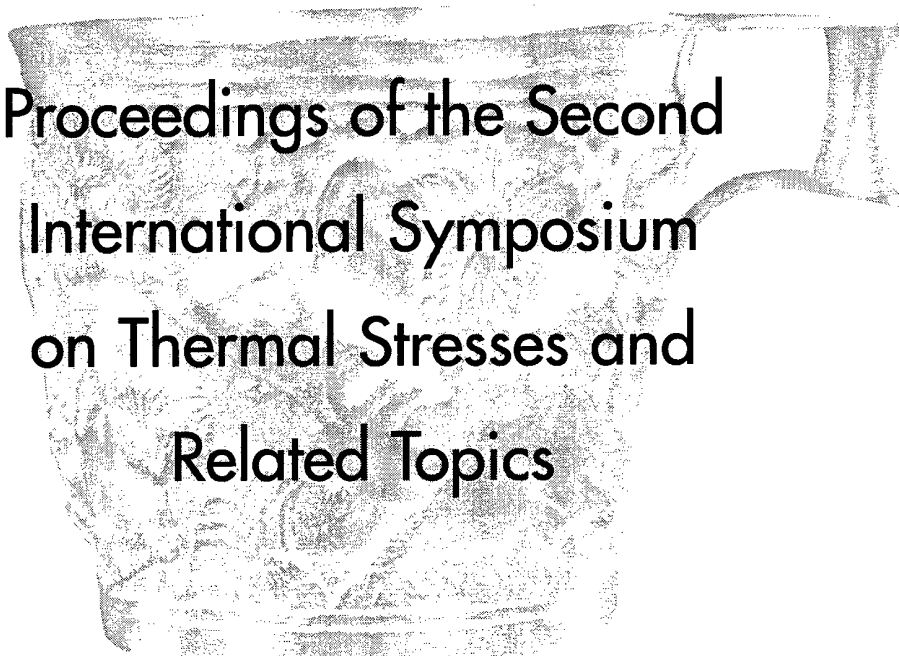


DTIC QUALITY INSPECTED

REPORT DOCUMENTATION PAGE			Form Approved OMB No. 0704-0188	
Public reporting burden for this collection of information is estimated to average 1 hour per response, including the time for reviewing instructions, searching existing data sources, gathering and maintaining the data needed, and completing and reviewing the collection of information. Send comments regarding this burden estimate or any other aspect of this collection of information, including suggestions for reducing this burden, to Washington Headquarters Services, Directorate for Information Operations and Reports, 1215 Jefferson Davis Highway, Suite 1204, Arlington, VA 22202-4302, and to the Office of Management and Budget, Paperwork Reduction Project (0704-0188), Washington, DC 20503.				
1. AGENCY USE ONLY (Leave blank)	2. REPORT DATE June 8-11, 1997	3. REPORT TYPE AND DATES COVERED Final Technical Report 1 Mar 97 - 31 Oct 97		
4. TITLE AND SUBTITLE Second International Symposium on Thermal Stresses and Related Topics Thermal Stresses 1997		5. FUNDING NUMBERS F49620-97-1-0174		
6. AUTHOR(S) Dr. Richard B. Hetnarski				
7. PERFORMING ORGANIZATION NAME(S) AND ADDRESS(ES) Rochester Institute of Technology 125 Tech Park Drive Rochester, NY 14623		8. PERFORMING ORGANIZATION REPORT NUMBER		
9. SPONSORING/MONITORING AGENCY NAME(S) AND ADDRESS(ES) AFOSR/NA 110 Duncan Avenue, Suite B115 Bolling AFB, DC 20332-8050		10. SPONSORING/MONITORING AGENCY REPORT NUMBER F49620-97-1-0174		
11. SUPPLEMENTARY NOTES				
12a. DISTRIBUTION AVAILABILITY STATEMENT Approved for public release; distribution unlimited.		12b. DISTRIBUTION CODE		
13. ABSTRACT (Maximum 200 words) The International conference brings together experts from across the world. It promises to advance the theoretical underpinnings of this important technological area, improve our collective ability to analyze stress in engineered systems, and advance our capability to design systems, structures, and products. The world has long depended on collaboration among members of the technical community. RIT values such international cooperation and is proud to play a role in the planning and implementation of this special symposium. The objective of Thermal Stresss '97 is to provided a forum for engineers and scientists engaged in industrial applications and basic research in the field of thermal stresses to exchange ideas and to extend further cooperation among the participants. The Thermal Stressses '97 enables engineers and researchers to meet at one place to present papers and conduct discussions. An extensive proceedings volume will be published. It will consist of 4-page extended abstracts of the papers submitted. The full text of papers will be published in "Journals on Mechanics", and in particular in the "Journal of Thermal Strcsses".				
14. SUBJECT TERMS			15. NUMBER OF PAGES 746	
			16. PRICE CODE	
17. SECURITY CLASSIFICATION OF REPORT Unclassified	18. SECURITY CLASSIFICATION OF THIS PAGE Unclassified	19. SECURITY CLASSIFICATION OF ABSTRACT Unclassified	20. LIMITATION OF ABSTRACT UL	

Thermal Stresses '97



Proceedings of the Second
International Symposium
on Thermal Stresses and
Related Topics



Rochester Institute of Technology
Rochester, New York, USA
June 8-11, 1997

19980615 052

R·I·T

Rochester Institute of Technology

Dean's Office
College of Engineering
James E. Gleason Building
77 Lomb Memorial Drive
Rochester, New York 14623-5603
716-475-2145 Fax 716-475-6879

June 1997

Dear Conference Participant:

I am pleased on behalf of the Rochester Institute of Technology to welcome you to *Thermal Stresses '97*.

This international conference brings together experts from across the world. It promises to advance the theoretical underpinnings of this important technological area, improve our collective ability to analyze stress in engineered systems, and advance our capability to design systems, structures, and products. I am pleased that you can bring your special expertise to bear on this subject.

The world has long depended on collaboration among members of the technical community. RIT values such international cooperation and is proud to play a role in the planning and implementation of this special symposium.

I hope this conference meets your expectations in all respects and that your stay here in Rochester will be personally and professionally rewarding. If any of us at RIT can help you in any way we would be pleased to do so.

Sincerely,



Paul E. Petersen
Dean, College of Engineering

RECENT INTERESTS IN THERMAL STRESSES

Thermal stress problems continue to attract the attention of a large international community of investigators. Based on a survey of 87 papers* published during 1996, a number of problem areas of major concern can be identified. One area of concentration, representing over one-fifth of the reviewed papers, involves thermo-mechanical behaviors of anisotropic and/or nonhomogeneous media. Among this group, 13 articles address problems associated with composite materials or structures, with 9 of this emphasizing response of laminated systems to various loads (e.g., thermal shock, combined mechanical and thermal loads, thermoelectric fields, etc.). Another area receiving considerable attention involves the potential utilization of advanced materials and "smart" structures for controlling thermal deformations; studies in this area have focused mainly on functionally graded media (6 articles) and piezoelectric ceramics (5). Thermally induced dynamic behaviors are investigated in 16 of the reviewed papers, with attention directed primarily at thermoelastic wave propagation (5), and free or forced vibrations (5) of beams, plates and shells. Other of the surveyed investigations treat: crack problems (8), including analysis of edge cracks in composite and functionally graded materials; stability problems (7) associated with thermal loading of beams, plates and shells; inelastic response (7), entailing viscoelastic, viscoplastic or elastic-plastic behaviors; development and application of numerical methods for thermal stress analysis, in particular, boundary element (4) and finite element techniques (3); thermoelastic contact problems (5); and experimental techniques (4) for determination of stress, damage or fracture, based upon thermoelastic data.

As evidence of the worldwide interest in thermal stresses, it is noted that of the nearly 50 articles published in the *Journal of Thermal Stresses* during 1996, the 82 contributing authors and co-authors represent 19 different countries, including: Bulgaria (2 authors), Egypt (2), France (3), Georgia (1), Germany (1), India (7), Iran (3), Italy (3), Japan (19), Korea (1), Kuwait (1), Poland (4), Romania (1), Russia (3), South Africa (1), Taiwan (7), Turkey (1), Ukraine (4), and United States (18).

T. R. Tauchert
Chair, National Organizing Committee

* Articles included in the survey were those appearing in Volume 19 of the *Journal of Thermal Stresses* plus those cited in the "Publications on Thermal Stresses" section of the journal.

A Note from the Principal Organizers of *Thermal Stresses '97*

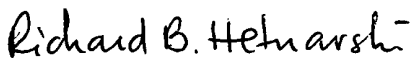
We take this opportunity to tell you, the Participants, that we have enjoyed working on the preparations leading to *Thermal Stresses '97*. After two years of effort we observe with amazement that the various pieces of the big jigsaw puzzle are starting to fall into place. Until very recently some of these pieces seemed to not fit well together. Now, with only a few weeks before the opening ceremony of *Thermal Stresses '97*, we are beginning to feel confident that things will work out. We hope that you will find our efforts worthwhile.

We express our thanks to Rochester Institute of Technology for allowing us to have *Thermal Stresses '97* on its campus. We thank various service departments of RIT for their friendly cooperation, especially the Catering Service, Resident Life, and the Physical Plant.

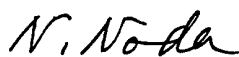
We express our appreciation to the School of Printing Management and Sciences, and in particular, we thank Professors Archibald D. Provan and Barbara Birkett for providing an excellent service for us, and to Keli McCreadie and Magda Knaflewska for taking great care in the design and printing of the Program, Proceedings Volume, and other materials.

Last but not least, we thank Mrs. Connie LaBarre, the secretary to Richard B. Hetnarski, for two years of dedicated hard work, often after hours and on weekends, on the preparations for *Thermal Stresses '97*.


We hope you will enjoy being a part of *Thermal Stresses '97*.



Richard B. Hetnarski
General Chair
James E. Gleason Professor of
Mechanical Engineering
Rochester Institute of Technology
Rochester, NY 14623, U.S.A



Naotake Noda
General Chair
Professor of Mechanical Engineering
Shizuoka University
Hamamatsu 432, Japan



Hany Ghoneim
Secretary
Associate Professor of
Mechanical Engineering
Rochester Institute of Technology
Rochester, NY 14623, U.S.A

General Chairs

R. B. Hetnarski (USA) and N. Noda (Japan)

Secretary

H. Ghoneim, Rochester Institute of Technology

Advisor General

B. A. Boley, Columbia University, USA

International Organizing Committee

Chairs

Y. Tanigawa, University of Osaka Prefecture, Japan

F. Ziegler, Technical University of Vienna, Austria

Members

J. Zarka, Ecole Polytechnique, France

G. England, Imperial College, United Kingdom

J. Ignaczak, Polish Academy of Sciences, Poland

Z. Mróz, Polish Academy of Sciences, Poland

T. Hata, Shizuoka University, Japan

K. Herrmann, University of Paderborn, Germany

J. Aboudi, Tel-Aviv University, Israel

R. Dhaliwal, University of Calgary, Canada

National Organizing Committee

Chairs

Carl Herakovich, University of Virginia

T. R. Tauchert, University of Kentucky

Members

G. Dvorak, Rensselaer Polytechnic Institute

V. Genberg, Eastman Kodak Company

G. R. Halford, NASA

D. Paul, U.S. Air Force Wright Lab

E. Suhir, Bell Laboratories

Program Committee

Chairs

Jim Barber, University of Michigan

Louis G. Hector, Jr., ALCOA

Members

K. Kokini, Purdue University

K. Tamma, University of Minnesota

L. Librescu, Virginia Polytech. Ins. & State University

Local Organizing Committee

Honorary Chairs

S. D. McKenzie, Provost and Vice President of
Academic Affairs, RIT

P. Petersen, Dean of the College of Engineering, RIT

Chairs

R. Budynas, J. Torok

Members

C. Haines, S. Kandlikar, S. Radziszowski, M. Scanlon,

L. Mikols, Joanne Mason, Mary Webster, Cynthia Gray

Sponsors

For their generous support, special thanks are extended to:

Wright Laboratory's

Flight Dynamics Directorate

Wright Patterson Air Force Base, OH

Air Force Office of Scientific Research

Bolling Air Force Base, Washington, DC

United States Air Force

European Office of Aerospace / Research and Development
London, U.K.

Department of the Air Force

Asian Office of Aerospace / Research and Development
Tokyo, Japan

* * *

The contributions of the following institutions are acknowledged:

Taylor & Francis, Publishers since 1798, Washington, DC

Local Organizing Committee, Thermal STresses, '95
Shizuoka University, Hamamatsu, Japan

Institute for Mechanics and Materials,
University of California, San Diego

Louis Skalny Foundation, Rochester, NY

Eastman Kodak Company, Rochester, NY

Gleason Foundation, Rochester, NY

U.S. Civilian Research & Development Foundation (CRDF)
Arlington, VA

The Kosciuszko Foundation, New York, NY

*Promoting Educational and Cultural Exchanges and Relations between the United States and
Poland since 1925*

Richard B. Hetnarski and Naotake Noda, General Chairs,
on behalf of the
International and National Organizing Committees
express thanks to

Dr. Albert J. Simone,

President of Rochester Institute of Technology,
for the support and interest shown to *Thermal Stresses '97*.

Special thanks are directed to

Dr. Stanley D. McKenzie,

Provost and Vice President for Academic Affairs,
Rochester Institute of Technology,
for the enthusiasm and assistance shown for the
organizational effort of *Thermal Stresses '97*.

Principal Lectures

Chairs:

Z. Sobotka

R.B. Hetnarski

N. Noda

Thermomechanics of Heterogeneous Media

George J. Dvorak

**Modeling of Thermal Cracking in Elastic and
Elastoplastic Solids**

K. P. Herrmann

**Thermal Stress-Focusing Effect Following Rapid
Uniform Heating of Spheres and Long Cylindrical Rods**

Toshiaki Hata

THERMOMECHANICS OF HETEROGENEOUS MEDIA

George J. DVORAK

*Center for Composite Materials and Structures and
Department of Mechanical Engineering, Aeronautical Engineering
and Mechanics
Rensselaer Polytechnic Institute, Troy, NY 12180*

Key Words: Composite Materials, Micromechanics, Thermomechanics, Graded Materials

1. Introduction

This lecture will survey some recently developed micromechanical modeling methods and certain results concerning the overall thermomechanical response, average local fields and heat conductivity of both elastic and inelastic composite materials, with either constant or variable volume fractions, and with extensions to polycrystals and laminated plates.

2. Thermoelastic composites and polycrystals

Initial connections between mechanical and thermal responses of heterogeneous media were established in the 1960s, primarily by Levin, who evaluated the overall strain due to a uniform change of temperature in a statistically homogeneous multiphase aggregate in terms of the overall and local elastic moduli, and thermal expansion coefficients and volume fractions of the phases. More recently, many other connections have been identified between the effects of mechanical loading and thermal changes in composite materials and laminates. Several such results were found using the method of uniform fields in heterogeneous media, which provides a class of exact solutions for local fields caused by certain overall loads and local eigenstrains. Superpositions of the uniform fields with those caused by other loading states offer interesting insights into the effect of thermal changes on the response of materials with complex microstructural geometry. For example, we will show that the local stress and strain fields due to a uniform change in temperature in a representative volume of a two-phase composite material can be related by exact connections to the respective fields caused by uniform mechanical loading. In certain multi-phase materials, such connections can be obtained for the averages of the thermal and mechanical fields. Another example will illustrate connections between thermal expansion and compliance coefficients of selected polycrystals, both in bonded and partially debonded configurations.

3. Elastic-plastic fibrous composites and laminates

Evaluation of the inelastic response of both metals and metal matrix composites and laminates relies, in part, on information about the initial yield surfaces and their motion in stress space during plastic loading. In heterogeneous solids, the overall yield surfaces are typically constructed using the local stresses and yield surfaces of the inelastic phases. Therefore, changes in the local fields induced by temperature variations may cause thermal hardening effects even in the absence of any local inelastic deformation. For fibrous metal matrix composites, the method of uniform fields predicts rigid body translation of the overall yield surface in stress space. Also, inelastic deformation of fibrous systems along a combined thermomechanical loading path is exactly simulated by purely mechanical loading along an equivalent path, in superposition with uniform local fields. This simplifies solution procedures and illuminates coupling between thermal and mechanical deformations in the fibrous systems.

4. Functionally graded materials

Thermomechanical modeling of composite materials with composition gradients often calls for solution of both heat conduction and thermoelasticity problems. Exclusive use of discrete models of the microstructure is not practical, hence homogenized models are required, such that provide accurate estimates of both the variable heat conductivities and thermoelastic moduli. Frequent concern is with nonlocal effects created by interactions of property and field gradients. Results of numerous comparative studies of local fields and overall response of both discrete and homogenized micromechanical models suggest that appropriate combinations of standard averaging techniques, which reflect the local microstructural arrangement, provide accurate homogenization procedures for graded material systems. The nonlocal effects are found to be significant only if local field gradients are large and field averages small, and may thus be neglected in most applications.

Modeling of thermal cracking in elastic and elastoplastic solids

K.P. Herrmann*), M. Dong**), and T. Hauck***)

*) Professor, Mechanical Engineering Department, University of Paderborn, Pohlweg 47-49, D-33098 Paderborn, Germany

**) Dr.-Ing., Staatliche Materialprüfungsanstalt, University of Stuttgart, Pfaffenwaldring 32, D-70569 Stuttgart, Germany

***) Dipl.-Ing., Motorola GmbH, Geschäftsbereich Halbleiter, AISL Europe, Schatzbogen 7, 81829 München

Key Words: Thermoelasticity, Thermoplasticity, Thermal Cracks, Dissimilar Material, Fracture Mechanical Parameters

1. Introduction

The study of thermal crack growth in multiphase materials is necessary for the assessment of the strength of composite structures because modern composite materials are often subjected to variable temperature fields. Furthermore, there exists experimental evidence for the appearance of different failure mechanisms in thermally loaded compounds, like curvilinear matrix and interface cracks, respectively, where these thermal cracks arise mostly under mixed-mode loading conditions. In this paper, a review is given about the fracture mechanical investigation of the thermal crack initiation and propagation in one of the segments or in the material interface of two- and three-dimensional self-stressed bimaterial structures.

2. Crack Path Prediction

The resulting boundary value problems of the stationary thermoelasticity and thermoplasticity for the cracked 2-D and 3-D two-phase compounds are solved by means of the finite element method. Moreover, by applying an appropriate crack growth criterion based on the numerical calculation of the total energy release rate of a quasistatic mixed-mode crack extension the further development of thermal crack paths starting at the intersection line of the material interface with the external stress-free surface of the 2-D and 3-D elastic bimaterials could be predicted. In case of the disk-like two-phase compounds the theoretically predicted crack paths show a very good agreement with results gained by associated cooling experiments. Several specimen geometries consisting of different material combinations and subjected to uniform as well as to non-uniform temperature distributions have been investigated by applying the relevant methods of fracture mechanics. As an important result could be stated that thermal cracks propagating in one segment of an elastic bimaterial only obey the rule $G_{II} = 0$, whereas for interface cracks a mixed-mode propagation is always existent where the G_{II} -values play an important role. Moreover, by applying the proposed crack growth criterion the possible crack

kinking direction ϑ^* of an interface crack tip out of the interface could be predicted under the consideration of the finite thickness of an interlayer (interphase). Furthermore, the influences of three-dimensional effects on the thermal crack propagation in axisymmetric two-phase composite structures have been studied by means of this crack growth criterion as well as by using the finite element method. The numerical results show some remarkable differences between 2-D and 3-D bimaterials concerning the thermal crack paths as well as the associated fracture mechanical parameters.

3. Local J-integral

Finally, an analysis of the stress and strain fields in the vicinity of thermal interface cracks in the discontinuity area of 2-D and 3-D elastoplastic two-phase compounds has been performed by using the FE-method. Moreover, a heat source $Q(x_i)$ was assumed in one of the two materials in the neighborhood of an interface crack tip. The resulting initial-boundary value problem of the instationary heat conduction equation has been solved by using the FE-method and under consideration of an appropriate semidiscretization procedure as well as by applying a Newtonian boundary condition for the heat transition from the specimen to the environment (temperature T_0) and an insulation condition concerning the interface crack surfaces. Furthermore, the corresponding stress states in the two-phase compounds and especially in the vicinity of an interface crack tip have been calculated by applying the incremental J_2 -plasticity as well as by using a bilinear hardening material law. Thereby the calculation of the stress states is based on a so-called sequentially coupled solution of the heat transfer and the thermal stress boundary value problem. The assessment in terms of failure is performed on the basis of the local J-integral which, for three-dimensional interface cracks, has recently been generalized by Herrmann and Hauck (1995) following the earlier work by Moran, Shih and Nakamura (1986,1987) and Nikishkov and Atluri (1987).

Thermal Stress-Focusing Effect Following Rapid Uniform Heating of Spheres and Long Cylindrical Rods

Toshiaki Hata*

*Faculty of Education, Shizuoka University, Shizuoka City, Shizuoka 422, JAPAN

Key Words: Thermoelasticity, Stress Waves, Thermal Shock, Cylinders, Spheres, Stress-Focusing, Ray Theory

1. Introduction

Stress waves, that develop following rapid uniform heating of linear-elastic spheres and long cylindrical rods, display a stress-focusing effect as they proceed radially towards the center in these geometries. The stress-focusing effect is the phenomenon that, under a rapid uniform heating, stress waves reflected from the free surface of the sphere or the cylindrical rod result in very high stresses at the center, even though the initial thermal stress should be relatively small. This phenomenon may be observed in the solid spheres subjected to the spherical symmetric heating and in the cylindrical rods subjected to the cylindrical symmetric heating.

The phenomenon of stress-focusing effect in a long cylindrical rod subjected to a sudden rise in temperature uniformly over its cross-section has been studied by Ho in 1976.

Consider a long cylindrical rod subjected to a sudden rise in temperature uniformly over its cross section. This type of temperature distribution may be developed by the absorption of infrared rays radiation or electromagnetic radiant energy from pulses that are typically of duration much less than 1 microsecond. Because the material is inertially restrained, the rapid heating results initially in a constrained thermal expansion and/or induced compressive thermoelastic stress in the rod. As the particles of the material begin to move, stress waves are created and propagate through the rod. Waves reflected from the cylindrical surface of the rod may accumulate at the center.

If the interest of the problem is in the maximum developed stresses due to the rapid heating of the rod, then the solution needs to be determined only for short elapsed time after the termination of heating, i.e., a time duration which is of the order b/c , where b and c are the radius of the rod and the elastic wave speed, respectively. For most materials, thermal diffusion time is much longer than b/c and so thermal conductivity can be neglected.

2. Subjects to be treated

This paper reviews recent extensions of the analytical methods for the problem of thermal shock in spheres and cylindrical rods, especially for the problem of thermal stress-focusing effect in spheres and cylindrical rods.

First, considering the problem of thermal shock in a hollow sphere subjected to the rapid uniform heating, if the ratio of the outer radius to the inner radius of the sphere increases, the peak tangential stress at the internal surface becomes higher and higher. As a limit case, for a solid sphere, it might be possible to observe the stress-focusing effect. Next, as for the analysis of a cylindrical rod due to the rapid uniform heating, stress waves also show the stress-focusing effect.

As for the analytical methods, the solutions are carried out by using Laplace transform on time. The inversion of Laplace transform is carried out by using the ray integrals in the case of the sphere, while by using the ray series in the case of the cylindrical rod. By using these methods, we show that the complicated Laplace transformed solutions of the problem lead to simple solutions.

Following the ray methods, we could obtain mathematically the order of singularity of the stresses in a cylindrical rod and a sphere subjected to the ramp heating, which is $O(\rho^{-2})$ for the cylindrical rod and $O(\rho^{-3})$ for the sphere. Furthermore, in order to clarify the strength of the stress-focusing effect, the stress focusing intensity factors can be defined.

As stated in the paper, many problems come out from the thermal stress-focusing effect. In the future the interaction between the cracks and the stress-focusing effect in a solid should be considered in the fracture mechanics.

Hence, the major accomplishment of this study is in gaining a better understanding of the thermal stress-focusing effect in the solid spheres, the cylindrical rods, and other geometries.

Session 1A

FRACTURE MECHANICS I

Chair: K. Kokini

Co-Chair: V.N. Hakobian

Thermomechanical Effects due to Rolling Contact On an Interface Crack Growth in a Surface of Layered Material

T. Goshima, T. Nishino, and T. Koizumi

Thermal Plastic Zone Size in an Infinite Solid with an External Axially Symmetric Crack

Janice S. Pawloski, Yu-Min Tsai

The Thermoelastic Problem of Uniform Heat Flow Disturbed by a Penny-Shaped Crack in a Finitely Deformed Incompressible Elastic Medium

Y. M. Tsai, Y. C. Shiah

Theoretical Analysis of Thermal Stress Intensity Factor for Nonhomogeneous Medium with a Penny-Shaped Crack

Sang-Pyo Jeon, Yoshinobu Tanigawa

Mixed Boundary Value Problem of Penny-Shaped Cut under Axially Symmetric Temperature Field

J. V. S. Krishna Rao, N. Hasebe

Thermomechanical Effects due to Rolling Contact on an Interface Crack Growth in a surface Layered Material

T. Goshima*, T. Nishino* and T. Koizumi**

* Faculty of Engineering, Toyama University, 3190, Gofuku, Toyama 930, JAPAN

** Faculty of Science and Engineering, Chuo University, 1-13-27 Kasuga, Bunkyo-ku, Tokyo 112, JAPAN

The two-dimensional interface crack problem in a surface coating layered material is considered under rolling/sliding contact with frictional heat generation. The interface crack is replaced by the distributed edge dislocations. The numerical results are given for some tribological material coatings on a steel substrate. The effects of the frictional coefficient, slide/roll ratio, the coating thickness and the crack length upon the stress intensity factors are considered numerically.

Key words: Elasticity, Thermal Stresses, Contact Problem, Coating Layered Material, Interface Crack

1. Introduction

The surface coating composite materials are more and more used to improve the mechanical and tribological behavior of surfaces in the industries. In most cases, rolling contacts are accompanied by frictional heat generation. Thermomechanical cracking can occur on the interface when they are subjected to the rolling/sliding contact. In recent years, a considerable effort has been devoted to thermomechanical contact problem in the various layered materials [1]-[2]. Most of these studies are not involved in the crack analysis. Therefore, one of the authors has dealt with a crack problem in a surface layered medium due to rolling contact [3]. However, this study do not involve in the interface crack analysis. In order to gain a better understanding for the conditions of fracture with debonding in layered materials due to rolling contact, the tribological and thermal effects due to rolling contact on the interface crack growth must be considered.

In this article, the two-dimensional interface crack problem in a surface coating layered material is considered under rolling/sliding contact with frictional heat generation. Attention here is focused on the stress intensity factors at the crack tips which provide the measure for quantifying the magnitude of crack growth. In this analysis, the crack is replaced by the distributed edge dislocations, and it is assumed that the crack face friction is neglected and that the temperature field is not disturbed by the crack with a large Peclet number. The problem is reduced to a pair of singular integral equations for dislocation densities. The singular integral equations can be solved numerically by considering the nature of the oscillatory singularities at the crack tips. The numerical results of the stress intensity factors are given for some tribological material coatings on a steel substrate. The effects of the frictional coefficient, slide/roll ratio, the coating thickness and the crack length upon the stress intensity factors are considered numerically.

2. Problem Formulation

Figure 1 shows the geometry and coordinate system for this study. The layered half-space is loaded by an arbitrarily distributed contact pressure $P_1(\tilde{x}_1)$ and tangential frictional load $fP_1(\tilde{x}_1)$ in the contact region. Where f is frictional coefficient. Then, the frictional heat generation $Q_1(\tilde{x}_1)$ is given as follows:

$$Q_1(\tilde{x}_1) = f V_s P_1(\tilde{x}_1) \quad (1)$$

Here V_s is the sliding velocity during rolling contact. In the analysis the following dimensionless quantities are used.

$$(x, y) = (\tilde{x}/c, \tilde{y}/c), (x_1, y_1) = (\tilde{x}_1/c, \tilde{y}_1/c), R_j = c V/a_j,$$

$$S_r = V_s/V, h = \tilde{h}/c, l = \tilde{l}/c, e = \tilde{e}/c, K = K_2/K_1,$$

$$G = G_2/G_1, P(x_1) = P_1(\tilde{x}_1)/P_0, \kappa_j = 3 - 4\nu_j$$

$$C_0 = 2G_2(1 - \alpha) / \{(\kappa_j + 1)(1 - \beta^2)\} \quad (2)$$

where a_j is thermal diffusivity, K_j is thermal conductivity, G_j is shear modulus, ν_j is the poisson's ratio, R_j is the Peclet number, S_r is the slide/roll ratio, P_0 is the maximum contact pressure and α, β are the Dundurs parameters [4]. The subscript $j=1, 2$ denote the coated and substrate regions respectively.

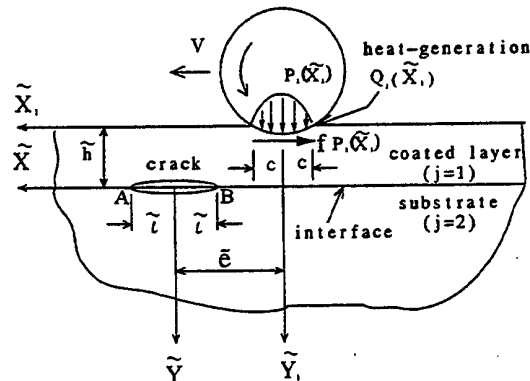


Fig.1 Problem configuration and coordinate system

The non-contact region is assumed to be thermally insulated, and the crack face friction is assumed to be neglected. Then, the thermal and mechanical boundary conditions can be given as:

$$\left(\frac{\partial T^{(1)}}{\partial y_1}\right) = \begin{cases} -f V S_r c P_0 P(x_1)/K_1, & |x_1| \leq 1, y_1=0 \\ 0, & |x_1| > 1, y_1=0 \end{cases} \quad (3)$$

$$\frac{\partial T^{(1)}}{\partial y_1} = K \frac{\partial T^{(2)}}{\partial y_1}, \quad y_1=h; \quad T^{(1)} = T^{(2)}, \quad y_1=h \quad (4); (5)$$

$$T^{(2)} = 0, \quad x_1^2 + y_1^2 \rightarrow \infty \quad (6)$$

$$\sigma_{yy}^{(1)} = \begin{cases} -P_0 P(x_1), & |x_1| \leq 1, y_1=0 \\ 0, & |x_1| > 1, y_1=0 \end{cases} \quad (7)$$

$$\sigma_{xy}^{(1)} = \begin{cases} -f P_0 P(x_1), & |x_1| \leq 1, y_1=0 \\ 0, & |x_1| > 1, y_1=0 \end{cases} \quad (8)$$

$$\sigma_{yy}^{(1)} = \sigma_{yy}^{(2)}, \quad y_1=h; \quad \sigma_{xy}^{(1)} = \sigma_{xy}^{(2)}, \quad y_1=h \quad (9); (10)$$

$$u_{yy}^{(1)} = u_{yy}^{(2)}, \quad y_1=h; \quad u_{xy}^{(1)} = u_{xy}^{(2)}, \quad y_1=h \quad (11); (12)$$

$$\sigma_{pq}^{(1)} = 0, \quad (p,q=x,y), \quad x_1^2 + y_1^2 \rightarrow \infty \quad (13)$$

$$\sigma_{xy}^{(1)} = 0, \quad y=0, \quad -l \leq x \leq l \quad (\text{on the crack face}) \quad (14)$$

$$\sigma_{xx}^{(1)} = 0, \quad y=0, \quad x \in x_{op} \quad (\text{on the crack face}) \quad (15)$$

$$u_{yy}^{(1)} = u_{yy}^{(2)}, \quad y=0, \quad x \in x_{cl} \quad (\text{on the crack face}) \quad (16)$$

where x_{op} and x_{cl} are the crack face opening and closing region, respectively.

3. Stress Analysis

Applying the Fourier transform to the quasi-stationary heat equation, the temperature solutions in the transformed space, which satisfies the boundary conditions Eqs.(3)-(6), can be obtained as follows [3].

$$\overline{T^{(j)}} = f c V S_r P_0 \overline{P(s)} F^{(j)}(s)/D_j, \quad (j=1, 2) \quad (17)$$

$$F^{(1)}(s) = \cosh(h-y_1)s_1 + K s_{12} \sinh(h-y_1)s_1$$

$$F^{(2)}(s) = \exp(h-y_1)s_2, \quad s_{12} = s_1/s_2, \quad s_j = (s^2 + i s R_j)^{1/2}$$

$$D_j = s_1 \sinh(hs_1) + K s_2 \cosh(hs_1), \quad i = \sqrt{-1}$$

where, s is the complex transform parameter.

The stress field $\sigma_{pq}^{(j)}$ in the cracked layered half-space subjected to the rolling-sliding contact is represented by superposition as follows.

$$\sigma_{pq}^{(j)} = \sigma_{pq}^{(0)} + \sigma_{pq}^{(1)} \quad (p,q=x,y), \quad (j=1,2) \quad (18)$$

Here, $\sigma_{pq}^{(0)}$ denote the thermal stresses in an uncracked layered half-space subjected to the rolling-sliding contact. The stresses $\sigma_{pq}^{(1)}$ denote the disturbance induced by the crack.

The thermal stresses in the Fourier transformed space due to the temperature field Eq.(17) are shown as:

$$\overline{\sigma_{xx}^{(0)}}/(2G) = -s^2 \overline{\phi_0^{(0)}} - s^2 y_1 \overline{\phi_3^{(0)}} - 2 y_1 \overline{\phi_3^{(0)}}' - \overline{\Omega^{(0)}}''$$

$$\overline{\sigma_{yy}^{(0)}}/(2G) = \overline{\phi_0^{(0)}}'' + y_1 \overline{\phi_3^{(0)}}'' - 2(1-\nu_j) \overline{\phi_3^{(0)}}' + s^2 \overline{\Omega^{(0)}}''$$

$$\overline{\sigma_{xy}^{(0)}}/(2G) = -is \{ \overline{\phi_0^{(0)}}' + y_1 \overline{\phi_3^{(0)}}' - (1-2\nu_j) \overline{\phi_3^{(0)}} + s^2 \overline{\Omega^{(0)}}' \} \quad (19)$$

where primes denote the differentiation with respect to y_1 . The stress functions and the thermoelastic potential in the transformed space are given as:

$$\overline{\phi_r^{(j)}} = C_r^{(j)} \exp(-sy_1) + (2-j) D_r^{(j)} \exp(sy_1) \quad (20)$$

$$\overline{\Omega^{(j)}} = \frac{(1+\nu_j) \alpha_j i}{(1-\nu_j) s R_j} \overline{T^{(j)}} \quad (r=0,3; j=1,2) \quad (21)$$

By applying the boundary conditions (7)-(12), the six coefficients $C_r^{(j)}$, $D_r^{(j)}$ can be solved from six algebraic equations. Consequently, the thermal stresses in an uncracked layered media, which satisfy the boundary conditions (7)-(13), are obtained by applying the inverse Fourier transform as

$$\sigma_{pq}^{(0)} = \frac{1}{\sqrt{2\pi}} \int_{-\infty}^{\infty} \overline{\sigma_{pq}^{(0)}} \exp(-isx_1) ds \quad (22)$$

To account for the disturbance $\sigma_{pq}^{(1)}$ by the crack, we consider the problem of a discrete edge dislocation b_x , b_y being at the interface ($x=\eta$) as shown in Fig.2. The induced stress field $\sigma_{pq}^{bx(1)}(x,y)$ and $\sigma_{pq}^{by(1)}(x,y)$ due to b_x and b_y , can be easily obtained. For example, the stresses at the interface are shown as:

$$\sigma_{xy}^{bx(1)}(x,0) = \frac{C_0 b_x}{\pi(x-\eta)}, \quad \sigma_{yy}^{bx(1)}(x,0) = -\beta C_0 b_x \delta(x-\eta) \quad (23)$$

$$\sigma_{yy}^{by(1)}(x,0) = \frac{C_0 b_y}{\pi(x-\eta)}, \quad \sigma_{xy}^{by(1)}(x,0) = \beta C_0 b_y \delta(x-\eta) \quad (24)$$

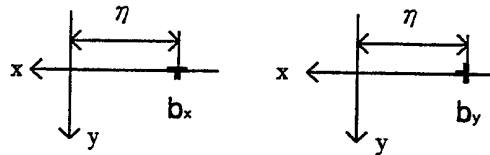


Fig.2. Geometry for the glide and climb dislocations (b_x and b_y) located at the interface

In order to remove the surface tractions and satisfy the boundary conditions Eqs.(9)-(13), additional stresses $\sigma_{pq}^{A(1)}$ must be considered. The stresses $\sigma_{pq}^{A(1)}$ can be obtained in the same manner as Eqs.(19)-(20) with $\Omega^{(0)}=0$. The unknown constants being equivalent to $C_r^{(1)}$, $D_r^{(1)}$ in Eq.(20) can be determined by solving algebraic equations to meet the boundary conditions Eqs.(9)-(13) and $\sigma_{yy}^{(1)} = \sigma_{xy}^{(1)} = 0$ on the surface ($y=0$).

Replacing b_x and b_y by distributed dislocation density $b_x(\eta)d\eta$ and $b_y(\eta)d\eta$ defined along the line of the crack, the stresses induced by the crack can be obtained by integration of η as follows.

$$\sigma_{pq}^{(i)} = \int_{-l}^l \{ \sigma_{pq}^{(i)}(x, y) + \sigma_{pq}^{(i)}(x, y) + \sigma_{pq}^{(i)} \} d\eta \quad (29)$$

Substituting Eqs.(22), (29) into Eq.(18) and the crack face boundary conditions Eqs.(14), (15), the following singular integral equations are obtained.

$$\beta \frac{C_0}{G_1} B_x(x) + \frac{C_0}{\pi G_1} \int_{-l}^l \frac{B_x(\eta)}{x-\eta} d\eta + \int_{-l}^l B_x(\eta) \Gamma_1(x, \eta) d\eta + \int_{-l}^l B_y(\eta) \Gamma_2(x, \eta) d\eta = - \left[\frac{\sigma_{xy}^{(i)}}{P_0} \right]_{y=0} \quad -l \leq x \leq l \quad (30)$$

$$-\beta \frac{C_0}{G_1} B_x(x) + \frac{C_0}{\pi G_1} \int_{-l}^l \frac{B_y(\eta)}{x-\eta} d\eta + \int_{-l}^l B_x(\eta) \Gamma_3(x, \eta) d\eta + \int_{-l}^l B_y(\eta) \Gamma_4(x, \eta) d\eta = - \left[\frac{\sigma_{xy}^{(i)}}{P_0} \right]_{y=0} \quad x \in x_{op} \quad (31)$$

where $B_x(\eta) = G_1 b_x / P_0$, $B_y(\eta) = G_1 b_y / P_0$ and the kernels $\Gamma_1, \Gamma_2, \Gamma_3, \Gamma_4$ are the functions of x and η . We must require in addition that the total Burgers vectors of the dislocations vanish, or that

$$\int_{-l}^l B_x(x) dx = 0, \quad -l \leq x \leq l \quad (32); \quad \int_{-l}^l B_y(x) dx = 0, \quad x \in x_{op} \quad (33)$$

as the conditions ensure that the displacements are single-valued.

4. Stress Intensity Factors

Replacing $\eta [-l, l]$ by $\zeta [-1, 1]$ ($\zeta = \eta / l$), $B_x(\eta)$ and $B_y(\eta)$ are written as

$$[B_x(\zeta), B_y(\zeta)] = \frac{[g_x(\zeta), g_y(\zeta)]}{(1-\zeta)^\gamma (1+\zeta)^\delta} \quad (34)$$

$$\gamma = \frac{1}{2} + i\omega, \quad \delta = \frac{1}{2} - i\omega, \quad \omega = \frac{1}{2\pi} \log \left(\frac{1+\beta}{1-\beta} \right) \quad (35)$$

Substituting Eq.(34) into Eqs.(30)-(33) and using the technique developed by Miller and Keer [5], the integral equations Eqs.(30)-(33) reduce to the simultaneous linear algebraic equations for g_x and g_y . In solving these equations, the region x_{op} or x_{cl} are determined by the iteration method under the condition of the absence of overlap of the materials at the interface. The boundary condition Eq.(16) can be satisfied by setting $g_y=0$ for the portion of $x \in x_{cl}$.

Defining the stress intensity factors by [6], K_I and K_{II} can be numerically determined as follows.

At the crack tip A,

$$[K_I, K_{II}] = P_0 C_0 \sqrt{cl(1-\beta^2)} [g_y(-1), g_x(-1)] / G_1 \quad (36)$$

At the crack tip B,

$$[K_I, K_{II}] = P_0 C_0 \sqrt{cl(1-\beta^2)} [g_y(1), -g_x(1)] / G_1 \quad (37)$$

5. Numerical Calculations

Numerical results were carried out for the case of some tribological material coatings on a steel substrate as Table 1. Contact pressure $P(x_1)$ was assumed to have a Parabolic distribution.

Table 1. Material properties

	Layer (j=1)				Substrate(j=2)
	Al ₂ O ₃	SiC	Si ₃ N ₄	Stellite III	Carbon steel
G _j (GPa)	158.5	142.0	117.6	93.4	80.0
ν_j	0.23	0.127	0.25	0.285	0.3
K _j (W/mK)	20.73	104.4	21.0	9.7	36.053
κ_j ($\mu\text{m}^2/\text{s}$)	4.99	49.0	0.98	2.77	9.72
α_j (μK^{-1})	7.19	5.01	2.6	11.3	10.0
β ($\times 10^{-3}$)	-59.27	7.648	-25.49	-12.81	

As the numerical results of stress intensity factors at the crack tip A were always larger than those at the crack tip B and K_I was very small compared to K_{II} , we show only the results of K_{II} at the crack tip A. In Figs.3, 4, the results of Al₂O₃ coating are plotted as functions of the crack location over a complete loading cycle showing the frictional and thermal (side/roll ratio) effects respectively.

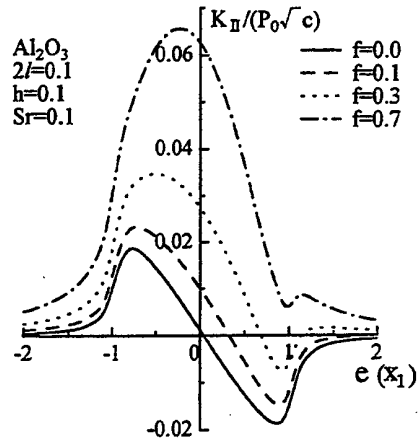


Fig.3 K_{II} as a function of e showing effects of f

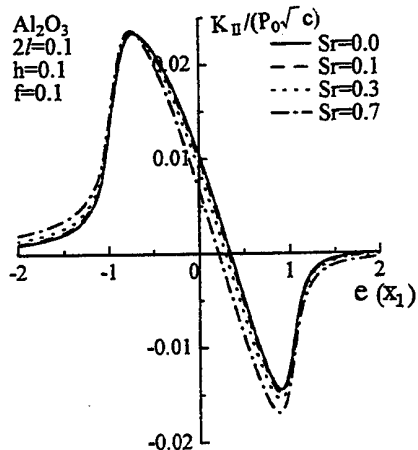


Fig.4 K_{II} as a function of e showing effects of S_r

The effects of frictional coefficient, slide/roll ratio, coating materials, layer thickness and crack length on the $\Delta K_{II} = (K_{II})_{max} - (K_{II})_{min}$ are shown in Figs.5-8.

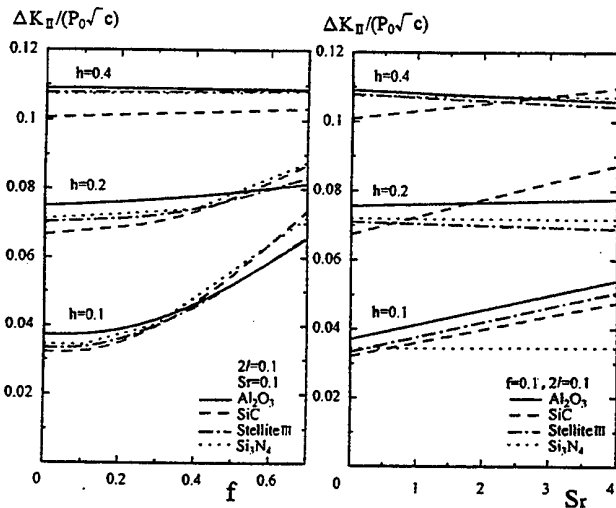


Fig.5 ΔK_{II} as a function of frictional coefficient f and slide/roll ratio Sr for various layer thickness

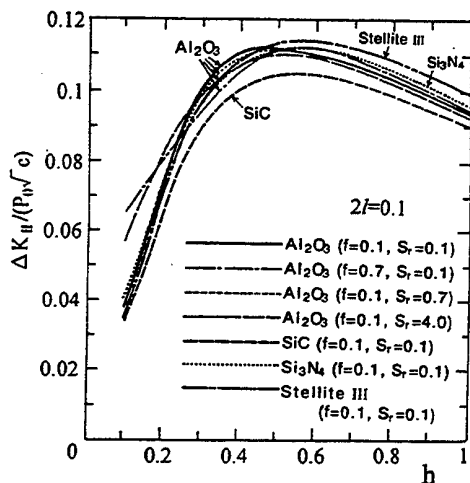


Fig.6 ΔK_{II} as a function of layer thickness

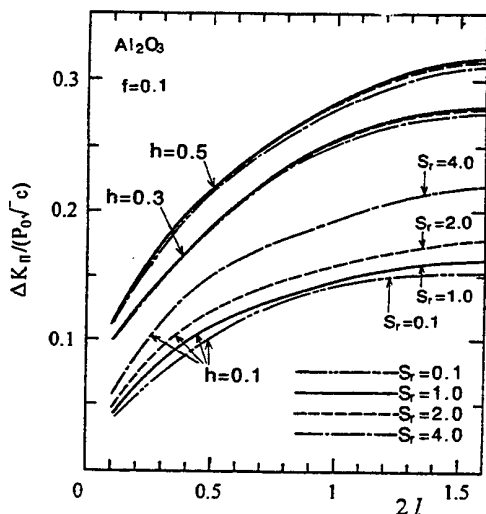


Fig.7 ΔK_{II} as a function of $2l$ showing effects of Sr

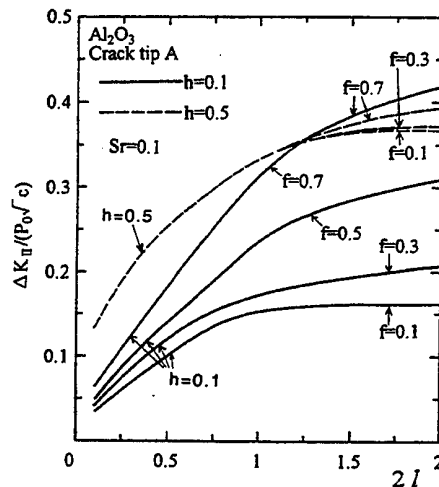


Fig.8 ΔK_{II} as a function of $2l$ showing effects of f

6. Conclusions

This work has analyzed the stress intensity factors K_{II} and ΔK_{II} for an interface crack in a surface layer bonded to a half-space under rolling-sliding contact loading. From numerical examples for some tribological material layers bonded to a steel substrate, thermomechanical effects on an interface crack growth were investigated. When f and Sr take small values, the value of ΔK_{II} for Al_2O_3 layer is larger than that for other material layers. As f and Sr increase, ΔK_{II} for SiC layer has the most remarkable thermomechanical effect. In the present numerical examples, the greatest value of ΔK_{II} occurs when $h=0.4\sim 0.6$. As the crack length increases, the values of ΔK_{II} increase. When f and Sr take small values, the increasing rate of ΔK_{II} decrease with an increase of crack length. However, especially for the case of thin layer, the increasing rate of ΔK_{II} is influenced significantly by the slide/roll ratio and frictional coefficient (thermomechanical effects).

References

- (1) Chen, T.Y. and Ju, F.D., Friction-Induced Thermo-Mechanical Cracking in a Coated Medium with a Near Surface Cavity, Trans. ASME J. Tribology Vol.111, p.270, 1989.
- (2) Chen, L. S. and Chu, H. S., Transient Thermal Stresses due to Periodic Moving Frictional Load in Layered Media, J. Thermal Stresses, Vol.12, p.169, 1989.
- (3) Goshima, T. and Takayama, H., Thermomechanical Cracking in a Surface Layered Medium due to Rolling Contact with Frictional Heating, Proc. the 1st Int. Sym. Therm. Stresses, p.67, 1995.
- (4) Dundurs, J., Discussion, Edge-Bonded Dissimilar Orthogonal Elastic Wedges Under Normal and Shear Loading, Trans. ASME J. Appl. Mech., Vol.36, p.650, 1967.
- (5) Miller, G.R. and Keer, L.M., Numerical Technique for the Solution of Singular Integral Equations of the Second Kind, Quart. J. Appl. Math., p.455, 1985.
- (6) Erdogan, F. and Gupta, G., The Stress Analysis of Multi-Layered Composite with a Flaw, Int. J. Solids Struct., Vol.7, p.39, 1971.

Thermal Plastic Zone Size In An Infinite Solid With An External Axially Symmetric Crack

Janice S. Pawloski and Yu-Min Tsai

*Department of Aerospace Engineering and Engineering Mechanics, Iowa State University
Ames, IA 50011, USA*

In this paper, an integral transform method is employed in order to determine the solution of the axially symmetric steady-state problem of an infinite linearly elastic, perfectly plastic solid with an external annular crack opened by an applied temperature over the crack surface. This problem is symmetric with respect to the plane of the crack. The Dugdale hypothesis is used to define the plastic zone. Two cases for the location of the plastic zone will be considered. The size of the plastic zone is determined by eliminating the singular stress at the beginning of the region of plastic behavior. The results for both cases are compared.

Key Words: Fracture, Thermal Stresses, Integral Transforms, Plastic Zone

1. Introduction

The problem of determining the axially symmetric thermal stress distribution in infinite bodies with annular cracks has been considered in several papers. The symmetric problem for a brittle material caused by applying a temperature to the crack surfaces is presented by Das⁽¹⁾. The anti-symmetric problem resulting from an applied heat flux on the crack surface is presented by Kassir⁽²⁾. The second paper also uses the hypothesis of Dugdale⁽³⁾ in determining the size of the plastic zone about the crack tip for an elastic-plastic material.

In this paper, an integral transform solution is employed to determine the temperature distribution, the normal stresses in the plane of the crack, and the displacement of the crack surface for an infinite elastic-plastic solid with an external crack opened by an applied temperature on the crack surface. Dugdale's hypothesis will also be used to determine the size of the plastic zone at the crack tip. It is assumed that a constant uniform tensile yield stress acts over an annular band near the crack tip. The singular stress at the beginning of the plastic region, and therefore the stress intensity factor, is in this case equal to zero.

2. Definition Of The Problem

Consider an infinite, isotropic elastic-plastic body containing a flat external crack. Cylindrical coordinates are used to describe the problem. Let r and z be the variables in the plane of the crack and perpendicular to the crack, respectively. The origin of this coordinate system lies in the plane of the crack

and at the centroid of the uncracked portion. Let d_s be the radial distance from the origin to the start of the plastic zone, d_T be the distance from the origin to the physical crack tip, and d_p be the distance from the origin to the end of the plastic zone. Two different cases will be considered:

Case One: The plastic zone starts at the physical crack tip, and extends over the crack surface. In this case, $d_s = d_T < d_p$. This is the same assumption used in the solution presented by Kassir⁽²⁾.

Case Two: The plastic zone exists over the uncracked portion of the solid, and ends at the physical crack tip. In this case, $d_s < d_T = d_p$.

Both mechanical and thermal loads are allowed to act along the crack surface. The conditions are symmetric with respect to the plane of the crack, so only the semi-infinite body, $z \geq 0$, will be considered. In addition, only conditions which are axially symmetric will be imposed, therefore variations with the angular coordinate θ can be neglected.

The temperature change from the stress-free state will be denoted by $T(r, z)$. The displacement vector $\bar{u}(r, z)$ has components u_r , u_θ , and u_z . The non-zero components of the stress tensor $\sigma(r, z)$ are σ_{rr} , $\sigma_{\theta\theta}$, σ_{zz} , and σ_{rz} . The symmetry of the temperature and stresses with respect to $z = 0$ gives rise to the following boundary conditions:

$$\frac{\partial T(r, 0)}{\partial z} = 0, \quad 0 < r < d_T, \quad (1)$$

$$u_z(r, 0) = 0, \quad 0 < r < d_s, \quad (2)$$

$$\sigma_{rz}(r, 0) = 0, \quad r > 0. \quad (3)$$

In addition, the crack face is subjected to a temperature and pressure distribution:

$$T(r, 0) = T_0 g(r), \quad r > d_T, \quad (4)$$

$$\sigma_{zz}(r, 0) = -p(r), \quad r > d_s. \quad (5)$$

3. The Heat Conduction Problem

In the linear theory of thermoelasticity, the temperature field can be determined independent of the stresses and displacements. For a steady-state conduction problem with no internal heat generation, the governing differential equation is simply Laplace's equation. The method of integral transforms leads to a general solution to this differential equation of the form

$$T(r, z) = \int_0^{\infty} A(\xi) e^{-\xi z} J_0(\xi r) d\xi. \quad (6)$$

Application of the boundary conditions found in Equations (1) and (4) leads to the following set of dual integral equations:

$$\int_0^{\infty} \xi A(\xi) J_0(\xi r) d\xi = 0, \quad 0 < r < d_T, \quad (7)$$

$$\int_0^{\infty} A(\xi) J_0(\xi r) d\xi = T_0 g(r), \quad r > d_T. \quad (8)$$

Equation (7) is identically satisfied if $A(\xi)$ has the form

$$A(\xi) = \int_{d_T}^{\infty} \tau(t) \sin(\xi t) dt. \quad (9)$$

Equation (8) can then be solved for the unknown function $\tau(t)$:

$$\tau(t) = -\frac{2T_0}{\pi} \frac{d}{dt} G(t). \quad (10)$$

where

$$G(t) \equiv \int_t^{\infty} \frac{\lambda g(\lambda) d\lambda}{\sqrt{\lambda^2 - t^2}}. \quad (11)$$

Once $\tau(t)$ has been determined, the temperature at any point can be found. In particular, in the plane of the crack over the uncracked portion,

$$T(r, 0) = -\frac{2T_0}{\pi} \int_{d_T}^{\infty} \frac{1}{\sqrt{t^2 - r^2}} \frac{dG(t)}{dt} dt, \quad r < d_T. \quad (12)$$

4. The Thermoelastic Problem

Once the temperature is known, the displacement field can be determined. The displacements are related to the change in temperature through the tensor expression

$$\text{div}(\text{grad } \bar{u}) + \frac{1}{1-2\nu} \text{grad}(\text{div } \bar{u}) = \frac{2(1+\nu)\alpha}{1-2\nu} \text{grad } T, \quad (13)$$

where α is the coefficient of thermal expansion and ν is Poisson's ratio. It is convenient to assume a displacement vector of the form

$$\bar{u} = \text{grad } \Phi + \bar{u}_1, \quad (14)$$

where Φ is called the thermoelastic displacement potential. Substituting Equation (14) into Equation (11) yields the decoupled set of equations:

$$\nabla^2 \Phi = \beta T, \quad (15)$$

where $\beta \equiv \frac{1+\nu}{1-\nu} \alpha$, and

$$\text{div}(\text{grad } \bar{u}_1) + \frac{1}{1-2\nu} \text{grad}(\text{div } \bar{u}_1) = 0. \quad (16)$$

A solution to Poisson's equation (15) gives an expression for the thermoelastic potential:

$$\Phi(r, z) = -\frac{\beta}{2} \int_0^{\infty} \xi^{-2} A(\xi) (1 + \xi z) e^{-\xi z} J_0(\xi r) d\xi. \quad (17)$$

A solution of the homogeneous equation (16) yields the following Airy stress function which satisfies the boundary condition of Equation (3):

$$\chi(r, z) = -2\mu \int_0^{\infty} \xi^{-3} C(\xi) (2\nu + \xi z) e^{-\xi z} J_0(\xi r) d\xi. \quad (18)$$

The non-zero displacements can be written in terms of these two functions:

$$u_r(r, z) = \frac{\partial \Phi}{\partial r} - \frac{1}{2\mu} \frac{\partial^2 \chi}{\partial r \partial z}, \quad (19)$$

$$u_z(r, z) = \frac{\partial \Phi}{\partial z} + \frac{1}{2\mu} \left(2(1-\nu) \nabla^2 \chi - \frac{\partial^2 \chi}{\partial z^2} \right). \quad (20)$$

The stress tensor can be found from the constitutive relation

$$\sigma = 2\mu \frac{\nu}{1-2\nu} (\text{div } \bar{u} - \frac{1+\nu}{\nu} \alpha T) \mathbf{I} + 2\mu \epsilon, \quad (21)$$

where μ is the shear modulus, \mathbf{I} is the unit tensor, and ϵ is the strain tensor, which is defined as the symmetric part of $\text{grad } \bar{u}$.

The dual integral equations for the thermoelastic problem are obtained by applying the boundary conditions of Equations (2) and (5):

$$\int_0^{\infty} \xi C(\xi) J_0(\xi r) d\xi = 0, \quad 0 < r < d_S, \quad (22)$$

$$\begin{aligned} \frac{\beta}{2} \int_0^{\infty} A(\xi) J_0(\xi r) d\xi + \int_0^{\infty} C(\xi) J_0(\xi r) d\xi \\ = \frac{1}{2\mu} p(r), \quad r > d_S. \end{aligned} \quad (23)$$

Equation (22) is identically satisfied if $C(\xi)$ has the form

$$C(\xi) = \xi \int_{d_S}^{\infty} F(t) \cos(\xi t) dt, \quad (24)$$

where

$$\lim_{t \rightarrow \infty} F(t) = 0. \quad (25)$$

Substituting Equations (9) and (24) into Equation (23) yields

$$\begin{aligned} \frac{\beta}{2} \int_{d_T}^{\infty} \tau(t) \int_0^{\infty} J_0(\xi r) \sin(\xi t) d\xi dt \\ - \int_{d_S}^{\infty} F'(t) \int_0^{\infty} J_0(\xi r) \sin(\xi t) d\xi dt \\ = \frac{1}{2\mu} p(r), \quad r > d_S. \end{aligned} \quad (26)$$

Equation (26) can be solved for the function $F(t)$.

Assuming that crack-tip blunting occurs at $r = d_p$, and that the crack tip opening displacement is equal to $u(d_p)$, consider the displacement of the crack outside the plastic zone. In terms of the function $F(t)$, the displacement is

$$u_z(r,0) = 2(1-\nu) \int_{d_s}^r \frac{F(t) dt}{\sqrt{r^2-t^2}}, \quad r > d_p. \quad (27)$$

The normal stress in the plane of the crack can also be expressed in terms of $F(t)$:

$$\sigma_{zz}(r,0) = 2\mu \int_{d_s}^{\infty} \frac{t F(t) dt}{(t^2-r^2)^{3/2}} - \beta\mu T(r,0), \quad r < d_s. \quad (28)$$

5. Solution Of Case One

If it is assumed that the physical crack tip coincides with the start of the plastic zone ($d_T = d_s$), then Equation (26) can be written as

$$\frac{\beta}{2} g(r) - \int_r^{\infty} F'(t) \frac{dt}{\sqrt{t^2-r^2}} = \frac{1}{2\mu} p(r), \quad r > d_s. \quad (29)$$

Assuming perfectly plastic behavior after yielding, uniform tension σ_0 exists throughout the plastic region. Let d_p locate the end of the plastic region, such that

$$p(r) = -\sigma_0 H(d_p - r), \quad r > d_s \quad (30)$$

where $H(d_p - r)$ is the Heaviside, or unit step, function. Using this assumption, equation (29) can be solved for $F(t)$:

$$F(t) = -\frac{\sigma_0}{\mu\pi} \sqrt{d_p^2 - t^2} H(d_p - t) - \frac{\beta}{\pi} G(t), \quad t > d_s. \quad (31)$$

For plastic deformation, the stress is no-where singular. Therefore, the stress intensity factor at the start of the plastic region should be zero. Assuming the location of the physical crack tip is known, the resulting equation can be solved for d_p , the end of the plastic region. The plastic zone width, non-dimensionalized with respect to the distance to the end of the plastic region, is given as

$$\omega_1 = \frac{d_p - d_s}{d_p} = 1 - \left[1 + \left(-\frac{\gamma G(d_s)}{d_s} \right)^2 \right]^{-1/2}, \quad (32)$$

where $\gamma \equiv \beta\mu T_0/\sigma_0$. Define the following terms:

$$\hat{u}_z(r,0) \equiv \frac{\mu}{(1-\nu)\sigma_0} \frac{u_z(r,0)}{d_p}, \quad (33)$$

and

$$\begin{aligned} \hat{u}_0(r) \equiv & -\frac{r}{d_p} \left[E\left(\frac{d_p}{r}\right) - E\left(\frac{d_p}{r}, \alpha_{sp}\right) \right] \\ & + \frac{(r^2 - d_p^2)}{r d_p} \left[K\left(\frac{d_p}{r}\right) - F\left(\frac{d_p}{r}, \alpha_{sp}\right) \right] \end{aligned} \quad (34)$$

where K and F are elliptic integrals of the first kind, E is an elliptic integral of the second kind, and $\alpha_{sp} \equiv \sin^{-1}(d_s/d_p)$. The crack displacement can be

expressed as

$$\hat{u}_z^{(1)}(r,0) = \frac{2}{\pi} \left\{ \hat{u}_0(r) - \frac{\gamma}{d_p} \int_{d_s}^r \frac{G(t) dt}{\sqrt{r^2-t^2}} \right\}, \quad r > d_p. \quad (35)$$

The normal stress in the plane of the crack reduces to

$$\frac{\sigma_{zz}^{(1)}(r,0)}{\sigma_0} = \frac{2}{\pi} \sin^{-1} \left(\frac{-\gamma G(d_s)}{\sqrt{d_p^2 - r^2}} \right), \quad r < d_s. \quad (36)$$

6. Solution Of Case Two

If the assumption is made that the plastic zone ends at the physical crack tip ($d_T = d_p$), Equation (26) can be written as

$$\frac{\beta}{2} \int_{d_T}^{\infty} \tau(t) \frac{dt}{\sqrt{t^2-r^2}} - \int_r^{\infty} F'(t) \frac{dt}{\sqrt{t^2-r^2}} = \frac{1}{2\mu} p(r), \quad d_s < r < d_p, \quad (37)$$

$$\frac{\beta T_0}{2} g(r) - \int_r^{\infty} F'(t) \frac{dt}{\sqrt{t^2-r^2}} = \frac{1}{2\mu} p(r), \quad r > d_p. \quad (38)$$

Let the prescribed stress assume the form given in Equation (30). Equations (37) and (38) then become

$$F(t) = -\frac{\sigma_0}{\mu\pi} \sqrt{d_p^2 - t^2} - \frac{\beta}{\pi} G(d_p), \quad d_s < t < d_p, \quad (39)$$

$$F(t) = -\frac{\beta}{\pi} G(t), \quad t > d_p. \quad (40)$$

Setting the stress intensity factor at the start of the plastic zone to zero, the width of the plastic zone, non-dimensionalized with respect to the distance to the end of the plastic region, is given as

$$\omega_2 = \frac{d_p - d_s}{d_p} = 1 - \sqrt{1 - \left(-\frac{\gamma G(d_p)}{d_p} \right)^2}. \quad (41)$$

The crack displacement can be expressed as

$$\begin{aligned} \hat{u}_z^{(2)}(r,0) = & \frac{2}{\pi} \left\{ \hat{u}_0(r) - \frac{\gamma}{d_p} (\alpha_p - \alpha_s) G(d_p) \right. \\ & \left. - \frac{\gamma}{d_p} \int_{d_p}^r \frac{G(t) dt}{\sqrt{r^2-t^2}} \right\}, \quad r > d_p, \end{aligned} \quad (42)$$

where $\alpha_p \equiv \sin^{-1}(d_p/r)$, and $\alpha_s \equiv \sin^{-1}(d_s/r)$. The normal stress in the plane of the crack reduces to

$$\frac{\sigma_{zz}^{(2)}(r,0)}{\sigma_0} = \frac{2}{\pi} \sin^{-1} \left(\frac{-\gamma G(d_p)}{\sqrt{d_p^2 - r^2}} \right), \quad r < d_s. \quad (43)$$

7. Some Specific Examples Of Prescribed Temperatures

7.1 INVERSE SQUARE OF THE DISTANCE

Assume that the temperature distribution over the physical crack surface is expressed as

$$g(\lambda) = -\frac{d_T^2}{\lambda^2}. \quad (44)$$

Then

$$G(d_T) = -\frac{\pi}{2}d_T, \quad (45)$$

and

$$\int_{d_T}^r \frac{G(t) dt}{\sqrt{r^2 - t^2}} = \frac{d_T^2}{r} \ln \left(\frac{r}{d_T} + \sqrt{\left(\frac{r}{d_T}\right)^2 - 1} \right). \quad (46)$$

The temperature distribution is

$$T(r,0) = -T_0 \left(\frac{d_T}{r} \right)^2 \left(1 - \sqrt{1 - \left(\frac{r}{d_T} \right)^2} \right), \quad r < d_T. \quad (47)$$

The width of the plastic zone for each case is given as

$$\omega_1 = 1 - 1/\sqrt{1 + \gamma^2 \frac{\pi^2}{4}} \quad (48)$$

and

$$\omega_2 = 1 - \sqrt{1 - \gamma^2 \frac{\pi^2}{4}}. \quad (49)$$

For small values of γ (less than 0.1), the values of ω for the two cases differ by less than 2.5 percent. However, as γ increases, the difference between the values of ω becomes more apparent.

The crack displacements and the normal stresses in the plane of the crack for each case can be found by substituting Equations (45) and (46) into Equations (35), (36), (42), and (43).

7.2 CONSTANT OVER AN ANNULAR REGION

An annular region of the crack face is maintained at a constant temperature below the reference state such that

$$g(\lambda) = -H(a - \lambda). \quad (50)$$

Then

$$G(d_T) = -\sqrt{a^2 - d_T^2}. \quad (51)$$

For $r < a$,

$$\int_{d_T}^r \frac{G(t) dt}{\sqrt{r^2 - t^2}} = -\frac{a}{d_T} \left[E\left(\frac{t}{a}\right) - E\left(\frac{t}{a}, \alpha_t\right) \right], \quad (52)$$

and for $r > a$,

$$\begin{aligned} \int_{d_T}^r \frac{G(t) dt}{\sqrt{r^2 - t^2}} &= -\frac{r}{d_T} \left[E\left(\frac{a}{r}\right) - E\left(\frac{a}{r}, \alpha_{ra}\right) \right] \\ &+ \frac{(r^2 - a^2)}{r d_T} \left[K\left(\frac{a}{r}\right) - F\left(\frac{a}{r}, \alpha_{ra}\right) \right]. \end{aligned} \quad (53)$$

The temperature distribution is

$$T(r,0) = -\frac{2}{\pi} T_0 \sin^{-1} \left(\frac{\sqrt{a^2 - d_T^2}}{\sqrt{a^2 - r^2}} \right), \quad r < d_T. \quad (54)$$

The width of the plastic zone for each case is given as

$$\omega_1 = 1 - 1/\sqrt{1 + \gamma^2 (\rho^2 - 1)} \quad (55)$$

and

$$\omega_2 = 1 - \sqrt{1 - \gamma^2 (\rho^2 - 1)}, \quad (56)$$

where $\rho \equiv a/d_T$. As expected, the wider the annular region of constant temperature, the wider the plastic region, and the more slowly the two solutions begin to differ.

The crack displacements and the normal stresses in the plane of the crack for each case can be found by substituting Equations (51), (52) and (53) into Equations (35), (36), (42), and (43).

7.3 EXPONENTIALLY DECAYING

The temperature difference decays exponentially from a maximum absolute value at the tip of the crack:

$$g(\lambda) = -e^{-c(\lambda - d_T)}, \quad (57)$$

where c is some constant. Then

$$G(d_T) = -e^{cd_T} d_T K_1(cd_T), \quad (58)$$

and the temperature distribution is

$$T(r,0) = -\frac{2}{\pi} T_0 e^{cd_T} \int_{d_T}^r \frac{ct K_0(ct) dt}{\sqrt{t^2 - r^2}}, \quad r < d_T, \quad (59)$$

where K_0 and K_1 are modified Bessel functions of the second kind. The width of the plastic zone for each case is given as

$$\omega_1 = 1 - 1/\sqrt{1 + \gamma^2 \left[e^{cd_T} K_1(cd_T) \right]^2} \quad (60)$$

and

$$\omega_2 = 1 - \sqrt{1 - \gamma^2 \left[e^{cd_T} K_1(cd_T) \right]^2}. \quad (61)$$

The slower the rate of temperature decay, the wider the plastic region, as is expected, and the more slowly the two solutions begin to differ.

The crack displacements and the normal stresses in the plane of the crack for each case can be found by substituting Equation (58) into Equations (35), (36), (42), and (43).

References

- (1) Das, B. R., Some axially symmetric thermal stress distributions in elastic solids containing cracks - I, an external crack in an infinite solid, *International Journal of Engineering Science*, Vol. 9, p 469-478, 1971.
- (2) Kassir, M. K., Size of thermal plastic zones around external cracks, *International Journal of Fracture Mechanics*, Vol. 5, No 3, p 167-177, 1969.
- (3) Dugdale, D. S., Yielding of steel sheets containing slits, *J. Mech. Phys. Solids*, Vol. 8, p 100-104, 1960.

The Thermoelastic Problem of Uniform Heat Flow Disturbed by a Penny-Shaped Crack in a Finitely Deformed Incompressible Elastic Medium

Y.M. Tsai and Y.C. Shiah

*Aerospace Engineering and Engineering Mechanics
Iowa State University
Ames, Iowa 50011*

The effect that the lateral normal stresses has on the thermal stresses for a penny-shaped crack is investigated on the basis of the theory of small deformations superposed on finite deformation. An infinite homogeneous incompressible isotropic elastic solid is initially subjected to an axisymmetrical tension of any amount at infinity. The deformation which is produced by a uniform heat flow disturbed by a penny-shaped crack is then superposed and characterized by a small displacement field. The equations of equilibrium are derived in terms of the temperature gradient and the lateral normal stress.

Using the techniques of Hankel transforms and multiple integrations, the thermal stresses and displacements in the crack plane are obtained in closed forms. The mode-II stress intensity factor is shown to be dependent upon the lateral normal stress. Both the superposed vertical displacement and the shear stress are symmetrical with respect to the crack plane. The superposed radial displacement and all the normal stresses are shown to be antisymmetrical with respect to the crack plane.

Key Words: Thermal stress, heat flow, finitely deformed medium, penny-shaped crack, mode-II fracture

1. Introduction

The final deformed state of a material body can often be reached by the composition of two deformations: an initial finite deformation and a superimposed infinitesimal deformation [1]. The stress distribution for a penny-shaped crack in an infinite elastic solid under infinitesimal deformation depends upon the tension normal to the crack plane, but is independent of the normal uniform stresses parallel to the crack plane. In the present work, the effect that the lateral normal stresses has on the thermal stresses for a penny-shaped crack is investigated on the basis of the theory of small deformations superposed on finite deformation [1, 2]. An infinite homogeneous isotropic elastic solid is initially subjected to an axisymmetrical tension of any amount at infinity. The deformation which is produced by a uniform heat flow disturbed by a penny-shaped crack is characterized by a small displacement field [3]. The equations of equilibrium are derived in terms of the temperature gradients and the lateral normal stress.

The current thermoelastic problem involves a system of three inhomogeneous partial differential equations

which are solved using the techniques of Hankel transforms. Superposed thermal stresses and displacements are solved and presented in closed forms.

2. Equations of equilibrium

An infinite homogeneous isotropic elastic solid is initially subjected to an axisymmetrical tension of any amount at infinity. The finite radial and axial stretches are denoted by μ and λ , respectively. The metric tensors and the strain invariants are calculated using cylindrical coordinates ($\theta_1=r$; $\theta_2=\theta$; $\theta_3=z$). In order to obtain explicit and closed-form solutions in later calculations, the material is assumed to be incompressible. Under this assumption, the non-vanishing components of the contravariant stress tensors have the following form [1, 2].

$$\tau^{11} = r^2 \tau^{22} = (\mu^2 - \lambda^2)(\Phi + \mu^2 \Psi) \quad (1)$$

$$\Phi = 2 \frac{\partial W}{\partial I_1}; \Psi = 2 \frac{\partial W}{\partial I_2} \quad (2)$$

and the strain energy function $W(I_1, I_2)$ is a function of the strain invariants I_1 and I_2 . The third strain invariant is equal to unity, i.e., $I_3 = 1 = \lambda^2 \mu^4$. The scalar pressure P is related to the derivatives of W as follows:

$$P = -\lambda^2 [\Phi + 2\mu^2 \Psi] \quad (3)$$

The above expression is obtained from the condition $\tau^{33} = 0$.

An infinitesimal thermoelastic displacement field is now superposed on the finitely deformed body. The temperature field considered is axisymmetrical with respect to the z -axis. Therefore, the associated thermoelastic problem has axisymmetrical deformations which can be characterized by the displacement components (u, v, w) . The actual strains are related to the derivatives of the displacement components. For a temperature change of θ , the normal thermal strain is equal to $\alpha_t \theta$ where α_t is the coefficient of linear thermal expansion. The superposed stress tensor τ'^{ij} are related to both the actual strains and the normal thermal strains. Following the procedures for obtaining the superposed stress tensor in [1, 2], the thermal strains are incorporated into the current stress tensor components as follows:

$$\tau'^{11} = \alpha_1 \left(\frac{\partial w}{\partial z} - \alpha_t \theta \right) + \alpha_2 \left(\frac{u}{r} - \alpha_t \theta \right) + p' \quad (4)$$

$$r^2 \tau'^{22} = \alpha_1 \left(\frac{\partial w}{\partial z} - \alpha_t \theta \right) + \alpha_2 \left(\frac{\partial u}{\partial r} - \alpha_t \theta \right) + p' \quad (5)$$

$$\tau'^{33} = \alpha_3 \left(\frac{\partial w}{\partial z} - \alpha_t \theta \right) + p' \quad (6)$$

$$\tau'^{13} = \alpha_4 \left(\frac{\partial w}{\partial z} + \frac{\partial w}{\partial r} \right), \tau'^{12} = \tau'^{23} = 0 \quad (7)$$

$$\alpha_2 = 2 \left[(\mu^4 - \mu^{-2}) \Psi - \mu^{-4} (\Phi + \mu^2 \Psi) \right] \quad (8)$$

$$\alpha_4 = \mu^{-4} (\Phi + \mu^2 \Psi) \quad (9)$$

$$\alpha_1 = 2 \left[(\mu^{-2} - \mu^4) A + (1 - \mu^{-6} - 2\mu^6) F + (\mu^{-4} - \mu^8) B - \mu^{-4} (\Phi + \mu^2 \Psi) \right] \quad (10)$$

$$\alpha_3 = 2\mu^{-4} \left[(1 - \mu^6) (\mu^{-4} A + 2B + 3\mu^{-2} F) + \Phi + \mu^2 \Psi \right] \quad (11)$$

$$A = 2 \frac{\partial^2 W}{\partial I_1^2}, B = 2 \frac{\partial^2 W}{\partial I_2^2}, F = 2 \frac{\partial^2 W}{\partial I_1 \partial I_2} \quad (12)$$

In terms of the expressions for τ'^{ij} in Eqs. (4)-(7), the equations of equilibrium in the absence of body forces

for the superposed field are obtained [1, 2] in the following forms:

$$\alpha_4 \frac{\partial^2 u}{\partial z^2} + (\alpha_1 + \alpha_4 - \tau^{11}) \frac{\partial^2 w}{\partial r \partial z} + \frac{\partial p'}{\partial r} - \beta_1 \frac{\partial \theta}{\partial r} = 0 \quad (13)$$

$$(\alpha_4 + \tau^{11}) \frac{\partial}{\partial r} \left(r \frac{\partial w}{\partial r} \right) + (\alpha_3 - \alpha_4) \frac{\partial^2 w}{\partial z^2} + \frac{\partial p'}{\partial z} - \beta_2 \frac{\partial \theta}{\partial z} = 0 \quad (14)$$

$$\beta_1 = (\alpha_1 + \alpha_2 - 3\tau^{11}) \alpha_t \quad (15)$$

$$\beta_2 = (\alpha_3 - 3\alpha_4 - 2\tau^{11}) \alpha_t \quad (16)$$

The condition of incompressibility has the following form:

$$\frac{1}{r} \frac{\partial}{\partial r} (ru) + \frac{\partial w}{\partial z} - 3\alpha_t \theta = 0 \quad (17)$$

3. Temperature field and formal solution

A penny-shaped crack with a radius a is assumed to be located in the interior of the medium. The z -axis is normal to the crack surface. The origin of the coordinate is located at the center of the crack. There is a uniform steady heat flow in the direction of the negative z -axis. The heat flow has a uniform temperature gradient ϵ . The disturbance due to the crack results in a temperature modification $\theta(r, z)$ of the original field. The surfaces of the crack are thermally insulated. The thermal boundary condition at $z=0$ can be written as [3].

$$\frac{\partial \theta}{\partial z} = -\epsilon, r \leq a; \theta = 0, r > a \quad (18)$$

The steady-state temperature field is governed by a Laplace equation. The thermal boundary value problem is solved by using the zeroth order Hankel transform. The transformed solution obtained can be written as:

$$\hat{\theta}^0 = C s e^{-sz}, Cs = \int_0^a Q \lambda J_0(\lambda s) d\lambda \quad (19)$$

Where the temperature field on the crack surface is:

$$Q = 2\epsilon(a^2 - r^2)^{1/2} / \pi, r \leq a \quad (20)$$

The disturbance temperature field produces thermal loadings. The thermoelastic boundary conditions at $z=0$ can be written as [2, 3]:

$$\tau'^{33} = 0 \text{ for all } r, u = \begin{cases} \phi(r), 0 \leq r \leq a \\ 0, a < r \end{cases} \quad (21)$$

To solve the system of three field equations and to satisfy the above boundary conditions, the first order Hankel transform is applied over Eq. (11), and the zeroth-order Hankel transform is applied over both Eq. (12) and (13). The transformed equations form a system of three inhomogeneous partial differential equations in terms of the transformed temperature field $\hat{\theta}^0$ in Eq. (17) as follows:

$$\alpha_4 \frac{\partial^2 \hat{u}^1}{\partial z^2} + \mu^6 \alpha_4 s \frac{\partial \hat{w}^0}{\partial z} - s \hat{p}'^0 = -\beta_1 s \hat{\theta}^0 \quad (22)$$

$$-\mu^6 \alpha_4 s^2 \hat{w}^0 + \alpha_4 \frac{\partial^2 \hat{w}^0}{\partial z^2} + \frac{\partial \hat{p}'^0}{\partial z} = \beta_2 \frac{\partial \hat{\theta}^0}{\partial z} \quad (23)$$

$$s \hat{u}^1 + \frac{\partial \hat{w}^0}{\partial z} = -3\alpha_t \hat{\theta}^0 \quad (24)$$

In the above expressions, the strain energy function is assumed to be of the Mooney type [1, 2] in order to have specific roots of the characteristics equation which is involved in obtaining the homogeneous solution of Eqs (22)-(24). The particular and homogeneous solutions of the three transformed equations are obtained and combined into the general solution with unknown constants which are determined by satisfying the boundary equations in Eq. (21). The formal solution obtained can be written in the following forms:

$$\hat{w}^0 = B_1 e^{-sz} + B_2 e^{-\mu^3 sz} + dz \hat{\theta}^0 \quad (25)$$

$$\hat{u}^1 = B_1 e^{-sz} + \mu^3 B_2 e^{-\mu^3 sz} + [3\alpha_t + d(sz-1)] \hat{\theta}^0 / s \quad (26)$$

$$\hat{p}'^0 = (1 - \mu^6) \alpha_4 s B_1 e^{-sz} + [(\mu^6 - 3) d + \beta_1 / \alpha_4 + 3\alpha_t + (1 - \mu^6) dsz] \alpha_4 \hat{\theta}^0 \quad (27)$$

$$d = [(\beta_2 - \beta_1) / \alpha_4 - 3\alpha_t] / 2(\mu^6 - 1) \quad (28)$$

$$(1 - \mu^6) \alpha_4 B_1 = \alpha_3 \hat{\phi}^1 - \{2\alpha_3 \alpha_t + [(\mu^6 - 3) d + \beta_1 / \alpha_4 + 3\alpha_t] \alpha_4\} C \quad (29)$$

$$\mu^3 B_2 = \hat{\phi}^1 - B_1 - (3\alpha_t - d) C \quad (30)$$

$$\hat{\phi}^1 = \int_0^a \lambda \phi(\lambda) J_1(\lambda s) d\lambda \quad (31)$$

4. Thermal stress and displacement

The superposed shear stress must be vanishing on the crack surfaces. To satisfy this condition, the first order Hankel transform is applied over the shear stress in Eq. (7). The transformed stress is then calculated in

terms of the transformed displacements. The Hankel inversion of the result at $z=0$ is:

$$\tau'^{13} = -KI_1 + MI_2 \quad (32)$$

$$I_1 = \int_0^\infty s^2 J_1(sr) \int_0^a \lambda \phi(\lambda s) J_1(\lambda s) d\lambda ds \quad (32)$$

$$I_2 = \int_0^\infty Cs^2 J_1(sr) ds \quad (33)$$

$$K = -\alpha_4(\mu^9 + \mu^6 + 3\mu^3 - 1) / \mu^3(\mu^3 + 1) \quad (34)$$

$$M = \left[\alpha_4(3\mu^{12} + 3\mu^9 + 7\mu^6 + 3\mu^3 - 2) - (\tau^{11} - \alpha_2) \right] \alpha \mu^{-3} (\mu^3 + 1)^{-2} \quad (35)$$

The shear stress vanishes for $r \leq a$. Under this condition, Eq. (32) becomes an integral equation, from which the crack shape function is solved [3] as follows:

$$\phi = 2M\epsilon r(a^2 - r^2)^{1/2} / 3\pi K \quad (36)$$

For $r > a$ at $z=0$, the shear stress has the following form [3]:

$$\tau'^{13} = 2M\epsilon a^3(r^2 - a^2)^{-1/2} / (3\pi r) \quad (37)$$

The other superposed stress components at $z=0$ are also calculated using the similar procedures the results are as follows:

$$\tau'^{11} = -(\alpha_1 + \alpha_2) \alpha_t \theta + \alpha_2 I_5 \quad (38)$$

$$+ \alpha_t(3\alpha_1 - 2\alpha_3) I_6 + (\alpha_3 - \alpha_1) I_7 \quad (39)$$

$$r^2 \tau'^{22} = -(\alpha_1 + \alpha_2) \alpha_t \theta - \alpha_2 I_5 + \alpha_t(3\alpha_1 - 2\alpha_3) I_6 + (\alpha_2 + \alpha_3 - \alpha_1) I_7 \quad (40)$$

where for $r < a$

$$I_5 = (a^2 - r^2)^{1/2} G, G = 2M\epsilon / 3\pi K \quad (41)$$

$$I_6 = 2\epsilon(a^2 - r^2)^{1/2} / \pi \quad (42)$$

$$I_7 = [2(a^2 - r^2)^{1/2} - r^2(a^2 - r^2)^{-1/2}] G \quad (43)$$

These three quantities vanish for $r > a$. From the shear stress in Eq. (37), the mode-II stress intensity factor is $K_{II} = 2\epsilon Ma^{3/2} / 3\pi^{1/2}$. The quantity M is a function of the lateral normal stress.

The superposed normal displacement at $z=0$ is obtained in the following form:

$$w = (K_2 I_3 + M_2 I_4) / \mu^3 (1 + \mu^3) \quad (44)$$

$$K_2 = 1 + \mu^3 - \alpha_3 / \alpha_4 \quad (45)$$

$$M_2 = \alpha_t(3 + 2\alpha_3 / \alpha_4) + (\mu^6 - 3)d + \beta_1 / \alpha_4 \quad (46)$$

The quantities I_3 and I_4 have two different expressions. For $r \leq a$

$$I_3 = G\pi(a^2 - 3r^2 / 2) / 4, \quad (47)$$

$$I_4 = \varepsilon(a^2 - r^2 / 2)2 \quad (48)$$

In the range outside the crack tip, i.e., $r > a$,

$$I_3 = 3G \left[a(r^2 - a^2)^{1/2} + (2a^3/3 - r^2) \sin^{-1}(a/r) \right] / 4 \quad (49)$$

$$I_4 = \varepsilon \left[a(r^2 - a^2)^{1/2} + (2a^2 - r^2) \sin^{-1}(a/r) \right] / 2\pi \quad (50)$$

The quantities τ'^{13} and w are symmetrical with respect to the plane $z=0$. However, the other four quantities τ'^{33} , τ'^{11} , $r^2\tau'^{22}$ and u are antisymmetrical with respect to the midplane $z=0$, and vanishing outside the crack surface on the crack plane.

References

- (1) Green, A.E. and Zerna, W., Theoretical elasticity, Clarendon Press, Oxford, 1968.
- (2) Tsai, Y.M., Initiation and propagation of a penny-shaped crack in a finitely deformed incompressible elastic medium, Engr. Frac. Mech. Vol. 14, pg. 627, 1981.
- (3) Tsai, Y.M., Transversely isotropic thermoelastic problem of uniform heat flow disturbed by a penny-shaped crack. J. Thermal Stresses, Vol. 6, pg. 379, 1983.

Theoretical Analysis of Thermal Stress Intensity Factor for Nonhomogeneous Medium with a Penny-Shaped Crack

Sang-Pyo Jeon* and Yoshinobu Tanigawa**

* Graduate Student, Osaka Prefecture University, 1-1, Gakuencho, Sakai, Osaka 593, JAPAN.

** Department of Mechanical Systems Engineering, Osaka Prefecture University.

In this study, an axisymmetrical thermoelastic singular stress problems for a nonhomogeneous medium is treated theoretically. It is assumed that the nonhomogeneous material properties of shear modulus of elasticity G , the coefficient of linear thermal expansion α , thermal conductivity λ vary with the axial coordinate z according to the power product forms, the material property of which has already proposed by Kassir. As an analytical model, a nonhomogeneous infinite body with a penny-shaped crack subject to axisymmetrical heat supply from the crack surface is considered. Distributions of displacements and stresses are analyzed using the fundamental equations system proposed in our previous paper and thereafter thermal stress intensity factor at the crack tip is evaluated theoretically. Numerical calculations are carried out for several cases taken into account the variety of nonhomogeneity of G , α and λ . The influence of these nonhomogeneous material constants affected on the thermal stress distribution and the thermal stress intensity factor is discussed.

Key Words: Thermal Stress Intensity Factor, Nonhomogeneous Medium, Axisymmetrical Problem, Crack Problem, Thermoelasticity.

1. Introduction

In recent years, among numerous advanced composite materials, nonhomogeneous materials such as Functionally Graded Materials have received considerable attention in the field of structural design subject to extremely high thermal loading. The material constants for such nonhomogeneous materials are described by an arbitrary function of the coordinate system. Therefore, the governing equations for the temperature field and the associated thermoelastic field become of nonlinear form in general case, thus, the theoretical treatment is very difficult and the exact solutions for both the temperature and thermoelastic fields are almost impossible to obtain.

However, under the assumption that the material property of shear modulus of elasticity G is given in the arbitrary power of an expression containing the variable of the axial coordinate z , the axisymmetric isothermal problems subject to mechanical loading for such nonhomogeneous materials have already developed by M.K.Kassir⁽¹⁾. And the analytical developments of thermoelastic problems for such nonhomogeneous body have been discussed by T.Hata⁽²⁾⁽³⁾. However, it can be seen from our verification that the analytical treatment could not be adaptable to the thermal stress problems with mechanical boundary conditions of being traction free.

Then, in our previous paper⁽⁴⁾, we have reconsidered the thermoelastic problems for such a nonhomogeneous body, and have reconstructed the fundamental equations system when the thermal

loading is acted.

In this study, making use of the fundamental equations system proposed in our previous paper, an axisymmetrical thermoelastic problem of singular stress field is treated, and the thermal stress intensity factor at the crack tip is evaluated theoretically. As an analytical model, we consider an infinite body with a penny-shaped crack subject to an axisymmetrical heat supply from the crack surfaces. Numerical calculations are carried out for several cases taken into account the variety of nonhomogeneity of shear modulus of elasticity G , the coefficient of linear thermal expansion α and the thermal conductivity λ .

2. Fundamental relations

Axisymmetrical isothermal elastic problems for the above-mentioned nonhomogeneous body have already discussed by Kassir, and the assumption is introduced for shear modulus of elasticity G and Poisson's ratio ν , which is given by

$$G(z) = G_0 \left(\frac{|z|}{a} + 1 \right)^m, \quad \nu = \text{const.} \quad (1)$$

where G_0 and m are the arbitrary constants, a is a typical length defined subsequently.

Now, the displacement components u and w in the radial and axial directions are defined by the following relations.

$$u = (z + a) \frac{\partial f}{\partial r}, \quad w = (z + a) \frac{\partial f}{\partial r} - f \quad (2)$$

Then, the fundamental equation for the displacement

function f can be derived from the equilibrium equations in the radial and axial directions, which is given by

$$\nabla^2 f + \frac{m}{z+a} \frac{\partial f}{\partial z} = 0 \quad (3)$$

$$\nabla^2 = \frac{1}{r} \frac{\partial}{\partial r} \left(r \frac{\partial}{\partial r} \right) + \frac{\partial^2}{\partial z^2} \quad (4)$$

Here, the following condition between ν and m is introduced.

$$\nu = \frac{1}{m+2}; \quad 0 < \nu < \frac{1}{2}; \quad 0 < m < \infty \quad (5)$$

Now, in order to establish the fundamental equation for the thermoelastic field, we now introduce the thermoelastic displacement potential function ϕ , which is defined by the following relations.

$$u = \frac{\partial \phi}{\partial r}, \quad w = \frac{\partial \phi}{\partial z} \quad (6)$$

Then, the fundamental equation for ϕ can also be derived from the equilibrium equations using the relations of Eqs.(1) and (5), which is shown as following form.

$$\nabla^2 \phi = -(m+3)(m+1)\alpha(z)T(r,z) \quad (7)$$

In which, $\alpha(z)$ and $T(r,z)$ are the coefficient of linear thermal expansion and the temperature change, respectively.

Thus, the displacement component u and w for the thermoelastic field are given by the method of superposition of Eqs.(2) and (6). Then, the thermal stress components can be evaluated from the stress-strain relations in terms of displacement components.

Now, we assume that the thermal conductivity $\lambda(z)$ is given by the following form.

$$\lambda(z) = \lambda_0 \left(\frac{|z|}{a} + 1 \right)^l \quad (8)$$

in which λ_0 and l are the arbitrary constants. Then the axisymmetric heat conduction equation in a steady state is given by

$$\nabla^2 T + \frac{l}{z+a} \frac{\partial T}{\partial z} = 0 \quad (9)$$

3. Analytical examples

As an analytical example, we now consider a nonhomogeneous infinite body with a penny-shaped crack of its radius a located at the plane $z=0$ as shown in Fig.1. Furthermore, we suppose that the temperature change is caused by the surface heat generation (heat sink) $q_0 F(r)$ from the crack surfaces.

3.1 TEMPERATURE ANALYSIS

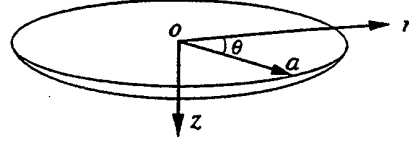


Fig.1 Coordinate systems of an infinite body

Heat conduction equation and the associated thermal boundary condition are represented in the following dimensionless forms.

$$\bar{\nabla}^2 \bar{T} + \frac{l}{\bar{z}} \frac{\partial \bar{T}}{\partial \bar{z}} = 0 \quad (10)$$

$$\bar{z} = 1; \quad \frac{\partial \bar{T}}{\partial \bar{z}} = F(\bar{r}) \cdot H(1-\bar{r}) \quad (11)$$

$$\bar{z} \equiv \bar{z} + 1, \quad \bar{\nabla}^2 = \frac{1}{\bar{r}} \frac{\partial}{\partial \bar{r}} \left(\bar{r} \frac{\partial}{\partial \bar{r}} \right) + \frac{\partial^2}{\partial \bar{z}^2} \quad (12)$$

where, $F(\bar{r})$ is an arbitrary dimensionless function associated to the surface heat source, $H(\cdot)$ is a Heaviside function.

Here, the following dimensionless quantities have been introduced to derive Eqs.(10)~(12).

$$\left. \begin{aligned} \bar{T} &= T/(q_0 a / \lambda_0), \quad (\bar{r}, \bar{z}) = (r, z)/a \\ \bar{\lambda}(\bar{z}) &= \lambda(z)/\lambda_0 \end{aligned} \right\} \quad (13)$$

where, q_0 is a typical value of surface heat generation (heat sink) per unit time and unit area. To solve the fundamental equation (10) under the conditions (11), we now introduce the method of Hankel transform of order zero over the variable \bar{r} . Then the temperature solution is given by

$$\bar{T}(\bar{r}, \bar{z}) = - \int_0^\infty \frac{F^*(s)}{s K_{\mu-1}(s)} \hat{z}^\mu K_\mu(s \bar{z}) \cdot s J_0(s \bar{r}) ds \quad (14)$$

$$\mu = \frac{1}{2}(1-l) \quad (15)$$

$$F^*(s) = \int_0^\infty F(\bar{r}) \bar{r} J_0(s \bar{r}) d\bar{r} \quad (16)$$

where, $J_\nu(\cdot)$ is a Bessel function of the first kind for order ν , and $K_\mu(\cdot)$ is a modified Bessel function of the first kind for order μ .

3.2 THERMOELASTIC ANALYSIS

Fundamental differential equation systems for the unknown functions f and ϕ are given in the following dimensionless forms.

$$\bar{\nabla}^2 \bar{f} + \frac{m}{\bar{z}} \frac{\partial \bar{f}}{\partial \bar{z}} = 0 \quad (17)$$

$$\bar{\nabla}^2 \bar{\phi} = -(m+3)(m-1)\bar{\alpha}(\bar{z})\bar{T}(\bar{r}, \bar{z}) \quad (18)$$

The corresponding displacement components and the stress components are represented in dimensionless forms as

$$\left. \begin{aligned} \bar{u}_r &= \hat{z} \frac{\partial \bar{f}}{\partial \bar{r}} + \frac{\partial \bar{\phi}}{\partial \bar{r}} \\ \bar{u}_z &= \hat{z} \frac{\partial \bar{f}}{\partial \hat{z}} - \bar{f} + \frac{\partial \bar{\phi}}{\partial \hat{z}} \end{aligned} \right\} \quad (19)$$

$$\left. \begin{aligned} \bar{\sigma}_r &= 2\bar{G}(\hat{z}) \left[\hat{z} \frac{\partial^2 \bar{f}}{\partial \bar{r}^2} - \frac{\partial \bar{f}}{\partial \hat{z}} + \frac{\partial^2 \bar{\phi}}{\partial \bar{r}^2} - (m+3)\bar{\alpha}(\hat{z})\bar{T}(\bar{r}, \hat{z}) \right] \\ \bar{\sigma}_{\theta\theta} &= 2\bar{G}(\hat{z}) \left[\hat{z} \frac{1}{\bar{r}} \frac{\partial \bar{f}}{\partial \bar{r}} - \frac{\partial \bar{f}}{\partial \hat{z}} + \frac{1}{\bar{r}} \frac{\partial \bar{\phi}}{\partial \bar{r}} - (m+3)\bar{\alpha}(\hat{z})\bar{T}(\bar{r}, \hat{z}) \right] \\ \bar{\sigma}_z &= 2\bar{G}(\hat{z}) \left[\hat{z} \frac{\partial^2 \bar{f}}{\partial \hat{z}^2} - \frac{\partial \bar{f}}{\partial \hat{z}} + \frac{\partial^2 \bar{\phi}}{\partial \hat{z}^2} - (m+3)\bar{\alpha}(\hat{z})\bar{T}(\bar{r}, \hat{z}) \right] \\ \bar{\sigma}_{rz} &= 2\bar{G}(\hat{z}) \left[\hat{z} \frac{\partial^2 \bar{f}}{\partial \bar{r} \partial \hat{z}} + \frac{\partial^2 \bar{\phi}}{\partial \bar{r} \partial \hat{z}} \right] \end{aligned} \right\} \quad (20)$$

Then, mechanical boundary conditions on the crack surface and its extended surface are given by the following relations.

$$\left. \begin{aligned} \hat{z} = 1; \bar{\sigma}_r &= 0 \quad (0 < \bar{r} < \infty) \\ \bar{\sigma}_z &= 0 \quad (0 < \bar{r} < 1) \\ \bar{u}_z &= 0 \quad (1 < \bar{r} < \infty) \end{aligned} \right\} \quad (21)$$

Here, the following dimensionless quantities have been introduced for Eqs.(17)~(21).

$$\left. \begin{aligned} (\bar{u}_r, \bar{u}_z) &= (u_r, u_z) / (\alpha_0 q_0 a^2 / \lambda_0) \\ (\bar{\sigma}_r, \bar{\sigma}_{\theta\theta}, \bar{\sigma}_z, \bar{\sigma}_{rz}) &= (\sigma_r, \sigma_{\theta\theta}, \sigma_z, \sigma_{rz}) / (\alpha_0 q_0 a G_0 / \lambda_0) \\ \bar{f} &= f / (\alpha_0 q_0 a^2 / \lambda_0), \quad \bar{\phi} = \phi / (\alpha_0 q_0 a^3 / \lambda_0) \\ \bar{G}(\hat{z}) &= G(\hat{z}) / G_0, \quad \bar{\alpha}(\hat{z}) = \alpha(\hat{z}) / \alpha_0 \end{aligned} \right\} \quad (22)$$

The solution for \bar{f} governed by Eq.(17) is represented by the following form.

$$\left. \begin{aligned} \bar{f} &= \int_0^\infty C_1(s) \hat{z}^p K_p(s\hat{z}) s J_0(s\bar{r}) d\bar{s} \\ p &= \frac{1}{2}(1-m) \end{aligned} \right\} \quad (23)$$

Similarly, the complementary solution $\bar{\phi}_c$ for $\bar{\phi}$ governed by Eq.(18) is represented by the following Hankel transformed form.

$$\bar{\phi}_c^* = C_2(s) e^{-s\hat{z}} \quad (24)$$

Now, we consider three different cases for nonhomogeneous material properties as shown in Table 1, the particular solutions $\bar{\phi}_p^*$ for these cases are given by the following forms.

$$\bar{\phi}_{p(case1)}^* = -(m+3)(m-1) \frac{F^*(s)}{2s^2} \hat{z} e^{-s(\hat{z}-1)} \quad (25)$$

Table 1 Numerical parameter of nonhomogeneous material properties

	$\bar{\lambda}(\hat{z})$	$\bar{\alpha}(\hat{z})$	$\bar{G}(\hat{z})$
Case 1	1	1	$1 \sim \hat{z} : 0 \leq m \leq 1$
Case 2	1	\hat{z}	$1 \sim \hat{z} : 0 \leq m \leq 1$
Case 3	\hat{z}^{-2}	1	$1 \sim \hat{z} : 0 \leq m \leq 1$

$$\bar{\phi}_{p(case2)}^* = -(m+3)(m-1) \frac{F^*(s)}{4s^3} (\hat{z} + s\hat{z}^2) e^{-s(\hat{z}-1)} \quad (26)$$

$$\bar{\phi}_{p(case3)}^* = -(m+3)(m-1) \frac{F^*(s)}{4s^3} \hat{z} (3 + s\hat{z}) e^{-s(\hat{z}-1)} \quad (27)$$

Then, the solution for $\bar{\phi}$ governed by Eq.(18) is represented by the following equation.

$$\bar{\phi} = \int_0^\infty [C_2(s) e^{-s\hat{z}} + \bar{\phi}_p^*] s J_0(s\bar{r}) d\bar{s} \quad (28)$$

Substituting Eqs.(23), (28) into Eqs.(19), (20), the components of displacement and stresses are formulated. To obtain an unknown coefficients $C_1(s)$, $C_2(s)$, we have to solve dual integral equation derived from boundary conditions (21), which is given by the following form.

$$\left. \begin{aligned} \int_0^\infty u \{1 + k(u)\} A(u) J_0(\alpha u) du &= F(\alpha) \quad (0 < \alpha < 1) \\ \int_0^\infty A(u) J_0(\alpha u) du &= 0 \quad (1 < \alpha < \infty) \end{aligned} \right\} \quad (29)$$

Then, the solution $A(u)$ is given by the form⁽⁵⁾.

$$A(u) = \frac{2}{\sqrt{\pi}} \int_0^1 h_1(t) \sin(ut) dt \quad (30)$$

Here, the unknown function $h_1(t)$ is a solution of Fredholm integral equation of the second kind given by

$$h_1(x) + \int_0^1 h_1(u) K(x, u) du = H(x) \quad ; 0 \leq x \leq 1 \quad (31)$$

where $K(x, u)$ and $H(x)$ are defined by

$$K(x, u) = (2\pi)^{-1/2} \{K_c(|x-u|) - K_c(x+u)\} \quad (32)$$

$$K_c(\tau) = \sqrt{\frac{2}{\pi}} \int_0^\infty k(t) \cos(\tau t) dt \quad (33)$$

$$H(x) = \sqrt{\frac{1}{\pi}} \int_0^x \frac{\xi F(\xi) d\xi}{\sqrt{(x^2 - \xi^2)}} \quad (34)$$

Eq.(31) can be solved numerically for $h_1(x)$. Knowing $h_1(x)$, we can evaluate the distributions of stresses and displacements and thermal stress intensity factor K_I at the crack tip.

The value of K_I is evaluated from the following equation.

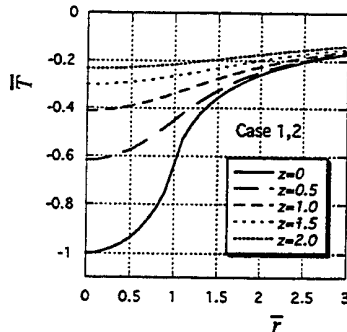
$$\bar{K}_I \equiv K_I \frac{\lambda_0}{G_0 \alpha_0 q_0 a \sqrt{a}} = \lim_{\bar{r} \rightarrow 1} \sqrt{2\pi(\bar{r}-1)} \bar{\sigma}_z|_{\hat{z}=1}$$

$$= -4h_1(1) \quad (35)$$

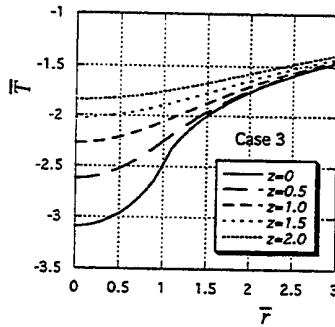
4. Numerical calculations

Assuming that $F(\bar{r})$ equal unity for surface heat source, numerical calculations are carried out for three cases represented by Table 1.

Fig.2 shows the temperature distribution \bar{T} in the radial direction. Namely, Fig.2(a) shows the result for Case1 and Case2 assumed as $\bar{\lambda}(\bar{z})=1$, Fig.2(b) shows one for Case3 assumed as $\bar{\lambda}(\bar{z})=\bar{z}^{-2}$.



(a) Case 1 and Case 2 ($\bar{\lambda}(\bar{z})=1$)



(b) Case 3 ($\bar{\lambda}(\bar{z})=\bar{z}^{-2}$)

Fig.2 Temperature distribution

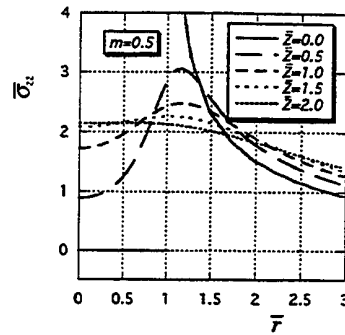
Fig.3 shows the axial stress distribution of $\bar{\sigma}_z$ for Case1 ~ Case3 when the nonhomogeneous parameter m equal 0.5, respectively. From these figures, it can be seen that the stress distribution is influenced by the variation of $\bar{\alpha}(\bar{z})$ and $\bar{\lambda}(\bar{z})$.

Fig.4 shows the thermal stress intensity factor \bar{K}_t for three different cases. It can be seen that the variation of \bar{K}_t is affected by the stress distribution and nonhomogeneous parameter m .

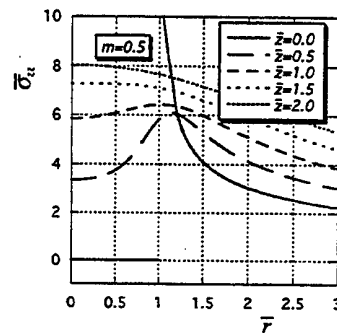
References

- (1) M. K. Kassir, Boussinesq Problems for Nonhomogeneous Solid, J. Eng. Mech. Division, ASCE, Vol.98(EM2), p.457-470, 1972.
- (2) T. Hata, Thermal Stresses in a Nonhomogeneous Thick Plate under Steady Distribution of Temperature, J. Thermal Stresses, Vol.5, no.1, p.1-11, 1982.
- (3) T. Hata, Thermal Stresses in a Nonhomogeneous Semi-infinite Elastic Solid under Steady Distribution of Temperature, Trans. JSME, Vol.51(A), p.1789-1795, 1985.

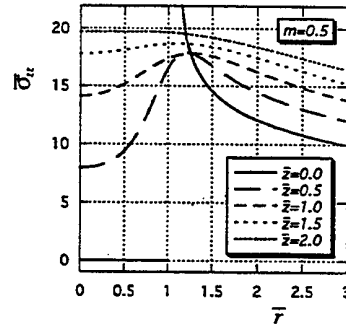
- (4) S. Jeon, Y. Tanigawa and D. Sone, Analytical Treatment of Axisymmetrical Thermoelastic Field with Kassir's Nonhomogeneous Material Properties and Its Adaptation to Boundary Value Problem of Slab under Steady Temperature Field, Journal of Thermal stresses (to be published).
- (5) I. N. Sneddon, Mixed Boundary Value Problems in Potential Theory, North-Holland Pub.Co., p.106-118, 1966.



(a) Case 1



(b) Case 2



(c) Case 3

Fig.3 Axial stress distribution of $\bar{\sigma}_z$

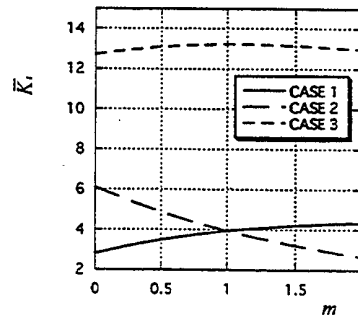


Fig.4 Variation of thermal stress intensity factor \bar{K}_t

Mixed Boundary Value Problem of Penny-shaped Cut under Axially Symmetric Temperature Field

J. V. S. Krishna Rao and N. Hasebe

*Department of Civil Engineering, Nagoya Institute of Technology,
Gokiso-cho, Showa-ku, Nagoya 466, JAPAN*

The axially symmetric problem for a Penny-shaped cut under thermal conditions is solved in the case the displacements are prescribed on its upper surface and stresses on its lower surface. The thermal conditions applied on the upper surface is different from the lower surface. Solution of the problem is obtained using Hankel transforms and Abel operator of the second kind. The boundary conditions of mixed boundary value problem reduce to a set of singular integral equations which are reduced to that of solving Riemann-Hilbert problem. Closed form solution is obtained. Explicit expressions are written for stress on the pane of the crack.

Key Words: *Mixed Boundary Value Problem, Disc-like Inclusion, Abel Operator, Hankel Transform*

1. Introduction

The class of problems which deal with the stress analysis of elastic bodies reinforced with inclusions which are either rigid or elastic, is of importance to the study of multiphase composite materials. In the majority of studies relating to inclusion problems it is assumed that perfect continuity or a bonded contact exists at the inclusion-elastic medium interface [3]. In the context of disc inclusion problems, Keer [4], Hunter and Gamblen [5] have investigated problems related to disc inclusions in which complete debonding occurs at plane face. In this paper we examine the behavior of the thermal stresses around a thin disc-like inclusion where debonding has occurred on one side while other side perfect bonding exists. The disc-like inclusion is subjected to general temperature conditions, that is, temperature applied on one face is different from the other.

To solve a class of crack and some inclusion problems a method is developed in the papers by Parihar and Krishna Rao [6] and Krishna Rao and Hasebe [1, 2]. The same method is used to solve the mixed boundary value problem. Problems considered in Ref. [1,2], the boundary conditions and general results obtained in terms of stress, displacement,

temperature and heat flux discontinuities at the crack plane reduces to that of solving Abel integral equations. But the mixed boundary value problem considered is reduced to a singular integral equations which intern reduced to that of Reimann-Hilbert problem. Even though the problem has closed form solution, evaluation of physical quantities like Stress Intensity Factors, Crack Opening Displacement, Energy required to open the crack etc. are of engineering interest and evaluation of them is not simple even in the special cases of thermal conditions. It is very important to mention here that the problems of thin disc-like or penny-shaped inclusions in three dimensions are natural analogue to the line inclusions in plane problems.

In the present paper, the problem considered is solved using the general results obtained in [1, 6] reducing to that of solving Riemann Hilbert problem. Closed form solutions are obtained to the unknown functions. Explicit expressions are given for stress components on the crack plane and order of the singularity rim of the crack is discussed.

2. Stress Field in the Neighbourhood of the Crack Plane Using Abel Operator of the Second Kind

Let the displacement components and temperature field in the upper half space ($z > 0$) be denoted by

$u_r^{(1)}(r,z)$, $u_z^{(1)}(r,z)$, $\theta^{(1)}(r,z)$ and their limiting values as $z \rightarrow 0+$ by $u_r^{(1)}(r,0)$, $u_z^{(1)}(r,0)$, $\theta^{(1)}(r,0)$ respectively. Similarly, let the displacement components and temperature field in the lower half space ($z < 0$) be denoted by $u_r^{(2)}(r,z)$, $u_z^{(2)}(r,z)$, $\theta^{(2)}(r,z)$ and their limiting values as $z \rightarrow 0-$ by $u_r^{(2)}(r,0)$, $u_z^{(2)}(r,0)$, $\theta^{(2)}(r,0)$, respectively. Using an obvious notation for stress components we set

$$\frac{\partial}{\partial \rho} \int_{\rho}^{\infty} \frac{\rho[u_r^{(1)}(r,0) - u_r^{(2)}(r,0)]}{\sqrt{r^2 - \rho^2}} dr = A(\rho), \rho > 0 \quad (1)$$

$$\frac{\partial}{\partial \rho} \int_{\rho}^{\infty} \frac{\rho[u_z^{(1)}(r,0) - u_z^{(2)}(r,0)]}{\sqrt{r^2 - \rho^2}} dr = B(\rho), \rho > 0 \quad (2)$$

$$\int_{\rho}^{\infty} \frac{\rho[\sigma_{rz}^{(1)}(r,0) - \sigma_{rz}^{(2)}(r,0)]}{\sqrt{r^2 - \rho^2}} dr = C(\rho), \rho > 0 \quad (3)$$

$$\int_{\rho}^{\infty} \frac{\rho[\sigma_{zz}^{(1)}(r,0) - \sigma_{zz}^{(2)}(r,0)]}{\sqrt{r^2 - \rho^2}} dr = D(\rho), \rho > 0 \quad (4)$$

$$\int_{\rho}^{\infty} \frac{\rho[\theta^{(1)}(r,0) - \theta^{(2)}(r,0)]}{\sqrt{r^2 - \rho^2}} dr = E(\rho), \rho > 0 \quad (5)$$

$$\int_{\rho}^{\infty} \frac{\rho[\frac{\partial}{\partial z} \theta^{(1)}(r,0) - \frac{\partial}{\partial z} \theta^{(2)}(r,0)]}{\sqrt{r^2 - \rho^2}} dr = F(\rho), \rho > 0 \quad (6)$$

then the Abel transforms of the second kind of stress and displacement components and temperature field $\sigma_r(r,z)$, $\sigma_{rz}(r,z)$, $u_r(r,z)$, $u_z(r,z)$, $\theta(r,z)$ are given in [1, 6] (See equations (2.19)-(2.24) of Ref.[6] and (45)-(51) of Ref.[1]). The limiting values of these stress, displacement and temperature fields as $z \rightarrow 0+$ and as $z \rightarrow 0-$ can be used to solve the mixed boundary value problem of disc-like or Penny-shaped inclusion in the plane $z=0$ which is subjected to loading conditions on one face, prescribed face displacements on the other side and general temperature conditions.

3. Penny-shaped Cut Under Mixed Mode Conditions and General Temperature Conditions

Let the circular disc-like (Penny-shaped) inclusion be situated in the plane $z=0$ of homogeneous isotropic infinite elastic body as shown in Fig.1. In terms of the cylindrical coordinates (r, ϕ, z) the position of the inclusion is $z = 0, 0 \leq r \leq a$. Here we consider debonding on

the upper surface ($0 < r < a, z \rightarrow 0+$) and perfect bonding on the lower surface ($0 < r < a, z \rightarrow 0-$) of the inclusion. The surface of the inclusion are subjected to general temperature conditions, that is, the temperature applied on the upper surface is different from the lower surface. The continuity and the boundary conditions may be written

$$u_r^{(1)}(r,0) = u_r^{(2)}(r,0), \quad r > a \quad (7)$$

$$u_z^{(1)}(r,0) = u_z^{(2)}(r,0), \quad r > a \quad (8)$$

$$\sigma_{zz}^{(1)}(r,0) = \sigma_{zz}^{(2)}(r,0), \quad r > a \quad (9)$$

$$\sigma_{rz}^{(1)}(r,0) = \sigma_{rz}^{(2)}(r,0), \quad r > a \quad (10)$$

$$\theta^{(1)}(r,0) = \theta^{(2)}(r,0), \quad r > a \quad (11)$$

$$\frac{\partial}{\partial z} \theta^{(1)}(r,0) = \frac{\partial}{\partial z} \theta^{(2)}(r,0), \quad r > a \quad (12)$$

$$\sigma_{rz}^{(1)}(r,0) = \tau(r), \quad 0 \leq r < a \quad (13)$$

$$\sigma_{zz}^{(1)}(r,0) = \sigma(r), \quad 0 \leq r < a \quad (14)$$

$$u_r^{(2)}(r,0) = U(r), \quad 0 \leq r < a \quad (15)$$

$$u_z^{(2)}(r,0) = V(r), \quad 0 \leq r < a \quad (16)$$

$$\theta^{(1)}(r,0) - \theta^{(2)}(r,0) = T_1^*(r), \quad 0 \leq r < a \quad (17)$$

$$\theta^{(1)}(r,0) + \theta^{(2)}(r,0) = T_2^*(r), \quad 0 \leq r < a \quad (18)$$

and the displacement, temperature fields are assumed to be continuous at the tip of the cut. Radial components of the displacement vanish at origin.

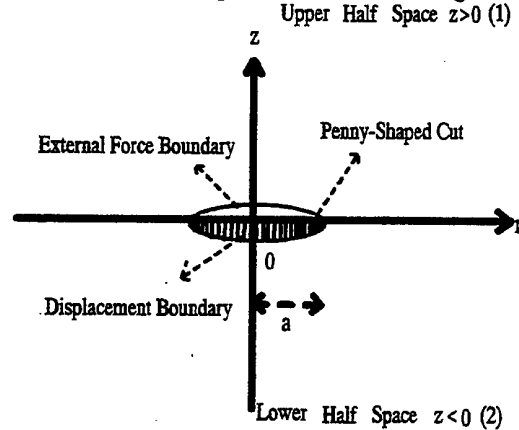


Fig.1 Mixed BVP for Penny-shaped Cut

Continuity conditions (7)-(12) give rise

$$A(\rho) = 0, B(\rho) = 0, C(\rho) = 0, \quad \rho > a \quad (19)$$

$$D(\rho) = 0, E(\rho) = 0, F(\rho) = 0, \quad \rho > a \quad (20)$$

Using (17), (5) and (11) we can write

$$E(t) = \int_t^a \frac{r T_1^*(r)}{\sqrt{r^2 - t^2}} dr, \quad 0 < t < a \quad (21)$$

Using the boundary conditions (13)-(16), (18),

equations (75), (90)-(93) of Ref. [1], equations (3.35)-(3.38) of Ref. [6] and (1)-(4) of the previous section the problem can be reduced to

$$\int_0^r \frac{F(t)dt}{\sqrt{r^2-t^2}} = -\frac{\pi}{2} T_2^*(r), \quad 0 < r < a \quad (22)$$

and a set of singular integral equations

$$(1-2\nu)\phi_1(t) - \phi_2(t) + \frac{2(1-\nu)}{\pi i} \int_{-a}^a \frac{\phi_1(s)ds}{s-t} = G(t), \quad -a < t < a \quad (23)$$

$$(3-4\nu)\phi_1(t) + (1-2\nu)\phi_2(t) + \frac{2(1-\nu)}{\pi i} \int_{-a}^a \frac{\phi_2(s)ds}{s-t} = H(t), \quad -a < t < a \quad (24)$$

where

$$G = \begin{cases} -8(1-\nu)[g_2(t) - ig_1(t)]/\pi, & 0 < t < a \\ -8(1-\nu)[g_2(-t) + ig_1(-t)]/\pi, & -a < t < 0 \end{cases} \quad (25)$$

$$H = \begin{cases} -8(1-\nu)[h_2(t) + ih_1(t)]/\pi, & 0 < t < a \\ -8(1-\nu)[h_2(-t) - ih_1(-t)]/\pi, & -a < t < 0 \end{cases} \quad (26)$$

The functions ϕ_1 and ϕ_2 are given by

$$\phi_1(s) = \delta(s) + i\gamma(s) = D(s) + iC(s), \quad (27)$$

$$\phi_2(s) = \alpha(s) + i\beta(s) = 2\mu[A(s) - iB(s)], \quad (28)$$

The loading term on the right hand side of equations (23)-(24) together with (25)-(26) are given by

$$g_1(t) = -\frac{\pi}{2} \int_0^t \frac{s\alpha(s)}{\sqrt{t^2-s^2}} ds + \frac{\pi\mu(1+\nu)\alpha}{4(1-\nu)} \int_0^t \frac{sT_2^*(s)}{\sqrt{t^2-s^2}} ds, \quad 0 < t < a \quad (29)$$

$$h_1(t) = -\frac{\mu\pi}{t} \frac{d}{dt} \int_0^t \frac{s^2 U(s)}{\sqrt{t^2-s^2}} ds - \frac{\pi\mu(1+\nu)\alpha}{4(1-\nu)} \int_0^t \frac{sT_2^*(s)}{\sqrt{t^2-s^2}} ds, \quad 0 < t < a \quad (30)$$

$$g_2(t) = \frac{\pi}{2} \int_0^t \frac{s\tau(s)}{\sqrt{t^2-s^2}} ds + \frac{\pi\mu(1+\nu)\alpha}{4(1-\nu)} E(t), \quad 0 < t < a \quad (31)$$

$$h_2(t) = \mu\pi \frac{d}{dt} \int_0^t \frac{sV(s)}{\sqrt{t^2-s^2}} ds + \frac{\pi\mu(1+\nu)\alpha}{4(1-\nu)} E(t), \quad 0 < t < a \quad (32)$$

Let $\kappa = 3 - 4\nu$; define the transformation

$$\begin{Bmatrix} \phi_1 \\ \phi_2 \end{Bmatrix} = \begin{Bmatrix} 1 & 1 \\ i\kappa^{1/2} & -i\kappa^{1/2} \end{Bmatrix} \begin{Bmatrix} \chi_1 \\ \chi_2 \end{Bmatrix}, \quad (33)$$

the set of coupled equations (23)-(24) can be written as uncoupled integral equations and are given by

$$(1-2\nu - i\kappa^{1/2})\chi_1(t) + \frac{2(1-\nu)}{\pi i} \int_{-a}^a \frac{\chi_1(s)ds}{s-t} = \frac{1}{2} (G(t) - i\kappa^{-1/2}H(t)), \quad -a < t < a \quad (34)$$

$$(1-2\nu + i\kappa^{1/2})\chi_2(t) + \frac{2(1-\nu)}{\pi i} \int_{-a}^a \frac{\chi_2(s)ds}{s-t} = \frac{1}{2} (G(t) + i\kappa^{-1/2}H(t)), \quad -a < t < a \quad (35)$$

The constants appeared in the solution of the singular integral equations can be settled using the conditions

$$\int_{-a}^a \phi_2(s)ds = 0; \quad \int_{-a}^a \phi_1(s)ds = C_0 \quad (36)$$

The Cauchy Integrals for $\chi_j, j=1, 2$ are given by

$$\Phi_j(u) = \frac{1}{2\pi i} \int_{-a}^a \frac{\chi_j(t)}{t-u} dt, \quad j=1, 2 \quad (37)$$

$\Phi_1^+; \Phi_1^-$ and $\Phi_2^+; \Phi_2^-$ are limiting values of Φ_1 and Φ_2 which are holomorphic functions of complex argument defined in the whole plane cut along $(-a, a)$. The functions χ_1 and χ_2 in terms of $\Phi_1^+; \Phi_1^-$ and $\Phi_2^+; \Phi_2^-$ are given by

$$\chi_1(s) = \frac{1}{2} [\phi_1(s) - i\kappa^{-1/2}\phi_2(s)] = \Phi_1^+(s) - \Phi_1^-(s) \quad (38)$$

$$\chi_2(s) = \frac{1}{2} [\phi_1(s) + i\kappa^{-1/2}\phi_2(s)] = \Phi_2^+(s) - \Phi_2^-(s) \quad (39)$$

Using (37)-(39), equations (34)-(35) can be reduced to Riemann-Hilbert problem [5, 7] and the solutions are given by

$$\Phi_1(u) = \frac{X_1(u)}{(\kappa - i\kappa^{1/2})4\pi i} \int_{-a}^a \frac{[G(t) - i\kappa^{-1/2}H(t)]dt}{X_1^+(t)(t-u)} \quad (40)$$

$$\Phi_2(u) = \frac{X_2(u)}{(\kappa + i\kappa^{1/2})4\pi i} \int_{-a}^a \frac{[G(t) + i\kappa^{-1/2}H(t)]dt}{X_2^+(t)(t-u)} \quad (41)$$

where, since the solution to the homogeneous problem is bounded at one end point, the arbitrary polynomial associated with the solution is zero and the Plemelj functions X_1 and X_2 corresponding to Φ_1 and Φ_2 respectively are given by

$$X_1(u) = [(u+a)/(u-a)]^{\gamma+1/4} \quad (42)$$

$$X_2(u) = [(u-a)/(u+a)]^{\gamma+1/4} \quad (43)$$

and γ is in terms of material constants and is written as

$$\gamma = (\log \kappa) / 4\pi i \quad (44)$$

The unknown functions A, B, C, D are given by the equations (38)-(41), (27), (28) and (19)-(20). The function E is given by (21) and F can be determined inverting the Abel integral equation (22)

and is given by

$$F(t) = -T_2^*(0) - \int_0^t \frac{t T_2^*(r) dr}{\sqrt{t^2 - r^2}}, \quad 0 < t < a \quad (45)$$

together with equation (20). Since the stress and displacements are in terms of A, B, C, D, E, F, therefore, in principle this completes the solution of the mixed boundary value problem.

4. Stress Components on the Plane of the Crack

The solution of the problem given in the previous section is complete but for application of the general results obtained we shall derive some physical quantities of engineering interest. Jump of the stress components on the crack surfaces are given by

$$\sigma_{zz}^{(1)}(r, 0) - \sigma_{zz}^{(2)}(r, 0) = -\frac{2}{\pi} \left[\frac{D(a)}{\sqrt{a^2 - r^2}} + \int_r^a \frac{D'(s) ds}{s \sqrt{s^2 - r^2}} \right], \quad 0 < t < a \quad (46)$$

$$\sigma_{rz}^{(1)}(r, 0) - \sigma_{rz}^{(2)}(r, 0) = -\frac{2}{\pi} \left[\frac{-aC(a)}{r \sqrt{a^2 - r^2}} + \int_r^a \frac{sC'(s) ds}{r \sqrt{s^2 - r^2}} \right], \quad 0 < t < a \quad (47)$$

Similarly, from equations (3.11)-(3.12) of Ref. [6] and (79)-(80) of Ref. [1] we can simplify stress component carrying out integration by parts we get

$$\begin{aligned} \sigma_{zz}^{(1)}(r, 0) + \sigma_{zz}^{(2)}(r, 0) &= -\frac{2\mu}{\pi(\lambda + 2\mu)} \left[\frac{2(\lambda + \mu)B(a) + C(a)}{\sqrt{a^2 - r^2}} \right] \\ &+ \frac{2\mu}{\pi(\lambda + 2\mu)} \int_0^a \frac{[2(\lambda + 2\mu)B'(t) + C'(t)] dt}{\sqrt{r^2 - t^2}} \\ &+ \frac{2\mu(1+\nu)\alpha \sqrt{r^2 - a^2}}{\pi(1-\nu)} \int_0^a \frac{s T_2^*(s) ds}{(r^2 - s^2) \sqrt{a^2 - s^2}} \end{aligned} \quad r > a \quad (48)$$

$$\begin{aligned} \sigma_{rz}^{(1)}(r, 0) + \sigma_{rz}^{(2)}(r, 0) &= -\frac{2\mu a}{\pi(\lambda + 2\mu)} \left[\frac{2(\lambda + \mu)A(a) - D(a)}{r \sqrt{a^2 - r^2}} \right] \\ &+ \frac{2\mu}{\pi(\lambda + 2\mu)} \int_0^a \frac{[2(\lambda + 2\mu)A'(t) - D'(t)] t dt}{\sqrt{r^2 - t^2}} \\ &- \frac{2\mu(1+\nu)\alpha}{\pi(1-\nu)r} \int_0^a \frac{t E'(t) dt}{\sqrt{r^2 - t^2}} \end{aligned} \quad r > a \quad (49)$$

5. Concluding Remarks

In the present paper it is illustrated that the general results developed in Ref. [1, 2, 6] to solve a class of boundary value problem also can be used for mixed boundary value problem. In the absence of the thermal conditions, the problem is same as that considered by Keer [5], and result are in complete agreement.

The expressions for stress components on the crack plane are given by (46)-(49). The stress components possess singularity of order 1/4 and singularity of the order 3/4. The computation of the functions $\phi_1(a) = D(a) + iC(a)$ and $\phi_2(a) = 2\mu[A(a) - iB(a)]$ should be done taking care of the oscillatory nature of the stresses in some special cases of the material constants. If the debonded and bonded surfaces of the thin disc-like inclusion are subjected different constant temperature conditions, Shear stress has unbounded nature at the rim of the crack.

6. References

- [1] Krishna Rao J. V. S., and Hasebe N., Axially Symmetric thermal Stresses of Penny-shaped Crack Subjected to General Surface Temperature, *Archive of Appl. Mech.*, Vol. 64, p. 481, 1994.
- [2] Krishna Rao J. V. S., and Hasebe N., Axially Symmetric Thermal Stress of Penny-shaped Crack under General Heat Flux, *J. of Thermal Stresses*, Vol. 18, p. 635, 1995.
- [3] Olesiak Z. and Sneddon I. N., The Distribution of Surface Stress Necessary to Produce a Penny-shaped Crack of Prescribed Shape, *Int. J. Engage. Sci.*, Vol. 7, p. 863, 1969.
- [4] Hunter S. C. and Gamblen D., The Theory of a Rigid Circular Disc Ground Anchor Buried in an Elastic Soil either with Adhesion or Without Adhesion, *J. Mech. Phys. Solids*, Vol. 22, p. 371, 1974.
- [5] Keer L. M., Mixed Boundary Value Problems for a Penny-shaped Cut, *J. of Elasticity*, Vol. 5, p. 89, 1975.
- [6] Parihar K. S. and Krishna Rao J. V. S., The Axially Symmetric Problem of a Penny-shaped Crack Under General Surface Loadings, *Int. J. Engage. Sci.*, Vol. 31, p. 953, 1993.
- [7] Muskhelishvili, N. I., *Some Basic Problems of the Mathematical Theory of Elasticity*, Noordhoff Int. Publ., Leyden 1975.

Session 1B

COMPOSITE MATERIALS I

Chair: L. Librescu

Co-Chair: M. R. Eslami

**Nonlinear Response of Sandwich Flat Panels under
Thermomechanical Loading Systems**

Terry Hause, Liviu Librescu, and Theodore F. Johnson

**Micromechanical Model for Thermal Analysis of
Particulate Composites**

Y. W. Kwon, C. Kim

**Thermal Stresses and Strains - The Achilles' Heal of
Continuous Fiber Reinforced Composites**

Gary R. Halford, Vinod K. Arya

**Thermal Stresses in Polymer Composites with Higher
Order Theories**

T. Kant, R. K. Khare

**Prediction of Thermal Free-Edge Stresses During
Processing of Graphite/PEEK Composite Laminates**

Moshe M. Domb, Jorn S. Hansen

NONLINEAR RESPONSE OF SANDWICH FLAT PANELS UNDER THERMOMECHANICAL LOADING SYSTEMS

Terry Hause*, Liviu Librescu* and Theodore F. Johnson**

* *Department of Engineering Science and Mechanics, Virginia Polytechnic Institute and State University, Blacksburg, VA 24061-0219*

** *Thermal Structures Branch, Structures Division, NASA Langley Research Center, Hampton, VA 23681-0001*

The study of the nonlinear response of sandwich flat panels exposed to thermomechanical loading systems constitutes the topic of this paper. The sandwich structure considered in this paper consists of a thick core-layer bonded by the face layers which are assumed to be symmetrically located with respect to the mid-plane of the overall structure. The loads involved in this analysis consist of biaxial compressive edge-loads, a lateral pressure as well as a non-uniform temperature field. The effects of the unavoidable initial geometric imperfections as well as the character of tangential boundary conditions are also incorporated and their implications upon the structural response are explored. In short, the results of this study are intended to provide pertinent information on the thermomechanical load carrying capacity of flat sandwich structures.

Key Words: Postbuckling, Sandwich Panel, Snap-through, Buckling Bifurcation, Thermal Load Carrying Capacity

1. Introduction

The structure of future supersonic and hypersonic flight and launch vehicles are likely to experience enormous challenges during their flight missions. These challenges are associated, among others, with the extremely high temperatures and mechanical loads they must withstand.

A typical laminated composite structure which, due to its exceptional properties, appears to be of great promise in the design of advanced supersonic/hypersonic space vehicle structures is the sandwich-type construction. Such structures consist of one or more high-strength, stiff face layers separated by a thick low-density flexible core.

Whereas the facings provide the primary load carrying capacity, the core carries the transversal load in terms of the shear stresses.

One of the problems, which for a better understanding and exploitation of load carrying capacity of sandwich panels is essential, is that associated with the determination of their non-linear response under complex thermomechanical loading conditions.

In spite of the high relevance of this problem in the design of high speed vehicle structures, to the best of the authors' knowledge, there are not pertinent studies in the available literature. For a most comprehensive and recent survey of the work done on the modeling of sandwich constructions and on the achievements in this area, the reader is referred to Ref. 1.

In the present study, the sandwich structure consists of a thick core-layer bonded by the face layers which consist of composite anisotropic materials, symmetrically laminated with respect to the mid-plane of the core-layer. The initial geometric imperfection consisting of a stress free initial transversal deflection will be also incorporated in the study. The loads under which the postbuckling response will be analyzed consist of biaxial compressive edge loads, a lateral pressure and a non-uniform thermal field.

Having in view that the generalized mixed representation of the governing equations of sandwich structures in terms of the Airy's potential function, transversal deflection and of a transverse shear potential function can be obtained in special cases only, in the present study a representation of governing equations in terms of displacement quantities will be supplied.

It should be noticed that the results presented in this paper constitute a generalization of the ones obtained in a number of previous papers [2-5].

2. Basic Assumptions and Conventions

The global middle plane of the structure σ , selected to coincide with that of the core layer, is referred to a curvilinear and orthogonal coordinate system x_α ($\alpha = 1, 2$).

The normal coordinate x_3 is considered positive when is measured in the direction of the inward normal. The uniform thickness of the core is $2\bar{h}$

while those of the upper and bottom faces are h'' and h' , respectively. As a result, $H (\equiv 2\bar{h} + h' + h'')$ is the total thickness of the structure.

The geometrically non-linear theory of doubly curved sandwich shells, of weak core, developed in the framework of the Lagrangian description is based on a number of assumptions, such as: i) the face sheets are constructed of a number of orthotropic material layers, the axes of orthotropy of the individual plies, being not necessarily coincident with the geometrical axes x_α of the structure, ii) the material of the core layer features orthotropic properties, the axes of orthotropy being parallel to the geometrical axes x_α . iii) a perfect bonding between the face sheets and between the faces and the core is postulated, and iv) the incompressibility in the transverse normal direction is postulated in both the core and facings,

3. Numerical Illustrations

In the numerical illustrations a temperature rise linearly varying through the thickness of the sandwich panel will be considered. This implies that herein $T(x_1, x_2, x_3) = x_3 \bar{T}(x_1, x_2)$. As a result, $\bar{T}(x_1, x_2) = -\frac{2}{H} T_u(x_1, x_2) = \frac{2}{H} T_l(x_1, x_2)$ where T_u and T_l are the temperature distributions on the external faces of the panel, $x_3 = -H/2$ and $x_3 = H/2$, respectively.

Throughout the numerical results a symmetric sandwich panel of a square projection on $P(L_1 = L_2 = L)$, whose core layer is of transversely-isotropic material and the faces of an isotropic material was considered. It was also assumed that $E_f/G_c = 100$, $\bar{h}/L = 0.03$ and $h/L = 0.002$.

In Fig. 1 the non-linear response of a geometrically perfect flat panel subjected to a temperature rise amplitude $\bar{T}_u (\equiv (1 - \nu^2)\alpha L^2 T_u / H^2)$ and to the uniaxial compressive edge load N_{11} as indicated in the graph was depicted. The results reveal that for fixed N_{11} , the upward deflection increases with the rise of \bar{T}_u . At the same time, the results show that with the increase of this compressive edge loads N_{11} , the upward deflections become larger and larger. The results also reveal that under the temperature rise \bar{T}_u , the panel does not feature buckling bifurcation.

Figure 2 represents the counterpart of Fig. 1 depicted in the plane (\bar{T}_u, Δ_1) , where $\Delta_1 (\equiv -(1/L_1/L_2) \int_0^{L_1} \int_0^{L_2} (\partial \xi_1 / \partial x_1) dx_1 dx_2)$ defines the end shortening in the x_1 -direction. The plot reveals that the end-shortening increases with both

the increase in \bar{T}_u and N_{11} .

Figure 3 depicts the non-linear behavior of a geometrically perfect flat panel subjected to a temperature rise \bar{T}_u and a lateral pre-load of amplitude $P (\equiv \bar{q}_{11})$. The results reveal that with the the temperature rise \bar{T}_u , the sensitivity to the variation of P diminishes.

Figure 4 depicts the behavior of a geometrically perfect flat sandwich panel subjected to the uniaxially compressive edge load rise N_{11} and a fixed temperature \bar{T}_u of various intensities. The results reveal that only in the absence of \bar{T}_u , the panel can experience buckling bifurcation. However, when the panel is exposed solely to a pre-determined temperature \bar{T}_u (i.e. when $N_{11} = 0$), the panel behaves like a geometrically imperfect panel, exhibiting a positive "initial imperfection" when $\bar{T}_u < 0$ and a negative "initial imperfection" when $\bar{T}_u > 0$. With the increase in the compressive edge load, N_{11} , the results reveal that the panel will experience positive or negative deflections, depending on whether $\bar{T}_u < 0$ and $\bar{T}_u > 0$, respectively. From the obtained plots it becomes also apparent that for $\pm \bar{T}_u$ the deformed shape of the panel is symmetrical with respect to the initial undisturbed configuration.

Figure 5 representing the counterpart of Fig. 4 depicted in the plane (N_{11}, Δ_1) reveals again that only in the absence of \bar{T}_u the panel features buckling bifurcation.

Figure 6 depicts the behavior of a geometrically perfect flat panel under a temperature rise \bar{T}_u and a pre-determined bi-axial compressive load system $L_R (\equiv N_{22}/N_{11})$. This edge had parameter is defined to be $L_R \leq 0$, and $L_R > 0$ when $N_{22} \leq 0$. (i.e. when the edges $x_2 = 0, L$ are subjected to a uniform tensile load), when $cal N_{22}$, respectively.

This figure obtained for a fixed $N_{11} = 1$, reveals that the tensile edge loads ($N_{22} < 0$) play a beneficial influence on the non-linear behavior, in the sense that with the increase of \bar{T}_u , for $N_{22} < 0$, the deflections are smaller than in the case $N_{22} \geq 0$. The same trend becomes apparent from Fig. 7 which depicts the behavior of a geometrically perfect panel subjected to a temperature rise and the pre-loads L_R and P .

All the previous results have been generated by assuming that all the edges are freely moveable.

Figure 8 represents the counterpart of Fig. 4 determined for the case of immovable edges $x_2 = 0, L$. The results of this plot compared with those of

Fig. 4 reveal that in the case of immovable edges the buckling load is lower as compared to that of the moveable edge case counterpart. However, as Fig. 8 reveals, for the same level of deflection, the panel is capable to carry much larger temperatures and compressive loads than in the moveable case counterpart.

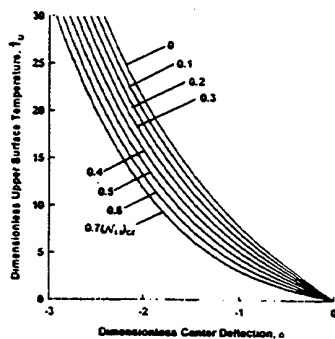
Finally, Figs. 9 and 10 reveal that in special cases, the flat panels can experience the snap-through phenomenon. In this sense, Fig. 9 shows that under a temperature rise \bar{T}_b , a flat panel featuring a negative imperfection subjected to the compressive pre-load N_{11} , can experience the snap-through buckling. The same phenomenon can occur (see Fig. 10) when a geometrically perfect flat panel is subjected to the pre-loads P and N_{11} and to a temperature rise \bar{T}_u .

4. Conclusions

A study of the non-linear behavior of sandwich flat panels under a system of thermomechanical loadings was presented. While the theory was developed in a more general context, the numerical illustrations concern only the case of symmetrical sandwich structures featuring a transversely isotropic weak core and isotropic face sheets.

The results have revealed among others, that under special conditions related with the magnitude of initial geometric imperfections and compressive edge pre-loads, the panel can exhibit snap-through buckling when subjected to a temperature rise varying anti-symmetrically through its thickness.

It is hoped that the results displayed in this paper will stimulate further studies on this topic and contribute to a better understanding of the behavior of sandwich panels under thermomechanical loadings.



Acknowledgement

The work reported herein was supported in part by NASA Langley Research Center under Grant NAG 1-1689.

References

1. Noor, A.K., Burton, W.S., Bert, C.W., "Computational Models for Sandwich Panels and Shells," *Applied Mechanics Reviews*, Vol. 4, No. 3, March 1996, pp. 155-199.
2. Librescu, L., Hause, T. and Camarda, C.J., "Geometrically Nonlinear Models of Initially Imperfect Anisotropic Sandwich Plates and Shells Incorporating Non-Classical Effects," *Proceedings of the 37th AIAA/ASME/ASCE/AHS/ASC Structures, Structural Dynamics and Materials Conference*, Paper AIAA 96-1350, Part 1, pp. 284-299, Salt Lake City, April 1995.
3. Hause, T., Librescu, L., and Camarada, C.J., "Postbuckling of Anisotropic Flat and Doubly-Curved Sandwich Panels Under Complex Loading Conditions," *11th DOD/NASA/FAA Conference on Fibrous Composites in Structural Design*, Forthworth, TX, 26-29 August, 1996
4. Librescu, L., Lin, W., Nemeth, M.P., and Starnes J.H., Jr. "Classical Versus Non-Classical Postbuckling Behavior of Laminated Composite Panels Under Complex Loading Conditions," *Non-Classical Problems of the Theory and Behavior of Structures Exposed to Complex Environmental Conditions*, AMD-Vol. 164, ASME, Ed. L. Librescu, pp. 169-182, 1993.
5. Librescu L., *Elastostatics and Kinetics of Anisotropic and Heterogeneous Shell-Type Structures*, Chapters V-VII, pp. 493-540, Noordhoff International Publishers, Leyden, The Netherlands, 1975.

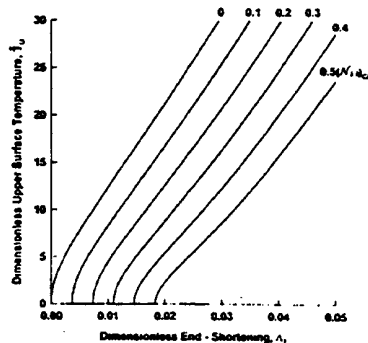


Fig. 1 Non-linear response of a flat sandwich panel subjected to a \bar{T}_u temperature rise and the uniaxial compressive edge preload N_{11} . Fig. 2 Counterpart of Fig. 1 depicted in the plane (\bar{T}_u, Δ_1) .

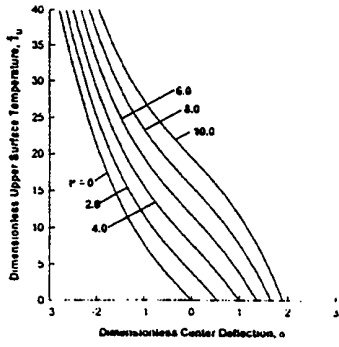


Fig. 3 Non-linear response of a flat sandwich panel subjected to the temperature rise amplitude \bar{T}_u and a lateral pre-load of intensity P .

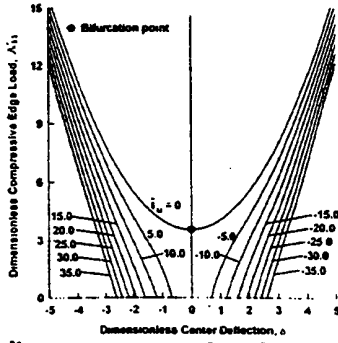


Fig. 4 Non-linear response of a flat sandwich panel subjected to the compressive edgeloading rise and temperature \bar{T}_u of given intensities.

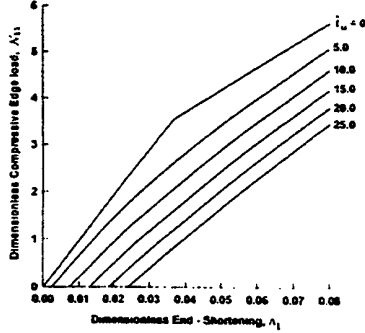


Fig. 5 The counterpart of Fig. 4 depicted in the plane (N_{11}, δ_1) .

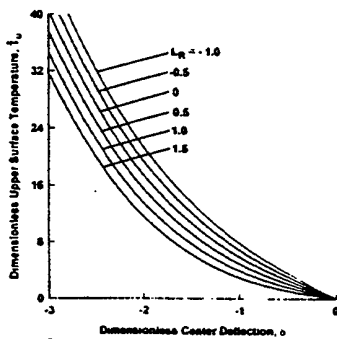


Fig. 6 Flat sandwich panel response under the temperature \bar{T}_u rise and the prescribed biaxially edge preload L_R ($\equiv N_{22}/N_{11}$ where $N_{11} = 1$ and $L_R < 0$ when $N_{22} < 0$ (implying compression)).

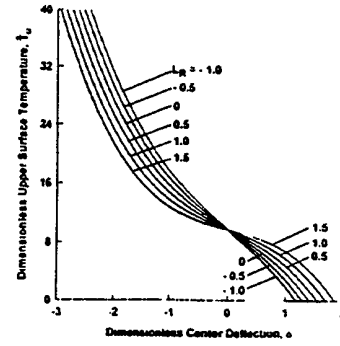


Fig. 7 Flat sandwich panel under the action of a temperature rise \bar{T}_u , of the prescribed biaxially edge preload L_R (with $N_{11} = 1$) and a lateral pre-load of intensity $P = 5$.

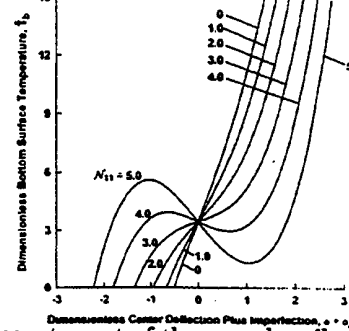


Fig. 8 The counterpart of the case described in Fig. 4 for the case of the immovable edges $x_2 = 0, L$.

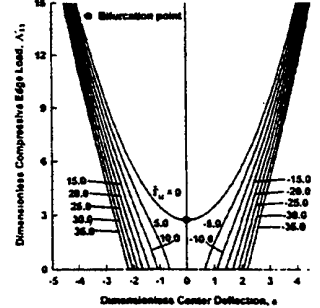


Fig. 9 Non-linear response of a flat geometrically imperfect ($\delta_o = -0.5$) sandwich panel under a temperature rise \bar{T}_b and a compressive edge preload N_{11} .

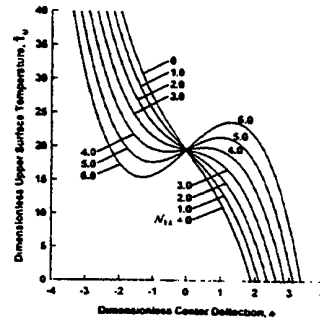


Fig. 10 Non-linear response of a flat-sandwich panel under a prescribed compressive edge pre-load and a fixed lateral pre-load.

Micromechanical Model for Thermal Analysis of Particulate Composites

Y. W. Kwon* and C. Kim**

* Mechanical Engineering Department, Naval Postgraduate School, Monterey, California, 93943

** School of Mechanical Engineering, Kookmin University, Seoul, Korea

Thermal stresses occur at the micromechanical level of a particulate composite caused by the mismatch of Coefficients of Thermal Expansion (CTE) of constituent materials like the particles and matrix binders. The stresses affect the service envelope of a composite under an external loading condition. Thus, a simplified, analytical, three-dimensional, micromechanical model is presented so that it can compute micro-thermal stresses occurring at the constituent materials as well as the effective CTE of a composite based on their materials properties. The analytical solutions compare very well with the results obtained from finite element analyses. In addition, a parametric study is conducted using the orthogonal array technique in order to determine the effects of each parameter of the constituent materials on the effective CTE, micro-thermal stresses, and the solution errors.

Key Words: Particulate Composite, Micromechanical Model, Thermal Stress, Orthogonal Array, Finite Element Analysis

1. Introduction

Thermal stresses can occur both at the microlevel and at the macrolevel of a composite structure. Microlevel thermal stresses result from different thermal properties of the constituent materials. Previous thermal analyses at the microlevel considered only fibrous composites [1, 2]. Therefore, this study presents a thermal analysis of a particulate composite material. A simple and accurate micromechanical model is derived for computing micro-thermal stresses as well as effective CTE's of particulate composite materials. The micro-stresses denote stresses in the particles and the matrix. The micro-model is a unit cell model and consists of eight subcells; one of which represents a particle and the rest of them denote the surrounding binding matrix of a particulate composite. A finite element analysis is also conducted to evaluate the developed micromechanical model.

2. 3-D MICROMECHANICAL MODEL

A three-dimensional, micromechanical model for a particle-reinforced composite is shown in Figure 1(a). A clear view of subcell locations is illustrated in Figure 1(b). Let subcell 1 denote the particle subcell and the rest of them be the binder matrix subcells. Planes 1-2, 2-3, and 3-1 are symmetric planes. Thus, an one-eighth of the full unit-cell model is shown in the figure. For simplicity, it is assumed that each subcell has constant stresses and strains, respectively. Equilibrium of subcell stresses at all interfaces must be satisfied as given below:

$$\sigma_{11}^1 = \sigma_{11}^2, \sigma_{11}^3 = \sigma_{11}^4, \sigma_{11}^5 = \sigma_{11}^6, \sigma_{11}^7 = \sigma_{11}^8 \quad (1)$$

$$\sigma_{22}^1 = \sigma_{22}^3, \sigma_{22}^2 = \sigma_{22}^4, \sigma_{22}^5 = \sigma_{22}^7, \sigma_{22}^6 = \sigma_{22}^8 \quad (2)$$

$$\sigma_{33}^1 = \sigma_{33}^5, \sigma_{33}^2 = \sigma_{33}^6, \sigma_{33}^3 = \sigma_{33}^7, \sigma_{33}^4 = \sigma_{33}^8 \quad (3)$$

where the subscripts denote stress components along the axes shown in Figure 1, and the superscript indicates the subcell number. Only normal stress components are considered in these equations. Similar equations can be written for shearing stress components. However, it is assumed that each subcell material is orthotropic or isotropic so that normal stress/strain components are not coupled with shear components. Thus, the present development is only for the normal components of stresses/strains. A similar development can be made for shearing stresses/strains.

It is assumed that subcells satisfy the following strain compatibility:

$$\begin{aligned} l_p \epsilon_{11}^1 + l_m \epsilon_{11}^2 &= l_p \epsilon_{11}^3 + l_m \epsilon_{11}^4 \\ &= l_p \epsilon_{11}^5 + l_m \epsilon_{11}^6 = l_p \epsilon_{11}^7 + l_m \epsilon_{11}^8 \end{aligned} \quad (4)$$

$$\begin{aligned} l_p \epsilon_{22}^1 + l_m \epsilon_{22}^3 &= l_p \epsilon_{22}^2 + l_m \epsilon_{22}^4 \\ &= l_p \epsilon_{22}^5 + l_m \epsilon_{22}^7 = l_p \epsilon_{22}^6 + l_m \epsilon_{22}^8 \end{aligned} \quad (5)$$

$$\begin{aligned} l_p \epsilon_{33}^1 + l_m \epsilon_{33}^5 &= l_p \epsilon_{33}^2 + l_m \epsilon_{33}^6 \\ &= l_p \epsilon_{33}^3 + l_m \epsilon_{33}^7 = l_p \epsilon_{33}^4 + l_m \epsilon_{33}^8 \end{aligned} \quad (6)$$

in which

$$l_p = V_p^{1/3} \quad (7)$$

$$l_m = 1 - l_p \quad (8)$$

and V_p is the particle volume fraction of a composite.

Each subcell has the constitutive equation

$$\epsilon_{ij}^n = C_{ijkl}^n \sigma_{kl}^n + \alpha_{ij}^n \Delta \theta \quad (9)$$

in which α_{ij}^n is CTE of the n^{th} subcell, either the particle or the matrix. For an isotropic material $\alpha_{ij}^n = \delta_{ij} \alpha^n$ in which δ_{ij} is the Kronecker delta. Further, $\Delta\theta$ is a change of temperature from the reference value. The subscripts i, j, k , and l vary from 1 to 3 while the superscript n changes from 1 to 8 for the present development, otherwise mentioned. Premultiplying both sides of Equation (9) by inverse of C_{ijkl}^n yields

$$\sigma_{ij}^n = E_{ijkl}^n \epsilon_{kl}^n - \tau_{ij}^n \quad (10)$$

where

$$\tau_{ij}^n = E_{ijkl}^n \alpha_{kl}^n \Delta\theta \quad (11)$$

and E_{ijkl}^n denotes the inverse of C_{ijkl}^n .

The unit-cell stresses and strains are obtained from the volume average of subcell stresses and strains. In other words,

$$\bar{\sigma}_{ij} = \sum_{n=1}^8 V^n \sigma_{ij}^n \quad (12)$$

$$\bar{\epsilon}_{ij} = \sum_{n=1}^8 V^n \epsilon_{ij}^n \quad (13)$$

Here, V^n is the volume fraction of the n^{th} subcell, and $\bar{\sigma}_{ij}$ and $\bar{\epsilon}_{ij}$ are the average unit-cell stresses and strains, respectively. These are the effective stresses and strains of a composite. Further, the constitutive equation of the effective stresses and strains is

$$\bar{\epsilon}_{ij} = \bar{C}_{ijkl} \bar{\sigma}_{kl} + \bar{\alpha}_{ij} \Delta\theta \quad (14)$$

in which \bar{C}_{ijkl} and $\bar{\alpha}_{ij}$ denote the effective mechanical and thermal material properties of a composite, respectively.

Algebraic manipulation of above equations results in the following matrix equation:

$$\{\epsilon\} = [R]\{f\} = [R_1]\{\Delta\tau\} + [R_2]\{\bar{\epsilon}\} \quad (15)$$

where $\{\epsilon\}$ is the vector consisting of three normal strain components of eight subcells. Vector $\{f\}$ is composed of three subvectors as given below:

$$\{f\}^T = \{\{\Delta\tau\}^T \{0\}^T \{\bar{\epsilon}\}^T\} \quad (16)$$

where $\{\Delta\tau\}$ is the column vector of 12×1 containing components τ_{ij}^n , and $\{0\}$ is the null vector of 9×1 , and $\{\bar{\epsilon}\}$ is the vector of 3×1 consisting of three effective, normal strains. Further,

$$[R] = \begin{bmatrix} [R_1] & [0] & [R_2] \end{bmatrix} \quad (17)$$

$24 \times 12 \quad 24 \times 9 \quad 24 \times 3$

The effective mechanical property matrix is computed from

$$[\bar{E}] = [V][E][R_2] \quad (18)$$

and the effective thermal property matrix is expressed as

$$\{\bar{\alpha}\} = -[\bar{E}]^{-1}[V]([E][R_1]\{\Delta\tau\} - \{\tau\})/\Delta\theta \quad (19)$$

in which $[E]$ is the matrix consisting of E_{ijkl}^n and vector $\{\tau\}$ consists of τ_{ij}^n . $[V]$ is the matrix composed of subcell volume fractions. Equation (18) indicates that the effective mechanical property is independent of thermal properties of subcells as expected. However, the effective thermal property is a function of mechanical as well as thermal properties of subcells as seen in Equation (19). The micro-thermal stresses at the subcells are computed as

$$\{\sigma\} = [E]([R_1]\{\Delta\tau\} + [R_2]\{\bar{\alpha}\}\Delta\theta) - \{\tau\} \quad (20)$$

3. Results and Discussion

A parametric study was conducted using an orthogonal array adopted in Taguchi's method [3] in order to determine the effects of each parameter of the constituent materials on the effective CTE's and micro-thermal stresses. The concept of orthogonality refers to the statistically independent or balanced parameters that make up the columns of the orthogonal array [3].

The variables used in the parametric study were elastic moduli, Poisson's ratios, CTE's of the constituent materials, and the particle volume fraction. Table 1 shows the variables. The full factorial analysis requires 625 cases. Instead, using an orthogonal array of $L_{25}(5^6)$ requires 25 analyses for the parametric study. Here, subscript of L , '25', represents the total number of cases, '5' denotes the number of levels, and '6' denotes the number of factors. This array is most suitable for the parameters given in Table 1.

For each case of the orthogonal array, the effective CTE and matrix thermal-stress were computed from the micromechanical model and the finite element analysis. The Rule Of Mixture (ROM) was also used to predict the effective CTE. The errors in the micromechanical model were less than four percent compared to the finite element results. On the other hand, ROM resulted in errors upto 16 percent. While the micromechanical model yielded relatively uniform errors, ROM resulted in a wide variation of errors. The ROM error was large when the matrix was much softer than the particle, the difference of the CTE's of the constituents was large, or PVF was large.

Figure 2 illustrates the effective CTE normalized with respect to the matrix CTE value. These graphs indicate the average effect of a single parameter over the variations of other parameters on the effective CTE value as expressed in the orthogonal array. The top left graph in Figure 2 indicates that the normalized, effective CTE is large when the modulus ratio is close to 1. However, the normalized, effective CTE became the minimum for the ratio of $E^p/E^m=100$, where superscripts 'p' and 'm' denote the particle and the matrix, respectively. A further increase of the modulus ratio increased the effective CTE. The CTE's of the constituents affected the effective CTE almost linearly. Similarly, PVF resulted in a linear variation of the effective CTE.

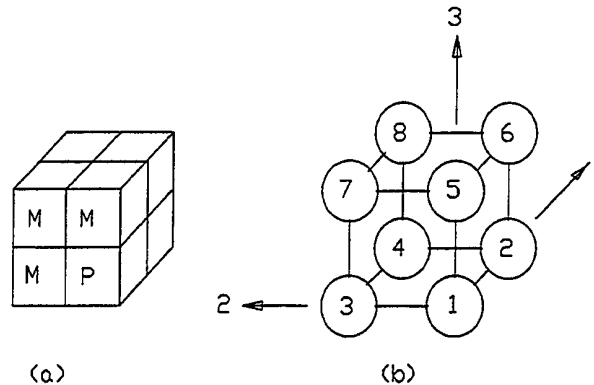


Figure 1. Micromechanical Model

The errors in micro-thermal stresses between the micromechanical and finite element results were compared. The average error was less than about six percent except for the case with a low PVF value of 0.2, which had a 10 percent error.

Figure 3 shows the plots of the matrix thermal stresses normalized with respect to the matrix elastic modulus. These stresses were computed for a unit degree of temperature change. The stress plots used absolute values when computing average values based on the orthogonal array. When comparing Figure 3 to Figure 2, the case with a smaller effective CTE value resulted in a greater thermal stress in the matrix. This observation was consistent for every parameter. The smaller effective CTE can be caused by a greater constraint from free deformation between the particle and the matrix. A greater constraint results in a larger thermal stress at the microlevel. When the modulus ratio was 100, the matrix thermal stress was the maximum but the effective CTE became the minimum. A larger difference in the constituent CTE values caused a greater thermal stress, as expected. Further, an increased PVF yielded a larger thermal stress, too. As far as the magnitude of the thermal stress was concerned, the CTE yielded the largest variation, as expected. The next largest variation resulted from PVF. On the other hand, elastic modulus ratios and Poisson's ratios varied the thermal stress in a less amount.

4. Conclusions

An analytical, three-dimensional, micromechanical model was developed to compute effective CTE's and micro-thermal stresses of particulate composites using constituents' mechanical and thermal properties. A simplified, unit-cell model was used for this purpose. The predictions obtained from the micromechanical model compared very well with the finite element results for both effective CTE values and micro-thermal stresses. The orthogonal array technique was adopted for a parametric study of particulate composites. This

method showed average effects of each parameter over wide variations of other parameters on the effective CTE and micro-thermal stress in the matrix material.

References

- (1) Hopkins, D. A. and Charnis, C. C., "A Unique Set of Micromechanics Equations for High-Temperature Metal Matrix Composites," *Testing Technology of Metal Matrix Composites* (Edited by DiGiovanni, P. R. and Adsit, N. R.), ASTM STP 964, American Society for Testing and Materials, 1988, pp. 159-176.
- (2) Aboudi, J., "Micromechanical Analysis of Composites by the Method of Cells," *Applied Mechanics Review*, Vol. 42, No. 7, July 1989, pp. 193-221.
- (3) Peace, G. S., *Taguchi Methods: A Hands-on Approach to Quality Engineering*, Addison-Wesley, Reading, Massachusetts, 1993.

Table 2. Variables for Orthogonal Array

Level No.	Modulus E^p/E^m	Pois. Ratio ν^p/ν^m	CTE α^p/α^m	PVF
1	1	0.20/0.36	0.10	0.20
2	10	0.24/0.26	0.25	0.35
3	10^2	0.28/0.36	0.50	0.50
4	10^3	0.32/0.36	0.75	0.65
5	10^4	0.36/0.36	1.00	0.80

* Superscripts p and m denote the particle and the matrix, respectively.

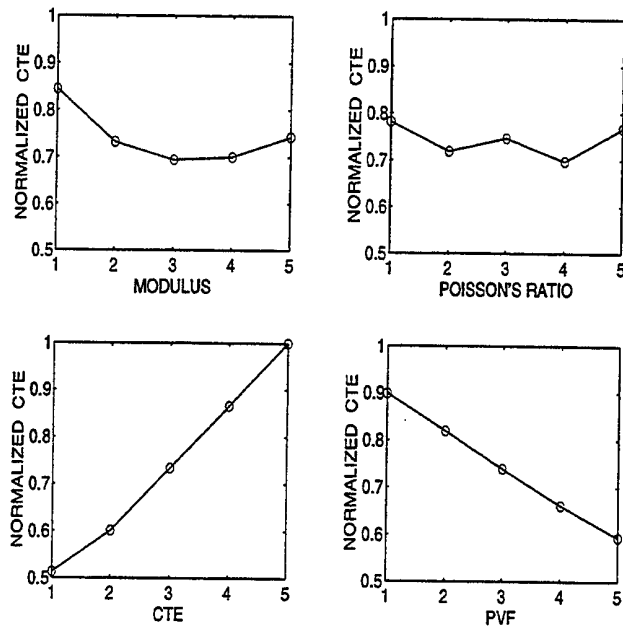


Figure 2. Variation of Average CTE Values Computed Based on the Orthogonal Array, Normalized With Respect to the Matrix CTE Value

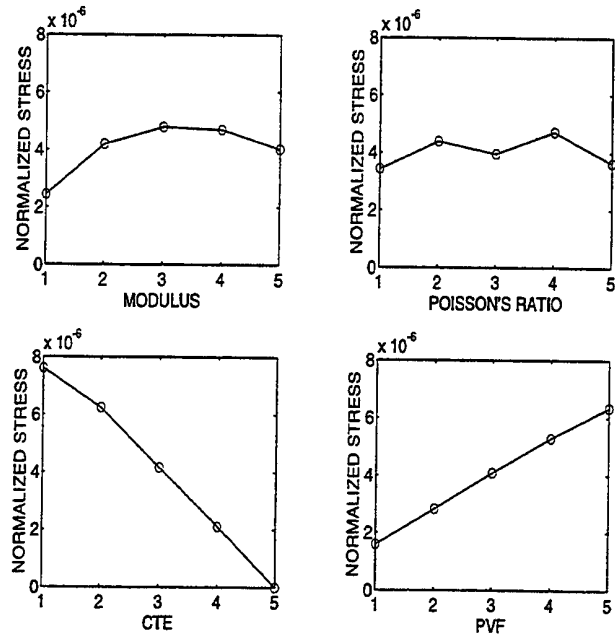


Figure 3. Variation of Average Matrix Thermal Stresses Computed Based on the Orthogonal Array, Normalized With Respect to the Matrix Elastic Modulus

Thermal Stresses and Strains - The Achilles' Heal of Continuous Fiber Reinforced Composites

Gary R. Halford* and Vinod K. Arya**

* Senior Research Scientist, Research and Technology Directorate, NASA-Lewis Research Center, 21000 Brookpark Road, Cleveland, Ohio 44135

** Resident Research Associate at NASA-Lewis Research Center, Department of Mathematics, University of Akron, Akron, Ohio 44325

This paper examines the thermal stresses and strains induced in unit cubes of a 33 volume percent continuous-fiber (silicon carbide, SCS6) reinforced titanium Metal Matrix (Ti-15-3) Composite (MMC). Stand-alone matrix material is also analyzed as a baseline of comparison. Each cube is exposed to a fixed heat flux on one face with the opposite face held at a fixed low temperature. Other faces are insulated and all faces are forced to remain parallel. Each cube is a sub-element of a much larger non-warping structural element. A comprehensive range of ply lay-ups and heat flux orientations are analyzed. Results are presented for global continuum- and local micro-mechanics linear elastic analyses. For every one of the 11 composite architectures studied, the micromechanical strains in the matrix in every direction exceed the maximum strains in the stand-alone matrix by approximately a factor two (75 to 118%). The combination of large thermal strains acting in very weak directions within MMCs is expected to reduce their thermal fatigue resistance far below that of monolithic materials.

Key Words: thermal stress, thermal strain, metal matrix composites, thermal fatigue, finite elements

1. Introduction

The potential structural benefits of unidirectional, continuous-fiber, metal matrix composites (MMCs) are legendary. Compared to their monolithic matrices, unidirectional MMCs possess superior properties such as higher stiffness and tensile strength, and lower coefficient of thermal expansion. Additionally, MMC density will be lower if the fibers are less dense than the matrix they replace. Their potential has been demonstrated unequivocally both analytically and experimentally, especially at ambient temperatures. Successes prompted Nationally funded efforts within the United States and elsewhere to extend the promise of MMCs into the temperature regime wherein creep, stress relaxation, oxidation, and thermal fatigue damage mechanisms lurk. This is the very regime for which alternative high-temperature materials are becoming mandatory, since further enhancement of state-of-the-art monolithic alloys is rapidly approaching a point of diminishing returns. Unfortunately, MMCs offer but limited improvement in creep, relaxation, and oxidation resistance, since these are governed largely by the matrix material *per se*, and the matrix is still very much in evidence in the MMC. More seriously, however, MMCs are at a distinct disadvantage over their monolithic matrix counterpart when it comes to resisting damage induced by repeated thermal cycling between ambient temperature and maximum service operating temperatures. As will be shown, thermal

cycling is the Achilles' heal of MMCs owing to the large internal thermal stresses and strains that develop in the constituent matrix and fibers because of their significant mismatch in thermal expansion α . A thermal expansion mismatch is inherent provided a mismatch in matrix/fiber moduli of elasticity is a desired characteristic. This is to be expected (see Halford⁽¹⁾) from the Grüneisen equation that inversely relates α to bulk modulus of elasticity K . Bulk and Young's moduli E are linearly related.

$$\alpha \propto (\gamma C_v / 3EV) \quad (1)$$

where γ is Grüneisen's constant that is related directly to the sum of the two powers in the equations for the attractive- and repulsive-force *versus* atomic spacing, C_v is the specific heat, and V is the molar volume.

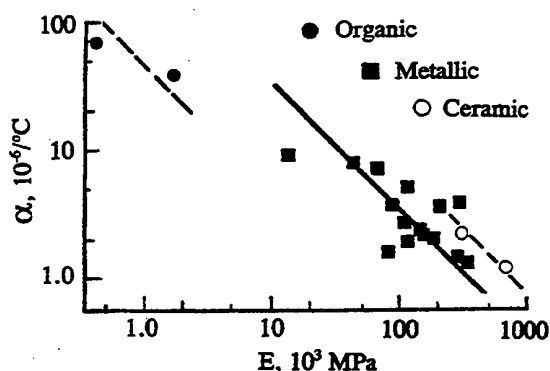


Fig. 1. Inverse relation between thermal expansion coefficient, α , and Young's modulus of elasticity, E . Data from Richards⁽²⁾.

Figure 1 depicts the inverse relation between thermal expansion and elastic modulus for three major classes of materials; organic, metallic, and ceramic⁽²⁾. The more disparate are the values of the moduli between fiber and matrix, the greater the thermal expansion mismatch and hence the greater will be the thermal stresses and strains for a given thermal excursion.

The current analytic research examines the thermal stresses and strains in unit cubes of MMCs induced by exposure of one face to a heat flux, Q , and the opposite face to a fixed temperature heat sink. Faces parallel to the x -direction heat flux were assumed insulated to make the analyses more tractable. A comprehensive range of simple ply lay-ups and heat flux orientations are analyzed. The objective is to determine the severity of thermally induced stresses and strains in MMCs and imply their potential impact on the thermal fatigue resistance of MMCs.

2. Material, Properties, Composite Cubes

Continuous fiber (silicon carbide, SCS6, 33% by vol.) reinforced titanium matrix (Ti-15-3) composites were analyzed. The temperature-dependent, time-independent material properties of the constituent materials (Table 1) were used in METCAN⁽³⁾ to compute discrete ply properties as a function of temperature (Halford and Arya⁽⁴⁾). These properties are shown in Table 2. The composite cubes consist of symmetric 12 ply lay ups with each ply having the dimensions $0.262 \times 0.262 \times 0.022$ cm. Several laminated architectures were selected to represent the extreme combinations of plies relative to the x -direction of heat flux, Fig. 2. One of the 12 cubes represents the stand-alone matrix material (Case 0). Four distinct laminate lay-ups (I, II, III, and IV) are positioned in three orientations (A-B-C) relative to the heat flux Q in the negative x -direction. Because Case

Table 1 - Mechanical and thermal properties of constituents

Temp.	°C	20	130	240	350	460	570	680	790	900
Fiber	E	8.98	8.88	8.79	8.68	8.58	8.47	8.36	8.23	8.11
	ν	0.1898	0.1878	0.1857	0.1835	0.1813	0.1790	0.1766	0.1741	0.1715
	α	0.1512	0.1546	0.1579	0.1616	0.1655	0.1695	0.1739	0.1786	0.1836
Matrix	E	1.78	1.67	1.56	1.44	1.30	1.15	0.98	0.78	0.48
	ν	0.3196	0.3005	0.2802	0.2582	0.2342	0.2075	0.1768	0.1395	0.0875
	α	0.2503	0.2609	0.2733	0.2811	0.3063	0.3298	0.3622	0.4160	0.5278

E: Young's modulus, $\times 10^6$ MPa ν : Poisson's ratio α : Coefficient of thermal expansion, $\times 10^{-5}$ °C⁻¹

Table 2- Orthotropic properties of the composite plies

T	°C	20	130	240	350	460	570	680	790	900
E ₁₁		2.6600	2.5200	2.3600	2.2200	2.0200	1.8100	1.5700	1.2600	0.8200
E ₂₂		4.1600	4.0600	3.9500	3.8300	3.7100	3.5700	3.4200	3.2400	3.0000
ν_{12}		0.1768	0.1634	0.1492	0.1342	0.1180	0.1004	0.0810	0.0588	0.0313
ν_{23}		0.2768	0.2633	0.2490	0.2336	0.2167	0.1981	0.1767	0.1509	0.1152
ν_{31}		0.3038	0.2874	0.2697	0.2504	0.2290	0.2049	0.1768	0.1417	0.0911
G ₁₂		1.0210	0.9670	0.9080	0.8450	0.7440	0.6940	0.6000	0.4820	0.3110
G ₂₃		1.0210	0.9670	0.9080	0.8450	0.7440	0.6940	0.6000	0.4820	0.3110
G ₃₁		1.0180	0.9770	0.9310	0.8800	0.8200	0.7510	0.6600	0.5520	0.3740
α_{11}		0.2096	0.2170	0.2254	0.2352	0.2471	0.2620	0.2820	0.3128	0.3786
α_{22}		0.1797	0.1829	0.1864	0.1899	0.1936	0.1974	0.2009	0.2039	0.2034

E = Young's modulus, $\times 10^6$ MPa ν = Poisson's ratio G = Shear modulus
 α = Coefficient of thermal expansion, $\times 10^{-5}$ °C⁻¹ $E_{22} = E_{33}$ $\alpha_{22} = \alpha_{33}$

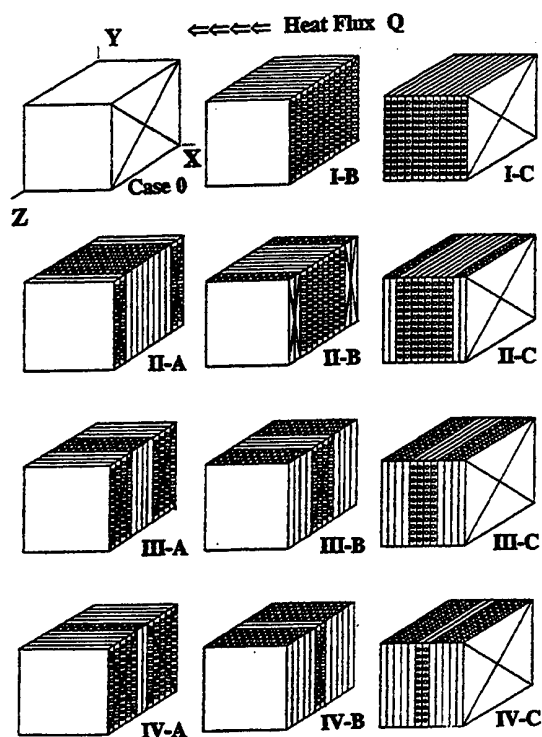


Fig. 2. Indexing scheme for describing ply lay-up architecture of composite cubes. Heat flux, Q , in negative X direction.

IA is equivalent to Case IC, Case IA is dropped and Case 0 is shown in its place. The Case indexing scheme follows a progression from a thick center laminate with no laminate faces (I) to a thin enter laminate and thick laminate faces (IV).

3. Thermal Loading and Finite Element Analyses

Each cube was thermally loaded with temperature rising slowly from 21°C to a maximum on the heated face while the opposite face was maintained at 21°C. Only steady-state thermal conditions were analyzed. Side faces were insulated. Maximum temperatures for the stand-alone matrix and composite cubes were determined by assuming both to be subjected to the same heat flux. For the arbitrarily prescribed maximum temperature of 800°C for the stand-alone matrix, thermal conductivity calculations based on a constant heat flux resulted in a maximum temperature of 910°C for the composite cubes owing to their lower thermal conductivity. Both continuum (Unit Cube with 1728 elements, 2197 nodes) and micromechanical (Unit Cell with 3072 elements, 3689 nodes) elastic finite element structural analyses were performed using MARC⁽⁵⁾ with 8-noded, solid hexagonal elements, Fig. 3. The micromechanical model is a sub-element of the continuum model which in turn is a sub-element from a larger non-warping

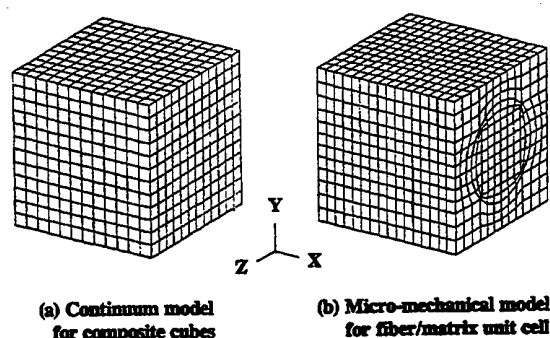


Fig. 3 Finite element models.

element. Consequently, parallel faces in both models were forced to remain parallel during thermal loading. The elastic analyses enable generalization of results to other ranges of thermal cycling. Sensitivity studies conducted by independently varying α and E permits extrapolation of results to other MMC systems with different combinations of expansion and moduli values (see for example, Halford and Arya⁽⁶⁾). In the current analyses, all of the computed stresses and strains are viewed as ranges for the case of slow, quasi-static, cyclic thermal loading between the minimum and maximum temperatures. Rapidly applied thermal transients would increase the thermal stresses and strains in the composite cubes to a greater extent than for the stand-alone matrix cube owing to the lower thermal conductivity of the composite.

4. Results

Thermal stress results for the stand-alone matrix (Case 0) are shown at the far left of Fig. 4. The maximum thermal stress range for this Case is 428 MPa (62 ksi) in the transverse (y and z) directions.

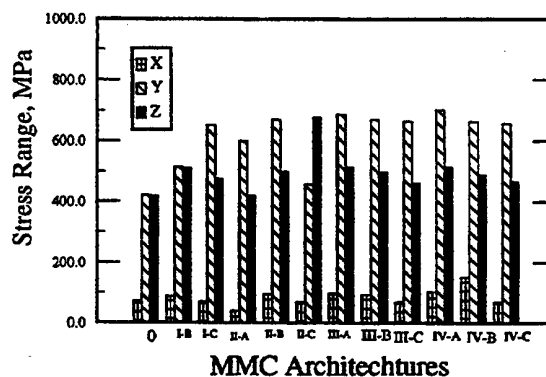


Fig. 4 Thermal stress ranges in composite cubes using continuum model.

Similarly, the maximum mechanical component of the thermally induced strain range is 0.48 % acting in the transverse directions (see far left of Fig. 5). Figure 4 also displays the maximum continuum stress range (and corresponding orthogonal stress ranges) found in each of the 11 composite Cases. The location of the maximum stress ranges are shown by the big X in Fig. 2. In every composite Case, every transverse stress range is greater than the maximum stress range in the stand-alone matrix material (Case 0). The maximum ranges are always at the cube face whose temperature cycled between the maximum and the minimum. The most benign Case (I-B) has a stress range 25% higher than that found in Case 0. Unfortunately, the direction of this high stress range is perpendicular to a fiber; the weakest possible direction in any composite. Combining the highest thermal stresses with the weakest directions will invariably give rise to much poorer thermal fatigue resistance than the stand-alone matrix, thereby negating any potential structural benefit of the composite for components loaded appreciably by thermal cycling. The extent of the poorer performance, while not experimentally evaluated herein, is indicated by the observations of others. For example, tensile strengths of [90] composites are well known to be considerably less than the tensile strength of stand-alone matrix material, and isothermal fatigue strengths of [90] composites can be as low as 10% of [0] fatigue strengths, Hashin and Rotem⁽⁶⁾. Furthermore, the thermal fatigue resistance of composites is expected to be even less than their isothermal fatigue resistance (Halford, Lerch, and Saltsman⁽⁷⁾). To better understand why this can be so,

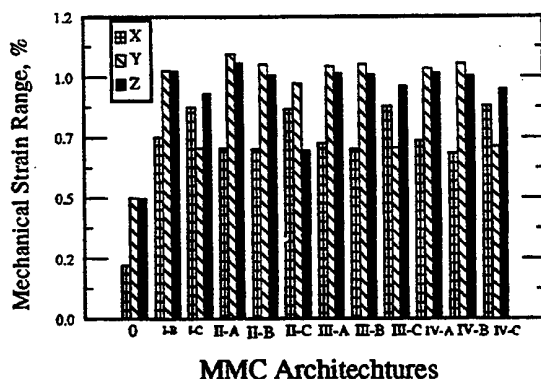


Fig. 5 Mechanical component of thermally induced strain ranges in matrix portion of unit cell using micro-mechanical model.

it is necessary to examine the thermal stresses and strains in the composite using a micromechanical structural analysis (Fig. 3). Figure 5 shows the mechanical component of the cyclic thermal strain range developed within the matrix material for each of the 11 composite Cases. Comparable maximum strain ranges are also shown for Case 0 for comparison. In

every Case, every strain range in every direction is higher than the maximum strain range in the stand-alone matrix material by 35 to 110%. Furthermore, the maximum strain ranges are always in a direction transverse to the local fiber direction.

5. Conclusions

The analytic results presented herein clearly demonstrate the extraordinarily large thermal stresses and strains that can be suffered by continuous-fiber reinforced metal matrix composites. The highest thermal stresses and strains are normal to the fibers; a notoriously weak direction. High stresses and strains in conjunction with weak directions are expected to severely limit the application of MMCs in structural applications involving appreciable thermal cycling. The broad range of ply lay-ups studied bounds the possible MMC architectures that could have been selected. For the same heat flux, none of the architectures offer a potential thermal fatigue resistance higher than the matrix material itself. Thermal fatigue resistance is not one of the structural advantages of metal matrix composites.

References

- (1) Halford, G. R., Obstacles to High Temperature Cyclic Structural Durability of Continuous-Fiber Composites, *Computational Mechanics '95, Theory & Application*, S. N. Atluri, G. Yagawa, and T. A. Cruse, Eds., Springer-Verlag, pp. 1128-1133, 1995.
- (2) Richards, C. W., *Engineering Materials Science*, Wadsworth, San Francisco, Tables A.1 - A.3, pp. 518-520, 1961.
- (3) Lee, H.-J., Gotsis, P. K., Murthy, P. L. N., and Hopkins, D. A., Metal Matrix Composite Analyzer (METCAN), *User's Manual, Version 4.0*, NASA TM-105244, 1991.
- (4) Halford, G. R. and Arya, V. K., Thermal Fatigue Limitations of Continuous Fiber Metal Matrix Composites, Materials and Structures Base Research and Technology Conference, NASA CP, NASA-Lewis Research Center, Cleveland, OH, May 1, 1997.
- (5) Anon., *MARC General Purpose Finite Element Program*, Vols. A-D, MARC Analysis Research Corp., Palo Alto, CA, 1992.
- (6) Hashin, Z. and Rotem, A., A Fatigue Failure Criterion for Fiber Reinforced Materials, *Journal of Composite Materials*, Vol. 7, pp. 448-464, 1973.
- (7) Halford, G. R., Lerch, B. A., and Saltsman, J. F., Proposed Framework for Thermomechanical Fatigue Life Modeling of Metal Matrix Composites, NASA TP-3320, July 1993.

Thermal Stresses in Polymer Composites with Higher Order Theories

T. Kant* and R. K. Khare**

*Department of Civil Engineering, Indian Institute of Technology Bombay, Powai, Mumbai-400076, INDIA.

** Department of Civil Engineering, Shri G.S. Institute of Technology and Science, Indore-452003, INDIA.

Closed-form and finite element discrete thermo-elastic solutions for flat and curved polymer composite laminates are obtained with a set of higher order two-dimensional (2D) displacement models incorporating improved transverse cross-sectional deformations.

Key Words: Thermal Stresses, Higher Order Theories, Composite Laminates, Plates, Shells

1. Introduction

Reliable evaluation of thermally induced deformations and stresses in components made of polymer composites in the form of plates and shells is important in the assessment of performance of the components. The growing applications of new composite materials especially in thermal environment have encouraged development of improved and refined analytical models for ultimate analysis. While studies in the aspects of mechanical behavior of advanced composites are extensive, very investigations have been carried out to-date few studies are available on their thermo-elastic behavior.

The three-dimensional (3D) analyses of laminates with a large number of laminae becomes intractable [1]-[3]. Researchers have, therefore, focused their attention on 2D theories. Noor and Burton [4,5] have identified four general approaches for constructing 2D theories: method of hypotheses, method of expansion, asymptotic integration technique and iterative methods.

Of these the method of hypotheses is a popular and general one for constructing 2D theories. An individual layer (lamina), for mathematical modeling purposes, is considered to be homogeneous and orthotropic (and thus the material properties are assumed to remain constant in each layer) while the laminate is heterogeneous through the thickness and generally anisotropic. The greater differences in the elastic properties between fiber filaments and matrix materials lead to a high ratio of in-plane Young's modulus-to-transverse shear modulus for most of the composite laminates fabricated to-date.

The classical lamination theory (CLT) is an extension of the Kirchhoff's thin plate/Love's thin shell theory and neglects the effects of out-of-plane strains and assumes each lamina to be in a

state of plane stress. It is observed that the CLT fails to predict accurately the static and dynamic response in case of composite laminates which are rather thick and/or exhibit high anisotropy ratios. Most importantly, it is found to be totally unsuitable for most sandwiches with high shear flexible cores. The very physical nature of a laminate makes transverse deformation significant. Thus the CLT is not suitable for modelling of laminates.

Theories which include the effects of transverse shear deformation energy and at times the transverse normal strain energy become necessary. The so-called first-order shear deformation theories (FOST) of Reissner [6] and Mindlin [7], based on assumed stress and displacement fields respectively, do remove some of the defects of the CLT. However, these too neglect the effects of transverse normal strain and assume a constant transverse shear strain through the laminated thickness. A shear correction coefficient, which is somewhat arbitrary, is thus used to correct the transverse shear strain energy of deformation. Transverse shear deformation assumes greater significance for fiber reinforced laminates and sandwiches, as compared to homogeneous plates and shells, due to large ratio of longitudinal elastic modulus to the transverse shear modulus.

The limitations of the FOSTs forced development of higher-order shear deformation theories (HOSTs) [8]-[14] which provide greater displacement accuracy and include the considerations of realistic parabolic variation of transverse shear stresses through the laminate thickness, warping of the transverse cross-sections and a few models do consider the complete 3D material constitutive law.

Kant and Khare [15] have recently used a nine degrees of freedom HOST in conjunction with a finite element technique for the thermal analyses flat laminates. In this presentation, we generalize the approach and develop a new flat facet element

for general curved laminates in addition to obtaining a few closed-form solutions with HOSTs.

2. Theory

Analytical models based on higher-order displacement field [15]:

HOST 12

$$u = u_0 + z\theta_y + z^2 u_0^* + z^3 \theta_y^* \\ v = v_0 - z\theta_x + z^2 v_0^* - z^3 \theta_x^* \quad (1)$$

$$w = w_0 + z\theta_z + z^2 w_0^* + z^3 \theta_z^* \\ \text{and two other models with changes in } w, \\ \text{HOST 11}$$

$$w = w_0 + z\theta_z + z^2 w_0^* \quad (2) \\ \text{and HOST 9}$$

$$w = w_0 \quad (3)$$

and the popular FOST based on,

$$u = u_0 + z\theta_y; v = v_0 - z\theta_x; w = w_0 \quad (4)$$

are developed and utilized here for general curved laminates. Starting from 3D elasticity equations proper material constitutive relations are taken as it is and 2D forms of strain-displacement relations are derived in a straight forward manner with help of Equations (1) - (4). 2D variationally consistent equilibrium equations and associated boundary conditions are derived using virtual work principle [11].

3. Results and discussion

Closed-form solutions for simply (diaphragm) supported cross-ply laminates and discrete solutions for general curved laminates using C^0 isoparametric flat facet quadrilateral finite elements are obtained. The formulations are first checked and validated by conducting numerical experiments on test problems described by Belytschko et al. [16] under mechanical loadings as pure 3D thermoelasticity solutions are scanty in literature. Numerical results on thermal problems analyzed by Khdeir et al. [17] and He [18] are presented in Tables 1 -3.

In addition, thermal effects are studied on new problems analyzed involving sandwich plates and shells both analytically and numerically. The difference between HOSTs and FOST is seen in low a/h ratios. This difference is more in plates than shells. HOST 12 results are closest to the 3D elasticity solutions.

References

- (1) Srinivas, S., Rao, A.K. and Joga Rao, C.V., Flexure of Simply Supported Thick Homogeneous and Laminated Rectangular Plates, *Z. Angew. Math. Mech.*, Vol.49, p.449, 1969.
- (2) Pagano, N.J., Exact Solutions for Composite Laminates in Cylindrical Bending, *J. Compos. Mater.*, Vol.3, p.398, 1969.
- (3) Ren, J.G., Exact Solution for Laminated Cylindrical Shells in Cylindrical Bending, *Compos. Sci. Technol.*, Vol.29(3), p.169, 1987.
- (4) Noor, A.K. and Burton, W.S., Assessment of Shear Deformation Theories for Multilayered Composite Plates, *ASME Appl. Mech. Rev.*, Vol.42(1), p.1, 1989.
- (5) Noor, A.K. and Burton, W.S., Assessment of Computational Models for Multilayered Composite Shells, *ASME Appl. Mech. Rev.*, Vol. 43(4), p.67, 1990.
- (6) Reissner, E., The Effect of Transverse Shear Deformation on the Bending of Elastic Plates, *ASME J. Appl. Mech.*, Vol.29(3), p.A69, 1945.
- (7) Mindlin, R.D., Influence of Rotary Inertia and Shear on Flexural Motions of Isotropic Elastic Plates, *ASME J. Appl. Mech.*, Vol.18, p.31, 1951.
- (8) Hilderbrand, F.B., Reissner, E. and Thomas, G.B., Notes on the Foundations of the Theory of Small Displacements of Orthotropic Shells, *NACA TN-1833*, 1949.
- (9) Lo, K.H., Christensen, R.M. and Wu, E.M., A Higher-Order Theory of Plate Deformation, *ASME J. Appl. Mech.*, Vol.44, p.663, 1977.
- (10) Murthy, M.V.V., An Improved Transverse Shear Deformation Theory for Laminated Anisotropic Plates, *NASA TP-1903*, 1981.
- (11) Kant, T., Numerical Analysis of Thick Plates, *Comput. Meth. Appl. Mech. Engng.*, Vol.31, p.1, 1982.
- (12) Kant, T., Owen, D.R.J. and Zienkiewicz, O.C., A Refined Higher-Order C^0 Plate Bending Element, *Comput. Struct.*, Vol.15, p.177, 1982.
- (13) Reddy, J. N., A Simple Higher-Order Theory for Laminated Composite Plates, *ASME J. Appl. Mech.*, Vol.51, p.745, 1984.
- (14) Pandya, B.N. and Kant, T., Higher-Order Shear Deformable Theories for Flexure of Sandwich Plates: Finite Element Evaluations, *Int. J. Solids Struct.*, Vol.24, p.1267, 1988.
- (15) Kant, T. and Khare, R.K., Finite Element Thermal Stress Analyses of Composite Laminates Using a Higher-Order Theory, *J. Thermal Stresses*, Vol.17, p.229, 1994.
- (16) Belytschko, T., Stolarski, H., Liu, W.K., Carpenter, N. and Ong, J.S.-J., Stress Projection for Membrane and Shear Locking in Shell Finite Elements, *Comput. Meth. Appl. Mech. Engng.*, Vol.51, p.221, 1985.

(17) Khdeir, A.A., Rajab, M.D. and Reddy, J.N., Thermal Effects on the Response of Cross-Ply Laminated Shallow Shells, Int. J. Solids Structures, Vol.29, p.653, 1992.

(18) He, J., Thermoelastic Analysis of Laminated Plates Including Transverse Shear Deformation Effects, Compos. Struct., Vol.30, p.51, 1995.

Table 1. Center deflections of simply (diaphragm) supported cross-ply shells subjected to sinusoidal thermal load

R/a	Present Closed Form				Present Finite Elements			Khdeir et al [17]		
	HOST12	HOST11	HOST9	FOST	HOST12	HOST 9	FOST	HSDT	FSDT	CST
Cylindrical shell (0°/90°) with a/b=1, h/a=0.1, R ₁ =∞, R ₂ =R										
5	1.1261	1.1261	1.1279	1.1272	1.1260	1.1278	1.1279	1.1235	1.1248	1.1280
10	1.1434	1.1434	1.1449	1.1444	1.1460	1.1468	1.1473	1.1421	1.1439	1.1447
50	1.1493	1.1493	1.1507	1.1501				1.1482	1.1501	1.1501
Spherical shell (0°/90°) with a/b=1, h/a=0.1, R ₁ =R ₂ =R										
5	1.0588	1.0588	1.0602	1.0578	1.0490	1.0553	1.0514	1.0545	1.0546	1.0660
10	1.1256	1.1256	1.1269	1.1258	1.1290	1.1304	1.1302	1.1235	1.1248	1.1280
50	1.1487	1.1487	1.1500	1.1493				1.1475	1.1493	1.1494
Plate	1.1497	1.1497	1.1510	1.1504	1.1470	1.1477	1.1478	1.1485	1.1504	1.1504
Ten layer cylindrical shell (0°/90°/.....) with a/b=1, h/a=0.1, R ₁ =∞, R ₂ =R										
5	1.0224	1.0224	1.0239	1.0234	1.0190	1.0203	1.0204	1.0216	1.0215	1.0247
10	1.0299	1.0299	1.0312	1.0307	1.0280	1.0293	1.0294	1.0303	1.0302	1.0310
50	1.0325	1.0325	1.0337	1.0330				1.0332	1.0330	1.0331
Plate	1.0326	1.0326	1.0339	1.0331	1.0320	1.0329	1.0328	1.0333	1.0331	1.0331

Table 2. Deflection and stress in a diaphragm supported symmetric cross-ply (0°/90°/0°) square laminate under sinusoidal thermal load

a/h	Quantity	Present Closed Form				Present Finite Elements				HE [18]
		HOST12	HOST11	HOST9	FOST	HOST12	HOST11	HOST9	FOST	
	\bar{w}	1.0823	1.0823	1.0874	1.0763	1.0832	1.0832	1.0874	1.0763	1.0904
	$\bar{\epsilon}_x^2 (z=-h/6)$	0.6628	0.6628	0.6616	0.6556	0.6614	0.6614	0.6602	0.6544	0.6712
	$\bar{\epsilon}_x^1 (z=-h/6)$	0.3024	0.3024	0.2736	0.1357	0.2762	0.2762	0.2484	0.1112	0.4776
	$\bar{\epsilon}_x^1 (z=-h/2)$	0.0122	0.0122	0.0826	0.4072	-0.5048	-0.5048	0.0110	0.3362	0.1478
	$\bar{\epsilon}_y^2 (z=-h/6)$	-0.8550	-0.8550	-0.9838	-1.0208	-0.9914	-0.9914	-1.0108	-1.0472	-0.8265
5	$\bar{\epsilon}_y^1 (z=-h/2)$	1.8538	1.8538	1.8590	1.8618	1.8494	1.8494	1.8556	1.8580	1.8450
	$\bar{\tau}_{xy}^1 (z=-h/2)$	1.0814	1.0814	1.0786	1.0722	1.0884	1.0884	1.0818	1.0754	1.0850
	$\bar{\tau}_{xz} (z=-h/6)$	0.1263	0.1263	0.1272	0.0795	0.1471	0.1471	0.1335	0.0864	0.0844
	$\bar{\tau}_{xz} (z=0)$	0.1433	0.1433	0.1448	0.0795	0.0676	0.0676	0.0612	0.0346	0.0674
	$\bar{\tau}_{yz} (z=-h/6)$	-0.1055	-0.1055	-0.1046	0.1060	-0.1007	-0.1007	-0.0958	0.0987	-0.1094
	$\bar{\tau}_{xz} (z=0)$	-0.0414	-0.0414	-0.0409	0.0424	-0.1022	-0.1022	-0.0934	0.0395	-0.0480
	\bar{w}	1.0489	1.0489	1.0501	1.0460	1.0490	1.0490	1.0501	1.0460	1.0517
	$\bar{\epsilon}_x^2 (z=-h/6)$	0.3308	0.3308	0.3306	0.3296	0.3302	0.3302	0.3300	0.3290	0.3325
	$\bar{\epsilon}_x^1 (z=-h/6)$	0.0581	0.0581	0.0540	0.0282	0.0447	0.0447	0.0404	0.0163	0.0960
	$\bar{\epsilon}_x^1 (z=-h/2)$	0.0165	0.0165	0.0266	0.0847	-0.0143	-0.0143	-0.0476	0.0490	0.0361
	$\bar{\epsilon}_y^2 (z=-h/6)$	-0.1590	-0.1590	-0.1630	-0.1621	-0.1706	-0.1706	-0.1741	-0.1719	-0.1436
10	$\bar{\epsilon}_y^1 (z=-h/2)$	0.9705	0.9705	0.9712	0.9715	0.9699	0.9699	0.9704	0.9700	0.9690
	$\bar{\tau}_{xy}^1 (z=-h/2)$	0.5192	0.5192	0.5188	0.5178	0.5212	0.5212	0.5205	0.5194	0.5200
	$\bar{\tau}_{xz} (z=-h/6)$	0.0433	0.0433	0.4336	0.0262	0.0524	0.0524	0.0516	0.0330	0.0293
	$\bar{\tau}_{xz} (z=0)$	0.0497	0.0497	0.0498	0.0262	0.0237	0.0237	0.0233	0.0132	0.0250
	$\bar{\tau}_{yz} (z=-h/6)$	-0.0355	-0.0355	0.0355	0.0349	-0.0277	-0.0277	-0.0110	-0.0113	-0.0316
	$\bar{\tau}_{yz} (z=0)$	-0.0144	-0.0144	0.0144	0.0140	-0.0281	-0.0281	-0.0276	-0.0281	-0.0234

Table 3. Deflection and stress in a diaphragm supported antisymmetric cross-ply ($0^\circ/90^\circ$) square laminate under sinusoidal thermal load

a/h		Present Closed Form				Present Finite Elements				
	Quantity	HOST12	HOST11	HOST9	FOST	HOST12	HOST11	HOST9	FOST	HE [18]
	\bar{w}	1.1478	1.1478	1.1530	1.1504	1.1501	1.1498	1.1530	1.1504	1.1557
	$\bar{\sigma}_x^2(z=0)$	0.0657	0.0657	0.0676	0.0700	0.0656	0.0656	0.06784	0.0702	0.0589
	$\bar{\sigma}_x^2(z=h/2)$	-1.7096	-1.7096	-1.7114	-1.7654	-1.7060	-1.7058	-1.7074	-1.7610	-1.6956
	$\bar{\sigma}_x^1(z=0)$	2.2160	2.2160	2.2320	2.3100	2.2140	2.2160	2.2380	2.3160	1.9444
	$\bar{\sigma}_x^1(z=h/2)$	-0.2410	-0.2410	-0.1818	-0.6148	-0.2928	-0.2946	-0.2562	-0.6930	-0.3077
5	$\bar{\sigma}_y^2(z=0)$	-2.2160	-2.2160	2.2320	-2.3100	-2.2140	-2.2160	2.2380	-2.3160	-1.9444
	$\bar{\sigma}_y^2(z=h/2)$	0.2410	0.2410	0.1818	0.6148	0.2928	0.2948	0.2562	0.6930	0.3077
	$\bar{\tau}_{xy}^2(z=h/2)$	-1.1576	-1.1576	-1.1556	-1.1354	-1.1714	-1.1704	-1.1592	-1.1388	-1.1653
	$\bar{\tau}_{xz}(z=0)$	-0.0365	-0.0365	-0.0354	-	-0.0108	-0.0138	-0.0262	-0.0076	-0.0740
	$\bar{\tau}_{yz}(z=0)$	-0.0365	-0.0365	-0.0354	-	-0.0108	-0.0138	-0.0261	-0.0076	-0.0740
	\bar{w}	1.1497	1.1497	1.1510	1.1504	1.1497	1.1497	1.1508	1.1502	1.1519
	$\bar{\sigma}_x^2(z=0)$	0.0339	0.0339	0.0347	0.0350	0.0339	0.0339	0.0348	0.0350	0.0334
	$\bar{\sigma}_x^2(z=h/2)$	-0.8748	-0.8748	-0.8753	-0.8827	-0.8741	-0.8741	-0.8742	-0.8809	-0.8728
	$\bar{\sigma}_x^1(z=0)$	1.1430	1.1430	1.1450	1.1550	1.1450	1.1450	1.1470	1.1550	1.1032
10	$\bar{\sigma}_x^1(z=h/2)$	-0.2547	-0.2547	-0.2460	-0.3074	-0.2856	-0.2856	-0.2785	-0.3433	-0.2638
	$\bar{\sigma}_y^2(z=0)$	-1.1430	-1.1430	-1.1450	-1.1550	-1.1450	-1.1450	-1.1470	-1.1550	-1.1032
	$\bar{\sigma}_y^2(z=h/2)$	0.2547	0.2547	0.2460	0.3074	0.2856	0.2856	0.2785	0.3433	0.2638
	$\bar{\tau}_{xy}^2(z=h/2)$	-0.5707	-0.5707	-0.5704	-0.5677	-0.5737	-0.5735	-0.5722	-0.5694	-0.5719
	$\bar{\tau}_{xz}(z=0)$	-0.0104	-0.0104	-0.0103	-	0.0006	0.0002	-0.0011	-0.0149	-0.0210
	$\bar{\tau}_{yz}(z=0)$	-0.0104	-0.0104	-0.0103	-	0.0006	0.0002	-0.0011	-0.0149	-0.0210

Superscripts 1 and 2 refer to layer numbers measured from $z = -h/2$.

Prediction of Thermal Free-Edge Stresses During Processing of Graphite/PEEK Composite Laminates

Moshe M. Domb[†] and Jorn S. Hansen

Institute for Aerospace Studies, University of Toronto, 4925 Dufferin St., Downsview, Ontario, CANADA M3H 5T6

A numerical model is developed for prediction of the process-induced thermal residual stresses in thermoplastic composite laminates. The model addresses the development of the residual stress state in fracture-critical free-edge regions as well as through-thickness stress variations. The current approach provides a unique capability for the investigation of the influence of thermal processing and structural parameters on the resulting buildup of residual stresses during manufacturing. Therefore, it can assist in the design and analysis of thermoplastic composites to tailor mechanical and strength characteristics. Thermal processing considered here includes solidification from the molten state at a specific surface cooling rate, and application of a posterior annealing cycle. A significant reduction in the free-edge stresses was obtained via a quench/anneal cycle in comparison to the recommended nominal cooling from the melt. Results are shown for the case of a quasi-isotropic APC-2 (graphite/PEEK) laminate.

Key Words: Residual Stress, Free Edge Stress, Processing, Thermoplastic, APC-2.

1. Introduction

The elevated processing temperatures and the large matrix/fiber thermoelastic property mismatch in thermoplastic composites may result in the development of thermal residual stresses of significant magnitude [1]. These process-induced stresses can considerably reduce the static and fatigue strength of the laminate, and can possibly lead to premature failures such as transverse matrix cracking, fiber buckling and inter-ply delamination. In particular, thermal residual stresses are critical in the vicinity of free edges, where high and localized interlaminar stresses arise. In addition, matrix crystallization during processing of semi-crystalline thermoplastics causes a large volumetric shrinkage which serves as an additional source of residual stress. As crystallization is strongly controlled by processing conditions, the resulting mechanism of stress buildup is also dependent upon processing parameters, such as the cooling rate from the melt and the annealing temperature [2].

As a result, prediction of the process-induced residual stresses is very important in relation to the design and performance of composite structures. Several studies which deal with modelling of the residual stress development during processing of thermoplastic laminates have been reported in the literature (a review of these models can be found in [3]). These studies utilize classical laminate theory as the basis for the residual stress anal-

ysis during processing, thus they provide information only about in-plane stress distributions in the thickness direction of the laminate. On the other hand, the current work presents a model which addresses the development of the three-dimensional residual stress state in free-edge regions, and in particular the interlaminar stress components, as well as through-thickness stress variations within the laminate. This model enables the investigation of the influence of thermal processing and structural parameters on the resulting buildup of residual stresses within the laminate. Thermal processing considered in the model includes solidification from the molten state at a specific cooling rate, and the application of a posterior annealing cycle [2]. Annealing is a recommended procedure applicable to semi-crystalline thermoplastics for the purpose of increasing an existing low level of crystallinity in the matrix; this to ensure an adequate environmental robustness.

Comparison of the process-induced free-edge stress profiles between a recommended nominal cooling from the melt and a proposed quench/anneal cycle is investigated here for a quasi-isotropic APC-2 (graphite/PEEK) laminate.

2. Model Description

The composite laminate considered in the present model is an infinitely-long composite strip with finite width $2W$ and finite thickness H , as depicted in Fig. 1. Since the external thermal loading can be viewed as uniform over all surfaces of the composite strip, both thermal and stress regimes

[†]Presently at deHavilland Inc., Garratt Blvd., Mail Stop N18-06, Downsview, Ontario, Canada M3K 1Y5

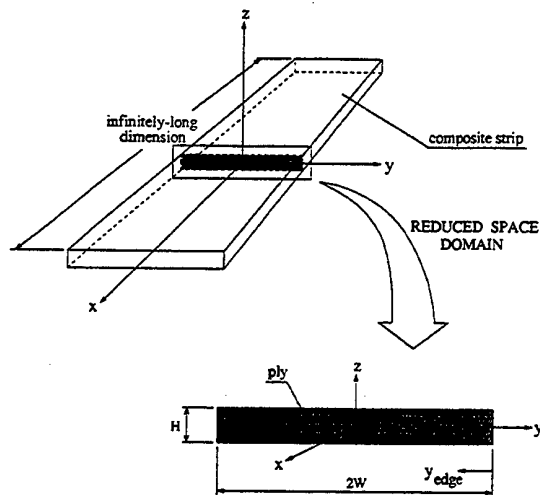


Figure 1: Reduced Space Domain of the Problem.

are invariant with the longitudinal direction of the structure (x -axis). This characteristic enables the reduction of the problem from a three-dimensional to a two-dimensional domain represented by the cross-sectional area of the laminate. This approach is referred to as Uniform Axial Extension [4]. Although the spatial domain of the problem is two dimensional, the stress analysis remains three-dimensional, as all displacement, strain and stress components are present in the formulation.

The model developed here consists of (1) a thermal analysis to determine the time-dependent temperature distribution over the cross-sectional area of the laminate, and (2) a quasi three-dimensional incremental stress analysis to predict the development of process-induced residual stresses within the domain. Both analyses are solved independently at every instant throughout the process using the Finite Element Method, however the analyses are coupled through the determination of the temperature- and crystallinity-dependent thermoelastic properties required for the stress calculation.

As the thermoelastic properties of the material and the volumetric shrinkage experienced during processing are strongly affected by the level of crystallinity in the matrix, a crystallization kinetics analysis of the non-isothermal crystallinity growth is required. Crystalline growth is strongly dictated by the thermal history and temperature rates encountered during processing. The non-isothermal crystallization kinetics model of Velisaris and Seferis [5] is implemented in the present study. Determination of the laminate's thermoelastic properties as a function of position and time is then performed. The corresponding properties for semicrystalline composites are derived using micromechanics models for the amorphous/crystalline and matrix/fiber systems in association with their respective volume fractions [3].

The stress analysis is based on an Uniform

Axial Extension incremental displacements approach using the Finite Element Method, in which incremental quantities are calculated and summed at each time during the processing. The model computes, in fact, changes in displacements, strains and stresses at each instant during the processing. Thus, implementation of the incremental approach enables complete modelling of the residual stress variations during processing in both the free-edge and through-thickness regions.

A complete and comprehensive description of the various analyses and solution techniques applied in the model can be found in [3].

3. Results

A quasi-isotropic $(+45_2, -45_2, 0_2, 90_2)_S$ APC-2 laminate has been investigated for the influence of the applied surface cooling rate from the molten state (380°C) and of a quench/anneal cycle on the free-edge stress profiles at room temperature (20°C). The present laminate has been exposed to (1) a quench cooling process (Q) at $6000^\circ\text{C}/\text{min}$ from the melt; (2) a nominal cool process (NC) at $30^\circ\text{C}/\text{min}$ from the melt; and (3) a quench/anneal cycle (Q/A) at 225°C for 1 minute. The discussion here concentrates only on the interlaminar stress components, while a detailed discussion on the in-plane stress components is presented in [3].

In order to show characteristic stress profiles, the overall room temperature distributions of the out-of-plane normal stress σ_z and shear stresses τ_{yz} and τ_{xz} for the NC case are presented in Fig. 2. At the free-edge region, typical stress concentrations are developed at the $0/90$ and $+45/-45$ interfaces for the three stress components. At the laminate interior region away from the free-edge, it is clear that no out-of-plane stresses develop through-the-thickness, this being consistent with the assumptions in the Classical Laminate Theory.

The room-temperature free-edge distributions of σ_z , τ_{yz} and τ_{xz} at various interfaces are depicted in Figures 3–6, respectively. Considering first the influence of cooling rate on the stress profiles, the results for the Q process can be compared to those from the NC case. It can be seen that the greater the surface cooling rate, the smaller the stress levels obtained at room temperature. The rationale behind this behavior comes from the fact that the cooling rate affects the onset temperature of crystallization in APC-2, where stress starts essentially to build up. The onset of crystallization is delayed as the cooling rate is increased [2], thereby reducing the temperature interval over which residual stresses build up, and resulting in lower stress levels at room temperature. In addition, all figures demonstrate the localized nature of the free-edge effect, where the interlaminar stresses assume significant magnitudes at the edge itself, however they level-out at a distance of about 1.0–1.5 times the laminate thickness measured in from the free-edge.

Evident from the results are the very large stress levels developed in the NC case and the sig-

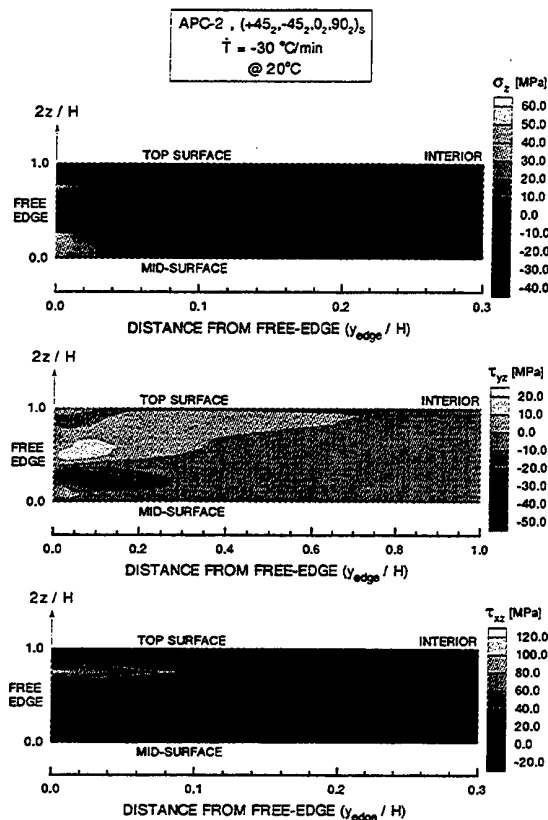


Figure 2: Room-Temperature Distribution of the Normal Stress σ_z and Shear Stresses τ_{yz} and τ_{xz} in the Cross-Section (First Quadrant) of a $(+45_2, -45_2, 0_2, 90_2)_S$ APC-2 Laminate Cooled at $30^\circ\text{C}/\text{min}$ (nominal cool) from the Molten State.

nificant stress reduction obtained in the Q process for all interlaminar stresses at both the 0/90 and $+45/-45$ interfaces. For σ_z (Figures 3 and 4), values ranging from -2 MPa (Q) to 59 MPa (NC), and from 18 MPa (Q) to 43 MPa (NC) are observed at these two free-edge interfaces, respectively. In relation to the assumed failure stress of 80 MPa , these tensile stresses indicate a significant reduction in the Mode-I delamination strength of the laminate at these locations. Regarding τ_{yz} and τ_{xz} (Figures 5 and 6), the critical location with respect to delamination are the 0/90 and $+45/-45$ free-edge interfaces, respectively. For the former, the stress level ranges from -17 MPa to -41 MPa , and for the latter, from 57 MPa to 98 MPa . Although these shear stress values are below the corresponding failure stresses of $\pm 80\text{ MPa}$ and $\pm 120\text{ MPa}$, respectively [3], they represent a considerable reduction in delamination strength. All interlaminar stresses vanish as the interior of the laminate is approached.

Although reduced free-edge stresses are obtained by quenching the laminate in contrast to the

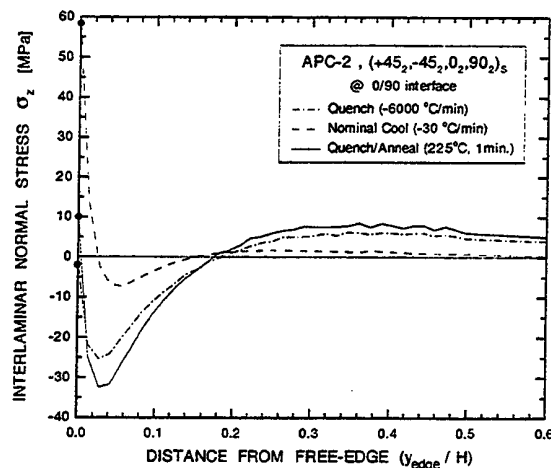


Figure 3: Effect of Thermal Process (Quench and Quench/Anneal versus Nominal Cool) on the Interlaminar Normal Stress σ_z Distribution at 20°C along the 0/90 Interface of a Quasi-Isotropic $(+45_2, -45_2, 0_2, 90_2)_S$ APC-2 Laminate.

slow-cool (NC) process, low levels of crystallinity are obtained in the rapid cooling process; an inadequate situation with respect to solvent resistance requirement and high-temperature retention of mechanical properties. An anneal cycle is then recommended in order to restore crystallinity, however, this results in some increase in the stress levels [3].

With regard to annealing effects, results from the Q/A cycle can be compared to those from the NC process. The Q/A cycle at 225°C for 1 minute produces almost identical levels of crystallinity to those obtained in the NC case, 22.69% and 23.21%, respectively. This enables the comparison in the stress distributions due exclusively to the difference in the crystallization kinetics between these processes. It is clear from Figures 3–6 that the quench/anneal process has significantly reduced the free-edge stress levels for all stress components. The reduced-stress percentages are 83.0% and 21.1% for σ_z and τ_{yz} at the 0/90 free-edge, respectively, and 38.0% and 3.1% for σ_z and τ_{xz} at the $+45/-45$ free-edge. These significant stress reductions are of great importance as they delay the onset of delamination at the free-edge. Consequently, an enhancement of the structural performance of the laminate is expected to be achieved.

4. Conclusions

A numerical model is developed for prediction of the process-induced thermal residual stresses in thermoplastic composite laminates. The model addresses the development of the residual stress state in free-edge regions as well as through-thickness stress variations. The model enables the investigation of the influence of different thermal processing

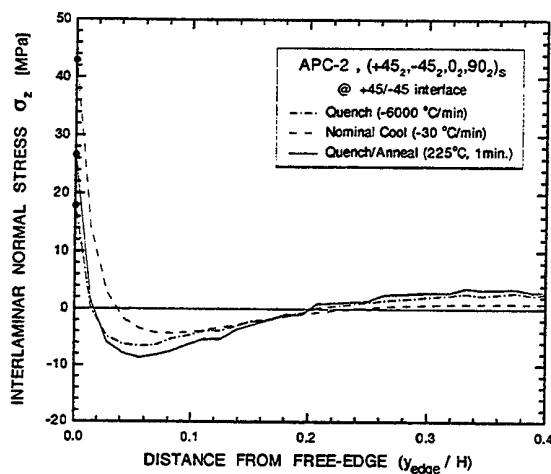


Figure 4: Effect of Thermal Process (Quench and Quench/Anneal versus Nominal Cool) on the Interlaminar Normal Stress σ_z Distribution at 20°C along the $+45/-45$ Interface of a Quasi-Isotropic $(+45_2, -45_2, 0_2, 90_2)_S$ APC-2 Laminate.

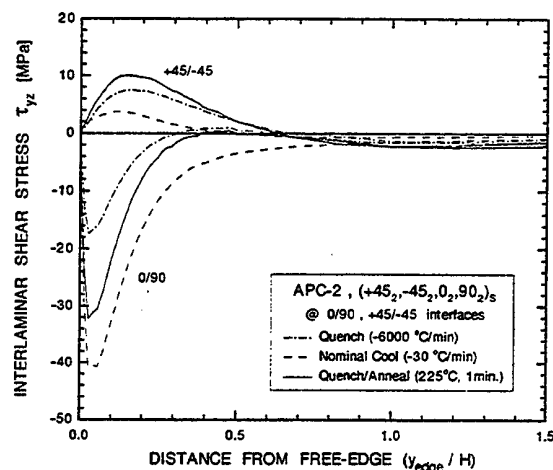


Figure 5: Effect of Thermal Process (Quench and Quench/Anneal versus Nominal Cool) on the Interlaminar Shear Stress τ_{yz} Distribution at 20°C along Various Interfaces of a Quasi-Isotropic $(+45_2, -45_2, 0_2, 90_2)_S$ APC-2 Laminate.

and structural parameters on the resulting buildup of residual stresses within the laminate.

A commonly-used APC-2 laminate configuration has been analyzed for various cooling rates from the molten state and in an annealing cycle. A significant reduction in the interlaminar free-edge stresses was obtained via application of a quench/anneal cycle in comparison to the recommended nominal cool, while maintaining a comparable and required crystallinity level in the matrix. This stress-reduction mechanism can contribute to enhanced static and fatigue strength, and therefore be beneficial in terms of structural performance of the laminate.

The results from the present study show that the present model can assist in the design and analysis of these laminates to tailor mechanical and strength characteristics. The degree of optimization offered by this model can therefore be of great benefit in terms of performance tailoring and weight-saving capabilities.

References

1. Nairn, J. A. and Zoller, P., The Development of Residual Thermal Stresses in Amorphous and Semicrystalline Thermoplastic Matrix Composites, Toughened Composites, ASTM STP 937, Philadelphia, PA, p. 328, 1987.
2. Unger, W.J. and Hansen, J.S., The Effect of Cooling Rate and Annealing on Residual Stress Development in Graphite Fibre Reinforced PEEK Laminates, Journal of Composite Materials, Vol. 27, No. 2, p. 108, 1993.
3. Domb, M.M., Analysis of Thermal Residual Stresses During Processing of Fibre-Re-

inforced Thermoplastic Composites, Ph.D. Thesis, Department of Aerospace Science and Engineering, University of Toronto, 1995.

4. Pipes, R.B. and Pagano, N.J., Interlaminar Stresses in Composite Laminates Under Uniform Axial Extension, Journal of Composite Materials, Vol. 4, p. 538, 1970.
5. Velisaris, C.N. and Seferis, J.C., Crystallization Kinetics of Polyether-ether-ketone (PEEK) Matrices, Polymer Engineering and Science, Vol. 26, No. 22, p. 1574, 1986.

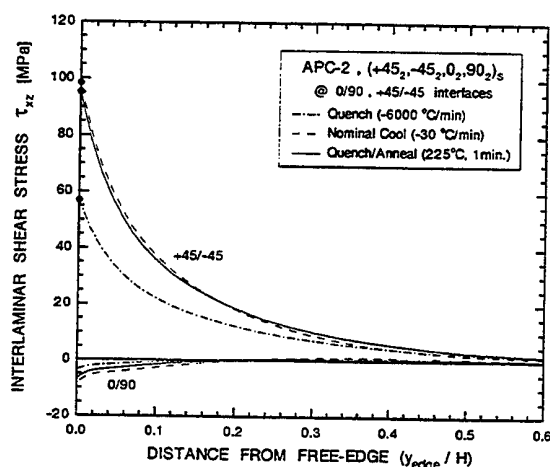


Figure 6: Effect of Thermal Process (Quench and Quench/Anneal versus Nominal Cool) on the Interlaminar Shear Stress τ_{xz} Distribution at 20°C along Various Interfaces of a Quasi-Isotropic $(+45_2, -45_2, 0_2, 90_2)_S$ APC-2 Laminate.

Session 1C

WAVE PROPAGATION I

Chair: K. L. Verma

Co-Chair: G. A. Harmain

**Stress-Focusing Effect in a Solid Cylinder Subjected to
Instantaneous Heating Based on the Theory of
Generalized Thermoelasticity**

X. F. Ding, T. Furukawa, and H. Nakanishi

Thermoelastic Soliton-Like Waves – A Survey

R. B. Hetnarski, J. Ignaczak

**Generalized Thermoelasticity in a Plate Subjected to
Partial Heating under Some Constraint Conditions**

T. Furukawa, M. Konishi, S. F. Ding, and H. Nakanishi

**Edge Waves in a Heat-Flux Dependent Micropolar
Thermo-Elastic Insulated Plate**

T. K. Chadha, Swaranjit Kaur

**A Nonstationery Rayleigh Wave on the Surface of a
Thermoelastic Heat-Insulated Torus**

Yuriy A. Rossikhin, Marina V. Shitikova

Stress-Focusing Effect in a Solid Cylinder Subjected to Instantaneous Heating Based on the Theory of Generalized Thermoelasticity

X.F. Ding, T. Furukawa and H. Nakanishi

*Department of Mechanical and System Engineering, Kyoto Institute of Technology,
Goshokaido-cho, Matsugasaki, Sakyo-ku, Kyoto 606, JAPAN*

When an isotropic and homogeneous solid cylinder is subjected to instantaneous heating at the surface, a stress wave at the surface proceeds radially inward to the center of the cylinder. The wave may accumulate at the center and give rise to very large stress magnitudes, even though the initial thermal stress is relatively small. This phenomenon is called the stress-focusing effect. In this paper, we use the fundamental equations of generalized thermoelasticity which include two different theories and treat the effects of these waves by means of the Laplace transform. The inversion of the Laplace transform is carried out numerically. The effects of the thermomechanical coupling and the relaxation times on the stress-focusing phenomena are examined.

Key words: Generalized Thermoelasticity, Stress-Focusing Effect, Stress Wave, Cylinder

1. Introduction

The analysis of a long cylindrical rod subjected to a sudden rise in temperature uniformly over its cross section has been studied by Ho [1] and Hata [2]. Due to the instantaneous heating, the stress waves reflected from the cylindrical surface of the rod may accumulate at the center and give rise to very high stresses, even though the initial thermal stress is relatively small. This phenomenon is called the stress-focusing effect.

The classical theory of dynamic thermoelasticity which takes into account the coupling effects between temperature and strain fields involves the infinite thermal wave speed. The theory of generalized thermoelasticity has been developed in an attempt to eliminate the paradox of the infinite velocity of thermal propagation. At present, there are two theories of the generalized thermoelasticity: the first is proposed by Lord and Shulman [3] (L-S theory), the second is proposed by Green and Lindsay [4] (G-L theory).

In this paper, we treat an isotropic and homogeneous infinitely long solid cylinder whose free surface is subjected to instantaneous heating. We use the fundamental equations of generalized thermo-

elasticity introduced by Noda et al. [5] which include the L-S theory and G-L theory. The Laplace transform technique is used and the inversion is carried out numerically. The effects of the thermomechanical coupling and the relaxation times on the stress-focusing phenomena are examined.

2. Analysis

We consider the one dimensional generalized thermoelasticity for an isotropic and homogeneous infinitely long cylinder of radius b . The cylinder is subjected to a sudden uniform temperature rise at the free surface. The fundamental equations which include the L-S and G-L theories consist of the heat conduction equation

$$\kappa \left(T_{,rr} + \frac{1}{r} T_{,r} \right) - (T + t_0 T_{,t})_{,t} = \frac{\delta}{\xi \alpha} \left[u_{,r} + \frac{u}{r} + \delta_{1k} t_0 (u_{,r} + \frac{u}{r})_{,t} \right]_{,t} \quad (1)$$

and the equation of motion represented by displacement component

$$u_{,rr} + \frac{1}{r} u_{,r} - \frac{u}{r^2} - \xi \alpha (T + t_1 T_{,r})_{,r} = \frac{1}{v_e^2} u_{,tt} \quad (2)$$

and the stress-strain-temperature relation

$$\begin{bmatrix} \sigma_{rr} \\ \sigma_{\theta\theta} \end{bmatrix} = 2\mu \begin{bmatrix} u_{,r} \\ u/r \end{bmatrix} + \lambda(u_{,r} + \frac{u}{r}) + (3\lambda + 2\mu)\alpha(T + t_1 T_{,t}) \quad (3)$$

Here u , T , σ_{rr} , $\sigma_{\theta\theta}$ are the radial displacement, temperature, radial stress and hoop stress, respectively, and λ and μ are Lamé's constants, α is the coefficient of linear thermal expansion, κ is thermal diffusivity, v_e is the velocity of propagation of longitudinal wave, $\xi = (1 + \nu)/(1 - \nu)$, ν is Poisson's

ratio, t_0 and t_1 are relaxation times, δ_{1k} is Kronecker's delta whose subscript k denotes the number of relaxation times, and δ is coupling parameter defined by

$$\delta = \frac{(3\lambda + 2\mu)^2 \alpha^2 \bar{T}}{(\lambda + 2\mu) \bar{\rho} c_v} \quad (4)$$

where \bar{T} is a reference temperature, $\bar{\rho}$ is density, c_v is the specific heat at constant volume. The comma indicate differentiation with respect to the independent variable indicated.

Let us introduce the following nondimensional variables

$$\begin{aligned} \rho &= \frac{r}{b}, \tau = \frac{\kappa t}{b^2}, \theta = \frac{T - T_0}{T_1 - T_0}, \beta = \frac{\kappa}{v_e b} \\ U &= \frac{u}{b\alpha(T_1 - T_0)}, t_0 = \frac{\kappa t_0}{b^2}, t_1 = \frac{\kappa t_1}{b^2} \quad (5) \\ \begin{bmatrix} \bar{\sigma}_{rr} \\ \bar{\sigma}_{\theta\theta} \end{bmatrix} &= \frac{1}{(\lambda + 2\mu)\alpha(T_1 - T_0)} \begin{bmatrix} \sigma_{rr} \\ \sigma_{\theta\theta} \end{bmatrix} \end{aligned}$$

Substituting these nondimensional variables to Eqs.(1), (2) and (3) and applying the Laplace transform denoted by asterisk (*) with parameter p under the initial condition

$$\tau = 0, \quad U = U_{,\tau} = 0, \quad \theta = \theta_{,\tau} = 0 \quad (6)$$

we have

$$\begin{bmatrix} \bar{\sigma}_{rr} \\ \bar{\sigma}_{\theta\theta} \end{bmatrix} = \begin{bmatrix} 1 \\ \eta \end{bmatrix} (U_{,\rho} + \frac{U}{\rho}) \pm (\eta - 1) \frac{U}{\rho} - \xi(1 + \tau_1 p) \theta^* \quad (7)$$

$$\begin{aligned} U_{,\rho\rho} + \frac{1}{\rho} U_{,\rho} - (\beta^2 p^2 + \frac{1}{\rho^2}) U^* \\ = \xi(1 + \tau_1 p) \theta_{,\rho}^* \end{aligned} \quad (8)$$

$$\begin{aligned} \theta_{,\rho\rho} + \frac{1}{\rho} \theta_{,\rho} - (1 + \tau_0 p) p \theta^* \\ = \frac{\delta}{\xi} (U_{,\rho} + \frac{U}{\rho}) (1 + \delta_{1k} \tau_0 p) p \end{aligned} \quad (9)$$

where $\eta = \nu / (1 - \nu)$.

From Eqs. (8) and (9), they follow that

$$\begin{aligned} U^* &= \xi(1 + \tau_1 p) [A_1 \xi_1 I_1(\xi_1 \rho) \\ &\quad + A_2 \xi_2 I_1(\xi_2 \rho)] \end{aligned} \quad (10)$$

$$\begin{aligned} \theta^* &= (\xi_1^2 - \beta^2 p^2) A_1 I_0(\xi_1 \rho) \\ &\quad + (\xi_2^2 - \beta^2 p^2) A_2 I_0(\xi_2 \rho) \end{aligned} \quad (11)$$

where A_1 and A_2 are integral constants and ξ_1 and

ξ_2 are the positive roots of the equation

$$\xi^4 - (B_0 p + B_1) p \xi^2 + (1 + \tau_0 p) \beta^2 p^3 = 0 \quad (12)$$

where

$$B_0 = \beta^2 + \tau_0 + \delta(\tau_1 + \delta_{1k} \tau_0), B_1 = 1 + \delta \quad (13)$$

Substituting Eqs.(10) and (11) into Eq.(7), the following equations can be obtained as

$$\begin{aligned} \begin{bmatrix} \bar{\sigma}_{rr} \\ \bar{\sigma}_{\theta\theta} \end{bmatrix} &= \xi(1 + \tau_1 p) \begin{bmatrix} 1 \\ \eta \end{bmatrix} [A_1 \xi_1^2 I_0(\xi_1 \rho) \\ &\quad + A_2 \xi_2^2 I_0(\xi_2 \rho)] \pm (\eta - 1) \frac{U}{\rho} - \xi(1 + \tau_1 p) \theta^* \end{aligned} \quad (14)$$

The boundary condition is represented by

$$r = b; \quad T = (T_1 - T_0) H(t) + T_0, \quad \sigma_{rr} = 0 \quad (15)$$

where $H(t)$ is Heaviside unit step function.

Substituting Eq.(5) to the above equation and applying Laplace transform, we obtain

$$\rho = 1; \quad \theta^* = \frac{1}{p}, \quad \bar{\sigma}_{rr} = 0 \quad (16)$$

Substituting Eqs.(10),(11) into Eq.(16) the unknown constants A_1, A_2 are obtained as

$$\begin{aligned} A_1 &= \frac{(\eta - 1) \xi_2 I_1(\xi_2) + \beta^2 p^2 I_0(\xi_2)}{(c_1 - c_2) p} \\ A_2 &= \frac{-[(\eta - 1) \xi_1 I_1(\xi_1) + \beta^2 p^2 I_0(\xi_1)]}{(c_1 - c_2) p} \end{aligned} \quad (17)$$

where

$$\begin{aligned} c_1 &= (\xi_1^2 - \beta^2 p^2) I_0(\xi_1) [\xi_2^2 I_0(\xi_2) + (\eta - 1) I_1(\xi_2) \xi_2] \\ c_2 &= (\xi_2^2 - \beta^2 p^2) I_0(\xi_2) [\xi_1^2 I_0(\xi_1) + (\eta - 1) I_1(\xi_1) \xi_1] \end{aligned} \quad (18)$$

Substituting Eq.(18) to Eqs.(10), (11) and (14), the solutions in the Laplace transform domain can be obtained.

3. Numerical Inversion of Laplace Transform

Let $F(p)$ be the Laplace transform of a function $f(t)$. The inversion formula for Laplace transform can be written as

$$f(t) = \frac{1}{2\pi i} \int_{d-i\infty}^{d+i\infty} e^{pt} F(p) dp \quad (19)$$

where d is an arbitrary real number greater than all the real parts of the singularities of $F(p)$.

We shall now outline two numerical methods used to find the solution in the physical domain.

The one is the Hosono's method [6]. The above integration is approximated the following infinite series form

$$f(t) = \frac{e^a}{t} \sum_{n=1}^{\infty} (-1)^n I_m \left\{ F\left(\frac{a + i(n-0.5)\pi}{t}\right) \right\} \quad (20)$$

where I_m represents the imaginary part. As the infinite series in Eq.(20) can only be summed up to a finite number N of terms, Euler's transformation is used to accelerate the convergence of the above series. We use Euler's transformation for last Np terms of this finite series.

The other method is proposed by Honig and Hirdes [7]. Taking $p=d+iy$, and expanding the function $h(t) = e^{-dt} f(t)$ in a Fourier series in the interval $[0, 2T]$, the approximate formula for the integral in Eq.(19) is presented by

$$f(t) = \frac{1}{2} c_0 + \sum_{n=1}^{\infty} \frac{e^{dt}}{T} \operatorname{Re} \left[e^{in\pi/T} F(d + in\pi/T) \right] + E_d \quad (21)$$

where E_d is the discretization error. As the infinite series in Eq.(21) can only be summed up to a finite number N of terms, the ε -algorithm is used to reduce the truncation error and, hence, to accelerate convergence.

4. Numerical Results

Numerical calculations are carried out for

$$\nu = 0.3, \beta = 0.01, \delta = 0.02$$

$$(L-S \text{ theory}) \quad \tau_0 = 5 \times 10^{-5}$$

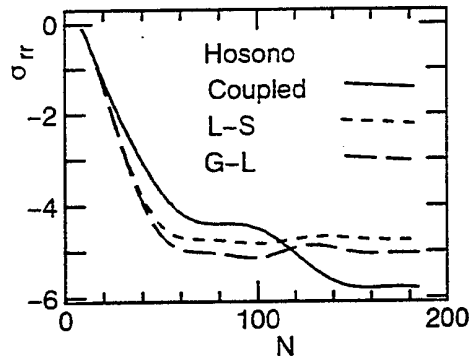
$$(G-L \text{ theory}) \quad \tau_0 = \tau_1 = 5 \times 10^{-5}$$

We adopt the parameters for Hosono as $a=8, Np=8$. The calculation for Honig and Hirdes is carried out by use of the subroutine program LAPIN appeared in their paper.

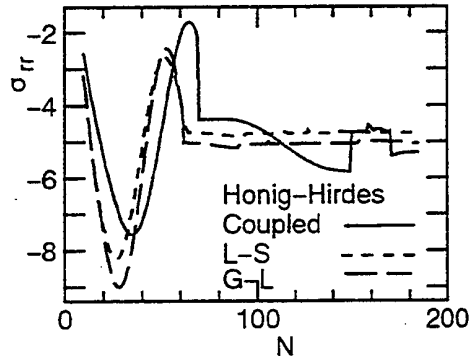
Figure 1 shows the relation between radial stress and the truncation term number for two numerical methods. The radial stresses for the position $\rho=0.01$

at the time when the first stress wave is reached are shown. From Fig. 1, we adopt the truncation term number $N=175$.

Figure 2 shows the radial stress distributions based on the coupled, L-S and G-L theories at various time before the first stress wave propagates to the

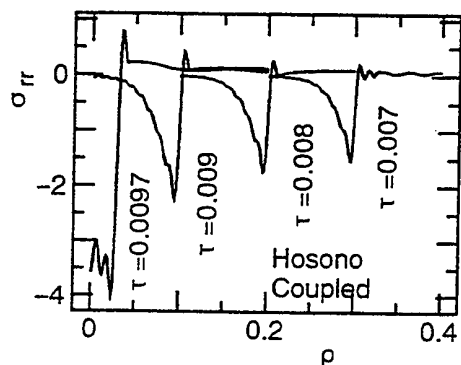


(a) Hosono's method

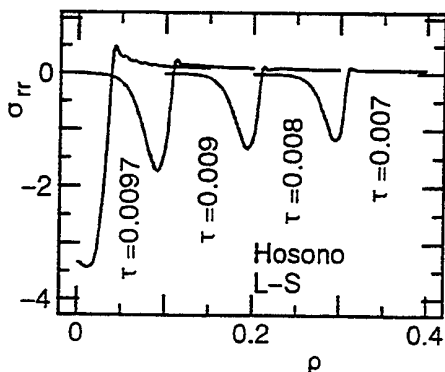


(b) Honig and Hirdes' method.

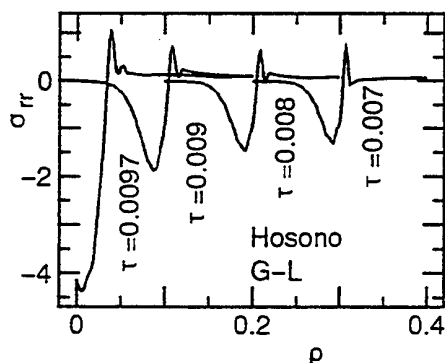
Fig.1 The relation between radial stress and truncation term number N .



(a) Coupled theory



(b) L-S theory



(c) L-S theory

Fig.2 Radial stress distribution

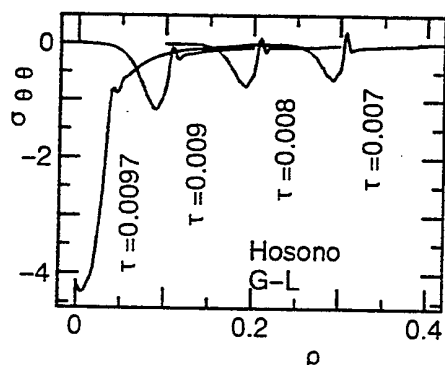


Fig. 3 Hoop stress distribution

center by use of Hosono's method. Large stress occurs as the stress wave front approaches to center. The hoop stress distribution based on the G-L theory are shown in Fig.3. The tendency of the hoop stress distribution is similar to that of the radial stress distribution.

The time variation of radial stress at the position $\rho = 0.01$ is shown in Fig. 4. The peak of stress appears periodically at interval $\tau = 0.02$.

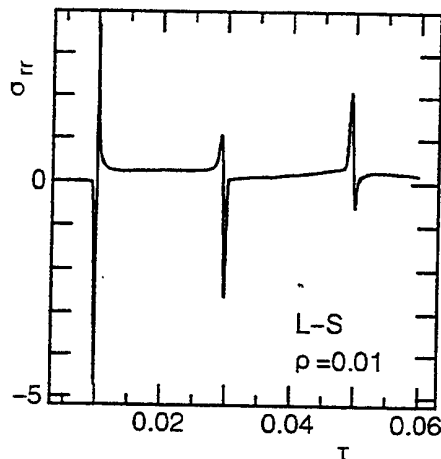


Fig. 4 Time variation of radial stress

References

- (1) Ho, C.-H., Stress Focusing Effect in a Uniformly Heated Cylindrical Rod, *J. Appl. Mech.*, Vol.43, p.464, 1976.
- (2) Hata, T., Reconsideration of the Stress-Focusing Effect in a Uniformly Heated Solid Cylinder, *J. Appl. Mech.*, Vol.61, p.676, 1994.
- (3) Lord, H.W. and Shulman, Y., A Generalized Dynamical Theory of Thermoelasticity, *J. Mech. Phys. Solids* Vol.15, p.299, 1967.
- (4) Green, A.E. and Lindsay, K.A., Thermoelasticity, *J. Elasticity*, Vol. 2, p.1, 1972.
- (5) Noda, N. Furukawa, T. and Fumihiro, A., Generalized Thermoelasticity in an Infinite Solid with a Hole, *J. Thermal Stresses*, Vol.12, p.385, 1989.
- (6) Hosono, T., Numerical Inversion of Laplace Transform and Some Application to Wave Optics, *Radio Sci.*, Vol. 16, p.1015, 1981.
- (7) Honig, G. and Hirdes, U., A Method for the Numerical Inversion of the Laplace Transform, *J. Comp. Appl. Math.*, Vol. 10, pp.113, 1984.

Thermoelastic Soliton-Like Waves – A Survey

R. B. Hetnarski* and J. Ignaczak**

* *Department of Mechanical Engineering, Rochester Institute of Technology,
Rochester, NY 14623, U.S.A.*

** *Center of Mechanics, Institute of Fundamental Technological Research,
Polish Academy of Sciences, Świętokrzyska 21, 00-049 Warsaw, Poland.*

One-dimensional soliton-like waves in a low-temperature nonlinear thermoelastic solid are reviewed. The thermoelastic solid is modeled within an extended nonlinear thermomechanics in which free energy and heat flux are generalized - in comparison to classical theory - to include an "elastic" heat flow that satisfies an evolution equation. When the absolute temperature T , heat flux q , and stress S depend on the space variable x and time t only, a soliton-like thermoelastic wave (T, q, S) is generated from a potential $\Phi = \Phi(x, t)$ and a displacement $u = u(x, t)$ ($|x| \leq \infty$, $t \geq 0$) that satisfy a nonlinear coupled system of partial differential equations subject to suitable end conditions at $x = \mp\infty$ for every $t \geq 0$. If $u \equiv 0$ and a thermoelastic coupling parameter vanishes, the nonlinear equations reduce to a single field equation for Φ that describes a soliton-like wave in a nonlinear rigid heat conductor. The survey focuses on soliton-like solutions to the nonlinear system of field equations as well as to the nonlinear single equation in a neighborhood of thermodynamical equilibrium when a low-temperature parameter is small. Explicit closed-form soliton-like waves that reveal "fountain" effect in a neighborhood of a wave front, as well as those represented by implicit solution to the nonlinear equations, are discussed.

Key Words: Generalized Nonlinear Thermoelasticity, Low Temperatures, Soliton-Like Waves.

1. Introduction

An attempt to describe low-temperature nonlinear thermoelastic waves has resulted in publication of a number of theoretical and experimental papers in this field. The survey covers theoretical results on low-temperature soliton-like thermal and thermoelastic waves. Most of the results were obtained by the present authors only recently. A nonlinear model of a homogeneous isotropic rigid heat conductor that has made significant impact on the development of these results was proposed in [1]. In that model both the free energy and the heat flux vector depend not only on the absolute temperature but also on "elastic" heat flow that satisfies an evolution equation. When this equation is combined with the energy conservation law one obtains a nonlinear coupled system of partial differential equations with a low-temperature parameter ω from which the absolute temperature and elastic heat flow fields are to be found. The model proposed in [1] was a starting point for writing the papers [2] and [3] in which problems of existence of low-temperature soliton-like thermal waves were discussed.

An attempt to generalize the nonlinear rigid heat conductor introduced in [1] to a nonlinear thermoelastic body in which soliton-like waves may propagate, has resulted in publication of papers [4], [5], and [6]. In the thermoelastic model both the free energy and the heat flux depend not only on the absolute temperature and the strain tensor but also on "elastic" heat flow that satisfies an evolution equation, and enters a modified Fourier law and a modified free energy formula through a linear term and a quadratic term, respectively. When the evolution equation is combined with the two laws of balance of forces and moments and with the geometric relations, a nonlinear coupled system of partial differential equations for the absolute temperature, displacement, and elastic heat flow, as unknown fields, is obtained. Apart from usual thermoelastic constants, a low-temperature parameter ω , similar to that of [1], is present in the nonlinear partial differential equations. In [4], soliton-like thermoelastic waves are discussed when $\omega = 1$. In [5] and [6] the results of [4] are generalized to include the case $\omega \in (0, 1]$, and obtain low-temperature soliton-like thermoelastic profiles for $\omega \rightarrow 0^+$.

It should be noted that a theory of nonlinear low-temperature waves propagating in a rigid heat conductor, based on a constitutive relation of Cattaneo type and a parabolic form of internal energy on the heat-flux axis, was proposed in [7]. Also, and extension of the theory in [7] to include a nonlinear thermoelastic model was given in [8]. However, no soliton-like waves were discussed in [7] and [8].

In Section 2 the fundamental system of field equations for a low-temperature nonlinear thermoelastic solid in terms of an elastic heat flow potential $\Phi = \Phi(x, t)$ and a displacement $u = u(x, t)$ is recalled, and associated initial-value problems are formulated. As a particular case, the governing equations and formulation for a low-temperature nonlinear rigid heat conductor are recovered. Section 3 is devoted to exact and approximate soliton-like solutions for a nonlinear thermoelastic solid, while in Section 4 soliton-like solutions for a nonlinear rigid heat conductor are reviewed.

2. Basic Field Equations

The model of a low-temperature nonlinear homogeneous thermoelastic solid appropriate for a one-dimensional case obeys the following dimensionless field equations (see eqs. (44) in [5]):

$$(\Phi_{tt} - \Phi_{txx} + \omega^2 \Phi_{tx}^2) \exp(-\omega \Phi_t) - \Phi_x \Phi_{xt} - \omega^{-1} [\Phi_{xx} + u_{xt} \exp(-\omega \Phi_t)] = 0 \quad (1)$$

$$\omega^{-1} (u_{xx} - \zeta^2 u_{tt}) + \epsilon^* \Phi_{xt} \exp(-\omega \Phi_t) = 0 \quad (2)$$

where $\Phi = \Phi(x, t)$ and $u = u(x, t)$ denote an elastic heat flow potential and a displacement in the x -direction, respectively, and t denotes time, while ω , ϵ^* , and ζ represent a low-temperature parameter, a generalized thermoelastic coupling constant, and an inertia parameter, respectively (see eqs. (23) in [5]). Subscripts are used for partial derivatives.

The absolute temperature $T = T(x, t)$, total heat flux $q = q(x, t)$, and stress $S = S(x, t)$ in the x -direction are given in terms of $\Phi = \Phi(x, t)$ and $u = u(x, t)$ by

$$T = \exp(-\omega \Phi_t) \quad (3)$$

$$q = \Phi_x + \omega \Phi_{xt} \exp(-\omega \Phi_t) \quad (4)$$

$$S = u_x - \epsilon^* [\exp(-\omega \Phi_t) - 1] \quad (5)$$

For the governing equations (1)-(2) the following Cauchy problem is formulated: Find a pair (Φ, u) that satisfies (1) and (2) with $|x| < \infty$, $t > 0$, subject to initial conditions

$$\begin{aligned} \Phi(x, 0) &= \Phi_0(x), \quad \Phi_t(x, 0) = \Phi_1(x) \\ u(x, 0) &= u_0(x), \quad u_t(x, 0) = u_1(x) \end{aligned} \quad (6)$$

where Φ_0 , Φ_1 , u_0 , and u_1 are prescribed functions suitably vanishing as $|x| \rightarrow \infty$. By virtue of eqs. (3)

and (4), a solution to the Cauchy problem generates a thermoelastic process (T, q, S) corresponding to the initial data

$$T(x, 0) = \exp[-\omega \Phi_1(x)] \quad (7)$$

$$q(x, 0) = \Phi'_0(x) + \omega \Phi'_1(x) \exp[-\omega \Phi_1(x)] \quad (8)$$

$$S(x, 0) = u'_0(x) - \epsilon^* \{\exp[-\omega \Phi_1(x)] - 1\} \quad (9)$$

where prime (') denotes a derivative with respect to x . If

$$(\Phi_1, \Phi'_1, \Phi'_0, u'_0)(x) \rightarrow (0, 0, 0, 0) \quad \text{as } |x| \rightarrow \infty$$

then

$$(T, q, S)(x, 0) \rightarrow (1, 0, 0) \quad \text{as } |x| \rightarrow \infty \quad (10)$$

Therefore, for suitably vanishing data at infinity, the Cauchy problem described by eqs. (1)-(2), and (6) complies with the initial thermodynamical equilibrium at which $T = 1$, $q = S = 0$ as $|x| \rightarrow \infty$. Also, note that if $\Phi_0 = \Phi_1 = u_0 = u_1 \equiv 0$ for $|x| \leq \infty$ and $\omega = 0$, the only solution to eqs. (1)-(2) subject to the conditions (6) is a trivial solution $(\Phi, u) = (0, 0)$ that corresponds to the thermodynamical equilibrium: $(T, q, S) = (1, 0, 0)$.

If $u = u(x, t) \equiv 0$ and $\epsilon^* = 0$, eqs. (1)-(5) reduce to those describing a low-temperature nonlinear rigid heat conductor (see eqs. (34) and (36) in [3], where ϵ is to be identified with ω of the present paper)

$$(\Phi_{tt} - \Phi_{txx} + \omega^2 \Phi_{tx}^2) \exp(-\omega \Phi_t) - \Phi_x \Phi_{xt} - \omega^{-1} \Phi_{xx} = 0 \quad (11)$$

$$T = \exp(-\omega \Phi_t) \quad (12)$$

$$q = \Phi_x + \omega \Phi_{xt} \exp(-\omega \Phi_t) \quad (13)$$

while the Cauchy problem given by eqs. (1)-(2), and (6) is formulated as follows: Find a function $\Phi = \Phi(x, t)$ that satisfies eq. (11) for $|x| < \infty$, $t > 0$, subject to the initial conditions

$$\Phi(x, 0) = \Phi_0(x), \quad \Phi_t(x, 0) = \Phi_1(x) \quad |x| < \infty \quad (14)$$

where Φ_0 and Φ_1 are prescribed functions.

A solution to the Cauchy problem stated by eqs. (11) and (14) generates a thermal process (T, q) corresponding to the initial conditions

$$T(x, 0) = \exp[-\omega \Phi_1(x)] \quad (15)$$

$$q(x, 0) = \Phi'_0(x) + \omega \Phi'_1(x) \exp[-\omega \Phi_1(x)] \quad (16)$$

and

$$(T, q)(x, 0) \rightarrow (1, 0) \quad \text{as } |x| \rightarrow \infty \quad (17)$$

if

$$(\Phi_1, \Phi'_0, \Phi'_1)(x) \rightarrow (0, 0, 0) \quad \text{as } |x| \rightarrow \infty \quad (18)$$

Clearly, if $\Phi_0 = \Phi_1 \equiv 0$ and $\omega = 0$, the only solution to eqs. (11) and (14) is a null solution $\Phi = 0$

corresponding to the thermodynamical equilibrium $(T, q) = (1, 0)$.

Existence and uniqueness theorems for the Cauchy problems (1)-(2), and (6); and (11) and (14) have not been formulated yet. The existence of particular soliton-like solutions to eqs. (1)-(2), and to eq. (11) is discussed in Sections 3 and 4, respectively.

3. Soliton-like thermoelastic waves

A solution (Φ, u) to eqs. (1)-(2) is sought in the form

$$\Phi = \Phi(s), \quad u = u(s) \quad (19)$$

where

$$s = x - vt \quad |s| \leq \infty \quad (20)$$

and v ($v > 0$) stands for a constant to be determined. Substituting eqs. (19) into eqs. (1)-(2) and (3)-(5), and eliminating u from eq. (1) by using eq. (2), results in the following equations

$$(\ddot{f} + v\dot{f} - f^2)\exp(-f) - (\omega v)^{-1}(1 + f)\dot{f} + \epsilon^* v(1 - \zeta^2 v^2)^{-1} \dot{f} \exp(-2f) = 0 \quad (21)$$

$$\frac{d}{ds} [\dot{u} - \epsilon^*(1 - \zeta^2 v^2)^{-1} \exp(-f)] = 0$$

and

$$T = \exp(-f), \quad q = \dot{f} \exp(-f) - (\omega v)^{-1} f$$

$$S = \dot{u} - \epsilon^* [\exp(-f) - 1] \quad (22)$$

where

$$f = f(s) = \omega \Phi_t = -\omega v \dot{\Phi} \quad (23)$$

and the superimposed dot stands for the derivative with respect to s ($\dot{} = d/ds$).

A soliton-like thermoelastic wave is defined as a triple (T, q, S) generated by a pair (f, \dot{u}) that satisfies the nonlinear equations (21) for $|s| < \infty$ subject to the boundary conditions

$$f(-\infty) = f(+\infty) = 0, \quad \dot{f}(-\infty) = \dot{f}(+\infty) = 0$$

$$\dot{u}(-\infty) = \dot{u}(+\infty) = 0 \quad (24)$$

The conditions (24) and eqs. (22) imply that

$$T(-\infty) = T(+\infty) = 1, \quad q(-\infty) = q(+\infty) = 0$$

$$S(-\infty) = S(+\infty) = 0 \quad (25)$$

Therefore, a soliton-like thermoelastic wave is represented by the localized constant profile functions $T = T(s)$, $q = q(s)$, and $S = S(s)$ on any plane $s = \text{const}$ propagating with a velocity v in the x -direction. Far away from the propagating plane the wave attains a thermodynamical equilibrium defined by $(T, q, S) = (1, 0, 0)$.

3.1 SOLITON-LIKE THERMOELASTIC WAVE OF ORDER ZERO

For a soliton-like wave of order zero

$$T = \exp(-\omega \Phi_t) \approx 1 - \omega \Phi_t \quad (26)$$

and eqs. (1)-(5), and (21)-(22) reduce to

$$\Phi_{xx} - \omega \Phi_{tt} + \omega(\Phi_{xx} + \frac{1}{2} \Phi_x^2)_t + u_{xt}(1 - \omega \Phi_t) = 0 \quad (27)$$

$$u_{xx} - \zeta^2 u_{tt} + \epsilon^* \omega \Phi_{xt} = 0$$

$$T = 1 - \omega \Phi_t, \quad q = \Phi_x + \omega \Phi_{xt}, \quad S = u_x + \epsilon^* \omega \Phi_t \quad (28)$$

and

$$\frac{d}{ds} [(c^2 - 1)f - \frac{1}{2}f^2 + c\omega^{1/2}\dot{f} + \frac{\epsilon^* c^2}{1 - \zeta^2 c^2} (f - \frac{1}{2}f^2)] = 0$$

$$\frac{d}{ds} [\dot{u} + \frac{\epsilon^*}{1 - \zeta^2 c^2} f] = 0 \quad (29)$$

$$T = 1 - f, \quad q = \dot{f} - (\omega v)^{-1} f, \quad S = \dot{u} + \epsilon^* f \quad (30)$$

where

$$c = v\omega^{1/2}, \quad \zeta = \zeta\omega^{-1/2} \quad (31)$$

while the boundary conditions remain as in (24).

3.2 SOLITON-LIKE THERMOELASTIC WAVE OF ORDER ONE

In this case T is approximated by

$$T = \exp(-\omega \Phi_t) \approx 1 - \omega \Phi_t + \frac{1}{2}(\omega \Phi_t)^2 \quad (32)$$

and eqs. (1)-(5) and (21)-(22) reduce to

$$\Phi_{xx} - \omega \Phi_{tt} + \omega(\Phi_{xx} + \frac{1}{2} \Phi_x^2)_t + u_{xt}(1 - \omega \Phi_t) - \frac{1}{2} \omega^2 [(\Phi_t^2)_{xx} - (\Phi_t^2)_t - u_{xt} \Phi_t^2] = 0 \quad (33)$$

$$u_{xx} - \zeta^2 u_{tt} + \epsilon^* \omega \Phi_{xt} - \frac{1}{2} \epsilon^* \omega^2 (\Phi_t^2)_x = 0$$

$$T = 1 - \omega \Phi_t + \frac{1}{2}(\omega \Phi_t)^2$$

$$q = \Phi_x + \omega \Phi_{xt} - \frac{1}{2} \omega^2 (\Phi_t^2)_x \quad (34)$$

$$S = u_x + \epsilon^* (\omega \Phi_t - \frac{1}{2} \omega^2 \Phi_t^2)$$

and

$$\frac{d}{ds} \{ (c^2 - 1)f - \frac{1}{2}f^2 + c\omega^{1/2} \frac{df}{ds} - \frac{1}{2} c\omega^{1/2} (\frac{d}{ds} + c\omega^{-1/2}) f^2 \}$$

$$+ \frac{c^2 \epsilon^*}{1 - \zeta^2 c^2} [(f - \frac{1}{2}f^2) - \frac{1}{2}(f - \frac{1}{2}f^2)^2] \} = 0 \quad (35)$$

$$\frac{d}{ds} \{ \frac{du}{ds} + \frac{\epsilon^*}{1 - \zeta^2 c^2} (f - \frac{1}{2}f^2) \} = 0$$

while the boundary conditions remain as given in eq. (24).

The soliton-like waves of order zero and one describe low-temperature thermoelastic disturbances for small ω . Soliton-like wave of order one is less restrictive than that of order zero.

It is shown that there are: (i) two implicit integral-form solutions to eqs. (21) and (24); (ii) two closed-form solutions to eqs. (29) and (24); and (iii) two implicit algebraic-form solutions to eqs. (35) and (24). It is also shown to what extent these solutions may be identified with the soliton-like thermoelastic waves. The solutions obtained in (ii) and (iii) are illustrated by a number of graphs.

4. Soliton-like thermal waves

These waves are obtained by a restriction in Section 3 to $u \equiv 0$ and $\epsilon^* = 0$. Therefore, a soliton-like thermal wave is described by a potential $\Phi = \Phi(x, t)$; $|x| < \infty$, $t > 0$, that satisfies eq. (11) subject to suitable end conditions; and the associated temperature $T = T(x, t)$ and heat flux $q = q(x, t)$ are given by eqs. (12) and (13), respectively.

Let

$$s = x - \frac{1}{\sqrt{\omega}} t \quad |s| \leq \infty \quad (36)$$

and look for a solution $\Phi = \Phi(s)$ to eq. (11). Then the following is obtained:

$$(\ddot{f} + \frac{1}{\sqrt{\omega}} \dot{f} - f^2) \exp(-f) - \frac{1}{\sqrt{\omega}} \dot{f}(1+f) = 0 \quad (37)$$

and

$$T = \exp(-f), \quad q = -\frac{1}{\sqrt{\omega}} f + \dot{f} \exp(-f) \quad (38)$$

where

$$f = f(s) = \omega \Phi_t = -\sqrt{\omega} \dot{\Phi} \quad (39)$$

A soliton-like thermal wave is defined as a pair (T, q) generated by a function $f = f(s)$ that satisfies the nonlinear equation (37) for $|s| < \infty$ subject to the boundary conditions

$$f(-\infty) = f(+\infty) = \dot{f}(-\infty) = \dot{f}(+\infty) = 0 \quad (40)$$

3.1 SOLITON-LIKE THERMAL WAVE OF ORDER ZERO

For a soliton-like thermal wave of order zero

$$T = \exp(-\omega \Phi_t) \approx 1 - \omega \Phi_t \quad (41)$$

and, with $c_0 = \frac{1}{\sqrt{\omega}}$, eqs. (11), (37)-(38) reduce to

$$\Phi_{xx} - \frac{1}{c_0^2} \Phi_{tt} + \frac{1}{c_0^2} (\Phi_{xx} + \frac{1}{2} \Phi_x^2)_t = 0 \quad (42)$$

$$\frac{d}{ds} (\dot{f} - \frac{1}{2\sqrt{\omega}} f^2) = 0 \quad (43)$$

$$T = 1 - f, \quad q = -\frac{1}{\sqrt{\omega}} f + \dot{f} \quad (44)$$

while the boundary conditions remain as given in eq. (40).

4.2 SOLITON-LIKE THERMAL WAVE OF ORDER ONE

In this case T is approximated by

$$T = \exp(-\omega \Phi_t) \approx 1 - \omega \Phi_t + \frac{1}{2} (\omega \Phi_t)^2 \quad (45)$$

and eqs. (11), and (37)-(38) reduce to

$$\begin{aligned} \Phi_{xx} - \frac{1}{c_0^2} \Phi_{tt} + \frac{1}{c_0^2} (\Phi_{xx} + \frac{1}{2} \Phi_x^2)_t \\ - \frac{1}{c_0^4} [(\Phi_t^2)_{xx} - (\Phi_t^2)_t] = 0 \end{aligned} \quad (46)$$

and

$$(1-f)\dot{f} - \frac{1}{\sqrt{\omega}} f^2 = 0 \quad (47)$$

$$T = 1 - f + \frac{1}{2} f^2, \quad q = -\frac{f}{\sqrt{\omega}} + \dot{f}(1-f) \quad (48)$$

while the boundary conditions are given by eq. (40).

It is shown that there is: (i) an implicit integral-form solution to eqs. (37) and (40); (ii) a closed form solution to eqs. (43) and (40); and (iii) an implicit algebraic-form solution to eqs. (47) and (40). Also, it is shown to what extent these solutions describe the soliton-like thermal waves.

REFERENCES

1. Ghoneim, H., and Dalo, D. N., Thermoviscoelasticity with Second Sound Effects, *J. Thermal Stresses*, Vol. 10, pp. 357-366, 1987.
2. Ignaczak, J., Solitons in a Nonlinear Rigid Heat Conductor, *J. Thermal Stresses*, Vol. 10, pp. 403-423, 1989.
3. Hetnarski, R. B., and Ignaczak, J., Soliton-Like Waves in a Low-Temperature Nonlinear Rigid Heat Conductor, *Int. J. Eng. Sci.*, Vol. 33, pp. 1725-1741, 1995.
4. Ignaczak, J., Soliton-Like Solutions in a Nonlinear Dynamic Coupled Thermoelasticity, *J. Thermal Stresses*, Vol. 13, pp. 73-98, 1990.
5. Hetnarski, R. B., and Ignaczak, J., Soliton-Like Waves in a Low-Temperature Nonlinear Thermoelastic Solid, *Int. J. Eng. Sci.*, Vol. 34, pp. 1767-1787, 1996.
6. Hetnarski, R. B., and Ignaczak, J., On Soliton-Like Thermoelastic Waves, submitted for publication in *Applicable Analysis*, special issue dedicated to the memory of G. Fichera.
7. Coleman, B. D., and Lai, P. H., Waves of Discontinuity and Sinusoidal Waves in the Theory of Second Sound in Solids, *Arch. Rational Mech. Anal.*, Vol. 126, pp. 1-20, 1994.
8. Oncu, T. S., and Moodie, T. B., Asymptotic Analysis of a Nonlinear Problem in Thermoelasticity, *Studies in Appl. Math.*, Vol. 93, pp. 163-186, 1994.

Generalized Thermoelasticity in a Plate Subjected to Partial Heating under Some Constraint Conditions

T. Furukawa*, M. Konishi**, X.F. Ding* and H. Nakanishi*

* *Department of Mechanical and System Engineering, Kyoto Institute of Technology,
Goshokaido-cho, Matsugasaki, Sakyo-ku, Kyoto 606, JAPAN*

** *Nagasaki Shipyard and Machinery Works, Mitsubishi Heavy Industries, Ltd.,
Akunoura-machi 1-1, Nagasaki 850-91, JAPAN*

This paper deals with the two dimensional generalized thermoelasticity based on the Lord and Shulman's theory and the Green and Lindsay's theory. The fundamental equations of generalized thermoelasticity which include both generalized theories are used. The generalized thermoelastic problems for a homogeneous and isotropic plate whose surfaces are traction free and subjected to a partial heating are analyzed by means of the Laplace transform and Fourier transform. The inversions of the Laplace transform and Fourier transform are carried out numerically. The numerical calculations for temperature and stresses under the generalized formulation are carried out.

Key Words: Generalized Thermoelasticity, Wave Propagation, Relaxation Time, Plate, Partial Heating

1. Introduction

The classical theory of dynamic thermoelasticity which takes into account the coupling between temperature and strain fields has been discussed in many papers. However, the dynamic coupled theory involves contradiction that thermal wave propagates at an infinite velocity. The theory of generalized thermoelasticity has been developed in an attempt to eliminate the paradox of the infinite velocity of thermal propagation. Therefore, the generalized theory is the dynamic coupled thermoelasticity which includes the time needed for acceleration of thermal wave.

At present there are two different theories of the generalized thermoelasticity: the first is proposed by Lord and Shulman [1] (L-S theory), the second is proposed by Green and Lindsay [2] (G-L theory). Furukawa et al. [3] used the fundamental equations of generalized thermoelasticity introduced by Noda et al. [4] which include the L-S theory and G-L theory and analyzed the one dimensional problem for a plate.

This paper deals with the two dimensional

generalized thermoelasticity for a homogeneous and isotropic plate based on the L-S theory and G-L theory. It is assumed that the plate is initially natural state. The surfaces of the plate are traction free and subjected to a partial heating. The temperature, displacement and stresses which satisfy the boundary conditions obtained by means of the Laplace transform and Fourier transform. The inversions of the Laplace transform and Fourier transform are carried out numerically.

2. Analysis

We consider the two dimensional generalized thermoelasticity for a homogeneous and isotropic plate of thickness l . The fundamental equations which include the L-S and G-L theories consist of the heat conduction equation

$$\kappa \nabla^2 T - (T + t_0 T_{,t})_{,t} = \frac{\delta}{m_1 \alpha} (e + \delta_{1k} t_0 e_{,t})_{,t} \quad (1)$$

and the equation of motion

$$\begin{aligned} \sigma_{xx,x} + \sigma_{xy,y} &= \rho u_{,tt} \\ \sigma_{xy,x} + \sigma_{yy,y} &= \rho v_{,tt} \end{aligned} \quad (2)$$

and the stress-strain-temperature relations

$$\begin{aligned} \begin{Bmatrix} \sigma_{xx} \\ \sigma_{yy} \\ \sigma_{zz} \end{Bmatrix} &= 2\mu \begin{Bmatrix} \varepsilon_{xx} \\ \varepsilon_{yy} \\ \varepsilon_{zz} \end{Bmatrix} + \lambda e \\ &\quad - (3\lambda + 2\mu)\alpha(T - T_0 + t_1 T_{,t}) \quad (3) \\ \sigma_{xy} &= 2\mu \varepsilon_{xy} \end{aligned}$$

where

$$\begin{aligned} \nabla^2 &= \frac{\partial^2}{\partial x^2} + \frac{\partial^2}{\partial y^2}, \quad m_1 = \frac{3\lambda + 2\mu}{\lambda + 2\mu} = \frac{1-\nu}{1+\nu} \\ \delta &= \frac{(3\lambda + 2\mu)^2 \alpha^2 T_0}{(\lambda + 2\mu) \rho c_v} \\ e &= \varepsilon_{xx} + \varepsilon_{yy} + \varepsilon_{zz} \quad (4) \end{aligned}$$

Here T : temperature, σ_{ij} : stress component, ε_{ij} : strain component, u, v : displacement components in the x and y directions respectively, t : time, κ : thermal diffusivity, α : coefficient of linear thermal expansion, δ : coupling parameter, ρ : density, c_v : specific heat at constant volume, λ, μ : Lamé's constants, ν : Poisson's ratio, T_0 : initial temperature, t_0, t_1 : relaxation times, δ_{1k} : Kronecker's delta whose subscript k denotes the number of relaxation times. The comma denotes the differentiation with following variable.

The strain components are

$$\begin{aligned} \varepsilon_{xx} &= u_{,x}, \quad \varepsilon_{yy} = v_{,y} \\ \varepsilon_{zz} &= c_1(y, t) + c_2(y, t)x \\ \varepsilon_{xy} &= \frac{1}{2}(u_{,y} + v_{,x}) \quad (5) \end{aligned}$$

where $c_1(y, t)$ and $c_2(y, t)$ are unknown function determined from z direction. We consider the conditions for z direction as follows:

(Case 1) The displacement are restrained.

(Case 2) The displacement are not restrained.

We introduce the following nondimensional quantities:

$$\begin{aligned} (X, Y) &= \frac{v_e}{\kappa}(x, y), \quad (\tau, \tau_0, \tau_1) = \frac{v_e^2}{\kappa}(t, t_0, t_1) \\ \theta &= \frac{T - T_0}{T_1 - T_0}, \quad (U, V) = \frac{v_e(u, v)}{\kappa\alpha(T_1 - T_0)}, \quad L = \frac{v_e}{\kappa}l \\ \bar{e} &= \frac{e}{\alpha(T_1 - T_0)}, \quad (C_1, C_2) = \frac{(c_1, c_2)}{\alpha(T_1 - T_0)} \\ (\sigma_{xx}, \sigma_{yy}, \sigma_{zz}, \sigma_{xy}) &= \frac{(\sigma_{xx}, \sigma_{yy}, \sigma_{zz}, \sigma_{xy})}{\mu\alpha(T_1 - T_0)} \quad (6) \end{aligned}$$

where v_e is the velocity of longitudinal wave given by $v_e = \sqrt{(\lambda + 2\mu)/\rho}$ and T_1 is the reference temperature.

Substituting these quantities and applying the Laplace transform defined by the relation

$$f^*(s) = \int_0^\infty f(\tau) \exp(-s\tau) d\tau \quad (7)$$

to Eqs.(1), (2) and (3), we have

$$\nabla^2 \theta^* - (1 + \tau_0 s) s \theta^* = \frac{\delta}{m_1} (1 + \delta_{1k} \tau_0 s) s e^* \quad (8)$$

$$\begin{aligned} \sigma_{xx,X}^* + \sigma_{xy,Y}^* &= m_2 s^2 U^* \\ \sigma_{xy,X}^* + \sigma_{yy,Y}^* &= m_2 s^2 V^* \quad (9) \end{aligned}$$

$$\begin{aligned} \sigma_{xx}^* &= m_2 U_{,X}^* + (m_2 - 2) V_{,Y}^* - m_1 m_2 (1 + \tau_1 s) \theta^* \\ &\quad - (m_2 - 2)(C_1^* + C_2^* X) \\ \sigma_{yy}^* &= m_2 V_{,Y}^* + (m_2 - 2) U_{,X}^* - m_1 m_2 (1 + \tau_1 s) \theta^* \\ &\quad - (m_2 - 2)(C_1^* + C_2^* X) \\ \sigma_{zz}^* &= (m_2 - 2)(U_{,X}^* + V_{,Y}^*) - m_1 m_2 (1 + \tau_1 s) \theta^* \\ &\quad - m_2 (C_1^* + C_2^* X) \\ \sigma_{xy}^* &= U_{,Y}^* + V_{,X}^* \quad (10) \end{aligned}$$

where the homogeneous initial conditions and the Eqs.(4) and (5) are used and

$$\nabla^2 = \frac{\partial^2}{\partial X^2} + \frac{\partial^2}{\partial Y^2}, \quad m_2 = \frac{\lambda + 2\mu}{\mu} = \frac{2(1-\nu)}{1-2\nu}$$

Substituting Eq.(10) into Eq.(9), we obtain

$$\begin{aligned} m_2 U_{,XX}^* + U_{,YY}^* + (m_2 - 1) V_{,XY}^* - m_2 s^2 U^* \\ = m_1 m_2 (1 + \tau_1 s) \theta_{,X}^* + (m_2 - 2) C_2^* \quad (11) \end{aligned}$$

$$\begin{aligned} m_2 V_{,YY}^* + V_{,XX}^* + (m_2 - 1) U_{,XY}^* - m_2 s^2 V^* \\ = m_1 m_2 (1 + \tau_1 s) \theta_{,Y}^* \\ + (m_2 - 2)(C_{1,Y}^* + C_{2,Y}^* X) \quad (12) \end{aligned}$$

We introduce the displacement potential ϕ and ψ defined by

$$U^* = \phi_{,X}^* + \psi_{,Y}^*, \quad V^* = \phi_{,Y}^* - \psi_{,X}^* \quad (13)$$

Substituting Eq.(13) and applying the Fourier transform defined by

$$\hat{f}(q) = \frac{1}{\sqrt{2\pi}} \int_{-\infty}^{\infty} f(y) \exp(-iqy) dy \quad (14)$$

to Eqs.(11) and (12), the following relations are obtained.

$$\begin{aligned} \hat{\phi}_{,XXXX}^* - (2q^2 + s_1) \hat{\phi}_{,XX}^* + (q^4 + q^2 s_1 + s_2) \hat{\phi}^* \\ = B_1 (C_1^* + C_2^* X) \quad (15) \end{aligned}$$

$$\hat{\psi}_{,XX}^* - (q^2 + m_2 s^2) \hat{\psi}^* = 0 \quad (16)$$

where

$$\begin{aligned} s_1 &= s\{1 + \delta + s[1 + \tau_0 + \delta(\delta_{1k} \tau_0 + \tau_1)]\} \\ s_2 &= (1 + \tau_0 s) s^3 \quad (17) \end{aligned}$$

$$B_1 = q^2 + s_1 - s^2 - 2(1 - \frac{1}{m_2})(q^2 + \frac{s_2}{s^2}) \quad (18)$$

The solutions of Eqs.(15) and (16) are

$$\hat{\phi}^* = m_1(1 + \tau_1 s)[A_{11} \exp(-k_1 X) + A_{12} \exp(k_1 X) + A_{21} \exp(-k_2 X) + A_{22} \exp(k_2 X)] + \frac{B_1}{q^4 + q^2 s_1 + s_2} (C_1^* + C_2^* X) \quad (19)$$

$$\hat{\psi}^* = m_1(1 + \tau_1 s)[A_{31} \exp(-k_3 X) + A_{32} \exp(k_3 X)] \quad (20)$$

where A_{ij} ($i=1,2,3; j=1,2$) are unknown constants determined from the boundary conditions and k_1 and k_2 are the positive roots of the equation

$$k^4 - (2q^2 + s_1)k^2 + q^4 + q^2 s_1 + s_2 = 0 \quad (21)$$

and expressed as

$$\begin{cases} k_1 \\ k_2 \end{cases} = \sqrt{\frac{1}{2}[2q^2 + s_1 \pm \sqrt{s_1^2 - 4s_2}]} \quad (22)$$

and k_3 is expressed as

$$k_3 = \sqrt{q^2 + m_2 s^2} \quad (23)$$

Similarly temperature is obtained as

$$\hat{\theta}^* = (k_1^2 - q^2 - s^2)[A_{11} \exp(-k_1 X) + A_{12} \exp(k_1 X)] + (k_2^2 - q^2 - s^2)[A_{21} \exp(-k_2 X) + A_{22} \exp(k_2 X)] - \frac{B_2}{q^4 + q^2 s_1 + s_2} (C_1^* + C_2^* X) \quad (24)$$

where

$$B_2 = \frac{-\delta s}{m_1} (1 + \delta_{1k} \tau_0 s) [2(1 - \frac{1}{m_2})q^2 + s^2] \quad (25)$$

Stress components are represented by displacement potentials as

$$\begin{aligned} \hat{\sigma}_{XX}^* &= (m_2 s^2 + 2q^2) \hat{\phi}^* + 2iq \hat{\psi}_{,X}^* \\ \hat{\sigma}_{YY}^* &= m_2 s^2 \hat{\phi}^* - 2 \hat{\phi}_{,XX}^* - 2iq \hat{\psi}_{,X}^* \\ \hat{\sigma}_{ZZ}^* &= (m_2 - 2)s^2 \hat{\phi}^* - 2m_1(1 + \tau_1 s) \hat{\theta}^* \\ &\quad - 4(1 - \frac{1}{m_2})(C_1^* + C_2^* X) \\ \hat{\sigma}_{XY}^* &= 2iq \hat{\phi}_{,X}^* - (m_2 s^2 + 2q^2) \hat{\psi}^* \end{aligned} \quad (26)$$

The unknowns C_1^* and C_2^* can be determined from the conditions for z direction.

Next we determine the remainder unknowns. As the surfaces of the plate are stress free, the next conditions are obtained

$$\begin{aligned} X=0; \quad \hat{\sigma}_{XX}^* &= \hat{\sigma}_{XY}^* = 0 \\ X=L; \quad \hat{\sigma}_{XX}^* &= \hat{\sigma}_{XY}^* = 0 \end{aligned} \quad (27)$$

We consider that the local heat source $r(y,t)$ is applied to the surface $x=l$. The thermal boundary condition represented by nondimensional form is

$$X=0; \quad \hat{\theta}_{,X}^* + H_a(1 + \tau_0 s) \hat{\theta}^* = 0 \quad (28)$$

$$X=L; \quad \hat{\theta}_{,X}^* + H_b(1 + \tau_0 s) \hat{\theta}^* = (1 + \tau_0 s) R^*$$

where H_a and H_b are Biot's numbers and R is the nondimensional form of the heat source r .

The remainder unknowns can be determined from Eqs.(27) and (28). The solutions for temperature, displacement and stresses are obtained in the Laplace and Fourier transformed domain.

3. Numerical Inversions of Laplace Transform and Fourier transform

We use the numerical method proposed by Hosono [3]. The inversion formula is presented by

$$f(\tau) \cong \frac{\exp(k)}{\tau} \sum_{n=1}^{N_h} (-1)^n \text{Im} \left\{ F \left(\frac{k}{\tau} + i \frac{n-0.5}{\tau} \pi \right) \right\} \quad (29)$$

We adopt the parameters as $k=6$ and $N_h=60$ by preliminary calculations.

We use the Fillon's method for the numerical inversion of Fourier transform represented by

$$f(y) \cong \frac{1}{\sqrt{2\pi}} \sum_{j=1}^{N_f} \int_{a_{2j-2}}^{a_{2j}} \hat{f}(q) \exp(iqy) dq \quad (30)$$

where $\hat{f}(q)$ is approximated to quadratic functions. We adopt the parameters as the upper limit $q=35$ and $N_f=115$ by preliminary calculations.

4. Numerical Results

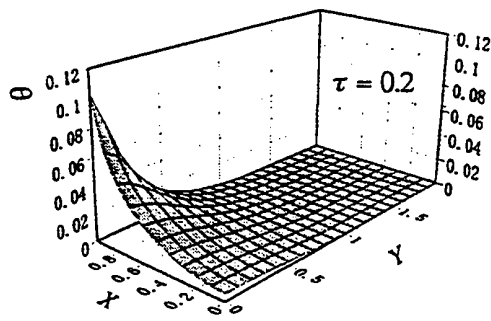
Numerical calculations are carried out for $\nu=0.3$, $H_a = H_b = 1$, $L=1$, $\delta=0.01$, $\tau_0=0.02$ and the heat source

$$R(Y, \tau) = \exp(-10|Y|) H(\tau) \exp(-\tau)$$

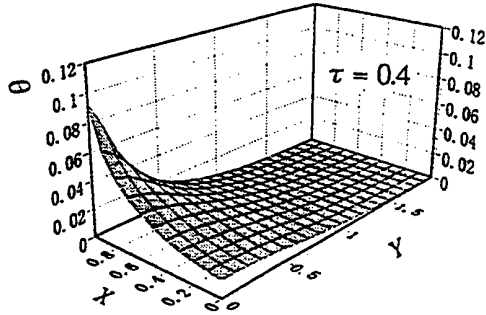
where $H()$ is Heaviside unit step function.

Figure 1 shows the temperature distributions for Case 1. The domain of influence of the heat source is spread over as increasing the time.

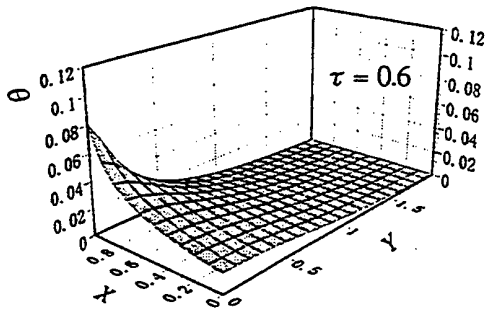
Figures 2 and 3 show the stress distributions σ_{XX} and σ_{YY} for Case 1, respectively.



(a) $\tau = 0.2$

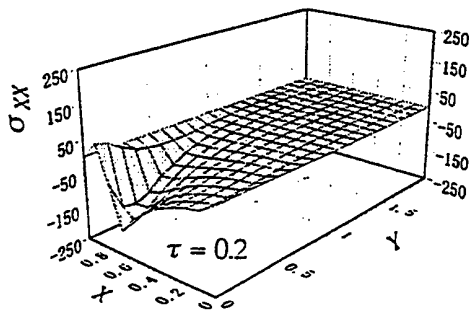


(b) $\tau = 0.4$



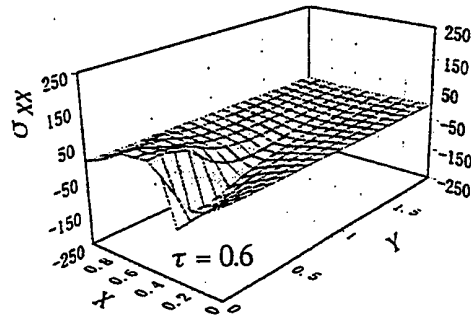
(c) $\tau = 0.6$

Fig. 1 Temperature distributions for Case 1.



(a) $\tau = 0.2$

The large variations occur at the time when the stress wave is arrived.



(b) $\tau = 0.6$

Fig. 2 Stress distributions σ_{xx} for Case 1

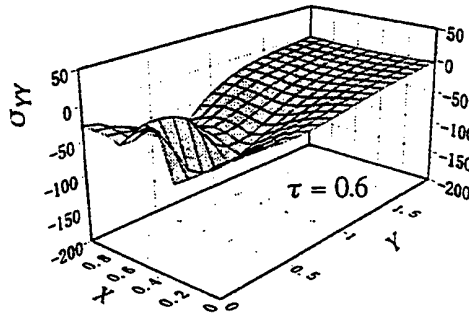


Fig. 3 Stress distributions σ_{yy} for Case 1.

References

- (1) Lord, H.W. and Shulman, Y., A Generalized Dynamical Theory of Thermoelasticity, J. Mech. Phys. Solids, Vol. 15, p.299, 1967.
- (2) Green, A.E. and Lindsay, K.A., Thermoelasticity, J. Elasticity, Vol. , p.1, 1972.
- (3) Noda, N., Furukawa, T. and Ashida, F., Generalized Thermoelasticity in an Infinite Solid with a Hole, J. Thermal Stresses, Vol.12, p.385, 1989.
- (4) Furukawa, T., Konishi, M., Ding, X. F. and Nakanishi, H., Generalized Thermoelasticity in One Dimensional Plate under Some Support Conditions, Thermal Stresses '95, p.283, 1995.
- (5) Hosono, T., Numerical Inversion of Laplace Transform and Some Applications to Wave Optics, Radio Sci., Vol. 16, p.1015, 1981.

Edge Waves in a Heat-Flux dependent Micropolar Thermo-elastic Insulated Plate

T.K. Chadha* and Swaranjit Kaur**

*Department of Mathematics, Guru Nanak Dev University, Amritsar, India

** S.R. Gout College for Women, Amritsar, India

Waves propagating along the edges of a thin plate of infinite length, which is in a state of plane stress are discussed for insulated edge conditions, lame's potentials are used to solve the system of the partial differential equations. The characteristic equations determining the phase speeds of symmetric and antisymmetric motions are derived. The cut-off frequencies are obtained for both cases. Frequency equation for a particular case of waves in a semi-infinite plate is derived and numerical results have been obtained to see the additional effect of micropolar on phase velocity. The results obtained are compared with earlier investigations.

Key Words : Thermal Stress, Micropolar, Thermoelasticity, Relaxation time.

1. Introduction

In recent years, many theories have been proposed to study the microstructural behaviour of the elastic solids. This theory is expected to find applications in the treatment of the mechanics of granular materials with elongated rigid grains and composite fibrous materials. Recent experiments by Gauthier and Jakesman [1] reveal that the micropolar waves can be excited and detected in typical solids, Yang and lakes [2] suggest, with a reasonable degree of confidence that human bone can adequately be used as a model for theory of micropolar elasticity.

Several attempts have been made to formulate generalized theory of thermoelasticity. Because of the experimental evidence available in favour of second sound effects, generalized thermoelasticity is of practical interest too. Chandrasekhariah [3] formulated generalized theory of micropolar thermoelasticity based upon Eringen's theory of micropolar elasticity [4] by including heat-flux among constitutive variables. Chandrasekhariah and Srikantiah [5] studied edge waves in a thermo-elastic plate in the context of temperature-rate-dependent thermoelasticity theory. In the present investigation, we have discussed edge waves in a heat-flux dependent micropolar thermo-elastic insulated plate in the context of theory proposed by Chandrasekhariah [3].

2. Basic Equations

We investigated plane waves which propagate along the edges of a plate, occupying the space

$$-\infty < x_1 < \infty, -H \leq x_2 \leq H, -L \leq x_3 \leq L.$$

We have assumed that both the faces $x_3 = \pm L$ and $x_2 = \pm H$ are stress free, couple stress free and are insulated. Then we have

$$\tau_{3i} = m_{3i} = \theta_{,3} = 0 \text{ on } x_3 = \pm L \quad (2.1)$$

$$\tau_{2i} = m_{2i} = \theta_{,2} = 0 \text{ on } x_2 = \pm H \quad (2.2)$$

where

$$\tau_{ij} = \lambda \delta_{ij} u_{k,k} + \mu (u_{i,j} + u_{j,i}) + k' \varepsilon_{ij} - \beta_T \theta \delta_{ij} \quad (2.3)$$

$$m_{ij} = \alpha' \xi_{k,k} \delta_{ij} + \beta' \xi_{i,j} + \gamma' \xi_{j,i} \quad (2.4)$$

$$\varepsilon_{ij} = u_{j,i} - \varepsilon_{ijr} \xi_r, \beta_T = (\lambda_1 + 2\lambda) a, \lambda_1 = (\lambda + 2\mu + k')$$

In these equations τ_{ij} are the components of force stress tensor, m_{ij} the components of couple stress, θ the temperature deviation above the uniform temperature $\theta_0 > 0$, u_α are the components of displacement, ξ microrotation vector, λ and μ Lamé's constants, α' , β' , γ' , k' micropolar constants, a the coefficient of linear thermal expansion, $\varepsilon_{\alpha\beta\gamma}$ the alternating tensor, $(\cdot)_{,j} = \partial(\cdot)/\partial x_j$.

It is assumed that plate is very thin, then (2.1) takes the form

$$\tau_{3i} = m_{3i} = \theta_{,3} = 0 \quad (2.5)$$

throughout the plate. Consequently, the plate remains in the state of plane stress and following the usual procedure, the equations of motion for an isotropic, homogeneous, micropolar thermoelastic material proposed by Chandrasekhariah [3] reduce to the following

$$(\mu + \lambda^*) u_{\beta,\alpha\beta} + \lambda_3 u_{\alpha,\beta\beta} - \beta^* \theta_{,\alpha} + k' \varepsilon_{\alpha\beta\gamma} \xi_{\gamma,\beta} = \rho \ddot{u}_\alpha \quad (2.6)$$

$$\gamma' \xi_{3,\beta\beta} + k' (u_{2,1} - u_{1,2}) - 2k' \xi_3 = \rho J \ddot{\xi}_3 \quad (2.7)$$

$$\theta_{,\alpha\alpha} = \theta_0 (1 + \tau_0 \partial/\partial t) (c^* \theta + \beta^* u_{\alpha,\alpha}) / k \quad (2.8)$$

$$\tau_{\alpha\beta} = \lambda^* \varepsilon_{\alpha\beta\gamma} \delta_{\alpha\beta} + (\mu + k') \varepsilon_{\alpha\beta} + \mu \varepsilon_{\beta\alpha} - \beta^* \theta \delta_{\alpha\beta},$$

$$m_{\alpha\beta} = \alpha' \xi_{\gamma,\gamma} \delta_{\alpha\beta} + \beta' \xi_{\alpha,\beta} + \gamma' \xi_{\beta,\alpha}$$

where

$$\vec{\xi} = (0, 0, \xi_3), \lambda^* = \lambda \lambda_2 / \lambda_1, \beta^* = \beta_T \lambda_2 / \lambda_1,$$

$$c^* = c(1 + \varepsilon), \varepsilon = \beta_T^2 / c \lambda_1, \lambda_2 = (2\mu + k'), \lambda_3 = \mu + k',$$

$$(\cdot) = \partial(\cdot)/\partial t, \alpha, \beta, \gamma = 1, 2.$$

In these equations J is rotational inertia, τ_0 relaxation time, ρ density, k thermal conductivity, c the specific heat at the constant strain.

Using $u_1 = \phi_{,1} + \psi_{,2}$, $u_2 = \phi_{,2} - \psi_{,1}$, where ϕ , ψ and ξ are functions of x_1 , x_2 and t , equations (2.6) - (2.8) reduce to

$$[\nabla^2 - (1/p^2) (\partial^2/\partial t^2)] \phi = \beta^* \theta / \rho p^2 \quad (2.9)$$

$$[\nabla^2 - (1/b^2) \partial^2/\partial t^2] \psi = -k^* \xi_3 / \lambda_3 \quad (2.10)$$

$$\{[\nabla^2 - (1/p^2) \partial^2/\partial t^2] \{ \nabla^2 - (1 + \tau_0 \partial/\partial t) (\theta_0/k^* \rho) \partial/\partial t \} - (1 + \tau_0 \partial/\partial t) (\varepsilon^*/k^*) \nabla^2 \partial/\partial t\} \phi = 0 \quad (2.11)$$

$$\{[\nabla^2 - (1/b^2) \partial^2/\partial t^2] \{ \nabla^2 - (2k^*/\gamma) - (\rho J/\gamma) \partial^2/\partial t^2 \} + (k^2/\gamma \lambda_3) \nabla^2\} \psi = 0 \quad (2.12)$$

where,

$$p^2 = (\lambda^* + \lambda_2) / \rho, k_1^* = k/\rho c^*,$$

$$\varepsilon_2^* = \beta^* \theta_0 / \rho^2 p^2 c^*, \nabla^2 = \partial^2/\partial x_1 \partial x_2, b^2 = (\mu + k^*)/\rho.$$

3. Solution of the problem

We take

$$\{\phi, \psi\} = \{\phi_0(x_2), \psi_0(x_2)\} \exp [i(\gamma_0 x_1 - \omega t)] \quad (3.1)$$

Here $\gamma_0 = \gamma_1 + i\gamma_2$, is complex number. ω is the angular frequency. Only real parts of (3.1) are physically relevant. Using (3.1) into (2.11) and (2.12) we get

$$\phi_0 = A_1 c_1^m + A_2 c_2^m + B_1 s_1^m + B_2 s_2^m \quad (3.2)$$

$$\psi_0 = A_3 s_1^1 + A_4 s_2^1 + B_3 c_1^1 + B_4 c_2^1 \quad (3.3)$$

where $A_1, A_2, A_3, A_4, B_1, \dots, B_4$ are arbitrary constants,

$$c_\alpha^m = \cosh m_{\alpha\alpha} x_2, s_\alpha^m = \sinh m_{\alpha\alpha} x_2, s_\alpha^1 = \sinh l_{\alpha\alpha} x_2,$$

$$c_\alpha^1 = \cosh l_{\alpha\alpha} x_2.$$

Here m_{01}, m_{02} are the complex roots of the equation

$$(\gamma_0^2 - m_0^2)^2 - [\omega^2/p^2 + (i\omega\theta_0/k^* \rho) \{1 + (\varepsilon^* \rho/\theta_0) - i\omega\tau_0(1 + \rho\varepsilon^*/\theta_0)\}] (\gamma_0^2 - m_0^2) + (i\theta_0\omega^3/\rho k^* p^2)(1 - i\omega\tau_0) = 0 \quad (3.4)$$

and l_{01} and l_{02} are the complex roots of the equation

$$(\gamma_0^2 - l_0^2)^2 - [(\omega^2/b^2) + (\rho J\omega^2/\gamma) - (2k^*/\gamma)] + (k^2/\gamma \lambda_3) (\gamma_0^2 - l_0^2) + (\omega^2/b^2) [(\rho J\omega^2 - 2k^*)/\gamma] = 0 \quad (3.5)$$

With the aid of (3.1) - (3.3), we get the following relations

$$\begin{aligned} u_1 &= (A_1 f_1 + B_1 g_1) \exp \{i(\gamma_0 x_1 - \omega t)\} \\ u_2 &= (A_1 f_2 + B_1 g_2) \exp \{i(\gamma_0 x_1 - \omega t)\} \\ \theta &= (A_1 f_3 + B_1 g_3) \exp \{i(\gamma_0 x_1 - \omega t)\} \\ \xi_3 &= (A_1 f_4 + B_1 g_4) \exp \{i(\gamma_0 x_1 - \omega t)\} \end{aligned} \quad (3.6)$$

where f_i and g_i are functions of x_2 ,

$$f_1 = i\gamma_0 (c_1^m - A_0' c_2^m) + (A_3/A_1) l_{01} c_1^1 + (A_4/A_1) l_{02} c_2^1$$

$$f_2 = m_{01} s_1^m - A_0' m_{02} s_2^m - i\gamma_0 [(A_3/A_1) s_1^1 + (A_4/A_1) s_2^1]$$

$$f_3 = (\rho p^2/\beta^*) (n_1 c_1^m - A_0' n_2 c_2^m)$$

$$f_4 = -(\lambda_3/k^*) [(A_3/A_1) n_3 s_1^1 + (A_4/A_1) n_4 s_2^1],$$

$$n_\alpha = m_{0\alpha}^2 - \gamma_0^2 + \omega^2/p^2, n_3 = l_{01}^2 + (\omega^2/b^2) - \gamma_0^2,$$

$$n_4 = l_{02}^2 + (\omega^2/b^2) - \gamma_0^2, A_0' = -(A_2/A_1),$$

g_1, g_2, g_3, g_4 are obtained from f_1, f_2, f_3, f_4 , by replacing A_0', A_1, A_3, A_4 by B_0', B_1, B_3, B_4 ; \cosh by \sinh and \sinh by \cosh respectively.

Since u_α , θ and ξ_3 are to be purely real, taking real parts in the right hand side of (3.6) and eliminating the trigonometric functions, we arrive at the following expressions

$$\begin{aligned} &(G_2' u_1 - F_2' u_2)^2 + (G_1' u_1 - F_1' u_2)^2 \\ &= (F_1' G_2' - F_2' G_1')^2 \exp(-2\gamma_2 x_1), \\ &(G_2' \xi_3 - H_2' u_2)^2 + (G_1' \xi_3 - H_1' u_2)^2 \\ &= (H_1' G_2' - H_2' G_1')^2 \exp(-2\gamma_2 x_1), \\ &(F_2' \xi_3 - H_2' u_1)^2 + (F_1' \xi_3 - H_1' u_1)^2 \\ &= (H_1' F_2' - H_2' F_1')^2 \exp(-2\gamma_2 x_1), \end{aligned} \quad (3.7)$$

where $F(x_2) = A_1 f_1 + B_1 g_1$, $G(x_2) = A_1 f_2 + B_1 g_2$,

$$H(x_2) = A_1 f_4 + B_1 g_4.$$

4. Frequency Equation

The boundary and thermal conditions (2.2) reduced to $\tau_{21} = \tau_{22} = \theta_{,2} = m_{23} = 0$ on $x_2 = \pm H$.

Using these edge conditions, eliminating constants A_1, \dots, A_4 and B_1, \dots, B_4 and introducing dimensionless variables, we get the following frequency equations

$$\begin{aligned} &\text{(i) FOR SYMMETRIC MOTION} \\ &\Gamma^2 k_1^2 M_1 M_2 s_1' s_2' L_1' L_2' c_{01}' c_{02}' \Omega^2 (N_1^2 - N_2^2) (N_4^2 - N_3^2) \\ &+ \Omega^2 [k_1 \Gamma^2 - (k_1 - 1) \Omega^2]^2 [M_2 s_2' c_1' (1 - N_2^2) \\ &- M_1 s_1' c_2' (1 - N_1^2)] T_1 = 0 \end{aligned} \quad (4.1)$$

$$\begin{aligned} &\text{(i) FOR ANTISYMMETRIC MOTION} \\ &\Gamma^2 k_1^2 M_1 M_2 c_1' c_2' L_1' L_2' s_{01}' s_{02}' \Omega^2 (N_1^2 - N_2^2) (N_4^2 - N_3^2) \\ &+ \Omega^2 [k_1 \Gamma^2 - (k_1 - 1) \Omega^2]^2 [M_2 s_2' c_1' (1 - N_2^2) \\ &- M_1 c_1' s_2' (1 - N_1^2)] T_2 = 0 \end{aligned} \quad (4.2)$$

We find from equations (3.4) and (3.5) that N_1 and N_2 satisfy the equation

$$N^4 - N^2 [1 - (1 + \varepsilon_0') / \Omega_0] - (1/\Omega_0) = 0 \quad (4.3)$$

and, N_3 and N_4 satisfy the equation

$$N^4 - N^2 [1 + J^* + H^*] + J^* = 0, \quad (4.4)$$

where, $\Gamma = \gamma H$, $\Omega = \omega H/b$, $V = \Omega b/\Gamma$, $L'_\alpha = l_{\alpha\alpha} H$,
 $M_\alpha = m_{\alpha\alpha} H$, $N_\alpha^2 = 1 - (p^2 n_\alpha / \omega^2)$, $N_{3,4}^2 = 1 - (b^2 n_{3,4} / \omega^2)$
 $\Omega_0 = i\Omega b k_1^* \rho / \theta_0 p^2 (H - i\Omega b \tau)$, $\varepsilon'_0 = \varepsilon_0^* \rho / \theta_0$,
 $J^* = (\rho J b^2 \Omega^2 - 2k^* H^2) / \Omega^2 \gamma'$, $H^* = k_1^* H^2 / \Omega^2 \gamma' (\mu + k)$,
 $T_1 = (1 - N_4^2) L'_2 s'_{01} c'_{02} - (1 - N_3^2) L'_1 s'_{02} c'_{01}$
 $T_2 = (1 - N_4^2) L'_2 s'_{02} c'_{01} - (1 - N_3^2) L'_1 s'_{01} c'_{02}$,
 $s'_\alpha = \sinh m_{\alpha\alpha} H$, $c'_\alpha = \cosh m_{\alpha\alpha} H$, $s'_{\alpha\alpha} = \sinh l_{\alpha\alpha} H$,
 $k_1 = 2 + (k'/\mu)$, $c_{\alpha\alpha}' = \cosh l_{\alpha\alpha} H$
 $L'^2_{1,2} = \Gamma^2 [1 - (V^2 N_{3,4}^2 / b^2)] = \Gamma^2 - \Omega^2 N_{3,4}^2$

We notice that the equations (4.1) and (4.2) may be regarded as equations connecting V and Γ . Accordingly, each of these equations, being transcendental, yields infinitely many discrete roots for V in terms of Γ , each root corresponding to a mode of vibration. Both symmetric and antisymmetric motions are obviously dispersive and the analysis of their behaviour in the general case is quite complicated. However, it is possible to obtain readily the cut-off frequencies by setting $\Gamma = 0$ in the frequency equations. The cut-off frequencies are governed by the following equations :

(i) FOR SYMMETRIC MOTIONS

$$N_2 (1 - N_2^2) \tan(\Omega b N_2/p) = N_1 (1 - N_1^2) \tan(\Omega b N_1/p) \quad (4.5)$$

$$N_4 (1 - N_4^2) \tan(\Omega N_4) = N_3 (1 - N_3^2) \tan(\Omega N_4) \quad (4.6)$$

(ii) FOR ANTISYMMETRIC MOTIONS

$$N_2 (1 - N_2^2) \tan(\Omega b N_1/p) = N_1 (1 - N_1^2) \tan(\Omega b N_2/p) \quad (4.7)$$

$$N_4 (1 - N_4^2) \tan(\Omega N_4) = N_3 (1 - N_3^2) \tan(\Omega N_4) \quad (4.8)$$

5. Limiting Case

For particular case, we have considered waves in a semi-infinite plate for large values of H . We suppose that

$$|\Gamma| > (b\Omega/p) |N_{1,2}|, \quad |\Gamma| > \Omega |N_{3,4}|, \quad \Omega \rightarrow \infty \quad (5.1)$$

Using these assumptions, equations (4.1) and (4.2) reduced to

$$-\Gamma^2 k_1^2 M_1 M_2 L'_1 L'_2 (M_1 + M_2) (L'_1 + L'_2) + [k_1 \Gamma^2 - (k_1 - 1) \Omega^2] [(\Omega^2 b^2 / p^2) - \Gamma^2 + (M_1^2 + M_2^2 + M_1 M_2)] [\Omega^2 - \Gamma^2 + (L_1'^2 + L_2'^2 + L_1 L_2')] = 0 \quad (5.2)$$

For $\Omega \rightarrow \infty$, the roots of equation (4.3) are given by

$$N_1^2 = 1 - (\varepsilon'_0 / \Omega_0), \quad N_2^2 = -(1 / \Omega_0) \quad (5.3)$$

provided the terms containing $1/\Omega_0^2$, $1/\Omega_0^3$ and $1/\Omega_0^4$ are neglected.

The roots of the equation (4.4) are given by

$$N_3^2 = 1 + H^*, \quad N_4^2 = J^* \quad (5.4)$$

Using (5.3) and (5.4) in (5.2), we get

$$-k_1^2 \tau_0^* H_0^* J_0^* [1 - (V^2 / V_0^2)]^{1/2} [\tau_1^* + \{1 - (V^2 / V_0^2)\}^{1/2}] (H_0^* + J_0^*) + [k_1 - (k_1 - 1) (V^2 / b^2)]^2 [1 - (V^2 / V_0^2)] \{1 + (\tau_0^* V_0^2 / p^2)\} + \tau_1^* \{1 - (V^2 / V_0^2)\}^{1/2} W_0^* = 0 \quad (5.5)$$

In the above equations, we have used, $\Omega_0 = - (V_0^2 / p^2)$,

$$\varepsilon'_0 = (\varepsilon_0^* \rho / \theta_0), \quad \tau_0^* = - (\varepsilon_0^* / \Omega_0), \quad \tau_1^* = (M_1 / \Gamma),$$

$$J_0^* = (L_2' / \Gamma), \quad H_0^* = (L_1' / \Gamma), \quad W_0^* = [1 - (V^2 / b^2)] (H^* + J^*) + J_0^* H_0^*$$

The equation (5.5) is the phase velocity equation for insulated edge conditions in a semi infinite plate.

6. Numerical results and discussion

Numerical results for a particular model having following values of parameters have been obtained in case of semi infinite plate :

$$\lambda = 5.17 \times 10^{11}, \quad \mu = 2.44 \times 10^{11}, \quad \rho = 2.638,$$

$$c_t = .2096, \quad a_t = .0421105 \times 10^{-6}, \quad \theta_0 = 20,$$

$$k = .337284$$

It is clear from Table 1 that longitudinal speed (p) and shear speed (b) increases as micropolar effect increases. As in classical theory, we see that speed of shear waves is always less than the speed of longitudinal waves for all values of k' . From Table 2 to Table 4, we observe that for fixed value of τ_0 , phase velocity increases as k' increases and for fixed value of k' , phase velocity decreases as τ_0 increases. It is seen that the speed of edge waves changes its trend, when we take into account microstructure of the material as well as relaxation time.

We get only one equation of the path in case of generalized thermoelasticity [5], but here we have obtained three equations (3.7). From these three equations of path, we get the similar type of result that size and shape of the orbits vary from one point to another and they decay with the advancement of the waves.

It is evident that the cut-off frequencies determined by equations are effected by the thermal field as well as micropolar field. These equations are similar as obtained in [5], but values of parameters involved are different. As in [5], from (5.5), here also waves are not dispersive but are influenced by the finiteness of the heat propagation speed. If we set $\tau_0^* = J^* = H^* = k' = 0$, then (5.8) reduce to the phase velocity equation of waves of classical elasticity.

Table 1.		
k'	p	b
0	5.292938×10^5	3.041287×10^5
$.002 \times 10^{11}$	5.293843×10^5	3.042533×10^5
$.005 \times 10^{11}$	5.295202×10^5	3.044402×10^5
$.008 \times 10^{11}$	5.296559×10^5	3.046269×10^5

Table 2.		
τ_0	k'	v
$.19839 \times 10^{-14}$	$.002 \times 10^{11}$	2.799561×10^5
$.19839 \times 10^{-14}$	$.005 \times 10^{11}$	2.801997×10^5
$.19839 \times 10^{-14}$	$.008 \times 10^{11}$	2.804431×10^5

Table 3.		
τ_0	k'	v
$.49508 \times 10^{-14}$	$.002 \times 10^{11}$	2.79955675×10^5
$.49508 \times 10^{-14}$	$.005 \times 10^{11}$	2.80199317×10^5
$.49508 \times 10^{-14}$	$.008 \times 10^{11}$	2.80442532×10^5

Table 4.		
τ_0	k'	v
$.73916 \times 10^{-14}$	$.002 \times 10^{11}$	2.79955303×10^5
$.73916 \times 10^{-14}$	$.005 \times 10^{11}$	2.80198945×10^5
$.73916 \times 10^{-14}$	$.008 \times 10^{11}$	2.80442209×10^5

References

- 1 Gauthier and Jaksman : Arch. Mech. 33, 717 (1981).
- 2 Yang and Lakes : J. Bio. Mech. 15, 91 (1982).
- 3 Chandrasekhariah : Int. J. Engng. Sci. Vol. 24, No. 8, 1389-1395 (1986).
- 4 Eringen A.C. : J. Math. and Mech. Vol. 15, p. 909, (1966).
- 5 Chandrasekhariah and Srikantiah : Int. J. Engng. Sci., 23, 65-77, (1985).

A Nonstationary Rayleigh Wave on the Surface of a Thermoelastic Heat-Insulated Torus

Yuriy A. Rossikhin and Marina V. Shitikova

*Voronezh State Academy of Construction and Architecture,
ul. Kirova 3-75, Voronezh 394018, Russia, MVS@vgasa.voronezh.su*

The effect of heat conduction on the propagation of a surface wave polarized in the sagittal plane along the surface of a torus is investigated. The modified Maxwell law is used instead of the Fourier law of heat conduction in order to take into consideration that small time what is necessary for the establishment of stationary heat conduction after the sudden occurrence of temperature gradient in a solid. The nonstationary surface wave is interpreted as the line on which temperature and components of the stress and strain tensors experience a discontinuity. The discontinuity line propagates with a constant normal velocity across the free from stresses and heat-insulated surface of the torus and is obtained by the exit onto the torus surface of the three strong discontinuity complex wave surfaces intersecting along this line: quasi-thermal, quasi-longitudinal and quasi-transverse volume waves. Applying the theory of discontinuities and using the kinematic, geometric and dynamic conditions of compatibility, the velocity and the intensity of the surface wave have been found. It has been shown that attenuation of the surface wave intensity is determined by the two factors: a consideration of the related strain and temperature fields and the change in curvature of the surface wave with time.

Key Words: Nonstationary Rayleigh Wave, Thermoelastic Heat-Insulated Torus

1. Introduction

Nayfeh and Nemmat-Nasser [1] pioneered in considering the problem on the propagation of a harmonic Rayleigh wave along the boundary of an isotropic thermoelastic half-space with allowance made for thermal relaxation. The half-space boundary was perceived to be free from stresses and thermal insulated. The equations for determining the Rayleigh wave velocity and its coefficients of attenuation both with depth and in the direction of propagation were obtained. The emphasis was on the thermal relaxation time dependence of the surface wave velocity. One of the methods of perturbation technique - the

asymptotic expansion matching principle - was used as the method of solution.

The propagation of nonstationary surface waves of the "diverging circles" type along the free from stresses surface of a right circular cone from a hexagonal monocrystal whose axis coincides with a crystal's axis of isotropy has been investigated by Rossikhin [2] without regard for thermal effects. The Sobolev method [3] was used as the method of solution. This method lies in the fact that the surface wave as a line of strong discontinuity is obtained as a result of the intersection of the conic surface either with one real conic volume shear wave of strong discontinuity (the surface wave of the "whispering gallery" type) or simultaneously with two complex conic volume waves of strong discontinuity: quasi-longitudinal and quasi-transverse waves (the nonstationary Rayleigh surface wave). This approach allows one to use the well-developed technique of the theory of discontinuous functions [4] whereby both the velocities of the surface waves and their intensities are calculated. It has been shown that the surface waves attenuate in the direction of their propagation, i.e. along cone generators, in accordance with a power law, and this attenuation is accounted for by the change in curvature of the surface waves with time.

In the present paper, this approach is used for the investigation of the nonstationary Rayleigh wave propagating along the free from stresses and heat-insulated surface of a thermoelastic isotropic torus.

2. Problem formulation

Assume that surface waves polarized in the sagittal plane propagate in the form of lines of strong discontinuity (the lines on which the components of the stress and strain tensors change abruptly) across the free from stresses and heat-insulated surface of a torus; in so doing a diverging (converging) circumference propagates across the surface of torus along

the arc of the circle generating the torus surface by its revolution around the torus axis (Fig.1).

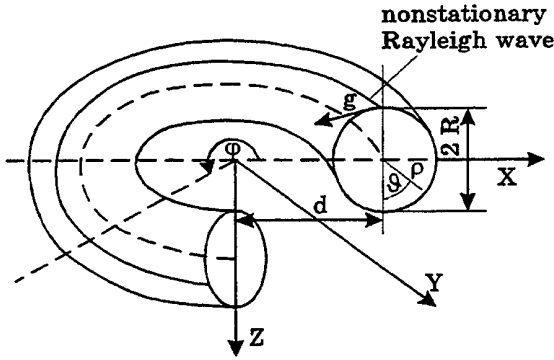


Fig 1. A scheme of a torus

The dynamic behavior of a linear thermoelastic material, from which the body under consideration is made, in the curvilinear systems of coordinates is described by the following set of equations:

$$q_{,i}^i + c_e \dot{\theta} + T_0 \gamma v_{,i}^i = 0 \quad (1)$$

$$q_i = -\lambda_0 \theta_{,i} - \tau_0 \dot{q}_i \quad (2)$$

$$\sigma_{,j}^{ij} = \rho \dot{v}^i \quad (3)$$

$$\dot{\sigma}_{ij} = \mu(v_{i,j} + v_{j,i}) + \lambda v_{,l}^l g_{ij} - \gamma \dot{\theta} g_{ij} \quad (4)$$

where σ^{ij} and σ_{ij} are the contravariant and covariant components of the stress tensor, respectively, v^i and v_i are the contravariant and covariant components of the displacement velocity vector, respectively, q^i and q_i are the contravariant and covariant components of the heat flow vector, respectively, g_{ij} are the covariant components of the metric tensor of the space, $\theta = T - T_0$ is the relative temperature of the body, T_0 is the body's temperature at the natural state, ρ is the density, λ and μ are Lamé's elastic constants, δ_{ij} is the Kronecker's symbol, c_e is the specific heat at constant strain, $\gamma = (3\lambda + 2\mu)\alpha_t$, α_t is the thermal linear expansion coefficient, λ_0 is the thermal conductivity, τ_0 is the thermal relaxation time, a Latin index after a comma denotes a covariant derivative with respect to the corresponding curvilinear spatial coordinate $x^1 = \rho$, $x^2 = \theta$ or $x^3 = \varphi$, on overdot labels a partial derivative with respect to the time t , and Latin indices take on the values 1, 2, and 3.

The boundary conditions

$$\sigma_{11} = 0, \quad \sigma_{12} = 0 \quad (5)$$

$$q_1 = 0 \quad (6)$$

should be added to the set of Eqs.(1)-(4), where σ_{11} and σ_{12} , ($\sigma_{13} = 0$ due to the symmetry of the problems under consideration) are the components of the stress tensor on the boundary surfaces of the relevant bodies, since for all the three bodies the coordinate $x^3 = \rho$ is perpendicular to the boundary surface at

each of its points (see Fig.1), and q_1 is the projection of the heat flow vector on the normal to the boundary surfaces of the three bodies.

3. The Method of Solution

In the subsequent discussion, we shall interpret the nonstationary volume wave of strong discontinuity Σ as a limiting layer of the thickness h at $h \rightarrow 0$, which surrounds the geometric surface Σ and within which the values σ_{ij} , σ^{ij} , v_i , v^i , q_i , q^i , and θ change monotonically and continuously from the magnitudes σ_{ij}^+ , σ^{ij+} , v_i^+ , v^{i+} , q_i^+ , q^{i+} , and θ^+ to the magnitudes σ_{ij}^- , σ^{ij-} , v_i^- , v^{i-} , q_i^- , q^{i-} and θ^- on the front and back boundaries of the wave layer, respectively.

Within the wave layer the following relationships are fulfilled for a certain function $Z(x^i, t)$:

$$Z_{,i} = \frac{dZ}{dn} \nu_i + g^{\alpha\beta} g_{ij} Z_{,\alpha} x_{,\beta}^j, \quad (7)$$

$$\dot{Z} = -G \frac{dZ}{dn} + \frac{DZ}{Dt},$$

where $dZ/dn = Z_{,i} \nu^i$ is the derivative with respect to the normal to Σ , ν_i are the covariant components of the unit normal vector, $g^{\alpha\beta}$ are the contravariant components of the metric tensor of the wave surface, $x_{,\beta}^j = \partial x^j / \partial u^\beta$, u^1 and u^2 are the curvilinear coordinates on the wave surface, Greek indices take on the values 1 and 2, a Greek index after a comma denotes a covariant derivative with respect to the corresponding surface coordinate, G is the normal velocity of the propagation of the surface Σ , D/Dt is the invariant derivative with respect to the time [4] which for the covariant and contravariant components of the unit normal vector to the wave layer has the form

$$\frac{D\nu_i}{Dt} = \frac{\delta\nu_i}{\delta t} - G\nu_m \Gamma_{in}^m \nu^n, \quad (8)$$

$$\frac{D\nu^i}{Dt} = \frac{\delta\nu^i}{\delta t} + G\nu^m \Gamma_{mn}^i \nu^n,$$

where $\delta/\delta t$ is the Thomas-derivative [4], and Γ_{mn}^i are the Christoffel symbols in the space.

Noting that at $h \rightarrow 0$ the second terms in (7) may be neglected as compared with the first ones, from Eqs.(1-4) we obtain

$$\frac{dq^i}{dn} \nu_i - G c_e \frac{d\theta}{dn} + T_0 \gamma \frac{dv^i}{dn} \nu_i = 0,$$

$$q_i = -\lambda_0 \frac{d\theta}{dn} \nu_i + \tau_0 G \frac{dq_i}{dn},$$

$$\frac{d\sigma^{ij}}{dn} \nu_j = -\rho G \frac{dv^i}{dn},$$

$$-G \frac{d\sigma_{ij}}{dn} = \lambda \frac{dv^l}{dn} \nu_l g_{ij} + \mu \left(\frac{dv_j}{dn} \nu_j + \frac{dv_j}{dn} \nu_i \right)$$

$$+\gamma G \frac{d\theta}{dn} g_{ij}. \quad (9)$$

Integrating relationships (9) with respect to n from $-h/2$ to $h/2$ and going to the limit at $h \rightarrow 0$, we find that the following relationships should take place on Σ :

$$\begin{aligned} [q^i] \nu_i - G c_\epsilon [\theta] + T_0 \gamma [v_i] \nu^i &= 0, \\ 0 &= -\lambda_0 [\theta] \nu_i + \tau_0 G [q_i], \\ [\sigma_{ij}] \nu^j &= -\rho G [v_i], \\ -G [\sigma_{ij}] &= \lambda [v_i] \nu^j g_{ij} + \mu ([v_i] \nu_j + [v_j] \nu_i) \\ &\quad + \gamma G [\theta] g_{ij}, \end{aligned} \quad (10)$$

where $[Z] = Z^+ - Z^-$.

Considering that $[v_i] = \omega \nu_i + g_{ij} W^\gamma x_{,\gamma}^j$, $[v^i] = \omega \nu^i + W^\gamma x_{,\gamma}^i$, and $\omega = [v_i] \nu^i$, $W_\gamma = [v_i] x_{,\gamma}^i$ from Eqs.(10) we obtain at $\omega \neq 0$

$$(G^2 - a^2)(G^2 - G_1^2) - G^2 \gamma^2 T_0 (\rho c_\epsilon)^{-1} = 0, \quad (11)$$

$$\begin{cases} [\sigma_{ij}] = -G^{-1} \{ 2\mu \nu_i \nu_j + \lambda g_{ij} + \rho(G^2 - G_1^2) g_{ij} \} \omega \\ [v_i] = \omega \nu_i, \quad [\theta] = (\gamma G)^{-1} \rho (G^2 - G_1^2) \omega \\ [q_i] = \lambda_0 (\tau_0 \gamma G^2)^{-1} \rho (G^2 - G_1^2) \omega \nu_i \end{cases} \quad (12)$$

where $a^2 = \lambda_0 (\tau_0 c_\epsilon)^{-1}$, and $\rho G_1^2 = \lambda + 2\mu$,

and at $\omega = 0$

$$\rho G^2 = \rho G_2^2 = \mu, \quad (13)$$

$$\begin{cases} [\sigma_{ij}] = -G^{-1} \mu (x_{,1}^i \nu_j g_{ij} + x_{,1}^j \nu_i g_{ji}) W^1, \\ [v_i] = g_{ij} x_{,1}^j W^1 \\ W^2 = [q_i] = [\theta] = 0 \end{cases} \quad (14)$$

Equation (11) defines the velocities $G^{(1)}$ and $G^{(2)}$ of two types of the volume waves of strong discontinuity: quasi-transverse Σ_1 and quasi-longitudinal Σ_2 , formulas (12) determine the relationships which are fulfilled on these waves. Equation (13) governs the velocity $G^{(3)}$ of the quasi-transverse wave of strong discontinuity, and formulas (14) are responsible for the relationships which are valid on this wave. Hereafter an upper index in brackets denotes an ordinal number of the wave.

To determine changes in the intensities of the three waves during their propagation, we write Eqs.(1)-(4) on the different sides of the each wave surface and take the difference of the corresponding equations written ahead of and behind the wave front. Having regard for the conditions of compatibility for discontinuities in the first-order derivatives [4] in arbitrary coordinates

$$[Z_{,i}] = [Z_{,i}] \nu^i \nu_i + g^{\alpha\beta} g_{ij} [Z]_{,\alpha} x_{,\beta}^j,$$

$$[\dot{Z}] = -G[Z_{,i}] \nu^i + D[Z]/Dt \quad (15)$$

as a result we obtain

$$\begin{aligned} Q_i \nu^i + g^{\alpha\beta} g_{ij} [q^i]_{,\alpha} x_{,\beta}^j - c_\epsilon G h + c_\epsilon \frac{D[\theta]}{Dt} \\ + T_0 \gamma (L_i \nu^i + g^{\alpha\beta} g_{ij} [v^i]_{,\alpha} x_{,\beta}^j) = 0 \end{aligned} \quad (16)$$

$$\begin{aligned} [q_i] = -\lambda_0 h \nu_i - \lambda_0 g^{\alpha\beta} g_{ij} [\theta]_{,\alpha} x_{,\beta}^j \\ + \tau_0 G Q_i - \tau_0 \frac{D[q_i]}{Dt}, \end{aligned} \quad (17)$$

$$S^{ij} \nu_j + g^{\alpha\beta} g_{ij} [\sigma^{ij}]_{,\alpha} x_{,\beta}^i = -\rho G L^i + \rho \frac{D[v^i]}{Dt}, \quad (18)$$

$$\begin{aligned} -G S_{ij} + \frac{D[\sigma_{ij}]}{Dt} = \lambda g_{ij} (L_i \nu^i + g^{\alpha\beta} g_{ik} [v^i]_{,\alpha} x_{,\beta}^k) \\ + \mu (L_i \nu_j + L_j \nu_i + g^{\alpha\beta} g_{ji} [v_i]_{,\alpha} x_{,\beta}^i + g^{\alpha\beta} g_{il} [v_j]_{,\alpha} x_{,\beta}^j) \\ + \gamma g_{ij} \left(Gh - \frac{D\theta}{Dt} \right), \end{aligned} \quad (19)$$

where $S_{ij} = [\sigma_{ij,i}] \nu^i$, $S^{ij} = [\sigma^{ij}] \nu^i$, $L_i = [v_i] \nu^i$, $L^i = [v^i] \nu^i$, $h = [\theta] \nu^i$, $Q_i = [q_i] \nu^i$.

Eliminating the values Q_i from Eqs.(16) and (17) and the values S_{ij} from Eqs.(18) and (19) and taking formulas (11)-(14), and the relationships

$$D\nu_i/Dt = D\nu^i/Dt = 0,$$

$$\nu_{,\alpha}^i = -g^{\sigma\gamma} b_{\sigma\alpha} x_{,\gamma}^i \quad (20)$$

into account yields

for the two quasi-longitudinal waves ($\omega \neq 0$)

$$\frac{D\omega}{Dt} = -\alpha\omega + G\Omega\omega, \quad \alpha = \frac{a^2(G^2 - G_1^2)}{2\tau_0(G^4 - a^2 G_1^2)},$$

$$L_i x_{,\gamma}^i = \omega_{,\gamma}, \quad (21)$$

$$h = \frac{\rho(G^2 - G_1^2)}{G\gamma} L_i \nu^i - \frac{\rho(G^2 + G_1^2)}{\gamma G^2} \frac{D\omega}{Dt} + \frac{2\rho G_1^2}{\gamma G} \Omega\omega,$$

and for the quasi-transverse wave ($\omega = 0$)

$$\frac{DW}{Dt} = G\Omega W, \quad W^2 = W_\gamma W^\gamma,$$

$$\frac{DW^\gamma}{Dt} = G\Omega W^\gamma + G W^\alpha b_{\alpha}^\gamma,$$

$$\frac{DW_\gamma}{Dt} = G\Omega W_\gamma - G W_\alpha b_\gamma^\alpha, \quad (22)$$

$$L_i \nu^i = -W_{,\alpha}^\alpha, \quad h = 0,$$

where Ω is the mean curvature of each wave surface, $b_{\sigma\alpha}$ are the coefficients of the second quadratic form of these surfaces, and $b_\gamma^\alpha = b_{\gamma\sigma} g^{\sigma\alpha}$.

Since the volume waves cropping out at the free thermal-insulated torus surface cross each other generating a surface wave, then the stress tensor and

heat flow vector components of each of the three volume waves should be added together on the surface wave. As a result from the conditions (5) and (6) on the surface wave can be written as

$$\sum_{i=1}^3 [\sigma_{11}]^{(i)} = 0, \quad \sum_{i=1}^3 [\sigma_{12}]^{(i)} = 0, \quad (23)$$

$$\sum_{i=1}^3 [q_1]^{(i)} = 0. \quad (24)$$

Using the condition of compatibility, we arrive at the equation for determination of the Rayleigh wave velocity g

$$\begin{aligned} & G_2^{-3} (1 - 2G_2^2 g^{-2})^2 (G^{(1)} + \chi G^{(2)}) \\ & + 4g^{-2} \left(\sqrt{1 - G^{(1)2} g^{-2}} + \chi \sqrt{1 - G^{(2)2} g^{-2}} \right) \\ & \times \sqrt{1 - G_2^2 g^{-2}} = 0 \end{aligned} \quad (25)$$

and the differential equation for defining its intensity

$$\frac{d\omega^{(1)}}{ds} + \alpha\omega^{(1)} + \frac{1}{R}\gamma\omega^{(1)} + \delta\omega^{(1)} = 0, \quad (26)$$

where

$$\chi = -\frac{G^{(2)2}(G^{(1)2} - G_1^2)\sqrt{1 - G^{(1)2}g^{-2}}}{G^{(1)2}(G^{(2)2} - G_1^2)\sqrt{1 - G^{(2)2}g^{-2}}},$$

s is the distance measured along the line of curvature, α , γ , and δ are the constant coefficient depending on the geometric and material constants of the thermoelastic torus.

The solution to Equation (26) has the form

$$\begin{aligned} \omega^{(1)} = c \exp(-\alpha R\theta) e^{[-i\theta(\gamma^* + \kappa_1^* + \kappa_2^*) + i\kappa_2^* f(\theta)]} \\ \times (d + R \sin \theta)^{-\kappa_3}, \end{aligned} \quad (27)$$

where c is the arbitrary complex constant, $\gamma^* = -i\gamma$, $\kappa_1^* = -i\kappa_1$, $\kappa_2^* = -i\kappa_2$, and κ_1 and κ_2 are constants.

The investigations carried out show that during the propagation of nonstationary Rayleigh waves (lines of discontinuity) along the free from stresses and heat-insulated surfaces of a thermoelastic torus along the lines of curvature the intensities of these waves attenuate by exponential and power laws at a time; in so doing the exponential attenuation occurs due to the connectedness of the strain and temperature fields, but the attenuation by the power law is caused by the presence of the time-dependent curvature of the surface wave. Besides the attenuation, the surface wave intensity oscillates with the time, in so doing the oscillation connects only with the curvature of the thermoelastic body surface.

REFERENCES

- [1] Nayfeh, A., and Nemmat-Nasser, S., Thermoelastic waves in solids with thermal relaxation, *Acta Mechanica*, Vol.12, 53-69, 1971.
- [2] Rossikhin Yu.A., Non-stationary Surface Waves of 'Diverging Circles' Type on Conic Surfaces of Hexagonal crystals, *Acta Mechanica*, Vol.92, 183-192, 1992.
- [3] Sobolev, S.L., Application of the plane wave theory to the Lamb problem (in Russian), *Trans. Seismol. Inst. Akad. Nauk SSSR*, N 18, 1-14, 1932.
- [4] Thomas T.Y., *Plastic Flow and Fracture in Solids*, New York: Academic Press, 1961.

Session 1D

PLASTICITY

Chair: Z Mróz

Co-Chair: W. K. Nowacki

**Modelling of Concrete Behaviour at Elevated
Temperatures within the Framework of Thermo-
Plasticity**

G. Heinfling, J. M. Reynouard, O. Merabet, and C. Duval

**Localization of Thermoelastoplastic Deformations in the
Case of Simple Shear**

Nguyen Huu Viem, W. K. Nowacki

**A Method of Inverse Problem of Thermomechanics with
Respect to Control of Thermostressed State of
Thermosensitive Piecewise-Homogeneous Solids**

A. V. Yasinskii, M. Y. Yuzvyak, and R. Y. Shypka

**Reformulation of Shakedown Theorems for Materials
with Temperature Dependent Yield Stress**

G. Borino, C. Polizzotto

Modelling of Transformation Induced Plasticity

L. Taleb, J. F. Jullien

Modelling of Concrete Behaviour at Elevated Temperatures within the Framework of Thermo-Plasticity

G. Heinfling*, J.M. Reynouard*, O. Merabet*, C. Duval**

* URGC-Structures, INSA de Lyon, Bât 304, 20 av A. Einstein, 69621 Villeurbanne Cedex, France

** Division Mécanique des Structures, EDF-SEPTEN, 12-14 av Dutrievoz, 69628 Villeurbanne Cedex, France

A numerical model for both compression and tension nonlinear behavior of concrete at elevated temperatures is presented here. A plasticity based model and algorithm for mode I cracking in concrete has been extended with temperature dependent properties. A fully implicit Euler backward algorithm has been applied to integrate the stresses and internal variables over a finite loading step. Thermo-mechanical interaction strains have been introduced to describe the influence of mechanical loading on the physical process of thermal expansion of concrete. Tests on plain concrete as well as on reinforced concrete structures have been simulated.

Key Words : Thermoplasticity, Cracking, Concrete, Structures, High temperatures, Interaction

1 Introduction

In severe accidental situations such as nuclear disease or fire, concrete structures are submitted to transient high temperature distribution. High temperatures induce strong micro-structural changes that alter the mechanical behavior of concrete. Hence, a numerical model for concrete under such conditions must include major induced phenomena: highly temperature dependent mechanical properties of the material and influence of mechanical loading on the physical process of thermal expansion. Up to now, only few authors [1]-[2] have considered cracking behavior of concrete in combination with elevated thermal loading. Here, a plasticity model and algorithm for mode I cracking in concrete has been extended with temperature dependent properties.

2 Plasticity based model for concrete at elevated temperatures

2.1 ASSUMPTIONS

Since no experimental data are available to evaluate the effect of the mechanical deformation process on the temperature field in concrete structures, the common approach of uncoupling the thermal and thermo-mechanical problems has been adopted. The total strain rate of concrete $\dot{\epsilon}$ is decomposed into the sum of an elastic strain rate $\dot{\epsilon}^e$, a plastic strain rate $\dot{\epsilon}^p$, a thermal expansion strain rate $\dot{\epsilon}^0$ and a thermo-mechanical interaction strain rate $\dot{\epsilon}^v$:

$$\dot{\epsilon} = \dot{\epsilon}^e + \dot{\epsilon}^p + \dot{\epsilon}^0 + \dot{\epsilon}^v \quad (1)$$

2.2 THERMO-MECHANICAL INTERACTION STRAINS

Investigation tests on plain concrete [4]-[6] have shown that to describe the response of this material under combined thermal and mechanical action it is necessary to abandon the usual assumption that thermal strain and mechanical strain can be treated as mutually independent components. Thermo-mechanical interaction strains have then to be taken into account.

A generalised multiaxial state of stress model has been proposed by Thelandersson [5] and by de Borst and Peeters [1] and has been successfully incorporated by Khennane and Baker [7] in a thermo-plasticity model. Hence, according to de Borst and Peeters [1], the thermo-mechanical interaction strain rate can be written as :

$$\dot{\epsilon}^v = H\sigma\dot{T} \quad (2)$$

where σ is the current stress vector, \dot{T} is the rate of heating, and H , for an isotropic material and for a plane stress state is given :

$$H = \frac{\alpha k}{f^c} \begin{bmatrix} 1 & -\gamma & 0 \\ -\gamma & 1 & 0 \\ 0 & 0 & \frac{1}{2}(1+\gamma) \end{bmatrix} \quad (3)$$

with α and f^c , respectively the coefficient of thermal expansion and the compression strength of concrete. k and γ can be evaluated from transient creep tests. For usual concrete, k varies from 1.8 [5] and 2.35 [11] and γ has been found to be equal to 0.285 [4].

2.3 THERMO-PLASTICITY MODEL AND ALGORITHM

A non smooth multisurface yield criterion is used to describe concrete behavior. Yield surfaces f_i , are function of stress σ , hardening parameter κ_i , and temperature T .

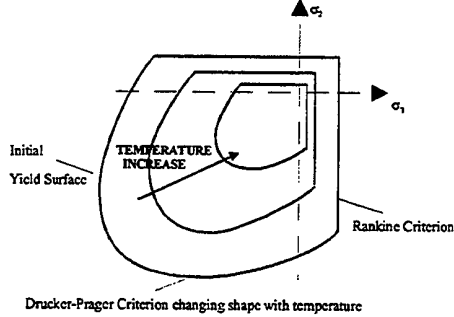


Fig.1. Yield surface in two dimensional space

The Drucker-Prager type criterion used for compression behavior, expressed in equation (4), is able to capture the changing shape of failure surfaces with temperature.

$$\sqrt{3J_2} + \left(\frac{\beta-1}{2\beta-1} \right) I_1 - \left(\frac{\beta}{2\beta-1} \right) f'_c = 0 \quad (4)$$

β is the ratio of the biaxial compression strength to the uniaxial compression strength. The experimental strength envelopes obtained by Kordina et al [8] are shown in figure 2 together with the model curves. Agreement between predicted and experimental strength envelopes is acceptable.

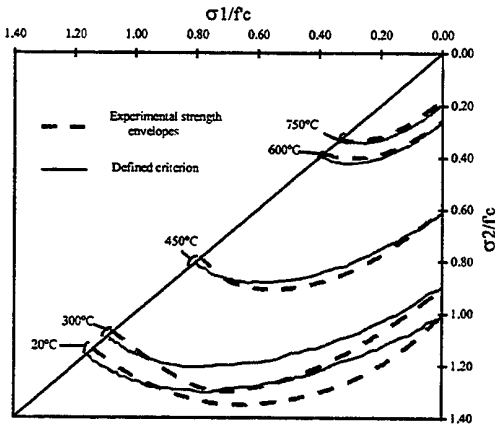


Fig.2. Biaxial compression strength envelopes

The concrete model implemented by Georgin [9] in the finite element code CASTEM 2000 is based on Feenstra [3] with regard to cracked concrete. The plasticity condition $f_i(\sigma, \kappa_i, T) = 0$ is imposed on each active surface during the integration process. Assumptions commonly used in plasticity theory with regard to mechanical hardening are adopted: normality of the plastic flow and isotropic

hardening. The isotropic Rankine flow theory proposed by Feenstra [3] is used to describe cracking behavior within the framework of plasticity. The ambiguity of plastic flow direction at the corner is removed by considering the contribution of each individual loading surface separately:

$$\dot{\varepsilon}^p = \dot{\lambda}_1 \frac{\partial f_1}{\partial \sigma} + \dot{\lambda}_2 \frac{\partial f_2}{\partial \sigma} \quad (6)$$

A trapezoidal Euler backward scheme proposed by Simo [10] is used. The updated stress vector σ_{n+1} is obtained by solving the system of equations :

$$\sigma_{n+1} = \sigma_c - D_{n+1} \left\{ \Delta \lambda_1 \frac{\partial f_1}{\partial \sigma} + \Delta \lambda_2 \frac{\partial f_2}{\partial \sigma} \right\}_{n+1} \quad (7)$$

The subscript $n+1$ refers to the time step and D_{n+1} is the Hooke matrix at temperature T_{n+1} . The thermo-elastic predictor σ_c is obtained by freezing inelastic flow during the time step :

$$\sigma_c = D_{n+1} (\Delta \varepsilon_{n+1} - \Delta \varepsilon_{n+1}^{th} - \Delta \varepsilon_{n+1}^{pr}) + \Delta D \varepsilon_n^c + \sigma_n \quad (8)$$

Solving system (7) finally consists of the determination of the inelastic multipliers which enforce the plasticity conditions at temperature T_{n+1} :

$$\begin{cases} f_1(\Delta \lambda_1, \Delta \lambda_2) = 0 \\ f_2(\Delta \lambda_1, \Delta \lambda_2) = 0 \end{cases} \quad (9)$$

A local Newton-Raphson method is used to solve system (9). Figure 3 shows the iterative return mapping process corresponding to this algorithm for the general case where two plasticity criteria are violated. The superscript (i) refers to the internal iterations during the solving process.

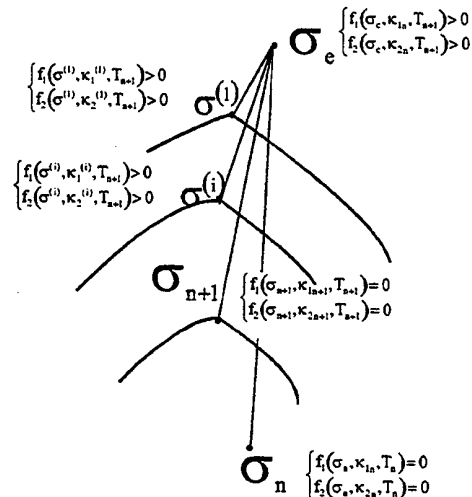


Fig.3. Iterative return mapping process

3 Simulations of tests on plain concrete

3.1 BIAxIAL ISOTHERMAL TESTS

Biaxial compression tests at different temperatures have been simulated. Figure 4 shows for example the stress-strain curve obtained at 450°C for $\sigma_1/\sigma_2 = 1$ together with the curve obtained by [8]. Simulation results emphasize a good description of the behavior of concrete under compression. Sensibility to hydrostatic pressure appears to be very important for high temperatures and high biaxial stress ratio.

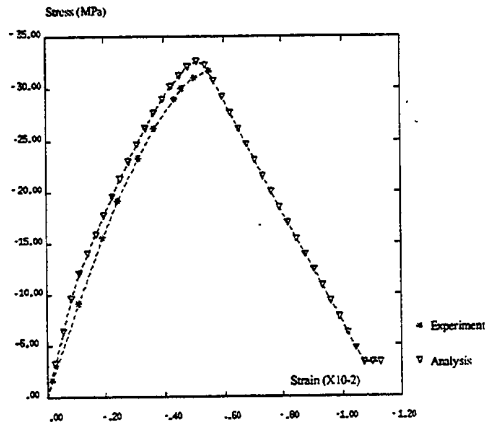


Fig.4. Biaxial compression test at 450°C, $\sigma_1/\sigma_2=1$

3.2 STRESS AND TEMPERATURE HISTORIES

The experiment conducted by Anderberg [11] has been simulated. The experiment consists, first, of heating a concrete specimen up to 400°C and then loading it, and second, loading a specimen to the required load and heating it under load. Figure 5 presents simulation results in both loading cases. These results validate the capacity of this model to describe stress and temperature history dependency.

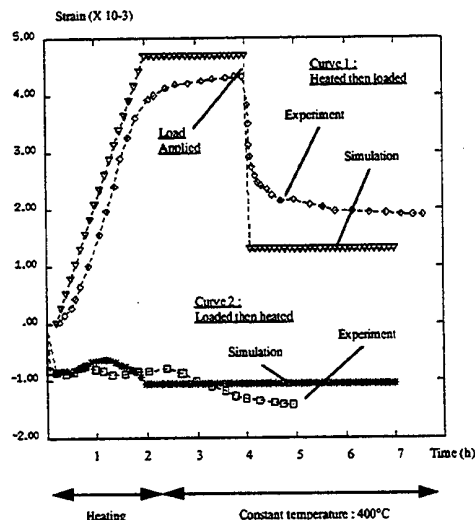


Fig.5. Deformational response of concrete under two different load and temperature histories

3.3 BIAxIAL TRANSIENT TESTS

Relaxation tests performed by Kordina et al [8] have been simulated. Figure 6 shows the model prediction for a relaxation test under uniaxial conditions for a normally stored concrete (20°C / 65% r.h.). Agreement between experimental and numerical results can be considered relatively good. Between 100°C and 250°C, shrinkage has been explicitly taken into account by decreasing strongly the coefficient of thermal expansion of concrete in this temperature range. The third peak of stress arising between 500°C and 600°C on the experimental curve results from chemical changes in concrete. This has not been modelled here.

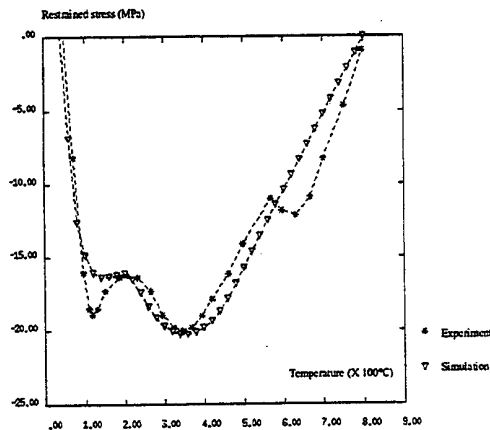


Fig.6. Restrained stress as function of temperature for a normal stored concrete specimen (65% r.h.)

Finally, transient creep tests performed by Kordina et al [8] have been simulated too. Numerical results emphasize that thermo-mechanical interaction strains have to be taken into account and that the presence of a sustained load during heating affects concrete behavior. Figure 7 shows for example the deformational behavior of a concrete specimen for a biaxial sustained load of 60% of the ultimate compressive strength.

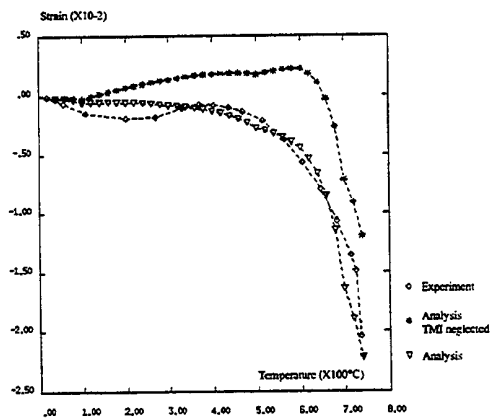


Fig.7. Total deformation of concrete during biaxial transient creep test. (load level 60% f'_c)

4 Simulations of deep beams subjected to transient high temperature distribution

Reinforced concrete deep beams subjected to an elevated surface temperature performed by Saito et al [12] have been simulated. The beams were first heated up to a certain surface temperature whereafter they were loaded to failure. Figure 8a presents the geometry of the tests. Reinforcement steel has been considered temperature dependent elastic-perfectly-plastic. Agreement between numerical and experimental results can be considered good. Figure 8b presents the global response of beam S3C heated up to 300° C. Figure 8c presents simulated and experimental crack pattern at failure. The results validate the capacity of the proposed crack model to describe accurately crack propagation in structures subjected to elevated temperatures.

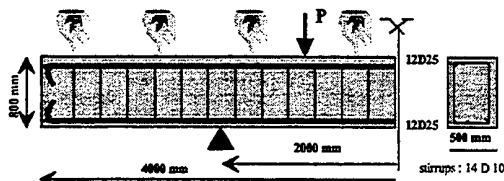


Fig.8a. Geometry of the tests

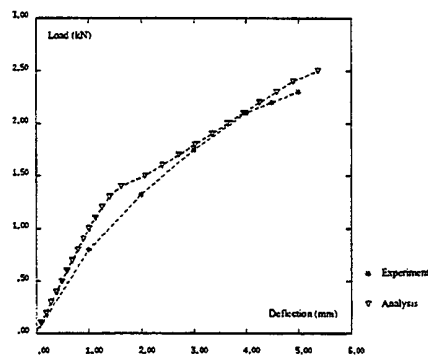


Fig.8b. Load-deflection curve for beam S3C.

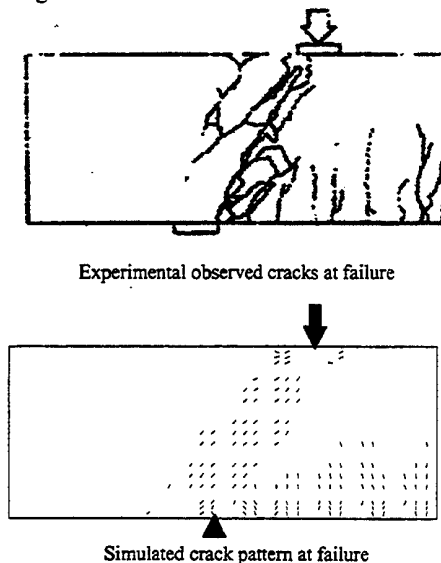


Fig.8c. Crack pattern at failure for beam S3C.

5 Conclusions

A model has been discussed for the analysis of concrete and reinforced concrete structures subjected to high temperatures. In particular, effectiveness and accuracy of a thermo-plasticity based model for cracking in concrete has been presented. The model used for thermo-mechanical interaction strains appeared to be suitable for this formulation and major effects of this phenomenon have been captured. A study has been undertaken concerning coupling of pore pressures appearing in concrete at elevated temperatures with this model. The perspectives of this study are interesting since spalling is a major issue for the assessment of integrity of high strength concrete structures subjected to elevated temperatures.

References

- (1) R. de Borst, P.P.J.M. Peeters, *Analysis of concrete structures under thermal loading*, *Comp. Meth. Appl. Mech. Engng.* 77, 293-310, 1989
- (2) R.J. van Foeken, *Numerical analysis of reinforced concrete structures at high temperatures including cracking, plasticity and creep*. *Numer. Meth. in Thermal problems*, vol 4, 1127-1183, 1985
- (3) P.H. Feenstra, R. de Borst, *A plasticity model and algorithm for mode-I cracking in concrete*, *Int. Journal Num. Meth. Engng.* Vol 38, 2509-2529, 1995
- (4) S. Thelandersson, *Modelling of combined thermal and mechanical action in concrete*, *Journal of Engineering Mechanics*, Vol 113, 893-903, 1987
- (5) U. Schneider, *Behavior of concrete at high temperatures*, *Deutscher Ausschuss für Stahlbeton*, Heft 337, 1982
- (6) G.A. Khoury, B.N. Grainger, P.J.E. Sullivan, *Transient thermal strain of concrete: literature review, conditions within specimen and behavior of individual constituents*, *Magazine of Concrete Research*, 37, 131-144, 1985
- (7) A. Khennane, G. Baker, *Thermoplasticity model for concrete under transient temperature and biaxial stress*, *Proc. R. Soc. Lond., A*, 439, 59-80, 1992
- (8) K. Kordina, C. Ehm, U. Schneider, *Effect of biaxial loading on the high temperature behavior of concrete*, *Proc. 1st Symp. of fire safety Science*, 1985
- (9) J.F. Georgin, J.M. Reynouard, O. Merabet, *Localisation in modelling of structures submitted to impact by viscoplasticity*, *5th COMPLAS, Barcelona*, 1997
- (10) J.C. Simo, J.G. Kennedy, S. Govindjee, *Npn-smooth multisurface plasticity and viscoplasticity*, *Int. J. Numer. Methods Engng.*, 26, 2161-2185, 1988
- (11) Y. Anderberg, S. Thelandersson, *Stress and deformation characteristics of concrete at high temperature:2*, *Bulletin 54, Lund Institute of technology, Lund*, 1976
- (12) H. Saito, M. Hiramoto, K. Saito, T. Miyashita, Y. Takeuchi, T. Mochida, *Ultimate strength of reinforced concrete members subjected to transient high temperature distribution*, *SMIRT 12, Paper H01/5*, 1993

Localization of Thermoelastoplastic Deformations in the Case of Simple Shear

Nguyen Huu Viem and W. K. Nowacki

Center of Mechanics, Institute of Fundamental Technological Research of Polish Academy of Sciences, ul. Swietokrzyska 21, 00-049 Warsaw, Poland

The results of tests of quasistatic and dynamic finite thermoelastoplastic plane shear is discussed. Use is made of a new shear device in which loading and displacements are controlled in compression. Using the thermovision technique the temperature changes of the sheared paths have been registered for various shear rates. The rate-independent constitutive relations are formulated for elastic-plastic metallic solids at finite strain. The constitutive relations are considered for an adiabatic process with combined isotropic-kinematic hardening. The analogous initial-boundary-value problem as in the experiment of simple shear is formulated for finite deformations. An exceptional homogeneity of the permanent strain and temperature fields is observed in experiments and numerical simulations, over the total length of the specimens, when the strain is less than 70%. For the largest deformations the zones of strain localization are observed.

Key Words: Plasticity, Dynamic Problem, Simple Shear, Strain Localization, Metal Sheets

1. Introduction

Numerical systems allow us to simulate the mechanical behaviour of thin-walled constructions, such as bodies of automobiles, buses, shells of wagons, air-planes, etc., submitted to the impact loading. Such systems require the knowledge of the dynamical behaviour of thin sheets of which these constructions are made. The mechanical characteristics of the thin-walled constructions are dependent on the metallurgical composition of the metal as well as on the manner of its production. It is indispensable to have the experimental data concerning this specific form of material. Tests in the case of simple shear are very important for the experimental investigation of the constitutive equations of materials. These experiments are supplementary to other tests realised in traction as well in compression or in pure shear.

A new shear device was used to perform tests of specimens having the form of slab such as metal sheets [1]. The loading and the displacements of this device are controlled by a Split Hopkinson Pressure Bar (SHPB) acting in compression. The special device was used to transform the compression to simple plane shear. For thin sheets in dynamic simple plane shear tests, it is the only known method to obtain a very good homogeneity of the permanent strain field over the total length of the specimen, without the localisation of deformations as in the case of torsion of thin-walled tubes [5].

The analogous initial-boundary-value problem of the simple shear was formulated in the case of

finite strains. We consider the rate-independent constitutive relations for an adiabatic process with combined kinematic-isotropic hardening at moderate pressures. The analytical solution is compared with the experimental data. The numerical calculations performed enabled the evaluation of the optimal dimensions of the specimen used in the case of dynamic loading.

2. Experiment

The shear device consists of two coaxial cylindrical parts (the external part is tubular and the internal part is massive). Both cylinders are divided into two symmetrical parts between which the sheet in testing is fixed. Two bands of the specimen between the internal and external parts of the device are in plane shear when these cylinders move axially one toward the other. Each band before test is rectangular and becomes almost a parallelogram having the constant length and the constant height.

First, the system is tested under quasi-static loading in order to verify its effectiveness. The dynamic test is similar but the loading is realized by the SHPB. The device with specimen is placed between two bars of the SHPB. In this case the mechanical impedance of the shear device and of the SHPB must be the same to avoid the noise in the interface signal. The impulse is created by the third projectile bar: the usual compression technique. We have to register the input, transmitted and reflected impulses: ε_i , ε_t and ε_r .

The specimens deformed quasi-statically or dyna

mically to 70 - 90 % as observed under the optical microscope, have a similar structure. The traversal lines marked on the specimens, on the gauge section, before the test remain parallel after the test. This fact indicates that the deformation is homogeneous in the considerable part of the specimen. However, the presence of free bounds of specimen produces the heterogeneity of stress field because the stress vector normal to the free surfaces must be zero, therefore we have assumed that the dimensions of the perturbed zone are small as compared to the dimensions of the specimen. The exceptional qualities of the homogeneity of the residual strain field show that the simplified analysis can be used in the zone of plastic deformations.

At the deformation of the order 70%, in the case of high strain rate we observe the formation of the tangled structure and of the dislocations cells. Their elongation and arrangement tend to be aligned along the length of the shear direction. In several grains the micro-bands of shear, parallel to the direction of x_1 axis (axis of compression) are observed. At the very high strain rate the shear macro-bands are observed. We can suppose that it is a critical strain at which the shear localization occurs. Before arriving at the critical strain, the deformation is homogeneous over the whole gauge length of the specimen. The work-hardening results from the creation, multiplication and interaction of the dislocations. In this case, a small part of the work of plastic deformation is stored in the material as elastic strain energy (about 6%) and the remaining part is converted into heat. In the paper [4] the temperature field due to plastic deformation is measured. The quasistatic tests on the behavior of stainless steel are performed. The goal of this paper was to obtain the mechanical curves as well as the temperature distributions in the simple plane shear areas. A change of temperature of the surface of these areas has been observed by the thermovision camera coupled with a system of data acquisition and conversion. The infrared radiation emitted by shear paths was measured. The results obtained enable present the temperature changes of the specimens subjected to the shear test with different rates of deformation, as well as to describe the macroscopic shear band, which develops at higher deformations. With this technique, it is possible to evaluate the stored energy due to the simple shear in the case of large deformations.

In the analysis, we must take into account that the loading of the specimen is not instantaneous. The loading compression wave must take some time to transmit from one end of the device to the other. However, in our tests, we have a very good equilibrium of forces on two sides of the shear device. We observe that the input and the output forces are very similar in shape (neglecting the small oscillations of the input force). So, in the simplified analysis we assume that the loading is homogeneous

and we proceed as in the case of quasi-static loading. The force is taken to be equal to the mean value of input and output force.

3. Theoretical simple shear analysis

The simple shear in the direction e_1 in the coordinate system (e_1, e_1) is defined by the relations

$$u_1 = \gamma(t) x_2, v_1 = \dot{\gamma} x_2 \text{ and } u_2 = u_3 = v_2 = v_3 = 0 \quad (1)$$

where $\gamma = \varepsilon_{12}$ and $\dot{\gamma}$ are the plastic shear strain and shear strain rate, respectively.

In the axis of x_i the Cauchy stress tensor σ and the back stress Π have the following non-zero components: $\sigma_{11}, \sigma_{22}, \sigma_{12}, \pi_{11}, \pi_{22}, \pi_{12}$. The presence of σ_{11} and σ_{22} is due to the fact that the distance between two parts of the shear device is constant during experiment i.e. $a = a_0 = \text{const}$.

The change in the temperature field ϑ is described as

$$\begin{aligned} \rho_0 c_v \dot{\vartheta} = & \left(1 - \frac{\pi}{\sigma_Y} \frac{\partial \sigma_Y}{\partial \pi} \right) (\bar{T} - \Pi) \cdot \mathbf{D}^p - \beta \text{div } \mathbf{q} - \\ & - \vartheta \alpha_v K_T \frac{\rho_0}{\rho} \text{tr } \mathbf{D} - \vartheta \frac{c_T}{c} \Pi \cdot \mathbf{D}^p \end{aligned} \quad (2)$$

where ϑ is the temperature, \mathbf{q} is the heat flux, π is the function determined from the stored energy [3], α_v is volumetric thermal expansion, K_T is the isothermal bulk modulus, c_v is specific heat at constant volume, c_T and c are constants [3]. In this relation terms of the right hand side denote: the dissipation of mechanical work, the heat exchange with environment, the heat of elastic deformations and the heat of internal rearrangement, respectively.

Using the rate-independent constitutive relations for the adiabatic process with combined isotropic-kinematic hardening at moderate pressures, and neglecting the thermal expansion, the heat of elastic deformation and the heat of internal rearrangement, we have the following set of equations [3] (these equations are similar in form to those employed in problems of small strains but are applicable to the whole range of deformation processes):

$$\begin{aligned} \ddot{\mathbf{T}} = & \beta \mathbf{L} \mathbf{D} - \frac{3j\mu\beta \mathbf{D} \cdot (\bar{\mathbf{T}} - \Pi)}{\sigma_Y^2 \mathcal{H}} [(\bar{\mathbf{T}} - \Pi) + \mathbf{P}] \quad (3) \\ j = & \begin{cases} 1 & \text{if } f = 0 \text{ and } \mathbf{D} \cdot (\bar{\mathbf{T}} - \Pi) \geq 0, \\ 0 & \text{if } f = 0 \text{ and } \mathbf{D} \cdot (\bar{\mathbf{T}} - \Pi) < 0 \text{ or } f < 0. \end{cases} \end{aligned}$$

where $\beta = \rho_0 / \rho$ is the ratio of densities in the reference and the actual configurations, $\mathbf{T} = \beta \boldsymbol{\sigma}$, $\ddot{\mathbf{T}} = \dot{\mathbf{T}} - \boldsymbol{\omega} \mathbf{T} + \mathbf{T} \boldsymbol{\omega}$ is the Zaremba-Jaumann rate, \mathbf{T}

is the deviatoric part of \mathbf{T} , \mathbf{L} is the fourth order tensor of elastic moduli, μ is the Lamé constant and f is the Huber-Mises yield criterion

$$f = \frac{3}{2}(\bar{\mathbf{T}} - \Pi) \cdot (\bar{\mathbf{T}} - \Pi) - \sigma_Y^2(\vartheta, \alpha) = 0 \quad (4)$$

here σ_Y is the yield stress in simple tension and α corresponds to the size of the yield surface

$$\dot{\alpha} = (\bar{\mathbf{T}} - \Pi) \cdot \mathbf{D}^P \quad (5)$$

The shift of the yield surface here is represented by the back stress Π for which the evolution law has the form of a linear kinematic hardening

$$\dot{\Pi} = c \mathbf{D}^P \quad (6)$$

where $c = \text{const}$ and \mathbf{D}^P is the plastic rate of deformation. The change in the temperature is described as

$$\rho_o c_v \dot{\vartheta} = (1 - \pi)(\bar{\mathbf{T}} - \Pi) \cdot \mathbf{D}^P \quad (7)$$

The first term on the right hand side of (7) represents the rate of energy dissipation and, therefore, π less than 1. For numerous metals π takes the value from 0.02 to 0.1. In the equation (3) \mathcal{H} is the hardening function

$$\mathcal{H} = 1 + \frac{c}{2\mu\beta} + \frac{1}{6\mu\beta} \frac{\partial(\sigma_Y^2)}{\partial\alpha} + \frac{(1-\pi)}{6\mu\beta\rho_o c_v} \frac{\partial(\sigma_Y^2)}{\partial\vartheta} \quad (8)$$

and tensor \mathbf{P} is obtained by expressing the term $(\omega^P \mathbf{T} + \mathbf{T} \omega^P)$ as a function of \mathbf{D}^P where ω^P is the plastic spin.

The equation for plastic spin can be assumed to be, according to Dafalias, Paulun and Pecherski [2] and others in the following form

$$\omega^P = \eta (\Pi \mathbf{D}^P - \mathbf{D}^P \Pi) \quad (9)$$

where η may depend on the invariants of \mathbf{D}^P and Π .

In the case of plane simple shear we have $\beta = 1$ and the equations above lead to

$$\begin{aligned} \dot{\sigma}_{11} - \dot{\gamma} \sigma_{12} &= -\frac{N_1}{\mathcal{H}} \dot{\gamma} [\sigma_{11} - \pi_{11} + M \sigma_{12}] \\ \dot{\sigma}_{12} - \dot{\gamma} \sigma_{11} &= \dot{\gamma} \left[\mu - \frac{N_1}{\mathcal{H}} (\sigma_{12} - \pi_{12} - M \sigma_{11}) \right] \\ \dot{\pi}_{11} - \dot{\gamma} \pi_{12} &= \frac{N_2}{\mathcal{H}} \dot{\gamma} (\sigma_{11} - \pi_{11}), \quad \sigma_{11} = -\sigma_{22} \\ \dot{\pi}_{12} + \dot{\gamma} \pi_{11} &= \frac{N_2}{\mathcal{H}} \dot{\gamma} (\sigma_{12} - \pi_{12}), \quad \pi_{11} = -\pi_{22} \end{aligned} \quad (10)$$

here $M = \frac{\eta}{\mu} [\pi_{11}(\sigma_{12} - \pi_{12}) - \pi_{12}(\sigma_{11} - \pi_{11})]$ and

$$N_1 = \frac{3j\mu}{2\sigma_Y} (\sigma_{12} - \pi_{12}), \quad N_2 = -\frac{3jc}{2\sigma_Y} (\sigma_{12} - \pi_{12})$$

Here, we use the relation for the multiplying function η occurring in the expression of plastic spin (9), in the form proposed in the paper [2].

In the case of plasticity with kinematic hardening we also have the analytical solutions. Then $\sigma_Y = \text{const}$ and now from (8) we have $\mathcal{H} = 1 + c/2\mu$.

Finally, after several calculations, we find the Cauchy stress components σ_{11} , σ_{12} and the back stress components π_{11} , π_{12} :

$$\begin{aligned} \pi_{11} &= \frac{c}{2\mathcal{H}} (\cos\phi - \cos\phi^*) \frac{\cos\phi}{(1 - a \cos\phi)} \\ \pi_{12} &= \frac{c}{2\mathcal{H}} (\cos\phi - \cos\phi^*) \frac{\sin\phi}{(1 - a \cos\phi)} \\ \sigma_{11} &= \frac{c}{2\mathcal{H}} (\cos\phi - \cos\phi^*) \frac{\cos\phi}{(1 - a \cos\phi)} + k_o \cos\phi \\ \sigma_{12} &= \frac{c}{2\mathcal{H}} (\cos\phi - \cos\phi^*) \frac{\sin\phi}{(1 - a \cos\phi)} + k_o \sin\phi \end{aligned} \quad (11)$$

where $a = \mu/k_o$, $k_o = \sigma_Y/\sqrt{3}$ is the yield value in shear; γ^* and ϕ^* are constants. Integrating the equation (7) the temperature field can be determined.

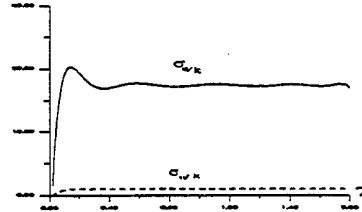


Fig. 1. Shear stress σ_{12} and normal stress σ_{11} vs. shear strain for kinematic hardening.

Solutions for stresses σ_{11} and σ_{12} in dimensionless form vs. shear strain γ , illustrated in Fig. 1, are obtained for kinematic hardening, with $\mu = 8 \cdot 10^4$ MPa, $c = 5333,33$ MPa, $k_o/\mu = 0.0577$. In the case of large plastic deformations the ratio σ_{11}/σ_{12} and σ_{22}/σ_{12} are much higher than in the case of small elastic deformations.

4. Numerical simulations of the experiment

A finite element method program was used for the numerical simulations of the formulated problem of quasistatic and dynamic simple shear of thin sheets. We assume the similar initial and boundary conditions as in the experiment. In the case of

dynamic deformations a simplified supposition is introduced. The process of wave propagation in the specimen is neglected. Due to the excellent equilibrium of input and output forces and quasi-constant value in the time period $50 \mu s < t < 500 \mu s$, we can treat our problem as quasistatic using a rate-independent constitutive equations. The amplitude of loading is determined from the dynamic experiment. We assume that in the contact between the specimen and bars the force is constant in time.

In the finite element method a rectangular mesh is introduced. Deformation of the mesh in time is determined. In the same time the components of the stress tensor σ_{12} and $\sigma_{22} = -\sigma_{11}$, the intensity of stress $\sigma_i = (3/2 s_{ij} s_{ij})^{1/2}$, the equivalent strain $e_i = (2/3 \varepsilon_{ij}^p \varepsilon_{ij}^p)^{1/2}$ and the temperature field are determined. First, the numerical simulation was made for the quasistatic loading of the sheet of stainless steel 1H18N9T, with $\mu = 8 \cdot 10^{-4}$ MPa, $\rho = 7.8 \text{ g/cm}^3$ and $\sigma_y = 280$ MPa.

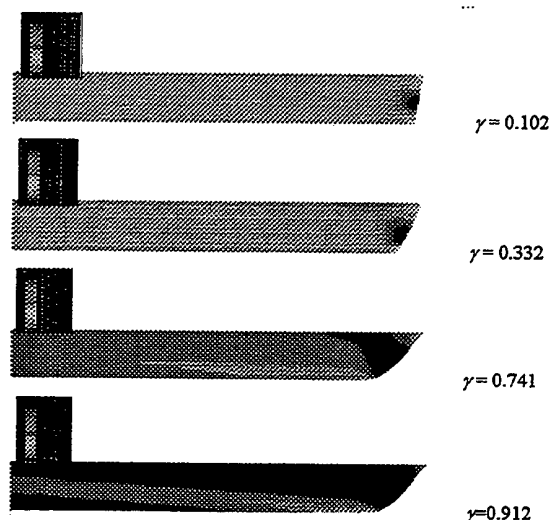


Fig. 2. Equivalent deformation.

Results of numerical simulation in the specimen subjected to the quasistatic simple shear are shown in Fig. 2. The equivalent deformation field is shown for a half part of the shear zone of the specimen. The deformation process is non-symmetric with respect to the axis x_2 . Successive sequences are presented for different values of shear strain defined as $\gamma = \Delta l(t)/a_0$, from $\gamma = 10.2\%$ to $\gamma = 91.2\%$. We observe for example the heterogeneity of the strain and stress fields at the free bounds of the specimen at the distance less than 1 % of the total length when the strain is 30% and less than 5 % of the total length when the strain is 70 %, exactly as in the experiments.

The shear zones are manifested by a significant temperature increase. At the ends of shear zones the theoretical predicted fields of strain heterogeneities are manifested by the increase of temperature,

particularly noticeable in the initial stage of shear. As the deformation continues, the line describing the position of maximum temperature departs from the shear direction. It gives evidence for the development of the macroscopic shear band, running along the specimen at a certain angle to the direction of shear.

5. Conclusions

An exceptional homogeneity of the permanent strain field at finite deformations over the total length of the specimens is observed in experiments and in the results of numerical simulation. In the case of a thin sheet, the proposed method is the only known test providing, homogeneous stress and strain fields in both dynamic and static tests. The method can be used to verify the proposed constitutive relations.

The simple shear test is particularly attractive, since the application of this type of loading path can result in large strains without the occurrence of plastic instability. But, after a certain strain on the order of 70-90%, the deformation becomes gradually localized. The material begins to be work-softening until fracture occurs.

Investigation of temperature distribution on the surface of the shear paths confirm the existence of the theoretically predicted fields of strain heterogeneity.

Acknowledgements. This paper is supported by the Polish Committee for Scientific Research, KBN Project No. 7T07A02608 on "Dynamic fracture of materials".

References

- (1) Gary, G., and Nowacki, W.K., Essai de cisaillement plan appliqué à des tôles minces, *Journal de Physique V, Colloque C8, supplément au Journal de Physique Vol. III*, p.65, 1994.
- (2) Paulun, J.E., and Pecherski, R.B., On the Relation for Plastic Spin, *Arch. of Appl. Mech.*, Vol.62, p.376, 1992.
- (3) Nguyen Huu Viem, Isothermal and Adiabatic Flow Laws of Metallic Elastic-Plastic Solids at Finite Strains and Propagation of Acceleration Waves, *Arch. Mech.*, Vol.44, p. 595, 1992.
- (4) Gadaj, P.S., Nowacki, W.K., Pieczyska, E., Changes of Temperature During the Simple Shear Test of Stainless Steel, *Arch. Mech.*, Vol. 48, p. 779, 1996.
- (5) Marchand, A., and Duffy, J., An Experimental Study of the Formation Process of Adiabatic Shear Bands in Structural Steel, *J. Mech. Phys. Solids.*, Vol.36, p.251, 1988.

A Method of Inverse Problem of Thermomechanics with Respect to Control of Thermostressed State of Thermosensitive Piecewise-Homogeneous Solids

A.V. Yasinskiĭ, M.Y. Yuzvyak and R.Y. Shypka

Department of Deformable Solids, Pidstryhach Institute for Applied Problems of Mechanics and Mathematics, National Academy of Sciences of Ukraine, 290601, Naukova Str., 3-b, Lviv, UKRAINE.

The optimal (in the sense of rapidity) problem of control by heating of thermosensitive solids of canonical forms (unbounded strip, hollow and continuous cylinder and sphere) under restrictions on the control function and maximal value of intensity of tangential thermostresses is considered. A case of elastoplastic deformation of solids under consideration is investigated within the theory of processes of deformation on the trajectories of small curvature. An algorithm of construction of numerical solution of the control problem is elaborated on the basis of a method of inverse problem of thermomechanics. Some numerical results of calculations are presented for typical data.

Key words: Inverse Problem, Optimal Control, Thermoplasticity, Heat Conductivity, Thermal Stresses

1. Introduction

The thermal processing of materials is often a constituent part of technological processes of manufacturing of design elements. Minimization of time of heating (cooling) of an item is one of factors, essentially influencing productivity of such processes. For maintenance of appropriate strength characteristics and functional properties of an item at determination of optimal regimes of its quickest heating (cooling) it is necessary to take into account the given restrictions on parameters of stressed and thermal states [1], [2]. The problems of the quickest heating of a body are also urgent for optimization of transient regimes of operation of responsible details and units of power equipment under conditions of intensive heat load.

In this paper the mathematical statement of the optimal (in the sense of rapidity) problem of control by heating of thermosensitive canonical solids (unbounded strip, hollow and continuous cylinder and sphere) under restrictions on control function and maximal value of intensity of tangential stresses is formulated for a case of elastoplastic deformation of material. The numerical algorithm for solving this problem is elaborated on the basis of a method of inverse problem of thermomechanics.

1. Formulation of the problem

Let a non-stationary temperature field in an isotropic piecewise-homogeneous body satisfies the heat conductivity equation

$$\frac{1}{\rho^j} \frac{\partial}{\partial \rho} \left(\lambda(T, \rho) \rho^j \frac{\partial T}{\partial \rho} \right) = c_*(T, \rho) \frac{\partial T}{\partial \tau} \quad (1)$$

$$k \leq \rho \leq 1 \quad \tau > 0 \quad j = 1, 2, 3$$

and the boundary and initial conditions

$$\lambda(T, k) \frac{\partial T(k, \tau)}{\partial \rho} - H_i(T) (T(k, \tau) - t_i(\tau)) = 0 \quad (2)$$

$$\lambda(T, 1) \frac{\partial T(1, \tau)}{\partial \rho} + H_i(T) (T(1, \tau) - t_i(\tau)) = 0 \quad (3)$$

$$T(\rho, 0) = f(\rho) \quad k \leq \rho \leq 1 \quad (4)$$

where $\lambda(T, \rho) = \lambda_*(T, \rho) / \lambda_0$ is the non-dimensional heat conductivity; $c_*(T, \rho) = c_v^*(T, \rho) / c_v^0$ is the specific non-dimensional heat capacity; $\lambda_*(T, \rho)$, $c_v^*(T, \rho)$ are the thermal conductivity and the specific heat capacity, respectively; λ_0 , c_v^0 are certain constants; $\rho = x / R_2$, $\tau = \lambda_0 \tau^* / c_v^0 R_2^2$ are non-dimensional coordinate and Fourier criterion; x , τ^* are the spatial coordinate and time; $k = 0$ for unbounded strip ($j = 0$) and continuous cylinder ($j = 1$) and sphere ($j = 2$); $k = R_1 / R_2$ for hollow cylinder and sphere; $H_i(T) = a_i(T) R_2 / \lambda_0$ ($i = 1, 2$) denote non-dimensional heat transfer coefficients; $a_i(T)$ ($i = 1, 2$) are heat transfer coefficients; $t_i(T)$ ($i = 1, 2$) are the temperatures of surrounding mediums.

We consider a case of elastoplastic deformation of material. The relations, which describe non-isothermic elastoplastic processes of deformation on trajectories of small curvature [3], are chosen as the governing equations of state. The thermal and mechanical characteristics are assumed to depend on temperature and spatial coordinate. For piecewise-homogeneous solid they are expressed by means of the aim of asymmetric step functions as for the whole body [4]

$$p(T, \rho) = p_1(T) + \sum_{i=1}^{n-1} (p_{i+1}(T) - p_i(T)) S_-(\rho - \rho_i)$$

where

$$S_-(x) = \begin{cases} 0 & x < 0 \\ 1 & x \geq 0 \end{cases}$$

n is a number of layers; i denotes the i -th layer; ρ_i is coordinate of interface between the i -th and layer and $(i+1)$ -th layers.

The optimization problem consists in determination of such control $u(\tau)$ (the temperature of heating medium $t_i(\tau)$ on one of boundary surface), which satisfies the condition

$$|u(\tau)| \leq U(\tau) \quad \tau \geq 0 \quad (5)$$

and the restriction on maximal value of intensity of tangential stresses

$$\max_{\rho} S(T) \leq S_*(T) \quad k \leq \rho \leq 1 \quad (6)$$

and provides heating of the body from the initial state (4) to the final state

$$T_* = \frac{1+j}{1-k^{1+j}} \int_k^1 \rho^j T(\rho, \tau_*) d\rho \quad j = 0, 1, 2 \quad (7)$$

over the minimum time $\tau_* = \min \tau$. Here $U(\tau)$ denotes the boundary admitted value of the control

function; $S = \left(\frac{1}{2} s_{ij} s_{ij} \right)^{1/2}$ is the intensity of tangential stresses; s_{ij} ($i, j = 1, 2, 3$) are the stress deviator components [3]; S_* denotes the boundary admitted value of the intensity of tangential stresses.

As the restriction (6) in a method of inverse problem of thermomechanics we can choose the following restrictions:

on maximal value of magnitude of accumulated plastic strain

$$\max_{\rho} \bar{A}_p \leq \bar{A}_p^* \quad k \leq \rho \leq 1$$

on maximal temperature difference

$$\max_{\rho} T(\rho, \tau_*) - \min_{\rho} T(\rho, \tau_*) \leq \delta T \quad k \leq \rho \leq 1$$

on gradients of temperature field

$$\frac{\partial T(1, \tau)}{\partial \rho} \leq S_1(T) \quad S_1(T) > 0$$

or

$$\frac{\partial T(k, \tau)}{\partial \rho} \geq S_2(T) \quad S_2(T) < 0$$

on velocity of temperature change

$$\frac{\partial T(\rho_0, \tau)}{\partial \tau} \leq \omega(T, \tau) \quad \rho = k, 1$$

on maximal temperature

$$\max_{\rho} T(\rho, \tau_*) \leq T_0 \quad T_0 = \text{const} \quad k \leq \rho \leq 1$$

and etc.

2. Solution of the problem

According to a method of inverse problem of thermomechanics [5], [6] the optimal (in the sense of rapidity) control is equal to the boundary admitted restriction

$$u(\tau) = U(\tau) \quad (9)$$

or provides the fulfillment of equality

$$\max_{\rho} S(T) = S_*(T) \quad k \leq \rho \leq 1 \quad (10)$$

Therefore, the solution of the optimal problem of control by heating (1)-(7) is constructed using stage by stage algorithm.

1. On the first stage it is assumed that the initial distribution of temperature field $f(\rho)$ satisfies the condition (6), and the direct problem of thermoplasticity is solved under condition (9).

The solution of the nonlinear heat conductivity problem is determined numerically using the finite-element method [7]-[9]. According to this method for finding unknown values of temperature at discretization points $T_i(\tau)$ we obtain the following system

$$\sum_{i=0}^N \left(C_{il} \frac{T_l(\tau + \Delta\tau) - T_l(\tau)}{\Delta\tau} + R_{il} \frac{T_l(\tau + \Delta\tau) + T_l(\tau)}{2} \right) = F_i(\tau + \Delta\tau / 2) \quad i = \overline{0, N} \quad (11)$$

where C_{il} , R_{il} are the coefficients of matrix of the heat capacity and heat conductivity, respectively; F_i denote the right-hand side vector components; $\Delta\tau$ is the time step.

The stressed-strained state of a body is determined from the solution of thermoelasticity problem. It is assumed that a body is free from external loads. The physical relations of the above-mentioned theory of thermoplasticity are as following

$$de_{ij} = \frac{ds_{ij}}{2G} - \frac{s_{ij}}{2G^2} \frac{\partial G}{\partial T} dT + de_{ij}^{(p)}$$

$$de_{ij}^{(p)} = (F_S dS + F_T dT) s_{ij} \quad i, j = 1, 2, 3 \quad (12)$$

where F_S and F_T are determined on the base of the instantaneous thermomechanical surface $\sigma = f(\varepsilon, T)$ as

$$F_S = \frac{3\sqrt{3}}{2\sigma} \left(\frac{1}{E_1} - \frac{1}{E} \right) \quad E_1 = \frac{\partial \sigma}{\partial \varepsilon}$$

$$F_T = \frac{3}{2\sigma} \left(\frac{\partial \varepsilon}{\partial T} + \frac{\sigma}{E^2} \frac{\partial E}{\partial T} \right)$$

Here $e_{ij} = \varepsilon_{ij} - \varepsilon_0 \delta_{ij}$, $e_{ij}^{(p)} = \varepsilon_{ij}^{(p)}$ are the deviator components of the total and plastic strains; ε_{ij} , $\varepsilon_{ij}^{(p)}$ are the tensor components of the total and plastic strains; $\varepsilon_0 = (\varepsilon_{11} + \varepsilon_{22} + \varepsilon_{33})/3$; σ_{ij} are the stress tensor components; G is the shear modulus; E is the Young modulus; δ_{ij} denotes Kronecker delta; ε is the total instantaneous strain [3].

The nonlinear thermoelasticity problem is linearized according to a method of additional strains [3], [10]. Therefore, the stress-strain relations are as follows

$$\sigma_{ij} = \frac{E_0}{1+\nu_0} \left(\varepsilon_{ij} - \varepsilon_{ij}^0 + \frac{3\nu_0}{1-2\nu_0} (\varepsilon_0 - \varepsilon_0^0) \delta_{ij} - \frac{1+\nu_0}{1-2\nu_0} \varepsilon_T \delta_{ij} \right) \quad i, j = 1, 2, 3 \quad (13)$$

The relations (13) express the Hooke law for isotropic homogeneous solid with the additional strains

$$\varepsilon_{ij}^0 = \frac{E(1+\nu_0)}{E_0(1+\nu)} \varepsilon_{ij}^{(p)} + \left(1 - \frac{E(1+\nu_0)}{E_0(1+\nu)} \right) (\varepsilon_{ij} - \varepsilon_T \delta_{ij}) + \left(1 - \frac{E(1-2\nu_0)}{E_0(1-2\nu)} \right) (\varepsilon_0 - \varepsilon_T) \delta_{ij} \quad i, j = 1, 2, 3 \quad (14)$$

Here ε_T is the thermal strain; ν is Poisson's ratio; E_0, ν_0 are certain constants.

The additional strains (14), which characterize deviation of equations (13) from Hooke law, take into account the plastic deformation of material and dependence of mechanical parameters on temperature.

The solution of elasticity problem for solids under consideration can be expressed in the analytical form using relations (13), (14).

Thus, the solution of thermoelasticity problem is reduced to a sequence of thermoelasticity problems for isotropic homogeneous solid with additional strains. The plastic strains are determined using a successive approximation method the base of instantaneous thermomechanical surface [3].

2. At the time moment $\tau = \tau_k$, when the maximal value of intensity of tangential stresses approaches the boundary admitted restriction we begin to solve the inverse thermoelasticity problem. Hence, it is necessary to find the heat influence - control function $u(\tau)$ taking into account the given boundary admitted restriction of the intensity of tangential stresses $S_*(T)$. For determining the control function a discrete analog of the heat conductivity problem with unknown function $u(\tau)$ is completed by condition (10). This condition can be written as a relation depending on temperature and additional strains on the base of

the analytical solution of the direct problem of thermoelasticity.

Unknown distribution of the plastic strains and control function at the time moment under consideration are determined using a successive approximation method. Plastic strains $\left(\varepsilon_{ij}^{(p)} \right)^{(k-1)}$ are chosen as initial approximation for plastic strains $\left(\varepsilon_{ij}^{(p)} \right)^{(k)}$. The initial approximation of the additional strains is calculated by formula (14) and the solution of the expanded system (10), (11) is determined using the iteration method. On the base of the obtained initial approximation of the control function we can find the first approximation of the plastic strains at the given time moment by solving the direct problem of thermoelasticity. Owing to formula (14) we can calculate a new approximation of the additional strains and find the first approximation of the control function as the solution of the inverse thermoelasticity problem. The process of successive approximations is finished when the condition

$$|u^{(s+1)} - u^{(s)}| \leq \delta_u |u^{(s)}|$$

is satisfied. Here $u^{(s+1)}, u^{(s)}$ denote two successive approximations of the control function; δ_u is the precision of solving the control problem.

When the control function $u(\tau)$ approaches the boundary admitted value the control problem is solved according to the first stage of the constructed algorithm. The calculations are finished when the final condition of heating (7) is satisfied.

3. Numerical results

As an example we consider the optimal (in the sense of rapidity) problem of control by heating two-layer unbounded hollow cylinder. The first layer is made from steel EI-437 and the second layer is made from steel SP-28. The physical and mechanical characteristics of materials are given in the work [11]. It is assumed that the initial temperature is 20°C and the inner surface $\rho = 0.2$ of the cylinder is heat insulated. The time distribution of the temperature of heating medium on the surface $\rho = 1$ is shown on Fig.1 by the dashed line 4. It is assumed that $H_2 = 10$ and that the conditions of ideal heat and mechanical contacts are fulfilled at the point $\rho = 0.6$.

The time distribution of maximal value of intensity of tangential stresses, maximal and minimal temperatures are shown on Fig.1 by the dashed lines 1-3, respectively. The optimal (in the sense of rapidity) regime of change of heating medium temperature is shown on Fig.1 by continuous line 4 under conditions $U = 700^\circ \text{C}$, $S(T) = 440 \text{ MPa}$, $T_* = 190^\circ \text{C}$. The behavior of the maximal value

of intensity of tangential stresses, maximum and minimum temperature are shown on Fig.1 by continuous lines 1-3. It can be seen from this figure the optimal control consists of three stages. At the first $[0, \tau_1]$ and third $[\tau_2, \tau_*]$ stages the optimal control is equal to boundary admitted restriction and at the second stage $[\tau_1, \tau_2]$ provides the fulfillment of equality (10).

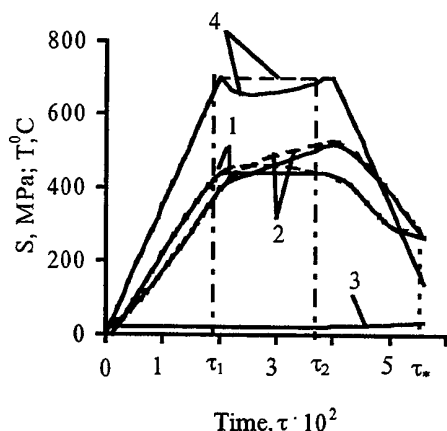


Fig. 1. Distribution of the maximal value of intensity of tangential stresses (1), maximal (2) and minimal (3) temperature and optimal control (4).

The numerical analysis shows that the conditions of the ideal heat and mechanical contact is fulfilled at the point of interface between layers in the hollow cylinder.

For estimation of plausibility of used equations of state the trajectories of deformation are constructed in the two-dimensional Ilyushin space $\dot{\gamma}_1, \dot{\gamma}_2$ [3], [11] at the point $\rho = 1.0$. The trajectory of deformation, when the condition (10) is fulfilled, is shown in Fig. 2. by continuous line. The dashed line shows the trajectory of deformation whith no restriction on the maximal value of intensity of tangential stresses. The point M on Fig.2. corresponds to the time moment $\tau = \tau_1$ and points N_1 and N_2 correspond to moment of unloading.

The estimation of values of curvature radia of constructed trajectories shows that they are trajectories of small curvature. That confirms a possibility of applying the relations of the theory of deformation processes on the trajectories of small curvature for finding the strained-stressed state of the hollow cylinder.

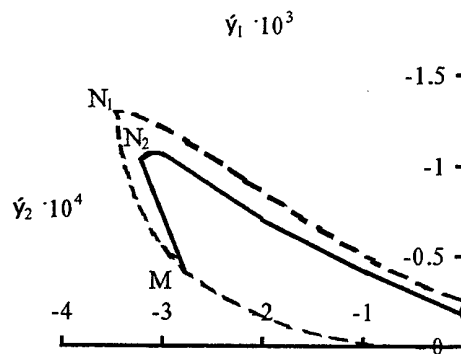


Fig. 2. Trajectories of deformation at the point $\rho = 1.0$

References

- (1) Butkovskii, A.H., Malyi, S.A., Andreyev, Y.N., Control by Heating of Metal, Metalurgiya, Moscow, 1981 (in Russian).
- (2) Rapoport, E.Y., Optimization of Processes of Induction Heating of Metal, Metalurgiya, Moscow, 1993 (in Russian).
- (3) Shevchenko, Y.N., Savchenko, V.H., Thermoviskoplasticity, Naukova Dumka, Kyjiv, 1987 (in Russian).
- (4) Kolyano, Y.M., Methods of Heat Conductivity and Thermoelasticity of Non-Homogeneous Solids, Naukova Dumka, Kyjiv, 1992 (in Russian).
- (5) Vihak, V.M., Optimal Control of Non-Stationary Temperature Regimes, Naukova Dumka, Kyjiv, 1979 (in Russian).
- (6) Vihak, V.M., Control by Thermal Stresses and Displacements, Naukova Dumka, Kyjiv, 1988 (in Russian).
- (7) Mitchel, A.R., Computational Methods in Partial Differential Equations, Wiley, London, 1969.
- (8) Zienkiewicz, O.C., The Finite Element Method in Engineering Science, McGraw-Hill, New York, 1971.
- (9) Strang, G., Fix, G., An Analysis of the Finite Element Method, Prentice Hall, New Jersey, 1973.
- (10) Birger, I.A., Shorr, B.F., Demyanushko, I.V., Thermal Strength of Machine Parts, Mashynostroeniye, Moskow, 1975 (in Russian).
- (11) Shevchenko, Y.N., Terekhov, R.H., Physical Equations of Thermoviskoplasticity, Naukova Dumka, Kyjiv, 1982 (in Russian).

Reformulation of Shakedown Theorems for Materials with Temperature Dependent Yield Stress

G. Borino and C. Polizzotto

*Dipartimento di Ingegneria Strutturale e Geotecnica, DISeG,
Università di Palermo, Viale delle Scienze, I-90128 Palermo, Italy.*

Elastic-plastic associative materials endowed with internal variables and obeying suitable thermo-plastic yielding laws are considered in the hypothesis that the yield function is convex (with respect to all arguments, including temperature), and that creep and thermal coupling phenomena are negligible. For structures composed of the above material and subjected to thermo-mechanical load programs, the static and kinematic shakedown theorem are restated.

Key Words: Thermoplasticity, Internal variables, Shakedown,

1. Introduction

The classic static and kinematic shakedown theorems [1-4] are well known analytical tools to characterize a specific limit state of elastic-plastic (thermally uncoupled) structures subjected to thermo-mechanical load programs. For load programs below the shakedown limit load, after a transient phase during which some limited plastic deformations occur, the structure responds elastically to the following thermo-mechanical loads —i.e. (elastic) shakedown occurs. The above theorems hold good also in the case in which the material yield stress is temperature dependent, provided that the thermal effects on the stress and on the yield function are taken into account for *every possible* thermo-mechanical load condition [5-8]. The latter requirement has heavy computational consequences. Additionally, when the yield stress is nonlinearly related to temperature, the kinematic theorem does not provide an upper bound statement for the shakedown limit load.

In a recent paper [13], these authors have addressed the above shakedown problem within the framework of a thermo-plasticity theory in the hypothesis that the yield function is convex in the space of all its arguments [9,10]. In the present paper internal variables are considered in order to account for the material hardening behaviour. Associative and thermally uncoupled plasticity is considered. The key idea is that entropy production is the sum of two

contributions, one related to the independent state variables, another related to the yield stress variation through temperature [10].

2. Thermodynamic considerations

Disregarding, for simplicity, heat propagation phenomena, the first thermodynamics principle can be written as [10]:

$$\dot{u} = \sigma : \dot{\varepsilon} \quad (1)$$

where $u = u(\varepsilon^e, \eta^e, \xi)$ is the internal energy density function, which depends on the elastic strain ε^e , the "reversible" entropy η^e , and the internal variables ξ ; also, σ is the stress, $\dot{\varepsilon}$ the total strain rate. Denoting by T the absolute temperature and introducing the free energy $\psi = u - T\eta^e = u - T(\eta - \eta^p)$, eqn (1) can be rewritten

$$T \dot{\eta} = \sigma : \dot{\varepsilon} - \dot{\psi} - \eta^e \dot{T} + T \dot{\eta}^p. \quad (2)$$

The l.h. side of (2), in absence of heat propagation, represents the entropy production rate which, by the second thermodynamics principle, is nonnegative, i.e.

$$\sigma : \dot{\varepsilon} - \dot{\psi} - \eta^e \dot{T} + T \dot{\eta}^p \geq 0 \quad (3)$$

which is the relevant Clausius-Duhem inequality.

Let ψ be assumed in the form

$$\psi = \psi_e(\epsilon^e, T) + \psi_{in}(\xi, T). \quad (4)$$

Substituting eqn (4) into (3) and noting that $\dot{\epsilon} = \dot{\epsilon}^e + \dot{\epsilon}^p$ gives:

$$\left(\sigma - \frac{\partial \psi_e}{\partial \epsilon^e} \right) : \dot{\epsilon}^e - \left(\eta^e - \frac{\partial \psi}{\partial T} \right) \dot{T} + \sigma : \dot{\epsilon}^p + T \dot{\eta}^p - \frac{\partial \psi_{in}}{\partial \xi} \cdot \dot{\xi} \geq 0 \quad (5)$$

Using classical arguments, we obtain the state equations as

$$\sigma = \frac{\partial \psi_e}{\partial \epsilon^e}, \quad \eta^e = -\frac{\partial \psi}{\partial T}, \quad \chi = \frac{\partial \psi_{in}}{\partial \xi} \quad (5)$$

as well as the dissipation density function, i.e.

$$\sigma : \dot{\epsilon}^p + T \dot{\eta}^p - \chi : \dot{\xi} \geq 0. \quad (7)$$

3. Associative thermo-plastic yielding laws

The material yielding function is assumed to depend on the state variables σ , $T = T_0 + \theta$ and χ , the thermodynamic forces related to the plastic mechanism variables $(\dot{\epsilon}^p, \dot{\eta}^p, \dot{\xi})$, i.e. $f(\sigma, \theta, \chi) \leq 0$, where by hypothesis f is smooth and convex with respect to all variables, including temperature. The thermo-plastic yielding laws are assumed as follows:

$$\dot{\epsilon}^p = \lambda \frac{\partial f}{\partial \sigma}, \quad \dot{\eta}^p = \lambda \frac{\partial f}{\partial \theta}, \quad \dot{\xi} = -\lambda \frac{\partial f}{\partial \chi} \quad (7a)$$

$$f(\sigma, \theta, \chi) \leq 0, \quad \dot{\lambda} \geq 0, \quad \dot{\lambda} f(\sigma, \theta, \chi) = 0 \quad (7b)$$

where λ is the consistency (or plastic) coefficient and the complementarity conditions (7b) account for the loading/unloading rule. Equations (7a,b) comply with the general normality rule to the yield surface $f=0$ in the (σ, θ, χ) -space.

Due to the convexity of f , the inequality

$$(\sigma - \bar{\sigma}) : \dot{\epsilon}^p + (\theta - \bar{\theta}) \dot{\eta}^p - (\chi - \bar{\chi}) : \dot{\xi} \geq 0 \quad (8)$$

holds for any sets (σ, θ, χ) and $(\dot{\epsilon}^p, \dot{\eta}^p, \dot{\xi})$ corresponding to each other through the constitutive equations (7a,b), as well as for any plastically admissible set $(\bar{\sigma}, \bar{\theta}, \bar{\chi})$, i.e. such that $f(\bar{\sigma}, \bar{\theta}, \bar{\chi}) \leq 0$.

The equality sign holds in eqn (8) if, and only if, either $\dot{\epsilon}^p = 0$, $\dot{\eta}^p = 0$, $\dot{\xi} = 0$ (in which case, $\bar{\sigma}, \bar{\theta}$ and $\bar{\chi}$ may be different from σ , θ and χ), or $\sigma = \bar{\sigma}$, $\theta = \bar{\theta}$, $\chi = \bar{\chi}$ (in which case $\dot{\epsilon}^p, \dot{\eta}^p, \dot{\xi}$ may be different from zero). Equation (8) is equivalent to a statement of maximum thermoplastic dissipation, which is the thermoplastic equivalent of Hill-Drucker [1,2] inequality. Thus, we can write (dropping the upper bars):

$$D(\dot{\epsilon}^p, \dot{\eta}^p, \dot{\xi}) = \max_{(\sigma, \theta, \chi)} \left(\sigma : \dot{\epsilon}^p + T \dot{\eta}^p - \chi : \dot{\xi} \right) \quad (9)$$

subject to: $f(\sigma, \theta, \chi) \leq 0$

where $T = T_0 + \theta$ and T_0 = ambient absolute temperature. The maximization problem (9) represents the maximum plastic dissipation theorem for the considered material. The Kuhn-Tucker conditions of problem (9) coincide with eqns. (7a,b).

4. The structural shakedown problem

A structure composed of the above material is subjected to thermo-mechanical loadings which vary in time in a quasi-static manner and depends on a set of independent parameters, say $\mathbf{P} = (\mathbf{P}^L, \mathbf{P}^\theta)$, \mathbf{P}^L for mechanical loads, \mathbf{P}^θ for thermal loads. \mathbf{P}^L and \mathbf{P}^θ are allowed to vary arbitrarily within the (closed) domains Π^L and Π^θ , which are assumed as polyhedra of, respectively, m^L , and m^θ vertices. Thus \mathbf{P} vary within $\Pi = \Pi^L \times \Pi^\theta$, with $m = m^L \cdot m^\theta$ vertices. The vectors \mathbf{P}_k , $k \in I(m) \equiv \{1, 2, \dots, m\}$, specifying the positions of these vectors, are referred to as the *basic* thermo-mechanical loads. Any \mathbf{P} inside Π can be represented as [12, 13]:

$$\mathbf{P} = \sum_{k=1}^m \gamma_k \mathbf{P}_k \quad (10)$$

where the γ s coefficients must satisfy the admissibility conditions:

$$\gamma_k \geq 0, \text{ for all } k \in I(m), \quad \sum_{k=1}^m \gamma_k = 1 \quad (11)$$

On letting the γ s vary in all possible ways, \mathbf{P} describes Π entirely; also taking the γ s as functions of $t \geq 0$, but complying with (11) for all t , a load path $\mathbf{P}(t)$ inside Π is obtained (*Admissible Load History*, ALH).

Equation (10) implies that the thermo-elastic stress response and the temperature corresponding to $\mathbf{P} = (\mathbf{P}^L, \mathbf{P}^0) \in \Pi$ can be represented as

$$\sigma^E = \sum_{k=1}^m \gamma_k \sigma_k^E(\mathbf{x}) \quad (12a)$$

$$\theta = \sum_{k=1}^m \gamma_k \theta_k(\mathbf{x}) \quad (12b)$$

where $\sigma_k^E(\mathbf{x})$ and $\theta_k(\mathbf{x})$ denote the analogous fields corresponding to basic load \mathbf{P}_k , $\forall k \in I(m)$.

In the following the static and kinematic theorems are phrased in a time-discrete form, in which only the basic thermo-mechanical loads are considered. This is possible due to the convexity of f .

4.1 STATIC SHAKEDOWN THEOREM

A necessary and sufficient condition in order that (elastic) shakedown occurs in an elastic-thermo-plastic structure subjected to thermo-mechanical loads variable in a (convex) polyedral domain Π with basic loads \mathbf{P}_k , $k \in I(m)$, is that there exist a time independent stress field, $\bar{\sigma}$, and a time-independent static internal variable field, $\bar{\chi}$, such that the sets $(\hat{\sigma}_k = \sigma_k^E(\mathbf{x}) + \bar{\sigma}, \theta_k, \bar{\chi})$ be plastically admissible for all $k \in I(m)$ everywhere in V , i.e.

$$f(\hat{\sigma}_k, \theta_k, \bar{\chi}_k) \leq 0, \quad \text{in } V, \quad \text{all } k \in I(m). \quad (13)$$

Proof. The procedure is similar to that of classic shakedown theory. The necessity part of the theorem is skipped being self-evident and we consider the sufficiency part only. Assume that eqn (13) be satisfied with some $\bar{\sigma}$, and $\bar{\chi}$. Let $\mathbf{P} = \mathbf{P}(t)$, $t \geq 0$, be any ALH and let the related elastic stress response and temperature distributions be expressed as in eqns (12a,b). Due to the convexity of f .

$$f(\sigma^E + \bar{\sigma}, \bar{\theta}, \bar{\chi}) \leq \sum_{k=1}^m \gamma_k f(\hat{\sigma}_k, \theta_k, \bar{\chi}_k) \leq 0 \quad \text{in } V \quad (14)$$

Thus, denoting by $\sigma, \varepsilon, \eta, \dots$ the actual response to the considered ALH, by eqn (8) and setting $\hat{\sigma} = \sigma^E + \bar{\sigma}$, one has

$$J = (\sigma - \hat{\sigma}) : \dot{\varepsilon}^P - (\chi - \bar{\chi}) : \dot{\xi} \geq 0, \quad \text{in } V, \quad \forall t \geq 0 \quad (15)$$

Assuming a linear elastic material behaviour, it is

$$\dot{\varepsilon}^P = \dot{\varepsilon} - \dot{\varepsilon}^E - \mathbf{C}^{-1} : \frac{d}{dt}(\sigma - \hat{\sigma}) \quad (16a)$$

$$(\chi - \bar{\chi}) : \dot{\xi} = \frac{d}{dt} \left\{ \psi_{in}(\xi) - \psi_{in}(\bar{\xi}) - \bar{\chi} : (\xi - \bar{\xi}) \right\} \quad (16b)$$

and thus, with an integration over V , eqn (15) gives

$$\begin{aligned} \int_V J dV = \int_V (\sigma - \hat{\sigma}) : (\dot{\varepsilon} - \dot{\varepsilon}^E) dV \\ - \frac{d}{dt} \int_V \left[\frac{1}{2} (\sigma - \hat{\sigma}) : \mathbf{C}^{-1} : (\sigma - \hat{\sigma}) \right. \\ \left. + \psi_{in}(\xi) - \psi_{in}(\bar{\xi}) - \bar{\chi} : (\xi - \bar{\xi}) \right] dV \end{aligned} \quad (17)$$

Since the first integral on the r.h. side of (17) vanishes by the virtual work principle and since $J \geq 0$ by eqn (15), follows

$$\begin{aligned} \frac{d}{dt} \int_V \left[\frac{1}{2} (\sigma - \hat{\sigma}) : \mathbf{C}^{-1} : (\sigma - \hat{\sigma}) \right. \\ \left. + \psi_{in}(\xi) - \psi_{in}(\bar{\xi}) - \bar{\chi} : (\xi - \bar{\xi}) \right] dV \leq 0 \end{aligned} \quad (18)$$

Considered that the above integral is positive definite and that therefore its value cannot become negative during the deformation process produced by the considered ALH, there must exist some time t^* such that for $\forall t \geq t^*$ it is $J = 0$, i.e. eqn (15) is satisfied as an equality, and as consequence $\dot{\varepsilon}^P, \dot{\eta}^P, \dot{\xi}$ vanishes at all $t \geq t^*$. That is, shakedown occurs. QED.

Let $\tilde{\mathbf{P}}_k$ denote some reference thermomechanical load with related temperature $\tilde{\theta}_k$ and let $\tilde{\sigma}_k^E$ be the corresponding elastic stress response. It can be easily shown that, if the sets $\hat{\sigma}_k = \beta_s \tilde{\sigma}_k^E + \bar{\sigma}$, $\theta_k = \beta_s \tilde{\theta}_k$ satisfy eqn (13) with some $\bar{\sigma}$, $\bar{\chi}$, then $\beta_s \leq \beta^*$, β^* being the relevant shakedown limit load.

4.2 KINEMATIC SHAKEDOWN THEOREM

A necessary and sufficient condition in order that elastic shakedown occurs in an elastic-thermo-plastic structure subjected to thermo-mechanical loads variable within a convex polyedral domain Π with basic loads \mathbf{P}_k , $k \in I(m)$ is that the inequality

$$E[\varepsilon_k^p, \eta_k^p, \xi_k] = \sum_{k=1}^m \int_V \left\{ D(\varepsilon_k^p, \eta_k^p, \xi_k) - \sigma_k^E : \varepsilon_k^p - \theta_k \eta_k^p \right\} dV \geq 0 \quad (19)$$

is satisfied for arbitrary choices of (noninstantaneous) mechanisms $\varepsilon^p = \varepsilon^p(u)$, with $u = 0$ on $S_u \subseteq \partial V$, and of thermoplastic strain path $\varepsilon_k^p, \eta_k^p, \xi_k$ such that

$$\sum_{k=1}^m \varepsilon_k^p = \varepsilon^p, \quad \sum_{k=1}^m \eta_k^p = \eta^p, \quad \sum_{k=1}^m \xi_k = 0, \quad \text{in } V. \quad (19)$$

The proof, similar to that presented in [12,13], is not reported here for lack of space. It can be shown that eqn. (19) written for $\sigma_k^E = \beta^* \tilde{\sigma}_k^E$, and $\theta_k = \beta^* \tilde{\theta}_k$ gives:

$$\beta^* \leq \frac{\sum_{k=1}^m \int_V D(\varepsilon_k^p, \eta_k^p, \xi_k) dV}{\sum_{k=1}^m \int_V (\tilde{\sigma}_k^E : \varepsilon_k^p + \tilde{\theta}_k \eta_k^p) dV} \quad (21)$$

which is an upper bound to β^* .

5. Conclusions

This paper provide an improved formulation of shakedown theory for thermo-mechanical processes with temperature-dependent yield stress. Thermal coupling and creep phenomena have been ignored, but they perhaps need to be considered in a refined theory, which is the object of an ongoing research work.

Acknowledgements: This paper is part of a research project supported by the Italian Ministero della Ricerca Scientifica e Tecnologica, (MURST 60%).

References

- (1) W.T. Koiter, General Theorems of elastic plastic solids, Progress in Solid Mechanics, eds. J.N. Sneddon, R. Hill, North Holland, Amsterdam, Vol. 1, 167-221, 1960.
- (2) J.B. Martin, Plasticity, fundamentals and general results, The MIT Press, Cambridge, Ma, 1975.

- (3) D.A. Gokhfeld and D.F. Chernavsky, Limit analysis of structures at thermal cycles, Sijthoff & Noordhoff, Alphen aan der Rijn, The Netherlands, 1980.
- (4) J. A. König, Shakedown of elastic-plastic structures, PWN-Polish Scientific Publishers, Warsaw, and Elsevier, Amsterdam, 1987.
- (5) W. Prager, Shakedown in elastic plastic media subjected to cycles of load and temperature, La plasticità nella Scienza delle Costruzioni, Proc. of the Symp. In honour of Arturo Danusso, Varenna, Italy, N. Zanichelli, Bologna, 239-244 1956.
- (6) J. . König, On some recent developments in the shakedown theory, Advances in Mechanics, 5, 237-258, 1982.
- (7) J. . König, Shakedown criteria in the case of loading and temperature variations, J. de Mécanique Théorique et Appliquée, Special Issue, 99-108, 1982.
- (8) J. . König, Quelques problemes recents dans la theorie de l'adaptation, Problèmes des rhéologie et mécanique des sols, Proc. Symp. Franco-Polonais, Nice, 233-243, 1974.
- (9) N. R. Hansen , H. L. Schreyer, A thermodynamically consistent framework for theories of elastoplasticity coupled with damage, Int. J. Solids Struct., 31, 359-389, 1994.
- (10) J.C. Simo and C. Miehe, Associative coupled thermoplasticity at finite strains: formulation, numerical analysis and implementation, Comput. Meths. Appl. Mech. Engng., 98, 41-104, 1992.
- (11) J. Lemaitre, J.-L. Chaboche, Mechanics of Solids Materials, Cambridge University Press, 1990.
- (12) C. Polizzotto, G. Borino, S. Caddemi and P. Fuschi, Shakedown problems for material models with internal variables, Eur. J. Mech. A/Solids, 10, 621-639, 1991.
- (13) G. Borino and C. Polizzotto, Shakedown theorems for a class of materials with temperature-dependent yield stress, in Proc. Complas 5, eds D.R.J Owen, E. Onate, E. Hinton, Pineridge press, 1997.

Modelling of Transformation Induced Plasticity

L. Taleb and J.F. Jullien

INSA, URGC/Structures, 20 avenue A. EINSTEIN 69621 Villeurbanne Cedex, FRANCE.
Tél. : (33) 4 72 43 87 04. Fax : (33) 4 72 43 85 23. e-mail : taleb@gcu-beton.insa-lyon.fr

The main objective of this paper is to give a description of the recent developments approach to the analysis of the Transformation Induced Plasticity (TIP) phenomenon. Both experimental and modelling aspects are reviewed. For the experimental one, the main parameters associated with TIP evolution are collected from a literature citations. A number of phenomenological and theoretical models are then considered in order to see if the chosen experimentally observed phenomena are well described. This work shows that these phenomena are not yet completely taken into account by the tested models. The phenomenological model presented by Videau et al. seems to be the one which is able to take into account the largest number of the observed effects. Unfortunately, this fact remains today mainly qualitative because up to now (to the best of our knowledge) no complete experimental identification of the model parameters has so far been made.

Key Words : Fe-C Alloys, Phase Transformation, Transformation Plasticity, Residual Stresses.

1. Introduction

Welding process of Fe-C alloys usually leads to the creation of a particular region called Heat Affected Zone (HAZ). The HAZ is the part of the material where the temperature remains below the melting point but sufficient to enable some structural transformations. If these transformations occur without external applied stress, normally no change of geometry is observed (except for the cases where the Fe-C alloy includes some segregations responsible of an effect of anisotropy which will have some macroscopic consequences). Otherwise, if the transformation occurs under an external applied stress, an irreversible deformation is observed even if the applied stress is significantly less than the yield stress of the weaker phase. This kind of irreversible deformation is called Transformation Induced Plasticity (TIP). The geometrical variation induced by this phenomenon has a significant part in the creation of the residual stresses in the material. It is therefore necessary to know accurately the importance of the latter after a welding process. The main goal of this paper is to give a description of the recent developments approach to the analysis of the TIP phenomenon. For this objective both experimental and modelling aspects are reviewed. In the second part of this paper some experimentally observed phenomena related to the TIP evolution are briefly described. The third part is devoted to a short presentation of the main constitutive equations of the chosen models followed by some comments related to the ability of these models to describe the considered phenomena.

2. Experimentally observed phenomena

The main experimentally observed phenomena collected from the literature citations are related to the TIP evolution versus the applied loading characteristics and the strain hardening state of the coexisting phases. These phenomena may be classified as follows :

(a) Level of the applied stress influence : the influence of the level of the applied stress on the final value (at the end of the transformation) of TIP has been studied by many authors [1]-[3]. The different obtained results seem agree with the fact that the final value of TIP is proportional to the applied stress (which remains constant) up to a certain fraction of the yield stress. According to [3], this fraction is about 1/2 for an applied tension or a combination of a tension and torsion and about 2/3 for an applied compression or a combination of a compression and a torsion.

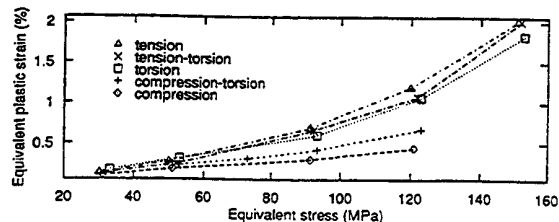


Figure 1 : TIP under various stress state [3]

(b) Direction of the applied stress effect : TIP evolution depend on the direction of the applied stress. At the end of a transformation, it seems that the

TIP absolute value is maximum for the tension and minimum for the compression [3] (see figure 1).

(c) Interaction between classical plasticity and TIP : there exists an interaction between the classical plasticity and TIP. In fact, it was shown [3] that the TIP evolution depends on the hardening state of the mother phase.

(d) Direction of TIP flow : some experimental results given in [3] show that TIP increment is colinear to the deviator of the effective stress instead of the stress itself. The effective stress is equal to the difference between the applied stress and the internal one. It was established that the latter has two components related respectively to the classical plasticity and TIP.

3. Considered Models. Comments

TIP is the plastic flow observed during the progress of a phase transformation under a moderate (less than the yield stress of the weaker phase) applied stress. This phenomenon is generally explained by two physical mechanisms : the first one [1] attributes TIP to the microscopic plasticity generated in the weaker phase (oriented by the applied stress) by the difference of specific volumes between the coexisting phases. This mechanism is related essentially to diffusional transformations (including bainitic one). The second mechanism [9] is related to martensitic transformation, it attributes the TIP phenomenon to the fact that under an external loading, the martensite plates are formed with a preferred orientation. In this paper only models based on the first mechanism will be considered.

For each considered model, the main constitutive equations are briefly presented followed by some comments related to their ability to describe the experimentally observed phenomena presented in the second part of this paper.

3.1 THEORETICAL MODELS

3.1.1 *The Model Proposed by Greenwood and Johnson*. This model doesn't give the evolution of TIP during transformation, it only allows to have the final value of TIP (at the end of a transformation) by the following equation :

$$\varepsilon^{pr} = \frac{5}{6} \frac{\sigma}{\sigma_y} \frac{\Delta V}{V} \quad (1)$$

where :

ε^{pr} is Transformation Induced Plasticity (TIP),

σ is the applied stress,

σ_y is the yield stress of the weaker phase,

$\Delta V/V$ is the relative variation of volume during transformation,

Comments :

- *phenomenon (a)* : not completely taken into account because the model supposes a full proportionality between the final value of TIP and the applied stress.

- *phenomenon (b)* : not taken into account because for the same absolute value of the applied stress, whatever its direction, the model forecasts the same TIP value.

- *phenomenon (c)* : not taken into account because no interaction between TIP and classical plasticity is considered.

- *phenomenon (d)* : not taken into account because the TIP flow is assumed to be colinear to the stress itself instead of the deviator of the effective stress.

3.1.2 *The Model Proposed by Abrassart*. This model gives the TIP evolution during the transformation. The proposed expression is as follows :

$$\varepsilon^{pr} = \frac{3}{4} \frac{\sigma}{\sigma_y} \frac{\Delta V}{V} \left(z - \frac{2}{3} z^{\frac{3}{2}} \right) \quad (2)$$

where :

ε^{pr} is the transformation induced plasticity,

σ is the applied stress,

σ_y is the yield stress of the weaker phase,

$\Delta V/V$ is the relative variation of the volume during the transformation,

z is the proportion of the new phase ($0 \leq z \leq 1$).

Comments : the same qualitative comments that the previous model could be made for this one. Quantitatively, at the end of the transformation ($z=1$), this model predicts a value less than the third of the one given by the Greenwood and Johnson model.

3.1.3 *The Model Proposed by Leblond*. This model is more recent, it gives the TIP evolution during the transformation. The proposed expressions considering ideal-plastic phases are as follows :

$$\dot{\varepsilon}^{pr} = \begin{cases} 0 & \text{if } z \leq 0.03 \\ -\frac{3\Delta\varepsilon_{1 \rightarrow 2}^{th}}{\sigma_y} \cdot \underline{S} \cdot h\left(\frac{\sigma^a}{\sigma_y}\right) \cdot (\ln z) \cdot \dot{z} & \text{if } z > 0.03 \end{cases} \quad (3)$$

where :

$$h\left(\frac{\sigma^a}{\sigma_y}\right) = \begin{cases} 1 & \text{if } \frac{\sigma^a}{\sigma_y} \leq 0.5 \\ 1 + 3.5 \left(\frac{\sigma^a}{\sigma_y} - \frac{1}{2} \right) & \text{if } \frac{\sigma^a}{\sigma_y} \geq 0.5 \end{cases} \quad (4)$$

$\Delta\varepsilon_{1 \rightarrow 2}^{th}$ is the difference of thermal deformation between the mother and the daughter phases ($=\Delta V/3V$).

σ_y is the yield stress of the weaker phase,

\underline{S} is the deviator of the stress tensor,

σ^{eq} is the equivalent applied stress (Von Mises),
 σ^y is the yield stress of the mixture,
 $h(\frac{\sigma^{eq}}{\sigma^y})$ is a function which takes into account the influence of the ratio : equivalent applied stress over the yield stress of the mixture,
 Z is the proportion of the new phase.

For the case where a linear isotropic hardening is considered, σ_i^y will depend on the effective plastic strain. If a linear kinematic hardening is considered, \underline{S} will be replaced by $(\underline{S}-\underline{A}_i)$ where \underline{A}_i is the internal stress due to the TIP evolution [7].

Comments :

- *phenomenon (a)* : qualitatively taken into account by the function $h(\frac{\sigma^{eq}}{\sigma^y})$.
- *phenomenon (b)* : not taken into account because the equivalent applied stress is given by the isotropic criterion of Von Mises.
- *phenomenon (c)* : not taken into account because no interaction between TIP and classical plasticity is considered. The internal stress tensor \underline{A}_i induced for the kinematic hardening case is only due to the TIP evolution.
- *phenomenon (d)* : taken into account when kinematic strain hardening is considered. In fact in the latter case, the direction of TIP flow is assumed to be the one of the deviator of the effective stress.

3.2 PHENOMENOLOGICAL MODELS

3.2.1 *The Model Proposed by Desalos.* Considering the results of some TIP experiments, Desalos [2] has established a relation between the TIP evolution, the proportion of the new phase and the uniaxial applied stress, the proposed expression is as follows :

$$\dot{\epsilon}^p = K \cdot \sigma \cdot f(z) \quad (5)$$

where :

K is a parameter depending on the transformation and on the material,

$f(z)$ is a function of the proportion of the new phase, for the considered test this function is equal to $(2-z)z$ ($f(0)=0$ and $f(1)=1$).

A generalization of the above equation for the multiaxial cases in addition to the ones where the stress is not constant was later proposed by Leblond [8] :

$$\dot{\epsilon}_{ij}^p = k \cdot S_{ij} \cdot g(z) \cdot \dot{z} \quad (6)$$

where :

\dot{z} is the rate of the new phase,

$\dot{\epsilon}_{ij}^p$ is the ij component of the TIP rate tensor ($\dot{\epsilon}^p$),

S_{ij} is the ij component of the deviator tensor (\underline{S}),

$g(z)$ is a function of the new phase proportion ($g = \frac{\partial f}{\partial z}$).

Comments :

- *phenomenon (a)* : not completely taken into account because the model supposes a full proportionality between the final value of TIP and the deviator of the applied stress.
- *phenomenon (b)* : not described because the equivalent applied stress is given by the isotropic criterion of Von Mises.
- *phenomenon (c)* : not taken into account because no interaction between TIP and classical plasticity is considered. In addition no internal stress whatever its origin is considered.
- *phenomenon (d)* : not considered because the direction of TIP flow is assumed to be the one of the stress deviator.

3.2.2 *The Model Proposed by Videau & al.* This model is the more recent of all. The evolution of the TIP rate is given by :

$$\dot{\epsilon}^p = \left(\sum_{i,j} K_{ij} z_i \langle \dot{z}_j \rangle \right) (\underline{S} - \underline{X}^p) \quad (7)$$

For diffusional transformations, the above equation is slightly modified as follows :

$$\dot{\epsilon}^p = \left(\sum_{i,j} K_{ij} \langle \dot{z}_j \rangle \right) (\underline{S} - \underline{X}^p) \quad (8)$$

where :

$$\langle X \rangle = X \text{ si } X \geq 0 \text{ et } \langle X \rangle = 0 \text{ si } X < 0$$

i and j mean : transformation, phase $i \rightarrow$ phase j ,

z_i is the proportion of phase i ,

\underline{S} is the stress deviator tensor,

\underline{X}^p is the internal stress tensor, it includes the effect of the interaction between TIP and classical plasticity, the sum $\sum_{i,j} K_{ij} z_i \langle \dot{z}_j \rangle = K^p$ replaces $2k(1-z)\dot{z}$

in the equation (6). In the presence of only two phases, $K^p = K_{12} z_1 \langle \dot{z}_2 \rangle + K_{21} z_2 \langle \dot{z}_1 \rangle$. Thus K^p allows to take into account the direction of the transformation ($i \rightarrow j$ or $j \rightarrow i$) because it is experimentally observed that K_{12} is different of K_{21} .

Comments :

- *phenomenon (a)* : not completely taken into account because the value of TIP at the end of a transformation is assumed to be fully proportional to the effective applied stress.
- *phenomenon (b)* : not described because the equivalent applied effective stress is given by the isotropic criterion of Von Mises.
- *phenomenon (c)* : qualitatively expressed because the considered internal stress tensor \underline{X}^p should include a classical plasticity effect.

- *phenomenon (d)* : expressed because the direction of TIP flow is assumed to be the one of the effective stress deviator.

4. Conclusion

Table 1 summarizes the conclusions concerning the ability of the considered models to take into account the selected experimentally observed phenomena. The first column contains the selected models and the first line refers to the considered phenomena. y and n mean respectively that the model take into account or not the chosen phenomenon. When both y and n are present the considered model take partly into account the chosen phenomenon.

Table 1 ability of considered models to describe experimentally observed phenomena (a), (b), (c) and (d).

	(a)	(b)	(c)	(d)
Greenwood & Johnson	y, n	n	n	n
Abrassart	y, n	n	n	n
Leblond	y	n	n	y
Desalos	y, n	n	n	n
Videau et al.	y, n	n	y	y

This table shows that the chosen experimentally observed phenomena are not yet completely taken into account by the tested models. The phenomenological model presented by Videau et al. seems to be the one which is able to take into account the largest number of the observed effects. Unfortunately, that remains today mainly qualitative because to the best of our knowledge no complete experimental identification of the model parameters has so far been made. Moreover in a welding process thermal gradients create some opposite thermal stresses for which the TIP evolution is not necessary the same (phenomenon (b)), this fact is not taken into account by this model and then the forecasts could be different from the reality.

The models proposed by Greenwood and Johnson and Abrassart cannot be used to predict the consequences of a welding process because, the first one only gives the value of TIP at the end of a phase transformation under a constant loading and the second one largely underestimates the TIP evolution.

The model proposed by Leblond is more general, it is normally applicable to predict TIP in a welding process. Quantitatively the forecasts could be different from the reality if (b) and (c) phenomena are significant. This model being essentially theoretical, more experimental results are necessary to its validation.

The tested models, except the one proposed by Videau et al., are established taking into account only one transformation, the variable z present in the proposed expressions is then defined as the proportion of the

new phase. That definition seems not sufficient when more than one phase transformation occur. In our opinion the forecasts will be better if z is taken as the sum of the proportions of the new phases which are formed under the external applied load.

Acknowledgment

The authors gratefully acknowledges Electricité De France (SEPTEN and DER) for their support of this work.

6. References

- (1) Greenwood G.W., Johnson R.H., The deformation of metals under small stresses during phase transformations, Proc. Roy. Soc. London, A283, p. 403-422, 1965.
- (2) Desalos Y., Comportement dilatométrique et mécanique de l'austénite métastable d'un acier A 533, Rapport IRSID n°95 34 94 01 MET 44, 1981.
- (3) Videau J.Ch., Cailletaud G., Pineau A., Experimental study of the transformation induced plasticity in a Cr-Ni-Mo-Al-Ti Steel, International seminar MECAMAT'95 : Mechanisms and mechanics of solid phase transformations, la Bresse, 16-19 mai, 1995.
- (4) Videau J.Ch., Cailletaud G., Pineau A., Modélisation des effets mécaniques des transformations de phases pour le calcul de structures, Journal de physique IV. Colloque C3, supplément au Journal de physique III, Vol. 4, février 1994.
- (5) Abrassart F., Influence des transformations martensitiques sur les propriétés mécaniques des alliages du système Fe-Ni-Cr-C. Thèse d'état université de Nancy I. 1972,
- (6) Leblond J.B., Devaux J., Devaux J.C., Mathematical modelling of transformation plasticity in steels- I. Case of ideal-plastic phases, Int. J. Of Plasticity, Vol.5, pp. 551-572, 1989.
- (7) Leblond J.B., Mathematical modelling of transformation plasticity in steels- II. Coupling with strain hardening phenomena, Int. J. Of Plasticity, Vol.5, pp. 573-591, 1989.
- (8) Leblond J.B., Simulation numérique du soudage-Modélisation mathématique des transformations métallurgiques-Etat d'avancement des travaux. Framatome, Internal report #TM/C DC/80.066, 1980.
- (9) Magee C.L., Transformation kinetics, microplasticity and ageing of martensite in Fe-31-Ni. Ph. D. Thesis Carnegie Mellon University, Pittsburgh, 1966.

Session 1E

RESIDUAL STRESSES I

Chair: C. C. Chamis

Co-Chair: W. Szyskowski

Temperature Field and Welding Residual Stresses in an Underwater Plasma-MIG Welded Single-Butt Weld

L. Lindhorst, O. Mahrenholtz

Influence of Low Tensile Residual Stresses due to Welding on the Fatigue Strength of High Strength Steels

Th. Nitschke-Pagel, H. Wohlfahrt

Numerical Analysis of Process-Induced Thermal Residual Stresses in Metallic Matrix Composites

A. Abedian, W. Szyszkowski, and S. Yannacopoulos

Fatigue Behaviour of Fully Compressive Loaded Welded Joints with High Tensile Residual Stresses due to Welding

J. Pucelik, Th. Nitschke-Pagel, and H. Wohlfahrt

A Numerical Procedure for Welding Residual Stresses Estimation

G. F. M. Souza, E. Goncalves

Temperature Field and Welding Residual Stresses in an Underwater Plasma-MIG Welded Single-Butt Weld

L. Lindhorst and O. Mahrenholtz

Offshore Section II, TU Hamburg-Harburg, D-21071 Hamburg, GERMANY

The influence of the water contact on underwater Plasma-MIG welding is regarded. An example of a rectangular plate with a single-butt weld is presented. The transient temperature field and the welding residual stresses are calculated using the finite element method (FEM). The results of the wet underwater welding process are compared to those of the dry welding process.

Key Words: Underwater Welding, Finite Element Method, Welding Residual Stresses

1. Introduction

Underwater welding is an important part of building and maintaining ships, oil rigs, and other off-shore equipment. Scuba divers with this skill have used arc welders to repair metal failures in all types of situations. Industry is still finding different areas where underwater welding is needed. Nuclear power has been identified as one of these areas. The pools of water which house spent uranium rods need constant maintenance to meet the rigorous standards of the industry. Automation is required to carry out repairs in such pools and the quality of the welds must be high.

Welding under water causes the material in the weld and in the region surrounding the weld to cool very rapidly. The quality of a weld is made up of several factors. Two such factors are the microstructure and the residual stresses in the welded structure. Both of these factors are affected adversely by a high cooling rate, which is not suited to applications requiring ductility. Fast cooling causes the metal to contract quickly. This often leads to regions of high stress in the weld. Cracking can be seen in these welds. As a result, the fracture mechanics of underwater welds are an area of concern (Lindhorst & Mahrenholtz [1]).

2. Theory

2.1 PLASMA-MIG WELDING

There are two components that make up the simulated welding process. These two components are the Plasma arc and the MIG arc as shown in Fig. 1 (Hamann [2]). Both belong to the 'Direct Light' processes. The Plasma-MIG technique works using a mechanically fed fusible metal electrode. The heat is created by the discharge of electrical energy when the positive and negative electrodes come in contact with each other. The positive electrode is the weld wire, which is fed at constant velo-

city to the welding head as the weld progresses. The ground, or negative electrode, is the weld specimen. The heat released from both the Plasma arc and the MIG arc melt the weld wire as well as the base metal. The MIG arc is surrounded by a region of hot inert gases. These gases protect the

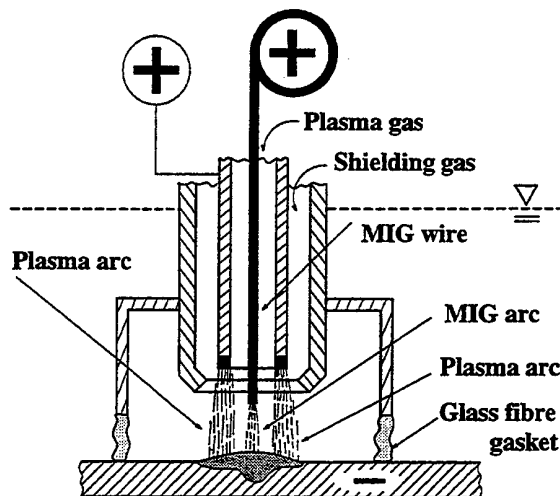


Fig.1. Schematic of Plasma-MIG welding.

weld from the atmosphere, in water and in the air. There is heat transfer to these gases, which is heat loss. This is accounted for by the efficiency of the welder. The efficiency of the welder is improved by trapping inert gases between the MIG arc and the Plasma arc. The Plasma gas is ionized which improves conductivity between the two electrodes. This stabilizes the Plasma arc, which in turn creates a weld that transfers material to the weld specimen without splattering. A schematic of the process is shown in Figure 1.

The Plasma-MIG welder simulation that is used in this simulation was developed by Hamann [2]. The heat flux by the arcs is approximated by a hemispherical (MIG arc) and a two-dimensio-

nal (Plasma arc) power distribution. The two processes are mathematically simulated by superimposing the power density function of the MIG arc with the power density function of the Plasma arc. This generates a three-dimensional power density distribution for the combined arcs.

2.2 HEAT TRANSFER TO WATER

The water contact influences mainly the temperature distribution inside the welded body in case of wet underwater welding. Hamann & Mahrenholtz [3] have investigated the influence of the water contact on the temperature field. They have developed a model for the calculation of the surface-heat-transfer coefficient, which takes into account the material effects, the orientation of the surface and the influence of undercooled boiling. The march of the surface-heat-transfer coefficient for the top and the bottom side of a horizontally orientated plate is shown in Fig. 2 (Hamann [2]).

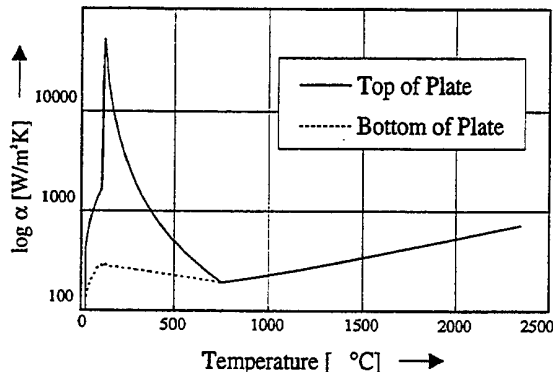


Fig.2. Heat transfer coefficient.

2.3 TEMPERATURE CALCULATION

The calculation of the instationary temperature field is separated into the problems of heat conduction, heat transfer to environment and simulation of welding process. The heat conduction problem is solved numerically because of the non-linear, temperature-dependent material properties. The internal energy accumulated by the deformation of the body is negligibly small (Banas *et al.* [4]) for the heat conduction problem of a conventional arc welding process. The balance of the internal energy for such a process is described by the Fourier heat conduction equation. The time integration is performed by using the unconditionally stable Dupont II scheme (Hogge [5]).

2.4 RESIDUAL STRESS CALCULATION

The welding residual stresses are caused by two physical mechanisms: the inhomogeneous volume change and the phase transformation. The first one arises from local heating and cooling, which leads to elastic-viscoplastic deformations.

The second leads to local volume changes and transformation stresses. Both types of stresses are equivalent from the mechanical point of view (Wu & Carlsson [6]).

The thermal loads due to heat input by the moving arcs are gradually applied in the FE analysis in order to determine the elastic or plastic strains. The total strain increment is given by the sum of the elastic, the plastic, the creep, the thermal and the strain increment due to phase transformation.

The creep strain increment is not considered due to the high cooling rate in case of wet underwater welding. The calculation of the strain increment due to phase transformation demands a coupled thermo-mechanical-metallurgical model of welding. It is very important to consider the temperature dependent material properties as correctly as possible working with such a model. So far, there is insufficient information on the temperature dependent material properties of low carbon steels in the temperature range above 1000 °C. For this reason, the strain increment due to phase transformation is not calculated but the effects of the transformation induced plasticity and the transformation induced volume change are considered in a simplified way. The transformation plasticity is approximated by elastic/ideal-plastic material behaviour between 300 °C and 400 °C as stated by Argyris & Mlejnek [7] and Goldak [8]. The transformation volume change is approximated by an artificial reduction of the thermal expansion coefficient in the transition temperature range (Goldak [8]).

3. Weld specimen

The geometry of the specimen is idealized to show a section of a V-joint weld 100 mm in length (Fig. 3). Since the V-joint is symmetrical, only half

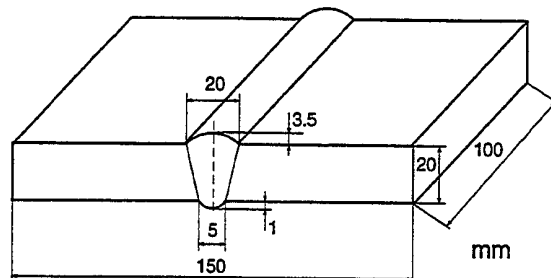


Fig.3. Geometry of the weld specimen.

of the weld is FE modeled (Fig. 4), saving processor time and making the simulation faster. The specimen is 150 mm in width and 20 mm thick. The weld is rounded at the top and the bottom. The top of the rounded weld reaches 3.5 mm above the top surface of the plate. The bottom of the weld reaches 1 mm below the bottom surface of the plate. The two parts to be welded do not touch. The distance

between the plates at the top surface is 20 mm while at the bottom surface is 5 mm. This forms the V for the weld metal to fill.

The specimen is oriented horizontally in the water with negligible pressure effects. The top of the plate lies parallel with the surface of the water. The specimen is divided into 2550 elements with 3276 nodes. The element type used is classified as an 8 node brick element (Fig. 4). The welding pro-

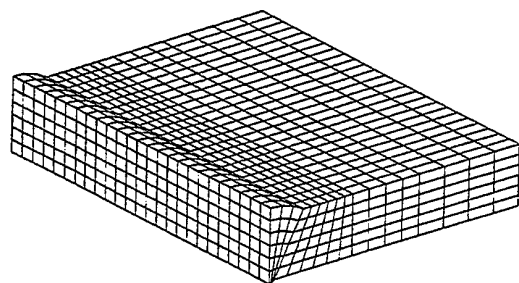


Fig. 4. FE-discretization of the weld specimen.

cess of laying molten metal onto a plate is simulated with a feature of the FE program ANSYS called 'birth and death'. The elements of the filler material have already been defined and created as a part of the geometry of the specimen, but to start the simulation, all these elements are defined as having a stiffness of 10^{-7} . The elements are brought to life according to the position of the welding torch by giving them their proper value of stiffness.

The material used in this simulation is the StE 355 off-shore steel. The temperature dependent material properties of this steel are taken from Lindhorst *et al.* [9].

4. Results

4.1 TEMPERATURE FIELD

Fig. 5 shows the temperature field at the time of 32 s after the beginning of the welding process. A comparison of the temperature field for the dry and the wet weld is presented. One half of each plate is shown in order to compare the temperature field inside the plates.

Fig. 5 reveals a perceptible difference between the temperature fields of both processes. Although the maximum temperature in the molten pool is about 1700 °C for the two plates, the molten pool in case of dry welding is about 20 % longer than in case of wet welding. The dimension of the heat affected zone is also bigger for the dry weld than that of the wet weld.

The temperature gradient in the vicinity of the weld seam is about 170 °C/mm for the wet weld and about 140 °C/mm for the dry weld, which is a difference of approximately 18 % between both conditions.

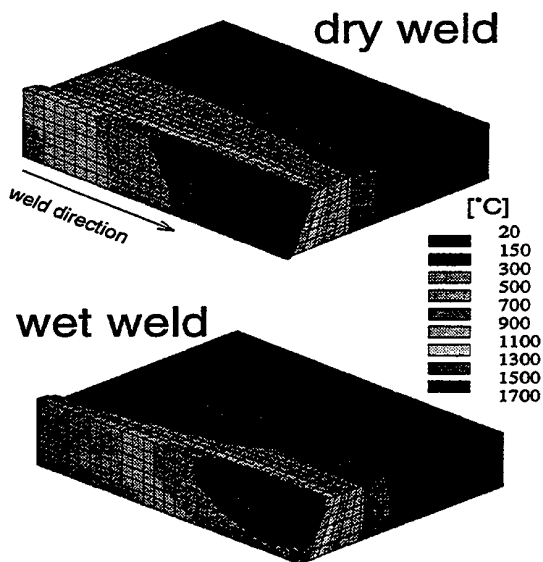


Fig. 5. Temperature field (time $t=32$ s).

4.2 WELDING RESIDUAL STRESSES

The water contact in case of wet underwater welding leads to a high cooling rate compared to that of the dry weld. The effect of the different cooling conditions of both plates is an perceptible influence on the welding residual stress distribution. Fig. 6 shows the welding residual stress component σ_x after cooling of the plates is finished. This stress component is chosen for presentation here, because it is of importance for cracks perpendicular to the welding direction. The direction of σ_x is the same as the opening direction of such cracks. That can lead to a propensity to crack propagation due to tensile stresses in x-direction.

The maximum σ_x value of the wet weld is about 350 MPa, which reaches nearly the yield stress of the base material. Compared to this, the maximum σ_x value of the dry weld is about 100 MPa smaller, which is a difference of approximately 30%. There is a perceptible stress gradient over the thickness (y-direction) of the plates, where σ_x reaches negative values on the plate surfaces and positive values inside the plates.

It is obvious that the stress distribution inside the dry weld and on its surface is nearly symmetric. In case of wet welding, the cooling rate of the plate is so high that the temperature field can not be equalized by heat conduction. Here, the distribution of the stress component σ_x is not symmetric.

In summary, one can say that the influence of the water contact in case of wet underwater welding leads to a deteriorated welding residual stress state compared to that of the dry weld for the regarded problem. The differences in the distribution of the presented stress component σ_x of the dry and

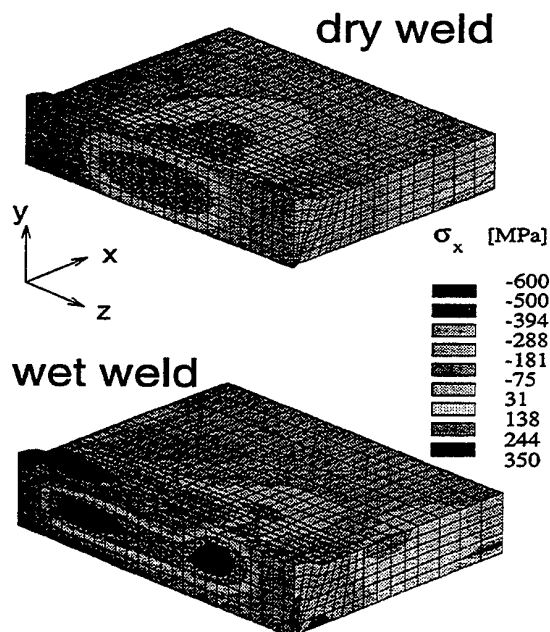


Fig.6. Stress component σ_x after cooling.

the wet weld are caused by the different boundary conditions. On the one hand there is water contact for the wet weld and on the other hand there is cooling in air atmosphere for the dry weld. This difference is the only difference between the input data of both calculations.

5. Conclusions

The influence of the water contact on the welding residual stresses in a wet underwater Plasma-MIG weld is shown in this paper. The instationary temperature field and the welding residual stresses are mainly influenced by the water contact. The results presented here show the importance of welding residual stresses in the defect assessment of wet underwater welded structures. The welding residual stresses of the wet weld are about 30 % bigger than that of the dry weld. They can contribute to satisfy the fracture criterion. They are of great concern in wet underwater welding and especially for materials with low fracture toughness. Therefore, further investigations on the influence of the water contact on welding residual stresses are necessary.

Acknowledgement

The authors are very grateful for the support of this research by the *Deutsche Forschungsgemeinschaft* of the Federal Republic of Germany (DFG).

References

- (1) Lindhorst, L. and Mahrenholtz, O., Influence of Welding Residual Stresses on Fracture Values, Symposium on Inelasticity and Damage in Solids Subject to Microstructural Change, St. John's, Newfoundland, Canada, 1996.
- (2) Hamann, R., Numerische Berechnung des instationären Temperaturfeldes im Schweißkörper für den nassen Plasma-MIG-Unterswasserschweißvorgang, Dissertation, VDI-Fortschrittsberichte, Reihe 2, Nr. 378, VDI-Verlag, 1996.
- (3) Hamann, R. and Mahrenholtz, O., On the Influence of the Surface Heat Transfer Coefficient on Wet Underwater Welds. Proceedings of the Fourth (1994) International Offshore and Polar Engineering Conference, Osaka, Japan, 112-119, 1994.
- (4) Banas, A., Hsu, T.R. and Sun, N.S., Coupled Thermoelastic-Plastic Stress Analysis of Solids by Finite Element Method, Journal of Thermal Stresses, 10 (4), 319-345, 1987.
- (5) Hogge, M., Numerical Methods in Heat Transfer, J. Wiley & Sons, 75-90, 1981.
- (6) Wu, X.R. and Carlsson, J., Welding Residual Stress Intensity Factors for a Half-Elliptical Surface Crack in Thin and Thick Plates, Engineering Fracture Mechanics, 19, 407-426, 1984.
- (7) Argyris, J. and Mlejnek, H.P., Die Methode der Finiten Elemente, F. Vieweg & Sohn, Braunschweig, 1986.
- (8) Goldak, J., Modeling Thermal Stresses and Distortion in Welds, In: David, S.A. and Vitek, J.M. (eds), Recent Trends in Welding Sciences and Technology, ASM International, 1989.
- (9) Lindhorst, L., Mahrenholtz, O. and Bartzsch, J., The Influence of the Water Contact on the Welding Residual Stresses of Wet Underwater Welds, Proceedings of the Sixth International Offshore and Polar Engineering Conference, Los Angeles, USA, 147-153, 1996.

Influence of Low Tensile Residual Stresses due to Welding on the Fatigue Strength of High Strength Steels

Th.Nitschke-Pagel*, H.Wohlfahrt*,

* Welding Institute, University of Braunschweig, Germany

Although in literature much discussion is found on the influence of residual stresses on the fatigue behaviour of welded structures, additional quantitative results are of importance. The paper reports on detailed quantitative investigations of the influence of tensile residual stresses on the fatigue strength of welded joints of fine-grained high strength structural steel StE 890. An important results is that in high strength structural steels tensile residual stresses with only medium magnitudes can be found at the weld toe. Nevertheless a remarkable influence of these residual stresses on the fatigue strength could be detected.

1. Introduction

The influence of residual stresses on the fatigue strength is well known for different base materials [14] and especially in high strength steels, the fatigue strength can be related to the magnitude of tensile residual stresses in the surface layers [8,16,17]. Tensile residual stresses are also frequently used to explain the low fatigue strength of weldments. Usually it is assumed that the tensile residual stresses in weldments always reach the yield strength of the base material [1,3,4,5,6]. However, investigations [10-13] have indicated that in weldments of high strength structural steels under normal welding conditions, the tensile residual stresses at the weld toe reach a magnitude significantly below the yield strength of the base material. On the other hand, in low strength steels the tensile residual stresses related to the yield strength may be higher, but the effectiveness of these residual stresses will exactly be lower or negligible. According to [8] the influence of tensile residual stresses in a base material can be approximated with

$$R_w = R_w^{RS=0} - m \cdot \sigma^{RS} \quad (1)$$

where R_w is the fatigue strength and $R_w^{RS=0}$ is the fatigue strength of the stress relieved material. The residual stress sensitivity factor m considers, that with

decreasing yield strength the influence of the residual stresses on the fatigue strength decreases more and more as a consequence of their reduction due to plastic deformations during the first load cycles [8,15]. Fig. 1, which shows the relationship between m and the ultimate strength of different steels [15] under consideration of the range of the ultimate strength for steels commonly used for welded components, evaluates, that the influence of the residual stresses on the fatigue strength of welded joints cannot be estimated without knowledge about the total amount of residual stresses and their efficiency at the weld toe.

In the model developed by Gurney [4] tensile residual stresses as high as the yield strength are anticipated. Superimposing the residual stresses and the load stresses during fatigue loading it is assumed, that the residual stresses will be reduced during the first load cycle. Then the sum of the load stress and the residual stresses will always reach the yield strength after the first load cycle and, therefore, the fatigue strength will not depend on the magnitude of an additionally applied mean stress because the upper stress will always be as high as the yield strength [4,6,9]. However, in high strength steels the magnitude of the tensile residual stresses due to welding depends on the combined effect of hindered shrinkage and phase transformation during cooling down [10-13]. If the phase transformation starts in the upper bainite or in the ferritic-perlitic state, the distribution of the residual stresses and the magnitude of the tensile residual stresses depends primarily on the degree of restraint of the weld seam. In the case of a high cooling velocity the transformation starts at a lower temperature and the distribution of the residual stresses will be strongly influenced by the compressive stresses occurring due to the hindered volume expansion in the transforming zones. Fig. 2 shows schematically possible distributions of the transverse residuals stresses as a consequence of different cooling conditions obtained using various heat inputs. The tensile residual stresses become higher with increasing heat input while the weld seam and the heat affected zone are broadened. However, the residual stresses at the weld toes are expected to only reach a magnitude of approximately 1/3

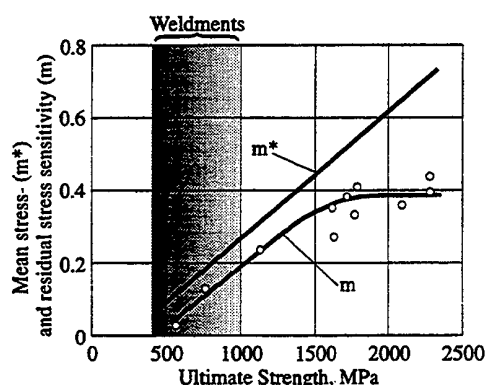


Fig. 1: Relation between the ultimate strength of different steels and the efficiency of mean stress (m^*) and residual stresses (m) [15].

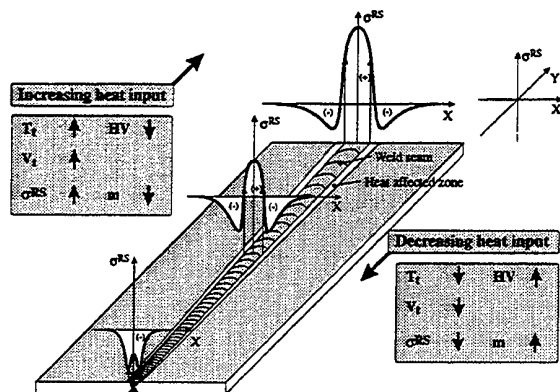


Fig. 2: Influence of the Heat input on the width of the weld seam, hardness, residual stresses and their efficiency for the fatigue strength. T_t =transformation temperature, v_t =cooling velocity

of the residual stresses in the weld centre line [7,18]. Otherwise, the hardness at the weld toe decreases with an increasing heat input, resulting in a lowering of the efficiency m of the higher tensile residual stresses. Consequently the residual stresses are not suitable to be used as an indicator for the expected fatigue strength if their efficiency at the weld toe is not taken into account.

2. Aim of the investigation and experimental procedures

Investigations on butt welded joints of various high strength structural steels ($R_m=525\ldots1040$ MPa) were conducted with the aim to show a quantitative relationship between the magnitude of the multiaxial state of the welding residual stresses and the fatigue strength. To examine, whether the m -factors of different base materials may be also used for welded joints, it was necessary to investigate the reduction of the residual stresses under an alternating load. The multiaxial residual stresses were determined in order to calculate the main residual stresses and their reduction after different numbers of load cycles.

Here results of investigations with a quenched and tempered structural steel StE 890 ($R_m=1040$ MPa, $R_e=1005$ MPa) with a six-layer double-V weld seam (plate thickness 10 mm) are presented. The specimens were TIG-welded with pulsed current using the parameters given in Tab. 1. The supply of the filler material was carefully controlled with the aim to create a reproducible flat weld seam with minimized notch geometry. The generation of various states of tensile residual stresses was obtained by using different levels of heat input during the welding of the cover-passes or by stress relief annealing of specimens welded under high heat input. After welding the cross section including the transverse butt weld of the specimens was reduced to a width of 50 mm by milling. The residual stresses were measured both after welding and after

milling and it could shown, that in the completely prepared specimens they were nearly as high as after the welding process. The notch factors α_k were determined using the formula given in [19] after measuring the height and width of the weld seam, the reinforcement angle and the radius of the macro notches at the weld toe. The angular distortion was always lower than 0.5° .

Table 1: Welding parameters (shielding gas 99.9% Ar)

	1+2	3+4	5+6	5+6
Voltage (V)	9.0	9.0	10.0	13.0
Base current (A)	110	110	100	230
Pulsed current (A)	180	190	210	300
Frequency(Hz)	8.40	8.40	8.55	8.62
Welding speed (cm/min)	10	10	10	10
Filler supply (cm/min)	30...40	30...40	40...60	40...60
Heat input (kJ/cm)	7.83	8.10	9.3	19.89

The distributions of the transverse and longitudinal residual stresses of each series of specimens were measured by means of X-rays ($CrK\alpha$ -radiation) before cyclic loading to prove the reproducibility of the induced residual stresses. Furthermore, the transverse and longitudinal stresses in the weld seam and at the weld toe were measured on at least 30 specimens of each series. The main residual stresses in the weld seam and at the weld toe were determined using three residual stress components. The measurements of the residual stresses were repeated in each of the experiments with different stress amplitudes after every decade of load cycles to examine the alteration of the multiaxial residual stresses during fatigue loading. Fatigue tests under tension-compression loading ($\kappa=-1$) were conducted for different stress amplitudes and six specimens on each stress amplitude. The S-N-curves for the 5%, 50% and 95%-fracture-probabilities were calculated by the $\arcsin\sqrt{P}$ -transformation.

3. Experimental results

3.1 RESIDUAL STRESS DISTRIBUTIONS

The scatterbands of the transverse residual stresses are given in Fig. 3. The figures show that in the specimens welded under a high heat input the greatest tensile residual stresses in the weld seam are higher than in the specimens welded under a low heat input. At the weld toe, however, the magnitude of the tensile residual stresses is nearly the same in both series. The high strength steel StE 890 was also investigated in the stress relief annealed state and an additional series of specimens welded under a high heat input was preloaded in tension-compression for ten cycles with a stress amplitude of 600 MPa, which was nearly as high as the cyclic yield strength of the base material. The comparison between the transverse residual stresses of

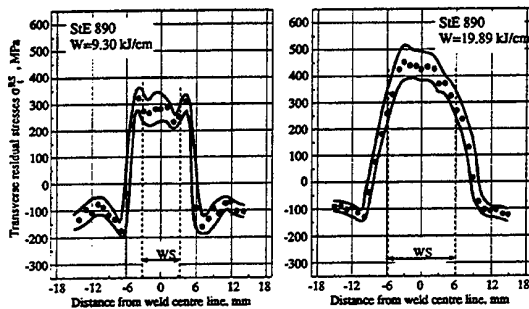


Fig.3: Scatterbands of the transverse residual stresses

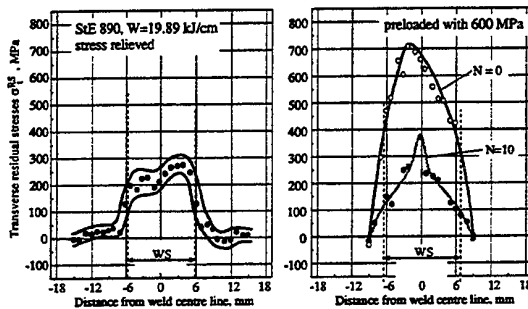


Fig.4: Scatterband of the transverse residual stresses after stress relieving and transverse residual stresses after preloading with 600 MPa

Table 2: Mean values of the residual stresses in MPa, notch factor, Vickers hardness, m-factors and product of m and σ_v^{RS} stresses at the weld toe

	W=9.30 kJ/cm	W=19.89 kJ/cm	stress relieved	preloaded
$\overline{\sigma}_t^{RS}$	270 ± 67	254 ± 73	96 ± 64	60 ± 35
$\overline{\sigma}_l^{RS}$	176 ± 60	190 ± 56	53 ± 70	70 ± 38
HV 5	420	340	325	340
α_k	1.05	1.05	1.05	1.05
$m \cdot \overline{\sigma}_v^{RS}$	78	54	16	17

the stress relieved specimens and the preloaded specimens in Fig. 4 illustrates that the residual stresses at the weld toe could be reduced through preloading to the same level as obtained through stress relieving. Tab. 2 contains the mean values of the residual stresses and the hardness of each series measured at the weld toe, the estimated factors m and the product of m and σ_v^{RS} . If the product of m and σ_v^{RS} is used to characterize the influence of the residual stresses on the fatigue strength, it can be expected that the specimens welded under the low heat input should show the lowest fatigue strength and the stress relief treatment should further the increase of the fatigue strength as much as preloading.

3.2 RESULTS OF THE FATIGUE TESTS

The assumptions that were made are confirmed by the results of the fatigue tests. The comparison of the

S-N-curves determined for the various specimens (Fig.5) indicates, that the difference in the fatigue strength of the specimens tested in the as welded state has the same order of magnitude as the difference of the product of m and σ_v^{RS} and the fatigue strength of the specimens welded under high heat input is higher, as it should be expected under consideration of the values in Tab. 3. On the other hand, the increase in the fatigue strength due to stress relieving or preloading is approximately as high as the decrease of the product of m and σ_v^{RS} .

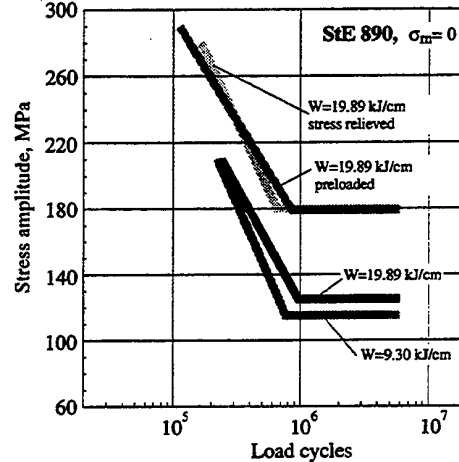


Fig.5: S-N-Curves of push-pull-loaded TIG-welded joints of Steel StE 890

3.2 RESIDUAL STRESS ALTERATION

Fig. 5 illustrates the V'Mises-stress distribution before fatigue loading and after the first load cycle with a stress amplitude of 300 MPa in a specimen welded under a high heat input. The distribution of the V'Mises stresses before fatigue loading shows that relatively high values of approximately 720 MPa are reached only in the weld seam. At the weld toe, the magnitude of the V'Mises stresses reaches only 500 MPa, about 50% of the yield strength of the base material. However, during the first load cycle the V'Mises stresses show an alteration in that way that the distribution becomes more homogeneous. The V'Mises stress at the weld toe is reduced from 500 MPa to 305 MPa. During fatigue loading, the V'Mises

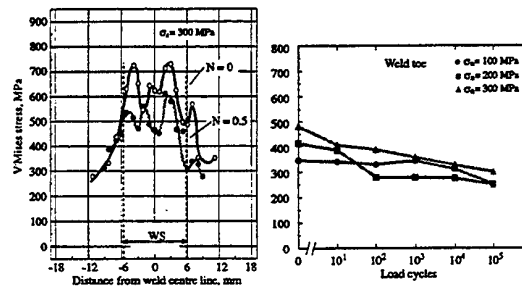


Fig. 6: Distribution of the V'Mises Stresses in a welded joint loaded with 300 MPa after the first load cycle and V'Mises stresses at the weld toe.

stresses at the weld toe are reduced under all of the stress amplitudes (Fig. 5), although they do not reach the magnitude of the cyclic yield strength or the yield strength. The magnitude of the reduction seems to depend on the magnitude of the stress amplitude. After 10^7 load cycles, the V-Mises stresses reach a magnitude of 250...300 MPa. This result is in accordance with the preceding statements in the influence of the residual stresses on the fatigue strength.

5. Conclusions

The results of this investigation have shown that the influence of tensile residual stresses due to welding on the fatigue strength can not be easily estimated such as through the comparison between the magnitudes of the tensile residual stresses of different weldments. Assumptions on the magnitude of the tensile residual stresses as presented in [4,5] are not confirmed by the results of the residual stress measurements made in this investigation. This is in agreement with results shown in [7,13]. At the weld toe, where the fatigue cracks start, the tensile residual stresses reach a magnitude significantly below the yield strength, especially in high strength steels as for instance StE 890. However, these relatively low tensile residual stresses can be important for the fatigue behaviour because their reduction during fatigue loading remains relatively small and thus they can become highly efficient due to the higher hardness or higher ultimate strength at the weld toe. A reliable estimation of the influence of these low tensile residual stresses on the fatigue strength requires the consideration of the efficiency factor m and possibly of the multiaxiality of stresses or, in other words, the consideration of both residual stress components at the weld toe.

The concept of using efficiency factors m offered reasonable results in these investigations. But nevertheless one has to conclude that this concept has to be revised for welded joints as it would probably overestimate the influence of very high magnitudes of tensile residual stresses on the fatigue strength. The results of the investigations indicate also, that small reductions of the residual stresses, in connection with lowering the local hardness and therefore lowering the efficiency of the residual stresses as induced by a stress relief heat treatment, can cause a significant increase in the fatigue strength.

Furthermore, the investigations on low strength steels show that differences in the fatigue strength can not be connected in any case with differences in the residual stress state. Even if the residual stresses are not considerably reduced during fatigue loading other influencing factors, as for instance the notch geometry, may have a dominating influence. One has to keep in mind that in weldments with sharp notches at the weld toe, such as after MAW- or MAG-welding, the fatigue

strength depends primarily upon the notch geometry at the weld toe and hence a lowering of the residual stresses through stress relief treatments has no effect.

The authors thank the German research association (DFG) for the support of the presented investigations.

References

- [1] Maddox, S.J.: In "Improving the fatigue strength of welded joints. The Welding Institute 1983, S.1-4
- [2] Trufjakov, V.I.: *British Welding Journal*, 5 (1958) No.11, S.491-498
- [3] Gurney, T.R.; Maddox, S.J.: IIFW-Doc. XV-342-73, 1973
- [4] Gurney, T.R.: *Fatigue of Welded Structures*, 2nd Edition (1979), Cambridge University Press
- [5] Maddox, S.J.: In "Residual Stress Effects in Fatigue". ASTM STP 776, American society of testing and materials, Philadelphia 1982, S.63-96
- [6] Haibach, E.: In VDI-Bericht 268 "Werkstoff- und Bauteilverhalten unter Schwingbeanspruchung". VDI-Verlag Dsseldorf 1976, S.179-192
- [7] Nitschke-Pagel, Th.; Wohlfahrt, H.: DVS-Bericht 133, DVS-Verlag Dsseldorf 1991, S.101-107
- [8] Wohlfahrt, H.: In "Dauerfestigkeit und Zeitfestigkeit", VDI-Bericht 661, VDI-Verlag Dsseldorf 1988, S.99-127
- [9] Eurocode No.3: Design of steel structures. Part 1: General rules and rules for buildings
- [10] Poje, R.: Dr.-Ing. thesis RWTH Aachen (1984)
- [11] Wohlfahrt, H.: *Härterei-Technische-Mitteilungen* 41(1986) Nr.5, S.248-257
- [12] Nitschke-Pagel, Th.; Wohlfahrt, H.: In "Residual Stresses-Measurement, Calculation and Evaluation". Ed. by V.Hauk, H.Hougarly and E.Macherauch. DGM-Verlag 1991, S.121-134
- [13] Nitschke-Pagel, Th.; Wohlfahrt, H.: In "Mechanical Effects of Welding". Ed. by L.Karlsson, L.E.Lindgren and M.Jonsson. Proc. of the IUTAM Symposium, 10.-14.6.1991 Lulea/Sweden. Springer Verlag 1992, S.123-134
- [14] Kloos, K.H.; Macherauch, E.: *Materialwissenschaft und Werkstofftechnik* 20 (1989). Teil 1: Nr.1, S.1-13; Teil 2: Nr.2, S.53-60; Teil 3: Nr.3, S.82-91
- [15] Starker, P.: Dr.-Ing. thesis TH Karlsruhe (1981)
- [16] "Residual Stresses - Measurement, Calculation and Evaluation". Ed. by V.Hauk, H.Hougarly and E.Macherauch. DGM-Verlag, Oberursel 1991
- [17] "Residual Stresses". Ed. by V.Hauk, H.Hougarly, E.Macherauch and H.-D.Tietz. DGM-Verlag, Oberursel 1993
- [18] Nitschke-Pagel, Th. Dr.-Ing. thesis, TU Braunschweig, 1995
- [19] Kumagai, II.: *Transactions of the Japan Society of Mechanical Engineers* 34, 1968, S.249-254

Numerical Analysis of Process-Induced Thermal Residual Stresses in Metallic Matrix Composites

A. Abedian, W. Szyszkowski, and S. Yannacopoulos

Mechanical Eng. Dept., Univ. of Saskatchewan, 57 Campus Dr., Saskatoon, Sk. S7N 5A9, Canada

Thermal stresses induced during cooling from the fabrication to ambient temperatures of SCS-6/Ti-6Al-4V and SCS-6/Ti-24Al-4Nb composites are analyzed applying the finite element method. The matrix is modeled as a bilinear elasto-plastic material with work and kinematic hardening. Thermo-mechanical properties of the fiber and the matrix are temperature dependent. It is shown that during cooling the material behavior is elasto-plastic at an intermediate stage only. At high temperatures, or when approaching room temperature, the stresses remain below the yield limit and the material is elastic.

Keywords: FEM, composite material, thermal residual stress, plastic deformation, micromechanics.

Introduction

When cooling composites from their high processing to low operating temperatures residual thermal stresses are generated due to the mismatch in the coefficient of thermal expansion (CTE) of the fiber and matrix materials. Such stresses may cause some damage and affect the performance of composites. Several experimental methods have been used to measure these stresses. However, in general, the experiments [1-3] are difficult to carry out and interpret. Normally, some of the experimental techniques cause redistribution and relaxation of the stresses. A good example is the X-ray diffraction technique [2,3] which requires material removal. Consequently, the accuracy of the stress and strain components obtained by experimental methods is usually not very high. Therefore, to understand the features of the process-induced residual stresses, one has to rely on analytical and numerical methods. The Finite Element Method (FEM) is used in the present study to model the thermal stress phenomena during cooling of metallic matrix composites (MMC) and intermetallic matrix composites (IMC).

The accuracy of the FEM simulation depends on the choice of numerical models which usually incorporate various geometrical and material assumptions. Typically, in such models the fibers are dispersed uniformly in the composite creating a pattern of identical volume cells. Consequently, only one representative cell, much smaller than the whole composite, is required to be modeled numerically. Clearly, the cell should be three dimensional. However, most of the FEM analyses of the residual thermal stresses in composite materials have been conducted using 2-D plane strain models [4-8].

It must be also mentioned that, in dealing with thermal stresses the material model should be capable of

handling the effects of temperature on the mechanical properties of the matrix and the fiber. If the processing temperature is relatively high, the process of cooling may induce inelastic (that is plastic and creep) deformation. Hence, such a material model should be capable of simulating elasto-plastic rate dependent behavior of the material over the temperature range considered.

In the work presented here, a 3-D model of the hexagonal volume unit is analyzed. Particularly, this model considers the fiber end effects. The matrix is modeled by a bilinear elasto-plastic material model with isotropic and kinematic hardening. All the material properties are temperature dependent. It is shown that for SCS-6/Ti-6Al-4V (MMC) composite some plastic deformation develops in model away from the fiber end. This is contrary to the results obtained in [4-6] for the same composite using 2-D models.

Material and Numerical Model

For FEM modeling of composites, it is usually assumed that the fibers are dispersed in the matrix in a regular pattern. Considering the symmetric aspects of the fibers distribution in a composite leads to a representative volume or a unit cell. Regarding the symmetry surfaces of the unit cells, the associated prism model can be established.

Here, the unit cell of a regular hexagonal pattern of long and straight fibers of circular section is modeled by a 3-D prism as shown in Fig. 1. The FEM model is meshed with the 8-nodded and 20-nodded brick elements of ANSYS, a commercial FEM software. Since high stress gradients are expected in the region at the fiber/matrix interface, the 20-nodded elements are used to mesh the model there. Due to symmetry of the volume cell the following boundary condition regimes are adopted. The nodes on line OO' are restrained in the x

and y directions while the nodes on the OO'B'B surface are restrained in the x-direction. The nodes on the OO'A'A surface are allowed to move in the OA-direction only and the AA'B'B surface remains planar. Also, the surface AOB is assumed to be planar to represent a plane of symmetry in the middle of the fiber. The surface A'O'B' represents a free surface and is free to deform in any direction.

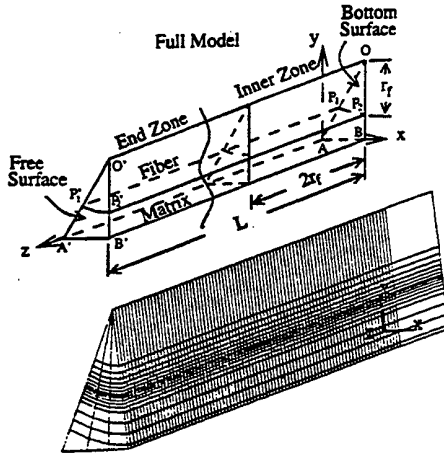


Fig. 1: FEM model.

As has been shown numerically in [7,9] and experimentally in [10], the fiber end effects disappear at a distance of about 2.5 to 3 fiber diameters away from the free surface. Further away (from the free surface) the axial strain component (in the z-direction) remains constant and is practically independent of the fiber length. This state of generalized plane strain dominates in the rest of the model. Here, in order to secure that the numerical model is able to simulate the end effects and the stress state away from the fiber end, the length of the model is assumed to be about five fiber diameters. The volume dominated by the generalized plane strain state is called the inner zone and the volume close to the free surface is referred to as the end zone. In elastic analyses a stress singularity is generated at the free surface on the fiber/matrix interface by the discontinuity in the material properties and is difficult to handle numerically as reported in [9,11].

In the present study, the thermal stresses in SCS-6/Ti-6Al-4V (MMC) and SCS-6/Ti-24Al-11Nb (IMC) composites induced during cooling processes from the fabrication temperature $T_f = 900^\circ\text{C}$ to the ambient temperature $T_r = 20^\circ\text{C}$ are investigated. The fibers are assumed to remain elastic during the process and the matrices are modeled as bilinear elastic-plastic strain hardening materials. The thermal and mechanical properties of the matrices used in this study are taken from [4] and are shown in Fig. 2 in function of temperature. In general, the thermal stresses increase when the composite cools down from the assumed stress-free fabrication temperature. However, during

cooling the yield stress of the matrix is also increasing (Fig. 3). Consequently, any plastic deformation will only be generated if the increase in thermal stress is greater than the increase in the yield stress.

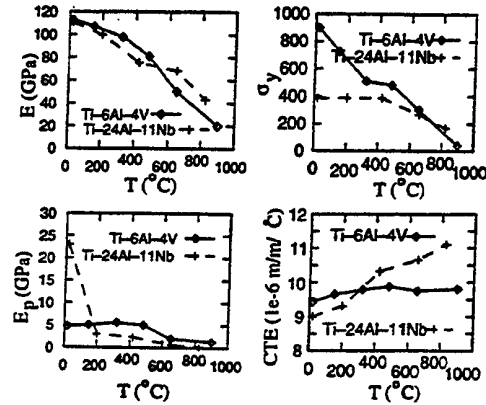


Fig. 2: Material properties.

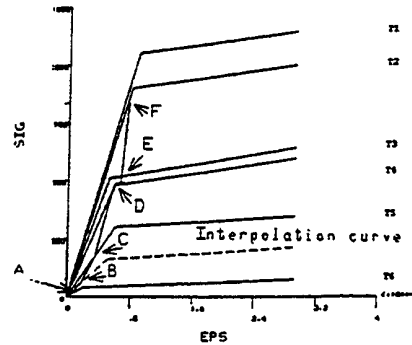
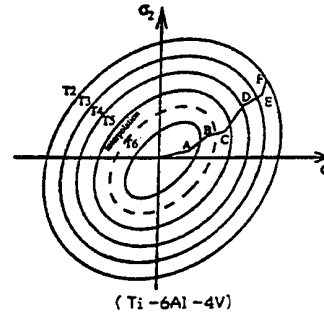


Fig. 3: Effects of temperature on the yield surface.

The von-Mises yield criterion along with the associated flow rule are used to define the onset and progression of plastic deformation. The strain hardening is indicated by the plastic modulus, E_p . The 3-D constitutive relations representing either kinematic or isotropic hardening (work hardening) are considered in the numerical calculations. It is noted that the current yield surface is dependent on the temperature and amount of plastic deformation accumulated as shown in Fig. 3 for isotropic hardening. The thermal stresses at $T_r = 20^\circ\text{C}$ are referred to as the residual stresses whether any plastic deformation is present or not.

Results and Discussion

The analysis of the SCS-6/Ti-6Al-4V composite has shown no sign of plastic deformation for cooling from the processing temperature (900°C) to about 360°C. The matrix starts to deform plastically at the end zone when the temperature drops below 360°C and the plastic area is gradually spreading into the inner zone where no plastic deformation has been calculated using 2-D plane strain models [4-6]. A plot of the history of the equivalent stress at points P_1 and P'_1 and the matrix yield stress during cooling is shown in Fig. 4. As the plot shows, the equivalent stresses are exceeding the yield stress in the temperature range of 360-150°C. At temperatures between 150°C and room temperature the matrix experiences no further increase in plastic deformation. Thus, the occurrence of plastic deformation is not monotonically dependent on the temperature increments. If the current equivalent thermal stresses which are increasing with temperature remain below the yield stress of the constituents (which is also increasing), no plastic deformation will be generated in either the fiber or the matrix.

This limited amount of plastic deformation has been observed in [1] utilizing the neutron diffraction technique and numerically calculated in [6]. However, in that study much higher CTE has been considered for the matrix than the values used in the present study.

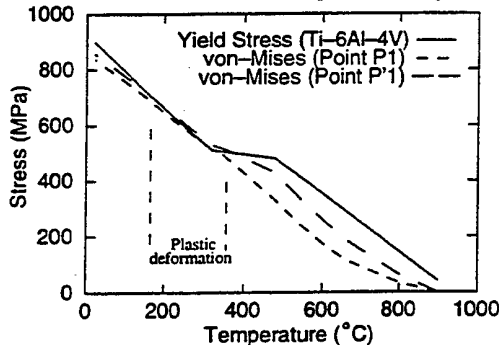


Fig. 4: Stress History at P_1 and P'_1 for Ti-6Al-4V matrix.

For the SCS-6/Ti-24Al-11Nb composite a history of the equivalent von-Mises stress in the matrix over the cooling period in both the inner zone and the end zone is shown in Fig. 5. Comparing the curve for the inner zone with the results of Ref. [4] for the rectangular fiber array unit cell shows that, for Ti-24Al-11Nb, the 3-D model predicts that yielding starts at lower temperatures (i.e. with higher stresses). The Ti-24Al-11Nb matrix, like the Ti-6Al-4V matrix discussed earlier, deforms plastically during cooling from the processing temperature. The plastic deformation starts at about 450°C and continues up to room temperature. The equivalent plastic strain profile of the matrix at room temperature is shown in Fig. 6, indicating that a significant portion of the matrix

has deformed irreversibly. Similar large plastic deformations have been reported in [4,12]. Such plastic deformations can significantly redistribute and relax the stresses. This phenomenon may highly affect the performance of the composite in service, in particular, when exposed to mechanical loads.

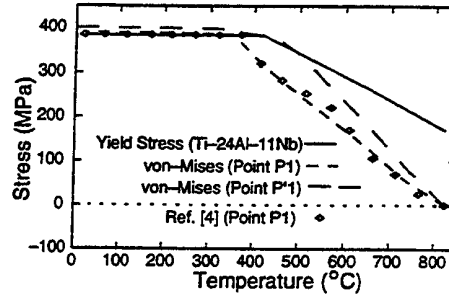


Fig. 5: Stress history at P_1 and P'_1 for Ti-24Al-11Nb matrix.

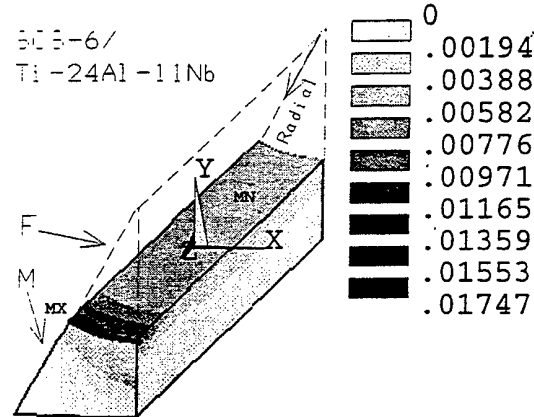


Fig. 6: Spreading the plastic strain zone in Ti-24Al-11Nb matrix.

The stress redistribution for Ti-24Al-11Nb matrix due to large plastic deformations is indicated in Fig. 7 where plots of the radial and hoop stress components in the inner zone for a temperature before the onset of plastic deformation and at room temperature are presented. The maximum of the compressive radial stress, which is initially located on line P_2B at point P_2 , due to the stress redistribution, is transferred at room temperature to point P_1 along line P_1A . The maximum hoop stress which first occurs at point P_1 (before yielding starts), moves to a point inside the matrix area close to the interface on line P_2B . Similar changes in location of the maximum and minimum stresses have been reported in [5] for Al/SCS-6 composite. In that paper these changes have been also attributed to the stress redistribution due to the matrix plastic deformation.

The plastic deformation changes the profile of the axial stress in the matrix, from relatively uniform before yielding starts, to a pattern with the stress reduction moving toward the fiber/matrix interface. Similar axial and hoop stress profiles have been experimentally

measured at room temperature in [3] utilizing X-ray diffraction for SCS-6/Ti-24Al-11Nb composite. Comparable results have also been obtained in [13].

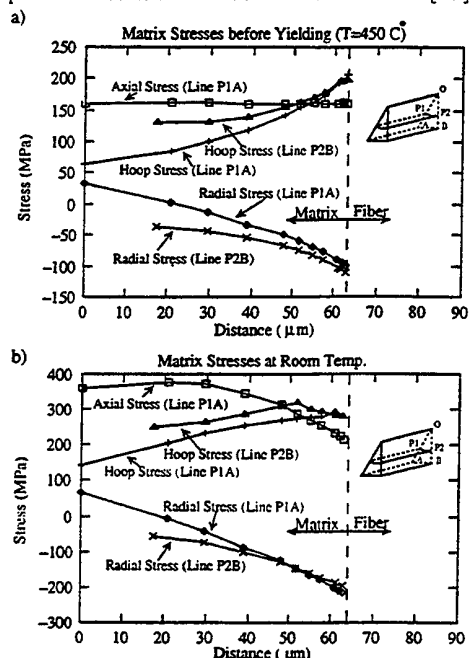


Fig. 7: The stress redistribution due to plastic deformations.

Conclusions

The following conclusions are drawn from the results of the present study:

- The analysis has revealed that during cooling the behavior of Ti-6Al-4V matrix is elastic at high temperatures and becomes elasto-plastic at an intermediate stage only. Any plastic deformation will only be generated if the increase in thermal stress is higher than the increase in the yield stress.
- the better agreement of the 3-D model results with experimental measurements indicates an advantage of the 3-D models over the widely used 2-D plane strain models.
- The relatively high tensile radial and hoop stresses that appear during the process may damage either the interfacial bonding (and cause circumferential cracking in the matrix) or initiate external and/or internal cracks.
- The final stress state depends on the amount of plastic deformation generated. High plastic deformation can cause relaxation and redistribution of the residual stresses.

References

- 1) Kupperman, D. S., Majumdar, S., Singh, P. J., and Sigal, A., Application of neutron diffraction time-of-flight measurement to the study of strain in composites, in measurement of residual and applied stress using neutron diffraction, Kluwer Academic Publisher, 439-450, 1992.
- 2) Brown, K. M., Hendricks, R. W., and Brewer, W. D., X-ray diffraction measurements of residual stresses in SiC/Ti composites, TMS Fall Meeting, Indianapolis, IN, 1989.
- 3) Rangaswamy, P., Revelos, W. C., and Jayaraman, N., Residual stresses in SCS-6/Ti-24Al-11Nb composite: Part I-Experimental, J. of Composites Technology & Research, 16(1), p. 47, 1994.
- 4) Chandra, N., Ananth, C. R., and Garmestani, H., Micromechanical modeling of process-induced residual stresses in Ti-24Al-11Nb/SCS-6 composite, J. of Composites Technology & Research, 16(1), p. 37, 1994.
- 5) Ananth, C. R., Chandra, N., Murali, K., and Garmestani, H., Effect of inelastic material behavior on residual stresses in metal matrix composites, Advanced Composites '93, Int. Conference on Advanced Composite Materials, Edited by Chandra, T., and Dhingra, A. K., The Minerals, Metals & Materials Society, p. 1,317, 1993.
- 6) Nimmer, R. P., Bankert, R. J., Russell, E. S., Smith G. A., and Wright, P. K., Micromechanical modeling of fiber/matrix interface effects in transversely loaded SiC/Ti-6-4 metal matrix composites, J. of Composites Technology & Research, 13(1), p. 3, 1991.
- 7) Rangaswamy, P. and Jayaraman, N., Residual stresses in SCS-6/Ti-24Al-11Nb composite: part II-finite element modeling, J. of Composites Technology & Research, 16(1), p. 54, 1994.
- 8) Durodola, J. F. and Ruiz, C., Thermal residual stresses in Ti-6-4/SiC_f metal matrix composite, Advanced Composites '93, Int. Conference on Advanced Composite Materials, Edited by Chandra, T., and Dhingra, A. K., The Minerals, Metals & Materials Society, 1,133, 1993.
- 9) Abedian, A. & Szyszkowski, W., Influence of the free surface on the thermal stresses in unidirectional composites, Accepted in Composites.
- 10) Biernacki, K., Szyszkowski, W., and Yannacopoulos, S., A study of large-scale model composite materials under thermal fatigue, Submitted to Composites.
- 11) King, J. A., A numerical study of thermal stress in composite materials, M. Sc. Thesis, Univ. of Saskatchewan, Saskatoon, SK., Canada, (1994).
- 12) Coker, D., Ashbaugh, N. E., and Nicholas, T., Analysis of thermomechanical cyclic behavior of unidirectional metal matrix composites, Thermomechanical fatigue behavior of materials, ASTM STP 1186, H. Sehitoglu, ED., American Society for Testing and Materials, Philadelphia, p. 50, 1993.
- 13) James, M. R., Behavior of residual stresses during fatigue of metal matrix composites, presented at the International Conference on Residual Stresses, ICRS-2, Tokushima, Japan, 1991.

Fatigue Behaviour of Fully Compressive Loaded Welded Joints with High Tensile Residual Stresses due to Welding

J.Pucelik*, Th.Nitschke-Pagel*, H.Wohlfahrt*

*Welding Institute, University of Braunschweig, Germany

Butt welded joints of the high strength structural steel StE 690 with high tensile residual stresses and stress relieved joints were investigated under compression loading. The residual stresses were measured by means of X-rays before and during fatigue loading, crack initiation was controlled by ultrasonic testing. The S-N curves determined for specimen fracture as well as the number of cycles to incipient cracks of the two treatments showed small differences. Therefore a significant influence of tensile residual stresses on the fatigue strength under cyclic compression loading can not be confirmed. The residual stresses within the weld were strongly reduced already during the first load cycles. Mostly the cracks started in the fine-grained zone, and that is to say in the region with very low tensile or even low compressive residual stresses. The conclusion is, that not the residual stresses, but the drop in hardness or strength, which represents a microstructural notch, is the dominating effect on crack initiation.

1. Introduction

Investigations carried out so far regarding the influence of residual stresses on the fatigue strength of welded structural and high strength fine-grained steels have looked mainly on the cyclic tension loading and alternating tension and compression loading. In this case, especially for joints loaded transverse to the weld seam, the fatigue strength is determined primarily by notches at the weld toe [1,2]. However, if the weld seam profile and the geometry of the weld toe are improved using optimized welding technology, the significance of notches decreases increasing the importance of welding induced residual stresses on the fatigue strength of transverse butt welds of high strength steels. The residual stresses due to welding are also of significance for the influence of mean stresses on the fatigue strength [3,4]. According to the model of Gurney [5] however, the fatigue strength of welded joints is independent of the amount of mean stress or the stress ratio, if tensile residual stresses within the welded seam and at the weld toe resemble the material yield strength. In this case, a quasistatic stress relief during the first cycle is assumed, if loading and residual stresses in the same direction are combined, exceeding the yield strength. Residual stresses should then be reduced to the extent by which the sum of load stresses and residual stresses exceeds the material yield strength and the maximum stress is adjusted to the magnitude of the yield strength independent of the stress ratio. Therefore, different tension mean stresses below the yield strength can result in the same fatigue strength. This model takes not into account, that the welding induced residual stresses within the weld seam and particularly at the weld toe mostly - especially in high strength steels - do not reach the yield strength. Additionally, the model does not consider the often significant relief of the residual stresses during cyclic loading, even if the sum of the loading and residual stresses does neither reach the yield strength nor the cyclic yield strength. It can be shown that residual and tensile mean stresses affect the fatigue behaviour of welded joints under cyclic tension or alternative tension compression loading if the magnitude of the tensile residual stresses is considerably below the yield

strength [4]. To day only a few results are available pertaining to the influence of tensile residual stresses on the fatigue strength of welded joints under compression loading [e.g 6,7]. These results are not sufficient for a safe and economic layout of structural members. It is assumed, that crack growth in welded joints under compression loading is possible in the case of presence of tensile residual stresses due to welding, because a compression-compression loading does not contain positive parts. Up to now, information on the possible relief of welding induced residual stresses during compression loading does not exist. It was the aim of the investigations presented here to contribute to the knowledge regarding the influence of tensile residual stresses on the fatigue behaviour of welded high strength steels under compression loading.

2. Materials and methods

The investigations were carried out using high strength fine-grained structural steel StE 690. The weld material was a welding wire with the same strength as the base material. The chemical composition and the strength values of both materials are given in Table 1. Sheet metal strips of 300x90x10 mm³ prepared for welding by shot peening were provided with a double-U weld preparation transversal to the direction of the applied load stress. A six-layer TIG-Welding with an alternating sequence of layers and the parameters shown in Table 2 was used to minimize angle distortion and notch sharpness at the weld toes. Relatively high residual stresses were generated using a sufficiently high heat input estimated according to the $t_8/5$ -equation [8]. Finally the testing cross section of 50x10mm² was carefully cut out using a rotary grinder under intensive cooling to prevent stress relief during manufacturing. Subsequently, some of the specimens were annealed for 30 minutes under gas shield at 600°C to relieve the residual stresses.

Table 1: Chemical composition and strength characteristics of base and filler material.

Chemical composition in weigh-% and strength characteristics													
	C	Si	Mn	P	S	Cr	Mo	Ni	V	R _m (MPa)	R _e (MPa)	A ₅ (%)	A _v (%)
StE 690	0.17	0.65	0.85	0.009	0.004	0.726	0.321	—	—	840	757	15	75 (T=-40°C)
Wire	0.1	0.6	1.6	—	—	0.3	0.25	1.0	0.1	>790	>690	16	>47 (T=-60°C)

Table 2: Welding parameters (shielding gas:99.99% Ar)

Pass	Base current (A)	Pulsed current (A)	Arc voltage (V)	Welding speed (cm/min)	Heat input (kJ/cm)	Pre-heating (°C)
1,2	170	240	10	10	12.3	120
3,4	200	280	11	10	15.8	120
5,6	225	320	12	10	19.6	20

The fatigue strength experiments were conducted under cyclic compression loading ($\kappa=1$) using a servohydraulic fatigue testing machine at a uniform cycle frequency of 20 Hz. At least six of the specimens, in both the as-wlded and stress-relieved state, were tested at four stress levels, two within the region of fatigue strength or finite life and the transition to fatigue strength. The number of cycles until incipient crack and the following crack growth within the weld seam was determined in some of the specimens by ultrasonic testing during fatigue loading. Since a specimen was able to transfer high compression forces, even with a high proportion of fatigue fracture, the determination of the number of cycles until fracture was difficult. In contrary to experiments under cyclic tension or tension compression loading, in this case the fatigue strength testing could not be terminated using distance limits. Full fatigue fractures with residual forced ruptures were rarely found, even at high stress amplitudes in the range of fatigue strength or finite life, although none of the specimens could be carried up to the maximum number of cycles (5×10^6) without incipient cracks. Only with a low tolerance for the set value of force, a self-contained halt of the testing machine at a high surface proportion of fatigue fracture, and thus the determination of the number of cycles until fracture could be obtained. The residual forced rupture of the specimens was carried out after the fatigue testing by static tensile strain. A fatigue fracture had to be assumed if the proportion of fatigue fracture area exceeded 50% of the cross section area or if a crack was running parallel to the weld seam throughout entire specimen. The calculation of the S-N-curves for fracture probabilities of 5%, 50% and 95% was carried out in accordance to the $\arcsin\sqrt{P}$ -transformation [9]. The distributions of welding transverse residual stresses before and after annealing were measured using Cr-K α -radiation in a stationary ψ -diffractometer with a point resolution of 1.5 mm. The {211}-interference of the ferritic steel was recorded at a 11 ψ -angles in a 2 θ -range from 152° to 160°. The calculation of residual stresses from the measured angles was carried out according to the $\sin^2\psi$ -method [10] using $1/2s_2=6.08 \cdot 10^{-6} \text{ MPa}^{-1}$.

3. Results

The transverse residual stresses transversal to the weld before and after annealing of a completely prepared specimen are shown in Fig.1. In the as-welded state high tensile residual stresses of approximately 400 to 500 MPa were found in the loading direction in the centre of the weld seam. The tensile transverse residual stresses quickly decrease with the distance to the weld centre and pass into the compression range in the base material. The compressive residual stresses in the base material have been introduced by shot peening the plates before

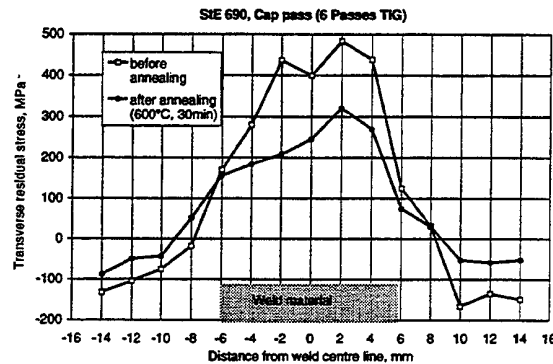


Fig. 1: Distribution of welding transverse residual stresses before and after annealing.

welding. In the weld toe tensile residual stresses of $\sigma^{RS}=175 \pm 78 \text{ MPa}$ (average of 40 specimens) exist. The distribution of the transverse residual stresses was not changed by annealing, but the curve was flattened. The highest stress relief is reached in the centre of the weld, down to values of approximately 200 to 300 MPa, transverse tensile residual stresses in the weld toe of the annealed specimens amounted to $\sigma^{RS}=101 \pm 46 \text{ MPa}$ (average of 4 measurements).

The hardness distributions of the cap passes of both treatments determined at a distance of 0.5 mm from the surface are shown in Fig.2. The hardness values of the specimen annealed after welding slightly exceeded those of the as-welded specimen. In both cases however, the hardness values decreased strongly in the transition zone to the base material, went through a minimum in the fine-grained zone of the heat-affected zone and then increased again up to the hardness of the base material.

In Fig.3 the S-N curves of the transverse butt weld specimens in the as-welded and in the stress-relieved state are shown under consideration of the number of

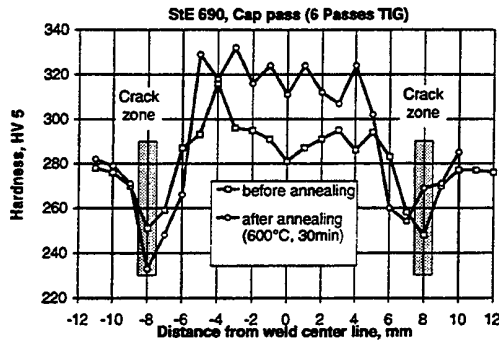


Fig. 2: Hardness Distributions before and after stress relief annealing

cycles until incipient cracks of approximately 1 mm depth, determined by ultrasonic testing. In most cases the cracks expanded very slowly after initiation and rarely extended over the entire diameter of the specimen. This was the reason for the method of defining fractures, as described before. The numbers of cycles until incipient cracks decreased with increasing stress amplitude and were comparable for both treatments, regarding the variation within the measurements. In spite of the early crack initiation all samples reached high numbers of cycles until fracture. At the lowest stress level ($\sigma_a=275$ MPa), for example, all samples went up to the maximum number of cycles (5×10^6). Comparing the specimen fractures, an overall lower variability of the stress-relieved samples is remarkable, which is the main reason for the distinct difference in the slopes of the fatigue strength lines for finite life of both treatments. The difference between the compressive fatigue strength

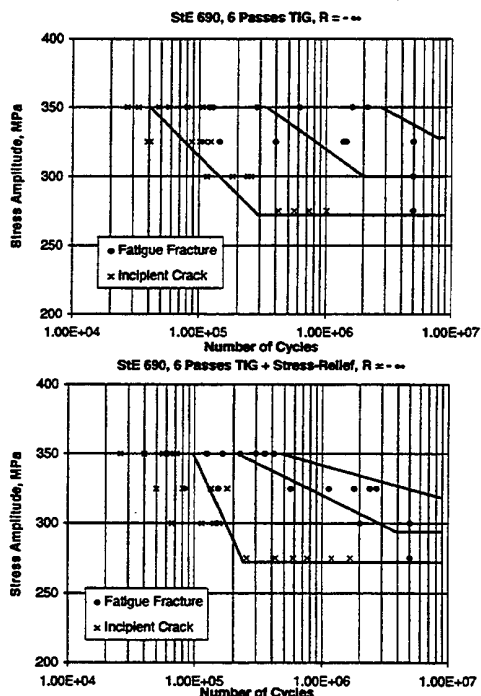


Fig. 3: S-N curves of compressive loaded transverse butt welds in the as-welded and stress-relieved state for fracture probabilities of 5%, 50% and 95%.

for the fracture probabilities shown in Fig. 3, however, is very small (as-welded: 300 MPa, stress-relieved: 294 MPa).

In some of the as-welded specimens, changes in residual stress under cyclic compression loading were determined after $N=1$ and $N=10$ cycles. These investigations confirmed a relief of the welding induced residual stress within the welding seam and in the weld toe, at high stress amplitudes, in the range of fatigue strength for finite life, already at the beginning of cyclic loading. An example for the reduction of residual stress is shown in Fig. 4 for a specimen which was loaded at a stress amplitude of 350 MPa under cyclic compression loading. The residual stresses at the weld toe were almost

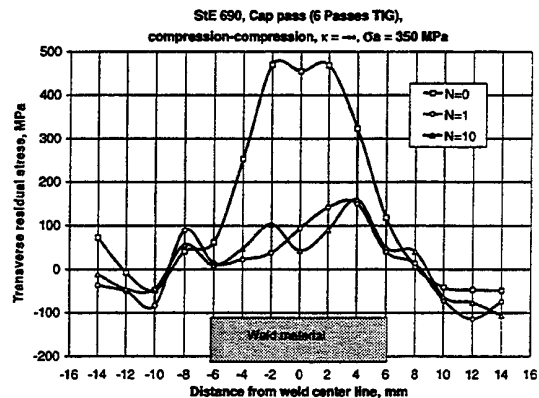


Figure 4: Distribution of the transverse residual stresses before and after after fatigue loading .

completely relieved. After 10 cycles with a stress amplitude of $\sigma_a=350$ MPa, transverse tensile residual stresses in the weld toe showed an average of $\sigma^{RS}=36 \pm 26$ MPa. Under stress amplitudes in the range of fatigue strength ($\sigma_a=100$ MPa and $\sigma_a=200$ MPa), no significant reductions of the residual stresses during the first cycle, and even up to 1000 cycles, were observed.

Apart from the pass structure in the transverse butt welds in Fig. 5 the location of incipient cracks and the further development of the fatigue fractures of a specimen loaded under cyclic compression in the as-welded state are shown. The incipient cracks are located on both sides of the weld at a constant distance to the weld toe in the area of the fine-grained zone. After crack initiation at the surface continued crack growth took place vertical to the applied cyclic compression loading. Additionally, it should be noticed that incipient cracks were found not only on the side of the specimen with high tensile residual stresses within the weld (second pass) but also on the side with low tensile or compressive residual stresses within the weld (first pass), as shown as an example in Fig. 5. The crack and fracture behaviour, as described before, is typical for both specimen treatments. In the as-welded, as well as in the subsequently annealed samples, the incipient crack was initiated at a distance of approximately 2 to 2.5 mm from the weld toe in the fine-grained zone of the heat affected zone. Subsequently, the cracks proceeded through the

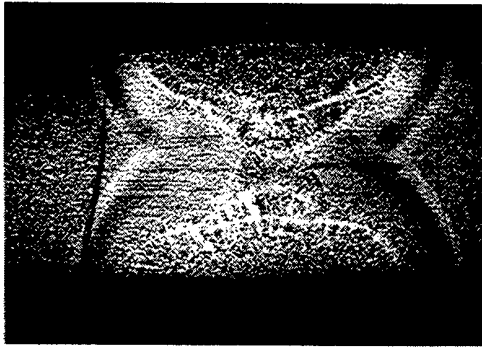


Figure 5: Weld profile and fatigue cracks after compression-compression loading ($\sigma_a = 350$ MPa).

specimen, parallel to the weld or the weld toe. No fatigue cracks appeared directly at the weld toe.

4. Conclusions

The results of this investigation have evaluated, that, as would be expected, the highest tensile residual stresses were found in the weld centre, however, the tensile residual stresses at the weld toe were also sufficiently high. The stress-relieved specimens showed similar residual stress distributions, but with overall lower tensile residual stresses. Obviously, the higher hardness values in the weld material of the subsequently annealed specimens are a consequence of the precipitation of vanadium during annealing [11]. The tendency of the weld material to harden under heat treatment was confirmed by the fact that the first cap pass, which was heated up for a short time during the application of the second cap pass, also showed slightly higher hardness values than the second cap pass. In both treatments however, a lower strength was found in the fine-grained area of the heat affected zone, which was confirmed by the drop of hardness in this area (see Fig.2). The numbers of cycles to incipient cracks were similar for the as-welded and the stress-relieved specimens. All of the cracks started in the fine-grained zone, and that is to say, in the region of the welds with very low tensile or even low compressive residual stresses. Cracks were located at a distance of 2 to 2.5 mm parallel to the weld toe in the region with the lowest hardness see Fig.2). The cracks occurred on both sides of the specimens independent of the magnitude of the initial residual stresses. Therefore, it can be concluded that the dominating factor for crack initiation is the microstructural notch caused by the drop in hardness or strength. In spite of the early occurrence of incipient cracks, the specimens of both treatments reached high numbers of cycles before fracture, as shown in Fig.3. The S-N curves determined for the specimen fracture of both specimen treatments showed only minor differences. For example the fatigue strengths of both treatments at a fracture probability of 50 % showed a negligible difference. Although the slope of the S-N-curve of the

as-welded specimens is higher, no further influence of the residual stresses on the endurance or the fatigue strength can be confirmed. It can only be assumed that the stress-relief treatment led to adverse material properties regarding fatigue strength under compressive loading within the welding seam.

The negligible influence of the residual stresses can also be confirmed by the change in the tensile residual stresses during the first cycles of compressive loading. Already after the first load cycle, the residual stresses were reduced to approximately 100 MPa over the whole range of the welding seam. The applied minimum stress resulted in an inhomogeneous elastic-plastic deformation within the fine-grained zone due to the lower strength in this region. Because of this reduction of the residual stresses by deformation, only very low tensile residual stresses were effective at the weld toe in the direction of loading. It is therefore not likely that welding induced residual stress can have an effect during a total cycle number of 5×10^6 . The S-N curves determined for the specimen fracture, as well as the number of cycles to incipient cracks of the two treatments showed only small differences which were not sufficient enough to confirm a significant influence of the residual stresses due to welding on the fatigue strength under cyclic compression loading. Neither the notch at the weld toe nor tensile residual stresses led to crack initiation within the weld toe which is the critical region under cyclic loading with load stress maxima in the tensile range. Obviously under pulsating compressive stresses the hardness minimum has a dominating effect on crack initiation.

The authors thank the Arbeitsgemeinschaft industrieller Forschungsvereinigungen (AIF) for the support of the investigations.

References

- [1] Heesch, J.; Nitschke, Th.; Wohlfahrt, H.: *Abschlußbericht zum DFG-Vorhaben Wo 344/1*, 1990
- [2] Prior, F.; Maurer, K.L.: *Mat.-wiss. u. Werkstofftech.* 26 (1995), pp. 161-171
- [3] Nitschke-Pagel, Th.; Wohlfahrt, H.: *DVS-Bericht 133*, DVS-Verlag Düsseldorf 1991, pp. 101-107
- [4] Nitschke-Pagel, Th.: *Dr.-Ing. thesis TU Braunschweig* 1995
- [5] Gurney, T.R.: *Fatigue of Welded Structures*, 2nd Edition, 1979, Cambridge University Press
- [6] Ponschab, H.; Lindner, W.: *Berg- und Hüttenmännische Monatshefte*, 133 (1988), pp. 237-245
- [7] Eide, O.I.; Berge, S.: *Fatigue crack growth in welded girders under compressive loading*. In „Weld failures“ Ed. by Harrison J.D. *International conference, The Welding Institute, Cambridge*, 1989, pp. 377-392
- [8] *Schweißgeeignete Feinkornbaustähle, SEW 088*, In „Taschenbuch der Stahl-Eisen-Werkstoffblätter“, Hrsg. Verein Deutscher Eisenhüttenleute, Verlag Stahleisen, Düsseldorf 1992
- [9] Dengel, D.: *Z. f. Werkstofftechnik* 6 (1975), pp. 253-288
- [10] Macherauch, E.; Müller, P.: *Z. angew. Physik* 13 (1961), pp. 305-312
- [11] Hannerz, N.E.: *Schweißen und Schneiden* 28 (1976), pp. 379-382

A Numerical Procedure for Welding Residual Stresses Estimation

G. F. M. Souza* and E. Goncalves*

*Department of Mechanical Engineering, São Paulo University, São Paulo, SP, CEP 05508-900, BRAZIL

This paper presents a study of thermal stresses during welding, considering the prediction of the longitudinal stresses acting on bead-on-plate and butt welds on plates or strips. The material is considered as strain hardening, and the weld is located at the plate center line or at the strip edge. It is applied the ordinary linear solution proposed by Rosenthal to represent the body temperature during welding.

Key Words: Welding, Thermal Stresses, Residual Stresses, Elastoplasticity

1. Introduction

The problem of predicting residual stresses due to welding has long been recognized by structures fabricators as very important but at the same time as very difficult one to analyze. The difficulty has its origin in the complex mechanism of residual stresses formation, which starts from the uneven temperature distribution caused by the intense, concentrated heat source associated with all fusion welding process. The incompatible strains that are formed as a consequence give rise in turn to self-equilibrating thermal stresses that remain in the weld structure after it has cooled down to ambient temperature, thus producing the so-called residual stresses. Figure 1 shows schematically the changes of temperature and stresses that occur during such a process.

In naval and marine, nuclear and petrochemical industries, there is the necessity of welding thick plates during construction and even during repair of structures, pressure vessels or reactors, that results in a complex residual stresses distribution in the welded part. These stresses have great influence on the mechanical behavior of the structure, particularly for fatigue, fracture and buckling analysis.

Taking in view the importance of residual stresses distribution prediction, this paper presents the development of a computer-aided analysis of thermal stresses in weldments, considering the prediction of longitudinal stress acting on bead-on-plate and butt welds on plates or strips. In order to check the proposed procedure for welding residual stresses estimation, it was conducted an experimental study on residual stresses distribution of thick strips, subjected to multipasses welding, comparing experimental results with analytical predictions.

2. Analysis of Thermal Stresses

The methodology that is presented in this paper aims the estimation of the residual stresses distribution parallel to the weld line, as a function of the lateral distance of the weld line. Such an analysis is referred to herein as the one-dimensional analysis. The basic assumption inherent in the one-dimensional stress analysis is that the only stress present is the one parallel to the weld line, σ_x , being a function of the transverse distance from the weld centerline only, and that σ_y and τ_{xy} , respectively transverse stress and shear stress, are zero, according to the coordinate system presented in Figure 2.

The algorithm for solving the problem is based on the method of successive elastic solution as proposed by Mendelson [1], taking into account the temperature dependence of material yield strength, considering also the material linear strain hardening. The analysis is based on the temperature distribution along the welding process, and the output of the algorithm, at each time step, consists of total strain, mechanical strain, plastic strain and thermal stress at each of the predetermined points located at various transverse distance from the weld centerline, as shown in Figure 3.

2.1 ANALYSIS OF HEAT FLOW

The methodology employs the Rosenthal, [2], analytical solution of the problem of heat flow during welding, which is based on the following assumptions: i) the welding is performed over a sufficient length so that the temperature distribution around the heat source would not change if viewed from a coordinate system moving with the heat source; ii) The physical properties of the conducting medium are constant; iii) The heat losses through the surface of the conducting medium to the surrounding atmosphere are neglected; iv) The conducting medium is semi-infinitely large in the three-dimensional analysis, when the heat source is considered as a point.

For a finite thick plate, the temperature distribution is calculated through the following expression:

$$T - T_0 = \frac{Q}{2\pi k} e^{-\frac{v}{2\lambda}\xi} \left\{ \frac{e^{-\frac{vR}{2\lambda}}}{R} + \sum_{n=1}^{\infty} \left[\frac{e^{-\frac{vR_n}{2\lambda}}}{R_n} + \frac{e^{-\frac{vR'_n}{2\lambda}}}{R'_n} \right] \right\} \quad (1)$$

Ttemperature at a given time step t
 T_0initial temperature
 Qtotal heat input, function of arc efficiency, welding current and arc voltage

$\xi = x - vt$ moving coordinate

varc travel speed

ttime

(x, y, z)fixed cartesian coordinate system

$$R = [\xi^2 + y^2 + z^2]^{1/2}$$

hthermal conductivity

$\lambda = \frac{k}{\rho c}$thermal diffusivity

ρdensity

cspecific heat

$$R_n = [\xi^2 + y^2 + (2nh - z)^2]^{1/2}$$

$$R'_n = [\xi^2 + y^2 + (2nh + z)^2]^{1/2}$$

2.2 STRESS CALCULATION

The stress calculation is based on the method proposed by Mendelson[1], for obtaining the elastoplastic stress and strain distribution in a thermally stressed plate, considering the temperature distribution constant along the specimen thickness.

Assuming σ_x the only nonzero stress, the stress-strain for a given point along the strip width, for a given time during welding process, considering the incremental behavior of plastic strain due to temperature time variation during welding, can be written as:

$$\epsilon_{x_n} = \frac{\sigma_{x_n}}{E} + \alpha T_{A_n} + \sum_{i=1}^{n-1} \Delta \epsilon_{x_i}^P + \Delta \epsilon_{x_n}^P \quad (2)$$

where:

σ_{x_n} longitudinal stress at a given time n

ϵ_{x_n} longitudinal strain at a given time n

α thermal expansion coefficient

E elasticity modulus

T_{A_n} temperature change from reference temperature

$\sum_{i=1}^{n-1} \Delta \epsilon_{x_i}^P$ cumulative plastic strain increments until the time before time n

$\Delta \epsilon_{x_n}^P$ plastic strain increment at time n

To simplify the analysis, equation 2 can be written in a nondimensional way, as follows:

$$\epsilon_{x_n} = \frac{S_{x_n}}{H} + \sum_{i=1}^{n-1} \Delta \epsilon_{x_i}^P + \Delta \epsilon_{x_n}^P + \tau_n \quad (3)$$

where

$$S_{x_n} = \frac{\sigma_{x_n}}{\sigma_0}, \quad \epsilon_{x_n} = \frac{\epsilon_{x_n}}{\epsilon_0}, \quad \tau = \frac{\alpha T_{A_n}}{\epsilon_0}, \quad H = \frac{E}{E_0}$$

$$\sum_{i=1}^{n-1} \Delta \epsilon_{x_i}^P = \frac{\sum_{i=1}^{n-1} \Delta \epsilon_{x_i}^P}{\epsilon_0}, \quad \Delta \epsilon_{x_n}^P = \frac{\Delta \epsilon_{x_n}^P}{\epsilon_0}$$

and $\epsilon_{m_x} = \epsilon_x - \tau$ mechanical strain (4)

and where the values with suffix zero represent reference values at room temperature.

Since there are no external forces, integrals for the net force and moment must satisfy the following condition:

$$\int_0^{\text{width}} S_x d\eta = 0 \quad \int_0^{\text{width}} S_x \eta d\eta = 0$$

$$\eta = \frac{y}{\text{width}} \quad (5)$$

and that $\epsilon_x = a + b\eta$, due to the assumption of $\tau_{xy} = \sigma_y = 0$, and taking in view equation 5, the

mechanical strain can be written as:

i) strip (weld at edge)

$$\begin{aligned} (\epsilon_{m_x})_n &= 4 \int_0^1 (\tau_n + \sum_{i=1}^{n-1} \Delta \epsilon_{x_i}^P + \Delta \epsilon_{x_n}^P) d\eta \\ &\quad - 6 \int_0^1 (\tau_n + \sum_{i=1}^{n-1} \Delta \epsilon_{x_i}^P + \Delta \epsilon_{x_n}^P) \eta d\eta + \\ &\quad + [12 \int_0^1 (\tau_n + \sum_{i=1}^{n-1} \Delta \epsilon_{x_i}^P + \Delta \epsilon_{x_n}^P) \eta d\eta \\ &\quad - 6 \int_0^1 (\tau_n + \sum_{i=1}^{n-1} \Delta \epsilon_{x_i}^P + \Delta \epsilon_{x_n}^P) d\eta] \eta - \tau_n \end{aligned} \quad (6)$$

ii) plate (weld at center line)

$$\begin{aligned} (\epsilon_{m_x})_n &= -\tau_n + \frac{1}{2} \int_{-1}^1 \tau_n d\eta - \frac{3}{2} \eta \int_{-1}^1 \tau_n \eta d\eta \\ &\quad + \frac{1}{2} \int_{-1}^1 \sum_{i=1}^{n-1} \Delta \epsilon_{x_i}^P d\eta + \frac{3}{2} \int_{-1}^1 \sum_{i=1}^{n-1} \Delta \epsilon_{x_i}^P \eta d\eta + \end{aligned}$$

$$+ \frac{1}{2} \int_1^1 \Delta e_{x_n}^P \, d\eta + \frac{3}{2} \eta \int_1^1 \Delta e_{x_n}^P \, \eta \, d\eta$$

(7)

At equations (6) and (7) the elasticity modulus is considered as a constant, with no variation with temperature.

Taking in view the above equations, it is possible to verify the dependance between the mechanical and plastic strain, at a given time. So the calculation of mechanical strain at a given time is iterative, beginning with the adoption of $\Delta e_{x_n}^P = 0$

and defining e_{x_n} . Through equation (5), it is

defined $(e_{x_n})_n$ and based on the stress-strain relation of the material, it is defined the stress and strain in the point. With this new value of

plastic strain, it is redefined the value $\Delta e_{x_n}^P$, and the calculation procedure is repeated. This procedure

is repeated until the convergence of $\Delta e_{x_n}^P$, with the definition of s_{x_n} .

It is also important to notice that the stress and strain state in a given point is dependent on the strain and stress of the other points along the width of the transversal cross section of the strip or plate, so the calculation must be done at several transverse positions simultaneously.

The temperature and thermal stresses calculation must be done at a given number of time values, through the welding process, including the heating and cooling periods, and the thermal stress distribution calculated at the last time step can be considered the residual stress induced by welding process.

This algorithm of residual welding stresses calculation for plates and strips was implemented in a computer program for IBM/PC microcomputers.

3. Experimental Studies of Residual Stresses

In studying thermal stresses during welding, it is important to compare experimental results with analytical predictions. Since most of the experimental techniques employed in residual stresses analysis are destructive, it is usually used test specimens for this analysis, welded to specific welding conditions, similar to those applied in industrial welding.

Figure 4 shows the test specimen geometry and location of strain gages. The material was ASTM-A131 Grade A carbon steel. The specimen was 500 mm long, 135 mm wide and 50 mm thick. Welding was done along the upper edge of the vertically positioned specimen, which was supported at both ends of the lower edge. The weld was 15 mm

thick, employing a multipass shielded metal arc welding. The reason why the specimen is unusually long is to permit the full development of the residual stress distribution through its width, near the mid length transverse cross section. Table 1 lists welding conditions for the two welded specimens used in this study.

After welding was complete and the specimen cooled to room temperature, twelve uniaxial strain gages were mounted along its midlength, on welded and lateral surfaces, in order to measure residual stresses acting on specimen surface, as shown in Figure 4.

For residual stresses measurements was employed the Stress Relaxation Method, [4], which is based on the hypothesis that the residual stress distribution is defined through the strain relieved measured by strain-gages, after the removal of small parts, containing the sensors, from the specimen.

For residual stresses measurements, a strip 50 mm wide was removed from the specimen and then, through the employment of splitting and slicing procedure, there were obtained the small parts of this blocks, containing the strain-gages. Amounts of stress relaxation were measured and residual stresses were determined through the application of Theory of Elasticity concepts.

4. Experimental And Theoretical Results for Residual Stresses Distribution

Figure 5 shows the distribution of surface longitudinal residual stresses, σ_x , along the midlength section, experimentally and theoretically defined.

The experimentally defined stress distribution can be interpreted as a combination of the following:

- i) The shrinkage of the weld causes high tensile residual stress in region near the weld and moderately low compressive stress in regions away from the weld. The tensile residual stresses values are almost equal to the material yield stress at room temperature.
- ii) The oxy-cutting process employed for specimen preparation causes relatively high tensile stress in the unwelded edge.

Reasonably good agreements were obtained between experimental data and analytical predictions, except for residual stress in the weld surface, where the effect of multipass weld procedure is more significant. Furthermore, the residual stresses theoretically predicted for the unwelded edge is lower than the experimental value, because the theoretical calculation procedure do not take in account the oxy-cutting process. The procedure presented in this paper predicted very well the high tensile stresses acting in the specimen near the weld line, which is very important, taking in view the detrimental effect that this tensile stress has on the structure behavior, mainly in brittle fracture or fatigue analysis.

5. Conclusions

The procedure presented in this paper has proved to be adequate for prediction of welded induced longitudinal residual stresses distribution acting on planar welding of plates or strips, being capable of estimating the high tensile stresses acting near the weld line, related to shrinkage of the weld, with a good accuracy. It could be used for analyzing longitudinal thermal and residual stresses induced by weld in structures composed by strip or plates with long weld lines, at least during the early design stages.

Since the program execution is rather inexpensive, it can be used as a tool to simulate various welding condition, in order to define the guidelines for the optimum welding procedure for a given structural geometry, taking in view the reduce of residual stress magnitude through the variation of welding current, arc voltage, or welding speed.

References

- (1) Mendelson, A., Plasticity: Theory and Application, Macmillan Co., New York, 1968.
- (2) Rosenthal, D., Mathematical Theory of Heat Distribution During Welding and Cutting, The Welding Journal, Vol. 20, n°5, Research Supplement, pp. 220s-234s, 1941.
- (3) Souza, G. F. M., Residual Stresses Analysis in Welded Structures, Master of Science Thesis, Polytechnic School, São Paulo University, 1990.
- (4) Goncalves, E., Residual Stress Analysis in Laser Butt Welded Joints, Department of Ocean Engineering, MIT, Cambridge, USA, 1977.

Table 1-Specimen Welding Parameters

Number of Passes.....	81
Electrode.....	AWS E7018
Current.....	150 A
Voltage.....	22 V
Speed.....	300 mm/min.

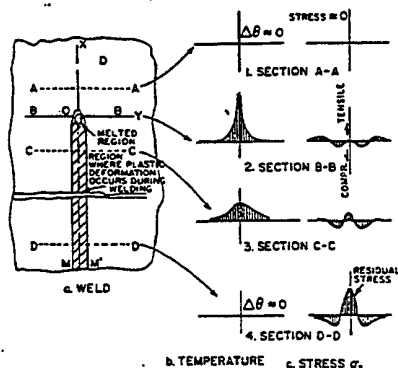


Fig. 1. Schematic Representation of Changes in Temperature and Stresses During Welding

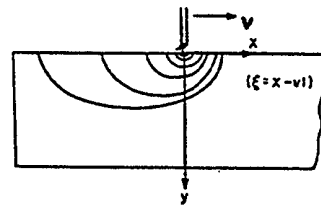


Fig. 2. Coordinate System.

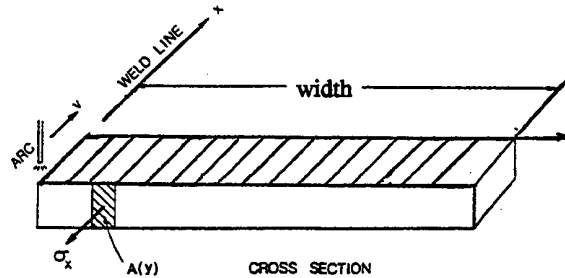


Fig. 3. Transverse Section Subdivision.

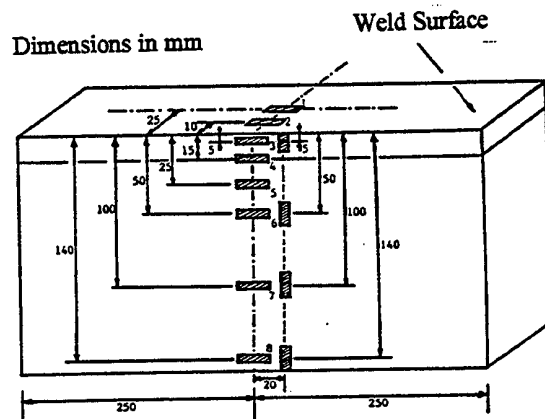


Fig. 4. Test Specimen

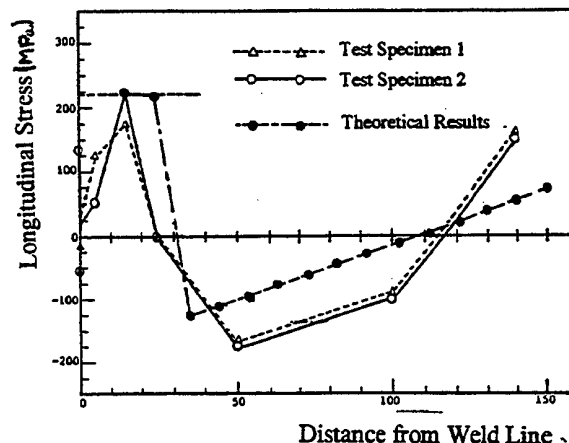


Fig. 5. Longitudinal Residual Stress Distribution in Test Specimen.

Session 1F

IMPERFECTIONS INHOMOGENEITY

Chair: E. Tsuchida

Co-Chair: M. Marin

**Frequency-Temperature Interaction of Stiffened Flat
Panels Featuring Initial Geometric Imperfections**

L. I. Librescu, M. A. Souza

**Deformation of Nickel Crystal by Embedded Atom
Method**

T. Tsuji, M. I. Baskes, A. Makino, and T. Koizumi

**Solution of an Elliptical Rigid Inclusion with Debondings
in an Infinite Plane under the Uniform Heat Flux**

N. Hasebe, K. Yoshikawa, and H. Irikura

**Steady State Thermal Stresses in an Elastic Thick Plate
Containing a Sliding Prolate Spheroidal Inhomogeneity
with the Regions of Both Plate Surfaces Being Heated
and Cooled**

E. Tsuchida, Y. Arai, and K. Esaki

**An Extension of the Cowin & Nunziato's Domain in
Initially Stressed Bodies with Voids**

Marin Marin

FREQUENCY-TEMPERATURE INTERACTION OF STIFFENED FLAT PANELS FEATURING INITIAL GEOMETRIC IMPERFECTIONS

L.I. Librescu* and M.A. Souza**

* *Department of Engineering Science and Mechanics, Virginia Polytechnic Institute and State University, Blacksburg, VA 24061-0219*

** *Technology Division, COREV America Inc., 11620 Brittmoore Park Drive, Houston, TX 77041, USA*

This study deals with the vibrational behavior of stiffened flat panels subjected to heating and a lateral pressure load. The effects played by the various reinforcement schemes and the initial geometric imperfection on the vibration in both prebuckling and postbuckling equilibrium ranges are considered and a number of pertinent conclusions are highlighted:

Keywords: Reinforced Plate, Frequency-temperature Interaction, Postbuckling.

1. Introduction

As the concept of high-speed, highly flexible and light structural weight aircraft capable of operating in a hostile flight environment gathers more impetus, the specialists are more and more challenged with a variety of new technical problems involving its design.

Such new problems are generated, among others, by the fact that the advanced supersonic and hypersonic flight vehicles are likely to experience, during their operational life, high temperatures and pressure gradients. Moreover, these vehicles will typically experience these loadings in a dynamic environment. Changes in the vibration characteristics of panels due to thermo-mechanical load interaction, affect their dynamic response and flutter-behavior. For this reason, understanding the effects of thermomechanical loads on vibration of flat and curved panels is a fundamental step in determining and understanding the dynamic behavior of structures exposed to such loading conditions. In spite of the great significance in the dynamic analyses of advanced flight vehicle structures, results on the vibrational response of *stiffened panels* under thermo-mechanical loadings appear to be extremely scarce. This paper is intended to supply information on this topic, namely on the frequency-load interaction of reinforced flat rectangular panels exposed to an elevated temperature field. The effect of initial geometric imperfection on frequency-load interaction of reinforced panels is assessed and conclusions on its implications are outlined.

2. Preliminaries. Basic Equations

Consider the case of rectangular isotropic flat panels reinforced by orthogonal stiffeners parallel to the panel edges. Consistent with the usual procedure, the stiffeners in the mutually orthogonal directions are assumed to deform independently. One assumes that the panel is exposed to a uniform through thickness temperature field

$$T(\xi_1, \xi_2, \xi_3) \equiv \bar{T}^0(\xi_1, \xi_2) \quad (1)$$

measured from a stress-free temperature T_r . In Eq. (1), ξ_1 and ξ_2 are the in-plane Cartesian orthogonal coordinates of the mid-plane of the plate, while ξ_3 is the transversal coordinate, positive in the inward direction.

The uniform temperature \bar{T}^0 can be defined as $\bar{T}^0 = (T_u + T_b)/2$ where $T_u \equiv T(\xi_1, \xi_2, \xi_3 = -h/2)$ and $T_b \equiv T(\xi_1, \xi_2, \xi_3 = h/2)$ denote the temperatures on the upper and bottom faces of the panel, respectively, while h denotes the uniform thickness of the panel. We will assume the existence of an initial geometric imperfection $\bar{V}_3^0(\xi_1, \xi_2, \xi_3) = \bar{v}_3^0(\xi_1, \xi_2)$ which refers to the transverse displacement in the unstressed configuration.

The main geometrical characteristics of stiffened panels in terms of which their cross-sectional properties are determined are depicted in Fig. 1.

From the constitutive equations, not displayed here, one can infer that in the presence of stiffeners, due to the asymmetry of the resulting panel, a

bending-stretching coupling is present. This fact which will be reflected further in the governing equations, implies, among others, that a uniform temperature field throughout the thickness of the panel and stiffeners will produce bending from the onset of heating. This reverts to the conclusion that in contrast to the case of non-stiffened and geometrically perfect panels, in the present case, the panel will not exhibit the thermal buckling bifurcation.

3. Governing System

In the present study, the nonlinear equations governing the thermomechanical response of stiffened flat panels are represented as a generalization of the classical von Kármán-Marguerre nonlinear plate theory, in the sense that the relevant equations include the effects of initial geometric imperfections and the presence of uni/biaxial stiffeners. As in the case of the non-stiffened classical plate theory, these equations are reduced to two partial differential equations in terms of the Airy stress function $F(\equiv F(\xi_1, \xi_2, t))$ and the transverse deflection $v_3(\xi_1, \xi_2, t)$ as:

$$\begin{aligned} & \bar{A}_1 F_{,2222} + \bar{A}_2 F_{,1111} + 2(\bar{B} + \bar{F}) F_{,1212} \\ & - (\bar{C}_1 + \bar{C}_2) v_{3,1122} - \bar{D}_1 v_{3,2222} - \bar{D}_2 v_{3,1111} \\ & + v_{3,11} v_{3,22} - v_{3,12} v_{3,12} + \dot{v}_{3,11} v_{3,22} \\ & + \dot{v}_{3,22} v_{3,11} - 2\dot{v}_{3,12} v_{3,12} \\ & + \bar{\lambda} \left(\Omega_1 \dot{T}_{,22} + \Omega_2 \dot{T}_{,11} \right) = 0, \end{aligned} \quad (2a)$$

$$\begin{aligned} & D \Delta \Delta v_3 - F_{,22} (v_{3,11} + \dot{v}_{3,11}) - F_{,11} (v_{3,22} + \dot{v}_{3,22}) \\ & + 2F_{,12} (v_{3,12} + \dot{v}_{3,12}) - O_1 F_{,1122} - O_2 F_{,1111} \\ & - O_3 F_{,2222} + O_4 v_{3,1122} + O_5 v_{3,1111} + O_6 v_{3,2222} \\ & - \bar{\lambda} (O_7 \dot{T}_{,11} + O_8 \dot{T}_{,22}) - q_3 + m_0 \ddot{v}_3 = 0. \end{aligned} \quad (2b)$$

Herein Δ denotes the 2-D Laplace operator, F is defined as $L_{\alpha\beta} = c_{\alpha\omega} c_{\beta\delta} F_{,\omega\delta}$ where $c_{\alpha\beta}$ is the permutation symbol and the Einstein summation convention over repeated indices is implied.

The coefficients appearing in Eqs. (2) are not displayed here. Equations (2a,b) are referred to herein as the von-Kármán type compatibility and transverse force equilibrium equation, respectively.

A simple inspection of the nature of coefficients O_7 and O_8 will disclose that the terms in the bending equations associated with the membrane

temperature subsist only in the case of a reinforced panel. This shows again that in reinforced panels the membrane temperature induces both stretching and bending.

In the present study the edges are considered to be simply supported. It is supposed also that the tangential motion of the panel, in the normal direction to the edge is unrestricted (movable edges). Denoting by n and t the in-plane directions normal and tangential to the panel edge, the pertinent boundary conditions are:

$$v_3 = 0; M_{nn} = 0; L_{nt} = L_{nn} = 0. \quad (3)$$

4. Numerical Illustrations and Discussion

Using the postbuckling governing equations not displayed here, an assessment of the effects played by an uniform through thickness temperature field and a lateral pressure on the natural frequency of stiffened flat panels will be accomplished. Throughout the numerical applications, the case of a simply supported square panel ($L_1 = L_2 \equiv L$) is considered. One also assumes that both the panel and stiffeners are of aluminum i.e. that $E_r \equiv E_s \equiv E = 10.4 \times 10^6$ psi, $\nu = 0.32$ and $\alpha = 13.15 \times 10^{-6}$ in/in/ $^\circ F$. It is also assumed, unless otherwise specified, that $L_1/h = 50$, $L_1 = 10$ in; $\ell_s/L = \ell_r/L = 5 \times 10^{-2}$; $\beta_s/L = \beta_r/L = 2 \times 10^{-3}$ and $b_r/L = b_s/L = 5 \times 10^{-2}$. For an uniaxially stiffened panel, say in the x_1 - direction, one should consider in the x_2 - direction that $b_r = \beta_r = 0$ and $L_r \Rightarrow \infty$.

The results are presented in the form of interaction curves that relate the magnitude of the average middle plane temperature amplitude \dot{T}_{11} to the square of the fundamental frequency, $\bar{\omega}^2 (\equiv \omega^2 m_0 L_1^4 / (\pi^4 D))$ as a function of geometric imperfection amplitude $\dot{\delta}_{11} (\equiv \dot{f}_{11}/h)$ and the intensity of the lateral pre-load $\bar{q}_{11} (\equiv q_{11} L_1^4 / (Dh))$.

The effects of uniform through thickness temperature increase on the fundamental vibration frequency of geometrically perfect flat panel are displayed in Fig. 2 where three scenarios are involved.

These concern the cases of the no reinforced, uniaxially and bi-axially reinforced panel. The results indicate that in the first situation, the fundamental frequency decreases linearly with increasing thermal load prior to buckling.

At buckling, the fundamental frequency is zero-valued. In the case of reinforced panels, due to the

coupling between bending and stretching induced by the non-symmetry of the panel, out-of-plane deflections are induced at the onset of the membrane thermal load and no buckling bifurcations are featured. The results from Fig. 2 show that in the absence of the temperature load $\dot{T}_{11} = 0$, the fundamental frequency of the bi-axially reinforced panel is larger than that of the uniaxially reinforced panel counterpart and both of them are larger than that of the no reinforced panel. In the case of reinforced panels the fundamental frequency decreases monotonically as the amplitude of the membrane temperature increases and their increases monotonically. This trend is due to the stiffening caused by the increased participation of the membrane stiffness as the deflection becomes larger. Another conclusion emerging from Fig. 2, concerns the amount of bending-stretching coupling featured by the uniaxially and bi-axially reinforced panels. As is readily seen, from Fig. 2, in the former case, the fundamental frequency reaches, at a certain value of \dot{T}_{11} , a rather close to zero value, whereas in the latter case the minimum value of the fundamental frequency is rather far from zero. The relative distance from zero of the fundamental frequency constitutes a measure of bending-stretching coupling involved in a reinforced panel.

It is also seen from Fig. 2 that for a bi-axially reinforced panel, the frequency minimum is shifted, as compared with the uni-axially and no-reinforced panels, towards larger amplitudes of the membrane temperatures.

From the same graph it also becomes evident that in the deep non-linear range the no-reinforced panel features larger frequencies than its uni-axially and bi-axially reinforced panel counterparts. This trend is attributed to the fact that in that range, there is an increased participation of the membrane stiffness in the non-reinforced panels as compared to that in the reinforced ones.

In Fig. 3 comparisons of the frequency-temperature interactions in non-reinforced, uniaxially and bi-axially reinforced panels subjected to lateral pre-loads of intensity $\bar{q}_{11} = 0$ and $\bar{q}_{11} = 50$ are presented.

The plots show that the lateral pre-load increases the minimum of the frequency featured by the panel in the absence of the lateral pre-load. It is also seen that beyond that temperature rendering the frequency minimum, the variation path of the frequency when $\bar{q}_{11} \neq 0$, follows closely that occurring in the case of $\bar{q}_{11} = 0$.

Finally, the effect of an initial geometric imperfection on the frequency-temperature interaction of a panel subjected to a lateral pre-load is presented in Fig. 4. Herein, the three scenarios concerning the non-reinforced, uniaxially and bi-axially reinforced panel are considered.

The results show that the initial geometric imperfection plays, on the frequency-temperature interaction, a similar role to that of the lateral pre-load. It is interesting to see also that an initial imperfection of the same amplitude plays a stronger role in increasing the minimum fundamental frequency in the bi-axially reinforced panels than in the uni-axially reinforced panel counterparts, and a much stronger influence as compared to the non-reinforced panels. Needless to say, in all the cases, due to the presence of the lateral pre-load and the existence of the initial geometric imperfection, the panel will not exhibit buckling bifurcation, and as such, the frequencies will not become zero valued quantities.

5. Conclusions

A parametric study of the vibration behavior of reinforced flat panels featuring initial geometric imperfections and subjected to thermal and mechanical loads has been presented. The loads considered in this study consists of a lateral pressure and a non-uniform membrane temperature field. Results are presented for simply-supported panels. The results identify the interactions of applied thermal and mechanical loads and the fundamental frequencies of the panel. The results show that the reinforcements, initial geometric imperfections, and transverse lateral pressure are all significant factors that should be considered in the dynamic design of panels subjected to a thermal field.

References

1. Noor, A.K. and Burton, W.S., "Computational Models for High-Temperature Multilayered Composite Plates and Shells," *Applied Mechanics Reviews*, 45 (10), 414-446, 1992.
2. Librescu, L. and Lin. W., "Thermomechanical Postbuckling of Plates and Shells Incorporating Non-Classical Effects," *Thermal Stresses IV*, Editor, R.B. Hetnarski, Elsevier, Amsterdam, Lausanne, New York, Oxford, Shanon, Tokyo, 379-452, 1996.
3. Souza, M.A. and Librescu, L., "Postbuckling of Reinforced Flat Panels Exposed to a High Temperature Environment," *Proceedings of the First International Symposium on Thermal*

Stresses and Related Topics, Thermal Stresses 1995, Shizuoka University, Hamamatsu, Japan, 235-239, 1995.

4. Librescu, L., *Elasto-Statics and Kinetics of Anisotropic and Heterogeneous Shell-Type Structures*, Noordhoff International Publ., The Netherlands, Leyden, 1975.
5. Bogdanovich, A.E., "Nonlinear Problems of the Dynamic Buckling of Reinforced Laminar Cylindrical Shells," *Prikladnaya Mekhanika*, Vol 22, 8, 57-66, 1986, Plenum Press, 1987.
6. Birman, V. and Bert, C. W., "Dynamic Stability of Reinforced Composite Cylindrical Shells in Thermal Fields," *Journal of Sound and Vibration*, 142, 2, 183-190, 1990.
7. Librescu, L., Lin, W., Nemeth, M.P. and Starnes, Jr., J.H., "Frequency-Load Interaction

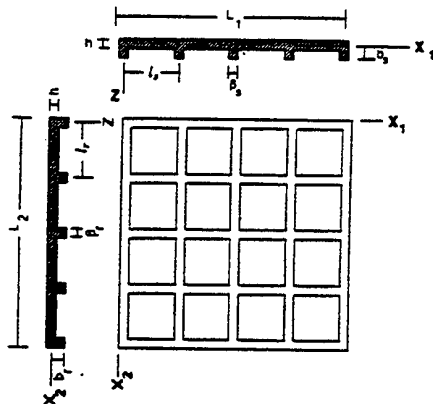


Fig. 1 Stiffened Plate Geometry.

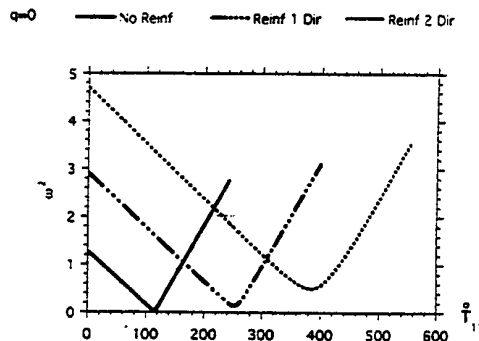


Fig. 2 Effects of the membrane temperature rise on the fundamental frequency of no-reinforced (—); uniaxially (---); and biaxially (.....) reinforced panels.

of Geometrically Imperfect Curved Panels Subjected to Heating," *AIAA Journal*, Vol. 34, No. 1, January, pp. 166-177, 1996.

8. Librescu, L., Lin W., Nemeth, M.P. and Starnes, Jr., J.H., "Vibration of Geometrically Imperfect Flat and Curved Panels Subjected to Thermal and Mechanical Loads," *Journal of Spacecraft and Rockets*, Vol. 33, No. 2, March-April, pp. 285-291, 1996.

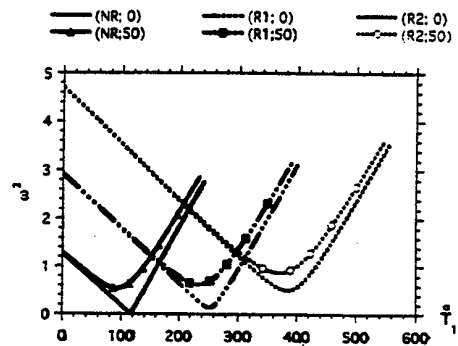


Fig. 3 Influence of the membrane temperature rise on the fundamental frequency of reinforced/no reinforced and loaded/unloaded panel by a lateral pressure. (—) no-reinforced, $\bar{q}_{11} = 0$); (---) no-reinforced, $\bar{q}_{11} = 50$); (.....) uniaxially reinforced, $\bar{q}_{11} = 0$); (— · —) uniaxially reinforced $\bar{q}_{11} = 50$); (— · — · —) bi-axially reinforced, $\bar{q}_{11} = 50$).

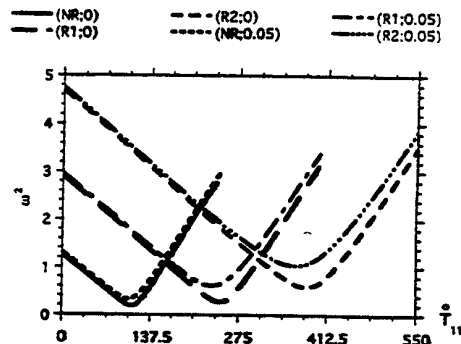


Fig. 4 Influence of the initial geometric imperfection and of the membrane temperature rise on the fundamental frequency of reinforced/no reinforced flat panel subjected to a fixed $\bar{q}_{11} = 10$ lateral pressure (—) no-reinforced, $\delta_0 = 0$); (---) no-reinforced, $\delta_0 = 0.05$); (.....) uniaxially reinforced, $\delta_0 = 0$); (— · —) uniaxially reinforced, $\delta_0 = 0.05$); (— · — · —) bi-axially reinforced, $\bar{q}_{11} = 0$); (— · — · — · —) bi-axially reinforced, $\delta_0 = 0.05$).

Deformation of Nickel Crystal by Embedded Atom Method.

T. Tsuji*, M. I. Baskes**, A. Makino* and T. Koizumi***

* Department of Mechanical Engineering, Shizuoka University, 3-5-1 Jyohoku, Hamamatsu 432, JAPAN

** Materials and Process Research Division, Sandia National Laboratories, Livermore, CA 94551, USA

*** Department of Precision Mechanics, Chuo University, 1-13-27, Kasuga, Bunkyo-ku, Tokyo 112, JAPAN

It is important to investigate atomic order analysis in order to understand microscopic deformation and/or fracture of material. Many investigators have been studying such the problems by using the molecular dynamics method. Moreover, it is important to consider temperature effect, because thermal stresses could be effective to the motion of a dislocation.

Therefore, in this paper, we analyzed temperature effect to the motion of a dislocation in nickel crystal by using newly proposed EAM (Embedded Atom Potential Method). We construct the cylindrical nickel crystal and put an $a[-1\ 0\ 0]$ dislocation by deforming the position of atoms by the dislocation theory. Temperature and/or strain are loaded to this cylinder and MD (Molecular Dynamic) simulations have been done. $a[-1\ 0\ 0]$ dislocation is separated to $a/3[-1\ 0\ 0]$, $a/6[-2\ -1\ -1]$ and $a/6[-2\ 1\ 1]$ dislocations with 0[K]. When the temperature is applied, these dislocations moved along $[1\ 1\ 1]$ and $[-1\ 1\ 1]$ directions. On the other hand, the dislocations moved along $[1\ -1\ -1]$ and $[-1\ -1\ -1]$ directions, when 1.6% uniaxial strain is applied along $[1\ 0\ 0]$ direction in 0[K]. Above 300[K], the movement of the dislocation occurs lower than the 1% strain.

Key Words : *Molecular Dynamic Method, Embedded Atom Method, Dislocation, Nickel Crystal, Missorientation, Temperature*

1. Introduction

Many efforts have been done to recognize a deformation of materials, and many atomic order investigations have been proceeded by experimental and computational methods. In order to study an atomic order deformation, it is important to have a method which can show structure of crystal. It is essential to use a potential, which can describe exactly defect energies such as the surface energy, when we proceed an atomic order simulation. On the other hand, it is well known that hydrogen effects to deformation of materials, and the computational simulations[1],[2] have been done.

In this paper, we propose the method to show the atomic order structure of crystal, and analyzes the deformation of nickel crystal. In section 2, the two kinds of method are proposed to show the structure of crystal by using the missorientation technique[3]. In section 3, we proceed the molecular dynamic simulation of nickel crystal by using newly proposed EAM (Embedded Atom Potential Method) [2], which can describe a fault energy appropriately and simulate the interactions of hydrogen and dislocations exactly. Strain, hydrogen, and temperature effect to the motion of a dislocation in the nickel crystal are studied.

2. Missorientation

It is difficult to see movement of dislocations or structure of crystal. Figure 1 shows pictures of deformed atom positions of a nickel crystal with 30% strain displayed by 4 different kinds of method. Figure

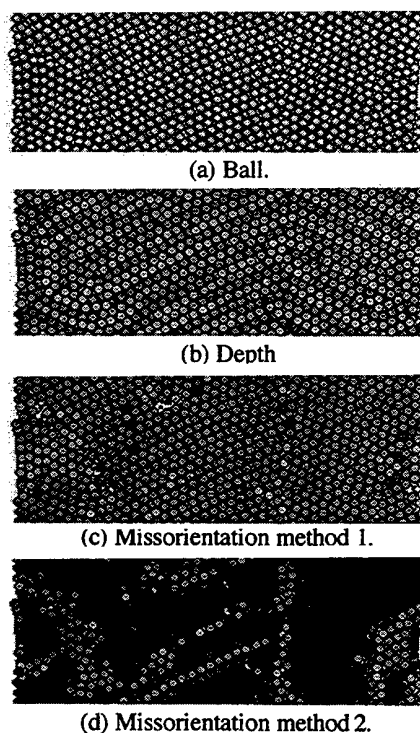


Fig. 1 Some methods to show position of atoms. (a) Ball. (b) Depth. The color shows the depth of atoms from you. Brighter atom is nearer to you. (c) Missorientation method 1. The color shows the missorientation angle to the perfect fcc crystal. (d) Missorientation method 2. The color shows the average missorientation angle between the atoms and the first nearest neighbor.

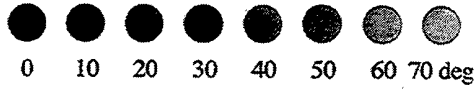


Fig. 2 Miss orientation color depth. Brightest atom shows 70 deg missorientation angle.

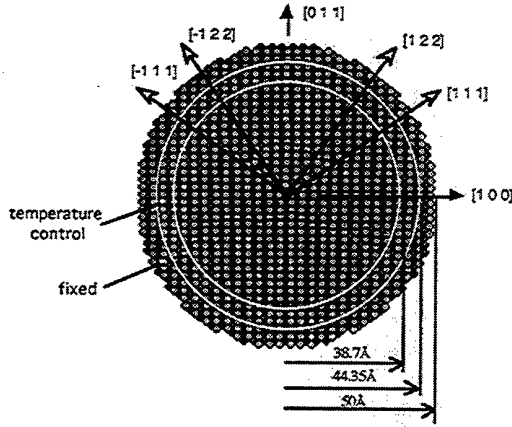


Fig. 3 Cylindrical Ni lattice model.

1 (a) shows atoms as balls. It is realistic but difficult to detect lattice structure or dislocations. Figure 1 (b) shows atoms by circle and put color depend on depth of atoms. Bright color note the atom near to you. We can see some lines, but it is still difficult to detect lattice structure. We propose two kinds of method to show atoms by using missorientation technique[3] as follows.

Method 1 : Rotation angle of missorientation from perfect lattice.

Method 2 : Average rotation angle of missorientation from first nearest neighbor.

Figure 1 (c) and (d) shows atoms which are displayed by these two methods respectively. The relationship between color depth and angle is shown in Fig. 2. In Fig. 1 (c), we can see some different structures, but it is still difficult to get detail of them. In Fig. 1 (d), we can see clearly many sections in the crystal by dark color and boundary of these sections by bright color, since the atom which have same lattice orientation shown by dark and region, where the orientation is changing, is shown by brighter color. On the other hand, when we study movement of dislocation, it is convenient to show atoms by method 1 as shown in following sections, because almost all part have perfect or same lattice structure.

3. Simulation of Cylindrical Ni Lattice

3.1 CYLINDRICAL MODEL

We construct the cylindrical nickel crystal as shown in Fig. 3. The axis of the cylinder is $[0 \ 1 \ 1]$ and the figure shows the surface normal to $(0 \ 1 \ 1)$. The radius r is 50 Å. Along the cylinder axis, we consider

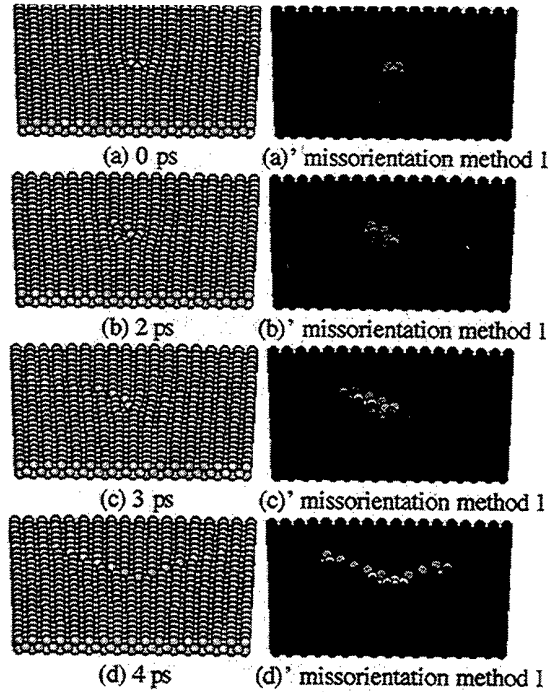


Fig. 4 Movement of $a[1 \ 0 \ 0]$ dislocation by relaxing to $T = 0$ K. Shown by balls and the missorientation method 1. Dark color denotes lower deg and highest color denotes 70 deg. (a) The initial atom position with an $a[1 \ 0 \ 0]$ dislocation. (b) The atom position after relaxed in 2 ps. $a[1 \ 0 \ 0]$ dislocation was started to move. (c) relaxed in 3 ps. (d) relaxed in 4 ps. The $a[1 \ 0 \ 0]$ dislocation were separated to $a/3[1 \ 0 \ 0] + a/6[2 \ 1 \ 1] + a/6[2 \ 1 \ 1]$. The position of dislocation are stable for more time.

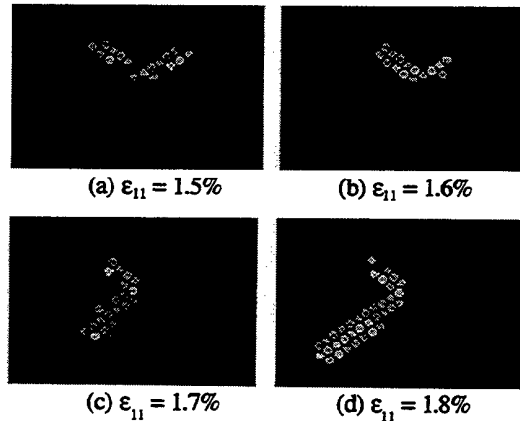


Fig. 5 Uniaxial stress is applied to the dislocation. Shown by the missorientation method 1. (a) The dislocations are stable before $\epsilon_{11} = 1.5\%$. (b) At $\epsilon_{11} = 1.6\%$, the dislocations started to move. (c) and (d) Dislocations are moved to along $[-1 \ -1 \ -1]$ and $[-1 \ 1 \ 1]$ direction.

periodic conditions with the length of periodicity 4.978 Å, which contains 4 layers of atoms. The atoms

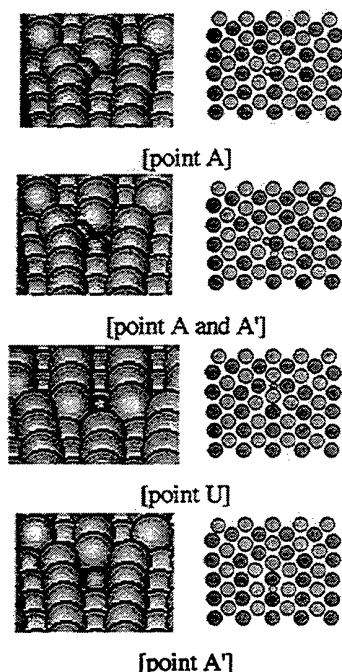


Fig. 6 Positions where hydrogen atoms are putted. Small balls show hydrogen atoms. Upper pictures show atoms (011) surface and tilted 60 deg along upper direction of the paper. Lower pictures show projection to [0 1 1] axis and same color shows same plane. 3.3 Hydrogen effects for $a[1\ 0\ 0]$ dislocation

in the region $r = 44.35$ to $50\ \text{\AA}$ and $r = 38.7$ to $44.35\ \text{\AA}$ are fixed to motion and temperature respectively.

3.2 $a[1\ 0\ 0]$ DISLOCATION at 0 K

$a[1\ 0\ 0]$ dislocation in the nickel crystal is made by deforming the positions of atom in order to the dislocation theory[4]. Figure 4(a) shows the applied $a[1\ 0\ 0]$ dislocation. This dislocation were separated to $a/3[1\ 0\ 0]$, $a/6[2\ 1\ 1]$ and $a/6[2\ 1\ 1]$ as shown in Fig. 4(b) to (c). Moreover, the misorientation angle of each atoms to the perfect crystal without dislocation is shown by colors in Fig. 4 (a)', (b)', (c)' and (d)'. By this figures, separation of the dislocation is shown clearly.

Uniaxial stress along $[1\ 0\ 0]$ axis is applied by scaling the position of each atoms. Scaling were proceeded by step 0.1% strain along $[1\ 0\ 0]$ and $-0.1\% \times v$ ($= 0.0374$) and relaxed 1ps for each steps. Figure 5 shows the misorientation angle of atoms by the method 1. The high angle region of misorientation is started to move with 1.6% strain and changing directions. Finally these regions are oriented to $[1\ 1\ 1]$ and $[1\ 1\ 1]$ direction.

3.3 HYDROGEN EFFECTS

One or two hydrogen atoms are putted near the separated dislocation, which is obtained in section 3.1 with 0 K and relaxed few pico seconds. It is

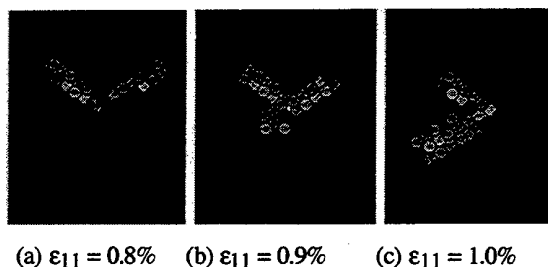


Fig. 7 One hydrogen in periodic position, that is two hydrogen atoms in two layers, are putted and applied strain with uniaxial condition along $[1\ 0\ 0]$ axis. Small ball shows the hydrogen. (a) Dislocations are stable before $\epsilon_{11} = 0.8\%$. (b) Dislocations start moving at $\epsilon_{11} = 0.9\%$. (c) Orientation of the dislocations are changed to $[-1\ -1\ -1]$ and $[-1\ 1\ 1]$ direction.

Table 1 Relationship between the critical strain, where dislocation starts moving, and the placement of hydrogen atoms.

point	A	A, A'	U	A'	no H
critical strain	0.9%	0.9%	1.2%	1.6%	1.6%

Table 2 Relationship between the critical strain, where dislocation starts moving, and temperature.

temperature [K]	0	100	300	500
critical strain	8%	5%	1%	0.6%

confirmed that the dislocation was not move by putting the hydrogen atoms. The positions, where hydrogen atoms are putted, are shown in Fig. 6. Figure 7 shows movement of the dislocation by applying strain with uniaxial stress condition. The dislocation starts moving at 0.9 % strain, that is 0.7 % lower than no hydrogen case. Table 1 shows the relationship between the critical strain, where dislocation starts moving, and the placement of hydrogen atoms. The lowest critical strain is obtained where the hydrogen is in the point A. In every cases shown in Fig. 6, the dislocation moved as same as no hydrogen case.

3.4 TEMPERATURE EFFECTS

Temperature effects are consider to the movement of $a[1\ 0\ 0]$ dislocation. Figures 8 shows the results with 100, 300 and 500 K. In all temperature, the dislocation separated along $[1\ 1\ 1]$ and $[1\ 1\ 1]$ directions with zero strain. This separations are different from 0 K case as shown in Fig.4 (d). When we dropped temperature from 100 K to 0 K, this structure in Fig.8 (a) is stable and total energy is 0.5 eV lower than the one of the structure with 0 K as shown in Fig. 4(d).

We applied strain with uniaxial condition to these cases. For all temperature, the dislocation moved along $[1\ 1\ 1]$ and $[1\ 1\ 1]$ directions, but the

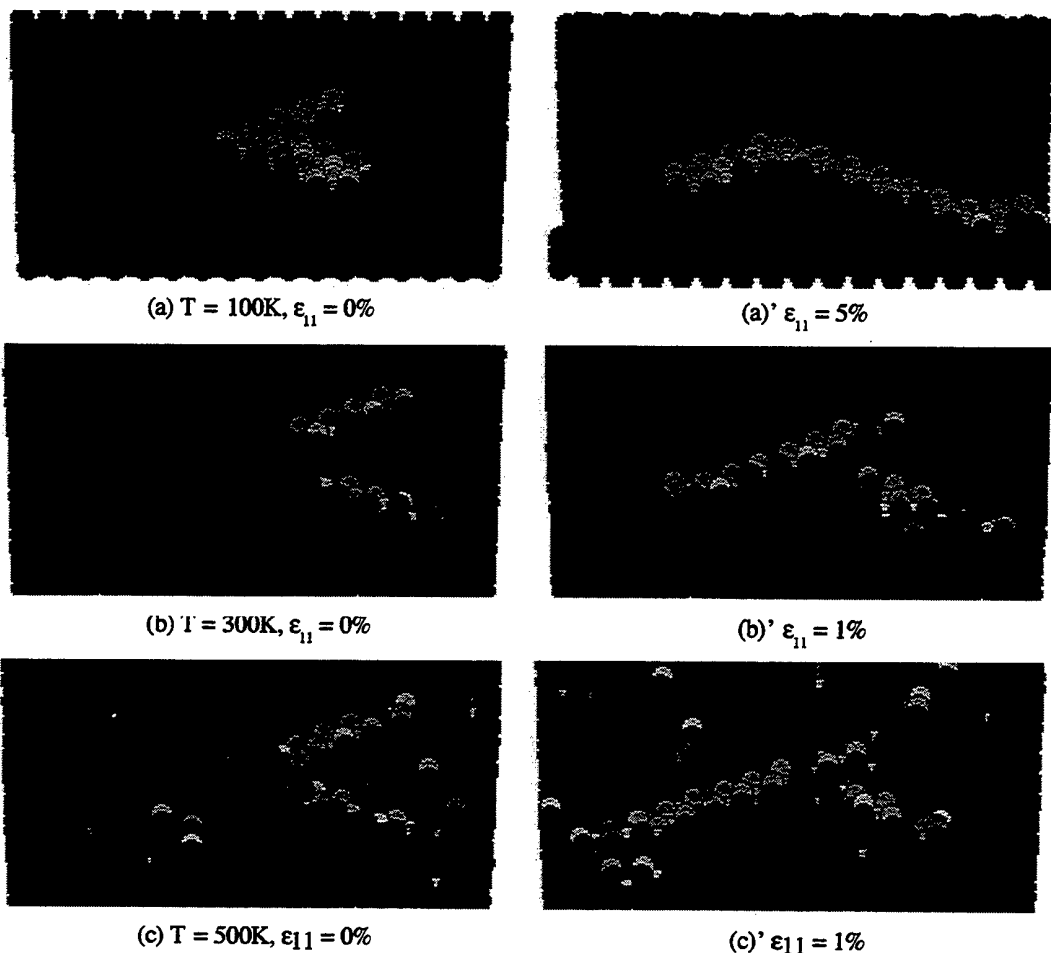


Fig. 8 Relaxed to (a) 100, (b) 300 and (c) 500 K, and applied (a)' 5%, (b)' 1% and (c)' 1% strain. Shown by the misorientation method 1. (a),(b) and (c) Separated $a[1\ 0\ 0]$ dislocations in Fig. 3 (d) are moved for each temperature. (a)',(b)' and (c)' the dislocations moved again along $[1\ -1\ -1]$ and $[-1\ -1\ -1]$ directions at 5%, 1% and 1% respectively.

strain where the movement occurs are not same. Table 2 shows the relationship between this critical strain and temperature. Above 300 K, the movement of the dislocation occurs lower than the 1% strain.

5. Conclusions

The two method, which describe the atomic order structure, are proposed, and the deformation simulation of nickel lattice has been proceeded with many different conditions. The following are summary of conclusions.

1. The misorientation angle is effective to consider structure of lattice.
2. Hydrogen and temperature reduce the critical strain where the dislocation starts to move.

Acknowledgments

The authors would like to thank D. A. Hughes for her many helpful discussions about the development of the misorientation calculations.

References

- (1) M. S. Daw and M. I. Baskes, 'Application of the Embedded Atom Method to Hydrogen Embrittlement.', Sandia Report, SAND86-8863,p.3-21, (1986).
- (2) J. E. Angelo, N. R. Moody and M. I. Baskes, 'Trapping of hydrogen to lattice defects in nickel.', Modelling Simul. Mater. Sci., Eng., Vol.3, pp.289-307, (1995).
- (3) C.T. Young, J. H. Steels, Jr., and J.L. Lyton, 'Characterization of Bicrystals Using Kikuchi Patterns.', Metallurgical Transactions, Vol.4, pp.2081-2089, (1973).
- (4) D. Hull and D. J. Bacon, Introduction to Dislocations, 3rd Ed., (Pergamon, Oxford), (1989).

Solution of an elliptical rigid inclusion with debondings in an infinite plane under the uniform heat flux

N.Hasebe*, K.Yoshikawa** and H.Irikura***

* Department of Civil Engineering, Nagoya Institute of Technology, Gokisocho Showaku, Nagoya 466, Japan

** Tokyu Construction Co., Ltd, Sibuya 1-16-14, Shibuyaku, Tokyo 150, Japan

*** Kajima Construction Co., Ltd, Akasaka 6-5-30, Minatoku, Tokyo 107, Japan

A problem of an elliptical rigid inclusion in an infinite plane subjected to uniform heat flux in an arbitrary direction and with n numbers of debonding on the interface of the elliptical rigid inclusion and the elastic matrix is solved. The rotation of the inclusion under the uniform heat flux is considered. The complex variable method is used and the closed form solution is obtained.

Key Words: Mixed Boundary Value Problem Thermal Stress, Uniform Heat Flux, Elliptic Rigid Inclusion

1. Introduction

Plane elastic boundary value problem can be roughly divided into three types; external force boundary value problem, displacement boundary value problem and mixed boundary value problem (displacement and external force boundaries exist simultaneously). In these boundary value problem, an infinite plane with a hole subjected to uniform heat flux has been considered widely before. For the external force boundary value problem, Florence and Goodier considered an infinite plate with an Ovaloid hole [1]; Takeuchi et al. considered an infinite plate with a polygonal hole [2], Sih studied an infinite plate with a crack [3]; Chao et al. considered an infinite plate with some circular crack on a circular line [4]; Hasebe et al. considered an infinite plate with a square hole [5] as well as a circular hole with a crack [6]. The general solution of an infinite plate with a rigid inclusion under the displacement boundary condition was derived by Hasebe et al. [7]. Sekine solved the line inclusion problem [8]. Furthermore, for the problem with mixed boundary condition, an infinite plate with a circular rigid inclusion with a crack was considered [9]. Kattis studied an arc-shaped inclusion and a straight line inclusion with debonding [10,11]. The above studies are all confined to the case that the number of external force and displacement boundaries is respective one. Compared with the problem to external force or displacement, the solution of the mixed boundary value problem with some segments of the external force and known displacement on the boundary has not been obtained so much before.

The purpose of the present paper is to find the general solution of the mixed boundary value problem of an infinite plate with an elliptical rigid inclusion with n debondings around the interface. The problem is solved by the mapping function and thermal dislocation method, and the problem becomes a Riemann Hilbert

problem so that the complex stress functions can be found. The heat flux is assumed not to pass across the interface of the inclusion in the analysis.

2. The method of analysis

2.1 The mapping function

Fig.1 shows an infinite plate with an elliptical hole (z -plane) which is mapped outside of the unit circle (ζ -plane) by the following mapping function:

$$Z = \omega(\zeta) = E_0 \zeta + \frac{E_1}{\zeta} \quad (1)$$

$$E_0 = \frac{(a+b)}{2}, \quad E_1 = \frac{(a-b)}{2}$$

where a and b denote the long and short radii of the ellipse.

2.2 The solution under the uniform heat flux without rotation

Fig.1 shows an infinite plate with an elliptical rigid inclusion or the constraint of displacement, q represents the uniform heat flux through unit time and unit area with an angle δ between the direction of the heat flux and the x -axis. The temperature and the

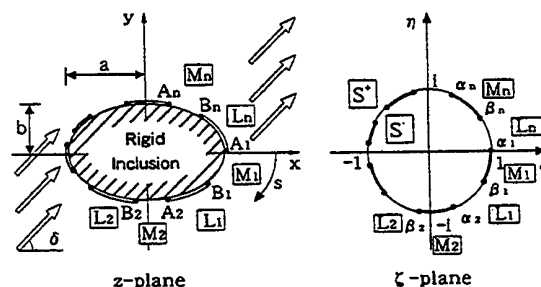


Fig.1 z -plane and ζ -plane

heat flux can be expressed by the mapping function and the complex temperature function. The complex temperature function is presented by [9]

$$\Psi(\zeta) = -\frac{q}{k} (E_0 \zeta e^{-i\delta} + \frac{\bar{E}_0}{\zeta} e^{i\delta}) \quad (2)$$

where k is the thermal conductivity. Stress analysis under uniform heat flux without rotation of the rigid inclusion is carried out. Fig.1 shows the case that there exist debondings of n segments between the inclusion and the elastic matrix. The external force boundaries by $L_j (j=1,2,\dots,n)$, and the displacement boundaries are denoted by $M_j (j=1,2,\dots,n)$. The coordinates of the both ends of M_j are denoted by α_j and β_j in order of clockwise direction. The outside region of the unit circle is denoted by S^+ , and the inner region by S^- .

The external force boundary condition is expressed by the regular complex stress functions as follows [12]

$$\phi(\sigma) + \frac{\omega(\sigma)}{\omega'(\sigma)} \overline{\phi'(\sigma)} + \overline{\psi(\sigma)} = C_j \quad \text{on } M_j (j=1,2,\dots,n) \quad (3)$$

where bar expresses conjugation of the complex function, C_j is the constant which denotes the resultant force on M_j , and has a relation $C_1 + C_2 + \dots + C_n = 0$ from equilibrium.

The displacement boundary condition is [9]

$$\begin{aligned} \kappa\phi(\sigma) - \frac{\omega(\sigma)}{\omega'(\sigma)} \overline{\phi'(\sigma)} - \overline{\psi(\sigma)} \\ = -2G\alpha' \int \Psi(\zeta) \omega'(\zeta) d\zeta \quad \text{on } L_j (j=1,2,\dots,n) \end{aligned} \quad (4)$$

The term in the right side of (4) denotes the displacement produced by the uniform heat flux, which is expressed by the complex temperature function and the first derivative of the mapping function. G is the shear modulus, ν is the Poisson's ratio, and α is the coefficient of thermal expansion. For plane strain state, $\alpha' = \alpha(1+\nu)$, $\kappa = 3-4\nu$; for generalized plane stress state, $\alpha' = \alpha$, $\kappa = (3-\nu)/(1+\nu)$.

Without losing the general property, the external force and displacement on the boundary are zero in (3) and (4). In order to eliminate the dislocation of displacement of the right term in (4), the function with dislocation is introduced and the complex stress functions to be obtained are expressed by [9]

$$\phi(\zeta) = \phi_1(\zeta) + \phi_2(\zeta), \quad \phi_1(\zeta) = A \log \zeta \quad (5)$$

$$\psi(\zeta) = \psi_1(\zeta) + \psi_2(\zeta), \quad \psi_1(\zeta) = B \log \zeta \quad (6)$$

Since the resultant force on the boundary must be zero, $B = \bar{A}$ can be obtained. Substituting (5) and (6) into (4), A can then be determined by eliminating the dislocation of the displacement in the right side of (4):

$$A = \frac{\alpha q R G}{2k} E_0 (\bar{E}_0 e^{i\delta} - E_1 e^{-i\delta}) \quad (7)$$

where $R = (1+\nu)/(1-\nu)$ for plane strain state, and

$R = (1+\nu)$ for generalized plane stress state.

By the principle of analytical continuation on the external force boundary, $\psi(\zeta)$ is expressed by

$$\psi(\zeta) = -\overline{\phi(1/\bar{\zeta})} - \frac{\omega(1/\bar{\zeta})}{\omega'(\zeta)} \phi'(\zeta) \quad (8)$$

Substituting (5), (6) and (7) into (3) and (4), the problem is transformed into Riemann Hilbert problem as:

$$\phi_2^+(\sigma) - \phi_2^-(\sigma) = C_j \quad (9)$$

$$\kappa\phi_2^+(\sigma) + \phi_2^-(\sigma) = H(\sigma) \quad (10)$$

$$H(\sigma) = \frac{\alpha q R G}{2k} (1+\kappa) \left(\frac{E_0^2 e^{-i\delta}}{2} \sigma^2 + \frac{\bar{E}_0 E_1 e^{i\delta}}{2\sigma^2} \right)$$

where $+$ denotes that ζ approaches the boundary of the unit circle from the out region S^+ , so does the signal $-$ from the inner region S^- . The general solution to satisfy (9) and (10) simultaneously on the whole boundary can be expressed as:

$$\begin{aligned} \phi_2(\zeta) = \frac{\chi(\zeta)}{2\pi i} \sum_{j=1}^n \int_{L_j} \frac{C_j}{\chi(\sigma)(\sigma-\zeta)} d\sigma \\ + \frac{\chi(\zeta)}{2\pi i} \sum_{j=1}^n \int_{M_j} \frac{H(\sigma)}{\chi(\sigma)(\sigma-\zeta)} d\sigma \end{aligned} \quad (11)$$

where $\chi(\zeta)$ is called Plemelj function, which is

$$\chi(\zeta) = \prod_{j=1}^n (\zeta - \alpha_j)^m (\zeta - \beta_j)^{1-m} \quad (12)$$

where $m = 0.5 - i(\ln \kappa)/2\pi$. The branching of $\chi(\zeta)/\zeta^m = 1$ is taken as $\zeta \rightarrow \infty$, and the following expressions hold,

$$\chi^+(\zeta) = \chi^-(\zeta) \quad \text{on } L_j (j=1,2,\dots,n) \quad (13)$$

$$-\kappa\chi^+(\zeta) = \chi^-(\zeta) \quad \text{on } M_j (j=1,2,\dots,n) \quad (14)$$

The second term of (11) can be expressed by the integration around the boundary $M(M_1+M_2+\dots+M_n)$ and is carried out by residue theorem. The final expression of $\phi(\zeta)$ can be obtained from (5) and (6) as

$$\begin{aligned} \phi(\zeta) = A \log \zeta \\ + \chi(\zeta) \frac{\alpha q R G}{2k} \left\{ \frac{E_0^2 e^{-i\delta}}{2} V + \frac{\bar{E}_0 E_1 e^{i\delta}}{2} \frac{\chi'(0)\zeta - \chi(0)}{\chi(0)^2 \zeta^2} \right\} \\ + \frac{\alpha q R G}{2k} \left\{ \frac{E_0^2 e^{-i\delta}}{2} \zeta^2 + \frac{\bar{E}_0 E_1 e^{i\delta}}{2} \frac{1}{\zeta^2} \right\} \\ + \frac{\chi(\zeta)}{2\pi i} \sum_{j=1}^n \int_{L_j} \frac{C_j}{\chi(\sigma)(\sigma-\zeta)} d\sigma \end{aligned} \quad (15)$$

where V in the second term of the right side is expressed as

$$n=1; \quad V = -\{\zeta + m\alpha_1 + (1-m)\beta_1\}$$

$$n=2; \quad V = -1$$

$$n \geq 3; \quad V = 0$$

The unknown constants $C_j (j=1, 2, \dots, n)$ can be determined by the condition that the stress components at infinity must be zero, i.e., $\phi'(\infty) = 0$. In order to satisfy this condition, the coefficients of the order more than the first order of ζ becomes zero. From this condition, $n-1$ number of equations about C_1, C_2, \dots, C_n can be established, and combining these equations with the condition that the resultant force must be zero, i.e., $C_1 + C_2 + \dots + C_n = 0$, C_1, C_2, \dots , and C_n can be decided.

In the expression of $\phi(\zeta)$, there exists integral term, however, the first derivative of the integral can be expressed explicitly without integral term involving ζ (see Appendix).

2.3 The solution of the rigid inclusion with rotation

If the inclusion under uniform heat flux is rotated, the rotation angle must be determined ε . It is taken positive in anti-clockwise direction about the origin. The boundary conditions can be defined as $p_x = p_y = 0$ on L_j and $u = -\varepsilon y$, $v = \varepsilon x$ on M_j , which are expressed as [12]

$$\phi^+(\sigma) - \phi^-(\sigma) = D_j \quad (16)$$

$$\kappa \phi^+(\sigma) + \phi^-(\sigma) = 2G\varepsilon i \omega(\sigma) \quad (17)$$

$D_j (j=1, 2, \dots, n)$ represents the resultant force on each M_j . The general solution that satisfies (16) and (17) can be obtained as

$$\begin{aligned} \phi(\zeta) = & \frac{\chi(\zeta)}{2\pi i} \sum_{j=1}^n \int_{L_j} \frac{D_j}{\chi(\sigma)(\sigma - \zeta)} d\sigma \\ & + \frac{2G\varepsilon i}{\kappa} \frac{\chi(\zeta)}{2\pi i} \sum_{j=1}^n \int_{M_j} \frac{\omega(\sigma)}{\chi(\sigma)(\sigma - \zeta)} d\sigma \end{aligned} \quad (18)$$

The integral of (18) on M_j can be carried out by line integration around the boundary M . Finally the complex stress function $\phi(\zeta)$ can be obtained as

$$\begin{aligned} \phi(\zeta) = & -\chi(\zeta) \frac{2G\varepsilon i}{1+\kappa} W + \frac{2G\varepsilon i}{1+\kappa} \omega(\zeta) \\ & + \frac{\chi(\zeta)}{2\pi i} \sum_{j=1}^n \int_{L_j} \frac{D_j}{\chi(\sigma)(\sigma - \zeta)} d\sigma \end{aligned} \quad (19)$$

W in the first term on the right side of (19) is

$$n=1; W = E_0 + \frac{E_1}{\zeta \chi(0)}$$

$$n \geq 2; W = \frac{E_1}{\zeta \chi(0)}$$

The unknown coefficients $D_j (j=1, 2, \dots, n)$ can be determined by the same method as that of the previous section. The another function $\psi(\zeta)$ is expressed by (8).

2.4 The resultant moment

The resultant moment on the displacement boundary must be calculated to obtain the rotation angle ε . From (15) and (19), the complex stress function can be expressed as

$$\phi(\sigma) = \chi(\sigma) f(\sigma) + g(\sigma) + e(\sigma) \quad (20)$$

The resultant moment M_{rot} about the origin on the displacement boundary can then be expressed as [12]

$$\begin{aligned} M_{rot} = & -\operatorname{Re} [f \chi(\sigma) f(\sigma) \overline{\omega}'(1/\sigma) \frac{1}{\sigma^2} d\sigma \\ & + f e'(\sigma) \overline{\omega}(1/\sigma) d\sigma] \end{aligned} \quad (21)$$

It is noted that $e(\sigma)$ denotes integral term in (15) and (19), $f(\sigma)$ denotes term with plemelj function (15) and (19), and $g(\sigma)$ is not related to the plemelj function, which does not appear in (21). The first derivative of $e(\sigma)$ is expressed without integral term (see to Appendix)

The solution of rigid inclusion rotating around the origin due to uniform heat flux from arbitrary direction is obtained by combining the solution of the inclusion without rotation and the solution of the inclusion with rotation under the condition that the resultant moment on the displacement boundary must be zero. In other words, the rotation angle of the inclusion can be determined by the condition that $M_{rot1} + M_{rot2} = 0$, where M_{rot1} is the resultant moment around the origin by making use of (15) in (21) and M_{rot2} is that by making use of (19) in (21).

3. Conclusions

Solutions (8) and (15) of the complex stress functions have been obtained for the case of the rigid elliptical inclusion with n number of segment of external force and displacement boundaries subjected to uniform heat flux in arbitrary direction and without rotation of the rigid inclusion. Besides this, the complex stress functions with a rotation subjected to uniform heat flux can be derived by superposing the complex stress function (19) only to (15). The rotation angle can be decided by the condition that the summation of the resultant moment due to (15) and (19) must be vanished.

Appendix

The first derivative of the $F(\zeta) = \chi(\zeta) \int_a^b \frac{d\sigma}{\chi(\sigma)(\sigma - \zeta)}$

The function is introduced

$$y^{-1}(\zeta) = \frac{1}{y(\zeta)} = \frac{1}{\chi(\zeta)} \prod_{k=1}^n (\zeta - \alpha_k)(\zeta - \beta_k) \quad (22)$$

Multiplying (22) by $1/(\sigma - \zeta)$ and the differential function by σ is considered

$$\frac{d}{d\sigma} \left\{ \frac{y^{-1}(\sigma)}{\sigma - \zeta} \right\} = \frac{\{y^{-1}(\sigma)\}'}{\sigma - \zeta} - \frac{y^{-1}(\sigma)}{(\sigma - \zeta)^2} \quad (23)$$

Multiplying the both terms of (23) by $d\sigma$, and

integrating from a to b , the both sides in (23) is expressed

the left side =

$$\int_a^b \frac{d}{d\sigma} \left\{ \frac{y^{-1}(\sigma)}{\sigma - \zeta} \right\} d\sigma = \left[\frac{y^{-1}(\sigma)}{\sigma - \zeta} \right]_a^b$$

$$= \frac{y^{-1}(b)}{b - \zeta} - \frac{y^{-1}(a)}{a - \zeta} = g_1(\zeta) \quad (24)$$

the right side =

$$\int_a^b \left[\frac{\{y^{-1}(\sigma)\}'}{\sigma - \zeta} - \frac{y^{-1}(\sigma)}{(\sigma - \zeta)^2} \right] d\sigma$$

$$= -f'(\zeta) \prod_{k=1}^n (\zeta - \alpha_k)(\zeta - \beta_k)$$

$$- f(\zeta) \sum_{j=1}^n \left(\frac{m}{\zeta - \alpha_j} + \frac{1-m}{\zeta - \beta_j} \right) \prod_{k=1}^n (\zeta - \alpha_k)(\zeta - \beta_k)$$

$$- g_2(\zeta) \quad (25)$$

where,

$$f(\zeta) = \int_a^b \frac{d\sigma}{\chi(\sigma)(\sigma - \zeta)}, \quad f'(\zeta) = \int_a^b \frac{d\sigma}{\chi(\sigma)(\sigma - \zeta)^2}$$

$g_2(\zeta)$ are the remaining term not including $f(\zeta)$ and $f'(\zeta)$. $f(\zeta)$ and $f'(\zeta)$ include the integral term by the following expression,

$$i(k) = \int_a^b \frac{\sigma^k}{\chi(\sigma)} d\sigma \quad (k = 0, 1, 2, \dots, n) \quad (26)$$

Arranging (24) and (25),

$$f'(\zeta) + H(\zeta)f(\zeta) + G(\zeta) = 0 \quad (27)$$

where,

$$H(\zeta) = \sum_{j=1}^n \left(\frac{m}{\zeta - \alpha_j} + \frac{1-m}{\zeta - \beta_j} \right)$$

$$G(\zeta) = \frac{g_1(\zeta) + g_2(\zeta)}{\prod_{k=1}^n (\zeta - \alpha_k)(\zeta - \beta_k)}$$

Equation (27) is the first differential equation of $f(\zeta)$, and the solution is expressed,

$$f(\zeta) \exp \left\{ \int H(\zeta) d\zeta \right\} + \int G(\zeta) \exp \left\{ \int H(\zeta) d\zeta \right\} d\zeta = \text{const} \quad (28)$$

Noting,

$$\exp \left\{ \int H(\zeta) d\zeta \right\} = \chi(\zeta) \times \text{const} \quad (29)$$

and substituting (29) into (28), the derivative function is obtained as follows:

$$\frac{d}{d\zeta} \{ \chi(\zeta) f(\zeta) \} = -\chi(\zeta) G(\zeta) \quad (30)$$

where $\{ \}$ in the left term of (30) is $F(\zeta) = \chi(\zeta) f(\zeta)$. The final expression of the first derivative function by using (22) can be obtained as

$$F'(\zeta) = -\chi(\zeta) \{ g_1(\zeta) + g_2(\zeta) \} \quad (31)$$

References

- [1] Florence.A.L. and Goodier.J.N., Thermal stresses due to disturbance of uniform heat flow by an insulated ovaloid hole, ASME J. Appl. Mech., Vol.27, pp.635-639, 1960.
- [2] Takeuchi.Y. and Noda.N., A new method for solving thermal stresses at an insulated hole under heat flow, Trans. Japan Soc. of Mech. Engrs, Vol.34, pp.411-417, 1968.
- [3] Sih.G.C., On the singular character of thermal stresses near a crack tip, ASME J. Appl. Mech., Vol.29, pp.587-589, 1962.
- [4] Chao.C.K. and Shen.M.H., Explicit solutions for curvilinear cracks in the thermoelastic medium, J. Thermal Stresses, Vol.16, pp.215-231, 1993.
- [5] Hasebe.N., Irikura.H. and Nakamura.T., Stress intensity factors of cracks initiating from a rhombic hole due to uniform heat flux, Engng. Fract. Mech., Vol.42, pp.331-337, 1992.
- [6] Hasebe.N., Tomida.A. and Nakamura.T., Thermal stresses of a cracked circular hole due to uniform heat flux, J. Thermal Stresses, Vol.11, pp.381-391, 1988.
- [7] Hasebe.N., Tomida.A. and Nakamura.T., Solution of displacement boundary value problem under uniform heat flux, J. Thermal Stresses, Vol.12, pp.71-81, 1989.
- [8] Sekine.H. and Mura.T., Thermal stresses around an elastic ribbonlike inclusion with good thermal conductivity, J. Thermal Stresses, Vol.2, pp.475-489, 1979.
- [9] Hasebe.N., Irikura.H. and Nakamura.T., A solution of the mixed boundary value problem for an infinite plate with a hole under uniform heat flux, ASME J. Appl. Mech., Vol.58, pp.996-1000, 1991.
- [10] Kattis, M.A., Thermal stress intensity factors for a partially bonded rigid fiber inclusion, Engng Fract. Mech., Vol.40, pp159-165, 1991.
- [11] Kattis.M.A. and Patia.A.P., Thermal stress problem for a partly debonded rigid circular-arc fiber inclusion in an infinite matrix, Engng. Fract. Mech., Vol.48, pp.359-366, 1994.
- [12] Muskhelishvili.N.I., Some Basic Problems of Mathematical Theory of Elasticity, fourth Edition, Noordhoff, The Netherlands, 1963.

Steady State Thermal Stresses in an Elastic Thick Plate Containing a Sliding Prolate Spheroidal Inhomogeneity with the Regions of Both Plate Surfaces Being Heated and Cooled

E.Tsuchida*, Y.Arai* and K.Esaki**

* Department of Mechanical Engineering, Saitama University, 255, Shimo-Okubo, Urawa, 338, JAPAN

** JR East Japan Co. Ltd.

The steady state thermal stresses in an elastic thick plate containing a prolate spheroidal sliding inhomogeneity, when the circle region of radius d of the upper surface is heated and lower one is cooled, are investigated. The interface between the inclusion and the matrix allows sliding. The solution is deduced with using thermoelastic displacement potential and Boussinesq's displacement functions. Numerical examples are given.

Key Words: Elasticity, Thermal stress, Thick plate, Inclusion, Steady state thermal stress

1. Introduction

New materials such as functionally gradient materials and MMC have developed recently. Then the thermal stresses near the inclusions are important for engineering design. In this paper, the steady state thermal stresses in an elastic thick plate containing a prolate spheroidal sliding inhomogeneity, when the circle region of radius d of the upper surface is heated and lower one is cooled, are investigated. The interface between the inclusion and the matrix allows sliding. The solution is deduced with using thermoelastic displacement potential and Boussinesq's displacement potentials. The related three-dimensional thermal stress problems of a spheroidal cavity or an inclusion embedded in a thick plate, were discussed in papers of Tsuchida and Nishikawa (1995)¹, Tsuchida et. (1996)², among others. Two sets of harmonic functions and two sets of biharmonic functions are given by simple expressions referring to cylindrical and prolate spheroidal coordinates. The boundary conditions on the surfaces of the thick plate and the inclusion are satisfied by using the relations between cylindrical and prolate spheroidal harmonics and biharmonics. Numerical results are presented for different heat or cool area, stiffness ratios, inclusion shapes and sizes, and the stress distributions in the neighbourhood of the inclusion are illustrated graphically.

2. Method of solution

2.1 Temperature distribution and thermoelastic displacement potential

Consider an elastic thick plate containing a prolate spheroidal inhomogeneity as shown in Fig.1. Denote the cylindrical and prolate spheroidal coordinates by (r, θ, z) and (α, β, γ) , respectively. They are related with each other by the equation

$$r = c\bar{q}\bar{p}, \quad \theta = \gamma, \quad z = cqp \quad (1)$$

in which c is the half distance between a pair of foci

and

$$\left. \begin{aligned} q &= \cosh \alpha, \quad \bar{q} = \sinh \alpha, \quad (q \geq 1) \\ p &= \cos \beta, \quad \bar{p} = \sin \beta \quad (|p| \leq 1) \end{aligned} \right\} \quad (2)$$

For convenience, r , z , q and \bar{q} henceforce will be regarded as dimensionless quantities referring to a typical length of the half thickness of the thick plate. The major and minor semi-axes of the prolate spheroidal inclusion are taken as b and a , where $b = c \cosh \alpha_0$, $a = c \sinh \alpha_0$.

The circular region of radius d of the upper surface of the thick plate is heated to constant temperature T_0 and lower one is cooled to $-T_0$, and other regions of surfaces are insulated.

First, we obtain the temperature distribution. T is the temperature rise from the initial uniform temperature $T = 0$.

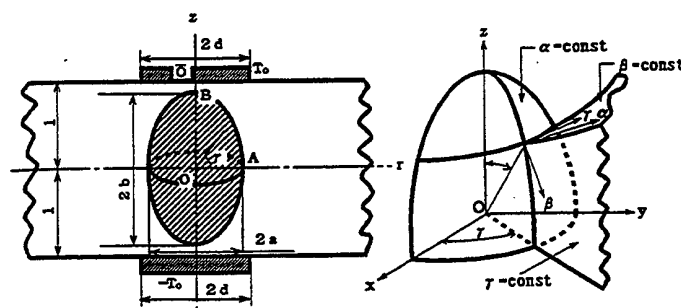


Fig.1 Coordinate system

Temperature distributions satisfy the Fourier heat conduction equation under steady state condition

$$\nabla^2 T = \nabla^2 \bar{T} = 0 \quad (3)$$

and satisfy the boundary condition:

- (i) On the surfaces of the thick plate $z = \pm 1$

$$(T)_{z=\pm 1} = \begin{cases} \pm T_0 & (r < d) \\ 0 & (r > d) \end{cases} \quad (4)$$

(ii) On the interface of the inclusion $\alpha = \alpha_0$

$$(T)_{\alpha=\alpha_0} = (\bar{T})_{\alpha=\alpha_0} \quad (5)$$

$$k \left(\frac{\partial T}{\partial \alpha} \right)_{\alpha=\alpha_0} = \bar{k} \left(\frac{\partial \bar{T}}{\partial \alpha} \right)_{\alpha=\alpha_0} \quad (6)$$

Here, k is the thermal conductivity. The quantities referring to the inclusion are denoted by a superior bar. We give the temperature functions as follows:

$$T = T_0 d \int_0^\infty \frac{\sinh \lambda z}{\sinh \lambda} J_1(\lambda d) J_0(\lambda r) d\lambda + T_0 \sum_{m=0}^\infty F_m Q_{2m+1}(q) P_{2m+1}(p) \quad (7)$$

$$+ T_0 \int_0^\infty \phi(\lambda) J_0(\lambda r) \sinh \lambda z d\lambda \quad (\alpha > \alpha_0)$$

$$\bar{T} = T_0 \sum_{n=0}^\infty \bar{F}_n P_{2n+1}(q) P_{2n+1}(p) \quad (\alpha < \alpha_0) \quad (8)$$

Here, $F_m, \bar{F}_n, \phi(\lambda)$ are unknown coefficients and an unknown function, which are determined from the boundary conditions. $J_n(\lambda r)$ is a Bessel function of the first kind and $P_n(p), Q_n(q)$ are Legendre functions of the first and second kinds respectively.

First, we use the following formulae to satisfy the boundary conditions (i) on the surfaces of the thick plate.

$$Q_n(q) P_n(p) = c \int_0^\infty i_n(\lambda c) J_0(\lambda r) e^{-\lambda z} d\lambda \quad (z > 0)$$

$$Q_n(q) P_n(p) = (-1)^n c \int_0^\infty i_n(\lambda c) J_0(\lambda r) e^{\lambda z} d\lambda \quad (z < 0) \quad (9)$$

where, $i_n(\lambda c)$ is

$$i_n(\lambda c) = i^{-n} j_n(i\lambda c) = \sqrt{\frac{\pi}{2\lambda c}} I_{n+\frac{1}{2}}(\lambda c)$$

and $i = \sqrt{-1}$.

From the boundary conditions, unknown function $\phi(\lambda)$ is found as follows.

$$\phi(\lambda) = - \sum_{m=0}^\infty c F_m i_{2m+1}(\lambda c) \frac{2}{e^{2\lambda} - 1} \quad (10)$$

Next, in order to satisfy the boundary conditions (ii) of the inclusion, we use the following formulae

$$J_0(\lambda r) \cosh \lambda z = \sum_{n=0}^\infty (4n+1) i_{2n}(\lambda c) P_{2n}(q) P_{2n}(p) \\ J_0(\lambda r) \sinh \lambda z = \sum_{n=0}^\infty (4n+3) i_{2n+1}(\lambda c) P_{2n+1}(q) \\ \times P_{2n+1}(p) \quad (11)$$

Satisfying the boundary condition (ii), we get

$$\sum_{n=0}^\infty \{ F_n Q_{2n+1}(q_0) + (4n+3)(\kappa_n + \delta_n) P_{2n+1}(q_0) \} \\ \times P_{2n+1}(p) = \sum_{n=0}^\infty \bar{F}_n P_{2n+1}(q_0) P_{2n+1}(p) \quad (12)$$

$$k \sum_{n=0}^\infty \{ F_n Q'_{2n+1}(q_0) + (4n+3)(\kappa_n + \delta_n) P'_{2n+1}(q_0) \}$$

$$\times P_{2n+1}(p) = \bar{k} \sum_{n=0}^\infty \bar{F}_n P'_{2n+1}(q_0) P_{2n+1}(p) \quad (13)$$

Here, δ_n, κ_n are

$$\delta_n = d \int_0^\infty \frac{J_1(\lambda d)}{\sinh \lambda} i_{2n+1}(\lambda c) d\lambda \quad (14)$$

$$\kappa_n = - \sum_{m=0}^\infty 2c F_m \int_0^\infty \frac{1}{e^{2\lambda} - 1} i_{2m+1}(\lambda c) i_{2n+1}(\lambda c) d\lambda$$

We obtain an infinite linear equation for F_n, \bar{F}_n . Solving these equations, we get T and \bar{T} .

Next, we seek the particular solution of the thermoelastic equation for the temperature function. As a particular solution for $\nabla^2 \Omega = T, \nabla^2 \bar{\Omega} = \bar{T}$, we give the following thermoelastic displacement Ω and $\bar{\Omega}$ for T and \bar{T} where, Ω and $\bar{\Omega}$ are thermoelastic displacement potentials for the matrix and the inclusion.

$$\Omega = T_0 d \int_0^\infty \frac{z \cosh \lambda z}{2\lambda \sinh \lambda} J_1(\lambda d) J_0(\lambda r) d\lambda + T_0 \sum_{m=0}^\infty \frac{F_m c^2 q p}{2(4m+3)} \{ Q_{2m+2}(q) P_{2m+2}(p) - Q_{2m}(q) P_{2m}(p) \} + T_0 \int_0^\infty \frac{1}{2\lambda} \phi(\lambda) J_0(\lambda r) z \cosh \lambda z d\lambda \quad (15)$$

$$\bar{\Omega} = T_0 \sum_{n=0}^\infty \frac{\bar{F}_n c^2 q p}{2(4n+3)} \times \{ P_{2n+2}(q) P_{2n+2}(p) - P_{2n}(q) P_{2n}(p) \}$$

Here, $\nabla^4 \Omega = \nabla^4 \bar{\Omega} = 0$.

2.2. Displacement potentials

The stresses caused by the above thermoelastic displacement potentials and temperature functions do not satisfy the boundary conditions on the surfaces of the thick plate and the inclusion interface. Then we use Boussinesq's displacement potentials. Boussinesq displacement potentials for the torsionless axisymmetric problem are given

$$2Gu_r = \frac{\partial \varphi_0}{\partial r} + z \frac{\partial \varphi_3}{\partial r} \\ 2Gu_z = \frac{\partial \varphi_0}{\partial z} + z \frac{\partial \varphi_3}{\partial z} - (3-4\nu)\varphi_3 \quad (16)$$

The boundary conditions in the case of sliding inclusion to be satisfied are :

(i) On the surfaces of the thick plate $z = \pm 1$

$$\pm \left(\frac{\sigma_z}{E\epsilon T_0} \right)_{z=\pm 1} = - \frac{1}{2(1-\nu)} \left\{ \int_0^\infty \left(\frac{dJ_1(\lambda d)}{\sinh \lambda} + \phi(\lambda) \right) \times \lambda \cosh \lambda J_0(\lambda r) d\lambda - \sum_{m=0}^\infty c F_m \int_0^\infty \lambda e^{-\lambda} i_{2m+1}(\lambda c) J_0(\lambda r) d\lambda \right\} \quad (17)$$

$$\left(\frac{\tau_{rz}}{E\epsilon T_0} \right)_{z=\pm 1}$$

$$= \frac{1}{2(1-\nu)} \left\{ \int_0^\infty \left(\frac{dJ_1(\lambda d)}{\sinh \lambda} + \phi(\lambda) \right) \right. \\ \times (\cosh \lambda + \lambda \sinh \lambda) J_1(\lambda r) d\lambda \\ \left. + \sum_{m=0}^\infty c F_m \int_0^\infty (\lambda - 1) e^{-\lambda} i_{2m+1}(\lambda c) J_1(\lambda r) d\lambda \right\}$$

(ii) On the surface of the inclusion $\alpha = \alpha_0$

$$\left(\frac{2Gu_\alpha}{E\epsilon T_0 h \bar{q}} \right)_{\alpha=\alpha_0} - \left(\frac{2G\bar{u}_\alpha}{E\epsilon T_0 h \bar{q}} \right)_{\alpha=\alpha_0} = u_\alpha^* \\ = \sum_{n=0}^\infty \left[-\frac{c^2}{2(1-\nu)} \left\{ \frac{k_{F1}}{4n-1} F_{n-1} + \frac{k_{F2}}{4n+3} F_n \right. \right. \\ + \frac{k_{F3}}{4n+7} F_{n+1} + k_{\kappa 1}(\kappa_{n-1} + \delta_{n-1}) \\ + k_{\kappa 2}(\kappa_n + \delta_n) + k_{\kappa 3}(\kappa_{n+1} + \delta_{n+1}) \} \\ + \frac{\epsilon_0(1+\bar{\nu})c^2}{2(1-\bar{\nu})(1+\nu)} \left\{ \frac{k_{\kappa 1}}{4n-1} \bar{F}_{n-1} + \frac{k_{\kappa 2}}{4n+3} \bar{F}_n \right. \\ + \frac{k_{\kappa 3}}{4n+7} \bar{F}_{n+1} \} \left. \right] P_{2n+1}(p) \\ \left(\frac{\sigma_\alpha}{E\epsilon T_0 c^2 h^4} \right)_{\alpha=\alpha_0} - \left(\frac{\bar{\sigma}_\alpha}{E\epsilon T_0 c^2 h^4} \right)_{\alpha=\alpha_0} = \sigma_\alpha^* \\ = \sum_{n=0}^\infty \left[-\frac{c^2}{1-\nu} \left\{ \frac{s_{F1}}{4n-5} F_{n-2} + \frac{s_{F2}}{4n-1} F_{n-1} \right. \right. \\ + \frac{s_{F3}}{4n+3} F_n + \frac{s_{F4}}{4n+7} F_{n+1} + \frac{s_{F5}}{4n+11} F_{n+2} \\ + s_{\kappa 1}(\kappa_{n-2} + \delta_{n-2}) + s_{\kappa 2}(\kappa_{n-1} + \delta_{n-1}) \\ + s_{\kappa 3}(\kappa_n + \delta_n) + s_{\kappa 4}(\kappa_{n+1} + \delta_{n+1}) \\ + s_{\kappa 5}(\kappa_{n+2} + \delta_{n+2}) \} + \frac{\epsilon_0(1+\bar{\nu})c^2 \Gamma}{(1-\bar{\nu})(1+\nu)} \\ \times \left\{ \frac{s_{\kappa 1}}{4n-5} \bar{F}_{n-2} + \frac{s_{\kappa 2}}{4n-1} \bar{F}_{n-1} + \frac{s_{\kappa 3}}{4n+3} \bar{F}_n \right. \\ + \frac{s_{\kappa 4}}{4n+7} \bar{F}_{n+1} + \frac{s_{\kappa 5}}{4n+11} \bar{F}_{n+2} \} \left. \right] P_{2n+1}(p) \\ \left(\frac{\tau_{\alpha\beta}}{E\epsilon T_0 c^2 h^4 \bar{q} \bar{p}} \right)_{\alpha=\alpha_0} = \tau_{\alpha\beta}^* \\ = \sum_{n=1}^\infty \left[-\frac{c^2}{2(1-\nu)} \left\{ \frac{t_{F1}}{4n-5} F_{n-2} + \frac{t_{F2}}{4n-1} F_{n-1} \right. \right. \\ + \frac{t_{F3}}{4n+3} F_n + \frac{t_{F4}}{4n+7} F_{n+1} + \frac{t_{F5}}{4n+11} F_{n+2} \\ + t_{\kappa 1}(\kappa_{n-2} + \delta_{n-2}) + t_{\kappa 2}(\kappa_{n-1} + \delta_{n-1}) \\ + t_{\kappa 3}(\kappa_n + \delta_n) + t_{\kappa 4}(\kappa_{n+1} + \delta_{n+1}) \\ + t_{\kappa 5}(\kappa_{n+2} + \delta_{n+2}) \} \left. \right] P'_{2n+1}(p) \\ \left(\frac{\bar{\tau}_{\alpha\beta}}{E\epsilon T_0 c^2 h^4 \bar{q} \bar{p}} \right)_{\alpha=\alpha_0} = \bar{\tau}_{\alpha\beta}^* \\ = - \sum_{n=1}^\infty \left[\frac{\epsilon_0(1+\bar{\nu})c^2 \Gamma}{2(1-\bar{\nu})(1+\nu)} \left\{ \frac{t_{\kappa 1}}{4n-5} \bar{F}_{n-2} \right. \right. \\ + \frac{t_{\kappa 2}}{4n-1} \bar{F}_{n-1} + \frac{t_{\kappa 3}}{4n+3} \bar{F}_n + \frac{t_{\kappa 4}}{4n+7} \bar{F}_{n+1} \\ + \frac{t_{\kappa 5}}{4n+11} \bar{F}_{n+2} \} \left. \right] P'_{2n+1}(p) \quad (18)$$

(iii) At infinity all stresses vanish.

Here, \prime denotes the differentiation. E is Young's modulus, ν is Poisson's ratio, ϵ the coefficient of linear expansion and $\epsilon_0 = \bar{\epsilon}/\epsilon$ is a ratio of coefficients of linear expansion. h is a local scale coefficient $h^2 = \frac{1}{c^2(q^2 - p^2)}$. Sample coefficients of k_{Fi} , s_{Fi} , t_{Fi} ($i = 1 \sim 3, l = 1 \sim 5$) are

$$k_{F1} = \frac{2n+1}{4n+1} \{ Q_{2n}(q_0) + q_0 Q'_{2n}(q_0) \} \quad (19)$$

Here, $q_0 = \cosh \alpha_0$, $\bar{q}_0 = \sinh \alpha_0$, $h_0^2 = \frac{1}{c^2(q_0^2 - p^2)}$. To satisfy these boundary conditions, we give the following harmonics for Boussinesq's displacement potentials φ_0 , and φ_3 .

For the matrix:

$$[I] \begin{cases} \varphi_0 = E\epsilon T_0 \sum_{m=0}^\infty A_m Q_{2m+1}(q) P_{2m+1}(p) \\ \varphi_3 = E\epsilon T_0 \sum_{m=0}^\infty B_m Q_{2m}(q) P_{2m}(p) \end{cases} \quad (20)$$

$$[II] \begin{cases} \varphi_0 = E\epsilon T_0 \int_0^\infty \psi_1(\lambda) J_0(\lambda r) \sinh \lambda z d\lambda \\ \varphi_3 = E\epsilon T_0 \int_0^\infty \lambda \psi_2(\lambda) J_0(\lambda r) \cosh \lambda z d\lambda \end{cases} \quad (21)$$

For the inclusion:

$$[III] \begin{cases} \varphi_0 = E\epsilon T_0 \sum_{n=1}^\infty \bar{A}_n P_{2n+1}(q) P_{2n+1}(p) \\ \varphi_3 = E\epsilon T_0 \sum_{n=1}^\infty \bar{B}_n P_{2n}(q) P_{2n}(p) \end{cases} \quad (22)$$

where, A_m , B_m , ($m = 0, 1, \dots$), \bar{A}_n , \bar{B}_n , ($n = 1, 2, \dots$) are unknown constants and $\psi_1(\lambda)$, $\psi_2(\lambda)$ are unknown functions of λ , which are determined from the boundary conditions. The above displacement potentials satisfy the boundary conditions (iii) automatically.

First, to satisfy the boundary conditions of the surfaces of the thick plate (i), we use the relation (9) and transform the displacement potentials [I] in the cylindrical coordinates and satisfy the boundary conditions. And the unknown functions $\psi_1(\lambda)$ and $\psi_2(\lambda)$ are found as follows:

$$\psi_1(\lambda) = \sum_{m=0}^\infty c \{ A_m i_{2m+1}(\lambda c) f_1(\lambda) \\ + B_m i_{2m}(\lambda c) f_2(\lambda) + \frac{1}{1-\nu} F_m i_{2m+1}(\lambda c) g_1(\lambda) \} \\ - \frac{1}{\lambda^2} \left\{ \frac{dJ_1(\lambda d)}{\sinh \lambda} + \phi(\lambda) \right\} \quad (23)$$

$$\psi_2(\lambda) = \sum_{m=0}^\infty c \{ A_m i_{2m+1}(\lambda c) f_3(\lambda) \\ + B_m i_{2m}(\lambda c) f_4(\lambda) + \frac{1}{2(1-\nu)} F_m i_{2m+1}(\lambda c) \\ \times g_2(\lambda) \} \\ - \frac{1}{2(1-\nu)\lambda^2} \left\{ \frac{dJ_1(\lambda d)}{\sinh \lambda} + \phi(\lambda) \right\} \quad (24)$$

Here,

$$f_1(\lambda) = \frac{3 - 4\nu - 2\lambda - e^{-2\lambda}}{\sinh 2\lambda - 2\lambda}$$

$$\begin{aligned}
f_2(\lambda) &= \frac{4(1-\nu)(1-2\nu)-2\lambda^2}{\lambda(\sinh 2\lambda-2\lambda)} \\
f_3(\lambda) &= \frac{\sinh 2\lambda-2\lambda}{3-4\nu+2\lambda+e^{-2\lambda}} \\
f_4(\lambda) &= \frac{\lambda(\sinh 2\lambda-2\lambda)}{\lambda^2(\sinh 2\lambda-2\lambda)} \\
g_1(\lambda) &= \frac{(1-\nu)(1-2\lambda-e^{-2\lambda})+\lambda^2}{\lambda^2(\sinh 2\lambda-2\lambda)} \\
g_2(\lambda) &= \frac{1-2\lambda-e^{-2\lambda}}{\lambda^2(\sinh 2\lambda-2\lambda)}
\end{aligned} \quad (25)$$

Next, to satisfy the boundary conditions of the interface of the inclusion (ii), we use the Equation (11) and rewrite [II]

$$[\text{II}]^* \begin{cases} \varphi_0 = E\epsilon T_0 \sum_{n=1}^{\infty} \alpha_n P_{2n+1}(q) P_{2n+1}(p) \\ \varphi_3 = E\epsilon T_0 \sum_{n=1}^{\infty} \beta_n P_{2n}(q) P_{2n}(p) \end{cases} \quad (26)$$

where

$$\begin{aligned}
\alpha_n &= (4n+3) \int_0^{\infty} \psi_1(\lambda) i_{2n+1}(\lambda c) d\lambda \\
\beta_n &= (4n+1) \int_0^{\infty} \lambda \psi_2(\lambda) i_{2n}(\lambda c) d\lambda
\end{aligned} \quad (27)$$

Deriving the stresses and displacements from [I], [II]*, [III], and satisfying the boundary conditions on the surface of the inclusion, we get

$$\begin{aligned}
&\sum_{n=0}^{\infty} \{k_{A1}A_n + k_{B1}B_n + k_{B2}B_{n+1} + k_{\alpha 1}\alpha_n \\
&\quad + k_{\beta 1}\beta_n + k_{\beta 2}\beta_{n+1}\} \\
&\quad - \frac{1}{\Gamma} \{ \bar{k}_{A1}\bar{A}_n + \bar{k}_{B1}\bar{B}_n + \bar{k}_{B2}\bar{B}_{n+1} \} P_{2n+1}(p) \\
&= u_{\alpha}^* \quad (28)
\end{aligned}$$

$$\begin{aligned}
&\sum_{n=0}^{\infty} \{s_{A1}A_{n-1} + s_{A2}A_n + s_{A3}A_{n+1} \\
&\quad + s_{B1}B_{n-1} + s_{B2}B_n + s_{B3}B_{n+1} + s_{B4}B_{n+2} \\
&\quad + s_{\alpha 1}\alpha_{n-1} + s_{\alpha 2}\alpha_n + s_{\alpha 3}\alpha_{n+1} + s_{\beta 1}\beta_{n-1} \\
&\quad + s_{\beta 2}\beta_n + s_{\beta 3}\beta_{n+1} + s_{\beta 4}\beta_{n+2}\} \\
&\quad - \{ \bar{s}_{A1}\bar{A}_{n-1} + \bar{s}_{A2}\bar{A}_n + \bar{s}_{A3}\bar{A}_{n+1} \\
&\quad + \bar{s}_{B1}\bar{B}_{n-1} + \bar{s}_{B2}\bar{B}_n \\
&\quad + \bar{s}_{B3}\bar{B}_{n+1} + \bar{s}_{B4}\bar{B}_{n+2} \} P_{2n+1}(p) \\
&= \sigma_{\alpha}^* \quad (29)
\end{aligned}$$

$$\begin{aligned}
&\sum_{n=1}^{\infty} \{t_{A1}A_{n-1} + t_{A2}A_n + t_{A3}A_{n+1} \\
&\quad + t_{B1}B_{n-1} + t_{B2}B_n + t_{B3}B_{n+1} \\
&\quad + t_{B4}B_{n+2} + t_{\alpha 1}\alpha_{n-1} + t_{\alpha 2}\alpha_n + t_{\alpha 3}\alpha_{n+1} \\
&\quad + t_{\beta 1}\beta_{n-1} + t_{\beta 2}\beta_n + t_{\beta 3}\beta_{n+1} + t_{\beta 4}\beta_{n+2}\} \\
&\quad \times P'_{2n+1}(p) = \tau_{\alpha\beta}^* \quad (30)
\end{aligned}$$

$$\begin{aligned}
&\sum_{n=1}^{\infty} \{ \bar{t}_{A1}\bar{A}_{n-1} + \bar{t}_{A2}\bar{A}_n + \bar{t}_{A3}\bar{A}_{n+1} \\
&\quad + \bar{t}_{B1}\bar{B}_{n-1} + \bar{t}_{B2}\bar{B}_n \\
&\quad + \bar{t}_{B3}\bar{B}_{n+1} + \bar{t}_{B4}\bar{B}_{n+2} \} P'_{2n+1}(p) \\
&= \bar{\tau}_{\alpha\beta}^* \quad (31)
\end{aligned}$$

Here, the sample coefficients are

$$\begin{aligned}
k_{A1} &= Q'_{2n+1}(q_0) \\
s_{A1} &= -\frac{2n(2n+1)}{(4n-1)(4n+1)} \{ \bar{q}_0^2 Q''_{2n-1}(q_0) \\
&\quad + q_0 Q'_{2n-1}(q_0) - (2n-1) Q_{2n-1}(q_0) \} \quad (32)
\end{aligned}$$

— $\Gamma=0.5$

— $\Gamma=2.0$

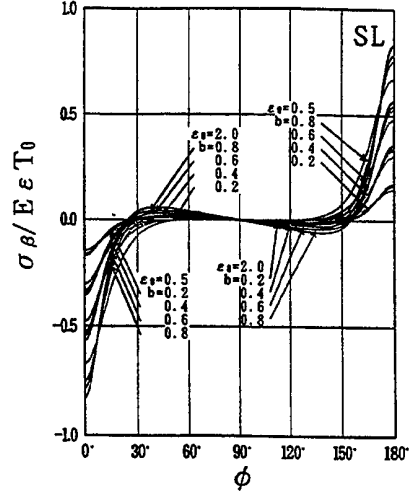


Fig.2 Variation of σ_{β} with ϕ on the surface of the inclusion, $s=0.5$, $d=1.0$, $\bar{k}/k=1.0$ SL

Here, Γ is $\Gamma = \bar{G}/G$. $\Gamma=0$ represents void, and $\Gamma=\infty$ is perfectly rigid. Equating the coefficients of $P_{2n+1}(p)$ and $P'_{2n+1}(p)$, in the left and right sides of equations (28)-(31), we obtain an infinite system of algebraic equations for A_n, B_n, \bar{A}_n and \bar{B}_n .

3. Numerical results

Numerical calculations were carried out for heat and cool regions radius $d=0.5, 1.0, 2.0$ changing, values of the semi-axis b , the shape ratio $s=a/b$, stiffness ratio $\Gamma = \bar{G}/G$ and ratio of the thermal expansion coefficients $\epsilon_0 = \bar{\epsilon}/\epsilon$.

The variation of σ_{β} with ϕ on the surface of the inclusion for $s=0.5$, $d=1.0$ is shown in Fig.2.

This work is supported in part by the Ministry of Education of Japan under the Grant-in-Aid for Scientific Research C (No.08650089) for 1996. The authors would like to appreciate the financial support.

REFERENCES

- (1) Tsuchida, E., Arai Y. and Nishikawa M., Steady State Thermal Stresses in an Elastic Thick Plate Containing a Prolate Spheroidal Inhomogeneity with Constant Temperature Applied on the Circle Regions of Both Plate Surfaces, Thermal Stresses'95, p.215, 1995.
- (2) Tsuchida, E. and Arai Y. and Esaki K., Steady State Thermal Stresses in an Elastic Thick Plate Containing a Prolate Spheroidal Cavity, Theor. and Appl. Mech. Vol.45, p.79, 1996.

An Extension of the Cowin & Nunziato's Domain in Initially Stressed Bodies with Voids

Marin Marin

Math. Dep., Univ. of Brasov, Str. I. Maniu, 50, 2200 Brasov, Romania

We prove that for a finite time $t > 0$, the displacement field u_i , the dipolar displacement field φ_{jk} , the temperature θ and the change in volume fraction σ generate no disturbance outside a bounded domain.

Key Words: Domain of influence, Initially stressed body, voids

1. Introduction

It is remarkable to note that the theory of materials with voids or vacuous pores was first proposed by Nunziato and Cowin [8]. In this theory the authors introduce an additional degree of freedom in order to develop the mechanical behavior of a body in which the skeletal material is elastic and interstices are voids of material. The intended applications of the theory are to geological materials like rocks and soil and to manufactured porous materials. The linear theory of elastic materials with voids was developed by Cowin and Nunziato in [3]. Here the uniqueness and weak stability of solutions are also derived. Iesan in [4] has established the equations of thermoelasticity of materials with voids. An extension of these results to cover the theory of micropolar materials with voids was been made in our study [6]. In the present paper we first consider the basic equations and conditions of the mixed initial-boundary value problem in the context of thermoelasticity of initial stressed bodies with voids. Next we

define the domain of influence B_t of the data at time t associated with the problem. We adopt the method used in [1] and [5] to establish a domain of influence theorem. The main result asserts that in the context of considered theory, the solutions of the mixed initial-boundary value problem vanishes outside B_t , for a finite time $t > 0$.

2. Basic equations

The basic equations from thermoelasticity of initial stressed bodies with voids are, [7]

$$\begin{aligned} (\tau_{ij} + \eta_{ij})_{,j} + \rho F_i &= \rho \ddot{u}_i, \\ \mu_{ijk,i} + \eta_{jk} + u_{j,i} Q_{ik} + \varphi_{ki} Q_{ji} - \\ - \varphi_{kr,i} N_{ijr} + \rho M_{jk} &= I_{kr} \ddot{\varphi}_{jr}, \end{aligned} \quad (1)$$

$$h_{i,i} + g + \rho L = \rho \kappa \dot{\sigma}, \quad (2)$$

$$\rho T_0 \dot{\eta} = q_{i,i} + \rho r. \quad (3)$$

The equations (1) are the motion equations, (2) is the balance of the equilibrated forces and (3) is the energy equation. We complete the above equations with

- the constitutive equations

$$\begin{aligned}\tau_{ij} &= u_{j,k} P_{ki} + C_{ijmn} \varepsilon_{mn} + G_{mni} \gamma_{mn} + \\ &+ F_{mnri} \chi_{mnr} + a_{ij} \sigma + d_{ijk} \sigma_{,k} - \alpha_{ij} \theta, \\ \eta_{ij} &= -\varphi_{jk} Q_{ik} + \varphi_{jk,r} N_{rik} + \\ &+ G_{ijmn} \varepsilon_{mn} + B_{ijmn} \gamma_{mn} + b_{ij} \sigma + \\ &+ D_{ijmnr} \chi_{mnr} + e_{ijk} \sigma_{,k} - \beta_{ij} \theta, \\ \mu_{ijk} &= u_{j,r} N_{irk} + F_{ijkemn} \varepsilon_{mn} + D_{mnijk} \gamma_{mn} + \\ &+ A_{ijkemn} \chi_{mnr} + c_{ijk} \sigma + f_{ijkm} \sigma_{,m} - \delta_{ijk} \theta, \\ h_i &= d_{mni} \varepsilon_{mn} + e_{mni} \gamma_{mn} + \\ &+ f_{mnri} \chi_{mnr} + d_i \sigma - a_i \theta + g_{ij} \sigma_{,j}, \\ g &= -a_{ij} \varepsilon_{ij} - b_{ij} \gamma_{ij} - c_{ijk} \chi_{ijk} - \\ &- \xi \sigma - d_i \sigma_{,i} + m \theta,\end{aligned}$$

$$\begin{aligned}S &= \alpha_{ij} \varepsilon_{ij} + \beta_{ij} \gamma_{ij} + \delta_{ijk} \chi_{ijk} + \\ &+ m \sigma + a_i \sigma_{,i} + a \theta, \\ q_i &= k_{ij} \theta_{,j};\end{aligned}\quad (4)$$

- the kinetic relations

$$\begin{aligned}\varepsilon_{ij} &= \frac{1}{2}(u_{i,j} + u_{j,i}), \gamma_{ij} = u_{j,i} - \varphi_{ij}, \\ \chi_{ijk} &= \varphi_{jk,i}, \theta = T - T_0, \sigma = \varphi - \varphi_0.\end{aligned}\quad (5)$$

In the above equations we have used the following notations: ρ - the constant mass density; S - the specific entropy; T_0 - the constant absolute temperature of the body in its reference state; I_{ij} - coefficients of inertia; κ - the equilibrated inertia; u_i - the components of displacement vector; φ_{jk} - the components of dipolar displacement tensor; φ - the volume distribution function which in the reference state is φ_0 ; σ - the change in volume fraction measured from the reference state; θ - the temperature variation measured from the reference temperature T_0 ; ε_{ij} , γ_{ij} , χ_{ijk} - kinematic characteristics of the strain; τ_{ij} , η_{ij} , μ_{ijk} - the components of the stress tensors; h_i - the components of the equilibrated stress vector; q_i - the components of the heat flux vector; F_i - the components of the body forces; M_{jk} - the

components of the dipolar body forces; r - the heat supply per unit time; g - the intrinsic equilibrated force; L - the extrinsic equilibrated body force; C_{ijmn} , B_{ijmn} , ..., k_{ij} - the characteristic functions of the material, and they obey the symmetry relations

$$\begin{aligned}C_{ijmn} &= C_{mni} = C_{jimn}, B_{ijmn} = B_{mni} \\ a_{ij} &= a_{ji}, d_{ijk} = d_{jik}, g_{ij} = g_{ji} \\ A_{ijkemn} &= A_{mnri}jk, F_{ijkemn} = F_{ijkemn} \\ G_{ijmn} &= G_{ijnm}, k_{ij} = k_{ji}, P_{ij} = P_{ji}.\end{aligned}\quad (6)$$

In (1) and (3) P_{ij} , Q_{ij} and N_{ijk} are prescribed functions which satisfy the following equations

$$(P_{ij} + Q_{ij})_{,j} = 0, N_{ijk,i} + Q_{jk} = 0.$$

The entropy inequality implies

$$k_{ij} \theta_{,i} \theta_{,j} \geq 0. \quad (7)$$

To the system of field equations (1)-(5) we adjoin the following initial conditions

$$\begin{aligned}u_i(x, 0) &= u_i^0(x), \dot{u}_i(x, 0) = u_i^1(x), \\ \varphi_{jk}(x, 0) &= \varphi_{jk}^0(x), \dot{\varphi}_{jk}(x, 0) = \varphi_{jk}^1(x), \\ \theta(x, 0) &= \theta^0(x), \sigma(x, 0) = \sigma^0(x), \\ \dot{\sigma}(x, 0) &= \sigma^1(x), x \in \bar{B},\end{aligned}\quad (8)$$

and the following prescribed boundary conditions

$$\begin{aligned}u_i &= \bar{u}_i \text{ on } \partial B_1 \times I, t_i = \bar{t}_i \text{ on } \partial B_1^c \times I, \\ \varphi_{jk} &= \bar{\varphi}_{jk} \text{ on } \partial B_2 \times I, \mu_{jk} = \bar{\mu}_{jk} \text{ on } \partial B_2^c \times I, \\ \sigma &= \bar{\sigma} \text{ on } \partial B_3 \times I, h = \bar{h} \text{ on } \partial B_3^c \times I, \\ \theta &= \bar{\theta} \text{ on } \partial B_4 \times I, q = \bar{q} \text{ on } \partial B_4^c \times I,\end{aligned}\quad (9)$$

where $t_i \equiv (\tau_{ij} + \eta_{ij})n_j$, $\mu_{jk} \equiv \mu_{ijk}n_i$, $h \equiv h_i n_i$, $q \equiv q_i n_i$, ∂B_1 , ∂B_2 , ∂B_3 and ∂B_4 with respective complements ∂B_1^c , ∂B_2^c , ∂B_3^c and ∂B_4^c are subsets of ∂B , $I = [0, t_0]$, n_i are the components of the unit outward normal

to ∂B , t_0 is some instant that may be infinite, u_i^0 , u_i^1 , φ_{jk}^0 , φ_{jk}^1 , θ^0 , σ^0 , σ^1 , \bar{u}_i , \bar{t}_i , $\bar{\varphi}_{jk}$, $\bar{\mu}_{jk}$, $\bar{\sigma}$, $\bar{\theta}$, \bar{q} and \bar{h} are prescribed functions in their domains.

Introducing (5) and (4) into equations (1), (2) and (3), we obtain the following system of equations

$$\rho \ddot{u}_i = [u_{j,k} P_{ki} - \varphi_{jk} Q_{ik} + \varphi_{jk,r} N_{rik} + (C_{ijmn} + G_{ijmn}) \varepsilon_{mn} + (G_{mni,j} + B_{ijmn}) \gamma_{mn} + (F_{mnrij} + D_{ijmnr}) \chi_{mnr} + (a_{ij} + b_{ij}) \sigma + (d_{ijk} + e_{ijk}) \sigma_{,k} - (\alpha_{ij} + \beta_{ij}) \theta]_{,j} + \rho F_i,$$

$$I_{kr} \ddot{\varphi}_{jr} = (u_{j,r} N_{irk} + F_{ijkmn} \varepsilon_{mn} + D_{mnijk} \gamma_{mn} + A_{ijkmnr} \chi_{mnr} + c_{ijk} \sigma + f_{ijkm} \sigma_{,m} - \delta_{ijk} \theta)_{,i} - \varphi_{ji} Q_{ki} + \varphi_{ji,r} N_{rki} + G_{jkmn} \varepsilon_{mn} + B_{jkmn} \gamma_{mn} + D_{jkmnr} \chi_{mnr} + b_{jk} \sigma + e_{jki} \sigma_{,i} - \beta_{jk} \theta + \rho M_{jk},$$

$$\rho \kappa \ddot{\sigma} = (d_{mni} \varepsilon_{mn} + e_{mni} \gamma_{mn} + f_{mnri} \chi_{mnr} + d_i \sigma + g_{ij} \sigma_{,j} - a_i \theta)_{,i} + \rho L - a_{ij} \varepsilon_{ij} - b_{ij} \gamma_{ij} - c_{ijk} \chi_{ijk} - \xi \sigma - d_i \sigma_{,i} + m \theta, \quad (10)$$

$$a \dot{\theta} = \frac{1}{\rho T_0} (k_{ij} \theta_{,j})_{,i} + \frac{1}{T_0} r - \beta_{ij} \dot{\varepsilon}_{ij} - \alpha_{ij} \dot{\gamma}_{ij} - \delta_{ijk} \dot{\chi}_{ijk} - m \dot{\sigma} - a_i \dot{\sigma}_{,i}. \quad (11)$$

By a solution of the mixed initial boundary value problem of the theory of thermoelasticity of initial stressed bodies with voids in the cylinder $\Omega_0 = B \times [0, t_0)$ we mean an ordered array $(u_i, \varphi_{jk}, \theta, \sigma)$ which satisfies the system (11) for all $(x, t) \in \Omega_0$, the boundary conditions (9) and the initial conditions (8).

3. Main result

We begin this section with the definition of the domain of influence. Next, we establish a domain of influence inequality, which

is a counterpart of the inequality established in [5]. Finally, we shall prove a domain influence theorem in the context of thermoelasticity of initial stressed bodies with voids.

In all what follows we shall use the following assumptions on the material properties

$$i) \quad \rho > 0, I_{ij} > 0, \kappa > 0, T_0 > 0, a > 0;$$

$$ii) \quad C_{ijmn} x_{ij} x_{mn} + 2G_{mnij} x_{ij} y_{mn} + B_{ijmn} y_{ij} y_{mn} + 2F_{mnrij} x_{ij} z_{mnr} + 2D_{ijmnr} y_{ij} z_{mnr} + A_{ijkmnr} z_{ijk} z_{mnr} + P_{ki} x_{jk} x_{ji} - 2Q_{ik} x_{ji} y_{jk} + N_{rik} x_{ji} z_{jkr} + 2a_{ij} x_{ij} \omega + 2b_{ij} y_{ij} \omega + 2c_{ijk} z_{ijk} \omega + 2d_{ijk} x_{ij} w_k + 2e_{ijk} y_{ij} w_k + 2f_{ijkm} z_{ijk} w_m + 2d_i w_i \omega + \xi \omega^2 + g_{ij} w_i w_j \geq \alpha(x_{ij} x_{ij} + y_{ij} y_{ij} + z_{ijk} z_{ijk} + w_i w_i + \omega^2), \quad \forall x_{ij} = x_{ji}, y_{ij}, z_{ijk}, w_i, \omega;$$

$$iii) \quad k_{ij} \xi_i \xi_j \geq \gamma \xi_i \xi_i, \quad \forall \xi_i.$$

These assumptions are in agreement with the usual restrictions imposed in the mechanics of continua. The assumption iii) represent a considerable strengthening of the consequence (7) of the entropy production inequality.

Let $U(x, s)$ be the function defined as

$$U(x, s) = \frac{1}{2} [\rho \dot{u}_i \dot{u}_i + I_{kr} \dot{\varphi}_{jr} \dot{\varphi}_{jk} + \rho \kappa \dot{\sigma}^2 + a \dot{\theta}^2 + C_{ijmn} \varepsilon_{ij} \varepsilon_{mn} + 2G_{ijmn} \varepsilon_{ij} \gamma_{mn} + B_{ijmn} \gamma_{ij} \gamma_{mn} + 2F_{mnrij} \varepsilon_{ij} \chi_{mnr} + 2D_{ijmnr} \gamma_{ij} \chi_{mnr} + A_{ijkmnr} \chi_{ijk} \chi_{mnr} + P_{ki} u_{j,k} u_{j,i} - 2Q_{ik} u_{j,i} \varphi_{jk} + 2a_{ij} \sigma \varepsilon_{ij} + 2N_{rik} u_{j,i} \varphi_{jkr} + 2b_{ij} \sigma \gamma_{ij} + 2c_{ijk} \sigma \chi_{ijk} + 2d_{ijk} \sigma_{,k} \varepsilon_{ij} + 2e_{ijk} \sigma_{,k} \gamma_{ij} + 2d_i \sigma \sigma_{,i} + 2f_{ijkm} \sigma_{,m} \chi_{ijk} + g_{ij} \sigma_{,i} \sigma_{,j} + \xi \sigma^2]. \quad (12)$$

We also define the function $K(x, s)$

$$K(x, s) = \frac{1}{2} [\rho \dot{u}_i \dot{u}_i + I_{kr} \dot{\varphi}_{jr} \dot{\varphi}_{jk} + \rho \kappa \dot{\sigma}^2 + a \dot{\theta}^2 + \varepsilon_{ij} \varepsilon_{ij} + \gamma_{ij} \gamma_{ij} + \chi_{ijk} \chi_{ijk} + \sigma^2 + \sigma_{,i} \sigma_{,i}](x, s). \quad (13)$$

Taking into account the assumptions i) and ii), from (12) and (13) we deduce

$$K(x, s) \leq U(x, s). \quad (14)$$

The next theorem is a necessary step to prove the main result.

Theorem 1. Let $(u_i, \varphi_{jk}, \theta, \sigma)$ be a solution to the system of equations (11) with the initial conditions (8) and the boundary conditions (9). Then for any $R > 0, t > 0$ and $x_0 \in B$, we have that

$$\begin{aligned} & \int_{D(x_0, R)} U(x, t) dV + \frac{1}{T_0} \int_0^t \int_{\Omega} k_{ij} \theta_{,i} \theta_{,j} dV ds + \\ & \leq \int_0^t \int_{\Omega} \rho (F_i \dot{u}_i + M_{jk} \dot{\varphi}_{jk} + L \dot{\sigma}) dV ds + \\ & + \int_0^t \int_{\Omega} \frac{1}{T_0} r \theta dV ds + \int_{\Omega_1} U(x, 0) dV + \\ & + \int_0^t \int_{\partial \Omega} (\bar{t}_i \dot{u}_i + \bar{\mu}_{jk} \dot{\varphi}_{jk} + \bar{h} \dot{\sigma}) dS ds + \\ & + \int_0^t \int_{\partial \Omega} \frac{1}{T_0} \bar{q} \theta dS ds, \end{aligned} \quad (15)$$

where $D(x_0, R) = \{x \in B : |x - x_0| < R\}$, $\partial D(x_0, R) = \{x \in \partial B : |x - x_0| < R\}$ and $\Omega = D[x_0, R + c(t - s)]$, $\Omega_1 = D[x_0, R + ct]$.

Based on the above estimations, we can now prove the main result of our study : the domain of influence theorem.

Let $B(t)$ be the set of points $x \in \bar{B}$ such that:

- (1) $x \in B \Rightarrow u_i^0 \neq 0$ or $u_i^1 \neq 0$ or $\varphi_{jk}^0 \neq 0$ or $\varphi_{jk}^1 \neq 0$ or $\sigma^0 \neq 0$ or $\sigma^1 \neq 0$ or $\theta^0 \neq 0$ or $\exists \tau \in [0, t]$ such that $F_i \neq 0$ or $M_{jk} \neq 0$ or $L \neq 0$ or $r \neq 0$;
- (2) $x \in \partial B_1 \Rightarrow \exists \tau \in [0, t]$ such that $\bar{u}_i \neq 0$,
- (3) $x \in \partial B_1^c \Rightarrow \exists \tau \in [0, t]$ such that $\bar{t}_i \neq 0$,
- (4) $x \in \partial B_2 \Rightarrow \exists \tau \in [0, t]$ such that $\bar{\varphi}_{jk} \neq 0$,
- (5) $x \in \partial B_2^c \Rightarrow \exists \tau \in [0, t]$ such that $\bar{\mu}_{jk} \neq 0$,
- (6) $x \in \partial B_2 \Rightarrow \exists \tau \in [0, t]$ such that $\bar{\sigma} \neq 0$,
- (7) $x \in \partial B_2^c \Rightarrow \exists \tau \in [0, t]$ such that $\bar{h} \neq 0$,

(8) $x \in \partial B_3 \Rightarrow \exists \tau \in [0, t]$ such that $\bar{\theta} \neq 0$,

(9) $x \in \partial B_3^c \Rightarrow \exists \tau \in [0, t]$ such that $\bar{q} \neq 0$.

The domain of influence of the data at instant t is defined as

$$B_t = \{x_0 \in \bar{B} : B(t) \cap \bar{S}(x_0, ct) \neq \emptyset\}, \quad (16)$$

where \emptyset is the empty set.

Theorem 2. Let $(u_i, \varphi_{jk}, \theta, \sigma)$ be a solution to the system of equations (11) with the initial conditions (8) and the boundary conditions (9). Then we have

$$u_i = 0, \varphi_{jk} = 0, \theta = 0, \sigma = 0,$$

on $\{\bar{B} \setminus B_t\} \times [0, t]$.

References

- (1) Carbonaro, B., Russo, R., *J. Elasticity*, 14, p.163, 1984
- (2) Chandrasekharaiah, D.S., *J. Elasticity*, 18, p.173, 1987
- (3) Cowin, S.C., Nunziato, J.W., *J. Elasticity*, 13, p.125, 1983
- (4) Iesan, D., *J. Elasticity*, 15, p.215, 1985
- (5) Ignaczak, J., Carbonaro, B., *J. Thermal Stresses*, 9, p.79, 1986
- (6) Marin, M., *C. R. Acad. Sci. Paris*, t. 231, Serie II b, p.475, 1995
- (7) Marin, M., *Int. J. Engng. Sci.*, 8, p.1229, 1994
- (8) Nunziato, J.W., Cowin, S.C., *Arch. Rat. Mech. Anal.*, 72, p.175, 1979

Session 2A

FRACTURE MECHANICS II

Chair: H. Hasebe

Co-Chair: C. Chaker

**Effects of Specimen Sizes and Cooling Media on the
Thermal Fatigue Crack Growth Behavior due to
Improved Quench Tests**

S. Ishihara, T. Goshima, T. Yoshimoto, and K. Nomura

**Crack Propagation in a Functionally Graded Material
Plate under Thermal Loading**

T. Fujimoto, N. Noda, S. Yasuda

**Interface Thermal Fracture of Ceramic Coatings in a
High Heat Flux Environment**

B. D. Choules, K. Kokini

**Rough Estimation of Extent of a Thermally Fractured
Zone in Hot Rock Masses Induced by Injecting Water
For More Efficient Extraction of Geothermal Energy**

M. Kurashige, M. Furuzumi, and S. Kamijo

**On Some Mixed Problems for a Compound Space,
Containing a Crack, with the Existence of a Stationary
Temperature Field**

V. N. Hakobian

Effects of Specimen Sizes and Cooling Media on the Thermal Fatigue Crack Growth Behavior due to Improved Quench Tests.

S. Ishihara*, T. Goshima*, T. Yoshimoto** and K. Nomura*

*Department of Mechanical Engineering, Toyama University, 3190 Gofuku, Toyama 930, JAPAN.

**Fujikoshi Cooperation, Ishigane, Toyama 930, JAPAN.

In this study, an improved quench testing method for a thermal shock resistance has been proposed. Repeated thermal shock tests were performed on cemented carbides to show the advantages of the new proposed method that enable us to estimate an intrinsic relationship between crack propagation rate and stress intensity factor, and the values of fracture toughness under the repeated thermal shocks. It was successfully shown that the cyclic thermal fatigue crack propagation behavior and fracture toughness values were independent of the specimen heights and the cooling media employed.

Key Words: Fatigue, Thermal Shock, Crack Propagation, Size Effect, Quenching Media, Cemented Carbides, Microstructure

1. Introduction

The quench tests [1]-[2] have been employed to evaluate the thermal shock resistance of the materials. In these tests, the critical temperatures T_c at which bending strengths after thermal shock drop abruptly due to initiations of thermal cracks is used as a scale of thermal shock resistance. The quench test has an advantage of being easily conducted at everywhere, but has a disadvantage of absence of the physical meaning in the parameter T_c . For examples, changes in the specimen sizes, specimen shapes and cooling media yield the different values of T_c , even if the same material would be tested. Therefore, it is impossible to obtain reliable T_c values, and also the quantitative relationship between subcritical crack growth rate and stress intensity factor under the repeated thermal shock tests.

In this study, an improved quench method for thermal shock experiments has been proposed. Repeated thermal shock tests by the new method were performed on cemented carbides to confirm that the cyclic thermal fatigue crack propagation behavior and fracture toughness values are independent of the specimen heights and cooling media with two different coefficient of kinematic viscosity.

2. Specimen and experimental procedures

2.1 SPECIMEN

The material tested was cemented carbides with 8.5 μ m WC grain size. Their chemical compositions are listed in Table 1. As seen from this table, the main compositions are WC, TiC and TaC. The final specimen

shape and dimensions are shown in Fig. 1. Two kinds of specimen, 8x4x25, 16x4x25 were prepared for the tests. All specimens were polished with diamond paste to the mirror-like finish prior to the tests. The mechanical properties after sintering are listed in Table 2. The values of fracture toughness are estimated as 12.7 MPa \sqrt{m} by bridge indentation method.

Table 1 Chemical compositions of the material used.

Wt(%)				
WC	TiC	TaC	NbC	Co
72	8	8	2	10

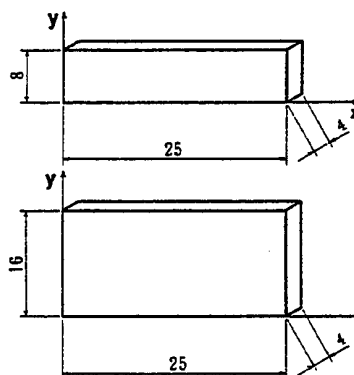


Fig. 1 The shapes and dimensions of the specimens.

Table 2 Mechanical properties of material.

Coefficient of linear expansion	5.34×10^{-6}
Young's modulus (GPa)	527.24
Poisson's modulus	0.222
K_{IC} (MPa $m^{1/2}$)	12.7

2.2 EXPERIMENTAL METHODS

2.2.1. Measurement of temperature distributions. All surfaces of the specimen but the bottoms were coated with a silicon resin to provide them with adiabatic boundary conditions. The surface without coating was planned to contact with the cooling media. The specimens were heated in the furnace at any temperatures for 20 minutes. Then the specimens were dropped down to contact with the cooling media of 293 K, and left at this condition for 5 minutes. Water and silicon oil were used for the cooling media in the present study. Their coefficient of kinematic viscosity are $0.89 \times 10^{-6} \text{ m}^2/\text{s}$ and $5 \times 10^{-6} \text{ m}^2/\text{s}$, respectively.

The repeated thermal shock tests were conducted using a timer-controlled motor that can lift or down the specimen between the furnace and the cooling media, as shown in Fig.2. From the preliminary experiments, temperature variations in the longitudinal and wide direction of the specimen were confirmed as a little. So, we can assume that only one dimensional temperature gradient is yielding in the specimen height. Measurements of temperature gradient along the specimen height were done by using the five Alumel-Chromel thermocouples with 0.2 mm diameter. These were attached to the specimen side at the distances 0, 1, 2, 4 and 8 mm for the 8 mm height specimens, and 0, 1, 2, 4 and 16 mm for the 16 mm height specimens from the cooled surface (bottom of the specimen). Figure 3 indicates these situations. The temperature measurements were done five times at the constant heating temperature. The averaged temperature distributions were used for the calculations of the dynamic thermal stresses induced during the thermal shock test.

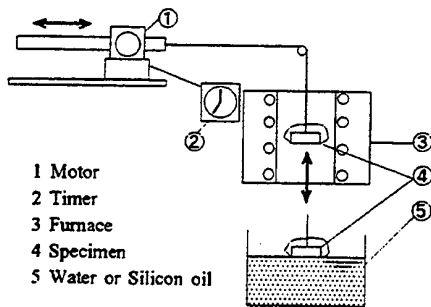


Fig.2 A schematic illustration of the thermal shock testing equipment.

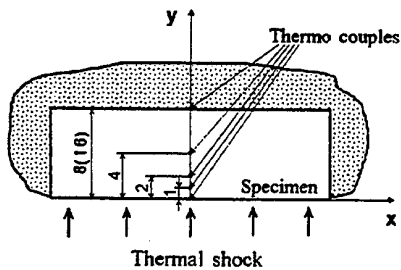


Fig.3 The locations of thermocouples attached to the specimen to measure the temperature distribution in the specimen height during the thermal shock.

2.2.2 Analysis of thermal stresses. When the temperature gradient does not occur in the longitudinal and transverse directions of the specimen but only in the direction of the specimen height, thermal stresses can be evaluated by the following expression [3],

$$\sigma_x(t, y) = -\frac{\alpha E T(t, y)}{1 - \nu} + \frac{1}{2c(1 - \nu)} \int_0^{2c} \alpha E T(t, y) dy + \frac{3y}{2c^3(1 - \nu)} \int_0^{2c} \alpha E T(t, y) y dy \quad (1)$$

where, α , E , ν denote coefficient of linear expansion, Young's modulus and Poisson's ratio of the material, respectively. In addition, $2c$ indicates the specimen height, and T denotes the temperature gradient. In this calculation, the variations of the thermal and mechanical properties with temperature were expected as a little, so the averaged values in the temperature's range were employed for the calculations. The numerical integral method was used for the calculation of the above expression.

2.2.3 Crack growth behavior during the repeated thermal shock test. Pre-crack was introduced at the center of the specimen by the bridge indentation method. Their lengths were ranged from 100 to 150 μm . The specimen surfaces containing the indentation were polished and eliminated about 40 μm to remove the effect of residual stresses induced by the bridging indentation. Crack length during fatigue process was measured by an optical microscope at magnification of 400–1000 by interrupting the test at the specified number of cycles. The relationship between $da/dN - K_{max}$ was obtained from the observed crack growth curve $2a - N$. Newmann-Raju expression [4] for surface crack in bending was employed in the calculation of K_{max} . The crack shapes for the surface cracks were investigated to be $b/a = 0.74$, where b and a denote a crack depth and a half crack length, respectively.

3. Experimental Results

3.1 TEMPERATURE DISTRIBUTION IN THE SPECIMEN DUE TO THERMAL SHOCK

Figure 4 show the temperature distribution in the direction of the specimen height at the elapsed time of 0.5 sec. The data was obtained for the case of heating temperature of 523 K. From Figure 4, a small difference can be seen between 8 and 16 mm height specimens in the temperature distributions, though sudden temperature changes near the cooled specimen surface due to thermal shock are commonly seen for both specimens. On the other hand, the temperature in silicon oil changes more slowly in the direction of specimen height and with time than in water.

3.2 DYNAMIC THERMAL STRESSES

The experimentally obtained temperature distributions were substituted into Equation (1) to calculate the dynamic thermal stresses induced in the specimen at the instance of the thermal shock.

Figure 5 shows the variations of the thermal stresses with the distance from the cooled surface for several elapsed times. This figure indicates the data for heating temperature of 523 K, specimen size 8x4x25 mm. As a cooling media, water was employed. We can see that the maximum thermal stresses always yield at the cooled specimen surface, and they are in tension. These tendencies are common to other experimental conditions.

Figure 6 show the changes of the thermal stresses, σ_{cool} , that yield at the cooled specimen surface as a function of time for the case of the heating temperature of 523 K. We can see that the maximum thermal stresses yield at the elapsed time of 0.5 second for both 8 and 16 mm heights specimens, but the absolute values of the thermal stresses differ with the specimen height, that is, the value for the 16 mm height specimen is 1.3 times larger than that for the 8 mm height specimen. In addition, we can see a different behavior between water and silicon oil in the variations of the thermal stresses. The maximum stresses σ_{max} for water yield at 0.5 sec, and the value is 470 MPa, while for silicon oil, it occurs at 6 sec and the value is 160 MPa. So, we notice that σ_{max} induced at thermal shock for silicon oil is only 0.34 times of those for water, and change very slowly as compared with that for water.

Figure 7 shows the variations of the maximum thermal stresses σ_{max} as a function of the heating temperature T_{max} of the specimen. As seen from this figure, the positive

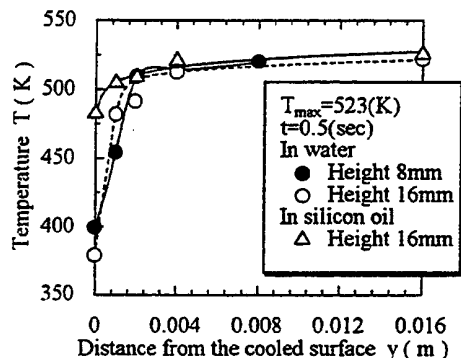


Fig.4 The effects of specimen heights and the cooling media on the temperature distributions in the direction of the specimen height.

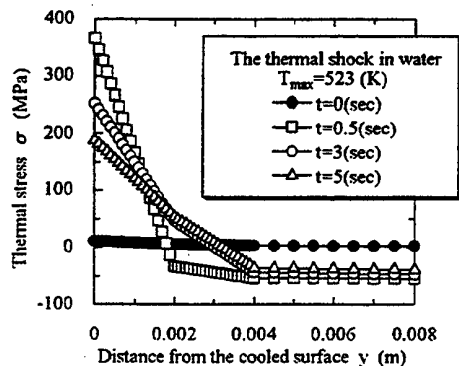


Fig.5 Distributions of the thermal stresses in the specimen induced by the thermal shock near the cooled surface with time.

linear relationships can be seen between σ_{max} and T_{max} . At a constant T_{max} , the maximum thermal stresses for 16 mm height specimen are larger than those for the 8 mm height specimen, though the slopes for both relations are almost same. On the other hand, the slope of the linear relationship in silicon oil is somewhat lower than in water.

3.3 CYCLIC CRACK GROWTH BEHAVIOR IN THE REPEATED THERMAL SHOCK TESTS

Figure 8 shows the relationship between crack growth rate, da/dN and stress intensity factor, K_{max} plotted on logarithmic paper under the repeated thermal shock tests for both 8 and 16 mm height specimens. In the tests, water was used as a cooling media. As seen from this figure, there is linear relationships between da/dN and K_{max} for both specimens, and no differences exist between them. As stated above, since there is no specimen size dependence on the relationships between da/dN and K_{max} , we can realize the effectiveness of the present method to get the crack growth behavior under the repeated thermal shock.

Figure 9 shows the effect of the cooling media on the relationships between da/dN and K_{max} under the repeated thermal shock. In the tests, the specimens with size of 16x4x25 mm were used. As seen from this figure, there is a linear relationship between da/dN and K_{max} on the log-log plot. In addition, the relationships are independent of the cooling media employed. This fact indicates that even if the thermal boundary conditions between the specimen

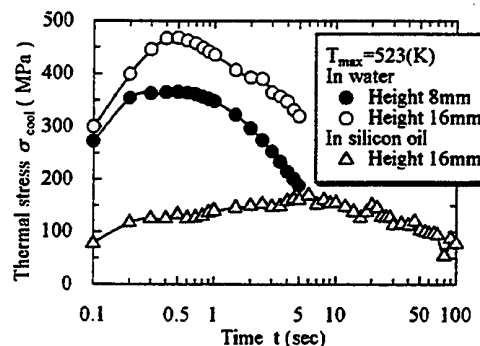


Fig.6 Variations of the thermal stresses σ_{cool} at the cooled specimen's surface with elapsed time.

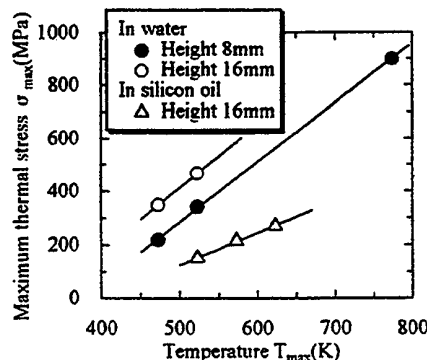


Fig.7 Changes of the maximum dynamic thermal stresses during the thermal shock as a function of the heating temperatures of the specimens.

surface and cooling media would be unexpected, we can evaluate the exact thermal stresses that yield along the cooled specimen surface by using the present method.

By applying the least square method to Fig. 8 and Fig. 9, we get the following intrinsic relationship between da/dN and K_{max} that is independent of the specimen size and the cooling media.

$$da/dN = 2.02 \times 10^{-7} (K_{max} - 3.3)^{1.56} \quad (2)$$

3.4 ESTIMATION OF THERMAL FRACTURE TOUGHNESS UNDER THERMAL SHOCK CONDITION

The heated temperatures of the specimen at which the precracks begin to propagate more than 100 μ m by a single thermal shock were investigated. By substituting these temperatures into Fig. 7, we can calculate the dynamic thermal stresses and evaluate thermal fracture toughness values K_{IC} using Newmann-Raju expression for surface crack in bending. The values of K_{IC} are listed in Table 3. As seen from this Table, the average fracture toughness values are estimated as 10.7 MPam^{1/2} for the

specimens of 8 mm height, and 9.8 MPam^{1/2} for the specimens of 16 mm. Though the value for the former is somewhat higher than for the latter, they are considered to be almost same. But these estimated values are smaller than those by Vickers-indentation method listed in Table 2. One of the reason for this difference is expected to come from oxidization of the specimen under high temperature, but the details of the mechanisms are unclear at the present.

Table 3 The values of fracture toughness obtained by the present method.

(a) Specimen height 8mm			
T_c (K)	σ_{max} (MPa)	$2a$ (μ m)	K_{IC} (MPam ^{1/2})
586	479.14	836	10.98
607	526.39	358.175	7.83
613	539.89	538.175	9.86
685	701.89	710	14.77
699	733.393	306.35	10.1
			Aver. 10.71

(b) Specimen height 16mm			
T_c (K)	σ_{max} (MPa)	$2a$ (μ m)	K_{IC} (MPam ^{1/2})
586	705.2	321.3	9.97
633	861.05	162.8	8.66
648	910.76	230.45	10.9
			Aver. 9.84

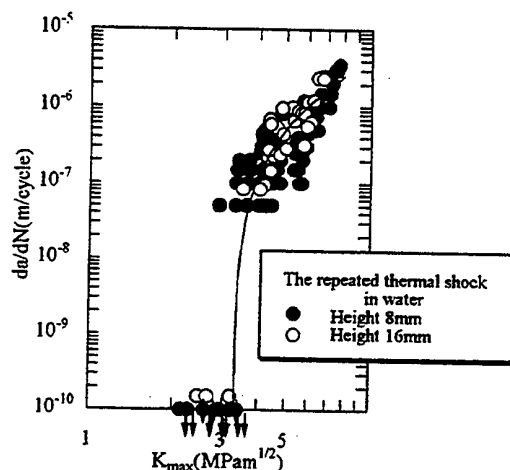


Fig.8 Effect of specimen heights on the relationship da/dN - K_{max} for the repeated thermal shock tests.

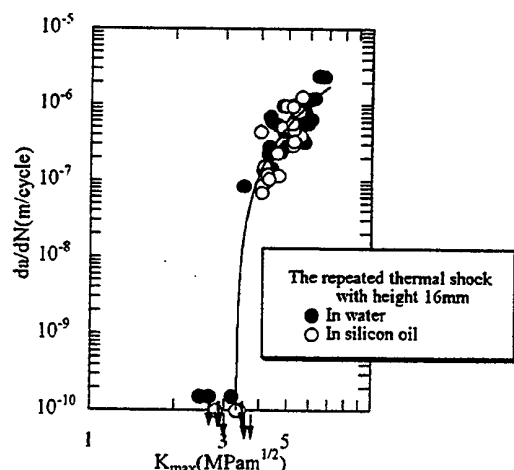


Fig.9 Effect of quenching media on the relationship da/dN - K_{max} for the repeated thermal shock tests.

4. Conclusions

The following results were reached from the present study.

- (1) The relationships between da/dN and stress intensity factor K_{max} and the values of fracture toughness under the repeated thermal shocks were studied using the new testing method. We confirmed that the relationships are independent of specimen sizes and the cooling media employed. The following intrinsic expression, $da/dN = 2.02 \times 10^{-7} (K_{max} - 3.3)^{1.56}$, was obtained for cemented carbides.
- (2) The values of fracture toughness investigated by the present method are independent of specimen sizes, but are lower as compared with those estimated by bridging indentation method. One of the reason for this, an oxidization of the specimen under high temperature environment is expected.

References

- (1) J.P. Singh, Y. tree and D.P.H. Hasselman, "Effect of bath and specimen temperature on the thermal stress resistance of brittle ceramics subjected to thermal quenching", J. Mater. Sci., 16, (1981), 2109-2118.
- (2) S. Ishihara, T. Goshima, K. Miyao, T. Yoshimoto and S. Takehana, "Study on the thermal shock behavior of cermets and cemented carbides", JSME Int. J., Ser. I, 34-316, A(1991), 490-495.
- (3) Y. Takeuti, Analyses of Thermal Stresses, (1989), 13-14, Nisshin.
- (4) J.C. Newman Jr. and I.S. Raju, NASA TP-1578, (1979)

Crack Propagation in a Functionally Graded Material Plate under Thermal Loading

T. Fujimoto, N. Noda, S. Yasuda

Department of Mechanical Engineering, Shizuoka University, 3-5-1, Johoku Hamamatsu Shizuoka 432, JAPAN.

Functionally graded materials (FGMs) have been developed as ultrahigh heat resisting materials in aircraft, space engineering, and nuclear fields. The formation and propagation of cracks in the FGM under severe thermal loading is often unavoidable. The crack path in an FGM plate under thermal loading tends to be straight or curvilinear. It is important to predict how the crack propagates on various conditions. In this paper, by use of mode I, mode II stress intensity factors and the maximum stress criterion, two-dimensional crack propagation in the FGM plate under thermal loading is studied by means of FEM.

Key Words : *Functionally graded materials, Mode I and mode II stress intensity factors, Kinked crack, Curvilinear crack path, Finite element method*

1. Introduction

Functionally graded materials (FGMs) have been developed as ultrahigh heat resisting materials in aircraft, space engineering, and nuclear fields. The application of FGMs in an extreme environment requires strength against thermal and mechanical loading. FGMs are composed of two quite different materials; engineering ceramics and light metal. The former is to resist severe thermal loading in a high temperature environment, and the latter is to maintain the structural rigidity. Thermal stress may produce cracks in FGMs which are subjected to extremely high thermal loading. Thermal stresses in the FGMs are deeply dependent on a composition rate of ceramics/metal and the thermal conditions. A suitable composition rate may prevent fractures. Therefore, it's important to study the FGMs from a view point of the fracture mechanics.

Thermal cracking problems have been investigated by many authors. Jin and Noda [1] investigated the steady thermal stress intensity factor of the functionally graded semi-infinite space with an edge crack subjected to thermal loading. Jin and Batra [2] studied the transient thermal stress intensity factor of functionally graded plate with an edge crack subjected to thermal shock. Thermal stresses may produce the straight or curvilinear crack. Bahr and Weiss et al. [3, 4] studied morphological transitions between single and multiple straight and oscillatory crack propagation in the homogeneous material. Herrmann et al. [5, 6] investigated curvilinear thermal cracks in bimetals or fibrous composites. Hibino et al. [7] experimentally observed the straight and curvilinear crack in functionally graded disk under thermal loading. Gu and Asaro [8] studied kink directions for several specimens which may be used to experimentally study fracture behavior of functionally graded materials.

In this investigation, we study the crack path in the FGM plate how to depend on an initial crack and thermal conditions. The crack propagation in the FGM plate under thermal loading is simulated to predict the crack path. Mode I and mode II thermal stress intensity factors and a fracture angle near a crack tip in the FGM plate are considered. Mode I and mode II stress intensity factors are obtained by solving the thermoelastic problem for plane strain case by means of the FEM. The crack propagation is investigated by use of the maximum stress criterion [9]. The straight and curvilinear crack paths are simulated.

2. Analysis

We consider crack propagation in an FGM plate as shown in Figure 1. The FGM plate is composed of the ceramics (PSZ) and the metal (Ti-6Al-4V). The FGM plate has an initial crack on the ceramics boundary which is subjected to thermal loading. The initial crack is composed of a main crack of length a_1 and a kinked crack of length a_2 . After the main crack propagates directly perpendicular to the surface of FGM plate, the kinked crack occurs with an angle of α_0 due to including impurities, particles, or any other reasons.

The FGM plate is suddenly heated from the initial temperature T_0 to the boundary temperature T_H on the ceramics surface and to the boundary temperature T_L on the metal surface. After the steady state is achieved, the FGM plate is suddenly cooled to the initial temperature T_0 on the both ceramics and metal surface, or is cooled by heat transfer which is characterized by the heat transfer coefficient h and the exterior temperature T_e on the ceramics surface.

The FGM plate with porosity is made by the continuously graded profile of the composition with change from the ceramics (PSZ) to the metal (Ti-6Al-4V). The volumetric ratio of the metal V_m and the porosity P are

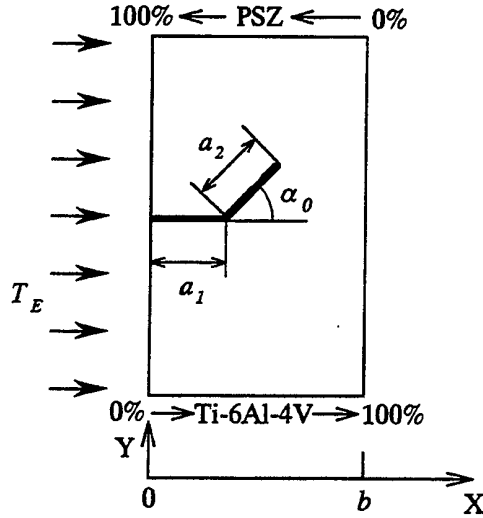


Figure 1 Model of functionally graded material plate with an initial crack

taken as :

$$V_m = \left(\frac{X}{b}\right)^m \quad P = A\left(\frac{X}{b}\right)^n \left[1 - \left(\frac{X}{b}\right)^k\right] \quad (1)$$

where

$$\left(\frac{n+k}{n}\right)^n / \left\{1 - \left(\frac{n}{n+k}\right)^k\right\} \geq A \geq 0$$

and m, n, k are arbitrary constants. b denotes a thickness of the FGM plate. For the material properties of the ceramics and the metal, those of experimental data [10, 11] are used. We apply the material properties of the FGM which expressed [12, 13] as :

$$\lambda = \frac{\lambda_0 \left\{ (1 - P^{2/3}) \lambda_0 + P^{2/3} \lambda_a \right\}}{P^{1/3} \lambda_0 + (1 - P^{1/3}) \left\{ (1 - P^{2/3}) \lambda_0 + P^{2/3} \lambda_a \right\}}$$

$$E = \frac{E_0(1 - P)}{1 + P(5 + \nu_0)(37 - 8\nu_0) / 8(1 + \nu_0)(23 + 8\nu_0)}$$

$$\alpha = \alpha_0 \quad \nu = \nu_0 \quad \rho = \rho_0(1 - P) + \rho_a P$$

$$C = \{C_0 \rho_0(1 - P) + C_a \rho_a P\} \quad (2)$$

where $\lambda, E, \alpha, \nu, \rho$, and C stand for the thermal conductivity, the Young's modulus, the linear thermal expansion coefficient, the Poisson's ratio, the mass density, and the specific heat, respectively, and

$$\lambda_0 = \lambda_c \left\{ 1 + \frac{3(\lambda_m - \lambda_c)V_m}{\{3\lambda_c + (\lambda_m - \lambda_c)(1 - V_m)\}} \right\}$$

$$E_0 = E_c \frac{E_c + (E_m - E_c)V_m^{2/3}}{E_c + (E_m - E_c)(V_m^{2/3} - V_m)}$$

$$\alpha_0 = \frac{\alpha_m V_m E_m / (1 - \nu_m) + \alpha_c (1 - V_m) E_c / (1 - \nu_c)}{V_m E_m / (1 - \nu_m) + (1 - V_m) E_c / (1 - \nu_c)}$$

$$\nu_0 = \nu_m V_m + \nu_c V_c \quad \rho_0 = \rho_m V_m + \rho_c V_c$$

$$C_0 = \frac{C_m \rho_m V_m + C_c \rho_c V_c}{\rho_m V_m + \rho_c V_c} \quad (3)$$

in which subscripts m, c , and a represent the metal, the ceramics, and the air, respectively. We assume that the material properties are independent of temperature.

Coordinate system near the crack tip is given in Figure 2. The angle α_0 represents the initial kink angle. The fracture direction makes the angle θ_c with the axis X' representing a normal direction on the crack tip. The crack tends to propagate in curves with the fracture angle θ_c being taken the positive. It tends to arrange itself to propagate perpendicular to the plate.

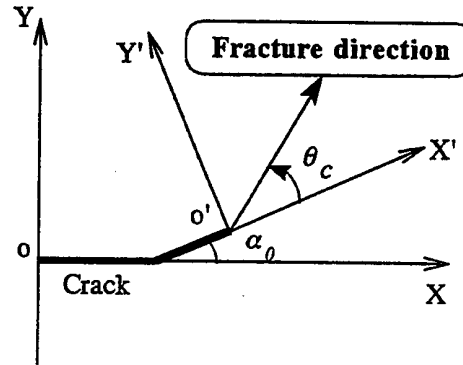


Figure 2 Coordinate systems near the crack tip and the fracture angle θ_c

We use the following criterion [9] for the crack propagation. On the $X'-Y'$ plane, the criteria can be written as follows:

- (a) The crack propagates perpendicular to the direction of greatest tension.

$$K_I \sin \theta + K_{II} (3 \cos \theta - 1) = 0 \quad (4)$$

- (b) The crack propagates when the mixed mode (mode I and mode II) stress intensity factor K exceeds the fracture toughness K_{Ic} .

$$K \left(= \cos \frac{\theta_0}{2} \left[K_I \cos^2 \frac{\theta_0}{2} - \frac{3}{2} K_{II} \sin \theta_0 \right] \right) \geq K_{Ic} \quad (5)$$

where the angle θ_0 stands for the direction along which the hoop stress σ_θ is maximum and the shear stress $\tau_{r\theta}$ is zero on the $X'-Y'$ plane. The fracture toughness K_{Ic} of the FGM plate is dependent on the position as follows :

$$K_{Ic} = V_m K_{cm} + (1 - V_m) K_{cc} \quad (6)$$

where K_{cm} and K_{cc} represent the fracture toughness of metal and ceramics, respectively. The angle θ_0 is found from the mode I and mode II stress intensity factors (K_I, K_{II}) by equation (4). The mixed mode stress intensity

factor K can be obtained from K_I , K_{II} , and θ_0 by equation (5).

Normalized stress intensity factors K^* , K_I^* , and K_{II}^* can be defined as stress intensity factors K , K_I , and K_{II} which are normalized by the fracture toughness K_{Ic} , respectively. Figure 3 shows typical relations among normalized stress intensity factors (K^* , K_I^* , and K_{II}^*), the angle θ_0 and cooling time. The variation of K_I^* is larger than that of K_{II}^* with the cooling time. When K_I^* is in the negative, the crack is closed by a compressive stress. The time when K_{II}^* takes into the positive is later than that of K_I^* . The normalized stress intensity factor of mixed mode K^* and the angle θ_0 are solved from K_I^* and K_{II}^* by equations (3) and (4). It is found by equations (3) and (4) that the angle θ_0 is decided by a ratio of K_I^* to K_{II}^* ; the angle θ_0 takes the positive when K_{II}^* is in the negative. t_f denotes the time when K^* has reached the fracture toughness K_{Ic} . When the cooling time has reached t_f , the crack propagates at the angle θ_0 on the X'-Y' plane. The angle θ_0 can thus be defined as a fracture angle θ_c at that time. One of the most important point to note is that K_{II}^* is in the negative for a while after the cooling. Since K_{II}^* is in the negative at t_f , the fracture angle θ_c takes the positive in Figure 3. Therefore, when K^* has reached the fracture toughness K_{Ic} with K_{II}^* being taken the negative, the crack tends to propagate in curves because the angle θ_c takes the positive.

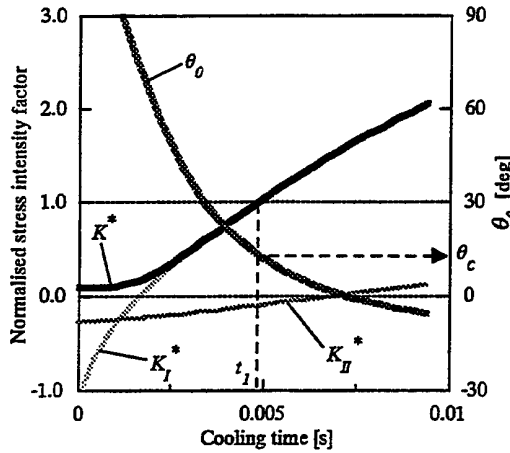


Figure 3 Typical relations between normalized stress intensity factors, the angle θ_0 and cooling time

The procedure for the simulation of crack propagation is shown in Figure 4. The crack extends incrementally as follows. The simulation of crack propagation starts from the initial crack which characterized by the main crack length a_1 , the kinked crack length a_2 , and the kink angle α_0 . The time $t_1^{current}$ when the mixed mode stress intensity factor K reaches the fracture toughness K_{Ic} and the fracture angle θ_c are obtained from the stress intensity factors K_I and K_{II} by the criterion. The current time $t_1^{current}$ when K reaches K_{Ic} is compared with the previous one. If the current time $t_1^{current}$ is later than the previous time $t_1^{previous}$, the crack propagation is stable;

thus the crack propagates along the fracture direction. If the current time $t_1^{current}$ is earlier than the previous time $t_1^{previous}$, the crack propagation is unstable. Therefore, the crack propagates along the normal direction on the crack tip; the fracture angle $\theta_c=0$ is taken.

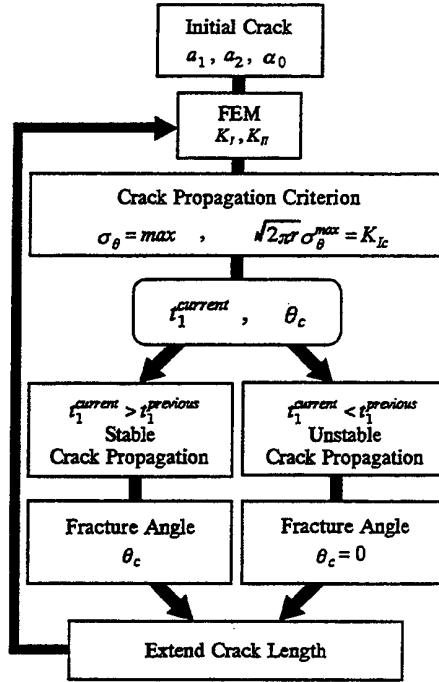


Figure 4 Procedure for the simulation of crack propagation

3. Numerical results

We simulate the crack propagation to predict the crack path which depends on the initial crack, thermal condition, and mechanical condition. The material properties of the ceramics and the metal are applied as follows :

$m = 1.0$	$A = 0.0$
$\lambda_c = 2.036 \text{ [W/mK]}$	$\lambda_m = 18.1 \text{ [W/mK]}$
$E_c = 117 \text{ [GPa]}$	$E_m = 66.2 \text{ [GPa]}$
$\alpha_c = 0.711 \times 10^{-5} \text{ [1/K]}$	$\alpha_m = 0.103 \times 10^{-4} \text{ [1/K]}$
$\nu_c = 0.333$	$\nu_m = 0.321$
$\rho_c = 5.60 \times 10^3 \text{ [kg/m}^3\text{]}$	$\rho_m = 4.42 \times 10^3 \text{ [kg/m}^3\text{]}$
$C_c = 615.6 \text{ [J/kgK]}$	$C_m = 808.3 \text{ [J/kgK]}$

The initial temperature $T_0=300\text{K}$ is taken. The heating temperature on the ceramics boundary $T_H=1300\text{K}$ is decided according to the result [7] that the crack occurred at the cooling process if the ceramics surface was heated to over around 1300K. The heating temperature on the metal boundary T_L is kept at the initial temperature. The ratio of kinked crack and main crack length $a_2/a_1=1/10$

is taken.

The crack path as shown in Figure 5 is simulated on condition that the crack increment takes from 0.05mm to 0.1mm. We selected the fracture toughness of ceramics $K_{Ic}=4.0\text{MPa}\sqrt{\text{m}}$ and that of metal $K_{Ic}=64.0\text{MPa}\sqrt{\text{m}}$ which are widely used. The ceramics boundary is cooled to the initial temperature T_0 . The fracture angle θ_c changes from the positive to the negative while the crack is propagating. Because the crack will still propagate and the fracture angle θ_c will take the negative, it can be predicted that the crack may arrange itself to propagate perpendicular to the FGM plate.

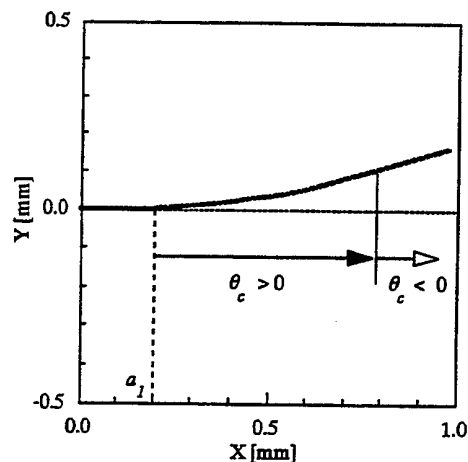


Figure 5 Simulation of crack propagation
($a_1=0.2\text{mm}$, $a_2=0.02\text{mm}$, $\alpha_0=5.0\text{deg}$)

Figure 6 shows a crack path simulated on the condition which differs from that of the previous simulation. The fracture toughness of ceramics $K_{Ic}=1.0\text{MPa}\sqrt{\text{m}}$ and that of metal $K_{Ic}=1.0\text{MPa}\sqrt{\text{m}}$ are used. The surface of ceramics is cooled by heat transfer ($h=1.0\times 10^6\text{W/m}^2\text{K}$, $T_f=300\text{K}$). The crack propagates in curves quite sharply. After the stable crack propagation, the unstable crack propagation occurred. The crack will still grow in around the Y direction by the unstable crack propagation.

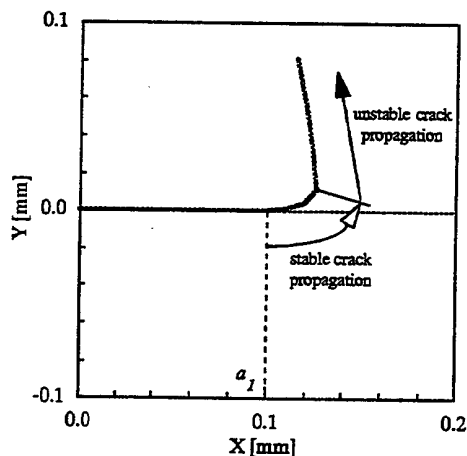


Figure 6 Simulation of crack propagation
($a_1=0.1\text{mm}$, $a_2=0.01\text{mm}$, $\alpha_0=5.0\text{deg}$)

4. Conclusion

In the FGM plate, straight and curvilinear crack paths under thermal loading are simulated by FEM including fracture mechanics. The crack path depends on the initial crack, thermal condition, or mechanical condition. When the mixed mode stress intensity factor reaches the fracture toughness with the mode II stress intensity factor being taken the negative, the crack tends to propagate in curves. On the other hand, when the mixed mode stress intensity factor reaches the fracture toughness with the mode II stress intensity factor being taken the positive, the crack tends to arrange itself to propagate perpendicular to the FGM plate.

References

- [1] Jin, Z. and Noda, N., "Edge crack in a nonhomogeneous half plane under thermal loading", *J. Thermal Stresses*, vol. 17, no. 4, pp. 591-599 (1994)
- [2] Jin, Z. and Batra, R. C., "Stress intensity relaxation at the tip of an edge crack in a functionally graded materials subjected to a thermal shock", *J. Thermal Stresses*, vol. 19, no. 4, pp. 317-339 (1996)
- [3] Bahr, H. -A., Gerbatsch, A., Bahr, U., and Weiss, H. -J., "Pattern selection in thermal cracking", *Proc. 1st Int. Sympo. Thermal Stress '95*, pp. 143-146 (1995)
- [4] Bahr, H. -A., Weiss, H. -J., Maschke, H. G., and Meissner, F., "Multiple crack propagation in a strip caused by thermal shock", *Theor. Appl. Fracture Mec.* 10, pp. 219-226 (1988)
- [5] Herrmann, K. P. and Dong, M., "Thermal crack growth in self-stressed two- and three-dimensional bimaterials", *Proc. 1st Int. Sympo. Thermal Stress '95*, pp. 131-134 (1995)
- [6] Ferber, F. and Herrmann, K. P., "Modelling of elementary failure mechanisms arising in thermomechanically loaded material models", *Proc. 1st Int. Sympo. Thermal Stress '95*, pp. 135-138 (1995)
- [7] Hibino, A., Kawasaki, A., and Watanabe, R., "Evaluation of thermal barrier property of FGM by burner heating test", *4th FGM Sympo.*, pp. 311-314 (1991)
- [8] Gu, P. and Asaro, R. J., "Crack deflection in Functionally graded materials" (1996)
- [9] Erdogan, F. and Sih, G. C., "On the crack extension in plates under plane loading and transverse shear", *Trans. ASME, J. Basic Eng.*, 85, pp. 519-527 (1963)
- [10] Cubberly, W. H., "Metals Handbook", vol. 3, 9th Ed., ASM (1989)
- [11] Touloukian, Y. S., "Thermophysical properties of matter", vol. 1, no. 2, IFI/Plenum (1973)
- [12] Kingery, W. D., Bowen, H. H., and Uhlmann, D. R., "Introduction of ceramics", John Wiley & Sons, New York (1976)
- [13] Kondo, R., "Porous materials", Gihoudo, Tokyo (1986)

Interface Thermal Fracture of Ceramic Coatings in a High Heat Flux Environment

B.D. Choules and K. Kokini

School of Mechanical Engineering, Purdue University, West Lafayette IN, 47907.

The effect of stress relaxation on interface crack formation in a single layer zirconia thermal barrier coating subjected to a high heat flux laser heating, followed by cooling is presented. Two coating thicknesses, 0.66 mm and 1.02 mm, were tested and modeled. A laser power of 200 Watts was used to heat the specimen surface for four seconds. The heating was followed by ambient air cooling. It was found that stress relaxation of the zirconia layer increased the strain energy release rate of an interface crack in the presence of a surface crack. Also, the resulting strain energy release rate was 189% higher in the 1.02 mm coating than the 0.66 mm coating.

Key Words: TBC, Interface Crack, High Heat Flux, Stress Relaxation, Surface Crack

2. Problem Formulation

1. Introduction

Ceramic coatings are being developed as a thermal barrier to high temperature environments such as diesel engines, gas turbines and aircraft engines [1]. Potential benefits include increased power output, improved efficiency and prolonged life of the metallic substrates. A limitation is that ceramic thermal barrier coatings experience thermal fracture which leads to coating spallation and delamination [2]-[4].

Lower heat fluxes and temperatures in diesel engines allow thick multilayer coatings to be used. These coatings made of partially stabilized zirconia (Y_2O_3 - ZrO_2) were found to experience stress relaxation. This resulted in reduction of compressive stresses at high temperature so that subsequent cooling resulted in tensile stresses leading to surface cracks [5]. The high heat fluxes and temperatures in gas turbines and aircraft engines require thin single layer coatings. In the current investigation a 1.5 kW CO_2 laser is used to provide a controlled high heat flux transient loading to single layer plasma sprayed partially stabilized zirconia coatings with thicknesses varying from 0.66 - 1.2 mm. In this paper, the effect of stress relaxation on an interface crack in the presence of a surface crack while subjected to a high heat flux environment is presented.

Steel beam samples coated with plasma sprayed partially stabilized zirconia were heated with a 1.5 kW CO_2 laser for 4 seconds. The samples were then allowed to cool to room temperature. During the ambient air cooling process surface and interface cracks were formed. A schematic of the specimen and experiment is shown in Figure 1. Coatings with two thicknesses were tested ($t_c = 0.66$ mm and 1.02 mm). The bond coat thickness (t_b) was 0.127 mm, the substrate thickness was 1.27 cm and the specimen length (L) was 3.2 cm. Experiments were performed with a laser power of 200 Watts. The laser beam diameter was 10 mm and the distribution is approximately Gaussian. Surface temperatures during the 4 seconds of laser heating, for the cases considered in this paper are shown in Figure 2. They approach 1000-1300°C. The substrate temperature remains near room temperature. Surface and interface cracks were initiated in the 1.02 mm thick coating during cooling after laser heating as shown in Figure 3. When the 0.66 mm thick coating was subjected to the same laser heating and cooling conditions only a surface crack was initiated.

This experiment is modeled as a quasi-steady state, uncoupled thermoelastic problem. The finite element method is used to solve for the transient temperature distributions. The maximum heat flux of the laser at 200 W of power is 2.3 W/mm². The ambient cooling conditions are $h=9$ W/m²K at the surface and $h=5$ W/m²K along the sides and bottom.

The crack faces are assumed to be insulated. The temperature distribution is then used to calculate deformations and thermal stresses in the body under plane stress conditions.

Partially stabilized zirconia has been found to experience time dependent behavior at high temperatures [5]. This time dependent behavior may be stress relaxation, sintering, and or phase changes. For simplicity, the time dependent behavior can be modeled using the following power creep law:

$$\frac{d\epsilon_c}{dt} = A \sigma^n e^{-\Delta H/RT} \quad (1)$$

where

ϵ_c - strain due to stress relaxation

σ - Von Mises equivalent stress

T - temperature

t - time

ΔH - activation energy = 277.3×10^3 (KJ/Kmol)

R - universal gas constant = 8.3143 (KJ/Kmol K)

A - experimental constant = 1.89×10^6 (Pa⁻ⁿ/s)

n - experimental constant = 1.59

The interface crack analyzed in the study is 250 μ m in length. The strain energy release rate (G) of the interface crack is calculated using the crack flank displacement method [6]. The crack flank displacements, (du -shearing and dv -opening), are calculated at a radius of 1 μ m from the crack tip. The temperatures near the interface crack are low enough that the material does not undergo stress relaxation in this region and the linear fracture parameter G may be used.

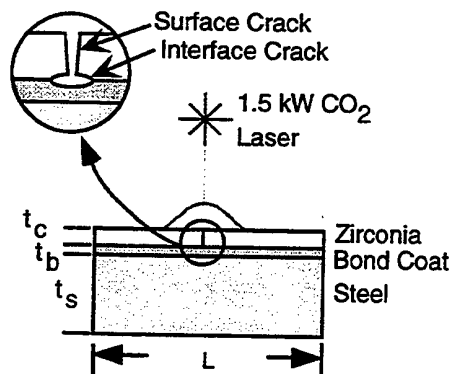


Figure 1. Schematic of specimen and experiment

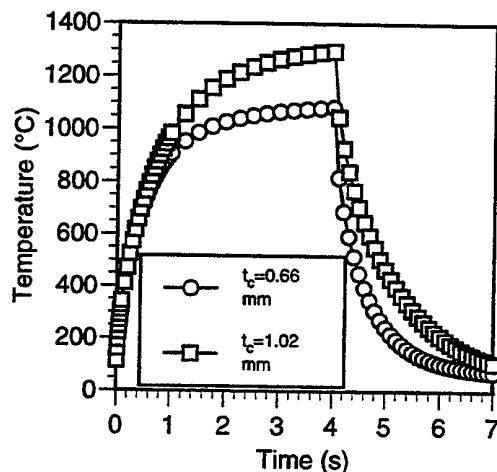


Figure 2. Surface temperature during 200 Watts laser heating followed by ambient cooling

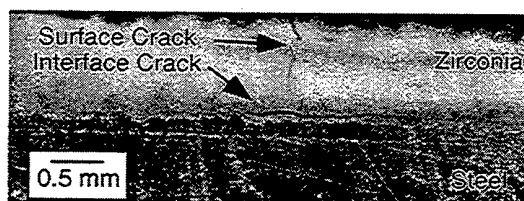


Figure 3. Surface and interface crack in 1.02 mm thick coating as a result of 200 W laser heating

3. Results and Discussion

The effect of stress relaxation on the surface stresses during laser heating and subsequent cooling was determined in the 0.66 mm thick coating *without* a surface crack. The comparison of the stresses when stress relaxation (S. R.) is or not included in the analysis is shown in Figure 4. When stress relaxation is not included, the surface stress remains compressive during the entire thermal cycle. However, when stress relaxation is included, the surface stress after heating is less compressive and becomes tensile upon cooling.

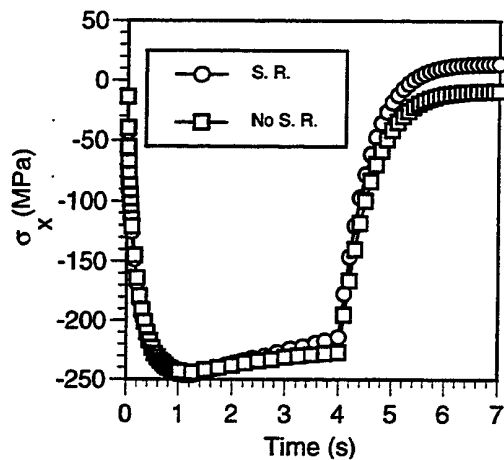


Figure 4. Center surface stress of 0.66 mm coating during laser heating without surface crack

In the case of the 0.66 mm thick specimen with a surface crack that extends to the interface crack, the comparison of the strain energy release rate (G) with and without stress relaxation is shown in Figure 5. As a result of stress relaxation, G of the interface crack is approximately 1.9 J/m^2 while it is approximately zero at 7 seconds. The corresponding crack flank displacements are presented in Figures 6 and 7. Stress relaxation increased du during cooling only $0.005 \text{ }\mu\text{m}$, whereas dv increased $0.018 \text{ }\mu\text{m}$. The tension in the coating resulting from stress relaxation facilitates the opening of the surface crack and the subsequent opening of the interface crack during cooling.

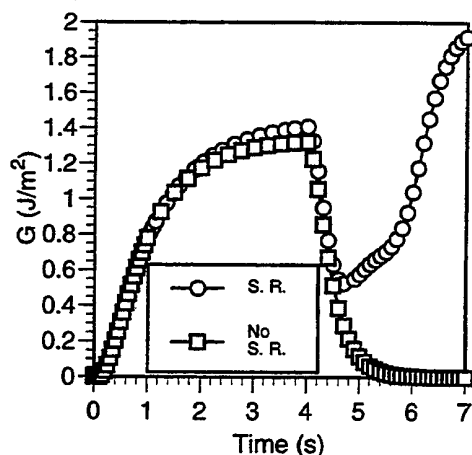


Figure 5. G of interface crack of 0.66 mm coating during laser heating with surface crack

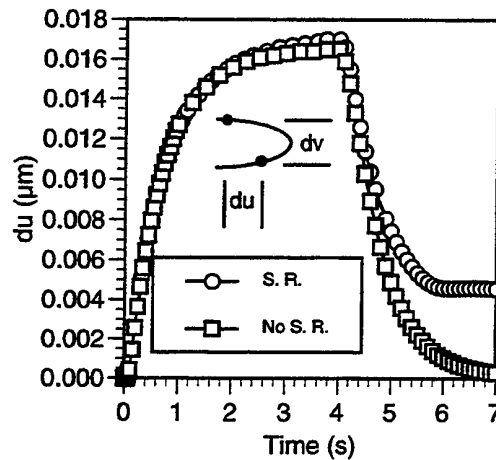


Figure 6. du of interface crack of 0.66 mm coating during laser heating with surface crack

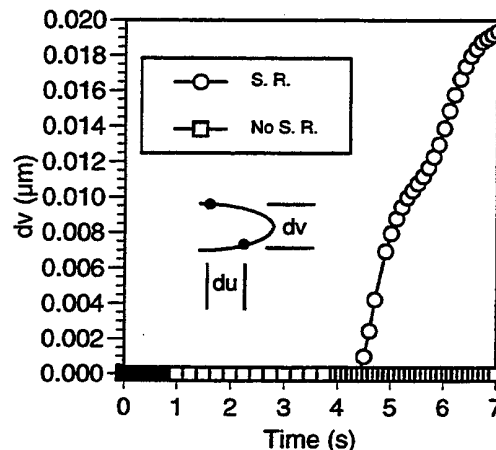


Figure 7. dv of interface crack of 0.66 mm coating during laser heating with surface crack

The strain energy release rate for the 1.02 mm thick coating and the corresponding crack flank displacements are presented in Figures 8-10. The thicker coating results in increased coating temperatures and stresses which increases the amount of stress relaxation. Thus, G of the interface crack increases from 0 J/m^2 to 5.5 J/m^2 at 7 seconds. This is caused by the increased opening and shearing at the interface crack tip. The interface crack of the 1.02 mm coating is subjected to a greater value of G (5.5 J/m^2) than the 0.66 mm coating (1.9 J/m^2). This may explain why in the experiment, the surface and interface cracks initiated in the 1.02 mm coating and only surface cracks initiated in the 0.66 mm coating.

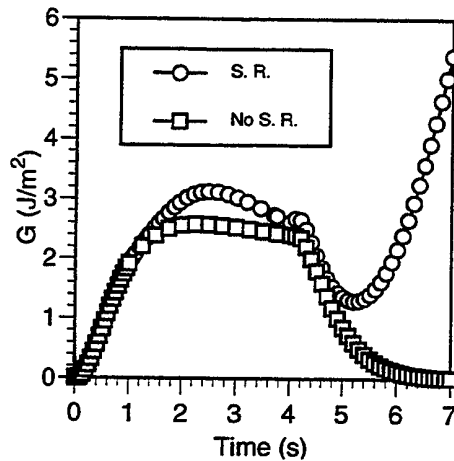


Figure 8. G of interface crack of 1.02 mm coating during laser heating with surface crack

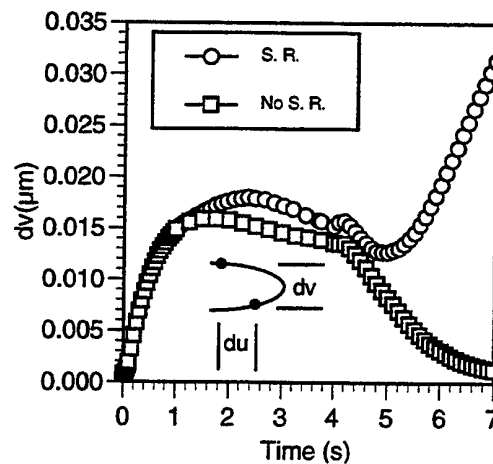


Figure 10. dv of interface crack of 1.02 mm coating during laser heating with surface crack

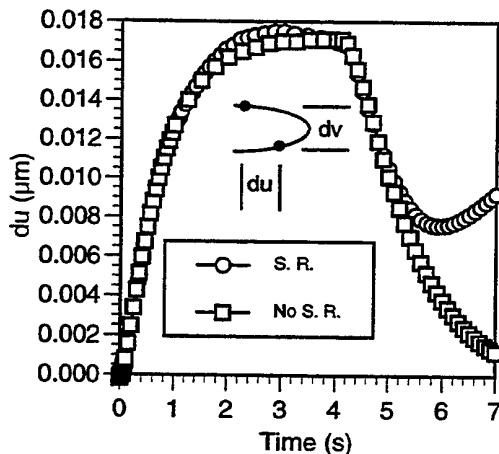


Figure 9. du of interface crack of 1.02 mm coating during laser heating with surface crack

4. Conclusions and Discussion

This analysis and the experiments lead to the following hypothesis: stress relaxation and surface cracking cause interface cracking in zirconia coatings subjected to a high heat flux thermal cycle. The present results are preliminary, and further experiments coupled with analysis are being performed in order to confirm this mechanism of interface cracking.

References

- (1) Brindley, W. (ed.), Workshop on Thermal Barrier Coatings, Proc. NASA Conference, Vol. 3312, 1995.
- (2) Liebert, C.H., and Miller, Robert A., Ceramic Thermal Barrier Coatings, Industrial and Engineering Chemistry Product Research and Development, Vol. 23, p. 344-349, 1984.
- (3) Brindley, W.J., Thermal Barrier Coating Life and Isothermal Oxidation of Low-Pressure Plasma-Sprayed Bond Coat Alloys, Surface and Coatings Technology, Vol. 43/44, p. 446-457, 1990.
- (4) Yonushonis, T.M., Hoag, K.L., Huston, P., Matarese, A. P., Novak, R. C. and Roehling, D. P., Thick Thermal Barrier Coatings for Diesel Engines, Proc. 25th Automotive Tech. Dev. Contractors Coordination Meeting, SAE Publication P2009, 1987.
- (5) Takeuchi, Y.R. and Kokini, K., Thermal Fracture of Multilayer Ceramic Thermal Barrier Coatings, ASME Trans. J. Gas Turbines Power, Vol. 116, p. 266-271, 1994.
- (6) Reynolds, R.R., Kokini, K., and Chen, G., The Mechanics of the Interface Crack using the Finite Element Method, ASME J. Eng. Mat. Tech., Vol. 112, p. 38-43, 1990.

Rough Estimation of Extent of a Thermally Fractured Zone in Hot Rock Masses induced by Injecting Water - For More Efficient Extraction of Geothermal Energy -

M. Kurashige*, M. Furuzumi, and S. Kamijo****

**Department of Mechanical Engineering, Iwate University, Ueda 4-3-5, Morioka 020, JAPAN*

***Department of Civil and Environmental Engineering, Iwate University, Morioka 020, JAPAN*

Rough size estimation has been analytically made of a thermally fractured zone which is induced around the borehole bottom by injecting cold water into a hot rock mass through an insulated inner pipe of the double pipe downhole system. The analysis has been done under spherical symmetry and steady state assumptions for three extreme thermal and mechanical conditions and brought the conclusion that the fractured zone size is about ten times the borehole radius and more if the convection appears within the fractured zone.

Key Words: Thermally Fractured Zone, Hot Rock Mass, Water Injection, Geothermal Energy

1. Introduction

Morita et al. [1] proposed a closed-system coaxial downhole heat exchanger with a thermally insulated inner pipe to extract geothermal energy from a deep thermal reservoir. This simple system has various merits: Among others, it has rather good efficiency in heat extraction from the rock masses because it has a coaxial double pipe system where injected cold water goes down the annulus and heated water up through the thermally insulated inner pipe (reverse circulation).

It is known that, for the deeper formation, the permeability is smaller and the heat conduction is predominant over the heat convection [2]. For the larger heat extraction efficiency, Morita [3] proposed a concept of making a fractured or failed zone around the borehole by thermal stresses: that is, by injecting cold water through the inner pipe before starting operation of this heat extraction system. We can expect strong convective heat transfer within the zone.

However, only a few researchers [4][5] dealt with a feasibility of the fracturing due to thermal stresses in the hot dry rock masses cooled by injecting cold water into a well. One of them [4] analyzed the thermal stresses induced around the borehole to make clear the fracturing mechanism. This analysis adopted the steady-state cylindrically symmetric "one-dimensional (that is, as a function of the radial coordinate only)" temperature field, which depended on the finite radius of outer boundary used instead of infinity in its analytical solution. This unacceptable dependence can be avoided by adopting a spherically symmetric or non-one-dimensional field in an infinite rock mass. (In this connection, we shall deal with the spherically symmetric case.) The other [5] calculated the tangential component of thermal stresses around the borehole and compared this stress with the tensile strength of rock;

they concluded that the fracture induced reaches to a distance of several times the borehole radius or more. They considered only a single fracture in the hot formation but not the fractured zone induced in it.

To the best of our knowledge, there seems to be no report on estimation of the extent or size of the fractured zone induced by thermal stresses. Before calculating the precise size and shape of it under various circumstances, it may be necessary to obtain some rough estimates of them under some "audacious" assumptions for simplicity.

In the present paper, we have sought rough estimates of only a size of the fractured zone induced by thermal stresses. We have used a spherical cavity instead of a semi-infinite cylindrical borehole and assumed complete spherical symmetry of the fields in most part of this paper. The tectonic stresses are also taken as hydrostatic or spherically symmetric. Exceptionally, an effect of the difference of the overburden stress from the horizontal tectonic stresses has been studied. Furthermore, we have considered only the steady state, which may induce the largest extent of the fractured zone.

In estimating the fractured zone extent, we have considered three extreme cases for thermal and mechanical conditions (Sections 6 to 8).

2. Temperature Field

Let us consider a spherically symmetric temperature field in an infinite rock mass with a spherical cavity having radius $r = a$. The cavity wall is cooled by the injected water. The semi-infinite region $r \geq a$ is divided into two regions: $a \leq r < R$ and $R \leq r < \infty$ with R remaining to determine later; the former is the thermally fractured zone with thermal conductivity κ_f , while the latter the non-fractured zone

of conductivity κ . Newton's law of cooling is applied to the boundary $r = a$; the relative heat transfer coefficient is denoted by h . T denotes a difference in rock temperature from the undisturbed rock temperature T_R ; $T_0 = T_w - T_R$ with T_w denoting the temperature of water in the cavity. Note that T and T_0 are negative.

For these boundary conditions, the temperature field is easily obtained in the form of

$$T = \Delta T_0 \left\{ \left(\frac{a}{r} \right) + \Delta \kappa \left(\frac{a}{R} \right) \right\} \text{ for } a \leq r < R, \quad (1-1)$$

$$T = \Delta T_0 (1 + \Delta \kappa) \left(\frac{a}{r} \right) \text{ for } R \leq r < \infty, \quad (1-2)$$

with

$$\Delta T_0 = T_0 / \{ \Delta \mu + \Delta \kappa (a/R) \}, \quad (2)$$

$$\Delta \mu = 1 + 1/(ah), \quad \Delta \kappa = \kappa_f / \kappa - 1,$$

where $\Delta \kappa = 0$ implies that the fracturing has no influence on the thermal conductivity, and ah is the associated Biot number.

3. Thermal Stresses

It is easy to obtain the thermal stresses induced by the temperature change (1). The thermal stresses which vanish at infinity and are accompanied with no tractions at the cavity wall surface are as follows: For the fractured zone ($0 \leq r < R$):

$$\sigma_r = \sigma_\theta = -\frac{E\alpha\Delta T_0}{1-\nu} \left[\frac{2}{3} \Delta \kappa \left(\frac{a}{R} \right) + \frac{1}{2} \left(\frac{a}{r} \right) + \left\{ \frac{1}{2} + \frac{1}{3} \Delta \kappa \left(\frac{a}{R} \right) \right\} \left(\frac{a}{r} \right)^3 \right]$$

$$\sigma_r = \sigma_\theta = -\frac{E\alpha\Delta T_0}{1-\nu} \left[\frac{2}{3} \Delta \kappa \left(\frac{a}{R} \right) + \frac{1}{2} \left(\frac{a}{r} \right) + \left\{ \frac{1}{2} + \frac{1}{3} \Delta \kappa \left(\frac{a}{R} \right) \right\} \left(\frac{a}{r} \right)^3 \right] \quad (3)$$

and for the non-fractured zone ($R \leq r < \infty$):

$$\sigma_r = -\frac{E\alpha\Delta T_0}{1-\nu} \left[(1 + \Delta \kappa) \left(\frac{a}{r} \right) - \left\{ \frac{1}{3} \Delta \kappa \left(\frac{R}{a} \right)^2 + 1 + \frac{2}{3} \Delta \kappa \left(\frac{a}{R} \right) \right\} \left(\frac{a}{r} \right)^3 \right]$$

$$\sigma_\theta = \sigma_r = -\frac{E\alpha\Delta T_0}{1-\nu} \left[\frac{1}{2} (1 + \Delta \kappa) \left(\frac{a}{r} \right) + \left\{ \frac{1}{2} + \frac{1}{3} \Delta \kappa \left(\frac{a}{R} \right) + \frac{1}{6} \Delta \kappa \left(\frac{R}{a} \right)^2 \right\} \left(\frac{a}{r} \right)^3 \right] \quad (4)$$

where E , ν , α are Young's modulus, Poisson's ratio, and the linear thermal expansion coefficient of the rock, respectively. For the case where the fracturing never influences on the thermal conductivity, the thermal stresses can be reduced from Eqs.(3) or (4).

4. Stresses due to Cavity Pressure and Tectonic Stresses

The pressure of injected water acting on the cavity wall, p_0 , and the tectonic stresses, γH , causes the stresses in the rock, which are given by

$$\sigma_r = -p_0 \left(\frac{a}{r} \right)^3 - \gamma H \left\{ 1 - \left(\frac{a}{r} \right)^3 \right\} \quad (5-1)$$

$$\sigma_\theta = \sigma_r = -\frac{1}{2} p_0 - \gamma H \left\{ 1 + \frac{1}{2} \left(\frac{a}{r} \right)^3 \right\} \quad (5-2)$$

where γ is the specific weight of the rock and H the distance of the cavity from the earth surface or the borehole depth.

5. Non-Hydrostatic Tectonic Stresses and Criterion of Failure

There are many cases that the overburden stress is different from the horizontal tectonic stresses, even though the borehole is very deep. We shall assume that the all-round horizontal stress is n times the overburden stress in their magnitude. For such a case, the last terms in Eqs.(5) must be replaced by the solutions borrowed from Lur'e.

For the sake of simplicity, the Mohr-Coulomb criterion shall be used to estimate the fracturing zone size; in addition, we will apply the tensile strength of rock to the region of tensile stress which may be expected to appear near the downhole.

6. Estimation of Fractured Zone Size - Full Loading Capacity Case -

In estimating the fractured zone extent, we have first considered the simplest case under the assumption that the fracturing affects neither on the loading capacity of a fractured rock formation nor on the temperature distribution within the formation; that is, the rock keeps the same elasticity and thermal conductivity as before fracturing and is never invaded into by the water injected.

In this case, $\Delta \kappa = 0$, which makes the symbol R expressing the fractured zone extent in Eqs.(1), (3) and (4) vanish, so that Eq.(1-1) and Eqs.(3) become identical to Eq.(1-2) and Eqs.(4), respectively, as expected. Summing Eqs.(3) with $\Delta \kappa = 0$ for the thermal stresses and Eqs.(5) for the downhole pressure induced stresses and tectonic stresses yields a total stress field in the infinite rock mass with the spherical cavity. Applying them to the failure criteria yields an equation to determine the fractured zone extent $r = R$.

To study an effect of the difference of the overburden stress from the all-around horizontal tectonic stress on the fractured zone size or shape, we here tentatively abandon the assumption of spherical symmetry in the stress field. For that case, Eqs.(5) should be replaced by the Lur'e solutions so that the total stress field depends on the meridian angle ϕ . Consequently, so does the fractured zone extent, that is, $R = R(\phi)$.

7. Estimation of Fractured Zone Size - Null Loading Capacity Case -

Next, as an extreme case, we have studied the case where the fractured zone completely loses its loading capacity and is fully invaded into by the borehole water; besides borehole pressure acting directly on the boundary between the fractured and yet-fractured zones, no more tractions act on that. The fracturing never makes any difference in the temperature also in this case, that is, $\Delta\kappa = 0$.

For this case, the cavity radius a must be replaced by the fractured zone extent R in Eqs.(5) and (3) with $\Delta\kappa = 0$ only when the radius relates to the stress boundary conditions but must not for the temperature field, since the stress boundary conditions are specified at the spherical surface $r = R$. Thus, we obtain the following total stress field:

$$\sigma_r = -p_0 \left(\frac{R}{r} \right)^3 - \gamma H \left[1 - \left(\frac{R}{r} \right)^3 \right] - \frac{E\alpha\Delta T_0}{1-\nu} \left(\frac{a}{R} \right) \left\{ \left(\frac{R}{r} \right) - \left(\frac{R}{r} \right)^3 \right\} \quad (6-1)$$

$$\sigma_\theta = \sigma_\phi = \frac{1}{2} p_0 \left(\frac{R}{r} \right)^3 - \gamma H \left[1 + \frac{1}{2} \left(\frac{R}{r} \right)^3 \right] - \frac{1}{2} \frac{E\alpha\Delta T_0}{1-\nu} \left(\frac{a}{R} \right) \left\{ \left(\frac{R}{r} \right) + \left(\frac{R}{r} \right)^3 \right\} \quad (6-2)$$

where ΔT_0 should be read as $T_0 / \Delta\mu$ since $\Delta\kappa = 0$ now. The procedure similar to that in the previous section may be applied to determine the fractured zone extent $r = R$.

8. Estimation of Fractured Zone Size - Enhanced Conduction Case -

Last, to discuss effects of an expected occurrence of heat convection within the fractured zone on the temperature and stress distributions and the change in a fractured zone size, we have introduced a "venturesome" assumption; we have introduced an appropriate increase in conductivity instead of the heat transfer enhancement caused by the convection within the fractured zone. In other words, we have employed an equivalent thermal conductivity κ_{fe} , which embodies the heat transfer enhancement by the convection within the fractured zone in terms of the enhanced conduction. We now have no knowledge of the equivalent conductivity and the equivalence relations remain to study in future. Here, we have used it as a parameter for a parameter survey; it may be reasonable since we know that the convection enhances the heat transfer so that the equivalent conductivity should be larger than the rock conductivity itself.

The procedure for seeking the fractured zone extent $r = R$ for this case is similar to that mentioned in the above.

9. Numerical Calculations and Discussion

We have carried out some numerical calculations to scrutinize the stress distributions around the cavity and the fractured zone sizes for each case. To obtain the radii of the zone R , the Newton-Raphson scheme is applied to the failure condition.

We have kept the Biot number $ah = 100$ for most cases. Furthermore, we have taken the cavity radius $a = 0.125$ m, the borehole depth $H = 2000$ m, the undisturbed rock temperature $T_R = 300^\circ\text{C}$, and the water temperature $T_w = 15^\circ\text{C}$ for almost all cases. The Young modulus, Poisson's ratio, linear thermal expansion coefficient and the density of the rock have been assumed to be $E = 24.1$ MPa, $\nu = 0.3$, $\alpha = 3 \times 10^{-5}$ 1/K and $\gamma = 25.5$ kN/m³. The shear strength and the coefficient of internal friction for the failure criterion have been specified as $\tau_0 = 24.1$ MPa and $\mu = \tan(66.5^\circ)$, respectively;

Tangential stress distributions together with the fractured zones are shown in Figures 1 and 2 for the full loading capacity case and the null loading capacity case, respectively. From Figure 1 for the full loading capacity case, we can see that the thermal stress contributions predominate over the tectonic stresses; the stresses due to the borehole pressure is very small. In contrast, for the null loading capacity case (Figure 2), the thermal stresses are comparable to the others or a little smaller than the tectonic stresses. The latter case assumes that the fractured zone never carries any internal forces but that the temperature is not affected by the fracturing, so that the thermal stresses are very much relaxed. Note that all stresses vanish in the fractured region in the figure.

The fractured zone sizes R versus the Biot number ah are drawn in Figure 3 for the above mentioned cases for the two well conditions of $H = 2000$ m, $T_w = 300^\circ\text{C}$ and $H = 6000$ m, $T_w = 500^\circ\text{C}$. The size increases as the Biot number does and becomes constant for the large Biot number, as justifies that we have kept the Biot number $ah = 100$ for almost all cases. Although the rock temperature is lower for the less deep well, the size of the fractured zone is larger for the shallower well because of the smaller tectonic stress. Furthermore, we can see from the figure that the full loading capacity case gives the larger size of the fractured zone than the null loading capacity case. This is understood from the thermal stress relaxation explained in the above. Our rough estimates of the fractured zone size are from 1.0 m to 1.3 m for the well with $H = 2000$ m and $a = 0.125$ m. In other words, the fractured zone radius is about ten or more times the borehole radius.

For the above two cases, we have assumed that the temperature field receives no influence from the fracturing. It can be, however, expected that the convection is induced within the fractured zone if the injected water invades into it and that this convection enhances the heat transfer so that the temperature may lower very much.

It may be difficult to take this convection into account in the theoretical analysis. To avoid this difficulty, we have made a "venturesome" assumption; we have introduced an appropriate increase in conductivity instead of the heat transfer enhancement caused by the convection within the fractured zone, so that we have studied the case of $\Delta\kappa \neq 0$.

Figure 4 describes the enlargement of the fractured zone size due to the fictitious improvement of the heat transfer within the fractured zone; the size increases almost linearly with the ratio κ_f/κ ($=1+\Delta\kappa$) of heat conductivity in the fractured zone to that of the yet-fractured zone. The convection within the fractured zone seems to accelerate the heat transfer and fractured zone extension to a great extent.

10. Conclusions

- (1) For the 2000 m or more deep thermal reservoir, the thermal stresses predominate over the tectonic stresses and those due to the hydrostatic pressure in the borehole, if the fracturing affects neither on the loading capacity of a fractured rock formation nor on the temperature distribution within the formation.
- (2) The fractured zone size is estimated from 1.0 m to 1.3 m for the well with the depth $H=2000$ m and the borehole radius $a=0.125$ m. In other words, the fractured zone size is about ten times the borehole radius.
- (3) We can expect that the zone size is larger than ten times the borehole radius, if the fractured zone is formed by water injection and the convection appears within it.

REFERENCES

1. K. Morita, O. Matsubayashi, and K. Kusunoki, Down-Hole Coaxial Heat Exchanger using Insulated Inner Pipe for Maximum Heat Extraction, Geothermal Resources Council, Trans., Vol.9, Part 1, pp.45-50, 1985.
2. Y. Yano, Y. Suda, and S. Tamairi, Data on Boreholes of Thermal Reservoirs in Japan Chisitsu-chousa Report, No.271, 1989.
3. K. Morita, New Method for Extraction of Geothermal Energy - Down-Hole Coaxial Heat Exchanger, Chinetsu, JGEA, Vol.28, No.1, pp.61-78, 1991.
4. H. Hayamizu, H. Kobayashi, and I. Matsunaga, Fracturing of Rock at Elevated Temperature with Borehole Cooling Method, J. Mining Metallurgical Inst. Japan, Vol.93, No.1077, pp.863-868, 1977.
5. Y. Sato, T. Yamaguchi, and M. Kuriyagawa, Stresses around a Well bored in a High Temperature Formation, Proc. Soc. Mining Mat. Processing Inst. Japan, pp.113-114, 1990.

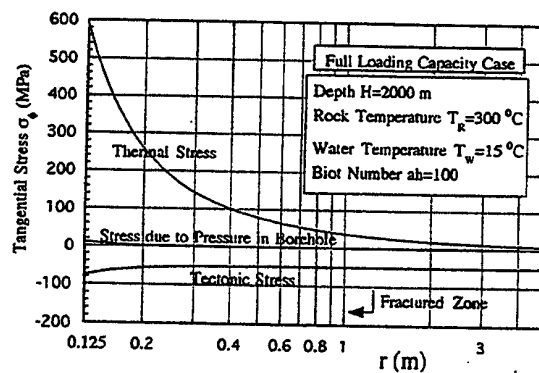


Fig.1 Tangential stresses (Full loading capacity case)

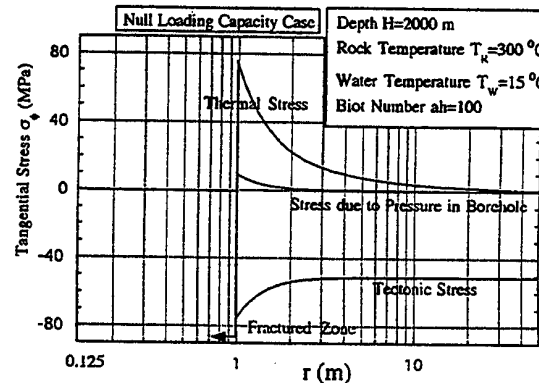


Fig.2 Tangential Stresses (Null loading capacity case)

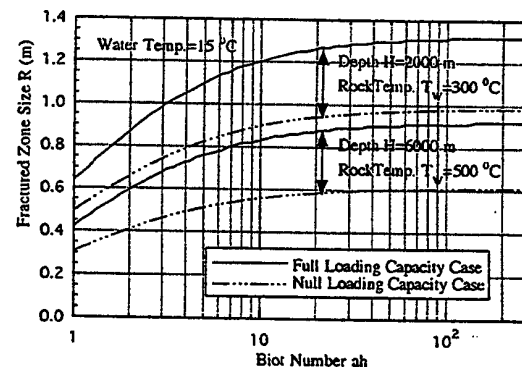


Fig.3 Fractured zone size (Full and null capacity cases)

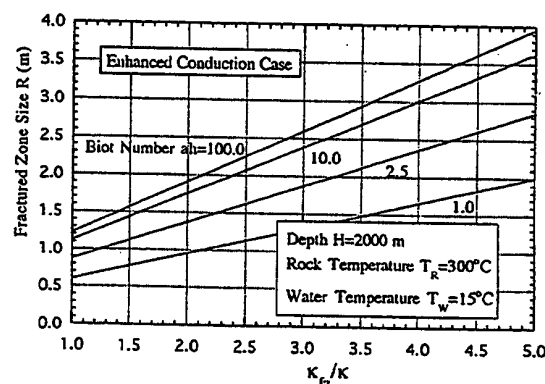


Fig.4 Fractured zone size (Enhanced conduction case)

On Some Mixed Problems for a Compound Space, Containing a Crack, with the Existence of a Stationary Temperature Field.

V.N.Hakobian

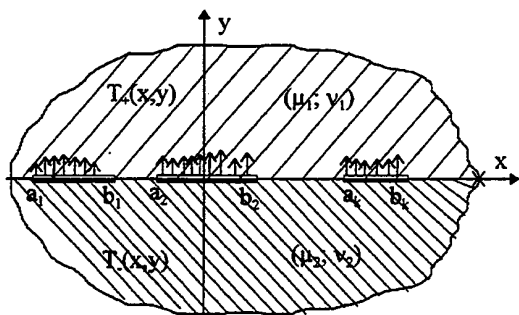
Institute of Mechanics of National Academy of Sciences, 24b, M.Baghramian ave., Yerevan 375019, Armenia

A plane strain state of compound elastic space, situated in a stationary temperature field, which consists of two homogeneous half-spaces, on the joining plane of which the space is weakened by one or several finite cracks, or by a system of periodical cracks, is considered. It is assumed that on one of the banks of all the cracks the components of the elastic displacements and temperatures are given and on the rest of the banks the components of stresses and the heat flow are given.

The problems are finally, formulated in the form of a system of two singular integral equation of the second kind and their closed solutions are built.

Key Words: Elasticity, Mixed Boundary Problem, Crack, Thermal Stress

Let an elastic compound plane situated in a stationary temperature field and consisting of two homogeneous half-planes with different modules of shears μ_1, μ_2 , Poisson's coefficient ν_1, ν_2 and the coefficients of heat extension α_1, α_2 , along the line of the joining line of the half-planes on the intervals (a_k, b_k) ($k=1, 2, \dots, n$) be weakened by cracks on the upper bank of which the stresses components $\chi_1(x) = \sigma_y^{(1)}(x, 0) - i\tau_{xy}^{(1)}(x, 0)$ and the values of heat flows $-\alpha_1 \partial T_+(x, 0) / \partial y = q_1(x)$ are given, and on the lower banks the components of displacements $W_2(x) = u_2(x, 0) + i v_2(x, 0)$ and temperature values $T_-(x, 0) = q_2(x)$ as well as the resultants p_k ($k=1, 2, \dots, n$) of the contact stresses acting there, are given (Pic. 1).



Pic. 1

It is supposed to determine the opening of the crack, the contact stresses acting on the lower banks of the cracks and out of the cracks on the joining line of two half-planes, as well as the intensities factors of these stresses at the end points of the cracks depending on efforts p_k ($k=1, 2, \dots, n$), displacements $W_2(x)$ and the temperature field.

At first we shall cite the solution of the temperature problem. With this aim let's introduce the functions

$$\begin{aligned} T(x) &= T_+(x, 0) - T_-(x, 0) \\ R(x) &= -\alpha_1 \partial T_+(x, 0) / \partial y + \alpha_2 \partial T_-(x, 0) / \partial y, \\ \left(x \in L; \quad L = \bigcup_{k=1}^n (a_k, b_k) \right) \end{aligned}$$

describing the jump of the temperature and the temperature flow on the banks of the cracks for the consideration. Then from the conditions on the banks of the cracks for determining these functions we shall have the following system of singular integral equations of the second kind

$$\begin{aligned} r_1(x) - \frac{\nu^*}{\pi} \int_L \frac{r_2(s)}{s-x} ds &= f_1(x) \\ r_2(x) - \frac{1}{\pi} \int_L \frac{r_1(s)}{s-x} ds &= f_2(x) \\ (x \in L) \end{aligned} \quad (1)$$

where

$$\begin{aligned} r_1(x) &= \alpha_1 T'(x); \quad r_2(x) = R(x); \\ f_1(x) &= \frac{\alpha_1 + \alpha_2}{\alpha_1} q_1(x); \\ f_2(x) &= -(\alpha_1 + \alpha_2) q_2(x); \quad \nu^* = \alpha_2 / \alpha_1 \end{aligned}$$

In this case the system of integral equations (1) should be considered together with the conditions

$$\int_{a_j}^{b_j} r_j(x) dx = 0. \quad (j=1, 2) \quad (2)$$

In order to build a closed solution of the system of integral equations (1), we shall multiply the second of them in $\pm \sqrt{\nu^*}$ and sum with the first one.

As a result, for determining the functions

$$\psi_j(x) = r_1(x) - (-1)^j \sqrt{v^*} r_2(x),$$

we shall get the following two separate singular integral equations

$$\psi_j(x) + \frac{(-1)^j \sqrt{v^*}}{\pi} \int_L \frac{\psi_j(s)}{s-x} ds = R_j(x) \quad (3)$$

$$(j=1,2; x \in L)$$

$$R_j(x) = f_1(x) - (-1)^j \sqrt{v^*} f_2(x),$$

In this case the conditions (2) will have the form

$$\int_{a_k}^{b_k} \psi_j(x) dx = 0; (j=1,2; k=1,2,...,n) \quad (4)$$

We shall notice that after having determined the functions $\psi_j(x)$ ($j=1,2$), it is easy to find the functions $T(x)$ and $R(x)$ by the formulae

$$T(x) = \frac{1}{2\alpha_1} \int_{a_1}^x [\psi_1(x) + \psi_2(x)] dx; (a_k < x < a_{k+1})$$

$$R(x) = \frac{1}{2\sqrt{v^*}} [\psi_1(x) - \psi_2(x)];$$

and determine the distribution of the temperature over the whole surface.

The general solution of the equations (3) is given by the formulae [1]

$$\psi_j(x) = \frac{R_j(x)}{1+v^*} - \frac{(-1)^j \sqrt{v^*} X_j^+(x)}{1+v^*} \times$$

$$\times \left\{ \frac{1}{\pi} \int_L \frac{R_j(s) ds}{X_j^+(s)(s-x)} + P_{n-1}(x) \right\} \quad (5)$$

$$(j=1,2; x \in L)$$

where $X_j^+(x)$ ($j=1,2$) is the value of the piece-wise analytic functions

$$X_j^+(z) = \prod_{k=1}^n (z-a_k)^{-\gamma_k} (z-b_k)^{\gamma_k-1}$$

$$\left(0 < \gamma_j = \frac{1}{2\pi} \arg \left(\frac{1-i(-1)^j \sqrt{v^*}}{1+i(-1)^j \sqrt{v^*}} \right) < 1 \right)$$

on the upper bank of the crack, and $P_{n-1}(x)$ is the polynomial of the degree $(n-1)$ with the unknown coefficients, which are determined from the condition (4).

Now we shall pass to the solution of a thermoelastic problem and we shall consider, that the temperature field is well-known and is equal to $T_+(x, y)$ when $y > 0$ and $T_-(x, y)$ when $y < 0$. Then introducing the functions

$$\chi(x) = [\sigma_y^{(1)}(x, 0) - i\tau_y^{(1)}(x, 0)] - [\sigma_y^{(2)}(x, 0) - i\tau_y^{(2)}(x, 0)]$$

$$W(x) / \theta_2^{(2)} = [u^{(1)}(x, 0) + i v^{(1)}(x, 0)] - [u^{(2)}(x, 0) + i v^{(2)}(x, 0)]$$

describing, correspondingly, the opening of the cracks and the jump of the stresses acting on different banks of the cracks, we come to the following system of determining integral equations:

$$W'(x) + \frac{ia_1}{\pi} \int_L \frac{W'(s)}{s-x} ds + \frac{ia_2}{\pi} \int_L \frac{\chi(s)}{s-x} ds = F_1^+(x)$$

$$\chi(x) - \frac{ib_1}{\pi} \int_L \frac{W'(s)}{s-x} ds + \frac{ib_2}{\pi} \int_L \frac{\chi(s)}{s-x} ds = F_2^+(x) \quad (6)$$

$$(x \in L)$$

which should be considered together with the conditions

$$\int_{a_k}^{b_k} \chi(x) dx = T_k; W(a_k) = W(b_k) = 0 \quad (k=1,2,...,n) \quad (7)$$

where

$$F_j^+(x) = F_j(x) + F_j^T(x); \quad (j=1,2)$$

$$F_1(x) = \frac{\theta_2^{(2)}}{\theta} \left[(\theta_1^{(1)} - \theta_1^{(2)}) \chi_1(x) - l_0 W_2'(x) \right];$$

$$F_2(x) = \frac{2}{\theta} \left[\frac{l_0}{2} \chi_1(x) + (\theta_1^{(2)} ((\theta_2^{(1)})^2 - (\theta_1^{(1)})^2) - \theta_1^{(1)} ((\theta_2^{(2)})^2 - (\theta_1^{(2)})^2)) W_2'(x) \right];$$

$$F_1^T(x) = \frac{\alpha_1 \theta_1^{(1)}}{\mu_1} \left(a_2 + \frac{d_0}{\theta} \right) Q_+(x) + \frac{\alpha_2 \theta_1^{(2)} a_2}{\mu_2} Q_-(x);$$

$$F_2^T(x) = \frac{\alpha_1 \theta_1^{(1)}}{\mu_1} \left(b_2 + \frac{b_0}{\theta} - 1 \right) Q_+(x) + \frac{\alpha_2 \theta_1^{(2)} (b_2 + 1)}{\mu_2} Q_-(x);$$

$$Q_{\pm}(x) = T_{\pm}(x, 0) \pm \frac{1}{i\pi} \int_{-\infty}^{\infty} \frac{T_{\pm}(s, 0)}{s-x} ds;$$

$$a_1 = \frac{\theta_2^{(1)} \theta_1^{(2)}}{\theta}; \quad a_2 = \frac{\theta_2^{(1)} \theta_2^{(2)}}{2\theta};$$

$$b_1 = \frac{2((\theta_2^{(1)})^2 - (\theta_1^{(1)})^2)}{\theta}; \quad b_2 = \frac{\theta_1^{(1)} \theta_2^{(2)}}{\theta};$$

$$\theta_1^{(j)} = \frac{\mu_j}{2 + \alpha_j}; \quad \theta_2^{(j)} = (1 + \alpha_j) \theta_1^{(j)};$$

$$\alpha_j = 1 / (1 - 2\nu_j); \quad d_0 = \frac{1}{2} (\theta_1^{(1)} - \theta_1^{(2)});$$

$$l_0 = \theta_2^{(1)} (\theta_2^{(1)} + \theta_2^{(2)}) - \theta_1^{(1)} (\theta_1^{(1)} - \theta_1^{(2)});$$

$$T_k = \int_{a_k}^{b_k} \chi_1(x) dx - p_k.$$

For the solution of the system of determining integral equations (6) a quadratic equation is considered

$$a_2 \lambda^2 - (a_1 - b_2) \lambda + b_1 = 0 \quad (8)$$

Discriminant of this equation

$$D = \frac{4\mu[\mu(v_1 - v_2)^2 - 4(1 - v_1)(1 - v_2)(3 - 4v_2)]}{[\mu(1 - 2v_1)(1 - 2v_2) + 2(1 - 2v_2)]^2};$$

$$(\mu = \mu_2 / \mu_1)$$

depending on the elastic constants of half-planes can be a zero or different from zero. In Table 1 for various values of Poissons' coefficients v_j ($j=1,2$) some numerical values of the parameter μ , in case of which $D=0$, are reduced:

Table 1.

$v_1 \backslash v_2$	0.1	0.2	0.3	0.4
0.1		633.6	113.4	33.6
0.2	748.8		403.2	67.2
0.3	163.8	492.8		233.2
0.4	62.4	105.6	302.4	

In case, when the discriminant D of this equation is different from zero, the solution of the system of determining integral equations is reduced to the solution of two separate singular integral equations of the second kind with respect to the functions $\varphi_j(x) = \chi(x) + \lambda_j W'(x)$ ($j=1,2$), where λ_j are the roots of the equation (8). These equations have the following form

$$\varphi_j(x) - \frac{q_j}{i\pi} \int_L \frac{\varphi_j(s) ds}{s-x} = Q_j^*(x) \quad (x \in L; j=1,2) \quad (9)$$

with this the conditions (7) obtain the form:

$$\int_{a_k}^{b_k} \varphi_j(x) dx = T_k, \quad (j=1,2; k=1,2,\dots,n) \quad (10)$$

here

$$Q_j^*(x) = Q_j(x) + Q_j^T(x); Q_j(x) = F_2(x) + \lambda_j F_1(x);$$

$$Q_j^T(x) = F_2^T(x) + \lambda_j F_1^T(x);$$

$$q_j = \frac{(a_1 + b_2) - (-1)^j \sqrt{D}}{2};$$

$$\lambda_j = \frac{(a_1 - b_2) - (-1)^j \sqrt{D}}{2a_2}; \quad (j=1,2)$$

and the solutions of the equations (9) are given by the formula [1]

$$\varphi_j(x) = \frac{1}{1-q_j^2} \left\{ \frac{q_j X_j^*(x)}{i\pi} \int_L \frac{Q_j^*(s) ds}{X_j^*(s)(s-x)} + Q_j^*(x) + P_{n-1}(x) X_j^*(x) \right\} \quad (11)$$

$$(x \in L; j=1,2)$$

where $X_j^*(x)$ is the value of the piecewise analytical function

$$X_j(z) = \prod_{k=1}^n (z - a_k)^{-\gamma_k} (z - b_k)^{\gamma_{k-1}};$$

$$\left(\gamma_j = \frac{\ln|g_j|}{2\pi i} + \frac{\theta_j}{2\pi} \right)$$

$$g_j = \frac{1+q_j}{1-q_j}; \quad 0 < \theta_j = \arg(g_j) < 2\pi.$$

On the upper bank of the section L , and $P_{n-1}(x)$ is the polynomial of $(n-1)$ the power with the unknown coefficients, which are determined from the condition (10).

After the determination of the functions $\varphi_j(x)$ it is easy to determine the rest of the important mechanical characteristics.

We shall notice that when $D > 0$

$$\gamma_j = \frac{1}{2} - i\beta_j \quad (\beta_j = \ln|g_j|/2\pi),$$

but in case of $D < 0$

$$\gamma_1 = \alpha - i\beta;$$

$$\gamma_2 = 1 - \alpha - i\beta; \quad (\alpha = \theta_1/2\pi; \beta = \ln|g_1|/2\pi).$$

We shall reduce the values of contact stresses, acting outside the cracks, on the line of the joining line of the half-planes and intensity factor of the stresses at the end points of the cracks with $n=1$ ($a_1 = -a; b_1 = a$), when $D < 0$:

$$\sigma_y^{(j)}(x,0) - i\tau_{xy}^{(j)}(x,0) =$$

$$= \frac{T_0}{a-x} \left[A \left| \frac{a+x}{a-x} \right|^{-\gamma_1} - \bar{A} \left| \frac{a+x}{a-x} \right|^{-\gamma_2} \right] +$$

$$+ \frac{1}{a-x} \left\{ \frac{Aq_1 \left| \frac{a+x}{a-x} \right|^{-\gamma_1}}{i(1-q_1^2) \sin(\pi\gamma_1)} \int_{-a}^a \frac{Q_1^*(s) ds}{\omega_1(s)(s-x)} - \right.$$

$$\left. - \frac{\bar{A}q_2 \left| \frac{a+x}{a-x} \right|^{-\gamma_2}}{i(1-q_2^2) \sin(\pi\gamma_2)} \int_{-a}^a \frac{Q_2^*(s) ds}{\omega_2(s)(s-x)} \right\}$$

$$(|x| > a)$$

$$K_j((-1)^j a) - iK_{jj}((-1)^j a) = (-1)^{j+1} A_j \left[T_1 + \frac{q_j}{i(1-q_j^2)\sin(\pi\gamma_j)} \int_{-a}^a \frac{Q_j^*(s)ds}{\omega_j(s)(s-(-1)^j a)} \right]$$

where

$$\begin{aligned} \omega_j(x) &= (a+x)^{-\gamma_j} (a-x)^{\gamma_j-1}; \quad A_1 = \bar{A}_2 = A \\ A &= \frac{i(l_3 - \lambda_2 l_2)}{\pi(\lambda_1 - \lambda_2)\Delta}; \quad l_2 = \theta_1^{(1)}\theta_2^{(2)} + \theta_2^{(1)}\theta_1^{(2)}; \\ l_3 &= \frac{2}{\theta_2^{(2)}} \left[(\theta_1^{(1)} + \theta_2^{(2)}) (\theta_1^{(1)}\theta_1^{(2)} - \theta_2^{(1)}\theta_2^{(2)}) + \right. \\ &\quad \left. + (\theta_1^{(1)} - \theta_2^{(2)}) (\theta_1^{(1)}\theta_2^{(2)} - \theta_2^{(1)}\theta_1^{(2)}) \right] \\ \Delta &= (\theta_2^{(1)} + \theta_2^{(2)})^2 - (\theta_1^{(1)} - \theta_1^{(2)})^2. \end{aligned}$$

In case, when $D=0$, the equation (8) has two similar roots, $\lambda_1 = \lambda_2 = (a_1 - b_2)/2a_2$. Then we only can obtain the first of the equations (4), where, this time, $q_1 = (a_1 + b_1)/2 > 1$. The solution of this equation is obtained by the first of formulae (11), with this $\gamma_1 = 1/2 - i\beta$. Later, substituting the value of the functions $\chi(x) = \varphi_1(x) + \lambda_1 W'(x)$ into the first of the equations (1) for determining the function $W'(x)$, we shall have exactly the same integral equation, as for the function $\varphi_1(x)$, with the only difference that the right part of this equation will be the following: $a_2 \varphi_1(x)/q_1 + F_1^*(x)$.

Building the solution of this equation in the same way, we shall find the function $W'(x)$, after which the function $\chi(x)$ will be found. The unknown

constants, entering the found functions are discovered with the help of the condition (7).

We shall reduce the formulae, obtained for the function $W'(x)$ in case of one crack:

$$\begin{aligned} W'(x) &= \frac{1}{1-q_1^2} \left\{ F_1^*(x) + \frac{a_2}{q_1(1-q_1^2)} Q_1^*(x) + \right. \\ &\quad \left. + \frac{q_1 \omega_1(x)}{i\pi} \int_{-a}^a \frac{F_1^*(s) + \frac{2a_2}{q_1(1-q_1^2)} Q_1^*(s)}{\omega_1(s)(s-x)} ds \right\} - \\ &\quad - \frac{q_1 a_2}{\pi^2(1-q_1^2)} \int_{-a}^a \frac{Q_1^*(s) \ln \frac{(a-x)(a+s)}{(a+x)(a-s)}}{\omega_1(s)(s-x)} ds + \\ &\quad + \frac{T_1 ch(\pi\beta)}{\pi(1-q_1^2)} \left(1 + \frac{q_1}{i\pi} \ln \frac{(a-x)}{(a+x)} \right) \omega_1(x) \end{aligned}$$

It is obvious from the obtained expressions that when $D=0$ the contact stresses have also a logarithmic singularity besides the power singularity at the points $x = \pm a$.

At the end we shall mention, that during the solution of the problem for a compound plane, containing a periodical system of collinear cracks, the obtained system of determining integral equations is identical with the system (6) and differs from it with Hilbert's kernel, figuring everywhere instead of Cauchy's kernel. Its solution is built in the same way.

Reference

- (1) Muskhelishvili N. Some Basic Problems of Mathematical Theory of Elasticity. "Nauka", M. 1966.

Session 2B

COMPOSITE MATERIALS II

Chair: Y. Shibuya

Co-Chair: Y. W. Kwon

**Thermal Stresses of Laminated Composite Plates
and Shells**

M. R. Eslami, B. Shiari, A. Y. N. Sofla, and H. Eslami

**Three-Dimensional Transient Thermal Stresses of a
Cross-Ply Laminated Rectangular Plate due to Partial
Heating**

Y. Ootao, R. Kawamura, and Y. Tanigawa

**Application of a Simplified Method Expressing Effects of
Anisotropic Ply to Thermal Stress Analysis of CFRP
Cross-Ply Laminates**

Y. Ozawa, K. Sugiura

Thermomechanical Fatigue of Metal Matrix Composites
Zhanjun Gao

**Deformation of Structural Elements from Anisotropic
Composite Materials under Thermal Loading**

L. Gracheva, N. Pankratova

Thermal Stresses of Laminated Composite Plates and Shells

M.R.Eslami*, B.Shiari*, A.Y.N.Sofla*, H.Eslami**

*Department of Mechanical Engineering, Amirkabir University of Technology, P.O.Box 15875-4413, Tehran, Iran

**Embry-Riddle Aeronautical University, Daytona Beach, FL 32114, USA

Accurate three dimensional interlaminar thermal stresses of unsymmetric laminated plates and shells due to uniform temperature rise are presented. Second order layerwise theory of Reddy is considered and applied to the plate while first order layerwise theory is used in shell formulation and the finite element method is used at inplane coordinates. Principle of virtual displacement is applied to derive finite element equations. Numerical examples are presented to show influence of layerwise theory to find interlaminar thermal stresses.

Key Words: Thermal Stresses, Layerwise, Finite Element, Plates and Shells

1. Introduction

In recent years, increasing need for high strength to weight ratios in structural components has led to the use of fiber-reinforced multilayered structures. High-performance composite materials can be used in the form of laminated plates and shells. The problem of interlaminar stresses in laminated plates and shell structures continues to be a popular topic for intensive research. Temperature changes often represent a significant factor, and sometimes the predominant cause of failure of composite structures subjected to harsh working conditions. Delamination and longitudinal cracks in the matrix are typical failure mechanisms in composite thin-walled members due to excessive stress levels caused by thermal stresses. Various first and higher order plates and shell theory are used to determine the interlaminar thermal stresses in laminated plates and shells subjected to thermal loadings [1-4]. These theories are often incapable of determining the three dimensional thermal stress field at ply-level. Thus analysis of thermal stresses may require the use of three dimensional elasticity theory or Layerwise laminate theory. In contrast to the single-layer theories, the Layerwise theory is developed by assuming that the displacement field is only C^0 continuous through the laminate thickness. Owing to the mathematical difficulties encountered in the analytical treatment of three dimensional thermoelasticity analysis of laminated plates and shells, the exact solutions are scarce [5-7]. The layerwise theories can be extended to find three dimensional thermal stress field at layer interfaces [8]. In the present paper three dimensional thermal stresses in laminated plates and shells based on second order layerwise theory of Reddy [9] due to uniform temperature rise are found.

The objective of this study is to investigate the interlaminar thermal stresses within unsymmetric laminated plates and shells. The Lagrangian interpolation function is used through the laminate thickness, and the finite element method is used at inplane coordinates.

2. Theoretical Formulation

Consider an N-layer orthotropic laminated composite, each being oriented arbitrarily with respect to the principal coordinates (α_1, α_2) . The displacements (u, v, w) at a generic point (α_1, α_2, z) in the laminate are assumed to be the form.

$$\begin{aligned} u(\alpha_1, \alpha_2, z) &= \sum_{j=1}^n U^j(\alpha_1, \alpha_2) \phi^j(z) \\ v(\alpha_1, \alpha_2, z) &= \sum_{j=1}^n V^j(\alpha_1, \alpha_2) \phi^j(z) \\ w(\alpha_1, \alpha_2, z) &= \sum_{j=1}^n W^j(\alpha_1, \alpha_2) \psi^j(z) \end{aligned} \quad (1)$$

where (U^j, V^j, W^j) denotes the nodal values of displacement field (u, v, w) , n is the number of nodes through the thickness, ϕ^j and ψ^j are global interpolation functions for discretization of the in-plane displacements through the thickness. For quadratic variation through each numerical layer these functions are given below:

$$\begin{aligned} \phi^1(z) &= \lambda_1^{(1)}(z) & z_1 \leq z \leq z_2 \\ \phi^{2I}(z) &= \lambda_2^{(2)}(z) & z_{2I-1} \leq z \leq z_{2I+1} \\ \phi^{2I+1}(z) &= \begin{cases} \lambda_3^{(I)}(z) & z_{2I-1} \leq z \leq z_{2I+1} \\ \lambda_1^{(I+1)}(z) & z_{2I+1} \leq z \leq z_{2I+3} \end{cases} \\ \phi^N(z) &= \lambda_3^{(N)}(z) & z_{N-2} \leq z \leq z_N \end{aligned}$$

$$\begin{aligned}\lambda_1^{(k)} &= (1 - \frac{\bar{z}}{h_k})(1 - \frac{2\bar{z}}{h_k}) \\ \lambda_2^{(k)} &= 4\frac{\bar{z}}{h_k}(1 - \frac{\bar{z}}{h_k}) \\ \lambda_3^{(k)} &= -\frac{\bar{z}}{h_k}(1 - \frac{2\bar{z}}{h_k})\end{aligned}\quad (2)$$

where $(I = 1, 2, 3, \dots, N_e)$, h_k is the thickness of the k -th layer, $\bar{z} = z - z_b^k$, and z_b^k denotes the z -coordinate of bottom of k -th numerical layer. The stresses in the k -th layer may be computed from the three dimensional stress-strain relation. For a k -th (orthotropic) lamina we have:

$$\begin{bmatrix} \sigma_{11} \\ \sigma_{22} \\ \sigma_{zz} \\ \tau_{22} \\ \tau_{1z} \\ \tau_{12} \end{bmatrix} = \begin{bmatrix} C_{11} & C_{12} & C_{13} & 0 \\ C_{12} & C_{22} & C_{23} & 0 \\ C_{13} & C_{23} & C_{33} & 0 \\ 0 & 0 & 0 & C_{44} \\ 0 & 0 & 0 & C_{45} \\ C_{16} & C_{62} & C_{63} & 0 \end{bmatrix} \begin{bmatrix} \epsilon_1 \\ \epsilon_2 \\ \epsilon_z \\ \gamma_{2z} \\ \gamma_{1z} \\ \gamma_{12} \end{bmatrix} - \begin{bmatrix} \bar{\beta}_{11} \\ \bar{\beta}_{22} \\ \bar{\beta}_{zz} \\ 0 \\ 0 \\ \bar{\beta}_{12} \end{bmatrix} T \quad (3)$$

where $[C_{ij}]_k$ and $[\beta_i]_k$ are trasformed stiffness and thermoelastic matrixes, respectively. The finite element model corresponding to this theory is developed by applying the principal of virtual displacements in absence of body forces to a representative physical element of the plate or shell. From the principle of vitual work:

$$\int_{v^e} [\sigma_{ij} \delta \epsilon_{ij}] dv = \int_{s^e} [T_i \delta u_i] ds \quad (4)$$

where σ_{ij} are the components of the stress tensor, ϵ_{ij} are the components of the strain tensor, T_i are the components of the surface traction. Formulations of plate and shell are completed in following sections.

2.1 PLATE FORMULATION

In plate coordinate (x, y, z) the linear strains associated with the displacement field in equation (1) are:

$$\begin{aligned}\epsilon_{xx} &= \sum_{j=1}^N \frac{\partial U^j}{\partial x} \phi^j \\ \epsilon_{yy} &= \sum_{j=1}^N \frac{\partial V^j}{\partial y} \phi^j \\ \epsilon_{zz} &= \sum_{j=1}^M W^j \frac{d\psi^j}{dz}\end{aligned}\quad (5)$$

$$\begin{aligned}\gamma_{yz} &= \sum_{j=1}^N V^j \frac{d\phi^j}{dz} + \sum_{j=1}^M \frac{\partial W^j}{\partial y} \psi^j \\ \gamma_{xz} &= \sum_{j=1}^N U^j \frac{d\phi^j}{dz} + \sum_{j=1}^M \frac{\partial W^j}{\partial x} \psi^j \\ \gamma_{xy} &= \sum_{j=1}^N (\frac{\partial U^j}{\partial y} + \frac{\partial V^j}{\partial x}) \phi^j\end{aligned}$$

Nodal displacements (U^j, V^j, W^j) in the finite element method solution are approximated by

$$\begin{aligned}U^j &= \sum_{i=1}^n U^{ji} N_i(x, y) \\ V^j &= \sum_{i=1}^n V^{ji} N_i(x, y) \\ W^j &= \sum_{i=1}^n W^{ji} N_i(x, y)\end{aligned}\quad (6)$$

where N_i is the linear shape function through the triangular elements.

2.2 SHELL FORMULATION

In curvilinear coordinate (α_1, α_2, z) , the linear strains associated with the displacement field in equation (1) for a cylidrical shell are:

$$\begin{aligned}\epsilon_{xx} &= \sum_{j=1}^N \frac{\partial U^j}{\partial x} \phi^j \\ \epsilon_{\theta\theta} &= \frac{1}{r(1 + \frac{z}{r})} (\sum_{j=1}^N \frac{\partial V^j}{\partial \theta} \phi^j + \sum_{j=1}^M W^j \psi^j) \\ \epsilon_{zz} &= \sum_{j=1}^M W^j \frac{d\psi^j}{dz} \\ \gamma_{x\theta} &= \sum_{j=1}^N \frac{\partial V^j}{\partial x} \phi^j + \frac{1}{r(1 + \frac{z}{r})} \sum_{j=1}^N \frac{\partial U^j}{\partial \theta} \phi^j \\ \gamma_{\theta z} &= \frac{1}{r(1 + \frac{z}{r})} \sum_{j=1}^N \frac{\partial W^j}{\partial \theta} \psi^j \\ &\quad + r(1 + \frac{z}{r}) \frac{\partial}{\partial z} [\frac{\sum_{j=1}^N V^j \phi^j}{r(1 + \frac{z}{r})}] \\ \gamma_{xz} &= \sum_{j=1}^N \frac{\partial W^j}{\partial x} \psi^j + \sum_{j=1}^N U^j \frac{d\phi^j}{dz}\end{aligned}\quad (7)$$

In order to complete the finite element formulation, the displacement (U^j, V^j, W^j) are approximated on the j th plane of the shell by:

$$\begin{aligned}U^j(\alpha_1, \alpha_2, z) &= \sum_{i=1}^3 U^{ji} N_i(\alpha_1, \alpha_2) \\ V^j(\alpha_1, \alpha_2, z) &= \sum_{i=1}^3 V^{ji} N_i(\alpha_1, \alpha_2)\end{aligned}\quad (8)$$

$$W^j(\alpha_1, \alpha_2, z) = \sum_{i=1}^3 W^{ji} N_i(\alpha_1, \alpha_2)$$

where U^{ji} , V^{ji} and W^{ji} are the displacement components u, v, w at the j th node of the two-dimensional finite element representation the j th plane of physical shell element. The functions $N_i(\alpha_1, \alpha_2)$ are two-dimensional Lagrangian interpolation polynomials associated with the i th node of two dimensional finite elements.

3. Numerical Results

To illustrate some of the thermal effects that occur in layered composite plates and shells, the numerical results will be presented. Typical properties for a graphite fiber/epoxy would be:

$$E_{11} = 180 \text{ GPa}, E_{22} = E_{33} = 10 \text{ GPa}, G_{13} = 7.1 \text{ GPa}, G_{23} = G_{12} = 7.1 \text{ GPa}, \nu_{13} = 0.3, \nu_{12} = \nu_{23} = 0.27, \alpha_{11} = 0.02 \times 10^{-6} \text{ m/}^\circ\text{C}, \alpha_{22} = \alpha_{33} = 22.5 \times 10^{-6} \text{ m/}^\circ\text{C}$$

Consider a crossply (0/90) graphite/epoxy rectangular plate. The boundary conditions are assumed simply supported ($w(x, 0) = w(x, 1) = 0$, $v(x, 0) = 0$). the plate is divided to ten elements in x and y directions and for observing the edge effects, the element sizes near the edges are chosen small. In thickness direction eight numerical layers (or seventeen nodes) are assumed. Figure (1) illustrates the deflection of the plate for 10^3°C temperature increasing. Figure (2) shows the transverse normal interlaminar stresses. It can be seen that the magnitude of transverse stresses become to maximum values near the edges. These high stresses could be cause the delamination. Figures(3) and (4) illustrate the transverse shear stresses. The magnitude of these stresses are increased near the edges of plate.

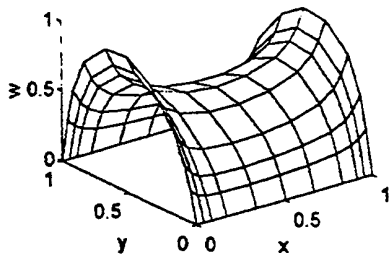


Fig.1.The deflection of crossply (0/90) graphite/epoxy plate.

Considering now a stacking sequence of crossply (0/90/0/90) graphite/epoxy cylindrical shell. The inner diameter and thickness of each layer are assumed 12.7 mm and 0.127 mm, respectively. Figure (5) and (6) show the axial, circumferential and

radial stresses in thickness direction. It can be seen, the interface between the outer 0° and 90° layers experiences a tensile radial stress.

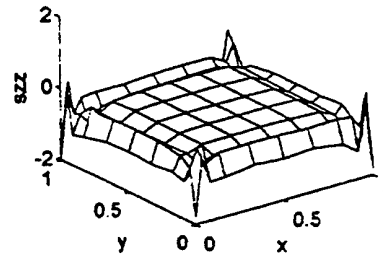


Fig.2.The transverse normal stresses in crossply (0/90) graphite/epoxy plate.

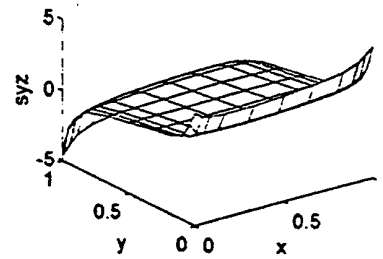


Fig.3.The transverse shear stresses in crossply (0/90) graphite/epoxy plate.

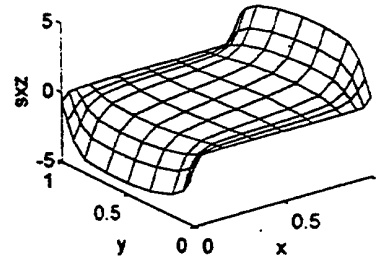


Fig.4.The transverse shear stresses in crossply (0/90) graphite/epoxy plate.

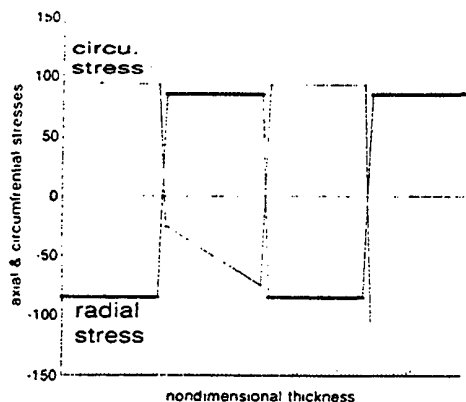


Fig.5.The axial and circumferential stresses in crossply (0/90/90/0) cylinder.

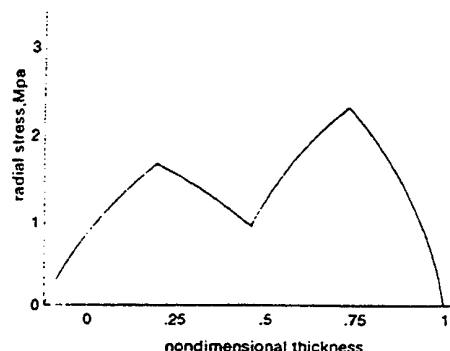


Fig.5.The radial stress in crossply (0/90/90/0) cylinder.

References

- [1] Stavsky, Y., "Thermoelasticity of Heterogeneous Anisotropic Plates", *J. Engng. Mech. Div., ASCE*, Vol. 89, p. 89-105, 1963.
- [2] Nemirovskii, Y.V., "On the Theory of Thermoelastic Bending of Reinforced Shells and Plates", *Mech. Composite Mater.*, Vol. 8, p. 750-759, 1972.
- [3] Wu, C.H. and Tauchert, T.R., "Thermoelastic Analysis of Laminated Plates, Part II: Antisymmetric Cross-ply and Angle-ply Laminates", *J. Thermal Stresses*, Vol. 3, p. 363-378, 1980.
- [4] Noor, A.K. and Burton, W.S., "Computational Models for High-Temperature Multilayered Composite Plates and Shells", *Appl. Mech. Rev.*, Vol. 45, p. 419-446, 1992.
- [5] Huang, N.N., and Tauchert, T.R., "Thermoelastic Solutions for Cross-ply Cylindrical Panels", *J. Thermal Stresses*, Vol. 14, p. 227-257, 1991.

- [6] Thanjitham, S., and Choi, H.J., "Thermal Stresses in a Multilayered Anisotropic Medium", *J. Appl. Mech.*, Vol. 58, p. 1021-1027, 1991.
- [7] Savoia, M., and Reddy, J.N., "Three-Dimensional Thermal Analysis of Laminated Composite Plates", *Int. J. Solid Struct.*, Vol. 32, p. 593-608, 1995.
- [8] Eslami, M.R., Sofla, A.Y.N., and Shiari, B., "Thermal Stresses of Laminated Composite Beams Based on Layerwise Theory", *Proceedings of First Conference of Aerospace Engineering*, Amirkabir University of Technology, 1997.
- [9] Reddy, J.N., and Robbins, D.J., "Theories and Computational Models for Composite Laminates", *Appl. Mech. Rev.*, Vol. 47, p. 147-169, 1994.

Three-Dimensional Transient Thermal Stresses of a Cross-Ply Laminated Rectangular Plate due to Partial Heating

Y. OOTAO*, R. KAWAMURA* and Y. TANIGAWA*

* Department of Mechanical Systems Engineering, Osaka Prefecture University,
1-1, Gakuen-cho, Sakai, 593, JAPAN

In this study, the theoretical analysis of a three-dimensional thermal stress problem is developed for a multilayered anisotropic laminated plate due to partially heat supply in a transient state. As an analytical model, we consider a laminated rectangular plate consisting of an orthogonal pile of layers having orthotropic material properties, i. e. a cross-ply laminate. We obtain the exact solutions for the three-dimensional temperature in a transient state and three-dimensional transient thermal stresses of a simple supported plate. As an example, numerical calculations are carried out for a 3-layered cross-ply laminate, and some numerical results for the temperature change, the displacement and the stress distributions are shown in figures.

Key Words : Elasticity, Thermal Stress, Composite Material, Cross-Ply Laminate, Rectangular Plate, Three-Dimensional Problem, Transient State

1. Introduction

Metal matrix composites have excellent material properties for heat resistance. They have been developed as new material that is adaptable for a high-temperature environment, for example, the structural components of a space-plane or a fusion reactor. It is necessary to take into account not only the effect of steady thermal stress but also effect of unsteady thermal stress. As one of the analytical modeling of the composite materials, the so-called laminated plate can be taken into account. Therefore, we can recognize that study of the thermal stress problems of these laminated plates becomes to be important and there are several analytical papers [1]-[4] concerned with these problems. However these papers restrict to the steady thermal bending problems using plate theory. On the other hand, one of cause of damage in these laminated plates includes delamination. In order to elucidate this phenomenon, the thermal stress analysis that considered the transverse shearing stress and the normal stress in the thickness direction are necessary. However, the study considered these effects are few. So far as we know, Tungikar and Koganti presented the three-dimensional exact solutions for thermal stress problem of simply supported rectangular orthotropic laminate [5]. However this paper restrict to the steady thermal stress problem. In our earlier paper [6], we analyzed the transient thermal stress problem of simply supported cross-ply laminate using the classical plate theory based on Kirchhoff-Love's hypothesis. However this paper didn't take into account the transverse shearing stress and the normal stress in the thickness direction.

From the viewpoint of above mentioned, we

analyzed the three-dimensional thermal stress problem involving a cross-ply laminated rectangular plate due to partially heat supply in the transient state.

2. Analysis

2.1 HEAT CONDUCTION PROBLEM

We consider that the laminated rectangular plate made of n layers as shown in Fig.1, the lengths of the sides and thickness of which are denoted by $2L_x$, $2L_y$, and B , respectively. We assume that each layer is composed of dissimilar plate with orthotropic material properties. And we consider an cross-ply laminate in which principal axis for each layer is parallel to the x or y axis. Throughout the paper, the indices i ($=1, 2, \dots, n$) are associated with i -th layer of laminated plate

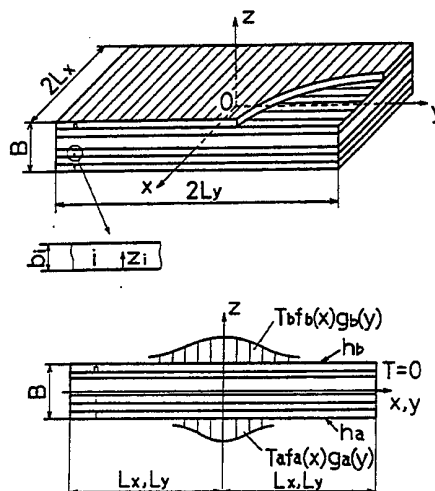


Fig.1 Analytical model and coordinate systems

from the lower side. Let b_i be the thickness of the i -th layer, and the origin of a local coordinate z_i is taken at the bottom side of i -th layer. We assume that the laminated rectangular plate is initially at zero temperature and is suddenly heated partially from the lower and upper surfaces by surrounding media with relative heat transfer coefficients h_a and h_b . We denote the temperature of the surrounding media by the functions $T_a f_a(x)g_a(y)$ and $T_b f_b(x)g_b(y)$, and assume that the end surfaces of the laminated plate are held at zero temperature. The transient heat conduction equation for the i -th layer in dimensionless form is shown as

$$\frac{\partial \bar{T}_i}{\partial \tau} = \bar{\kappa}_x \frac{\partial^2 \bar{T}_i}{\partial \bar{x}^2} + \bar{\kappa}_y \frac{\partial^2 \bar{T}_i}{\partial \bar{y}^2} + \bar{\kappa}_z \frac{\partial^2 \bar{T}_i}{\partial \bar{z}^2}; i=1 \sim n \quad (1)$$

and the initial and thermal boundary conditions in dimensionless form are taken in the following forms:

$$\tau = 0; \bar{T}_i = 0; i=1 \sim n \quad (2)$$

$$\bar{z}_i = 0; \frac{\partial \bar{T}_i}{\partial \bar{z}_i} - H_a \bar{T}_i = -H_a \bar{T}_a f_a(\bar{x})g_a(\bar{y}) \quad (3)$$

$$\bar{z}_i = \bar{b}_i, \bar{z}_{i+1} = 0; \bar{T}_i = \bar{T}_{i+1}; i=1 \sim (n-1) \quad (4)$$

$$\bar{\lambda}_{z_i} \frac{\partial \bar{T}_i}{\partial \bar{z}_i} = \bar{\lambda}_{z_{i+1}} \frac{\partial \bar{T}_{i+1}}{\partial \bar{z}_{i+1}}; i=1 \sim (n-1) \quad (5)$$

$$\bar{z}_n = \bar{b}_n; \frac{\partial \bar{T}_n}{\partial \bar{z}_n} + H_b \bar{T}_n = H_b \bar{T}_b f_b(\bar{x})g_b(\bar{y}) \quad (6)$$

$$\bar{x} = \pm \bar{L}_x; \bar{T}_i = 0 \quad (7)$$

$$\bar{y} = \pm \bar{L}_y; \bar{T}_i = 0 \quad (8)$$

In expressions (1)-(8), we have introduced the following dimensionless values:

$$(\bar{T}_i, \bar{T}_a, \bar{T}_b) = \frac{(T_i, T_a, T_b)}{T_0}, (\bar{L}_x, \bar{L}_y, \bar{b}_i) = \frac{(L_x, L_y, b_i)}{B}$$

$$(\bar{x}, \bar{y}, \bar{z}, \bar{z}_i) = \frac{(x, y, z, z_i)}{B}, \bar{\kappa}_k = \frac{\kappa_k}{\kappa_0}; k=x, y, z$$

$$\bar{\lambda}_{z_i} = \frac{\lambda_{z_i}}{\lambda_0}, \tau = \frac{\kappa_0 t}{B^2}, (H_a, H_b) = (h_a, h_b)B \quad (9)$$

where T_i is temperature change, κ_k ($k=x, y, z$) is thermal diffusivity, λ_{z_i} is thermal conductivity, t is time, and T_0 , κ_0 , and λ_0 are typical values of temperature, thermal diffusivity, and thermal conductivity, respectively. For the sake of brevity, we introduce the following symmetric conditions for the temperature functions $f_a(\bar{x})$, $f_b(\bar{x})$, $g_a(\bar{y})$ and $g_b(\bar{y})$ without loss of generality:

$$f_a(-\bar{x}) = f_a(\bar{x}), f_b(-\bar{x}) = f_b(\bar{x}) \quad (10)$$

$$g_a(-\bar{y}) = g_a(\bar{y}), g_b(-\bar{y}) = g_b(\bar{y})$$

Introducing the finite cosine transformation and Laplace transformation, the solution of equation (1) can be obtained so as to satisfy the conditions (2)-(8).

$$\bar{T}_i = \sum_{k=1}^{\infty} \sum_{l=1}^{\infty} \bar{T}_{kl} \cos q_k \bar{x} \cos s_l \bar{y} \quad (11)$$

where

$$\begin{aligned} \bar{T}_{kl} = & \frac{4}{\bar{L}_x \bar{L}_y} \left[\frac{1}{F} (\bar{A}_i' \cosh \rho_{kl} \bar{z}_i + \bar{B}_i' \sinh \rho_{kl} \bar{z}_i) \right. \\ & + \sum_{j=1}^m \frac{2 \exp(-\mu_j^2 \tau)}{\mu_j \Delta'(\mu_j)} (\bar{A}_i \cosh \beta_{ij} \bar{z}_i + \bar{B}_i \sinh \beta_{ij} \bar{z}_i) \\ & \left. + \sum_{j=m+1}^{\infty} \frac{2 \exp(-\mu_j^2 \tau)}{\mu_j \Delta'(\mu_j)} (\bar{A}_i \cos \gamma_{ij} \bar{z}_i + \bar{B}_i \sin \gamma_{ij} \bar{z}_i) \right] \quad (12) \end{aligned}$$

And in Eqs.(11) and (12), q_k , s_l , ρ_{kl} , β_{ij} , and γ_{ij} are as follows:

$$q_k = \frac{(2k-1)\pi}{2\bar{L}_x}, s_l = \frac{(2l-1)\pi}{2\bar{L}_y}$$

$$\rho_{kl} = \sqrt{(\bar{\kappa}_x q_k^2 + \bar{\kappa}_y s_l^2) / \bar{\kappa}_z}$$

$$\beta_{ij} = -\frac{\mu_j^2 - \bar{\kappa}_x q_k^2 - \bar{\kappa}_y s_l^2}{\bar{\kappa}_z} \quad \text{if } \mu_j^2 / \bar{\kappa}_z - q^2 - s^2 < 0$$

$$\gamma_{ij} = \frac{\mu_j^2 - \bar{\kappa}_x q_k^2 - \bar{\kappa}_y s_l^2}{\bar{\kappa}_z} \quad \text{if } \mu_j^2 / \bar{\kappa}_z - q^2 - s^2 > 0 \quad (13)$$

and μ_j represents the j -th positive roots of the following transcendental equation:

$$\Delta(\mu) = 0 \quad (14)$$

and the condition for the eigenvalue μ_j is given as

$$\mu_1 < \mu_2 < \dots < \mu_m < \sqrt{\bar{\kappa}_x q^2 + \bar{\kappa}_y s^2} < \mu_{m+1} < \dots \quad (15)$$

For the sake of brevity, the detail of the temperature solution is omitted here.

2.2 THERMAL STRESS PROBLEM

In the associated thermoelastic field, we now develop the three-dimensional analysis for transient thermal stresses in simply supported cross-ply laminated rectangular plate. We introduce the following dimensionless values.

$$\begin{aligned} \bar{\sigma}_{kli} &= \frac{\sigma_{kli}}{\alpha_0 E_0 T_0}, (\bar{u}_i, \bar{v}_i, \bar{w}_i) = \frac{(u_i, v_i, w_i)}{\alpha_0 T_0 B} \\ \bar{\alpha}_{ki} &= \frac{\alpha_{ki}}{\alpha_0}, \bar{C}_{ki} = \frac{C_{ki}}{E_0} \end{aligned} \quad (16)$$

where σ_{kli} is the stress components, (u_i, v_i, w_i) are the displacement components, α_{ki} is the coefficient of linear thermal expansion, C_{ki} is the stiffness constant of elasticity, and α_0 and E_0 are the typical values of the coefficient of linear thermal expansion and Young's modulus of elasticity, respectively.

Substituting the stress-strain relations and displacement-strain relations into the equilibrium equations, the displacement equations of equilibrium are written as

$$\begin{aligned} & \bar{C}_{11i} \bar{u}_{i, \bar{x}\bar{x}} + \bar{C}_{66i} \bar{u}_{i, \bar{y}\bar{y}} + \bar{C}_{55i} \bar{u}_{i, \bar{z}\bar{z}} + (\bar{C}_{12i} + \bar{C}_{66i}) \bar{v}_{i, \bar{x}\bar{y}} \\ & + (\bar{C}_{13i} + \bar{C}_{55i}) \bar{w}_{i, \bar{x}\bar{z}} = -(\bar{C}_{11i} \bar{\alpha}_{xi} + \bar{C}_{12i} \bar{\alpha}_{yi} + \bar{C}_{13i} \bar{\alpha}_{zi}) \\ & \times \sum_{k=1}^{\infty} \sum_{l=1}^{\infty} \bar{T}_{kl} q_k \sin q_k \bar{x} \cos s_l \bar{y} \end{aligned} \quad (17)$$

$$\begin{aligned} & (\bar{C}_{66i} + \bar{C}_{12i}) \bar{u}_{i, \bar{x}\bar{y}} + \bar{C}_{66i} \bar{v}_{i, \bar{x}\bar{x}} + \bar{C}_{22i} \bar{v}_{i, \bar{y}\bar{y}} + \bar{C}_{44i} \bar{v}_{i, \bar{z}\bar{z}} \\ & + (\bar{C}_{23i} + \bar{C}_{44i}) \bar{w}_{i, \bar{y}\bar{z}} = -(\bar{C}_{12i} \bar{\alpha}_{xi} + \bar{C}_{22i} \bar{\alpha}_{yi} + \bar{C}_{23i} \bar{\alpha}_{zi}) \end{aligned}$$

$$\times \sum_{k=1}^{\infty} \sum_{l=1}^{\infty} \bar{T}_{kl} s_l \cos q_k \bar{x} \sin s_l \bar{y} \quad (18)$$

$$(\bar{C}_{13i} + \bar{C}_{55i}) \bar{u}_{i, \bar{y}} + (\bar{C}_{44i} + \bar{C}_{23i}) \bar{v}_{i, \bar{y}} + \bar{C}_{55i} \bar{w}_{i, \bar{x}} + \bar{C}_{44i} \bar{w}_{i, \bar{y}} + \bar{C}_{33i} \bar{w}_{i, \bar{z}} = (\bar{C}_{13i} \bar{\alpha}_{xi} + \bar{C}_{23i} \bar{\alpha}_{yi} + \bar{C}_{33i} \bar{\alpha}_{zi})$$

$$\times \sum_{k=1}^{\infty} \sum_{l=1}^{\infty} \bar{T}_{kl} \bar{z} \cos q_k \bar{x} \cos s_l \bar{y} \quad (19)$$

If the lower and upper surfaces are traction free, the the boundary conditions of lower and upper surfaces and the conditions of continuity at the interfaces can be represented as

$$\begin{aligned} \bar{z}_1 &= 0; \quad \bar{\sigma}_{z1} = 0, \quad \bar{\sigma}_{xz1} = 0, \quad \bar{\sigma}_{yz1} = 0 \\ \bar{z}_n &= \bar{b}_n; \quad \bar{\sigma}_{zn} = 0, \quad \bar{\sigma}_{xz n} = 0, \quad \bar{\sigma}_{yz n} = 0 \\ \bar{z}_i &= \bar{b}_i, \quad \bar{z}_{i+1} = 0; \quad \bar{\sigma}_{zi} = \bar{\sigma}_{z, i+1}, \quad \bar{\sigma}_{xi} = \bar{\sigma}_{x, i+1} \\ \bar{\sigma}_{yi} &= \bar{\sigma}_{y, i+1}, \quad \bar{u}_i = \bar{u}_{i+1}, \quad \bar{v}_i = \bar{v}_{i+1}, \quad \bar{w}_i = \bar{w}_{i+1} \quad (20) \end{aligned}$$

We now consider the case of a simply supported plate. The mechanical boundary conditions are given as follows:

$$\begin{aligned} \bar{x} &= \pm \bar{L}_x; \quad \bar{\sigma}_{xz} = 0, \quad \bar{v}_i = 0, \quad \bar{w}_i = 0 \\ \bar{y} &= \pm \bar{L}_y; \quad \bar{\sigma}_{yz} = 0, \quad \bar{u}_i = 0, \quad \bar{w}_i = 0 \quad (21) \end{aligned}$$

The boundary conditions (21) are satisfied automatically if the displacement components are given the following forms:

$$\begin{aligned} \bar{u}_i &= \sum_{k=1}^{\infty} \sum_{l=1}^{\infty} \{U_{ckl}(\bar{z}_i) + U_{pkl}(\bar{z}_i)\} \sin q_k \bar{x} \cos s_l \bar{y} \\ \bar{v}_i &= \sum_{k=1}^{\infty} \sum_{l=1}^{\infty} \{V_{ckl}(\bar{z}_i) + V_{pkl}(\bar{z}_i)\} \cos q_k \bar{x} \sin s_l \bar{y} \\ \bar{w}_i &= \sum_{k=1}^{\infty} \sum_{l=1}^{\infty} \{W_{ckl}(\bar{z}_i) + W_{pkl}(\bar{z}_i)\} \cos q_k \bar{x} \cos s_l \bar{y} \quad (22) \end{aligned}$$

In expressions (22), the first term of right side shows the homogeneous solution of Eqs.(17)-(19) and the second term of right side shows the particular solution of Eqs.(17)-(19). Then $U_{ckl}(\bar{z}_i)$, $V_{ckl}(\bar{z}_i)$, and $W_{ckl}(\bar{z}_i)$ are given by the following expressions:

$$\begin{aligned} U_{ckl}(\bar{z}_i) &= \sum_{J=1}^3 \{F_{klJ} C_{klJ}(\bar{z}_i) + G_{klJ} S_{klJ}(\bar{z}_i)\} \\ V_{ckl}(\bar{z}_i) &= \sum_{J=1}^3 L_{klJ} \{F_{klJ} C_{klJ}(\bar{z}_i) + G_{klJ} S_{klJ}(\bar{z}_i)\} \\ W_{ckl}(\bar{z}_i) &= \sum_{J=1}^3 R_{klJ} \{G_{klJ} C_{klJ}(\bar{z}_i) + \alpha_{klJ} F_{klJ} S_{klJ}(\bar{z}_i)\} \quad (23) \end{aligned}$$

where

$$\begin{aligned} C_{klJ}(\bar{z}_i) &= \cosh(m_{klJ} \bar{z}_i), \quad S_{klJ}(\bar{z}_i) = \sinh(m_{klJ} \bar{z}_i) \\ m_{klJ} &= \sqrt{\gamma_{klJ} + \frac{B^{(ii)}}{3A^{(ii)}}}, \quad \alpha_{klJ} = 1 \text{ if } r_{klJ} + \frac{B^{(ii)}}{3A^{(ii)}} > 0 \\ C_{klJ}(\bar{z}_i) &= \cos(m_{klJ} \bar{z}_i), \quad S_{klJ}(\bar{z}_i) = \sin(m_{klJ} \bar{z}_i) \\ m_{klJ} &= \sqrt{-\left(\gamma_{klJ} + \frac{B^{(ii)}}{3A^{(ii)}}\right)}, \quad \alpha_{klJ} = -1 \text{ if } r_{klJ} + \frac{B^{(ii)}}{3A^{(ii)}} < 0 \quad (24) \end{aligned}$$

$$r_{klJ} = 2\sqrt{-\frac{d_i}{3}} \cos \left[\frac{\phi_i + 2(J-1)\pi}{3} \right]; \quad J=1,2,3$$

$$\phi_i = \cos^{-1} \left[\frac{-f_i \sqrt{27}}{2(-d_i)^{3/2}} \right], \quad d_i = - \left[\frac{3C^{(ii)} A^{(ii)} + (B^{(ii)})^2}{3(A^{(ii)})^2} \right]$$

$$f_i = - \left[\frac{2(B^{(ii)})^3 + 9A^{(ii)} B^{(ii)} C^{(ii)} + 27D^{(ii)} (A^{(ii)})^2}{27(A^{(ii)})^3} \right]$$

$$\begin{aligned} A^{(ii)} &= \bar{C}_{33i} \bar{C}_{44i} \bar{C}_{55i} \\ B^{(ii)} &= q_k^2 \{ \bar{C}_{44i} (\bar{C}_{11i} \bar{C}_{33i} - \bar{C}_{13i}^2) + \bar{C}_{55i} (\bar{C}_{33i} \bar{C}_{66i} - 2\bar{C}_{13i} \bar{C}_{44i}) \} \\ &\quad + s_l^2 \{ \bar{C}_{55i} (\bar{C}_{22i} \bar{C}_{33i} - \bar{C}_{23i}^2) + \bar{C}_{44i} (\bar{C}_{33i} \bar{C}_{66i} - 2\bar{C}_{23i} \bar{C}_{55i}) \} \\ \bar{C}^{(ii)} &= -q_k^4 \{ \bar{C}_{66i} (\bar{C}_{11i} \bar{C}_{33i} - \bar{C}_{13i}^2) + \bar{C}_{55i} (\bar{C}_{11i} \bar{C}_{44i} - 2\bar{C}_{13i} \bar{C}_{66i}) \} \\ &\quad + q_k^2 s_l^2 \{ -\bar{C}_{11i} (\bar{C}_{22i} \bar{C}_{33i} - \bar{C}_{23i}^2) - 2(\bar{C}_{12i} + \bar{C}_{66i})(\bar{C}_{13i} + \bar{C}_{55i}) \\ &\quad \times (\bar{C}_{23i} + \bar{C}_{44i}) - 2\bar{C}_{44i} \bar{C}_{55i} \bar{C}_{66i} + 2\bar{C}_{11i} \bar{C}_{23i} \bar{C}_{44i} \\ &\quad + \bar{C}_{12i} \bar{C}_{33i} (\bar{C}_{12i} + 2\bar{C}_{66i}) + \bar{C}_{13i} \bar{C}_{22i} (\bar{C}_{13i} + 2\bar{C}_{55i}) \} \\ &\quad - s_l^4 \{ \bar{C}_{66i} (\bar{C}_{22i} \bar{C}_{33i} - \bar{C}_{23i}^2) + \bar{C}_{44i} (\bar{C}_{22i} \bar{C}_{55i} - 2\bar{C}_{23i} \bar{C}_{66i}) \} \\ D^{(ii)} &= q_k^6 \bar{C}_{11i} \bar{C}_{55i} \bar{C}_{66i} + q_k^4 s_l^2 \{ \bar{C}_{55i} (\bar{C}_{11i} \bar{C}_{22i} - \bar{C}_{12i}^2) \\ &\quad + \bar{C}_{66i} (\bar{C}_{11i} \bar{C}_{44i} - 2\bar{C}_{12i} \bar{C}_{55i}) \} + q_k^2 s_l^4 \{ \bar{C}_{44i} (\bar{C}_{11i} \bar{C}_{22i} - \bar{C}_{12i}^2) \\ &\quad + \bar{C}_{66i} (\bar{C}_{22i} \bar{C}_{55i} - 2\bar{C}_{12i} \bar{C}_{44i}) \} + s_l^6 \bar{C}_{22i} \bar{C}_{44i} \bar{C}_{66i} \quad (25) \end{aligned}$$

Substituting Eqs.(22) and (23) into the displacement-strain relations and the stress-strain relations, the stress components are obtained. In Eq.(23), F_{klJ} and G_{klJ} ($i=1 \sim n$, $J=1,2,3$) are unknown constants, which should be determined from mechanical conditions (20).

3. Numerical results

As an illustration of numerical calculations, we assume that each layer of laminated plate consists of the same orthotropic plate, and consider the three-layered ($0^\circ/90^\circ/0^\circ$) cross-ply laminated plate composed from alumina (Al_2O_3) fiber reinforced aluminum composite. And, numerical results are presented for the following values.

$$H_a = H_b = 5.0, \quad \bar{T}_a = 0, \quad \bar{T}_b = 1.0, \quad \bar{L}_x = \bar{L}_y = 3.0$$

$$f_b(\bar{x}) = H(1.0 - |\bar{x}|), \quad g_b(\bar{y}) = H(1.0 - |\bar{y}|) \quad (26)$$

where $H(x)$ is Heaviside's function. The material constants are shown in Table 1. In Table 1, the subscript L denotes the longitudinal direction of fiber and the subscript T denotes the transverse direction of fiber. The typical values of material properties such as κ_0 , λ_0 , α_0 and E_0 , used to normalize the numerical data, are based on those in fibre direction.

The variations of the temperature, the thermal

Table 1 Material Properties

Thermal diffusivity	[m ² /s]	$\kappa_L = 41.1 \times 10^{-6}$	$\kappa_T = 29.5 \times 10^{-6}$
Coefficient of thermal expansion	[1/K]	$\alpha_L = 7.6 \times 10^{-6}$	$\alpha_T = 14.0 \times 10^{-6}$
Thermal conductivity	[W/(mK)]	$\lambda_L = 1.05 \times 10^2$	$\lambda_T = 0.75 \times 10^2$
Young's modulus of elasticity	[GPa]	$E_L = 1.5 \times 10^2$	$E_T = 1.1 \times 10^2$
Shear modulus of elasticity	[GPa]	$G_{LT} = 0.35 \times 10^2$	$G_{TT} = 0.41 \times 10^2$
Poisson's ratio		$\nu_{LT} = 0.33$	$\nu_{TT} = 0.33$ $\nu_{TL} = 0.242$

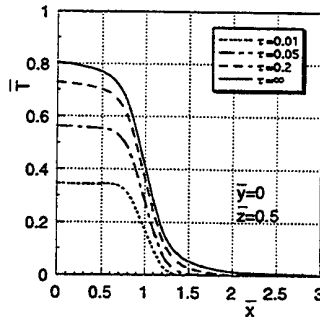


Fig.2 Variation of the temperature on the heated surface ($\bar{y}=0$, $\bar{z}=0.5$)

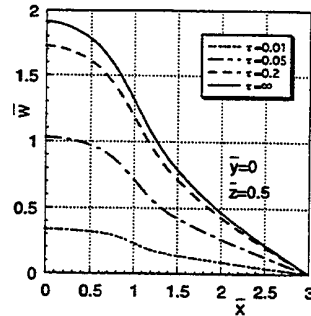


Fig.3 Variation of the thermal displacement \bar{w} on the heated surface ($\bar{y}=0$, $\bar{z}=0.5$)

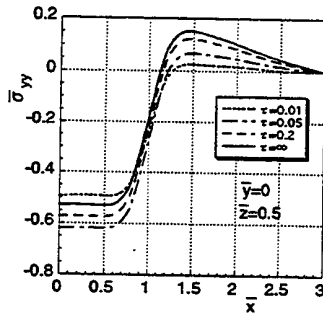


Fig.4 Variation of the thermal stress $\bar{\sigma}_{yy}$ on the heated surface ($\bar{y}=0$, $\bar{z}=0.5$)

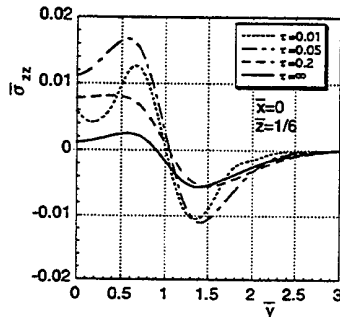


Fig.5 Variation of the thermal stress $\bar{\sigma}_{zz}$ on the interface between the second layer and the third layer ($\bar{x}=0$, $\bar{z}=1/6$)

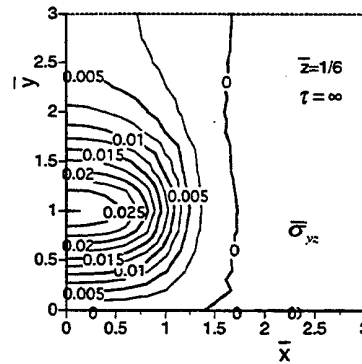


Fig.6 Distribution of the stress $\bar{\sigma}_{yx}$ in a steady state on the interface between the second layer and the third layer ($\bar{z}=1/6$, $\tau=\infty$)

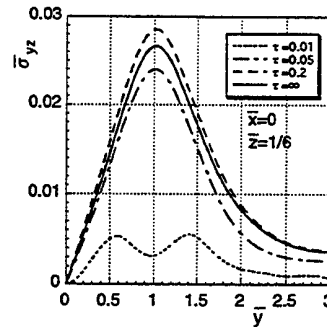


Fig.7 Variation of the thermal stress $\bar{\sigma}_{yx}$ on the interface between the second layer and the third layer ($\bar{x}=0$, $\bar{z}=1/6$)

displacement \bar{w} and the thermal stress $\bar{\sigma}_{yy}$ on the heated surface ($\bar{y}=0$, $\bar{z}=0.5$) are shown in Figures 2 to 4. Figures 5 to 7 show the variations of the thermal stresses on the interface ($\bar{z}=1/6$) between the second layer and the third layer. The variations of the normal stress $\bar{\sigma}_{zz}$ and the transverse shear stress $\bar{\sigma}_{yx}$ along the y axis ($\bar{x}=0$) are shown in Figures 5 and 7. The distribution of the transverse shear stress $\bar{\sigma}_{yx}$ in a steady state is shown in Figure 6.

References

- (1) C.H.Wu and T.R.Taucher, J. Thermal Stresses, Vol.3, p.247, 1980.
- (2) C.H.Wu and T.R.Taucher, J. Thermal Stresses, Vol.3, p.365, 1980.
- (3) J.N.Reddy and Y.S.Hsu, J. Thermal Stresses, Vol.3, p.475, 1980).
- (4) A.A.Khdeir and J.N.Reddy, J. Thermal Stresses, 14(1991), p.419.
- (5) V.B.Tungikar and K.M.Rao, Compos. Struct. , Vol..27, p.419, 1994.
- (6) Y.Tanigawa, Y.Ootao and T.Takahara, Trans. JSME, Ser. A, Vol.58, p.712, 1992 (in Japanese).

Application of a Simplified Method Expressing Effects of Anisotropic Ply to Thermal Stress Analysis of CFRP Cross-Ply Laminates.

Y. Ozawa* and K. Sugiura*

* *Department of Mechanical Engineering, Faculty of Education, Fukushima University, Matsukawa-machi, Fukushima 960-12, JAPAN.*

We have investigated the failure behavior of CFRP cross-ply laminates under thermal loading, by the use of a simplified method which could express effects of an anisotropic ply. In this report, the finite element method analysis is applied to the extension of a transverse crack in the outer ply of CFRP cross-ply laminates under uniform thermal loading. Making a comparison between the result of FEM analysis and that of our simplified method, we discuss the practical application of our simplified method to the transverse ply cracking in CFRP cross-ply laminates for various values of elastic constants of plies and configurations of laminates.

Key Words: CFRP Cross-Ply Laminates, Ply Cracking, FEM Analysis, Anisotropic Ply, Application of Simplified Method.

1. Introduction

Recently, with the increasing use of fibre reinforced composite materials as space structure components, the study of thermal fatigue strength of composite materials has received wide attention. The fracture process of composite materials, especially CFRP cross-ply laminates, is very complicated and the thermal fatigue strength is affected considerably by the laminate structure and the micro fracture [1].

When a laminates, consisting of a stack of laminae bonded together, is subjected to a thermal load, the response depends on the properties of the individual laminae and the way they interact with each other [2]. It is well known that the properties of laminae are not isotropic. An orthotropic laminae has three mutually perpendicular planes of material symmetry and the properties at any point are different in three mutually perpendicular directions. Therefore, it is necessary to discuss the fracture of composite materials from the viewpoint of the elasticity of an anisotropic bodies. However, it is very difficult to have the analytical solution for the anisotropic bodies.

In the previous papers [3, 4], we have investigated the failure behavior of CFRP cross-ply laminates under thermal loading. We proposed a new model of anisotropic plies in the theoretical analysis of the transverse ply-cracking in the cross-ply laminates. A simplified method with this model could express the effects of elastic constants of anisotropic plies and their configurations. By using the simplified method, we discussed the extension of the transverse cracks [3] and their multiplication [4] in the plies of laminates under thermal loading and the thermal stresses around them. This method could reduce mathematical intricacies of the problem.

In this report, the finite element method analysis (FEM analysis) is applied to the problem of transverse ply cracking in the outer ply of CFRP cross-ply laminates under uniform thermal loading. FEM program MARC K5.2 and Pre/Post-processor MENTAT II ver.1.2 are used in this study. Making a comparison between the result of FEM analysis and that of our simplified method, we discuss the application of our simplified method to the transverse ply cracking in the laminates in the case that the laminates have various values of elastic constants of plies and various configurations. By considering the assumption of our model of anisotropic plies, we clarify the application limit of our simplified method to the transverse ply cracking in the laminates.

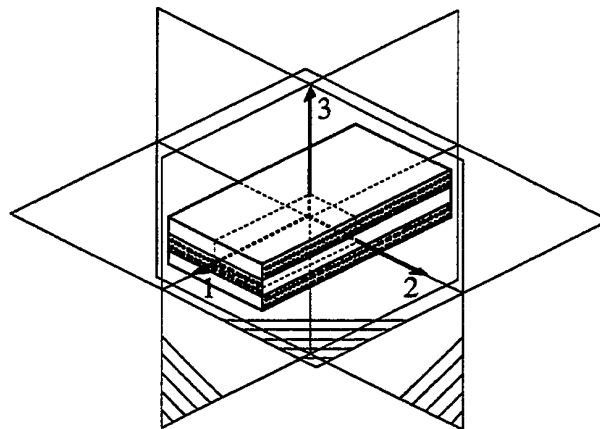


Fig. 1. CFRP cross-ply laminates and three mutually perpendicular planes of material symmetry.

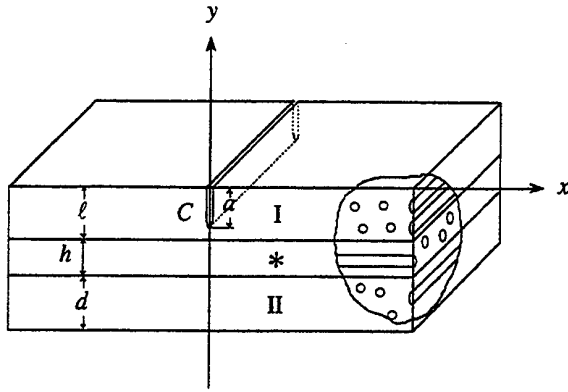


Fig. 2. A transverse crack from the surface of an outer ply and coordinate system.

2. Formulation of the Problem and Boundary Conditions

Consider the thermal stresses around an edge crack parallel to the fibres in the outer transverse ply of the laminate $[90^\circ/0^\circ/90^\circ]_s$ under uniform thermal loading (Fig. 2). The transverse plies I and II treated here are assumed to be homogeneous and transverse isotropic and to obey the Duhamel-Neumann relation. The longitudinal ply * is homogeneous and orthotropic. The transverse plies are perfectly bonded to the longitudinal ply. The crack of length a is perpendicular to the fibres in longitudinal ply. In the analysis, a rectangular coordinate system is employed as shown in Fig. 2. The symmetry condition of the problem will be used.

The boundary conditions of this problem can be written as follows:

(i) From the condition for stresses on the surface of the edge crack C,

$$\sigma_{xl} + i\tau_{xyl} = 0 \quad (x=0, -a < y < 0). \quad (1)$$

In what follows, the subscripts I and II refer to quantities associated with the transverse plies I and II, respectively.

(ii) Since the edge surface of the outer transverse ply I is free from tractions, this condition gives

$$\sigma_{yl} + i\tau_{xyl} = 0 \quad (y=0). \quad (2)$$

(iii) Considering the symmetry condition of the problem, we obtain

$$\tau_{xyl} = 0, v_{ll,x} = 0 \quad (y=-(\ell+h+d)). \quad (3)$$

(iv) From the continuity condition for stresses and displacements on the interface between the ply I and the longitudinal ply *, we obtain

$$\begin{aligned} \sigma_{yl} + i\tau_{xyl} &= \sigma_{y*} + i\tau_{x*y*} \\ u_{l,x} + i v_{l,x} &= u_{*,x} + i v_{*,x} \quad (y=-\ell). \end{aligned} \quad (4)$$

The asterisk will refer to quantities associated with the longitudinal ply.

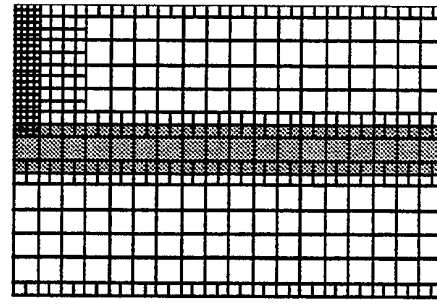


Fig. 3. An example of finite element model.

Table 1. Mechanical Properties of CFRP Laminates [5].

Longitudinal modulus, E_{11}	138 GPa
Transverse modulus, E_{22}	11.7 GPa
In-plane shear modulus, G_{12}	4.56 GPa
Transverse shear modulus, G_{23}	4.18 GPa
In-plane Poisson's ratio, ν_{12}	0.29
Out-plane Poisson's ratio, ν_{23}	0.4
Coefficient of thermal expansion, α_1	$0.09 \times 10^{-6} \text{ K}^{-1}$
Coefficient of thermal expansion, α_2	$28.8 \times 10^{-6} \text{ K}^{-1}$

(v) On the interface between the ply II and the longitudinal ply *,

$$\begin{aligned} \sigma_{yII} + i\tau_{xyl} &= \sigma_{y*} + i\tau_{x*y*} \\ u_{II,x} + i v_{II,x} &= u_{*,x} + i v_{*,x} \quad (y=-(\ell+h)). \end{aligned} \quad (5)$$

(vi) When the composite is subject to a constant increment of temperature ΔT , we have

$$\begin{aligned} T(x, y) &= 0 \quad (t=0) \\ T(x, y) &= \Delta T \quad (t>0) \end{aligned} \quad (6)$$

In this case, there is no difference in temperature between two points on the different crack surfaces.

3. Finite Element Analysis

In the plane strain condition, the FEM analysis is applied to the problem of transverse ply cracking in the outer ply of CFRP cross-ply laminates under uniform thermal loading. Considering the symmetry condition of the problem, we set up the finite element model for the region $(x \geq 0)$ in Fig. 2. The plate of CFRP laminate is divided into 513 eight-node quadrilateral elements. Fig. 3 shows an example of finite element model of the CFRP laminate. The total number of the nodes is 1800. This analysis is performed by the FEM program MARC K5.2 and Pre/Post-processor MENTAT II ver. 1.2.

The unsteady heat conduction analysis is carried out under the temperature condition as follows:

$$\begin{aligned} T_i &= 0 \quad (t=0) \\ T(x, 0) &= \Delta T, \quad T(x, -(\ell+h+d)) = \Delta T \quad (t>0) \end{aligned} \quad (7)$$

Viewing the reference [5], the mechanical properties of the laminate are assumed as shown in Table 1.

4. A Simplified Method

We have investigated the failure behavior of CFRP cross-ply laminates under thermal loading by using a new model of anisotropic plies [3, 4]. This model could express the effects of elastic constants of anisotropic plies and their configurations. By using the simplified method, we discussed the extension of the transverse cracks and their multiplication in the plies of laminates under thermal loading and the thermal stresses around them. Here we will show a summary of this simplified method.

Let us consider the continuity conditions for stresses and displacements on the interfaces between the transverse plies and the longitudinal ply. The component of the displacement u_x in the longitudinal ply is supposed to be uniform through the thickness, when the constant thickness of the longitudinal ply h is small. Therefore, the continuity conditions for displacements on the interface between the transverse plies and the longitudinal ply give

$$\frac{\partial u_I}{\partial x} = \frac{\partial u_{II}}{\partial x} = \frac{\partial u_{III}}{\partial x}, \quad \frac{\partial v_I}{\partial x} = \frac{\partial v_{II}}{\partial x} \quad (8)$$

Moreover, from the continuity condition for stresses on the interface, we obtain

$$\sigma_{yI} = \sigma_{yII} = \sigma_{yIII} \quad (9)$$

The equilibrium of the force due to σ_{xx} and the tangential force acting on the interface of the thin reinforced phase yields

$$\tau_{xyI} - \tau_{xyII} + h \frac{\partial \sigma_{xx}}{\partial x} = 0 \quad (10)$$

Let us try to transform Equations (10) in the plain strain condition, the constitutive equations for the orthotropic longitudinal ply are given by

$$\sigma_{xx} = c_{11} \frac{\partial u_x}{\partial x} + c_{12} \frac{\partial v_x}{\partial y}, \quad \sigma_{yy} = c_{12} \frac{\partial u_x}{\partial x} + c_{22} \frac{\partial v_x}{\partial y} \quad (11)$$

Here c_{ij} are elastic constants of the longitudinal ply. From the constitutive equations for the transverse plies, we obtain

$$\frac{\partial u_I}{\partial x} = \frac{1-\nu^2}{E} \sigma_{xI} - \frac{\nu(1+\nu)}{E} \sigma_{yI} \quad (12)$$

where E is Young's modulus in the transverse ply and ν Poisson's ratio.

In view of Equations (8), (9) and (12), eliminating $\partial v_x / \partial y$ from (11) and substituting it into (10), it follows that

$$\tau_{xyI} - \tau_{xyII} + p_1 \frac{\partial \sigma_{xI}}{\partial x} - p_2 \frac{\partial \sigma_{yI}}{\partial x} = 0 \quad (13)$$

where

$$p_1 = h \left(c_{11} - \frac{c_{12}^2}{c_{22}} \right) \frac{1-\nu^2}{E}$$

$$p_2 = h \left(\left(c_{11} - \frac{c_{12}^2}{c_{22}} \right) \frac{\nu(1+\nu)}{E} - \frac{c_{12}}{c_{22}} \right) \quad (14)$$

Consequently, the continuity conditions for displacements and stresses on the interface of the thin longitudinal ply give Equations (8), (9) and (13) instead of Equations (4) and (5). Here it should be noted that the problem reduces to the two phases problem of the regions of the plies I and II.

Following Muskhelishvili [6], the stresses and the displacement gradients can be expressed, in the absence of body forces, in terms of the temperature potential functions $\theta(z)$ and the elastic potential function $\Phi(z)$ and $\Psi(z)$:

$$\begin{aligned} \sigma_{xj} + \sigma_{yj} &= 2 \left\{ \Phi_j(z) + \overline{\Phi_j(z)} \right\} \\ \sigma_{yj} - i \tau_{xyj} &= \Phi_j(z) + \overline{\Phi_j(z)} + z \overline{\Phi_j'(z)} + \overline{\Psi_j(z)} \\ \frac{E}{1+\nu} (u_{j,x} + i v_{j,x}) &= (3-4\nu) \Phi_j(z) - \overline{\Phi_j(z)} - z \overline{\Phi_j'(z)} \\ &\quad - \overline{\Psi_j(z)} + E \alpha \theta_j(z) \quad (j = I, II) \end{aligned} \quad (15)$$

where α is the coefficient of thermal expansion.

To find the solution, the edge dislocation will be distributed continuously along the cracks C . By paying attention to the behavior of the temperature potential function at infinity, we have the potential functions $\theta_I(z)$, $\Phi_I(z)$ and $\Psi_I(z)$ of the ply I [3].

$$\begin{aligned} \theta_I(z) &= \Delta T \\ \Phi_I(z) &= \frac{\mu}{2(1+\nu)} \varepsilon - \frac{\mu}{4\pi(1-\nu)} \int_0^a b(s) \left[\frac{i}{z+is} \right. \\ &\quad \left. - \int_0^\infty \{ A(m) \exp[im(z+is)] + B(m) \exp[-im(z-is)] \} dm \right] ds \\ \Psi_I(z) &= -\frac{\mu}{1+\nu} \varepsilon + \frac{\mu}{4\pi(1-\nu)} \int_0^a b(s) \left[\frac{i}{z+is} + \frac{s}{(z+is)^2} \right. \\ &\quad \left. + \int_0^\infty \{ [C(m) - imzA(m)] \exp[im(z+is)] \right. \\ &\quad \left. + [D(m) + imzB(m)] \exp[-im(z-is)] \} dm \right] ds \end{aligned} \quad (16)$$

where

$$\varepsilon = -\alpha \Delta T \frac{1-\frac{\alpha}{\lambda}}{1+\frac{\ell+d}{h} \frac{\lambda+2\mu}{c_{11}}}, \quad \lambda = \frac{E\nu}{(1+\nu)(1-2\nu)}, \quad \mu = \frac{E}{2(1+\nu)} \quad (17)$$

where ε is the elastic strain in the transverse ply I when the composite is subject to a constant increment of temperature ΔT . $\Phi_I(z)$ and $\Psi_I(z)$ include the terms of a density function of edge dislocation $b(s)$ distributed along C . Substituting the potential functions into the boundary condition (1), we obtain a set of singular integral equations for the dislocation density function.

The density function $b(s)$ is assumed in the form of the product of an unknown function $g(s/a)$ and the weight function of Jacobi polynomials [3, 7]. Once the unknown $g(s/a)$ has been determined from the singular integral equation, the stress intensity factor and the stresses along the interface and in the transverse ply are obtained in terms of $g(s/a)$ by substituting Equation (16) into (15).

The stress intensity factor for the opening mode at the tip of the transverse crack C is expressed in the form

$$K_I(-a) = \alpha \Delta T \sqrt{\pi \ell} g(1) \quad (18)$$

5. Numerical Calculations and Results

The FEM analysis is applied to the problem of transverse ply cracking in the outer ply of CFRP cross-ply laminates under uniform thermal loading. Numerical calculations are performed for the stress intensity factor of the transverse crack in the outer transverse ply. In this case we introduce the following non-dimensional parameter Γ relating to the stiffness of the longitudinal ply:

$$\Gamma = \frac{h}{\ell} \frac{c_{11}}{\mu} \quad (19)$$

The results are plotted in terms of the geometrical parameters and the Γ . The ratio of the thickness of the transverse ply II to that of the ply I d/ℓ is 1.0.

Making a comparison between the results of FEM analysis and that of our simplified method, we will discuss the application of our simplified method to the transverse ply cracking in the laminates.

The values of stress intensity factor at the crack tip are shown in Table 2. It is found that the stress intensity factors K_I of the simplified method are in good agreement with the K_I of FEM analysis when the adjacent longitudinal ply is thin, and the ratio of the elastic constant in the fibre direction of the longitudinal

ply to the Lamé constant of the outer ply c_{11}/μ is large. In the case that the longitudinal ply is somewhat thick and the ratio of the elastic constant is small, the quantitative agreement between two methods is not good.

Let us consider the assumption of the model of anisotropic plies. We made the assumption that the component of the displacement u_x in the longitudinal ply is supposed to be uniform through the thickness when the constant thickness of the longitudinal ply h is small. Therefore, our simplified method is applicable to the transverse ply cracking in the laminates in the case that the adjacent longitudinal ply is thin, and the ratio c_{11}/μ is large.

From the numerical calculations by the simplified method, the variation of the stress intensity factor K_I at the tip of the transverse crack C is shown versus the ratio of crack length a/ℓ for $\Gamma = 10$ in Fig. 4. As the value of a/ℓ increases, the stress intensity factor K_I increases gradually, taking the extreme value, and then tends to zero at $a/\ell = 1$. The short-dashed line indicates the K_I when the longitudinal ply is isotropic. It can be recognized from this figure that the K_I takes larger values than that in the case of the orthotropic ply. We understand from another calculation that the factor K_I increases as Γ increases.

Table 2. Stress intensity factors ($\Gamma = 10$ and $a/\ell = 0.8$).

h/ℓ	c_{11}/μ	FEM	Simplified Method
0.1	100	0.41	0.412
0.3	33	0.41	0.412
0.5	20	0.39	0.412
1.0	10	0.35	0.412

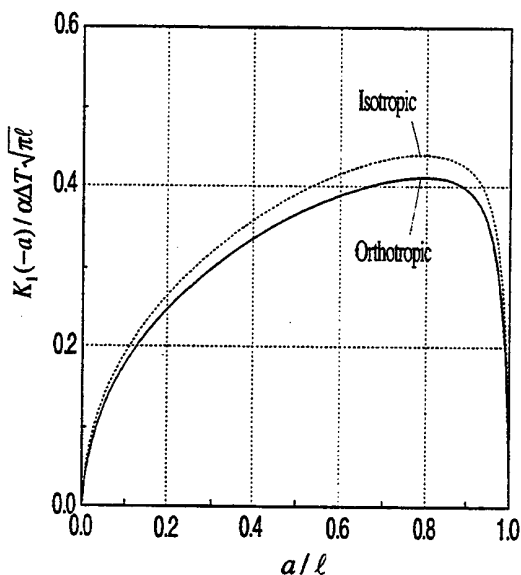


Fig. 4. Stress intensity factors versus crack length ($\Gamma = 10$).

References

- (1) Adams, D. S., Bowles, D. E. and Herakovich, C. T., "Thermally Induced Transverse Cracking in Graphite-Epoxy Cross-Ply Laminate," *Journal of Reinforced Plastics and Composites*, Vol. 5, p.152, 1986.
- (2) Hull, D., *An Introduction to Composite Materials*, Cambridge University Press, Cambridge, 1981.
- (3) Ozawa, Y., Haraguchi, S., and Sugiura, K., "Ply Cracking in the Longitudinal and Transverse Plies of CFRP Laminates Under Thermal Loading," *The 72th JSME Fall Annual Meeting* No. 940-30, p.166, 1994. (in Japanese)
- (4) Ozawa, Y., Sugiura, K. and Noguchi, K., "Ply Cracking in the Outer and Inner Plies of CFRP Laminates Under Thermal Loading," *Thermal Stresses '97*, in Rochester, (1997-6).
- (5) Han, Y. M., Hahn, H. T. and Croman, R. B., "A Simplified Analysis of Transverse Ply Cracking in Cross-Ply Laminates," *Composites Science and Technology*, Vol. 23, p.165, 1988.
- (6) Muskhelishvili, N. I., *Some Basic Problems of the Mathematical Theory of Elasticity*, 4th Edn., P. Noordhoff, Groningen, 1963.
- (7) Erdogan, F., *Mechanics Today* Vol. 4, Nemat-Nasser, S., ed., Pergamon Press, p.1, 1978.

Thermomechanical Fatigue of Metal Matrix Composites

Zhanjun Gao

Eastman Kodak Company, 1669 Lake Avenue, Rochester, NY 14652-4333

The damage of metal matrix composites under a general thermomechanical fatigue is considered. A criterion to determine the stiffness reduction is established. It is shown that the characteristic damage state of the materials is related directly to the most damaging loading level at which the combined load and temperature yield the maximum stress-strength ratio during cycling. Stiffness reduction of metal matrix composite materials are predicted for room temperature as well as in-phase and out-of-phase fatigue.

Key Words: Damage, stiffness reduction, thermomechanical fatigue, metal matrix composites

Stiffness Reduction

Today, metal matrix composites are being considered for a variety of applications in high temperature and aggressive environmental conditions. In this paper, an analytical model is presented for predicting fatigue damage of metal matrix composite laminates in terms of stiffness reduction under a general nonisothermal fatigue.

The damage accumulation and stress redistribution of a laminate depend on micromechanical properties, including properties of fibers, matrix, interface, etc. Johnson et al. [1] studied the stiffness reduction for $[0/90]_{2s}$ lay-ups of a SCS-6/Ti-15-3 laminate, and showed the elastic modulus dropped about 78% during the first few cycles, then remained almost constant until just before the final failure. Reifsnider [2] investigated the spacing between cracks in the -45° plies of a $[0/90/\pm 45]_s$ AS-3501-5 graphite epoxy laminate as a function of quasi-static load level and cycles of loading. He found that matrix cracks developed quite early in the life and quickly stabilized to a very nearly constant level with a fixed spacing for both quasi-static and cyclic loading. The crack patterns for both quasi-static and cyclic loading were essentially identical, regardless of load history. This indicates that the load re-distribution for such a laminate occurs only during the first part of the loading cycles. After these cycles, the damage in the laminate reaches a stable level, called characteristic damage state (CDS) (Reifsnider, [2]). Reifsnider [2] pointed out that the CDS is completely defined by the properties of fiber, matrix, interface and fiber orientations, etc., and is independent of loading history. A scrutiny by the current authors on the numerous data from Neu

[3] on stiffness change for titanium matrix composite laminates ($[0]_4$, $[0/90]_s$ and $[0/\pm 45/90]_s$) at different thermomechanical fatigue loading also suggests that the existence of CDS.

Room Temperature Fatigue

Since the stiffness of the laminate at the CDS level is a characteristic material property of the laminate, and independent of loading history, it is to our advantage to determine the stiffness reduction under a static loading condition.

After the damage initiation, the transverse normal stress in the 90° plies, σ_{22} (of 90°) in a cross-ply laminate, is not completely relaxed. Instead, it is necessary that this stress remains at a level equal to transverse strength Y so that additional damage can be accumulated up to the CDS level. Thus, the reduced modulus E_2 in the 90° plies can be approximately obtained by solving the equation

$$\sigma_{22} (\text{of } 90^\circ) = Y. \quad (1)$$

The algorithm is as follows:

(1) For an applied static load exceeds the level at which damage in the 90° plies begins to initiate, let all the elastic parameters of the 0° plies be the initial values. The current stiffness, E_2 , of the 90° plies is reduced by an amount of $dE_2 = 0.001E_2$. Other parameters, E_1 , G_{12} , ν_{12} remain their initial values. Stress distributions in each ply are obtained through a laminate analysis.

(2) If the stress σ_{22} (of 90°) is larger than Y , repeat the first step until the Eqn. (1) is satisfied.

(3) The final reduced value of E_2 of the 90° plies is then used to obtain the extensional stiffness of the laminate.

When the static applied load is equal to the value of the ultimate tensile strength (UTS) of the laminate, the maximum possible stiffness reduction is reached since any load level above UTS causes immediate fracture of the laminate. Therefore, the characteristic stiffness are found from the above scheme at the static load level equal to UTS.

Figure 4 shows the stiffness reduction analysis using the above procedure for a SCS-6/Ti-15-3 laminate with $[0/90]_{2s}$ lay-ups at room temperature. Before the load reaches the level of 500 MPa, E_2 of the 90° plies and therefore, the axial stiffness of the laminate remain unchanged, and the stress-strength ratio, σ_x (of 0°)/ X , of the 0° plies increases linearly. Then with further increase of the applied load, the stiffness E_2 of the 90° plies is sharply reduced and results in the reduction of the axial stiffness of the laminate. When the load approaches the ultimate tensile strength (UTS) level, the stress-strength ratio, σ_x (of 0°)/ X , of the 0° plies approaches 1, indicating the 0° plies are about to fracture. The axial stiffness of the laminate approaches a characteristic value, $E_x = E_{xc}$.

The characteristic stiffness, E_{xc} , can be approximately obtained as the stiffness value corresponding to applied load equal to the ultimate tensile strength, which is 944 MPa for the laminate. The predicted value of E_{xc} is equal to 76% of the initial axial stiffness. The prediction agrees with experimental data of Johnson et al. [1]. The lamina material properties used in the calculations of Fig. 4 are given in [4]. Similar procedure can be established for $[0_2/\pm 45]_s$ and $[0/90/\pm 45]_s$ laminates [4].

In-phase Fatigue

During the in-phase fatigue, the temperature changes from 150°C to 650°C at the same frequency with the applied mechanical load. The maximum mechanical load occurs at maximum temperature, 650°C . The equation to determine the stiffness reduction of the 90° plies in the cross-ply laminate, Eqn. (1), is written as

$$\sigma_{22} \text{ (of } 90^\circ) = Y(T_{\max}) \quad (2)$$

where $Y(T_{\max}) = 227$ MPa, is the strength of the 90° plies in the transverse direction at $T = T_{\max} = 650^\circ\text{C}$. The reduced axial stiffness after initial damage is predicted to be 107.2 GPa using Eqn. (2) with UTS = 637 MPa at 650°C .

Out-of-Phase Fatigue

The maximum and minimum temperatures for the out-of-phase fatigue, Fig. 2, remain the same as those of the in-phase fatigue, i.e., $T_{\max} = 650^\circ\text{C}$ and $T_{\min} = 150^\circ\text{C}$. For the out-of-phase fatigue, since the maximum load occurs at the minimum temperature, $T_{\min} = 150^\circ\text{C}$, the stiffness reduction is determined from the equation

$$\sigma_{22} \text{ (of } 90^\circ) = Y(T_{\min}) \quad (3)$$

where $Y(T_{\min}) = 380$ MPa is the transverse tensile strength of the unidirectional laminates at 150°C . The reduced axial stiffness after initial damage is predicted to be 141.26 GPa.

General Thermomechanical Fatigue

In a general thermomechanical loading for which both temperature and applied load change periodically, but not obeying in-phase or out-of-phase pattern, the temperature and load levels suitable for the determination of stiffness reduction are not that obvious. In general, the stiffness reduction is directly related to the most damaging state of stress at which the stress-strength ratio is maximum. The stress-strength ratio indicates how close the materials is to failure. A value of the stress-strength ratio closer to 1 suggests a more severe damage than that of much less than 1. When the ratio is equal to 1, complete fracture occurs. Examining the equations used in stiffness reduction for room temperature as well as in-phase and out-of-phase fatigue, it is clear that in each case, the load and temperature level used give the maximum stress-strength ratio in the cycles. For room temperature (or isothermal fatigue) the strength of the material is constant, and therefore, the maximum stress to stiffness ratios occurs at maximum applied load. For in-phase fatigue, the strength of the material decreases as temperature increases. Therefore, the maximum stress-strength ratio is obtained at the maximum applied load at

which the temperature is the highest and the strength is the lowest. For an out-phase fatigue, Fig. 2, however, when the applied load reaches its maximum value, the temperature is lowest, and the strength is also maximum. It is not clear whether the maximum stress-strength ratio occurs at the maximum applied load. This needs to be verified from calculation of the stress-strength ratio in the entire cycle. As shown in Fig. 3, as the stress in the 90° plies increases from 0 to its maximum, the transverse strength of the composite also increases as a result of the temperature drop. Although Fig. 4 show the maximum stress-strength ratio also occurs at the maximum applied load for the metal matrix composite considered, this should be taken with caution. It is quite possible that for a different material, the strength curve in Fig. 3 is more steep so that the maximum stress-strength ratio occurs at a location where the applied stress is not maximum. In a general thermomechanical fatigue, the stiffness reduction should be determined by

$$\begin{aligned} &\sigma_{22} \text{ (of } 90^\circ \text{) at the load level of maximum stress-} \\ &\text{strength ratio} \\ &= Y \text{ at the temperature corresponding to the load} \\ &\text{level of maximum stress-strength ratio} \quad (4) \end{aligned}$$

The maximum applied stress, together with the associated temperature, represents a critical state of loading, of the fatigue process. This critical state of loading dictates a unique state of damage represented by stiffness reduction of the off-axis plies of the total laminate.

Concluding Remarks

An analytical model has been presented to predict fatigue damage of metal matrix laminates containing off-axis plies under general isothermal and nonisothermal fatigue loading. For the room temperature fatigue, in-phase and out-of-phase fatigue considered, the maximum applied stress, together with the associated temperature, represents the most "damaging" thermomechanical loading, called the critical state of loading, during fatigue. This state of loading dictates a unique state of damage represented by stiffness reduction of the off-axis plies of the total laminate. After first few cycles, further damage is dominated by the 0° plies of the laminate. In a general nonisothermal fatigue,

the stiffness reduction is determined by the load and temperature levels which give the maximum stress-strength ratio as shown in Eqn. (4). The stiffness reduction formulations, Eqns. (1) - (3) for room temperature, in-phase and out-of-phase fatigue can be considered as special cases of Eqn. (4).

The new concept of the critical state of loading suggests that what matters most is the maximum applied stress and related temperature, which is the most damaging state of loading. From this point of view, the differences between in-phase and out-of-phase fatigue reported are not the results of phase lags between the thermal and mechanical loading, but rather the consequences of temperature difference at the maximum applied stress. For instance, the damage mechanism of the out-of-phase fatigue with $T_{\min}=150^\circ\text{C}$ should be basically the same as the isothermal fatigue at 150°C . At the temperature of 150°C , the matrix material is relatively brittle, and the yield stress of the matrix is higher than that needed for the formation of matrix cracks. The damage mechanisms for both out-of-phase and isothermal fatigue are matrix cracking. On the other hand, If the minimum temperature for the out-of-phase fatigue, T_{\min} , is relatively high, (e.g., $T_{\min}=550^\circ\text{C}$, $T_{\max}=650^\circ\text{C}$), the damage will be fiber dominated similar to the in-phase fatigue with the same temperature range. This is because at 550°C , the matrix material is relatively ductile with a relatively lower yield strength. Matrix yielding occurs before matrix cracks are formed. The fiber strain in this case is much higher to keep up with the viscoplastic deformation in the matrix material, which causes fiber fracture.

The above observation is very important for engineering applications where the loading pattern in general is neither in-phase nor out-of-phase. However, the critical state of loading, which may or may not occur at the maximum applied stress, will play an important role in determining the dominated damage modes and fatigue life of the composite laminates.

References

- [1]. Johnson, W. S., Lubowinski, S. J. and Highsmith, A. L. 1990. 'Mechanical Characterization of Unnotched SCS₆/Ti-15-3 Metal

Matrix Composites at Room Temperature,' Thermal Behavior of Metal Matrix and Ceramic Matrix Composites, ASTM STP 1080, J. M. Kennedy, H. H. Moeller, and W. S. Johnson, Eds., American Society for Testing and Materials, Philadelphia, pp 193-218.

[2]. Reifsnider, K. L. 1990. Fatigue of Composite Materials, Elsevier Science Publishers B. V., New York.

[3]. Neu, R. W. 1992. 'Thermomechanical Fatigue in Metal Matrix Composites: Mechanistic Life Prediction Model and Experiments,' Final Report, Contributive Research and Development, Vol. 60. Wright Laboratory Materials Directorate, Wright-Patterson AFB, OH.

[4]. Gao, Z and Zhao, H. "Life Predictions of Metal Matrix Composite Laminates under Isothermal and Nonisothermal Fatigue," Journal of Composite Materials, Vol. 29, pp. 1142-1168, 1995.

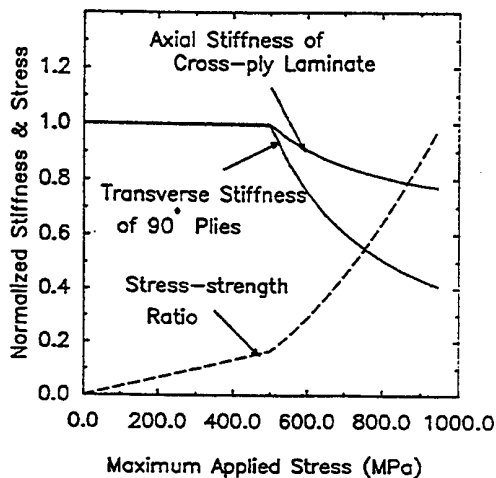


Fig. 1. Stiffness reduction and stress redistribution of the $[0/90]_{2s}$ laminate under a static loading.

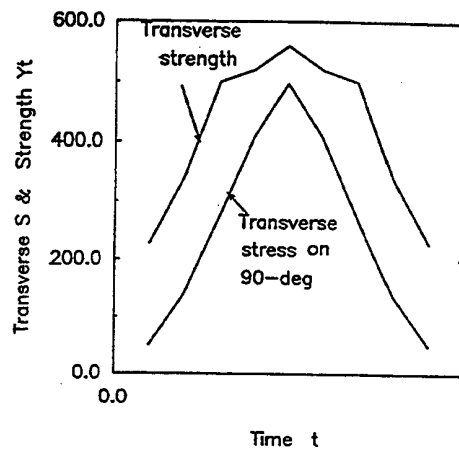


Fig. 3. Stress and strength of the 90° plies in the out-of-phase fatigue.

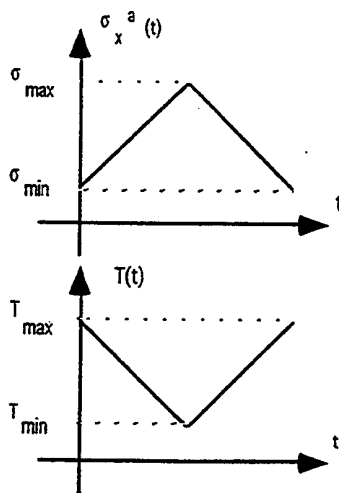


Fig. 2. Load and temperature in the out-of-phase fatigue.

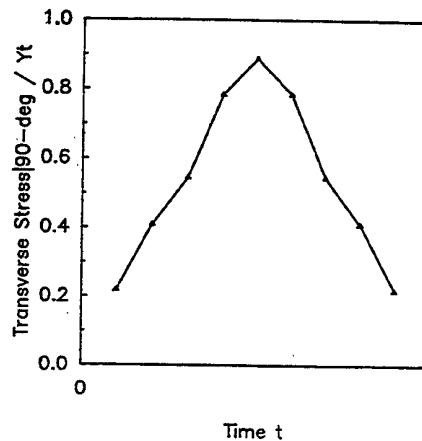


Fig. 4. Stress-strength ratio of the 90° plies in the out-of-phase fatigue.

Deformation of Structural Elements from Anisotropic Composite Materials under Thermal Loading.

L. Gracheva* and N. Pankratova**

*Institute for Problems of Strength, National Academy of Sciences of Ukraine
2 Timiryazevskaya Str., Kiev 252014, UKRAINE.

**Institute of Mechanics, National Academy of Sciences of Ukraine
3 Nesterova str., Kiev 252057 UKRAINE.

A problem of the stress-strain state of structural elements of anisotropic composite materials (CM's) was solved considering distribution of physical and mechanical characteristics obtained on a unique equipment designed and manufactured for the purpose at the Institute for Problems of Strength; it allows us to simulate real working conditions for an object of study. Computations of the stress-strain state of high temperature structural elements involve some data on properties of materials not only in relation to the temperature but also in duration of thermal load application, a character of heat conveyance, material anisotropy, chemical composition, and nature of a gas medium. We obtained some distributions of tangential ($\tau_{\theta\theta}$, τ_{zz}) stresses in length and in width of a cylindrical heat-proof coating made of a carbon-filled reinforced plastic (CFRP); the coating is designed to meet conditions of re-entry of aircraft.

Key Words: Thermal Stress, Composite Material, Heat Deformation, Anisotropy, Heat-Proof Coatings

1. Introduction

A specific feature in the behavior of heat-protective polymeric composite materials (CMs) at high temperatures is a considerable dependence of their physical and mechanical properties on duration of exposure to heat, and a character of heat conveyance. This dependence, related to thermal destruction of the CM binders, has to be considered when defining functional relationships between stresses and strains generated in the materials in heating.

Deformation and fracture behavior of carbon CM's is characterized by an appreciable instability, particularly if they are exposed to a repetitive thermal loading (this is despite the fact that destructive processes in such materials are completed at the stage of fabrication).

Here we consider some aspects associated with determination of thermal stress state for laminated anisotropic hollow elastic bodies; we assume that they have a cylinder shape, nonuniform in thickness, and exposed to a uniform temperature field. A solution of such problems is required, in particular, when evaluating strength and load-carrying capacity of heat-protective coatings for high-temperature structures.

2. Experimental methods and results

One of the main processes in fracture mechanics of high-temperature CM's is thermal (shrinking) deformation. There is a strong relationship between the coefficient of thermal deformation and the whole spectrum of physical and mechanical characteristics of a material: elasticity modulus, E , tensile and

compressive ultimate strengths, σ_{ut} , σ_{uc} , Poisson's ratio, etc.

Fracture of a heat-proof coating might be caused by crumbling, partial melting, erosive ablation, separation of some segments, and outer surface cracking. Frequently, cracking behavior is complicated due to the action of gas pressure generated as a result of pyrolysis of inner layers, local material defects, etc. More often cracks propagate along formation lines of cylindrical or conic coatings and are caused by tensile stresses. Experimental study of thermal deformation and strength in reinforced plastics, with maximum allowance made for service conditions and data obtained for stress-state calculations of heat-proof structural components is justified by an urgent demand to improve thermal resistance and life time of a heat-proof coating for a space vehicle.

To study how efficient a heat-proof coating made of a carbon-filled reinforced plastic (CFRP) we studied physical and mechanical characteristics of CFRP in conditions simulating real ones: varying temperature, heating rate, components and pressure of a gaseous medium.

Temperature values in a layer of CFRP in a process of heating up and cooling down are shown on Fig. 1 (Severov [2]). Temperature was averaged over a thickness of an outer layer of the heat-proof coating.

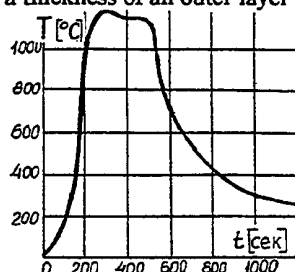


Fig. 1. Temperature variation in heat-proof carbon-plastic coating in re-entry trajectory

To obtain reliable values of thermal deformation of the heat-proof coating CFRP samples were studied at different heating rates that do correspond to those in a re-entry path. Some characteristics of change of thermal deformation of a carbon plastic in neutral and in an oxidizing gaseous media are presented on Fig. 2 (Gracheva [3]). The figure shows that in the neutral

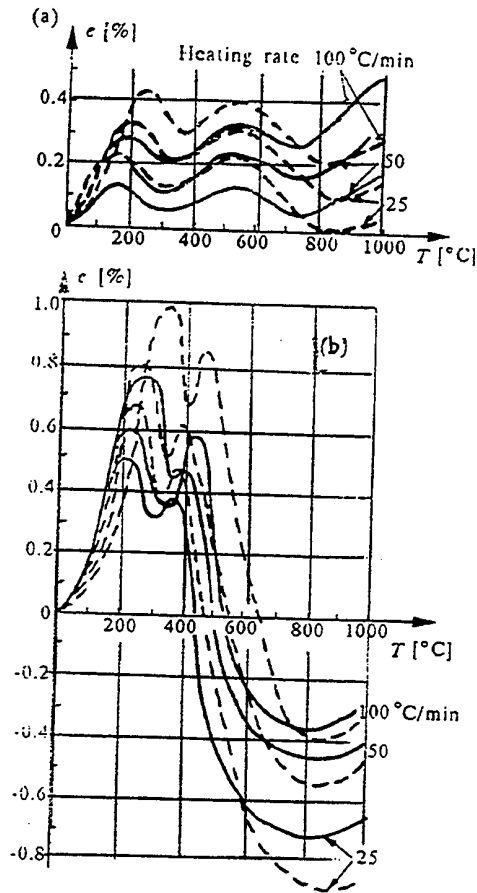


Fig. 2. Dependence of thermal deformation in carbon-plastic on heating rate in neutral (solid lines) and oxidizing (broken lines) atmospheres: (a)-along the warp, (b) - along the weft

medium (solid lines) the intensity of deformation processes is different as compared to that of in the oxidizing one (dashed lines). In addition, one can see that the extremes on the expansion diagrams for specimens cut along the warp tend to increase in the neutral medium and to decrease in the oxidizing one.

The change in the elasticity modulus of the carbon plastic depending on temperature (Fig. 3) was received in the neutral medium at a heating rate of 100 degrees/min (Eskin [4]).

Obtained experimental characteristics of changes in physical and in mechanical properties of the material are necessary to calculate parameters of a

stress-deformed state of elements of heat-proof coatings operating in real conditions.

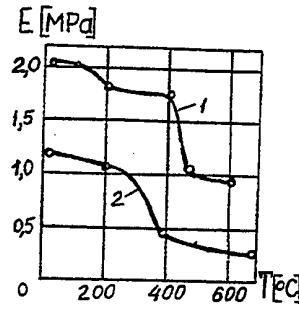


Fig. 3. Temperature dependence of Elasticity modulus: 1 - in stretching 2 - in bending

3. Calculation of a thermal stressed state of a cylindrical construction element

We consider a stress-deformed state of the construction element having a shape of a non-homogeneous anisotropic cylinder, and we employ a solution to a set of equations of an elasticity theory problem. Our method is based on using a combination of equations of elasticity theory, those of heat conductivity, and some numerical analysis.

As initial equations of the three-dimensional problem, an equation of elasticity theory in the curvilinear system of coordinates α, β, γ is taken. There is one plane of elastic symmetry tangential at each point to a body surface $\gamma = \text{const}$ or perpendicular to the axis of rotation $\alpha = \text{const}$. The Hook generalised law for the i -th layer ($\gamma_i \leq \gamma \leq \gamma_{i+1}$, $i=1, \dots, N$) has the form

$$\begin{aligned} \bar{e}^i &= B^i \bar{\sigma}^i + \bar{f}^i, \bar{e}^i = \{e_{\alpha}^i, e_{\beta}^i, e_{\gamma}^i, e_{\alpha\beta}^i, e_{\alpha\gamma}^i, e_{\beta\gamma}^i\}, \\ \bar{\sigma}^i &= \{\sigma_{\alpha}^i, \sigma_{\beta}^i, \sigma_{\gamma}^i, \tau_{\alpha\beta}^i, \tau_{\alpha\gamma}^i, \tau_{\beta\gamma}^i\}, B^i = \|b_{lp}^i(i)\|, \\ l, p &= 1, 2, \dots, 6, \\ b_{m4}^i &= b_{m5}^i = b_{4m}^i = b_{5m}^i = 0, (m=1, 2, 3, 6) \text{ for } \gamma = \text{const}, \\ b_{m5}^i &= b_{m6}^i = b_{5m}^i = b_{6m}^i = 0, (m=1, 2, 3, 4) \text{ for } \alpha = \text{const}, \\ \bar{f}^i &= \{\alpha_{\alpha}^i T, \alpha_{\beta}^i T, \alpha_{\gamma}^i T, \alpha_{\alpha\beta}^i T, \alpha_{\alpha\gamma}^i T, \alpha_{\beta\gamma}^i T\} \end{aligned}$$

Here, $e_{\alpha}^i, e_{\beta}^i, e_{\gamma}^i, e_{\alpha\beta}^i, e_{\alpha\gamma}^i, e_{\beta\gamma}^i$ are the strain tensor components, $\sigma_{\alpha}^i, \sigma_{\beta}^i, \sigma_{\gamma}^i, \tau_{\alpha\beta}^i, \tau_{\alpha\gamma}^i, \tau_{\beta\gamma}^i$ are the stress tensor components. Elastic constants b_{lp}^i , coefficients of linear thermal expansion $\alpha_{\alpha}^i, \alpha_{\beta}^i, \alpha_{\gamma}^i$ in the directions α, β, γ , coefficients of temperature shift $\alpha_{\alpha\beta}^i, \alpha_{\alpha\gamma}^i, \alpha_{\beta\gamma}^i$ are functions of the coordinate γ that makes it possible to take into account an arbitrary variability of material properties through the elastic cylinder thickness.

Taking into consideration the equations of equilibrium, the expressions for deformations by displacements, the Hook law for a non-homogeneous anisotropic body the system of differential equations

for definition of the stress-deformed state of a laminated hollow body is received.

The solution to the problem must satisfy conditions on the limiting surfaces $\gamma = \gamma_0$, $\gamma = \gamma_N$ and conditions of layers conjugation $\gamma = \gamma_i$. In most cases there is a rigid conjugation when layers of the body are deformed without slipping and breaking off, the continuity conditions $\sigma_j^i = \sigma_j^{i+1}$, $j = 1, 2, \dots, 6$ are fulfilled for all $\bar{\sigma}$ components. Sometimes these conditions can be violated and some of the components of $\bar{\sigma}^i$ can break, i.e. $\sigma_j^i \neq \sigma_j^{i+1}$.

A rigid conjugation of layers for a non-homogeneous cylinder (cylindrical coordinate system z, θ, r) may be written for an i -th layer in the form

$$\begin{aligned} \sigma_r^i &= \sigma_r^{i+1} & \tau_{rz}^i &= \tau_{rz}^{i+1} & \tau_{r\theta}^i &= \tau_{r\theta}^{i+1} \\ (3) & & & & & \\ u_r^i &= u_r^{i+1} & u_z^i &= u_z^{i+1} & u_\theta^i &= u_\theta^{i+1} \end{aligned}$$

The temperature field for the i -th layer of the cylinder is defined by the equation of heat conductivity which in cylindrical coordinate system is expressed by

$$K_r^i \frac{\partial}{\partial r} \left(\frac{\partial T^i}{\partial r} \right) + r K_z^i \frac{\partial^2 T^i}{\partial z^2} + \frac{K_\theta^i}{r} \frac{\partial^2 T^i}{\partial \theta^2} = 0 \quad (4)$$

where $K_r^i = K_r^i(r)$, $K_z^i = K_z^i(r)$, $K_\theta^i = K_\theta^i(r)$ - the coefficients of heat conductivity acting in the directions r, z, θ . It is assumed that thermal continuity conditions of layers over the entire surface of contact are fulfilled

$$T^i = T^{i+1} \quad K_r^i \frac{\partial T^i}{\partial r} = K_r^{i+1} \frac{\partial T^{i+1}}{\partial r} \quad (5)$$

Further, we deal with the case when the butt-ends of the cylinder $z = 0$, $z = l$ do not displace in their planes and are free from a normal load. Taking the resolving functions as basic ones we can formulate conditions on the limiting surfaces $r = r_0$, $r = r_N$ and the interfaces of the layers r_i ; making transformations of the initial equations of elasticity (1) and equations of heat conductivity (4), performing separation of variables for each pair of k and n values

for the i -th layer we come to a following system (Pankratova [6]).

$$\begin{aligned} \frac{d\bar{\sigma}_{kn}^i}{dr} &= C_{kn}^i \bar{\sigma}_{kn}^i + \bar{f}^i \\ \bar{\sigma}_{kn}^i &= (\sigma_{r, kn}^i, \tau_{rz, kn}^i, \tau_{r\theta, kn}^i, u_{r, kn}^i, u_{z, kn}^i, u_{\theta, kn}^i, T_{kn}^i, T'_{kn}^i) \\ C_{kn}^i &= \|c_{mq, k}^i(r)\| \\ \bar{f}^i &= (f_1^i, f_2^i, \dots, f_8^i) \\ m, q &= 1, 2, \dots, 8 \end{aligned}$$

Here σ_r - radial stress, τ_{rz} , $\tau_{r\theta}$ - tangential stresses, u_r , u_z , u_θ - radial, axial, and circumference displacements, respectively, T - temperature, T' - temperature gradient.

The matrix elements C_{kn}^i depend on mechanical characteristics of a layer of the material. Integration of Eqs (6) is done by means of a robust numerical method; it gives us a solution with a high degree of precision. Selection of basic values to formulate contact conditions for layer conjugation makes it possible to get solutions easily for a prescribed number of layers.

Then we studied the stress-state of a heat-proof coating in the form of a hollow cylinder in a quasi-static setting using the method described above. In agreement with the prescribed experimental data relating to layer thickness, mechanical properties, and temperature field we broke the cylinder into separate layers $[r_i, r_{i+1}]$ ($i=1, 2, \dots, 7$). Specified characteristics in each of these layers are given by their own expressions

$$\begin{aligned} T &= A_i + B_i r & \nu &= C^{(i)}_0 + C^{(i)}_1 T + C^{(i)}_2 T^2 \\ E &= C_i + D_i T & \alpha_T T &= a_i + b_i T \end{aligned} \quad (7)$$

being approximated by the initial data. Here E - modulus of elasticity, ν - Poisson ratio, α_T - coefficient of linear temperature expansion.

Some results of the solution to the problem for maximum values of stresses τ_{rz} , $\tau_{r\theta}$ in external (subjected to heating) layer ($0 \leq r \leq 10 \text{ mm}$) are shown on Fig. 4.

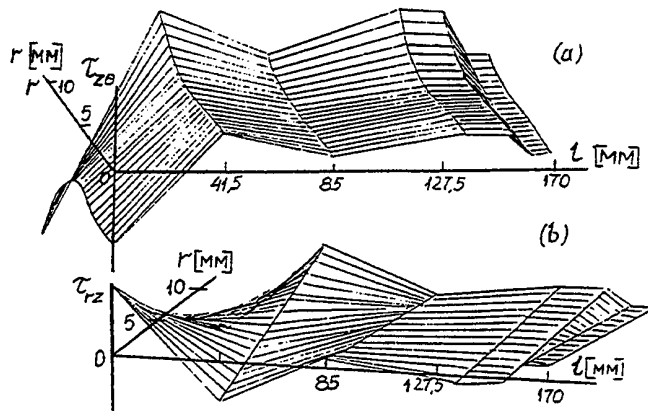


Fig. 4. Distribution of tangential stresses $\tau_{r\theta}$ and τ_{rz} through the thickness and along the length of a carbon-plastic cylindrical coating in re-entry trajectory:

- (a) $\tau_{r\theta \max} = 55.54 \text{ MPa}$
 $\tau_{r\theta \min} = -115.36 \text{ MPa}$
- (b) $\tau_{rz \max} = 45.66 \text{ MPa}$
 $\tau_{rz \min} = -37.01 \text{ MPa}$

Calculations for a thermo-stressed state is done for a hollow carbon-plastic cylinder of length $L = 340$ mm, radius of the mid-surface $R = 90$ mm, and the thickness $r = 10$ mm. Temperature field values are varied from a room temperature up to 1200°C (Fig. 1). Elasticity modulus $E_z = E_{\theta}$ (curve 1, Fig. 3), E_r (curve 2, Fig. 3), and shear modulus $G_{z\theta} = G_{rz} = G_{r\theta}$. Coefficients of linear temperature expansion are determined from experimental data on thermal deformation: α_z (Fig. 2, a), α_{θ} (Fig. 2, b), α_r (Borisenko [7]).

Tangential stresses $\tau_{z\theta}$ and τ_{rz} vary through thickness of the cylinder according to some nonlinear law (Fig. 4). These stresses are considered to be the most dangerous ones for the integrity of a carbon-plastic heat-proof coating under heating it up from 200 to 700°C .

It is known (Gracheva [8]) that thermal destruction of phenol-phormaldehyde binder of the carbon-plastic occurs in this temperature range; as a consequence, there is an appreciable shrinkage deformation. Due to thermal deformations of both signs tangential stresses develop in the material. In multiple heatings tangential stresses are conducive to acceleration of the destruction process; it takes place as a result of thermal destruction without application of external forces.

4. Conclusions

A comprehensive experimental and theoretical study has been done on influence of thermal deformations upon the stressed state of structural elements made of high-temperature CM's.

On the basis of a developed approach to the problem of a stress-deformed state of a hollow thick-walled body we studied how inhomogeneity and anisotropy of elastic properties of the material influence stress level and deformability of a laminated body having a shape of a cylinder.

We obtained some dependencies of a level of ultimate stresses in hollow cylindrical bodies made of an anisotropic CM on change in its physical and mechanical properties; the dependencies are obtained at different temperatures, heating rates, composition, and pressure of gaseous medium.

We did some analysis of a thermo-stressed state of a cylindrical heat-proof coating made of a carbon

plastic for conditions that simulate real ones for re-entry of aircraft into dense layers of the atmosphere.

References

- (1) G. N. Tretyachenko, L. I. Gracheva, Heat Deformation and Strength of Composite Materials at High Temperatures, *Mechanics of Composite Materials*, 1986, No. 5, p. 800.
- (2) A. Severov, L. I. Gracheva, V. N. Koloskova, and V. V. Vengzgen, Thermal Deformation of a Heat-Proof Material at re-entry trajectories, *Strength of Materials*, Vol. 24, No. 4, (1992), pp. 409-413.
- (3) L. Gracheva and N. Pankratova, Influence of Thermal Deformation on the Stress State of Heat-Proof Coatings, *Journ. of Theoret. and Applied Mechanics*, No. 3, Vol. 32 (1994), p. 675-687.
- (4) E. A. Eskin and V. K. Fedchuk, Influence of Temperature on physical and mechanical characteristics of carbon-filled plastics, *Strength of Materials*, Vol. 12, No. 7 (1980), p. 610-613.
- (5) S. G. Lehnitsky, *Theory of Elasticity of Anisotropic Body*, Moscow, Nauka, 1977 (in Russian).
- (6) N. D. Pankratova, A. A. Mukoed, Deformation of The Thick Laminated Orthotropic Plate, XXXV Symposium 'Modelling in Mechanics', Gliwice 1995, pp. 251-256.
- (7) V. A. Borisenko, L. I. Gracheva, and N. D. Pankratova, Methods for investigation of Composite Materials Thermal Deformation by Optical Dilatometers, *Recent Advances in Experimental Mechanics*, Rotterdam, 1994, Vol. 2, pp. 837-841.
- (8) L. I. Gracheva, Peculiarities of Stress-State Curves of Carbon Plastics at High Temperatures, *Strength of Materials*, Vol. 14, No. 3, (1982), pp. 390-393.

Session 2C

WAVE PROPAGATION II

Chair: K. L. Verma

Co-Chair: G. A. Harmain

**Numerical Solutions of a Coupled Thermoelastic
Interaction with Second Sound**

G. A. Harmain

**Wave Propagation In Thermoelastic Cylindrical Shell
Containing Fluid**

A. Sarkisyan

**Coupled Problem of a Thermoelastic Plate in Elliptical
Shape**

D. Trajkovski, R. Cukic

**Propagation of Generalized Thermoelastic Free Waves in
Plate of Anisotropic Media**

K. L. Verma

Numerical Solutions of a Coupled Thermoelastic Interaction with Second Sound

G. A. Harmain

Dept. of Mechanical Eng., University of Victoria, Victoria, B. C., Canada V8W 3P6.

Thermal and elastic waves resulting from a suddenly applied change in the normal stress and/or temperature at the surface of a cylindrical cavity in an unbounded isotropic medium, initially unstressed and at a uniform temperature are obtained using numerical methods. We consider two linear thermoelastic theories, which are governed by systems of hyperbolic partial differential equations and predict a finite speed of propagation of thermal effects (second sound).

Key Words: Second Sound-Thermoelasticity-Method of Characteristics-MacCormack's Method.

1 Introduction

Several review papers on second sound have appeared recently in literature [1, 2, 3]. It is well known that if Fourier's Law for heat conduction is assumed along with the Principle of Local State, an infinite speed of propagation of thermal effects is predicted, consequently the theory is flawed. Several theories have been proposed which take into consideration the finite speed propagation of thermal signals. In this research two theories of second sound have been applied. We obtain the first theory, henceforth described as Theory 1 when Maxwell-Cattaneo Law replaces Fourier's Law of heat conduction. The following inequality

$$\mathbf{q} \cdot \text{grad} T \leq 0, \quad (1)$$

where \mathbf{q} and T are heat flux vector and temperature, respectively, follows from Clausius-Duhem inequality when the Principle of Local State is assumed, regardless of heat conduction law. The Clausius-Duhem inequality follows, in turn, from the Second Law of Thermodynamics when entropy flux is due solely to heat conduction [4]. However, inequality (1) may be violated for certain problems when Theory 1 is adopted. The significance of this violation is investigated for the problem considered. The second theory considered, henceforth described as Theory 2, is a linearized version of a theory proposed by Green and Lindsay [5]. This theory is not based on Principle of Local State and is thermodynamically consistent.

Second sound theories involve one or more thermal relaxation times, for example Green and Lindsay's theory involves two relaxation times, and these relaxation times are assumed equal. Results are obtained for relaxation times representative of metals which are of the order of magnitude 10^{-11} s.

Two independent numerical schemes are used to obtain the solutions to these problems. The first scheme is based on application of method of characteristics and is discussed in detail in a recent reference of Harmain *et al.*, [6]. The second scheme is based on application of MacCormack's method which is a predictor-corrector type of scheme for solution of a system of hyperbolic equations. Numerical results are obtained from finite difference forms of the relations along the five families of the characteristics and from MacCormack's method. The method of characteristics indicates that there are two wave speeds one which is essentially mechanical and the other essentially thermal. It was found that MacCormack's method does not always give satisfactory results when thermal wave speed is greater than mechanical wave speed.

The results indicate that, for the problem considered, the stress and heat flux distributions predicted for various theories are almost identical however, the temperature distributions are significantly different for times of the order of magnitude of the relaxation time. The classical coupled thermoelastic theory is governed by a system of parabolic partial differential equations consequently the above numerical schemes are not applicable.

We consider cylindrically symmetric longitudinal waves propagating from a cylindrical cavity, in an unbounded medium which is initially unstressed, at rest and at a uniform reference temperature T_0 . Assuming a plane strain condition and we define a cylindrical polar coordinate system with the z -axis aligned with the longitudinal axis of the cylinder, r the radial distance from the axis, a is the cavity radius and ϕ denotes the azimuthal angle.

The initial conditions for the problems are:

$$\sigma_r(r, 0) = \sigma_\phi(r, 0) = \theta(r, 0) = 0, \quad (2)$$

where σ_r and σ_ϕ are the radial and circumferential stress components, respectively, and $\theta = T - T_0$, and T the temperature. Furthermore, we assume $\frac{\theta}{T_0} \ll 1$. The boundary conditions for the first problem are:

$$\sigma_r(a, t) = \sigma_0 H_1(t), \theta(a, t) = 0, \quad (3)$$

where σ_0 is a constant, and $H_1(t)$ is the unit step function. For the second problem, the boundary conditions are

$$\begin{aligned} \sigma_r(a, t) &= 0, \\ \theta(a, t) &= f(t)H_1(t), \end{aligned} \quad (4)$$

where $f(t) = t\theta_0/t_1$, and $f(t) = \theta_0$ for $t \geq t_1$, and $\theta_0 \ll T_0$ is a constant.

2 Governing Equations

Equation of motion, with body forces neglected is,

$$\frac{\partial v}{\partial t} - \frac{1}{\rho} \left(\frac{\partial \sigma_r}{\partial r} + \frac{\sigma_r - \sigma_\phi}{r} \right) = 0, \quad (5)$$

where ρ is the mass density, v is the particle velocity in the radial direction. Furthermore, for both theories the non-trivial infinitesimal strain components are given by

$$e_r = \frac{\partial u}{\partial r}, \quad (6)$$

$$e_\phi = \frac{u}{r}. \quad (7)$$

From time derivatives of Equations (6 and 7) we obtain the compatibility equations,

$$\frac{\partial e_r}{\partial t} - \frac{\partial v}{\partial r} = 0, \quad (8)$$

$$\frac{\partial e_\phi}{\partial t} - \frac{v}{r} = 0. \quad (9)$$

The constitutive equations are given by,

$$\sigma_r = 2\mu e_r + \lambda(e_r + e_\phi) - K\alpha(\theta + n\tau\dot{\theta}). \quad (10)$$

$$\sigma_\phi = 2\mu e_\phi + \lambda(e_r + e_\phi) - K\alpha(\theta + n\tau\dot{\theta}). \quad (11)$$

The energy equation is given by,

$$\begin{aligned} \rho c(n\tau\ddot{\theta} + \dot{\theta}) + K\alpha(\dot{e}_r + \dot{e}_\phi)(T + n\tau\dot{\theta}) \\ + \frac{\partial q}{\partial r} + \frac{q}{r} = 0. \end{aligned} \quad (12)$$

where superposed dot denotes partial differentiation with respect to time, μ and λ are Lamé's constants. $K = (2\mu/3 + \lambda)$ is the bulk modulus, α is the volume coefficient of thermal expansion, τ is the relaxation time and $n = 0(1)$ for Theory 1(2), and c is the specific heat(per unit mass) at constant strain. It follows from the analysis given by Green and Lindsay [5], that Fourier's Law for heat conduction

$$q = -k \frac{\partial \theta}{\partial r}. \quad (13)$$

where k is the thermal conductivity, is valid for Theory 2, so that there is a further compatibility equation

$$\frac{\partial q}{\partial t} = -k \frac{\partial \dot{\theta}}{\partial r}. \quad (14)$$

The following nondimensionalization scheme has been introduced.

$\bar{T} = T/T_0$, $\bar{\theta} = \theta/T_0$, $\bar{v} = v/c_0$, $\bar{t} = t/\tau$, $\bar{r} = r/(c_0\tau)$, $\bar{\sigma}_r = \sigma_r/(2\mu + \lambda)$, $\bar{\sigma}_\phi = \sigma_\phi/(2\mu + \lambda)$, $\bar{q} = q/((2\mu + \lambda)c_0)$, $\bar{s} = s/c$, $\bar{K} = K/(2\mu + \lambda)$, $\bar{\alpha} = \alpha T_0$, where s denotes the entropy, $c_0 = ((2\mu + \lambda)/\rho)^{1/2}$.

In nondimensionalized equations, a superposed dot denotes partial differentiation with respect to nondimensionalized time. Henceforth, unless, otherwise indicated, nondimensionalized quantities are used and the overbars are omitted for convenience. The wave speeds which appear later are nondimensionalized by dividing by c_0 . The governing equations in the nondimensionalized form for the given nondimensionalization scheme is in matrix form as follows.

$$\begin{aligned} \begin{bmatrix} e_r \\ e_\phi \\ q \\ \theta \\ v \end{bmatrix}_t + \begin{bmatrix} 0 & 0 & 0 & 0 & -1 \\ 0 & 0 & 0 & 0 & 0 \\ 0 & 0 & 0 & M & 0 \\ 0 & 0 & N & 0 & L \\ -1 & -P & 0 & F & 0 \end{bmatrix} \begin{bmatrix} e_r \\ e_\phi \\ q \\ \theta \\ v \end{bmatrix}_r \\ + \begin{bmatrix} 0 \\ v/r \\ q \\ Lv/r \\ -Q(e_r - e_\phi)/r \end{bmatrix} = 0. \end{aligned} \quad (15)$$

Here the constants have the following meanings, $F = \alpha K T_0 / \rho c_0^2$, $L = K\alpha / \rho c$, $M = k T_0 / (2\mu + \lambda) \tau c_0^2$, $N = (2\mu + \lambda) / \rho c T_0$, $P = \lambda / \rho c_0^2$, $Q = 2\mu / \rho c_0^2$, $\zeta = (FL)^{1/2}$ is the coupling coefficient of classical thermoelasticity, and $\eta = (MN)^{1/2}$ is the uncoupled thermal wave speed. The subscripts r and t with matrices denote partial derivatives of the quantities within matrices w.r.t subscripts.

The governing equations for Theory 2 are

$$\begin{bmatrix} e_r \\ e_\phi \\ q \\ \theta \\ v \end{bmatrix}_t + \begin{bmatrix} 0 & 0 & 0 & 0 & -1 \\ 0 & 0 & 0 & 0 & 0 \\ 0 & 0 & 0 & M & 0 \\ 0 & 0 & N & 0 & L \\ -1 & -P & 0 & F & 0 \end{bmatrix} \begin{bmatrix} e_r \\ e_\phi \\ q \\ \theta \\ v \end{bmatrix}_r + \begin{bmatrix} 0 \\ -v/r \\ 0 \\ \dot{\theta} + Lv/r \\ -qG - Q(e_r - e_\phi)/r \end{bmatrix} = 0 \quad (16)$$

where $G = \alpha K c_0^2 \tau / k$.

3 Methods of Solution

3.1 Method of Characteristics

The system of equations given above in Equation (15) represents the five families of characteristics in (r, t) plane,

$$\frac{dr}{dt} = \pm \lambda_1, \frac{dr}{dt} = \pm \lambda_2, \frac{dr}{dt} = 0, \quad (17)$$

where, λ_1, λ_2 are the wave speeds, and are given by, $\lambda_{(1)} = (G + \sqrt{G^2 - 4H})/2$, $\lambda_{(2)} = (G - \sqrt{G^2 - 4H})/2$ where $FL + MN + 1 = G$ and $MN = H$. The relations along the characteristics can be obtained using the procedure in Whitham [7] and are

$$\frac{de_\phi}{dt} - \frac{v}{r} = 0, \quad (18)$$

on $\frac{dr}{dt} = 0$.

$$\begin{aligned} \frac{de_r}{dt} + P \frac{de_\phi}{dt} - (\lambda_i - \lambda_i^{-1}) \frac{N}{L} \frac{dq}{dt} - \\ (\lambda_i^2 - 1) \frac{1}{L} \frac{d\theta}{dt} - \lambda_i \frac{dv}{dt} - P \frac{v}{r} \\ - (\lambda_i - \lambda_i^{-1}) \frac{Nq}{L} - (\lambda_i^2 - 1) \frac{v}{r} \\ + \frac{Q(e_r - e_\phi)\lambda_i}{r} = 0, \end{aligned} \quad (19)$$

on $\frac{dr}{dt} = \pm \lambda_i$, $i \in \{1, 2\}$.

3.2 MacCormack's Method

An alternative numerical method for solving hyperbolic systems of partial differential equations was proposed by MacCormack [8], which is a finite difference predictor-corrector scheme. The independent variables for Theory 1 are

$$U = \{e_r, e_\phi, v, q, \theta\}, \quad (20)$$

Similarly for Theory 2 the independent variables are

$$W = \{e_r, e_\phi, v, q, \dot{\theta}\}, \quad (21)$$

where U , and W denote the independent variables in general for Theory 1 and Theory 2 respectively. The above systems of equations for Theory 1 can be expressed as:

$$\frac{\partial U}{\partial t} + \frac{\partial \{H(U)\}}{\partial r} + b(U) = 0, \quad (22)$$

where $H(U)$ and $b(U)$ are functions of U . For this system, the implementation of MacCormack's method is for predictor step as:

$$U_j^{(\overline{m+1})} = U_j^m - \frac{\Delta t}{\Delta R} \{H(U_{j+1}^m) - H(U_j^m)\} - \Delta t b(U_j^m). \quad (23)$$

Similarly for corrector step the resulting equations are in the form,

$$U_j^{(m+1)} = \frac{1}{2} (U_j^m + U_j^{(\overline{m+1})}) - \frac{\Delta t}{\Delta r} \{H(U_j^{(\overline{m+1})}) - H(U_{j-1}^{(\overline{m+1})})\} - \Delta t b(U_j^{(\overline{m+1})}). \quad (24)$$

The term U_j^m represents the finite difference approximation for U at a grid point $(1 + j\Delta r, m\Delta t)$. The superscript refers to an index of a discrete time step Δt , and the subscript refers to an index of discrete space step Δr . The overbar notation has been used to indicate the predictor components, and notation without any overbar indicates the corrector components.

4 Discontinuity relations

Since the above systems of equations are in conservation form, the discontinuity relations, which relate the jumps in $\{e_r, v, q, \theta\}$ for Theory 1, and $\{e_r, v, q, \dot{\theta}\}$ for Theory 2 can be obtained as per methodology given by Whitham [7]. The jump relations for Theory 1 are as follows,

$$V[e_r] + [v] = 0, \quad (25)$$

$$V[q] - M[\theta] = 0, \quad (26)$$

$$V[\theta] - N[q] - L[v] = 0, \quad (27)$$

$$V[v] + [e_r] - F[\theta] = 0, \quad (28)$$

where V is the velocity of the discontinuity and the brackets $[\]$ denote the jump of the enclosed quantity across a discontinuity.

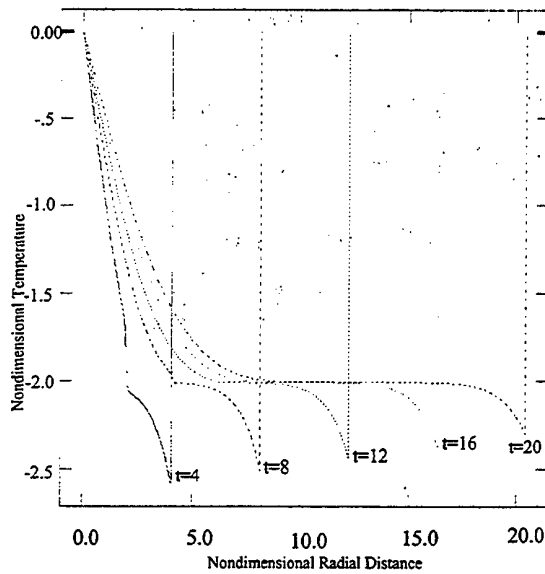


Figure 1: The plot for temperature for relaxation time $8 \times 10^{-12}s$ for Theory 1.

Since linear theory is considered, the discontinuity velocities are given by $V = \pm \lambda_1$ and $V = \pm \lambda_2$, that is discontinuities travel along characteristics. A detailed discussion regarding stress and temperature discontinuities has been given by Achenbach [9]. Also, for material integrity, the radial displacement component is continuous, and hence $[e_\phi] = 0$. These points also hold for Theory 2.

5 Results

Results were obtained from finite difference schemes based on the method of characteristics and MacCormack's method for relaxation time $\tau = 8.0 \times 10^{-12}s$ and for $\tau = .5 \times 10^{-12}s$ for an aluminum alloy. The following property values, typical for an aluminium alloy have been used,
 $k = 217W/mK$, $c = 946J/kgK$,
 $\alpha = 7.7 \times 10^{-5}/K$, $c_0 = 6198m/s$,
 $K = 68.6Gpa$, $\rho = 2700kg/m^3$
 $T_0 = 293K$.

For this set of data the value of λ_1 and λ_2 are 1.0208 and .51506 respectively for a relaxation value of $8.0 \times 10^{-12}s$, 2.112581 and 0.99552 for a relaxation time of $.5 \times 10^{-12}s$.

The results indicate that two sets of discontinuities propagating along the slow and fast characteristics. When $\eta < (1+(\zeta)^2)^{1/2}$ then fast wave is essentially mechanical, while for the cases $\eta > (1+(\zeta)^2)^{1/2}$ the fast wave is essentially thermal. Some of the results are presented in Figures 1 and 2, for Theory 1.

References

- [1] Joseph, D. D., *et al.*, "Heat Waves," Rev. Mod. Phys. vol 61 no 1 (1989).

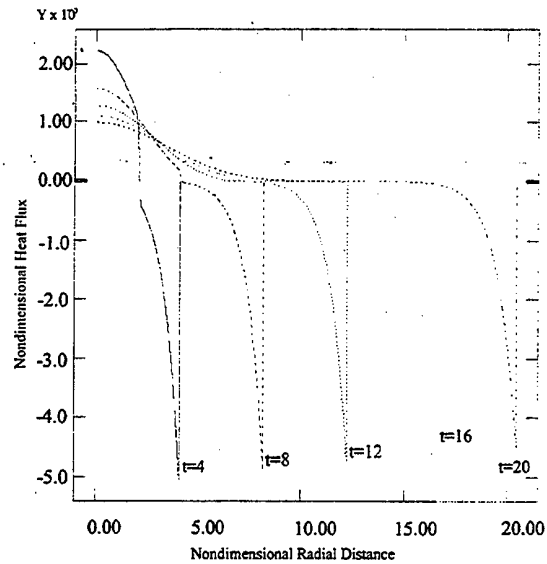


Figure 2: The plot for heat flux for relaxation time $8 \times 10^{-12}s$ for Theory 1.

- [2] Özisik, M. N., and Tzou, D. Y., "On the Wave Theory in Heat Conduction," HTD-Vol 227 Fundamental Issues in Small Scale Heat Transfer, ASME, (1992).
- [3] Chandrashekharaiiah, D. S., "Thermoelasticity with Second Sound," Appl. Mech. Rev., Vol 39, No 3, (1986).
- [4] Lavenda, B. H., "Thermodynamics of Irreversible Processes," Dover, (1993).
- [5] Green, A. E., and Lindsay, K., "Thermoelasticity," J. Elasticity, Vol. 2, pp 1-7, (1972).
- [6] Harmain, G. A., Wegner, J. L., Su, J., Had-dow, J. B., "Coupled Radially Symmetric Linear Thermoelasticity," Accepted for Publication in International Journal of Wave Motion.
- [7] Whitham, G. B., "Linear and Nonlinear Waves," Wiley Interscience, New York, (1974).
- [8] MacCormack, R. W., "The Effect of Viscosity in Hypervelocity Impact Cratering," AIAA paper, pp. 69-354, Cincinnati, Ohio, (1969).
- [9] Achenbach, J. D., "The Influence of Heat Conduction on Propagating Stress Jumps," J. Mech. Phys. Solids, Vol. 16, pp. 273 -282, (1968).

Acknowledgements

Financial and computational support of Professor James W. Provan, Dean faculty of Engineering of University of Victoria, B. C., Canada is greatly appreciated.

Wave Propagation In Thermoelastic Cylindrical Shell Containing Fluid

A. Sarkisyan*

* Department of Solid Mechanics, Yerevan State University, A. Manukyan str. 1, Yerevan, 375049, ARMENIA

The shell-fluid and shell-temperature systems are considered for solution of wave propagation problem in thermoelastic cylindrical shell containing ideal fluid: one-dimensional and two-dimensional. For these cases we get expressions for wave propagation velocity; numerical realization is done for these cases. The same problem is done taking into account unimoment consideration of problem for shell containing one-dimensional model of fluid as well as two-dimensional model. Results are compared. Well-known Zhukovski's formula is generalized on case of presence of temperature field.

Key Words: Wave Propagation, Shell, Thermal Stresses, Fluid.

1. Formulation of the problem and introduction of basic equations.

We consider axis-symmetric wave propagation of infinitely long isotropic cylindrical shell (radius R , thickness h , density ρ , Young modulus E) containing ideal fluid with density ρ_0 . Suppose that shell vibrations pass through thermo-delivery process which creates thermal stresses, i.e. we have thermal connected problem. Let temperature field within shell varies by the following way [1]:

$$T = \theta_1 + z \theta_2. \quad (1)$$

Shell motion equations are known from [2]

$$\frac{\partial T_1}{\partial x} = \rho h \frac{\partial^2 u}{\partial t^2}, \quad (2)$$

$$\frac{\partial^2 M_1}{\partial x^2} - \frac{T_2}{R} + T_0 \frac{\partial^2 w}{\partial x^2} + P = \rho h \frac{\partial^2 w}{\partial t^2}$$

where P - fluid pressure, T_1 , T_2 - loads, T_0 - initial loading of shell middle surface, u, w - displacements of middle surface.

Taking into account expression (1) we have following thermoconductivity equations [3]

$$\frac{\partial \theta_1}{\partial t} - \chi \frac{\partial^2 \theta_1}{\partial x^2} + \frac{2k^*}{c_p \rho h} \theta_1 +$$

$$+ \eta \chi \left[\frac{\partial^2 u}{\partial t \partial x} + \frac{1}{R} \frac{\partial w}{\partial t} \right] = 0, \quad (3)$$

$$\frac{\partial \theta_2}{\partial t} - \chi \frac{\partial^2 \theta_2}{\partial x^2} + \left[\frac{12\chi}{h^2} + \frac{6k^*}{c_p \rho h} \right] \theta_2 -$$

$$- \eta \chi \frac{\partial^3 w}{\partial x^2 \partial t} = 0$$

where χ - thermoconductivity coefficient, k^* - coefficient of body surface thermochanging, c_p - unit thermocapacity, $\eta = (3\lambda + 2\mu)\alpha T / c_p \rho \chi$, α - temperature expansion coefficient, λ, μ - Lamé constants.

2. Shell containing two-dimensional model of fluid.

For two-dimensional model of fluid we know from [4] following equations

$$\Delta \varphi = 0, \quad (4)$$

$$P = \rho_0 \frac{\partial \varphi}{\partial t}$$

where φ - potential function, Δ - Laplas operator.

We can introduce potential function by means of Bessel's functions [5]. Then introducing solution of thermoelasticity system (2)-(3) by means of exponential function, we get new representation of fluid pressure

$$P = \rho_0 w_0 \frac{\omega^2 I_0(kR)}{k I_1(kR)} \exp(\omega t - kx) \quad (5)$$

here w_0 - unknown coefficient, $I_0(kR)$, $I_1(kR)$ - Bessel's functions, k - wave number, ω - frequency.

For this general case we get sixth order dispersion equation. For case of absence of temperature field we get forth order dispersion equation.

Table 1. Values for Bessel's functions.

$1/kR$	1	2	5	10
$I_0(kR)/I_1(kR)$	2.24	4.12	10.05	20.02

From following given quantities: $\rho_0/\rho = 0.94$, Poisson coefficient $\nu = 0.3$, $T_0/Eh = 0.15$ and from values of table 1 for $h/R = 1/20$ dimensions shell in shell-fluid system for waves with small frequencies

($\frac{\partial^2 u}{\partial t^2} = 0$) we have following representation (fig. 1):

$$\frac{v}{c} = \sqrt{\frac{1 + \frac{T_0}{Eh} + \frac{(kR)^2}{12(1-v^2)} \left(\frac{h}{R}\right)^2}{1 + \frac{\rho_0 I_0(kR)}{\rho I_1(kR)} \frac{1}{kh}}} \quad (6)$$

where $c^2 = E/\rho$ is known Moense-Kortevég' formula [6].

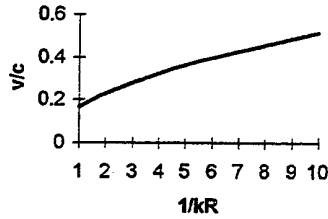


Figure 1. Shell containing two-dimensional model of fluid.

Taking into account unmoment consideration of problem ($M_1 = T_0 = \theta_2 = 0$) we get fifth order dispersion equation. Analogously, the order of equation decreased in absence of temperature field till forth order, and for small frequencies waves (fig.2) by the same condition we get

$$\frac{v}{c} = \frac{1}{kR \sqrt{1 + \frac{\rho_0 I_0(kR)}{\rho I_1(kR)} \frac{1}{kh}}} \quad (7)$$

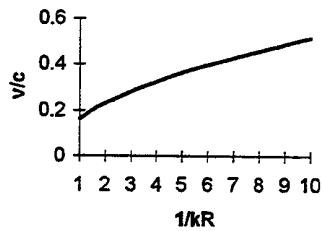


Figure 2. Shell containing two-dimensional model of fluid (unmoment consideration).

As it is seen approximately there are no differences between these two cases.

3. Shell containing one-dimensional model of fluid.

For one-dimensional model of fluid there are following equations [7]

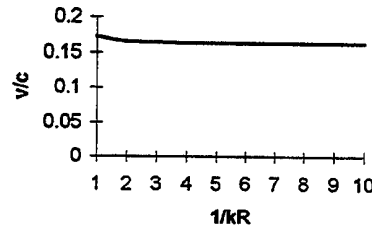
$$\begin{aligned} \frac{1}{\rho_0} \frac{\partial P}{\partial x} + \frac{\partial v}{\partial t} &= 0, \\ \frac{\partial v}{\partial x} + \frac{2}{R} \frac{\partial w}{\partial t} &= 0 \end{aligned} \quad (8)$$

Here we also get sixth order dispersion equation. In shell-fluid system we get forth order dispersion equation, and in this system in case of $\frac{\partial^2 u}{\partial t^2} = 0$ we get (fig. 3)

$$\frac{v}{c} = \sqrt{\frac{1 + \frac{T_0}{Eh} (kR)^2 + \frac{k^4 R^2 h^2}{12(1-v^2)}}{(kR)^2 + \frac{2\rho_0 R}{\rho h}}} \quad (9)$$

Comparing figures 1 and 3 we can see that in case of wave propagation problem in shell containing one-dimensional model of fluid the velocity of wave propagation decreased while in case of two-dimensional model the velocity is increased.

Figure 3. Shell containing one-dimensional model of fluid.



For the same problem but in unmoment consideration we get (fig.4)

$$\frac{v}{c} = \frac{1}{\sqrt{(kR)^2 + \frac{2\rho_0 R}{\rho h}}} \quad (10)$$

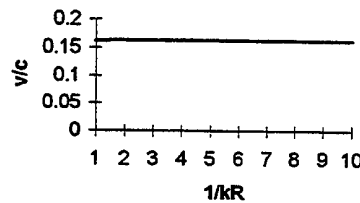


Figure 4. Shell containing one-dimensional model of fluid (unmoment consideration).

From figures 2 and 4 (in point of view of unmoment consideration problem) we can see that for two-dimensional models of fluid velocity increases while for one-dimensional velocity remains quasi-constant. Considering so called "dry" shell, i.e. wave propagation problem without any fluid, we indicate quasi-linear dependency (fig.5)

$$\frac{v}{c} = \sqrt{\frac{1}{(kR)^2} + \frac{k^2 h^2}{12(1-v^2)}} \quad (11)$$

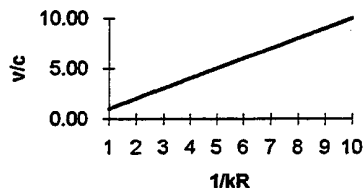


Figure 5. "Dry" shell.

4. Shell-temperature system.

We consider shell-temperature system taking into account unmoment consideration of problem. In case of smallness of inertial term ($\frac{\partial^2 u}{\partial t^2} = 0$), from thermoelasticity equations the problem comes to following system:

$$\frac{\partial T_1}{\partial x} = 0, \quad (12)$$

$$\frac{T_2}{R} + \rho h \frac{\partial^2 w}{\partial t^2} = 0,$$

$$\frac{\partial \theta_1}{\partial t} - \chi \frac{\partial^2 \theta_1}{\partial x^2} + \frac{2k^*}{c_p \rho h} \theta_1 +$$

$$+ \eta \chi \left[\frac{\partial^2 u}{\partial t \partial x} + \frac{1}{R} \frac{\partial w}{\partial t} \right] = 0,$$

from which dispersion equation obtained:

$$[1 + \alpha \eta \chi (1 + \nu)] \omega^3 - i \left(\chi k^2 + \frac{2k^*}{c_p \rho h} \right) \omega^2 - \frac{E}{\rho R^2} (1 + 2\alpha \eta \chi) \omega + \frac{E i}{\rho R^2} \left(\chi k^2 + \frac{2k^*}{c_p \rho h} \right) = 0 \quad (13)$$

In case of absence of connection for frequencies we have

$$\omega_{1,2} = \pm \frac{1}{R} \sqrt{\frac{E}{\rho}} \quad (14)$$

$$\omega_3 = \frac{i \left(\chi k^2 + \frac{2k^*}{c_p \rho h} \right)}{(1 + \alpha \eta \chi (1 + \nu))}$$

Approach roots of this equation introduced in such form which takes into account smallness of thermal connection (η). Then, introducing solution of equation (13) in form

$$(\omega - \omega_1 + a_1) (\omega + \omega_2 + a_2) (\omega - \omega_3 + a_3) = 0 \quad (15)$$

where a_i - small quantities which characterize smallness of connection.

Comparing equation (13) with equation (15) for a_i we get

$$\text{Re} a_{1,2} = \frac{\pm \frac{1}{2} \frac{E}{\rho R^2} \alpha \eta \chi (1 - \nu) (1 + \alpha \eta \chi (1 + \nu))}{\left(\chi k^2 + \frac{2k^*}{c_p \rho h} \right)^2 + \frac{E}{\rho R^2} (1 + \alpha \eta \chi (1 + \nu))^2} \quad (16)$$

a_3 -image number characterized damping process.

Therefore, we get expression for velocity of wave propagation in thermoelastic cylindrical shell

$$v = \pm \frac{1}{kR} \sqrt{\frac{E}{\rho}} \left[1 - \frac{\frac{1}{2} \frac{E}{\rho R^2} \alpha \eta \chi (1 - \nu) (1 + \alpha \eta \chi (1 + \nu))}{\left(\chi k^2 + \frac{2k^*}{c_p \rho h} \right)^2 + \frac{E}{\rho R^2} (1 + \alpha \eta \chi (1 + \nu))^2} \right] \quad (17)$$

5. Zhukovskii's formula in case of temperature field.

Here we generalize well-known formula of pulse-wave velocity [6].

Supposing $T_1 = 0$ and

$$T_2 = E h (w/R - \alpha \theta_1) \quad (18)$$

thermoconductivity equation in this case is

$$[1 + \alpha \eta \chi (1 + \nu)] \frac{\partial \theta_1}{\partial t} - \chi \frac{\partial^2 \theta_1}{\partial x^2} + \frac{2k^*}{c_p \rho h} \theta_1 + \quad (19)$$

$$+ \frac{\eta \chi}{R} (1 - \nu) \frac{\partial w}{\partial t} = 0$$

Considering blood as a one-dimensional model we have equations (8).

Taking into account (18), shell motion equation will be

$$E h \left[\frac{1}{R} \frac{\partial^2 w}{\partial x^2} - \alpha \frac{\partial^2 \theta_1}{\partial x^2} \right] = 2 \rho_0 \frac{\partial^2 w}{\partial t^2} \quad (20)$$

which in couple with thermoconductivity equation (19) is closed system from which we get cubic dispersion equation

$$[1 + \alpha \eta \chi (1 + \nu)] \omega^3 - i \left(\chi k^2 + \frac{2k^*}{c_p \rho h} \right) \omega^2 - \omega \frac{E h k^2}{2 \rho_0 R} (1 - 2\alpha \eta \chi \nu) + \frac{E h k^2}{2 \rho_0 R} i \left(\chi k^2 + \frac{2k^*}{c_p \rho h} \right) = 0 \quad (21)$$

In case of absence of connection

$$\omega_{1,2} = \pm k \sqrt{\frac{Eh}{2\rho_0 R}} \quad (22)$$

$$i \left(\chi k^2 + \frac{2k^*}{c_p \rho h} \right)$$

$$\omega_3 = \frac{(1 + \alpha \eta \chi (1 + \nu))}{(1 + \alpha \eta \chi (1 + \nu))}$$

from which for wave propagation velocity $c^2 = Eh/2\rho_0 R$. This formula is obtained in [6] and it is called Zhukovski's formula.

Now let's introduce the roots of equation (21) in form which takes into account smallness of connection, i.e. in form (15).

Analogously to previous case for wave propagation velocity in case of temperature field we get

$$v = \pm \sqrt{\frac{Eh}{2\rho_0 R}} \left[1 - \frac{\frac{Eh k^2}{4\rho_0 R} \alpha \eta \chi (1 + 3\nu)(1 + \alpha \eta \chi (1 + \nu))}{\left(\chi k^2 + \frac{2k^*}{c_p \rho h} \right)^2 + \frac{Eh k^2}{2\rho_0 R} (1 + \alpha \eta \chi (1 + \nu))^2} \right] \quad (23)$$

This formula is generalization of Zhukovski formula,

which is well-known in biomechanics as a pulse wave propagation velocity.

References

1. Parkus, G., Nonstationar Thermal Stresses, (in Russian), Moscow, p.252, 1963.
2. Novozhilov, V., Theory of Thin Elastic Shells, (in Russian), Leningrad, p.275, 1962.
3. Novatcki, V., Dynamic Problems of Thermoelasticity, (in Russian), Moscow, p.255, 1970.
4. Sedov, L., Solid Mechanics, (in Russian), Moscow, Vol., 1973.
5. Korenev, B., Some Problems of Elasticity Theory, solving by means of Bessel's Functions, (in Russian), Moscow, p.450, 1960.
6. Caro, C., Pedley, T., Schroter, R., Seed, W., The Mechanics of Circulation, Oxford University Press, New York, Toronto, 1978.
7. Ambartsumyan, S., Movsisyan, L., On Problem of Pulse Wave Propagation, Mechanics of Polymers, Riga, #4, pp.696-702, 1978.

Coupled Problem of a Thermoelastic Plate in Elliptical Shape

D. Trajkovski* and R. Cukic**

* Faculty of Technical Engineering, University St. Kliment Ohridski, Ivo Ribar Lola b.b., 97000 Bitola
MACEDONIA

** Faculty of Mechanical Engineering, University in Belgrade, 27 Marta 80, 11000 Belgrade
YUGOSLAVIA

Coupled dynamic problem of a thermoelastic plate in elliptical shape due to a thermal shock on its surface is analyzed. By making use of the integral transform method the system of partial differential equations of the coupled problem is reduced to a system of integral equations regarding to time. The solutions are given in forms of series of Mathieu functions of first and second kind both for a free supported and a clamped plate.

Key words: Elliptical Plate, Coupled Dynamic Problem, Thermoelasticity, Integral Transforms

1. Introduction

Rapid thermal processes, caused by a thermal shock, are very interesting from a view point of thermoelasticity since they introduce coupling between the temperature and deformation fields. In solving contour two dimensional problems the integral transform method has many advantages over the method of separating the variables. At present, many transformations in a rectangular and a circular domain, for various kinds of boundary conditions have been developed [1], [2]. Coupled dynamic problems for a rectangular and circular plate have also been solved by Boley and Barber [3], Ignaczak and Nowacki [4], Kovalenko and Karnayukhov [5] and Cukic [6].

In most of the works on a circular plate boundary conditions are satisfied approximately - it is usually assumed that $\nabla^2 w = 0$ on the contour. By taking into a consideration the coupling phenomenon, a frequency change of the vibrations has been found but that correction is far less than the error made by the simplification of the boundary conditions. In this paper it is found a solution of a coupled problem with exact boundary conditions.

2. Basic equations

The equations of the coupled dynamic problem of thermoelasticity for plates has the following nondimensional form [7]:

$$\begin{cases} \nabla^4 \bar{w} + \partial_{\bar{t}} \bar{w} + (1+\nu) \cdot \nabla^2 \bar{\tau} = 0 \\ \nabla^2 \bar{\tau} - \delta \cdot \bar{\tau} - \frac{1}{\bar{\kappa}_1} \cdot \partial_{\bar{t}} \bar{\tau} + \bar{\eta} \cdot \partial_{\bar{t}} \nabla^2 \bar{w} = -\bar{\alpha} \cdot \bar{\Theta}_+ \end{cases} \quad (1)$$

$\bar{\Theta}_+(X^1, X^2, \bar{t}) = \bar{\Theta}(X^1, X^2) \cdot h(\bar{t})$ in the domain of the ellipse $\Omega = \{(0 \leq X^1 \leq \xi) \cap (0 \leq X^2 \leq 2\pi)\}$,

with homogenous initial conditions regarding $\bar{w}, \bar{\tau}, \partial_{\bar{t}} \bar{w}$ and boundary conditions corresponding to a free supported (2,3) or clamped plate (2,4)

$$\bar{w}(X^1 = \xi) = 0, \quad (2)$$

$$\bar{M}_{11}(X^1 = \xi) = -\left[\nabla^2 \bar{w} - \frac{1-\nu}{\bar{\rho}} \cdot \left(\partial_{22} \bar{w} + \frac{\bar{e}^2}{2} \cdot \frac{\sinh 2X^1}{\bar{\rho}} \cdot \partial_1 \bar{w} - \frac{\bar{e}^2}{2} \cdot \frac{\sin 2X^2}{\bar{\rho}} \cdot \partial_2 \bar{w} \right) + (1+\nu) \cdot \bar{\tau} \right]_{X^1=\xi} = 0, \quad (3)$$

$$\partial_1 \bar{w}(X^1 = \xi) = 0, \quad (4)$$

$$\bar{\tau}(X^1 = \xi) = 0, \quad (5)$$

where X^1, X^2 are elliptical coordinates, linked with the Cartesian coordinates with the following relations $Z^1 = e \cdot \cosh X^1 \cdot \cos X^2$, $Z^2 = e \cdot \sinh X^1 \cdot \sin X^2$ (6)

$\nabla^2 = \frac{1}{\bar{\rho}} (\partial_{11} + \partial_{22})$ - the Laplace differential operator,

$$\partial_i = \partial / \partial X^i \quad (i = 1, 2), \quad \nabla^4 = \nabla^2 (\nabla^2), \quad \xi = \text{Arccosh} \frac{1}{\bar{e}}$$

$$\bar{\rho}(X^1, X^2) = \frac{\bar{e}^2}{2} \cdot (\cosh X^1 - \cos X^2); \quad \bar{e} = \frac{e}{a} - \text{nondi-}$$

mensional eccentricity of the ellipse; a, b, e - the longer and shorter axes and the linear eccentricity of the ellipse; $h(\bar{t})$ - the Heavyside function; The nondimensional variables are defined as follows: $\bar{w} = w/a$,

$$\bar{t} = t/(a^2/K), \quad \bar{\tau} = \alpha \cdot \tau, \quad \delta = 12(a/h)^2 \left(1 + \frac{h\alpha}{2\lambda} \right),$$

$$\bar{\kappa}_1 = \frac{\bar{\kappa}}{1+\varepsilon}, \quad \bar{\kappa} = K \cdot \kappa, \quad \bar{\Theta}_+ = \alpha \cdot \Theta_+, \quad \bar{\alpha} = 12 \frac{h\alpha}{2\lambda} \frac{a^3}{h^3},$$

$$\bar{\eta} = \frac{E\alpha_i T_0}{(1-\nu)\lambda\kappa}, \quad \bar{M}_{ij} = \frac{a\bar{M}_{ij}}{D} \quad (i, j = 1, 2), \quad \varepsilon = \frac{1+\nu}{1-2\nu} \bar{\kappa}\bar{\eta}$$

$$\kappa = \lambda/(\rho_0 c_e), \quad K = \sqrt{\rho_0 h/D}, \quad D = Eh^3/(12(1-\nu^2)).$$

The meaning of other constants is accordingly to [7].

3. Transformation of the equations of the system

The system of equations (1) is transformed by means of the Mathieu finite integral transform [8]

$$\mathcal{T}[f(X^1, X^2); X^1, X^2 \rightarrow m, n] = f_{2m, n}^c = \int_0^{2\pi} \int_0^{\xi} f(X^1, X^2) \times \\ \times \rho(X^1, X^2) \text{Ce}_{2m}(X^1, q_{2m, n}) \text{ce}_{2m}(X^2, q_{2m, n}) dX^1 dX^2 \\ m=0, 1, 2, \dots \quad n=1, 2, \dots, \quad (7)$$

where ce_{2m} , Ce_{2m} are the Mathieu functions of first and second kind with even index [9]; $q_{2m, n}$ ($m=0, 1, 2, \dots$) is the n -th root of the transcendental equation

$$\text{Ce}_{2m}(X^1 = \xi, q) = 0 \quad m=0, 1, 2, \dots \quad (8)$$

The inverse transformation is:

$$\mathcal{T}^{-1}[f_{2m, n}^c; m, n \rightarrow X^1, X^2] = f(X^1, X^2) = \\ = \sum_{m=0}^{\infty} \sum_{n=1}^{\infty} \frac{f_{2m, n}^c}{W_{2m, n}} \text{Ce}_{2m}(X^1, q_{2m, n}) \text{ce}_{2m}(X^2, q_{2m, n}), \quad (9)$$

$$W_{2m, n} = \int_0^{2\pi} \int_0^{\xi} \rho(X^1, X^2) [\text{Ce}_{2m}(X^1, q_{2m, n}) \text{ce}_{2m}(X^2, q_{2m, n})]^2 dX^1 dX^2 \quad (10)$$

Both the functions \bar{w} and $\bar{\tau}$, when developed into series in the form (9), satisfy identically the conditions of periodicity, continuity and symmetry with regard to the ellipses axes.

The Laplace transformation [10] is used for transformation the equations (1) from the time domain into the domain of the complex variable p and vice versa:

$$\mathcal{L}[f(\bar{t}); \bar{t} \rightarrow p] = \int_0^{\infty} e^{-p\bar{t}} f(\bar{t}) d\bar{t} = f^*(p) \quad (11)$$

$$\mathcal{L}^{-1}[f^*(p); p \rightarrow \bar{t}] = \frac{1}{2\pi i} \int_{c-i\infty}^{c+i\infty} e^{p\bar{t}} f^*(p) dp, \quad i = \sqrt{-1}.$$

By making application of the transformations (7), (11) onto the equations (1), taking into consideration the rules for transformation the derivatives [10], after inserting the initial and boundary conditions (2), (3), (4) we arrive at

$$(p^2 + \Lambda_{2m, n}^2) \bar{w}_{2m, n}^c - (1 + \nu) \Lambda_{2m, n} \bar{\tau}_{2m, n}^c = S_{2m, n} \sum_{i=0}^{\infty} A_{2i}^{(2m, n)} \Phi_{2i}^* \\ \Lambda_{2m, n} \bar{\kappa}_1 \bar{\eta} p \bar{w}_{2m, n}^c + [p + \bar{\kappa}_1 (\Lambda_{2m, n} + \delta)] \bar{\tau}_{2m, n}^c = \bar{\alpha} \bar{\kappa}_1 \frac{\bar{\theta}_{2m, n}^c}{p} \quad (12)$$

where: $\Lambda_{2m, n} = 4q_{2m, n} / \bar{e}^2$, $S_{2m, n} = \text{Ce}_{2m}'(X^1 = \xi, q_{2m, n})$ $A_{2i}^{(2m, n)}$ are coefficients in the series of Mathieu functions with even index:

$$\text{ce}_{2m}(x, q_{2m, n}) = \sum_{i=0}^{\infty} A_{2i}^{(2m, n)} \cos 2ix. \quad (13)$$

Φ_{2i}^* is a finite cosine transform of the function $\Phi(X^2, \bar{t}) = \nabla^2 \bar{w}(X^1 = \xi, X^2, \bar{t})$,

$$\Phi_{2i} = \int_0^{2\pi} \Phi(X^2) \cdot \cos 2iX^2 dX^2, \quad i=0, 1, 2, \dots \quad (14)$$

The transform Φ_{2i}^* will be found later from the bo-

undary condition (3) or (4). From the system (12) it follows immediately

$$\bar{w}_{2m, n}^c = \frac{1}{p \cdot \Delta_{2m, n}(p)} (1 + \nu) \bar{\alpha} \bar{\kappa}_1 \Lambda_{2m, n} \bar{\theta}_{2m, n}^c + \\ + \frac{1}{\Delta_{2m, n}(p)} [p + \bar{\kappa}_1 (\Lambda_{2m, n} + \delta)] S_{2m, n} \sum_{i=0}^{\infty} A_{2i}^{(2m, n)} \Phi_{2i}^*, \quad (15)$$

$$\bar{\tau}_{2m, n}^c = \frac{1}{p \cdot \Delta_{2m, n}(p)} \bar{\alpha} \bar{\kappa}_1 (p^2 + \Lambda_{2m, n}^2) \bar{\theta}_{2m, n}^c - \\ - \frac{1}{\Delta_{2m, n}} \cdot \frac{\varepsilon_1}{1 + \nu} \Lambda_{2m, n} S_{2m, n} p \sum_{i=0}^{\infty} A_{2i}^{(2m, n)} \Phi_{2i}^*, \quad (16)$$

where $\varepsilon_1 = (1 + \nu) \bar{\kappa}_1 \bar{\eta} = (1 - 2\nu) \frac{\varepsilon}{1 + \varepsilon}$ is the coefficient of coupling between the fields of temperature and deformations for plates; $\Delta_{2m, n}(p) = (p^2 + \Lambda_{2m, n}^2) [p + \bar{\kappa}_1 (\Lambda_{2m, n} + \delta)] + \varepsilon_1 \Lambda_{2m, n} p \approx$

$$\approx [(p^2 + \gamma_{2m, n})^2 + \lambda_{2m, n}^2] \cdot (p + \beta_{2m, n}), \quad (17)$$

$$\gamma_{2m, n} = \frac{\varepsilon_1}{2} \sigma_{2m, n} \mu_{2m, n}, \quad \lambda_{2m, n} = \Lambda_{2m, n} \left(1 + \frac{\varepsilon_1}{2} \sigma_{2m, n}\right),$$

$$\beta_{2m, n} = \mu_{2m, n} (1 - \varepsilon_1 \sigma_{2m, n}), \quad \sigma_{2m, n} = \frac{\Lambda_{2m, n}^2 \mu_{2m, n}}{\Lambda_{2m, n}^2 + \mu_{2m, n}^2}, \\ \mu_{2m, n} = \bar{\kappa}_1 (\Lambda_{2m, n} + \delta). \quad (18)$$

The approximate form for $\Delta_{2m, n}(p)$ is convenient for inversion of the Laplace transforms (15), (16). After applying the inverse transformations (8), (11) we obtain the deflection \bar{w} and the temperature moment $\bar{\tau}$ in the geometrical-time domain:

$$\begin{pmatrix} \bar{w}(X^1, X^2, \bar{t}) \\ \bar{\tau}(X^1, X^2, \bar{t}) \end{pmatrix} = \sum_{m=0}^{\infty} \sum_{n=1}^{\infty} \frac{\text{Ce}_{2m}(X^1, q_{2m, n}) \text{ce}_{2m}(X^2, q_{2m, n})}{W_{2m, n}} \times \\ \times \begin{pmatrix} f_{2m, n}^{(1)}(\bar{t}) \\ f_{2m, n}^{(2)}(\bar{t}) \end{pmatrix} + \int_0^{\bar{t}} \begin{pmatrix} f_{2m, n}^{(2)}(\bar{t} - \theta) \\ -f_{2m, n}^{(4)}(\bar{t} - \theta) \end{pmatrix} \sum_{i=0}^{\infty} A_{2i}^{(2m, n)} \Phi_{2i}(\theta) d\theta \quad (19)$$

In the above equation $f_{2m, n}^{(1)}(\bar{t}) \dots f_{2m, n}^{(4)}(\bar{t})$ are the following inverse Laplace transformations [11]:

$$f_{2m, n}^{(1)}(\bar{t}) = \mathcal{L}^{-1} \left[\frac{1}{p \Delta_{2m, n}(p)} (1 + \nu) \bar{\alpha} \bar{\kappa}_1 \Lambda_{2m, n} \bar{\theta}_{2m, n}^c; p \rightarrow \bar{t} \right]$$

$$f_{2m, n}^{(2)}(\bar{t}) = \mathcal{L}^{-1} \left[\frac{1}{\Delta_{2m, n}(p)} (p + \mu_{2m, n}) S_{2m, n}; p \rightarrow \bar{t} \right]$$

$$f_{2m, n}^{(3)}(\bar{t}) = \mathcal{L}^{-1} \left[\frac{1}{p \Delta_{2m, n}(p)} \bar{\alpha} \bar{\kappa}_1 (p^2 + \Lambda_{2m, n}^2) \bar{\theta}_{2m, n}^c; p \rightarrow \bar{t} \right]$$

$$f_{2m, n}^{(4)}(\bar{t}) = \mathcal{L}^{-1} \left[\frac{p}{\Delta_{2m, n}(p)} \frac{\varepsilon_1}{1 + \nu} \Lambda_{2m, n} S_{2m, n}; p \rightarrow \bar{t} \right] \quad (20)$$

If the thermal shock is induced under the action of uniform temperature field at the surface $Z^3 = h/2$ in the whole region of the plate than the transform $\bar{\theta}_{2m, n}^c$ can be found as

$$\bar{\theta}_{2m, n}^c = \bar{\theta}_0 \int_0^{2\pi} \int_0^{\xi} \rho(X^1, X^2) \text{Ce}_{2m}(X^1, q_{2m, n}) \text{ce}_{2m}(X^2, q_{2m, n}) dX^1 dX^2 \quad (21)$$

4. Finding the function Φ

The last boundary condition (3), after inserting equation (19/1), taking into account the boundary condition (3), becomes

$$\sum_{i=0}^{\infty} \left[a_{k,i} \Phi_{2i}(\bar{t}) - \int_0^{\bar{t}} K_{k,i}(\bar{t}-\theta) \Phi_{2i}(\theta) d\theta \right] = g_k(\bar{t}) \quad \bar{t} \geq 0 \quad k=0,1,\dots \quad (22)$$

The kernels $K_{k,i}$ and the functions g_k on right sides of the integral equations (22) are given in form of series

$$K_{k,i}(\bar{t}) = \pi a_{\xi} \sum_{m=0}^{\infty} \sum_{n=1}^{\infty} \frac{S_{2m,n} A_{2k}^{(2m,n)} A_{2i}^{(2m,n)}}{W_{2m,n}} f_{2m,n}^{(2)}(\bar{t}), \quad (23)$$

$$g_k(\bar{t}) = \pi a_{\xi} \sum_{m=0}^{\infty} \sum_{n=1}^{\infty} \frac{S_{2m,n} A_{2k}^{(2m,n)}}{W_{2m,n}} f_{2m,n}^{(1)}(\bar{t}) \quad k,i=0,1,2,\dots,$$

where $a_{\xi} = \frac{2(1-\nu)}{\xi^2} \sinh 2\xi$, and

$$a_{k,i} = \begin{cases} \left(\frac{1}{2}, k=0 \right) \cdot \left(\cosh^2 2\xi + \frac{1}{2} \right), & k=i \\ -\cosh 2\xi, & |k-i|=1 \\ 1/4, & |k-i|=2 \\ 0 & \text{otherwise} \end{cases} \quad (24)$$

Similarly, in the case of a clamped plate, the boundary condition (4) leads us to a different kind of integral equation:

$$\sum_{i=0}^{\infty} \int_0^{\bar{t}} K_{k,i}(\bar{t}-\theta) \Phi_{2i}(\theta) d\theta = -g_k(\bar{t}), \quad \bar{t} \geq 0 \quad k=0,1,2,\dots \quad (25)$$

$K_{k,i}$ and g_k have been previously defined (eq. (23)).

5. Numerical example

If we insignificantly sacrifice calculus accuracy, the systems (22) and (25) can be reduced to first several equations. It was observed that number of $N=3..6$ equations was sufficient. The cosine transform $\Phi_{2i}(\bar{t})$ ($i=0,1,\dots,N$) of the function $\Phi(X^2, \bar{t}) = \nabla^2 \bar{w}|_{X^1=\xi}$ can be than found from these reduced systems. The deflection \bar{w} and temperature momentum $\bar{\tau}$ in an arbitrary point (X^1, X^2) of the plate at the given time \bar{t} is calculated according to equation (19).

On fig. 1. and 2. first N members of the transform $\Phi_{2i}(\bar{t})$ that correspond to a simply supported ($N=2$) and clamped plate ($N=5$) are shown. It is assumed the plate is made of brass, with longer axis $a=0.5$ m, thickness $h=5$ mm and relative eccentricity $e=0.707$ ($\xi=0.85$). The elastic and thermal properties of the material are given by the following coefficients:

$$\begin{aligned} E &= 12 \cdot 10^{11} \text{ N/m}^2, \quad \nu = 0.42, \quad \alpha_{\tau} = 18.4 \cdot 10^{-6} \text{ K}^{-1}, \\ \rho_0 &= 8600 \text{ kg/m}^3, \quad \lambda = 93 \text{ W/(m} \cdot \text{K)}, \quad \alpha = 20 \text{ W/(m}^2 \cdot \text{K)}, \\ \kappa &= 2.838 \cdot 10^{-5} \text{ m}^2/\text{s}, \quad \vartheta_0 = 320 \text{ K}, \quad T_0 = 293 \text{ K}, \\ D &= 1518 \text{ Nm}, \quad K=0.168 \text{ s/m}^2, \quad \xi = 0.85, \quad \delta = 1.2 \cdot 10^5, \end{aligned}$$

$$\begin{aligned} \bar{\alpha} &= 6452, \quad \bar{\eta} = 1311, \quad \bar{\vartheta}_0 = 5.9 \cdot 10^{-3}, \quad \varepsilon = 0.0558, \\ \bar{\kappa}_1 &= 4.53 \cdot 10^{-6}, \quad \varepsilon_1 = 8.43 \cdot 10^{-3}. \end{aligned}$$

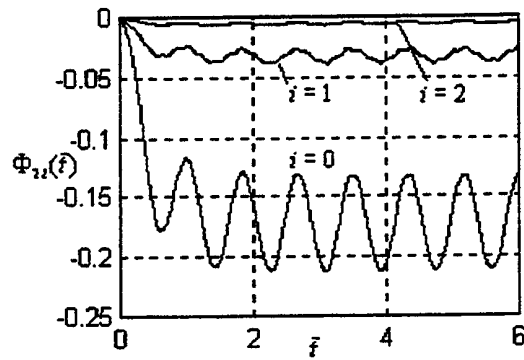


fig.1

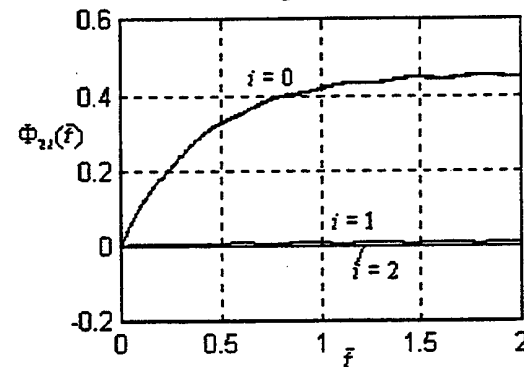


fig.2

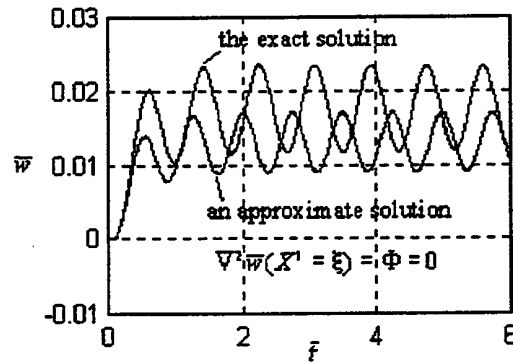


fig.3

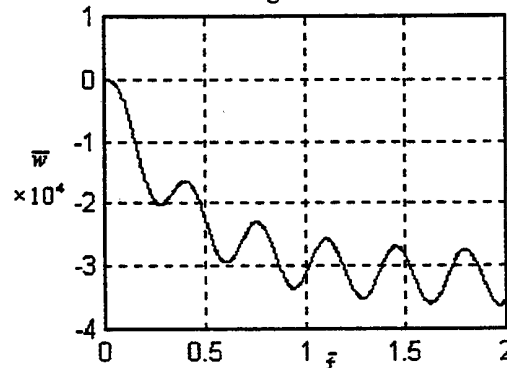


fig.4

On fig. 3. and 4. the deflections in the middle of the plate ($X^1 = 0, X^2 = \pi/2$) versus time are shown. On fig. 5., 6. deflections in one quarter of the elliptical region at the moment $\bar{t} = 1$ are presented.

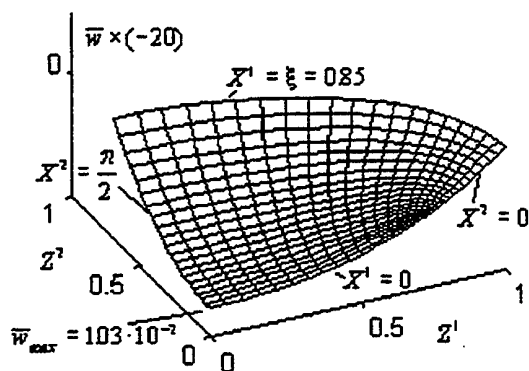


fig.5

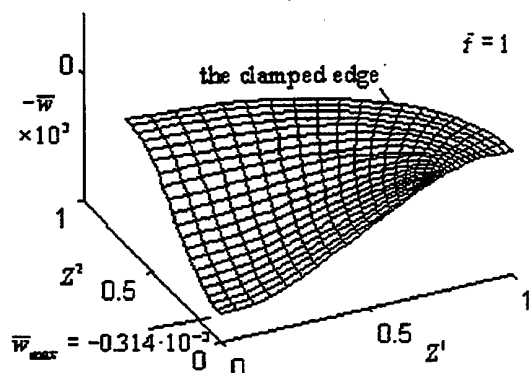


fig.6

The systems (22), (25) were numerically solved. In all sumes in eq. (23) only eigenvalues $q_{2m,n} \leq 35$ ($\Lambda_{2m,n} \leq 280$) were kept. The step of integration depends on the frequency $\lambda_{\max} \approx \Lambda_{\max} \approx 280$ and it should not exceed $\Delta \bar{t}_{\max} = 0.2 \cdot 2\pi / \lambda_{\max} \approx 0.004$

6. Conclusion

1. Involving the function $\Phi(X^2, \bar{t})$ on the contour $X^1 = \xi$ is unnecessary in calculating \bar{t} according to equation (19) (the error is less than 0.4%). The function Φ exerts an influence both on the quantity and frequency of deflections (increasing the quantity by 20% and decreasing the frequency of the fundamental mode by 11%, fig.3.). It means that the plate behaves less rigid at the exact solution.

2. The coupling effect increases the frequency by the factor $1 + \varepsilon_1/2$. This correction is, however, less than the error made when the function Φ and its cosine transform Φ_{2i} are neglected in the equation (19).

3. In the case of stationary temperature field, when $\bar{t} \rightarrow \infty$ for example, the systems (22), (25) are reduced to systems of algebraic equations regarding Φ_{2i} .

4. For the application of the described method it is sufficient to transform only the differential equations of the problem, leaving one or more boundary conditions unsatisfied. The solution obtained by inversion should be inserted into the remaining conditions so that they would be reduced to integral equations regarding some function on the contour (Φ_{2i} in this case). The method is rather universal and increases the flexibility of the integral transform method.

References

- (1) Sneddon I. Preobrazovaniya Furie. Moskva, IL, 1965
- (2) Lukovskii I.A., Galicyn A.S., Zhukovskii A.N. Nekotorye integralnye preobrazovaniya dlya ellipticheskikh oblastei.-in the book: Analiticheskie, chislenie i analogovye metody v zadachah teploprovodnosti. Kiev, "Naukova Dumka", 1977
- (3) Boley B.A., Barber A.D. Dynamic Response of Beams and Plates to Rapid Heating, J. Appl. Mech., 24 (1957), 413
- (4) Ignaczak J., Nowacki W. Transferzal Vibration of a Plate Produced by Heating, Arch. Mech. Stos., 13 (1961), No.5.
- (5) Kovalenko D.A., Karnayukhov G.V. Kolebaniya krugloi plastiny zumovleni teplovym udarom, AN URSS, Ser. A., 1968, No.2.
- (6) Cukic R. Coupled and Uncoupled Problem of Thermoelastic Vibration of a Circular Plate, Bull. de L'Academie Pol. des Sciences, Vol XXII, No.2., 1974
- (7) Nowacki W. Thermoelasticity, PWN publishers, Warszawa, 1986.
- (8) Gupta R.K. A Finite Transform Involving Mathieu Functions and Its Application, Proc. Nat. Inst. Ici. India, 1964, A30, 6.
- (9) Janke E., Emde F., Losch F. Tafeln Hoherer Funktionen, Stuttgart, B.G. Teubner Verlagsgesellschaft, 1960.
- (10) Thomson W.T. Laplace Transformation, Prentice-Hall, New York, 1950.
- (11) Makarov I.M., Menskii B.M. Tablica obratnyh preobrazovanii Laplasy i obratnyh zpreobrazovanii, Moskva, "Vyshaya Shkola", 1978

Propagation of Generalized Thermoelastic Free Waves in Plate of Anisotropic Media

K.L. Verma

Department of Mathematics, Govt. Post Graduate College, Hamirpur, Himachal Pradesh, INDIA 177 005.

Analysis for the propagation of free waves in homogenous anisotropic generalized thermoelastic plate is developed. Secular equation for the monoclinic plate in closed form and isolate the mathematical conditions for symmetric and antisymmetric wave mode propagation in completely separate terms is derived. Material systems of higher symmetry, such as orthotropic, transversely isotropic, cubic and isotropic are contained implicitly in the analysis. It is shown that the motion for SH modes decouple which is not effected by thermal variations from the rest of motion if propagation occurs along an in-plane axis of symmetry. Finally the numerical solution for a isotropic plate is carried out and the dispersion curves for symmetric and antisymmetric are presented by varying the relaxation time.

Key Words: Anisotropic, media, Guided Wave, Thermal Relaxation time, Free wave, Thermoelasticity.

1. Introduction

The study of thermoelastic wave propagation in anisotropic materials is of great practical use in engineering applications especially in the context of modified/generalized theories of thermoelasticity.

Recently, attempts have been made to extend this generalized theory of thermoelasticity to anisotropic elastic media. Banerjee and Pao [1] investigated the propagation of plane harmonic waves in infinitely extended anisotropic solids, taking into account the thermal relaxation time. They showed that four characteristic wave speeds are possible in such types of solids. They further studied the velocity, slowness as well as the wave surfaces of the thermoelastic waves.

Propagation of free guided waves in anisotropic homogeneous plate has been studied in detail by authors [2]-[4]. These studies provide an interesting picture of the rich dispersion characteristic of these guided waves. Several others authors [5]-[11] have studied free Lamb waves.

Propagation of plane harmonic waves in homogenous transversely isotropic heat conducting elastic materials has been investigated [12]-[13]. Recently, the generalized theory of thermoelasticity advanced by Lord and Shulman [14] has been extended to anisotropic elastic bodies by Dhaliwal and Sherief [15].

The present paper is aimed at to study the propagation of free thermoelastic waves in homogeneous anisotropic thermally conducting elastic plate. The analysis for waves to the monoclinic plate is carried to derive the secular equation in the closed form and isolate the mathematical conditions for symmetric and

antisymmetric wave mode propagation in completely separate terms. Materials system of higher symmetry, such as orthotropic, transversely isotropic, cubic and isotropic are contained implicitly in the analysis. It has been found that SH wave which is not effected by temperature variations decoupled from the rest of motion if the propagation occurs along an in-plane axis of symmetry. The results in the case of coupled thermoelasticity can be obtained as special cases by setting $\tau_0 = 0$ in the present analysis. Finally the numerical solution for a isotropic plate is carried out and the dispersion curves for symmetric and antisymmetric are presented by varying the relaxation time τ_0 .

2. Formulatin of the Problem

Consider a homogeneous monoclinic thermally conducting elastic plate, having thickness d , whose normal is aligned with the x_3 - axis of a reference cartesian coordinate system $x_i = (x_1, x_2, x_3)$. The midplane of the plate is chosen to coincide with the $x_1 - x_2$ plane. With respect to this primed coordinate system, the equations of motion and heat conduction equation are [15]

$$\sigma'_{ij,j} = \rho' \ddot{u}_i \quad \dots(1)$$

$$K'_{ij} T'_{,j} - \rho' C_e' (\dot{T} + \tau_0 \ddot{T}) = T_0 \beta'_{ij} (\dot{u}_{i,j} + \tau_0 \ddot{u}_{i,j}) \quad \dots(2)$$

where

$$\begin{aligned} \sigma'_{ij} &= C'_{ijkl} e'_{kl} - \beta'_{ij} T'; \\ \beta'_{ij} &= C'_{ijn} \alpha'_{in} \quad i,j,k,l=1,2,3 \end{aligned} \quad \dots(3)$$

α'_{in} is the thermal expansion tensor, K'_{ij} is the thermal conductivity tensor, ρ' , C_e' and τ_0 are respectively the density the specific heat at constant strain, and thermal relaxation time. In the analysis

usual summation convention holds. The comma notation is used for spatial derivatives and super posed dot for time differentials.

Since σ_{ij} , e_{kl} , α_{kl} and C_{ijkl} are tensors and as here conducting analysis in the global x_i coordinates, any orthogonal transformation of the primed to the non-primed coordinates i.e. x'_i to x_i , transforms according to

$$\begin{aligned}\sigma_{mn} &= \gamma_{mi} \gamma_{nj} \sigma'_{ij} \\ e_{op} &= \gamma_{ok} \gamma_{pl} e'_{kl} \\ C_{mnop} &= \gamma_{mi} \gamma_{nj} \gamma_{ok} \gamma_{pl} C'_{ijkl} \\ \alpha_{kl} &= \gamma_{ki} \gamma_{lj} \alpha'_{ij}\end{aligned}\quad \dots(4)$$

where γ_{ij} is the cosine of the angle between x'_i and x_j , respectively. For rotation of angle ϕ in the $x'_1 - x'_2$ plane, the transformation tensor γ_{ij} reduces to

$$\gamma_{ij} = \begin{bmatrix} \cos \phi & \sin \phi & 0 \\ -\sin \phi & \cos \phi & 0 \\ 0 & 0 & 1 \end{bmatrix} \quad \dots(5)$$

using (4) and (5) in (3) yields

$$\sigma_{ij} = C_{ijkl} \epsilon_{kl} \quad \dots(6)$$

For monoclinic materials having $x'_1 - x'_2$ as a plane of mirror symmetry, $C_{14} = C_{24} = C_{34} = C_{15} = C_{25} = C_{35} = C_{46} = C_{56} = 0$.

$$\dots(7)$$

where the transformation relations between C_{pq} and C'_{pq} are as in [2].

In terms of the rotated coordinate system x_i , the equations of motion and heat conduction transforms to

$$\sigma_{ij,j} = \rho \ddot{u}_i \quad \dots(8)$$

$$K_{ij} T_{,ij} - \rho C_e (\dot{T} + \tau_0 \ddot{T}) = T_0 \beta_j (\dot{u}_{i,j} + \tau_0 \ddot{u}_{i,j}) \quad \dots(9)$$

3. Analysis

Substituting from equation (6)-(7) into equation (8) and (9) results in a system of four coupled equations for the displacements u_1, u_2, u_3 and temperature T . Since the plane wave propagation along the x_1 - direction is independent of x_2 , a formal solution for these displacements and temperature can be written as

$$(u_1, u_2, u_3, T) = (1, V, W, S) e^{i\xi(x_1 + \alpha x_3 - ct)} \quad \dots(10)$$

where ξ is the wave number $i = \sqrt{-1}$, c is the phase velocity ($= \omega/\xi$), ω is the circular frequency, α is still an unknown parameter, V, W are ratios of the displacement amplitudes of u_2 and u_3 to that of u_1 , respectively and S is the ratio of temperature T to that of displacement amplitude u_1 . Although solutions (10) are explicitly independent of x_2 , an implicit dependence is contained in the transformation and transverse displacement component is non-vanishing in equation (10). This choice of solutions leads to the four coupled equations.

$$M_{pq}(\alpha) U_q = 0 \quad p, q = 1, 2, 3, 4 \quad \dots(11)$$

where the summation convention is implied,
 $M_{ij} = M_{ji}$, $i, j = 1, 2, 3$ are same as given in [2]

and

$$\begin{aligned}M_{14} &= i\beta_3/\xi \quad M_{24} = i\beta_6/\xi \quad M_{34} = i\beta_3\alpha/\xi \\ M_{41} &= i\xi T_0 c^2 \tau \beta_1 \quad M_{42} = i\xi T_0 c^2 \tau \beta_6 \\ M_{43} &= i\xi T_0 c^2 \tau \beta_3 \alpha \\ M_{44} &= K_1 + K_3 \alpha^2 - \rho c^2 C_e \tau, \quad \tau = \tau_0 + i/\omega \quad \dots(12)\end{aligned}$$

The system of equations (11) has non-trivial solution if the determinant of the coefficients of U_1, U_2, U_3 and U_4 vanishes, which leads to the eighth degree polynomial equation

$$\alpha^8 + A_1 \alpha^6 + A_2 \alpha^4 + A_3 \alpha^2 + A_4 = 0 \quad \dots(13)$$

where

$$A_1 = [-K_3 A_1 + \Delta' Q_1 + (C_{45}^2 - C_{44} C_{55}) Q_2 \beta_3^2] / \Delta$$

$$\begin{aligned}A_2 &= [-K_3 A_2 + A_1 Q_1 \\ &- \{ (C_{11} C_{44} - 2C_{16} C_{45} + C_{55} C_{66}) - (C_{44} + C_{55}) \beta_3^2 \\ &+ C_{33} C_{55} \beta_6^2 + C_{33} C_{44} \beta_1^2 \\ &- (2C_{13} C_{44} - C_{36} C_{45} + 2C_{44} C_{55} - C_{45}^2) \beta_1 \beta_3 \\ &- 2C_{33} C_{45} \beta_1 \beta_6 \\ &- (2C_{36} C_{45} - 2C_{13} C_{45}) \beta_3 \beta_6 \} Q_2] / \Delta.\end{aligned}$$

$$\begin{aligned}A_3 &= [-K_3 A_3 + A_2 Q_1 - \{ (C_{33} C_{66} + C_{36}^2 + 2C_{36} C_{45} \\ &+ C_{44} C_{55} + C_{45}^2 - (C_{33} + C_{45}) \rho c^2 \} \beta_1^2 \\ &+ ((C_{11} C_{33} - C_{13}^2 - 2C_{13} C_{55}) - (C_{33} + C_{55}) \rho c^2) \beta_6^2 \\ &- ((C_{11} - C_{11} C_{66}) + (C_{11} + C_{66}) \rho c^2 - \rho^2 c^4) \beta_3^2 \\ &- (2C_{13} C_{66} + 2C_{55} C_{66} - C_{16} C_{36} - C_{16} C_{45} - 2 \\ &(C_{13} + C_{55}) \rho c^2) \beta_1 \beta_3 \\ &- (2C_{13} C_{16} - C_{13} C_{36} - 2C_{13} C_{45} - 2C_{36} C_{55} - C_{44} C_{55} \\ &- C_{45} \rho c^2) \beta_1 \beta_6 \\ &- (2C_{11} C_{36} + 2C_{11} C_{45} - 2C_{13} C_{16} - 2C_{16} C_{55} - 2 \\ &(C_{36} + C_{45}) \rho c^2) \beta_3 \beta_6 \} Q_2] / \Delta.\end{aligned}$$

$$\begin{aligned}A_4 &= [A_3 Q_1 - \{ (C_{55} - C_{66} - (C_{55} + C_{66}) \rho c^2 + \rho^2 c^4) \beta_1^2 \\ &+ (C_{11} C_{55} - (C_{11} + C_{55}) \rho c^2 + \rho^2 c^4) \beta_6^2 \\ &+ (2C_{16} C_{55} - 2C_{16} \rho c^2) \beta_1 \beta_6 \} Q_2] / \Delta. \quad \dots(14)\end{aligned}$$

$$\begin{aligned}\Delta &= -K_3 \Delta' \\ Q_1 &= \rho c_e c^2 \tau - K_1 \\ Q_2 &= T_0 c^2 \tau\end{aligned}\quad \dots(15)$$

A_1, A_2, A_3 and Δ' are the coefficient of corresponding equation of sixth degree polynomial for elastic waves [2]. Equation (13) admits eight solutions for α (having the properties)

$$\alpha_2 = -\alpha_1, \alpha_4 = -\alpha_3, \alpha_6 = -\alpha_5, \alpha_8 = -\alpha_7 \quad \dots(16)$$

For each α_q , $q = 1, 2, 3, \dots, 8$, we can use the relations (12) and express $V_q = U_2/U_{1q}$, $W_q = U_3/U_{1q}$ and $S_q = U_4/U_{1q}$ as $V_q = L_1(\alpha_q)/L(\alpha_q)$, $W_q = L_2(\alpha_q)/L(\alpha_q)$, $S_q = L_3(\alpha_q)/L(\alpha_q)$

$$\dots(17)$$

where

$$\begin{aligned}L_1(\alpha_q) &= M_{11} M_{23} M_{34} + M_{12}^2 M_{24} + M_{12} M_{14} M_{33} \\ &- M_{13} M_{14} M_{23} - M_{11} M_{24} M_{33} - M_{12} M_{13} M_{34} \\ L_2(\alpha_q) &= M_{12}^2 M_{34} + M_{11} M_{23} M_{34} + M_{13} M_{14} M_{22} \\ &- M_{12} M_{14} M_{23} - M_{12} M_{13} M_{24} - M_{11} M_{22} M_{24} \\ L_3(\alpha_q) &= M_{12}^2 M_{33} + M_{12}^2 M_{22} + M_{12}^2 M_{11} \\ &- 2M_{12} M_{13} M_{23} - M_{11} M_{22} M_{33} \\ L(\alpha_q) &= M_{14} M_{23}^2 + M_{12} M_{24} M_{33} + M_{13} M_{22} M_{34} \\ &- M_{12} M_{23} M_{34} - M_{13} M_{23} M_{24} - M_{14} M_{22} M_{23} \dots\end{aligned}\quad \dots(18)$$

Combining the equations (17), with the stress strain and temperature relations and using superposition, we finally write the formal solutions for the displacements, temperature, stress and temperature gradient as

$$(u_1, u_2, u_3, T) = \sum_{q=1}^8 (U_1 V_q, W_q, S_q) U_{1q} e^{i\xi(x_1 + \alpha_q x_3 - ct)} \quad \dots(19)$$

$$(\sigma_{13}, \sigma_{13}, \sigma_{23}, T') = \sum_{q=1}^8 (D_{1q}, D_{2q}, D_{3q}, D_{4q}) U_{1q} e^{i\xi(x_1 + \alpha_q x_3 - ct)} \quad \dots(20)$$

Incorporating equations (16) and (17) - (21) and inspecting the resulting relations such as

$$\begin{aligned} W_{j+1} &= -W_j, D_{2j+1} = -D_{2j}, D_{3j+1} = -D_{3j} \\ V_{j+1} &= V_j, D_{1j+1} = D_{1j}, S_{j+1} = S_j, j=1,3,5,7 \dots(21) \end{aligned}$$

$$\begin{aligned} D_{1q} &= [i\xi(C_{13} + 2C_{36}V_q + C_{33}\alpha_q W_q) - \beta_3 S_q] \\ D_{2q} &= [i\xi(2C_{55}(\alpha_q + W_q) + C_{45}\alpha_q V_q)] \\ D_{3q} &= [i\xi(2C_{45}(\alpha_q + W_q) + 2C_{44}\alpha_q V_q)] \\ D_{4q} &= [i\xi\alpha_q S_q] \quad \dots(22) \end{aligned}$$

Calculating the stresses σ_{13} , σ_{23} and temperature gradient T' of (20) at the upper and lower faces

$x_3 = d/2$ and $x_3 = -d/2$ respectively and setting them equal to zero to invoke the stress - free boundary conditions finally yield the eight equations relating the propagation amplitude U_1, U_2, \dots, U_8 , whose determinant of coefficients after algebraic manipulations and reductions leads to the two uncoupled characteristic equations.

$$D_{11} G_1 \cot(\gamma\alpha_1) - D_{13} G_3 \cot(\gamma\alpha_3) + D_{15} G_5 \cot(\gamma\alpha_5) - D_{17} G_7 \cot(\gamma\alpha_7) = 0 \quad \dots(23a)$$

$$D_{11} G_1 \tan(\gamma\alpha_1) - D_{13} G_3 \tan(\gamma\alpha_3) + D_{15} G_5 \tan(\gamma\alpha_5) - D_{17} G_7 \tan(\gamma\alpha_7) = 0 \quad \dots(23b)$$

Corresponding to symmetric and antisymmetric modes respectively with

$$G_1 = \begin{vmatrix} D_{23} & D_{25} & D_{27} \\ D_{33} & D_{35} & D_{37} \\ D_{43} & D_{45} & D_{47} \end{vmatrix}, G_3 = \begin{vmatrix} D_{21} & D_{25} & D_{27} \\ D_{31} & D_{35} & D_{37} \\ D_{41} & D_{45} & D_{47} \end{vmatrix}$$

$$G_5 = \begin{vmatrix} D_{21} & D_{23} & D_{27} \\ D_{31} & D_{33} & D_{37} \\ D_{41} & D_{43} & D_{47} \end{vmatrix}, G_7 = \begin{vmatrix} D_{21} & D_{23} & D_{25} \\ D_{31} & D_{33} & D_{35} \\ D_{41} & D_{43} & D_{45} \end{vmatrix}$$

$$\gamma = \frac{\xi d}{2} = \frac{\omega d}{2c} \quad \dots(24)$$

4. Orthotropic Material

If x_1 and x_2 of equation (3) are chosen to coincide with the in-plane principal axes for orthotropic symmetry then

$$C_{16} = C_{26} = C_{36} = C_{45} = 0, \alpha_{12} = 0 \quad \dots(25)$$

Further more, for transverse isotropy

$$C_{33} = C_{22}, C_{13} = C_{12}, C_{55} = C_{66}$$

$$C_{22} - C_{33} = 2C_{44}, \alpha_{22} = \alpha_{33} \quad \dots(26)$$

and for cubic symmetry

$$\begin{aligned} C_{11} &= C_{22} = C_{33}, C_{12} = C_{13} = C_{23} \\ C_{44} &= C_{55} = C_{66}, \alpha_{11} = \alpha_{22} = \alpha_{33} \quad \dots(27) \end{aligned}$$

4.1 PROPAGATION ALONG AXES OF ROTATIONAL SYMMETRY

Notice that the axis x_1 and x_2 coincide with the azimuthal angles $\phi = 0$ and $\phi = 90^\circ$ respectively. Substitute from equation (25), which particularize the constitutive relations (3) to orthotropic media, it is observed that M_{12} , M_{23} , M_{31} and M_{42} of (12) vanishes. This result means that SH wave motion decouple from the rest of motion.

As a consequence equation (13) for $\phi = 0$, reduces to

$$\alpha^4 + B_1 \alpha^2 + B_2 \alpha^2 + B_3 = 0 \quad \dots(28)$$

$$\text{and } C_{66} + C_{44} \alpha^2 - \rho c^2 = 0 \quad \dots(29)$$

where

$$\begin{aligned} B_1 &= [-K_3 F_1 - F_2 \rho c^2 + C_{33} C_{55} Q_1 - C_{55} \beta_3^2 Q_2] / \Delta_1 \\ B_2 &= [-K_3 F_3 + (F_1 - F_2 \rho c^2) Q_1 - (C_{33} \beta_1^2 + (C_{11} - \rho c^2) \beta_3^2) Q_2] / \Delta_1 \\ B_3 &= [F_3 - (C_{55} \rho c^2) \beta_1^2 Q_2] / \Delta_1 \quad \dots(30) \end{aligned}$$

$$\Delta_1 = -K_3 C_{33} C_{55}$$

$$F_1 = C_{11} C_{33} - C_{13}^2 - 2 C_{13} C_{55}$$

$$F_2 = C_{33} + C_{55}$$

$$F_3 = C_{11} C_{55} - (C_{11} + C_{55}) \rho c^2 + \rho^2 c^4 \quad \dots(31)$$

Equation (28) admits six solutions for α with properties

$$\alpha_2 = -\alpha_1, \alpha_4 = -\alpha_3, \alpha_6 = -\alpha_5 \quad \dots(32)$$

and equation (29) leads to

$$\alpha_7 = -\alpha_8 = [(\rho c^2 - C_{66}) / C_{44}]^{1/2} \quad \dots(33)$$

Here, notice that α_7, α_8 of equation (33) corresponds to the (SH) motion, while those of equation (32) corresponding to the sagittal plane.

By employing the same procedure and following the same steps as used in obtaining the results of equations (23) the reduced uncoupled characteristic equations are

$$D_{11} G_1 \cot(\gamma\alpha_1) - D_{13} G_3 \cot(\gamma\alpha_3) + D_{15} G_5 \cot(\gamma\alpha_5) = 0$$

$$D_{11} G_1 \tan(\gamma\alpha_1) - D_{13} G_3 \tan(\gamma\alpha_3) + D_{15} G_5 \tan(\gamma\alpha_5) = 0 \quad \dots(34a,b)$$

$$\sin(2\gamma\alpha_7) = 0 \quad \dots(35)$$

with γ as defined in (24).

and

$$G_1 = \begin{vmatrix} D_{23} & D_{25} \\ D_{43} & D_{45} \end{vmatrix}, G_3 = \begin{vmatrix} D_{21} & D_{25} \\ D_{41} & D_{45} \end{vmatrix}, G_5 = \begin{vmatrix} D_{21} & D_{23} \\ D_{41} & D_{43} \end{vmatrix} \quad \dots(36)$$

$$\begin{aligned} D_{1q} &= [i\xi(C_{13} - C_{33}\alpha_q W_q) - \beta_3 S_q] \\ D_{2q} &= [i\xi(C_{55}(\alpha_q + W_q))] \\ D_{4q} &= i\xi\alpha_q, q=1,2,\dots,6 \quad \dots(37) \end{aligned}$$

$$W_q = \frac{M_{11}M_{34} - M_{13}M_{14}}{M_{14}M_{33} - M_{13}M_{34}}, S_q = \frac{M_{11}M_{43} - M_{13}M_{41}}{M_{14}M_{43} - M_{13}M_{44}} \quad \dots(38)$$

The results (34a,b) with their parameter defined in equations (32) and (37), constitute the characteristic equations for symmetric and antisymmetric modes for waves propagating along an in-plane axis of symmetry of an orthotropic plate. Equation (35), is the characteristic equation of a horizontally-polarized SH wave on the same plate, which is clearly independent of thermal

variations, Further more, the relation (34) implicitly contains corresponding results for materials possessing higher than orthotropic symmetry. These include transversely isotropic, cubic, and isotropic. Here, one needs only to exploit the appropriate restrictions on the thermoelastic properties as described in equations (26) and (27).

5. Numerical Results and Discussion

In this section, the analytical results derived in the previous sections are used to present phase velocity (Λ, Λ_1 nondimensional) dispersion curves plotted as a function of the $\gamma = \xi d/2$; at $\tau_0 = 0.2, 0.5, 0.001$. These curves have been calculated from expression based on the dispersion relation in equation (34) suitably modified according to detail of symmetry class. Computation for the symmetric and antisymmetric modes have been carried out for carbon steel for which the physical data is

$$\lambda = 9.3 \times 10^{10} \text{ Nm}^{-2} \quad \mu = 8.4 \times 10^{10} \text{ Nm}^{-2}$$

$$\rho = 7.9 \times 10^3 \text{ Kg m}^{-3}$$

$$T_0 = 293.1^\circ \text{ K}, \quad \varepsilon = 0.34,$$

$$C_e = 6.4 \times 10^2 \text{ J Kg}^{-1} \text{ deg}^{-1}$$

It is found that the phase velocity of the thermoelastic waves get modified and is influenced by the thermal relaxation time and agree in general with the results obtained by [16] when thermoelastic coupling constant $\varepsilon = 0$ for isotropic material. as is in following figures

Fig.1 $\tau_0 = 0.2$

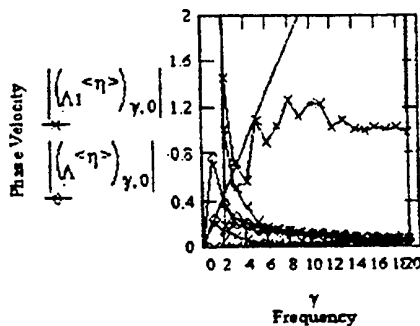


Fig.2 $\tau_0 = 0.5$

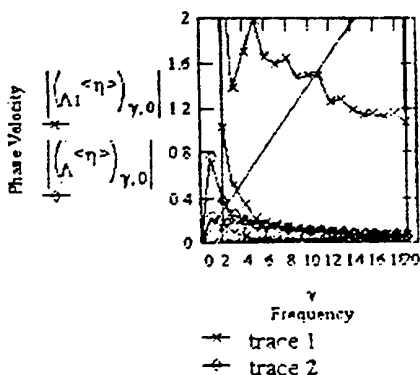
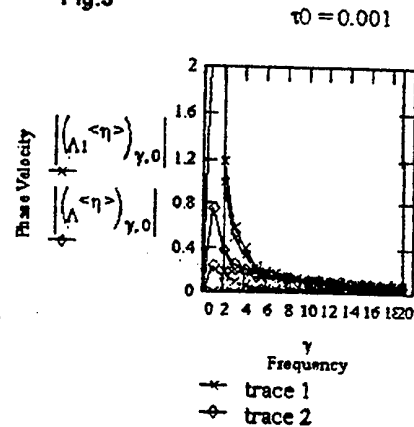


Fig.3



6. References

- (1) Banerjee D. K., and Pao Y.H., J. Acoust. Soc. Am. 56 p 1444, 1974.
- (2) Nayfeh A.H., and Chementi, D.E., J. Appl. Mech. Vol. 56 p881, 1989.
- (3) Li, Y., and Thompson, R.B., J. Acoust. Soc. Am. Vol. 87 p1911, 1990.
- (4) Karunasena W.M., Shah, A.H., and Datta, S.K., J. Appl. Mech. Vol. 58 p1028, 1991.
- (5) Kaul R.K., and Mindlin, R.D., J. Acoust. Soc. Am. Vol. 34 p1902, 1962.
- (6) Abubakar, I. P., and Auld, B.A., J. Acoust. Soc. Am. Vol. 15 p129, 1962.
- (7) Solie, I.P., and Auld, B.A., J. Acoust. Soc. Am. Vol. 54 p50, 1973.
- (8) Bylis, E.R., and Green, W.A., J. Sound and Vib. Vol. 110 p1, 1986.
- (9) Mal, A.K., Wave Motion Vol. 10 p 257, 1988.
- (10) Datta, S.K., Shah, A.H., Bratton, R.I., and Chakraborty, T. J. Acoust. Soc. Am. Vol. 83 p2020, 1988.
- (11) Dayal, V., and Kinra, V.K., J. Acoust. Soc. Am. Vol. 85 p2268, 1989.
- (12) Chadwick, P., and Seet, L.T.C., Mathematica 17 p255, 1970.
- (13) Chadwick, P., J. Thermal Stress, 2 p193, 1979.
- (14) Lord, H.W., and Shulman, Y., J. Mech. Phys. Solids, 15 p299, 1967.
- (15) Dhaliwal, R.S., and Sherief, H.H., Quart. Appl. Math., 88 p1, 1980.
- (16) Tolstoy, I and E. Usdin Geophysics, Vol. 18 p844, 1953.

Session 2D

**CONSTITUTIVE EQUATIONS FOR
INELASTIC BEHAVIOR**

Chair: J. Skrzypek

Co-Chair: J. C. Lambropoulous

**Thermal-Mechanical Coupling and Path-Dependence in
Underground Cavities**

H. Wong

**Thermal Stress Relaxation During Growth of
Cylindrical Shells**

John C. Lambropoulos

Modeling of Damage Effect on Heat Transfer in Solids

A. Ganczarski, J. Skrzypek

**On the Macro-Model for Unsafe Points of Structures to
Evaluate LCF Resistance**

D. A. Gokhfeld, O. S. Sadakov, and V. B. Poroshin

**A Constitutive Model for Thermal-Hydro-Chemo-Mech-
anical Response of Decomposing High Performance
Concrete Under High Temperature**

M. Jouhari, I. Laalai

Thermal-Mechanical Coupling and Path-Dependence in Underground Cavities

H. Wong

Laboratoire Géomatériaux-Département Génie Civil et Bâtiment, Ecole Nationale des Travaux Publics de l'Etat, rue Maurice Audin, 69518 Vaulx-en-Velin Cedex, France (CNRS URA 1652).

The problem of a tunnel subjected simultaneously to pressure loading and thermal gradient is discussed, with an emphasis on the concept of loading path and its influence on the current equilibrium state. For the case of internal heating and monotone pressure drop, path independence seems to apply both to perfect plasticity and softening behavior, while the contrary holds in the case of cooling.

Key Words : *Loading Path, Thermal-Softening, Thermal Stress, Tunnels, Corner Flow*

1. Introduction

A few closed form solutions of a tunnel subjected to internal pressure and to an axisymmetric time-dependent temperature field are presented. Starting from the reference case : positive temperature increase (heating) and constant material parameters, notably the strength (i.e. perfect plasticity), generalizations to the cases of temperature decrease (cooling), and thermal softening (strength decreases with heating) are briefly discussed and illustrated. Models on internal heating can for example be applied to studies of nuclear waste disposals or geothermal extraction wells, while the model on internal cooling is useful in the estimation of tunnel lining stresses induced by ventilation. Such closed form solutions constitute very useful design tools to appreciate the importance of thermal effects in underground cavities.

2. Problem Definition and Basic Assumptions

We consider an infinite, isotropic, homogeneous medium, with an elastoplastic behavior, obeying Tresca's criterion :

$$F(\underline{\sigma}) = \sigma_i - \sigma_k - 2C = 0 \quad (1)$$

where $\sigma_i > \sigma_j > \sigma_k$ are the ordered principal stresses, and C the cohesion. The strain rate tensor, under the assumption of small strains, can be decomposed into the following components :

$$\dot{\underline{\epsilon}} = \left[\frac{1+\nu}{E} \dot{\underline{\sigma}} - \frac{\nu}{E} \text{tr}(\dot{\underline{\sigma}}) \underline{1} \right] + \alpha \dot{T} \underline{1} + \dot{\underline{\epsilon}}^P \quad (2)$$

where E and ν are Young's modulus and Poisson's ratio, and $T(r,t)$ is the time-dependent excess temperature field with respect to a reference initial temperature T_0 . The plastic strain rate tensor $\dot{\underline{\epsilon}}^P$ is supposed to be derived from an associative flow rule ($\dot{\lambda}$ and $\dot{\lambda}_{ij}$ positive):

$$\begin{aligned} \dot{\underline{\epsilon}}^P &= \dot{\lambda} \frac{\partial F(\underline{\sigma})}{\partial \underline{\sigma}} & \text{if } \sigma_i > \sigma_j > \sigma_k \\ \dot{\underline{\epsilon}}^P &= \dot{\lambda}_{ij} \frac{\partial F_{ij}(\underline{\sigma})}{\partial \underline{\sigma}} + \dot{\lambda}_{ik} \frac{\partial F_{ik}(\underline{\sigma})}{\partial \underline{\sigma}} & \text{if } \sigma_i > \sigma_j = \sigma_k \end{aligned} \quad (3)$$

The second form of $\dot{\underline{\epsilon}}^P$ applies when the stress tensor is at a corner of the Tresca's prism, and corner flow regime intervenes [1]-[2]. A circular tunnel of radius a is excavated, the effect of the retreating excavation front being simulated by a fictitious internal pressure, which decreases monotonically from the initial geostatic pressure P_∞ to an intermediate value $P_i \in [P_\infty, 0]$. This constitutes the first stage: the mechanical loading stage.

Maintaining P_i at its previous value, an internal thermal loading gives rise to an axisymmetric time-dependent temperature field $T(r,t)$. This constitutes the second stage: the thermal loading stage. Under the hypothesis of perfect plasticity (C constant), the following cases are considered :

Case 1 : an internal heating, leading to $T > 0$, $\partial_r T > 0$, $\partial_r T < 0$ for all (r,t) .

Case 2 : an internal cooling, leading to $T < 0$, $\partial_r T < 0$, $\partial_r T > 0$ for all (r,t) .

3. Model 1 : Perfect Plasticity (C Constant), Internal Heating

This problem has been treated by Wong [1]-[2]. We shall only retrieve the main events and the most salient features. For the particular case of mechanical loading with $\dot{T}=0$, followed by thermal loading with $\dot{P}=0$ (see def. below), the elastoplastic zones appear in the sequence (P1, P2, P3, then P4), illustrated by figure 1. In order to discuss the concept of path-dependence (i.e. dependence on loading history), we construct a loading plan, with $\Delta P = \frac{P_\infty - P_i}{C}$, a dimensionless mechanical loading parameter, as abscissa, and $\theta(a,t) = \frac{E\alpha T(a,t)}{2C(1-\nu)}$, a dimensionless temperature, as ordinate (both monotone increasing), as shown in figure 2. The particular loading history $\dot{T}=0$ then $\dot{P}=0$, corresponds to path L, and the subregions P1 to P4 traversed correspond to the respective configurations encountered in the same order. The path L' is a more general case where

mechanical and thermal loads vary simultaneously (admitted by the model). The configurations encountered will then appear in the order (P1, P2, P3, P4, P3), of which figure 3 is a more precise representation.

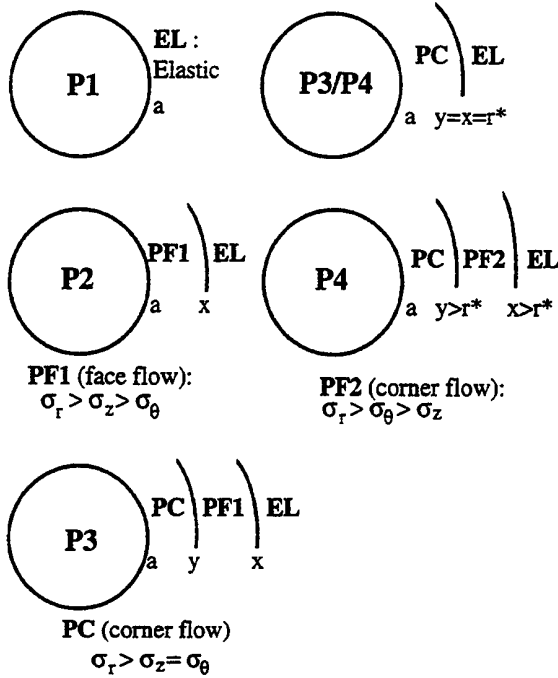


Fig. 1 Sequence of elastoplastic zones.

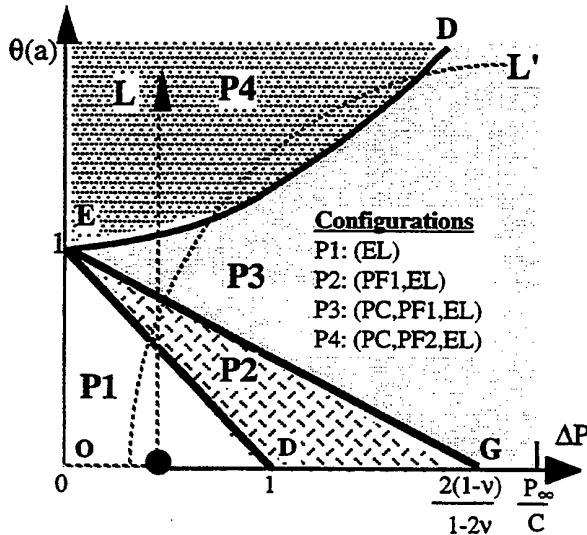


Fig. 2 Loading plane and loading path.

4. Model 2 : Perfect Plasticity (C Constant), Internal Cooling

This leads us to consider the lower half plane $\theta < 0$. Analytical results from Wong [1] show that the subregion corresponding to elastic behavior is an

extension of the triangle ODE of figure 2 ($\theta(a) > 0$, $\Delta P > 0$, $\Delta P + \theta(a) < 1$) to a polygon OABCD as shown in figure 4.

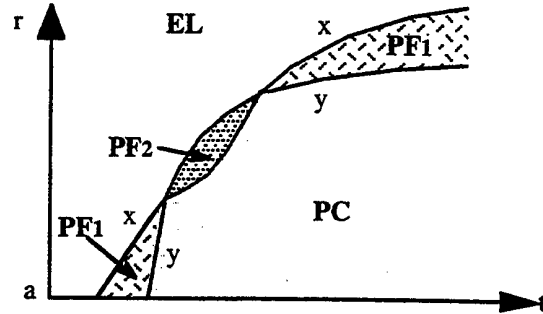


Fig. 3 Evolution following path L'.

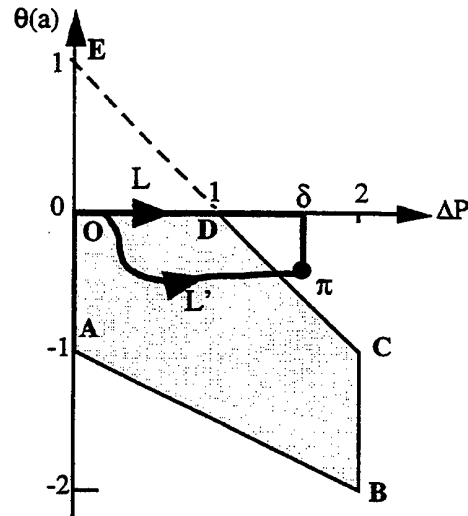


Fig. 4 Elastic subregion and loading paths L, L'.

Theoretically the yield criterion can be reached at each of the boundary segments of this polygon. Practically, for geotechnical problems, temperature rises are usually much less than the characteristic temperature $T^* = 2C(1-\nu)/E\alpha$ of ordinary geomaterials, in other words $\theta(a) \ll 1$. Thus we need only consider the segment CD, defined by $\Delta P + \theta(a) = 1$ as for ED, but with $\theta(a)$ negative. It can clearly be seen that cooling increases the threshold of mechanical loading causing plastification. This phenomenon, first observed by Guenot & Maury [9], is now widely exploited in the petroleum industry in the stabilization of wellbores by cooling the drilling mud.

To appreciate semi-quantitatively the effect of cooling, take for example two different loading paths L (isothermal) and L' (non-isothermal) such that the part of L' outside the elastic subregion is entirely horizontal. For path L, the relative convergence U_i (change of radius divided by the initial radius) at the state δ is given by:

$$\frac{E}{C} U_i = 2(1-\nu^2)e^{(\Delta P-1)} - (1+\nu)(1-2\nu)\Delta P$$

whereas for L' , the convergence at π equals :

$$\frac{E}{C} U_i = 2(1-\nu^2)(1-\theta(x,t))\left(\frac{x}{a}\right)^2 - (1+\nu)(1-2\nu)\Delta P$$

x being the unique root of the equation :

$$1 - \Delta P - \theta(x) + \ln\left(\frac{x}{a}\right)^2 = 0 \quad (4)$$

For illustrative purposes, take a temperature profile $\theta(r) = \theta_a [1 - \beta \ln(r/a)]$, with $\beta = 1/\ln(b/a)$, which corresponds quite well to real temperature profiles. Substitution into equation (4) gives :

$$\frac{x}{a} = \exp\left[\frac{\Delta P + \theta_a - 1}{2 + \beta \theta_a}\right]$$

and the convergence :

$$\frac{E}{C} U_i = 2(1-\nu^2) \frac{1 + \frac{\theta_a(\beta \Delta P - 2)}{2}}{1 + \frac{\theta_a \beta}{2}} \exp\left(\frac{\Delta P + \theta_a - 1}{1 + \beta \theta_a/2}\right) - (1+\nu)(1-2\nu)\Delta P$$

For $b/a=10$, the variation of EU_i vs. θ_a is shown in the following figure, which clearly illustrates the influence of cooling on the convergence. Note that the value of U_i is relatively insensitive to the ratio b/a ($\theta(b)=0$) for $b/a > 10$.

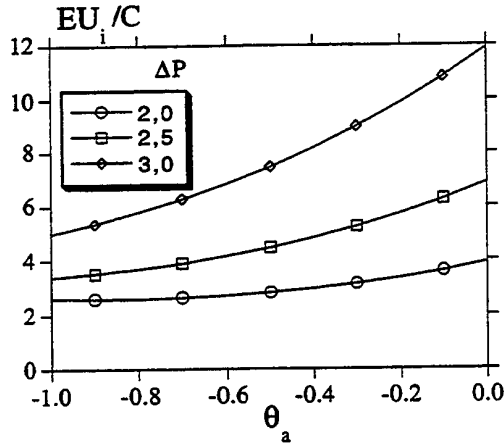


Fig. 5 Influence of cooling on convergence.

Contrary to the case of heating ($\theta > 0$), the state of equilibrium now depends on the loading path even when ΔP and θ are both monotone. For example, had we followed the loading path $O\delta\pi$, we would have the same convergence at states δ and π , since the portion $\delta\pi$ corresponds to elastic unloading, with no variation of the convergence. A particular example of such situations can be found in deep tunnels with high in-situ temperatures (due to geothermal gradient). The problem to be solved is the estimation of stress reduction (so the risk of encountering traction) in the tunnel lining, when fresh air is sent for ventilation purposes at the opening of service. This scenario corresponds well to the loading path $O\delta\pi$, and the

medium would have an incrementally elastic behavior for the portion $\delta\pi$. It is an established result that the tunnel radius is insensitive to temperature variations in elastic behavior. Thus cooling of the medium alone would not change anything; the effect is simply not "felt" by the lining. In the contrary, cooling of the lining leads to contraction, thus additional convergence, thereby altering the equilibrium lining-massif. Suppose the initial equilibrium reached under isothermal conditions (P_{i0} , U_{i0}) is given by the solution of the simultaneous equations (K =lining stiffness):

$$P_i = f_M(U_i); \quad P_i = K(U_i - U_d)$$

Subsequent variation of convergence due to cooling can be written as :

$$\delta U_i = \alpha |T| + \frac{\delta P_i}{K}$$

The first term is simply the thermal contraction (which induces positive convergence), whereas the second term, of opposite sign, represents the reduction of the pressure from the massif, and counterbalances partially the thermal contraction. Denoting $P_i' = P_i + \delta P_i$ and $U_i' = U_i + \delta U_i$, it can easily be shown that the new equilibrium state is the solution of the modified system here-below:

$$P_i = f_M(U_i); \quad P_i = K[(U_i - U_d) - \alpha |T|]$$

which admits a simple graphical interpretation as shown in figure 6.

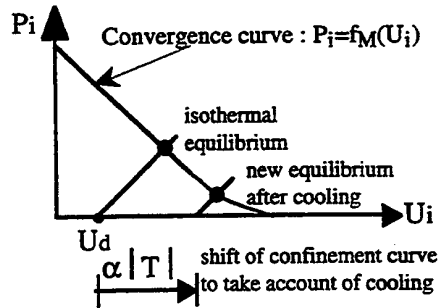


Fig. 6 Change of equilibrium due to cooling.

This model has been used to estimate the possible thermal stresses in the lining of an Alpine tunnel.

5. Model 3 : Thermal Softening ($\partial_T C(T) < 0$), Internal Heating

The decrease of mechanical strength with temperature increase has been reported by many authors, of which we can mention the experimental work of Chayé & Sirieys [3], Hommand & Houpert [4], Hueckel [5], Rousset [6] and Wong [7]. One particular example, reconstructed from Rousset[6],

illustrates the typical drop of strength to be expected in deep clays (Fig. 7).

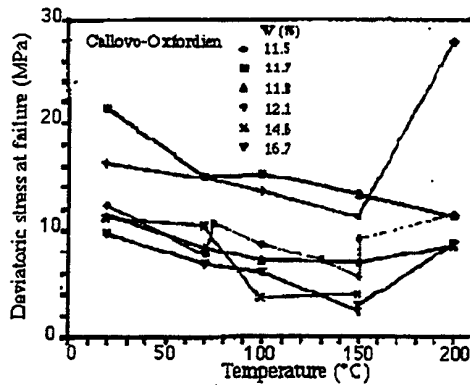


Fig. 7 Thermal softening in deep clays.

This suggests a generalization of the reference model to a thermal-softening behavior:

$$\partial_T C(T) < 0 \quad \text{for } T > 0, \partial_T T > 0, \partial_T T < 0 \quad (5)$$

For example, data in figure 7 can be approximated by the following function:

$$C(T)/C(T_0) = 1 - A[1 - e^{-0.027(T-T_0)}]$$

with A lying between 0.25 to 0.55. This model can be useful in, for example, the design of underground nuclear waste disposals or geothermal extraction wells, where one would be interested by the effects of strength reduction on the borehole stability and convergence.

Note that plastic strains only occur if the stress tensor stays on the yield surface, while softening stipulates that the latter shrinks with temperature, i.e. $D_T F(\underline{\sigma}, T) = \underline{\sigma} : \partial_{\underline{\sigma}} F(\underline{\sigma}, T) + T \partial_T F(\underline{\sigma}, T) = 0$. As $\dot{T} > 0$ and $\partial_T F(\underline{\sigma}, T) > 0$, we deduce that $\underline{\dot{\sigma}} : \partial_{\underline{\sigma}} F(\underline{\sigma}, T) < 0$, hence $\underline{\dot{\sigma}} : \underline{\dot{\epsilon}}^p < 0$, violating the "stability" requirement set forth by Drucker (see for example Palmer et al [8]). In consequence, uniqueness of the solution is not theoretically guaranteed. Notwithstanding, only one consistent solution has been found which verifies all the necessary conditions of consistency. Detailed theoretical developments will be published in a separate paper. It is interesting that this solution leads to the same sequence of elastoplastic zones (figure 1) and admits the same qualitative descriptions such as the sub-division of the loading plane. However, this time, the boundaries are not fixed beforehand. The new element in this solution is a dimensionless field function $C(T)$, defined by $C(T) = C(T)/C(T_0)$, representing the degree of softening inside the medium. For example, the yield condition of P1: $\Delta P + \theta(a) = 1$ becomes: $\Delta P + \theta(a) = C(T_a)$ where $T_a = T(a, t)$ is the temperature at tunnel wall. The plastic boundary

$x(t)$ in the configuration P2 is now given by (cf. equation (4)):

$$\theta(x(t), t) - C[T(x(t), t)] = -\Delta P + 2 \int_a^{x(t)} \frac{C(\xi, t)}{\xi} d\xi$$

Putting $C(T) = C(T_0)$ gives the solution of model 1, demonstrating the consistency of the two models.

Conclusions

The three thermal-mechanical models presented here, thanks to their analytical character, allow a more comprehensive study of thermal effects in underground cavities. Their simplicity also facilitates greatly numerical computations, and sensitivity studies become routine matters. These facilities make them an ideal complement to more elaborate numerical tools in a design office, especially at the preliminary design stage.

References

- (1) H. Wong, *Comportement des Galeries Souterraines Soumises à un Chargement Thermique*, Ph.D Thesis, E.N.P.C., Paris, France (1994).
- (2) H. Wong, 'Thermoplastic and thermo-viscoplastic behaviours of underground cavities', *Proc. 8 Int. Congress on Rock Mech.*, Tokyo, Japan, 2, pp. 479-483, Balkema (1995).
- (3) D. Chayé and P. Sirieys, 'Anisotropie et dilatabilité thermique des roches calcaires', *C. R. Acad. Sci.*, 314, série II, pp. 1259-1265 (1992).
- (4) F. Hommand-Etienne and R. Houper, 'Données récentes sur le comportement des roches en fonction de la température', in P. Berest and Ph. Weber (eds.) *La Thermomécanique des roches*, 304-312, BGRM Editions (1986).
- (5) T. Hueckel, 'Temperature effects on brittle-plastic transition in dehydrating rocks in subduction : a continuum mechanics approach', *International Workshop on Thermo-mechanics of Clays and Clay Barriers*, Bergamo, Italy (1993).
- (6) G. Rousset, 'Etude expérimentale du comportement de l'argile de l'Aisne - Partie I & II', *Internal reports G.3S*, 92-002 & 92-005 (1992).
- (7) T. F. Wong, 'Effects of temperature and pressure on failure and post-failure behavior of Westerly granite', *Mechanics of Materials*, 1, 3-18 (1982).
- (8) A. C. Palmer, G. Maier, D. C. Drucker, 'Normality relations and convexity of yield surfaces for unstable materials or structural elements', *J. Applied Mechanics* Vol. 30, pp. 464-470 (1967).
- (9) A. Guenot & V. Maury, 'Stabilité des forages profonds', in P. Berest and Ph. Weber (eds.) *La Thermomécanique des roches*, pp. 292-303, BGRM Editions (1986).

THERMAL STRESS RELAXATION DURING GROWTH OF CYLINDRICAL SHELLS

John C. Lambropoulos

Department of Mechanical Engineering, University of Rochester, Rochester, NY 14627

We examine thermal stress relaxation during growth from the melt of shaped crystals in the form of thin circular cylindrical shells, using the Haasen-Alexander constitutive law, in which the creep strain-rates and dislocation generation-rate depend on the current levels of temperature, stress, and dislocation density. Unlike problems in time-independent domains, growth problems have vanishing tractions and non vanishing traction-rates which are proportional to the growth rate. Once the stress- and dislocation-rates are computed, they are integrated starting from the solid-liquid interface. Such integration requires knowledge of stresses and dislocation density at the solid-liquid interface, significant microstructural parameters describing the solidification process and critically affecting the resulting stress relaxation and dislocation density, including the final density.

Key words: cylindrical shell, thermal stress, relaxation, dislocation density, crystal growth, silicon, semiconductors.

1. Introduction

As the efficiency of Si-based photovoltaic cells increases, photovoltaic energy becomes more attractive as an alternative form of clean, inexpensive energy. ⁽¹⁾ Experimental efficiencies in the range 13%-23% have been reported. The recent series of articles edited by Sinke ⁽²⁾ outlines some of the materials issues for with photovoltaic energy. To further enhance efficiency, dislocation density must be minimized.

A common method for the growth of thin Si plates from the melt for photovoltaic applications is Edge-defined Film-fed Growth (EFG): Si plates are grown either directly in the form of rectangular panels, or as polygonal cylindrical tubes which are subsequently sectioned by laser cutting into rectangular panels, thus increasing productivity. ⁽³⁾

Growth of flat sheet ⁽⁴⁾ or polygonal tubes ⁽⁵⁾ gives rise to inhomogeneous thermal and residual stress distributions caused by inhomogeneous temperature gradients. For comparison, see Lambropoulos. ⁽⁶⁾ Since the temperature is also very high during growth from the melt, large amounts of creep by dislocation generation and multiplication also lead to stress relaxation at the cost of significant dislocation density and residual stresses.

We consider the simplified geometry of thin cylindrical shells of circular cross section, as the limiting case of a polygonal tube in which the number of facets increases to infinity. The interaction of various factors leading to dislocation generation is investigated. Such factors include the rate of temperature decay away from the solid-liquid interface, the rate of crystal growth, the radius and thickness of the growing shell, as well as the boundary conditions, in terms of the initial dislocation density and initial stress prevailing along the solid-liquid interface.

2. Constitutive law

High-temperature inelastic deformation of Si is described by decomposing strain-rate into elastic (assumed isotropic), thermal, and creep parts:

$$\begin{aligned}\dot{\epsilon}_{ij} &= \dot{\epsilon}_{ij}^e + \dot{\epsilon}_{ij}^{th} + \dot{\epsilon}_{ij}^c \\ \dot{\epsilon}_{ij}^e &= \frac{1+\nu}{E} \left(\dot{\sigma}_{ij} - \frac{\nu}{1+\nu} \dot{\sigma}_{kk} \delta_{ij} \right) \\ \dot{\epsilon}_{ij}^{th} &= \alpha(T) T \dot{\delta}_{ij}\end{aligned}\quad (1)$$

with a super-posed dot denoting material derivatives.

Several different models have been used to describe the creep strain-rate, including power-law creep, and exponential dependence of strain-rate on stress via an activation volume. ^(6, 11) Such models view dislocation generation as a steady-state process, so that the total dislocation density is constant. As a result, these models can not predict an evolving dislocation density.

For dislocation generation in semiconductors such as Si, Alexander and Haasen ⁽⁷⁾ proposed a constitutive law in which the inelastic strain-rate and dislocation generation rate both depend on temperature, stress, and on the dislocation density. This constitutive model predicts, for example, the presence of upper and lower yield points in a uniaxial tensile test at fixed loading rate and temperature. Extensive data and review of the model assumptions are in George and Rabier. ⁽⁸⁾ The Alexander-Haasen constitutive law was introduced in the study of EFG flat plate Si crystal growth by Dillon et al., ⁽⁹⁾ and has also been used to describe dislocation generation during Czochralski crystal growth. ^(10, 11)

As the state of stress during crystal growth is multiaxial and inhomogeneous, we use the multiaxial form of the Alexander-Haasen constitutive law

$$\dot{\epsilon}_{ij}^{cp} = \phi b B_0 \exp(-Q/R_g T) (\tau_e - A \sqrt{N})^m N \frac{s_{ij}}{\tau_e} \quad (2)$$

$$\dot{N} = K B_0 \exp(-Q/R_g T) (\tau_e - A \sqrt{N})^{m+1} N$$

$\dot{\epsilon}_{ij}^{cp}$ is creep strain-rate, N is dislocation density, $s_{ij} = \sigma_{ij} - \sigma_{kk} \delta_{ij}/3$ is stress deviator, δ_{ij} is Kronecker delta, and τ_e is effective shear stress $\tau_e = (s_{ij} s_{ij}/2)^{1/2}$. $\langle x \rangle = x$ if $x > 0$, and 0 otherwise. For Si: $\phi \approx 1/2$, b is Burgers vector (0.38 nm), exponent $m = 1.1$, and constants $B_0 = 8.6 \times 10^{-4} \text{ m}^3 \cdot 2 \text{ N}^{-1} \cdot \text{s}^{-1}$, $K = 3.1 \times 10^{-4} \text{ mN}^{-1}$, $A = 4 \text{ Nm}^{-1}$ (describing back stress of dislocations already present). Activation energy of dislocation motion is $Q = 211 \text{ kJ mol}^{-1}$, and $R_g = 8.314 \text{ J mol}^{-1} \text{ K}^{-1}$ is the gas constant.

3. Problem formulation

A circular cylindrical shell is semi-infinite in the growth x -direction. The growth rate is p_0 . The shell has radius R , thickness t , and bending rigidity $D = Et^3/[12(1-\nu^2)]$.

The solid-liquid interface is at $x = 0$, with z measuring from the shell middle surface. As the shell is subjected to axisymmetric loading, the kinematic relations of strain-rates and velocities \dot{w} , \dot{u} in the radial (z) and axial (x) directions, are, respectively,

$$\dot{\epsilon}_x = \frac{d\dot{u}}{dx} - z \frac{d^2 \dot{w}}{dx^2}, \quad \dot{\epsilon}_\theta = \frac{\dot{w}}{R} \quad (3)$$

and the incremental equations of equilibrium are

$$\dot{N}_x = 0, \quad \frac{d\dot{Q}_x}{dx} + \frac{\dot{N}_\theta}{R} = 0, \quad \frac{d\dot{M}_x}{dx} - \dot{Q}_x = 0 \quad (4)$$

When steady-state growth conditions are attained (long shell), field quantities do not change in a fixed laboratory frame of reference, and material derivatives are then converted to spatial derivatives by

$$\dot{\phi} = p_0 \frac{d\phi}{dx} \quad (5)$$

The differential equation for the radial velocity is

$$\frac{d^4 \dot{w}}{dx^4} + 4\beta^4 \dot{w} = \dot{F}_1(x) + \frac{d^2 \dot{F}_2(x)}{dx^2} \quad (6)$$

where $\beta = [3(1-\nu^2)]^{1/4}/\sqrt{Rt}$ and

$$\begin{bmatrix} \dot{F}_1(x) \\ \dot{F}_2(x) \end{bmatrix} = \begin{bmatrix} \frac{\dot{N}^{th}}{DR} + \frac{\dot{N}_\theta^{cp} - \nu \dot{N}_x^{cp}}{DR(1-\nu^2)} \\ -\frac{\dot{M}^{th}}{D(1-\nu)} - \frac{\dot{M}_x^{cp}}{D(1-\nu^2)} \end{bmatrix} \quad (7)$$

Thermomechanical force-resultant rates are

$$\dot{N}^{th} = \int_{-t/2}^{+t/2} E \alpha \dot{T} dz, \quad \dot{M}^{th} = E \alpha \int_{-t/2}^{+t/2} E \alpha \dot{T} z dz \quad (8)$$

$$\begin{bmatrix} \dot{N}_x^{cp} \\ \dot{N}_\theta^{cp} \\ \dot{M}_x^{cp} \end{bmatrix} = \begin{bmatrix} \int_{-t/2}^{+t/2} E (\dot{\epsilon}_x^{cp} + \nu \dot{\epsilon}_\theta^{cp}) dz \\ \int_{-t/2}^{+t/2} E (\dot{\epsilon}_\theta^{cp} + \nu \dot{\epsilon}_x^{cp}) dz \\ \int_{-t/2}^{+t/2} E (\dot{\epsilon}_x^{cp} + \nu \dot{\epsilon}_\theta^{cp}) z dz \end{bmatrix}$$

Traction-free boundary conditions $M_x = Q_x = 0$ at the solid-liquid interface $x = 0$ lead to boundary conditions in terms of the force- and moment-rates

$$\dot{M}_x = p_0 Q_x = 0, \quad \dot{Q}_x = p_0 \frac{dQ_x}{dx} = -p_0 \frac{N_\theta}{R} \quad (9)$$

Thus, the traction-rate boundary conditions require knowledge of the transverse force N_θ (equivalently, the stress σ_θ) at the interface.

The radial velocity rate was found by a Green's function iterative approach and numerical integration in the axial direction. The integration grid pattern was finely spaced near the solid-liquid interface (where stresses are expected to vary rapidly). High order Gauss quadrature rule was used to find the stress profile in the thickness direction so as to obtain the sectional loading rates $\dot{N}_x^{cp}, \dot{N}_\theta^{cp}, \dot{M}_x^{cp}$. For stability and convergence, a one-dimensional line search was used to obtain the optimum step length for the radial velocity and curvature-rate in each new iteration.

Once the stresses are computed, the dislocation density and creep strain-rates are found by integrating equations (2) in the direction of crystal growth, where $N(x=0, z) \equiv N_0(z)$ is the initial dislocation density along the solid-liquid interface. The initial dislocation density N_0 can not be determined a priori, as it is set by the physical mechanism of solidification.

The temperature distribution is taken to be

$$T(x, z) = T_r + (T_m - T_r + T_z \frac{z}{t}) e^{-\gamma x} \quad (10)$$

where T_r is the room temperature, T_m is the melting temperature, and T_z is the temperature difference between the outer surface and the inner surface of the shell. We assumed that N_0 is uniform through the shell thickness. For the shell geometry we use typical radius $R = 5$ cm, and thickness $t = 100$ μ m.

4. Thermoelastic results

We first use the thermoelastic approximation, neglecting the creep strain-rates as compared to the thermal and elastic strain-rates, with the dislocation density level determined from the thermoelastic stress values.

Fig. 1 shows the effect of the initial dislocation density at the solid-liquid interface on the final dislocation density at the outer shell surface as a function of the ratio γ/β describing the rate of temperature decay with respect to the geometrical dimensions of the shell.

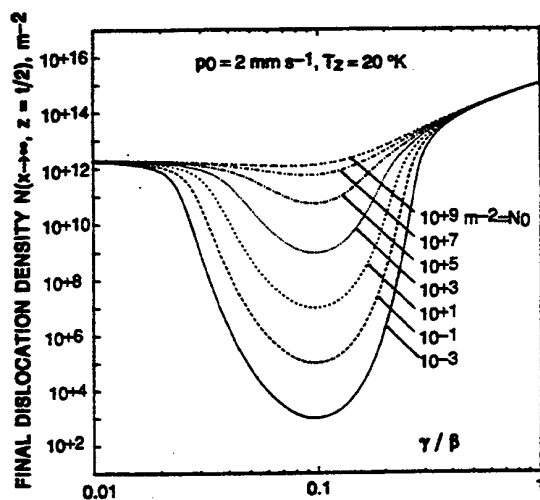


Fig. 1 The final dislocation density at the outer shell surface $z=t/2$ vs. the dimensionless ratio γ/β for various values of the initial dislocation density N_0 at the solid-liquid interface.

For slow temperature decay ($\gamma/\beta \ll 1$), each material element of the shell spends a longer time interval at higher temperatures, and the high rate of dislocation generation makes the final dislocation density insensitive to the initial value ("temperature-driven" dislocation multiplication).

On the other hand, for rapid temperature decay, γ is of order β or larger, and severe thermal stresses also

make the final dislocation density insensitive to the initial value at the solid-liquid interface ("stress-driven" dislocation multiplication).

For intermediate values of γ/β , the effect of the initial dislocation density is significant, with lower initial values leading to lower final values.

When the initial dislocation density is small, the maximum creep strain-rate is negligible when we are not in the "temperature-driven" or "stress-driven" regimes of dislocation multiplication. At intermediate values of γ/β the creep strain rates are negligible and thermoelastic calculation of stresses is justified.

5. Stress relaxation

The problem formulation outlined above introduces two important material parameters at the solid-liquid interface, the initial stress $\sigma_{\theta,0}$ which induces a generally non-vanishing tangential force N_0 at the interface, see equation (6), and the initial dislocation density N_0 at the interface. In this aspect, growth problems of the type described above are different in their formulation from problems in which the material has a constant mass.

The effect of stress relaxation at the interface will be examined by using

$$\sigma_{\theta,0} = f [(\sigma_{\theta})_{\text{elastic}}]_{x=0} \quad (11)$$

where $(\sigma_{\theta})_{\text{elastic}}$ is the thermoelastic stress based on the temperature distribution used. Multiplicative factor f describes the effect of stress relaxation (for $f = 1$, there is no stress relaxation). It is expected that f and N_0 are inversely related: When N_0 is large, there is significant stress relaxation ($f \rightarrow 0$).

In Figures 2-3 we show the computed effects of the initial dislocation density N_0 , and relaxation factor f on the maximum final dislocation density. Slow growth leads to high final dislocation density, because each shell element spends a longer time interval at higher temperatures. Larger dislocation density, in turn, produces large creep strain-rates and strains and, hence, larger residual stresses. Uniform temperature through the shell thickness produces the lowest final dislocation density and residual effective stress. Higher initial density at the interface $x=0$ generally leads to higher final dislocation density, since dislocation multiplication rate depends on the current dislocation density.

For complete stress relaxation at the interface ($f = 0$), the final dislocation density is low because of the stress dependence of the dislocation multiplication rate. For little relaxation ($f \rightarrow 1$), the large stresses prevailing at the interface induce high dislocation multiplication rate, and hence high final density.

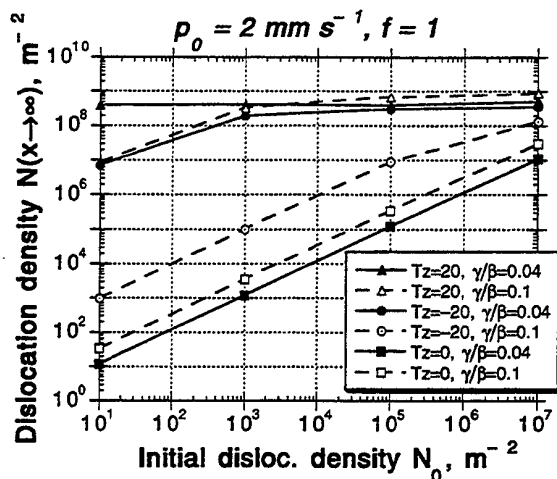


Fig. 2: Dependence of the final dislocation density on the initial dislocation density at the solid-liquid interface. Solid symbols are for slow temperature decay, and open symbols for intermediate decay.

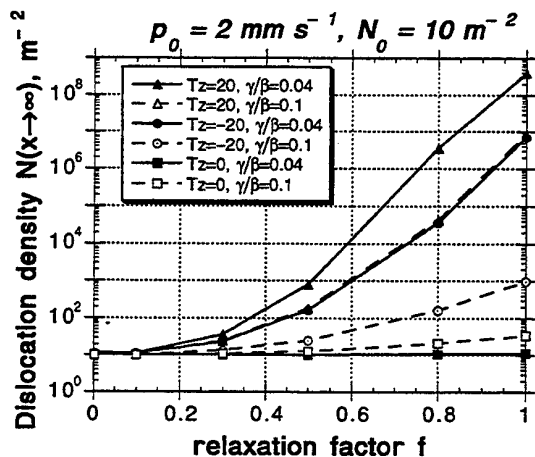


Fig. 3: Dependence of final dislocation density on the initial stress at $x=0$. For $f=0$, full stress relaxation at the interface; For $f=1$, no relaxation.

6. Conclusions

We have outlined an approach for computing thermal stress, stress relaxation, and dislocation density during growth of thin shells from the melt.

Problems of combined growth and stress relaxation require knowledge of the stress tensor along the growth interface, in contrast to problems requiring specification of the traction vector when mass is

conserved. When the Alexander-Haasen model is used to describe the multiplication of dislocations during crystal growth, the initial dislocation density at the solid-liquid interface additionally must be specified.

Initial stress and dislocation density along the interface are used as initial conditions for finding the stresses and dislocation density everywhere in the crystal, by integrating the stress-rates and dislocation multiplication rate in the growth direction. These rates vary rapidly within a short distance from the interface, and soon reach a constant value. The mechanical and microstructural state of the solid-liquid interface is thus identified as a significant aspect of the crystal growth problem.

Acknowledgment

We acknowledge the financial support by the National Science Foundation via Grants DMR-9023436 and MSS-8857096.

REFERENCES

1. H.M. Hubbard, Photovoltaics today and tomorrow, Science 244, 297 (1989).
2. W.C. Sinke (ed.), Materials for Photovoltaics, MRS Bulletin XVIII No. 10, 18 (1993).
3. D.S. Harvey, Recent progress in octagon growth using edge-defined film-fed growth, J. Crystal Growth 104, 88 (1990).
4. J.C. Lambropoulos, J.W. Hutchinson, R.O. Bell, B. Chalmers, and J.P. Kalejs, Plastic deformation effects on stress generated during Si sheet growth at high speeds, J. Cryst. Growth 65, 324 (1983).
5. C.-H. Wu and J.C. Lambropoulos, Thermoelastic analysis of dislocation generation during Edge-defined Film-fed Growth of polygonal shells, J. Crystal Growth 155, 38 (1995).
6. J.C. Lambropoulos, High temperature inelastic deformation during shaped crystal growth from the melt, J. Crystal Growth 104, 1 (1990).
7. H. Alexander and P. Haasen, Dislocations and plastic flow in the diamond structure, Solid State Phys. 22, 28 (1968).
8. A. George and J. Rabier, Dislocations and plasticity in semiconductors. I - Dislocation structures and dynamics. II - The relation between dislocation dynamics and plastic deformation, Revue Phys. Appl. 22, 941, 1327 (1987).
9. O.W. Dillon, C.T. Tsai, and R.J. DeAngelis, Dislocation dynamics during the growth of Si ribbon, J. Appl. Phys. 60, 1784 (1986).
10. C.T. Tsai, On the finite element modeling of dislocation dynamics during semiconductor crystal growth, J. Crystal Growth 113, 499 (1991).
11. J.C. Lambropoulos and C.-H. Wu, Mechanics of shaped crystal growth from the melt, J. Mater. Res. 11, 2163 (1996).

Modeling of Damage Effect on Heat Transfer in Solids

A. Ganczarski[†] and J. Skrzypek[‡]

*Institute of Mechanics and Machine Design, Cracow University of Technology
Warszawska 24, 31-155 Kraków, POLAND, e-mail: zmco@cut1.mech.pk.edu.pl*

The paper deals with a modeling of coupling between the damage evolution and heat transfer in solids, that undergo brittle deterioration from creep. Three models that account for: direct conductivity drop with damage, simultaneous conductivity drop and radiation increase, and substitutive conductivity and radiation through partly damaged solid, are formulated. As examples, cylinders subject to creep damage under pure thermal gradient are considered, and corresponding failure mechanisms are compared.

Key Words: Rheology, Continuum Damage Mechanics, Thermal Fracture Conductivity, Radiation

1. Introduction

Creep process and associated material deterioration are temperature sensitive. The classical approach consists in accounting for the effect of temperature on the material constants in constitutive equations of creep and creep damage. This approach was applied by the authors in [1] where an annular disk, subject to creep under combined peripheral radial tension and stationary radial temperature gradient, was considered.

When more advanced approach is used, the thermo-damage coupling is required in order to take into account changes of the temperature field, caused by deterioration, and vice versa.

2. Basic equations

2.1 HEAT EXCHANGE IN SOLIDS SUBJECT TO DAMAGE EVOLUTION

Tanigawa [2] formulated basic thermo-elastic equations and problems for time-independent non-homogeneous structural materials $\lambda(r)$ in the form:

$$\frac{1}{r} \frac{d}{dr} \left[r \lambda(r) \frac{dT}{dr} \right] = 0. \quad (1)$$

The problem becomes more complicated when the time-dependent creep process in the presence of temperature field, and the associated material deterioration, is considered. The material non-homogeneity becomes time-dependent $\lambda(r, t)$, following damage accumulation in a solid. Hence, when isotropic nature of damage is assumed (governed by a single scalar parameter D (cf. Kachanov

[3]), a more general form instead of Eqn.(1) is required:

$$\frac{1}{r} \frac{\partial}{\partial r} \left[r \lambda(r, t) \frac{\partial T}{\partial r} \right] = c_v \rho \frac{\partial T}{\partial t}. \quad (2)$$

In order to specify a thermal conductivity function $\lambda(r, t)$ the damage evolution with time $D(t)$, that results in temperature redistribution, is used.

The simplest model is based on the assumption of the linear heat conductivity drop with damage (cf. Ganczarski and Skrzypek [4]):

$$\lambda^D(r, t) = \lambda(r) [1 - D(r, t)], \quad (3)$$

where $\lambda(r)$ denotes non-homogeneous, in general, distribution of thermal conductivity in a virgin (undamaged) solid, whereas scalar parameter D defines current damage level, $D \in [0, 1]$.

Further extension of the previous model allows for an additional heat flow term through the damaged surface element portion, by application of the Stefan-Boltzmann radiation law. Hence, when both conductivity and radiation mechanisms of heat transfer are admitted, the following extension of Eqn.(2) is proposed:

$$\frac{1}{r} \frac{\partial}{\partial r} \left[r \lambda^D(r, t) \frac{\partial T}{\partial r} - \sigma \epsilon D(r, t) T^4 \right] = c_v \rho \frac{\partial T}{\partial t}, \quad (4)$$

with $\lambda^D(r, t)$ given by (3). This model was suggested by the authors in [4], and applied to the radial flow in an originally homogeneous cylinder subject to constant temperatures at the edges, when the scalar damage growth rule was applied. A combined conductivity/radiation mechanism allows for a heat flux even though the damage at a point reaches level 1 (due to radiation across the microcracks). However, it will be shown further, the model exhibits the essential inconsistency. Namely, the form of term associated with radiation suggests,

[†]Assistant Professor at Cracow University of Technology

[‡]Professor at Cracow University of Technology

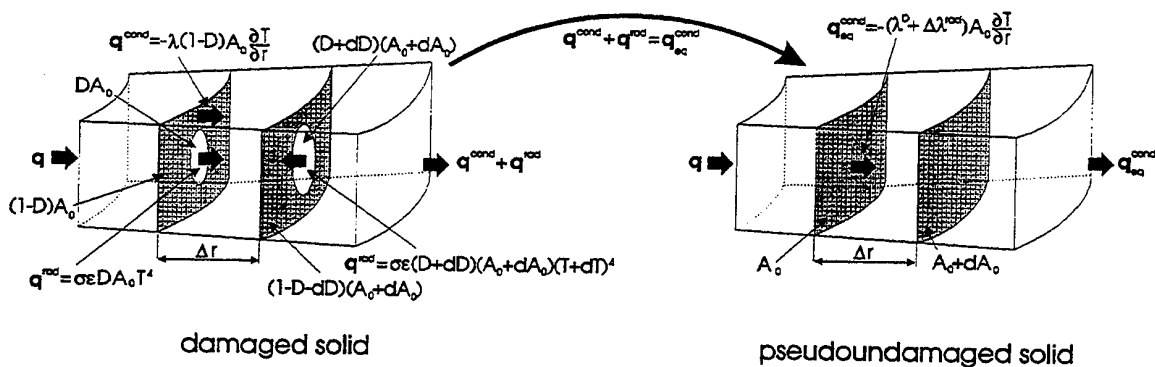


Fig.1. Schematic of heat transfer through partly damaged material element and hypothesis of heat equivalence

that there exists heat exchange caused by a redistribution of damage only, even though the temperature gradient is locally zeroth. Hence, to omit this inconsistency, it is necessary to use of second law of thermodynamics, and to cut off inadmissible temperature distribution.

Another way consists in accounting for a combined heat exchange, when the conductivity is assumed as dominant phenomenon characterized by the substitutive coefficient of thermal conductivity (cf. Staniszewski [5]), modified in order to take into account simultaneous influence of conductivity through point r and radiation from r to $r + \Delta r$, Fig.1. Equivalent coefficient of thermal conductivity is expressed, therefore, by the equation:

$$\lambda_{eq}(r, t, T) = \lambda^D(r, t) + \Delta\lambda^{rad}(r, t, T). \quad (5)$$

The equivalent (substitutive) coefficient of thermal conductivity is obtained by equating heat flux due to radiation through a partly damaged cross section and heat flux due to conductivity through fictitious pseudodamaged cross section:

$$\Delta\lambda^{rad}(r, t, T) = \sigma\epsilon \left[4D + \frac{\partial D/\partial r}{\partial T/\partial r} T \right] T^3 \Delta r. \quad (6)$$

In a simplified case, when changes of D with r are small, the last term in the parenthesis may be disregarded. Consequently, the equation of heat transfer (2) may be rewritten in the following form:

$$\frac{1}{r} \frac{\partial}{\partial r} \left[r \lambda_{eq}(r, t, T) \frac{\partial T}{\partial r} \right] = c_v \rho \frac{\partial T}{\partial t}, \quad (7)$$

with $\lambda_{eq}(r, t, T)$ given by Eq.(5) and (6).

Concluding: in the model (7), a combined conductivity and radiation mechanism through undamaged (solid) and damaged (voided) material, respectively, is reduced to the equivalent conductivity through the fictitious, pseudodamaged material, when a substitutive nonlinear coefficient of

thermal conductivity function $\lambda_{eq}(r, t, T)$ through the pseudodamaged material is introduced to the Fourier conductivity law for partly damaged material (4) instead of linearly decreasing with damage coefficient $\lambda^D(r, t)$ in the model (3). Note, that in the model under consideration (7), in case when the material damage parameter reaches locally level $D = 1$ (macrocrack initiation), the equivalent coefficient $\lambda_{eq}(D = 1)$ remains non-zeroth and, hence, the residual fictitious heat conductivity through the pseudodamaged (fictitious) surface element, equivalent to the heat radiation through the completely damaged (true) element, remains non-zeroth as well. On the other hand, the model (7), in contrast to the model (4), is free from an inadmissible heat exchange phenomenon caused by the damage redistribution, when the temperature gradient locally drops to zero.

A complete 3D model, with the term $\partial D/\partial r$ taken into account, is a subject of separate paper.

2.2 GENERAL EQUATIONS OF MECHANICAL STATE

When the geometrically linear theory of small displacements is applied and decomposition of total strains into elastic, creep, and thermal parts is used: $\epsilon = \epsilon^e + \epsilon^c + \epsilon^{th}$, the problem might be formulated via the stress function:

$$\mathcal{F}[\phi, T] = 0 \quad \text{for } t = 0, \\ \mathcal{F}[\phi, T] = \frac{E}{1-\nu^2} \left\{ \nu \dot{\epsilon}'_r + \right. \\ \left. -(1-\nu) \dot{\epsilon}'_\theta + \frac{\dot{\epsilon}'_r - \dot{\epsilon}'_\theta}{r} \right\} \quad \text{for } t > 0, \quad (8)$$

where the linear differential operator $\mathcal{F}[\phi, T]$ takes the form (primes and dots denote derivatives with respect to r and t , respectively):

$$\mathcal{F}[\phi, T] = \phi'' + \frac{\phi'}{r} - \frac{\phi}{r^2} + \frac{E}{1-\nu} \alpha T'. \quad (9)$$

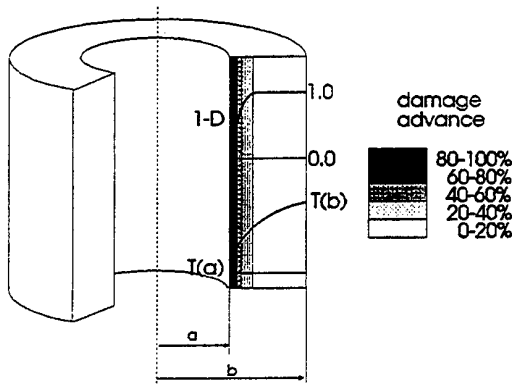


Fig. 2. Boundary conditions imposed on a cylinder

The stress components and their rates are defined as follows:

$$\left. \begin{aligned} \sigma_r &= \phi/r, \quad \sigma_\theta = \phi', \\ \sigma_z &= \nu(\sigma_r + \sigma_\theta) - E\alpha T, \end{aligned} \right\} \text{ for } t = 0$$

$$\left. \begin{aligned} \dot{\sigma}_r &= \dot{\phi}/r, \quad \dot{\sigma}_\theta = \dot{\phi}', \\ \dot{\sigma}_z &= \nu(\dot{\sigma}_r + \dot{\sigma}_\theta) - E\alpha \dot{T} + E(\dot{\epsilon}_r^c + \dot{\epsilon}_\theta^c), \end{aligned} \right\} \text{ for } t > 0 \quad (10)$$

Constitutive equations for coupled creep-damage problem are defined by the similarity of deviators, based on the flow theory

$$\dot{\epsilon}_{kl}^c = \frac{3}{2} \frac{\dot{\epsilon}_{eq}^c}{\sigma_{eq}} s_{kl}, \quad k, l = r, \theta, z, \quad (11)$$

and the time hardening hypothesis associated with the Kachanov isotropic brittle rupture law (4):

$$\dot{\epsilon}_{eq}^c = (\sigma_{eq}^{net})^{m(T)} \dot{f}(t), \quad \dot{D} = C(T) \left\langle \frac{\sigma_I}{1-D} \right\rangle^{n(T)}, \quad (12)$$

where $f(t)$ is a given time function, $\langle \rangle$ denote Macauley brackets, and σ_I refers to the maximum principal stress. In case of the plane strain conditions and creep incompressibility the intensities of the stress, the net stress (with the effect of deterioration taken into account), and the strain rates, are defined by the following formulae [4]:

$$\sigma_{eq} = \sqrt{\frac{3}{2} s_{kl} s_{kl}}, \quad \sigma_{eq}^{net} = \frac{\sigma_{eq}}{1-D}, \quad (13)$$

$$\dot{\epsilon}_{r/\theta}^c = \frac{\sigma_{eq}^{m(T)-1}}{(1-D)^{m(T)}} \left(\sigma_{r/\theta} - \frac{\sigma_{\theta/r} - \sigma_z}{2} \right) \dot{f}(t).$$

In the above formulation, damage rate and strain rates are defined by temperature dependent material functions $m(T)$, $C(T)$, $n(T)$.

3. Formulation of boundary problems

Let us consider a cylinder of the inner and outer radii a and b , respectively, under the plane strain condition, subject to radial temperature gradient Fig.2. Stresses and their rates satisfy Eqn.(8) as

well as homogeneous boundary conditions:

$$\begin{aligned} \phi(a) &= 0, \quad \phi(b) = 0, \quad \text{for } t = 0, \\ \dot{\phi}(a) &= 0, \quad \dot{\phi}(b) = 0, \quad \text{for } t > 0. \end{aligned} \quad (14)$$

The homogeneous, stationary equations of heat transfer (2), (4) and (7) are compared. Temperature redistribution due to damage are considered here as quasistatic, hence right-hand sides of Eqs.(2), (4), (7) are disregarded. In general, for the very high damage rates preceding failure, this term might be significant.

Temperature at both inner and outer edges of the cylinder is held constant in time, hence, the following boundary conditions have to be satisfied:

$$T(a) = T_a, \quad T(b) = T_b. \quad (15)$$

As the initial solution (for $t = 0, D \equiv 0$), the classical logarithmic distribution of temperature is obtained from all boundary problems (2), (4) and (7), with (15) taken as boundary conditions for temperature field.

4. Numerical algorithm for thermo-creep-damage problem

The elastic solution when $D \equiv 0$, and the classical distribution of the temperature are assumed as the initial conditions of the creep damage problem. Then, for the subsequent time step "new" values of strain $\epsilon_{r/\theta}$, stresses $\sigma_{r/\theta/z}$, damage parameter and temperature are computed. In all cases under consideration, and each step of time, the equation of heat transfer is solved by use of subiterations either of the Finite Difference Method, associated with the relaxation method, or the Modified Midpoint Method. Material functions $m(T)$, $C(T)$, $n(T)$ are updated as well. The procedure is repeated until the first macrocrack is initiated.

5. Results

All numerical examples presented in this paper deal with the cylinder made of stainless steel (rolled 18 Cr, 8 Ni, 0.45 Si, 0.4 Mn, 0.1 C, Ti, Nb stabilized, austenitic, annealed at 1070°C, air cooled ASTM 321) of the following properties [6], [7]: $E = 15.0 \times 10^3$ kG/mm², $\sigma_{0.2} = 12.0$ kG/mm², $\nu = 0.3$, $\alpha = 1.85 \times 10^{-5}$ 1/K, $\lambda = 23$ W/mK, $a/b = 0.5$, $\sigma = 5.669 \times 10^{-8}$ W/m²K⁴, $\epsilon = 0.50$, the temperature dependent material functions for creep rupture are:

T (°C)	m	n	σ_{cB}^5 (kG/mm ²)	C (kG ⁻ⁿ s ⁻¹)
600	4.5	3.1	10.0	1.68×10^{-22}
650	4.0	2.8	6.0	1.29×10^{-20}
700	3.5	2.5	3.8	6.36×10^{-19}

where σ_{CB}^5 denotes the stress necessary to cause creep rupture after 10^5 hr.

5.1 EXAMPLES

5.1.1 Thermo-Damage Coupling in a Cylinder Disregarded.

Disregarding the effect of damage accumulation on heat transfer Eqn.(1), the sampling solution is obtained. In this case temperature remains unchanged, the accompanying hoop stress relaxation is slow enough to reach at finite upper-band estimation of the lifetime.

5.1.2 Pure Heat Conductivity Case.

In case of simplified equation of heat transfer (2), where radiation through the damaged part of wall is disregarded ($\epsilon = 0$), the significant temperature redistribution is observed. The hoop stress relaxation is now comparable with the sampling case except for the tertiary creep period, hence lifetime is eventually shorter ($85\%t_I$).

5.1.3 Combined Conductivity-Radiation Case.

Combined conductivity / radiation mechanism taken into account cause that saturation of temperature precedes rupture. Hence, appropriate cutting-off procedure, to avoid thermodynamically inadmissible temperature fields, must be introduced. The high temperature gradients are observed in the inner zone, that result in a change of sign of the hoop stress and, eventually, the lower-band estimation of the lifetime ($38\%t_I$).

5.1.4 Equivalent Conductivity Concept.

The concept of equivalent conductivity-radiation exhibits the essential differences dependent on whether the derivative $\partial D/\partial T$ is disregarded or taken into account. When the exact formula (6) is applied a characteristic hoop stress discontinuity is formed at the point of most advanced damage. In case of $\partial D/\partial T = 0$ concept (7) slightly differs from (2). Concluding, as the most reliable, the equivalent conductivity concept Eq.(7), is recommended.

A comparison of the lifetimes for all considered cases is presented in Table 1.

relative lifetime	Examples			
	5.1.1	5.1.2	5.1.3	5.1.4
	t_I	$0.853t_I$	$0.381t_I$	$0.789t_I$

Table 1 Comparison of lifetimes of cylinders

References

- (1) Ganczarski, A. and Skrzypek, J., On Optimal Design of Disks with Respect to Creep Rupture, Proc. of IU-TAM Symp. Creep in Struct., Springer, pp. 571-577, 1991.
- (2) Tanigawa, Y., Some basic thermoelastic problems for nonhomogeneous structural materials, ASME, 48, 6, pp.287-300, 1995.
- (3) Kachanov, L.K., Introduction to Continuum Damage Mechanics, Martinus Nijhoff Publishers, 1986.

- (4) Ganczarski, A., Skrzypek, J., Concept of Thermo-Damage Coupling in Continuum Damage Mechanics, Proc. Thermal Stresses'95, 46, 4, pp.83-86, 1995.
- (5) Staniszewski, B., Thermodynamics, PWN, Warsaw, 1982 (in Polish).
- (6) Odqvist, F.K.G., Mathematical Theory of Creep and Creep Rupture, Oxford, Clarendon Press, 1974.
- (7) Holman, J.P., Heat Transfer, McGraw-Hill, 1990.

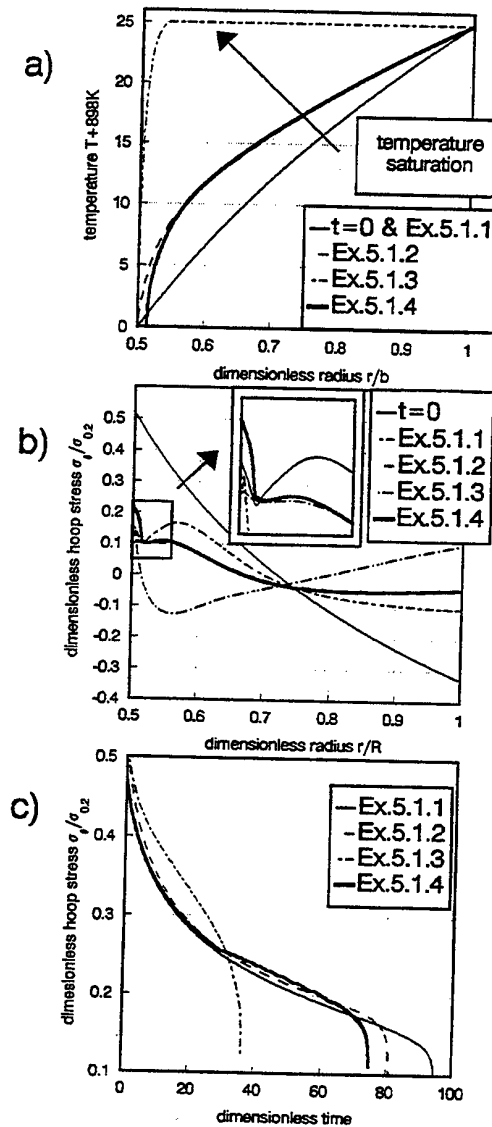


Fig.3. Comparison: a) temperature redistribution, b) relaxation of hoop stress, c) evolution of hoop stress with time

Acknowledgments

The authors gratefully acknowledge grant KBN 7 T07A 028 11 (421/T07/96/11).

On the Macro-Model for Unsafe Points of Structures to Evaluate LCF Resistance

D.A. Gokhfeld, O.S.Sadakov, V.B.Poroshin

Cheliabinsk State University of Technology, 454080 Cheliabinsk, Russia

A rational design procedure is suggested which includes associated rheological and durability analysis of structures with local inelastic zones subjected to variable repeated mechanical and thermal actions. The approach is based on the structural model of elasto-visco-plastic medium and the ideas which follow from.

Key Words: Repeated Loading, Plasticity, Creep, Damage Accumulation, Macro-model of Structure

1.Introduction

In many cases lifetime of structures subjected to variable repeated actions of load and temperature is limited by situations which exist in their inelastic zones (IZ): rise of inelastic strains is here the most likely. Meanwhile, application of the traditional methods of inelastic stress-strain analysis to such problems usually leads to excessive computational volumes. Hence necessity of some approximate approaches follows, by which sufficiently realistic durability prognosis can be made at essentially smaller labour input. As an example, the known Neuber's approach could be served: however, its possibilities are restricted by analysis of stress concentration zones under monotonous loading condition: besides, in some cases the obtained results lack accuracy. Utilization of the structural model of elasto-visco-plastic medium [1] and of regularities that it implies (in particular, the generalised similarity principle [2]) allows to find solutions for the problems which appear at diverse loading conditions. In difference from the Neuber's and other authors' (Stowell, Makhutov) supposition, use of any universal formula is not assumed here. By the deduced regularities inelastic deformation process in unsafe point x_0 of a structure generated at any loading program can be determined proceeding from outcomes of stress-strain analysis (carried out by any way) at initial loading.

The offered approach expands a wide circle of the problems and is not restricted by the cases of expressed stress concentration: it remains valid when inelastic strain domains in a design are relatively small (at least, situation is not close to the limit equilibrium state). And in any case, due to use of the structural model, the peculiarities of non-isothermal plasticity and creep under repeated loading are rather adequately reflected.

Lifetime evaluation (in accordance with the criterion of a macro-crack formation) is based on the suggested version of damage accumulation model of kinetic type. The latter is associated with the mentioned structural (rheological) model as they both are defined by common state parameters. This essentially simplifies the corresponding design procedure.

2.The structural model of medium

It should be reminded that the mentioned type of rheological models [1-3] is based on the concept of the actual materials micro-inhomogeneity. The most simple way to reflect this property goes back to the known Masing scheme (in the Western countries for such models they frequently use terms "composite" and "layers"). Accordingly, deformation behavior of a body element is here imitated by a package of *perfectly viscous* subelements (SEs) having equal strains ε (or, in general, strain tensors ε) and temperature T . Creep rate of any is supposed to be a function of temperature and individual stress (or corresponding elastic strain r). It has been assumed, that all these functions are similar to some common rheological function (RF) $\Phi(x, T)$ which is specific for each material.

Typical RF at constant temperature, being plotted in semi-logarithmic coordinates, usually can be approximated by two intersecting straight lines. It reflects two different inelastic deformation regimes. The first (marked as $\dot{p}_p^*(s)$ in Fig.1) is distinguished by relatively high strain rates in a narrow elastic strain range. This type of inelastic deformation is

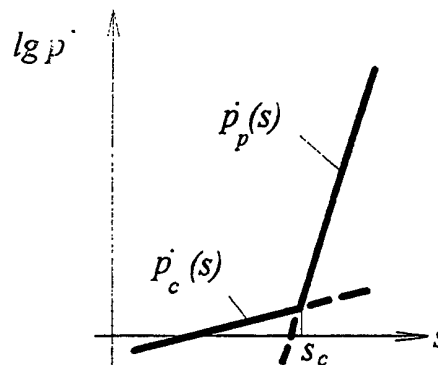


Fig.1. The rheological function

usually considered as a scleronomic one (plasticity). The second ($\dot{p}_c^*(s)$) is typical for creep (s is the state parameter of the simulated medium, explanation of its essence and physical interpretation will be given

below, by points the time derivatives - d/dt - are denoted).

It is evident, that in any case (excluding the intersecting zone) one of the two inelastic regimes - viscous or plastic (and the corresponding type of damage accumulation, see p.5) has prevailing meaning; however, they both are realized simultaneously:

$$p^* = A_p(T) \exp(B_p s) + A_v(T) \exp(B_v s). \quad (1)$$

3. The similarity principle

Cyclic steady deformation behavior of a structure is here considered. It is supposed that loading which is realized in the IZ is close to proportional (this often takes place even in spite of disproportionate changes of forces and/or thermal strains). In the general case, history of an arbitrary external action can be presented by adequate field of fictitious elastic strains $r_e(x, t)$ which is related linearly with corresponding stresses in the structure. In connection with any local IZ it is sufficient to know strains $r_e(x, t)$ in the zone only [3].

Moreover, taking into account the assumption made for loading conditions in such zones, we can rely on the generalized similarity principle (GSP); it should be reminded that the GSP has been deduced (on the base of general equations of the structural model) for arbitrary design subjected for proportional variable repeated loading [2]. Then, due to respective similarity of actual stress, strain and displacement fields generated in a structure, the necessary initial information can be reduced to fictitious elastic strain history in its any representative point x_0 (e.g. in a point which is supposed to be unsafe).

Below the necessary equations are written assuming that the stress state is linear. Their generalization for the case of arbitrary stress state is trivial, except a peculiarity: instead of effective values of tensors, the corresponding *scalar measures* here should be used, which differ from the formers by possibility to change their signs.

Let $r_e(x)$ in any point of the IZ at any time instant t be proportional to a common parameter $R \equiv r_e(x_0)$; analogously, $T(x, t) \approx T(t) \Psi(x)$, where $T(t) \equiv T(x_0, t)$. Functions $R(t)$, $T(t)$ determine the prescribed loading program.

Current state which exists in the IZ (designated below as $S(t)$) represents a set of actual elastic and total strain fields $r(x), e(x)$; accordingly, parameter E determines total strain in point x_0 of IZ (here and after only power part of actual strain is meant, i.e. thermal strain component is excluded). Creep rate field $p^*(x, t)$ is determined as a non-linear function of state S and temperature T . Let us remind, that any volume element of structure is represented by a bundle of perfectly viscous SEs.

Let initial loading of a structure at constant power strain rate $E^* = b$ and temperature $T = T_b$ be

taken as the basic one. The corresponding one-parametric set of states S_b will be termed as the basic one (M_b); any of its elements is identified by parameter R ($S_b(R) \in M_b$). Initial loadings corresponding to different values of E^*, T form a set of states M_2 . Accordingly to the GSP, the latter proves to be two-parametric: any state S corresponding to arbitrary values of R, E^*, T is similar to some state S_b :

$$S(R, E^*, T) = s S_b(R/s); \quad (2)$$

$$s = \Phi^0(E^*/b, T). \quad (3)$$

Here and after upper zero denotes corresponding inverse function (Φ^0 is function inverse to the RF with respect to the first argument). In addition, here such normalization of the RF is used, that $\Phi(1, T_b) = b$. In particular, if the basic loading determines the diagram

$$R = f(E), \quad (4)$$

the diagrams obtained in other trials are similar to the mentioned one with respect to the coordinate origin:

$$R = sf(E/s). \quad (5)$$

At repeated loading similarity of the states S ceases, but the differences $S_* = S - S_v$ (S_v denote the state in the last reversal) prove to be similar to the states S_b [2]:

$$S_*(R_*, E^*, T) = \kappa S_b(R/\kappa); \quad (6)$$

$$\kappa = S - S_v. \quad (7)$$

Accordingly,

$$R_* = \kappa f(E/\kappa). \quad (8)$$

The asterisks mark changes of the corresponding parameters on a comparison with their values have been reached at the last reversal moment (index v).

Expressions (2) and (4)-(8) can be used also at variable rate E^* and temperature T as some approximation; however use of expression (3) can lead to some errors. For example, stress relaxation in a zone IZ at value E^* which is close to zero is possible, but this does not mean that parameter s is equal to zero. In such situations the latter parameter can be represented as a functional of the deformation history; the defining equation is based on a similarity assumptions (1), (4) and can be obtained by time differentiation of expression (8) taking into account (3).

By introducing parameter $\pi = E - R$ which is linearly related with state S , we come to the state equation

$$\pi^* = \Phi(s, T)(1 - f'(E/\kappa)); \quad (9)$$

parameters s and E/κ can be determined using parametric equation (8); here and below derivatives are marked by dashes. The state equation (9) can be used on any stage of loading history (on the initial one it should be adopted $E^* = s, r = R, v = 0$). Specifically, from (9) at $E^* = \text{const}$, $T = \text{const}$ expression (3) follows.

Unfortunately, the "memory rules" by which conditions of the sequential reversals appearance and erasing from the memory cannot be considered here; largely, they are analogous to those used in the case of the similarity principle formulated for the structural model of medium [1,2].

4. On the computational procedure

The characteristic functions RF ($\Phi(s, T)$) and $R = f(E)$ be used as the identification functions for the suggested macro-model. The first one can be determined by process of scaling over dependence of secondary creep rate of the material on elastic strain r and temperature T ($p^* = \varphi(r, T)$):

$$\Phi^0(x, T) = \Phi^0(x, T) / \Phi^0(b, T_b). \quad (9)$$

To determine function f it is necessary to analyze the states of the structure under initial loading characterized by the two different conditions:

- supposing perfect elasticity ($\Phi = 0$) - to connect parameters of external thermo-mechanical action with loading parameter R ;
- be based on the given RF (i.e. determined by expression (9)) and the basic value of parameter $E^* = b$. Variation of the external load rate should be fitted in such way that the actual power strain rate in unsafe point x_0 be approximately constant; then, this value is accepted as the basic one ($E^* = b$). The RF here is supposed to be independent on temperature ($T = T_b$).

Comparing the results one can determine dependence (3) between parameters R and E .

Note, that there is no necessity to prescribe the loading program for the basic computations in detail. It is enough to reproduce situations (i.e. external forces and thermal strains) which correspond to the extreme states in the IZ.

5. Lifetime evaluation of a structure

It is offered to use here the variant of LCF damage accumulation model associated with the structural (rheological) model of medium by utilization of identical state parameters (its initial version is discussed in [3]).

It is supposed that total damage consists of "cyclic" part ω_c which is due to alternating inelastic strain, and the "static" one ω_s related with cyclic

strain accumulation (below attention is attracted to the first part only). Experiments show that component ω_s should be divided, in its turn, into two parts which correspond to plastic and creep deformation processes, respectively (see Fig.1). This is conditioned by a specific effect: damage caused by creep under tension decreases after creep under compression (this peculiarity is often interpreted as «damage curability»). Thus we obtain:

$$\omega_s = \omega_p + \omega_c \quad (10)$$

In the most simple case of tension-compression loading cycle the suggested equations take the form:

$$\omega_p^* = D_p(s, T) v^\alpha |p_p^*|; \quad (11)$$

$$\omega_c^* = H(\omega_s) D_c(s, T) v^\alpha |p_c^*|, \quad (12)$$

here $D_i(s, T)$ are the damage functions depending on state parameters s and T (see p.2); the third state parameter is presented by relation $v = p/r$, (inelastic and elastic strains p, r in point x_0 should be account off from the last reversal point); H denotes Heavyside function ($H(x) = 0$ at $x < 0$, otherwise $H(x) = 1$).

Inelastic strain rates p_p^* and p_c^* should be determined in accordance with the state equation (the similarity principle [1]) of the structural model of medium

$$p_\beta^* = \Phi_\beta(s, T)(1 - \varphi(E/\kappa)) \quad (\beta = p, c) \quad (13)$$

where functions Φ_p, Φ_c correspond to the two branches of the RF which are shown in Fig.1. Parameter v in equations (11), (12) is uniquely connected with argument E/κ of state equation (8). It is important, that state parameters s and E/κ for the IZ as a whole and for macro-stresses in point x_0 coincide. Due to this peculiarity the both computations concerning deformation kinetics and damage accumulation can be carried on in a parallel way.

Identification of the model is reduced to experimental determination of damage functions $D_\beta(s, T)$ and exponent $\alpha(T)$. The functions can be found from LCF tests data at varied deformation rates in tension and compression half-cycles; the LCF diagram exponent is determined by a slope of plotted in logarithmic coordinates. As an example, damage functions for a high-temperature Cr-Ni steel is shown in Fig.2. Note, that identification of the damage model can be simplified if piecewise-linear (line 2) or, all the more, piecewise-constant (3) approximation of the functions is used.

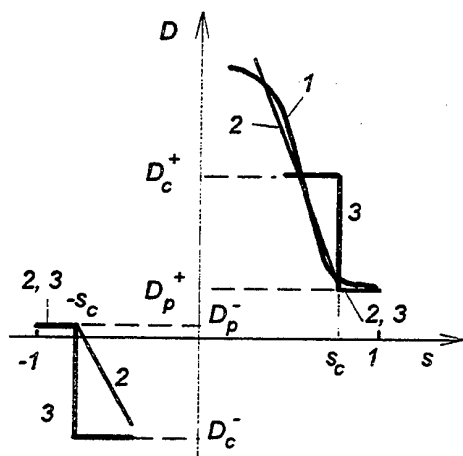


Fig.1. The damage functions

Verification of the suggested damage accumulation model confirmed that it reflects the main LCF regularities [5] with quite satisfactory accuracy. Moreover, at loading programs which include hold-time periods and/or non-isothermal loading stages, numbers of cycle to failure predicted by the suggested model correspond to experimental data something better than other known damage models. Possibly, it is related with state parameters v and s has been adopted as defining for the damage process (as well as for viscous and plastic deformation processes). It has been shown [1,2] that the parameters can be interpreted in terms of physics of metals: the first one represents relative number of activated sliding planes while the second- relative loading intensity of the latter.

6. Conclusion

Due to the suggested generalized model of structure, the rather cumbersome methods which are used now for stress-strain analysis of inelastic structures subjected to variable repeated loading, in some actual cases can be substituted by procedures which need essentially less computational volumes. The approach has required use of some simplified assumptions, in particular, isochronism of strain reversals in all the points of the considered structure; the Masing principle validity for viscous solids; similarity of state of any structure with respect to its basic state which corresponds to initial loading stage. Verification of model has shown that the inaccuracies caused by the assumptions prove to be rather small.

It should be noted that only cyclical component of a structure response (and accordingly LCF damage) is considered above: the static component (strain accumulation which often accompanies cyclic loading and can essentially decrease durability of structures) has not been taken into account. But in the case of local IZ influence of the latter on lifetime

can be usually neglected. In more common cases, approximate limit strain accumulation can be determined accordingly to the acting loading cycle parameters using some special procedure [6].

This study is a part of the project sponsored by the Russian Fund for Fundamental Research (grant 95-01-00230)

References

- (1) Gokhfeld, D. A. and Sadakov, O.S. On the Main Approaches to Strength and Lifetime Evaluation of Structures Under Variable Repeated Load and Temperature, *Inelastic Solids and Structures* (Antoni Sawchuk Mem. Vol., M. Kleiber and J.-A. Konig, Eds), Pineridge Press, Swansea, U.K., p.415, 1990.
- (2) Gokhfeld, D.A. and Sadakov, O.S. Generalized Similarity Principle for Plasticity and Creep Analysis of Structural Elements, *Trans. 11th Intern. SMiRT Conf. (Tokyo, Japan)*, V. L, p.581, 1991.
- (3) Gokhfeld, D.A., Poroshin, V.B. and Sadakov O.S. On LCF Lifetime Prediction in the Case of Stress Concentration Zone, *Trans. 4th Intern. Confer. on Comput. Plasticity (COMPLAS-4)*, Barcelona, Pineridge Press, Swansea, UK, p.1033, 1995.
- (4) Gokhfeld, D.A., Poroshin, V.B. and Sadakov, O.S. Plasticity and Creep, LCF and Crack Propagation Processes: Related State Equations, *Trans. SMiRT 11th Intern. Confer., Tokyo, Japan, Vol.L*, p.283, 1991.
- (5) Manson, S.S., The Challenge to Unify Treatment of High Temperature Fatigue. A Partisan Proposal Based on Strainrange Partitioning, *ASTM Spec. Techn. Publ.*, N520, p.74, 1973.
- (6) Gokhfeld, D.A. and Sadakov, O.S., Steady Cyclic State of a Structure: Methods of Its Direct Determination, *Inelastic Behaviour of Structures under Variable Loads*, Z.Mroz, D.Weichert, St.Doros Eds, Kluwer Academic Publ., Dordrecht, Boston, London, p.449, 1995.

A Constitutive Model for Thermo-Hydro-Chemo-Mechanical Response of Decomposing High Performance Concrete Under High Temperature.

M. Jouhari* and I. Laalal*

* Ecole Nationale des Ponts et Chaussées, Centre d'Enseignement et de Recherche en Analyse des Matériaux (ENPC-CERAM), 6 et 8 avenue Blaise Pascal, Cité Descartes Champs-sur-Marne, F-77455 MARNE-LA-VALLEE Cedex 2, FRANCE.

We have developed a thermo-hydro-chemo-mechanical constitutive model for decomposing high performance concrete subjected to high temperature. The model is based on the poroelasticity theory and includes analysis of the mass loss of the skeleton due to thermochemical decomposing, gas pressure inside the pores and stresses. The numerical results show the influence of the rate of heating and the values of the material parameters on temperature gradient, stress fields and water vapour pressure and especially the influence of the chemical shrinkage due to dehydration on the spalling.

Key Words: High Temperature, High Performance Concrete, dehydration, Stresses and Pore pressure.

1. Introduction

Over the last few years, experimental studies have shown premature damage in certain high performance concretes (HPC) during exposure to high temperature. These types of concrete are dense, with a number of excellent properties, but the density is a potential problem with regard to fire resistance. High temperatures induce a loss of strength and stiffness, increase both the elastic deformability and the creep, alter the chemical-physical composition of the hardened mortar (transmigration and vaporisation of the free water, loss of the combined and adsorbed water, dissociation of the calcium hydroxide at 450°C, shift from α quartz to β quartz in the crystalline silicon dioxide at 575°C) [1]. When concrete is exposed to high temperature, the liquid water in the concrete will change into water vapour. The dehydration of the C-S-H also produces a water vapour. These two phenomenon combined to the low porosity and low coefficients of fluid transfer lead to a considerable increase of the pressure of fluid inside the concrete. Then the risk of spalling is very high even explosive spalling has been reported [2]. In order to get a better understanding of this phenomenon and a greater degree of predictability, it is necessary to acquire more knowledge about the thermo-hydro-chemo-mechanical mechanisms that cause this kind of damage.

2. Mass Conservation and Thermodynamic

We have developed a thermo-hydro-chemo-mechanical constitutive model for decomposing high performance concrete subjected to high temperature and overall loading. The model is based on the poroelasticity theory and includes analysis of the mass loss of the skeleton due to thermochemical decomposing, gas pressure inside the pores and the thermal stress. The underlying ideas to model such a dehydration in the framework of reactive porous

media are mass conservation considerations and thermodynamics of open porous media. For the general theory of open reactive nonsaturated porous media, the interested reader is referred to Coussy [3,4]. At the level of the porous media, the dehydration may be roughly viewed as follows: the reactant phase corresponds to the hydrates and the product phase to the free water vapour. Let m^s and m^f be respectively the mass increase of fluid and the mass loss by the skeleton. The mass conservation for each phase reads as follows:

$$\frac{dm^s}{dt} = -\text{Div } \underline{M} + m^0 \quad (1)$$

$$\frac{dm^f}{dt} = m^0 \quad (2)$$

where m^0 is the rate of mass of fluid produced by the dehydration and $-\text{Div } \underline{M}$ is the external rate of fluid mass supply. Equations (1) and (2) give:

$$\frac{dm}{dt} = -\text{Div } \underline{M} \quad (3)$$

where $m = m^s - m^f$ is the mass increase due only to the external flow of fluid.

Using thermodynamics of open porous medium, the second law of thermodynamics can be written as follows:

$$\sigma : \dot{\epsilon} - \dot{\Psi} - \dot{S}T + g_m^s \dot{m}^s - g_m^f \dot{m}^f - (g_m^s - g_m^f) m^0 - \frac{\underline{Q}}{T} \cdot \underline{\text{Grad}} T - \frac{\underline{M}}{\rho^s} \cdot \underline{\text{Grad}} p \geq 0 \quad (4)$$

where an overdot denotes time derivation; σ , S and g_m^j are stress tensor, entropy and free enthalpies per unit mass, they are the thermodynamic forces associated in dissipation to the rate of the strain tensor ϵ , temperature T and mass m^j ($j = g, s$); and \underline{Q} and \underline{M} are the vectors of the heat flux and the fluid flux.

$\phi_i = \sigma : \dot{\varepsilon} - \dot{\Psi} - \dot{S}T + g_m^s \dot{m}^s - g_m^s \dot{m}^s$ is the dissipation related to the intrinsic mechanisms; $\phi_d = -\left(g_m^s - g_m^s\right)m^0$ is the dissipation associated to the dehydration reaction; $\phi_t = -\frac{Q}{T} \cdot \text{Grad}T$ is the dissipation associated with the transport of heat and $\phi_f = -\frac{M}{\rho^s} \cdot \text{Grad}p$ is the dissipation associated with the transport of fluid.

Substituting equation (2) into (4), the second law of thermodynamic can be written as:

$$\sigma : \dot{\varepsilon} - \dot{\Psi} - \dot{S}T + g_m^s \dot{m}^s - \frac{Q}{T} \cdot \text{Grad}T - \frac{M}{\rho^s} \cdot \text{Grad}p \geq 0 \quad (5)$$

A comparison between (4) and (5) allows us to consider the mass loss m^s as an internal variable, denoted in the following by x and its associated thermodynamic force by A . A is the affinity of the chemical reaction of dehydration and \dot{x} its reaction rate (because its evolution cannot be controlled by external flow). The thermodynamics forces derive from free energy $\Psi = \Psi(\varepsilon, T, m, x)$.

Classically, we obtain:

$$\sigma = \frac{\partial \Psi}{\partial \varepsilon}; \quad S = -\frac{\partial \Psi}{\partial T}; \quad g_m^s = \frac{\partial \Psi}{\partial m}; \quad A = -\frac{\partial \Psi}{\partial x} \quad (6)$$

3. Constitutive equations

To complete the description of the mechanical behaviour, we have worked out from specifying expression of free energy of the system a constitutive equations in the framework of physical linearization and infinitesimal transformation:

$$\sigma = \sigma_0 1 + \lambda \text{tr} \varepsilon + 2\mu \varepsilon - Mb \frac{m}{\rho_0^s} 1 - 3\alpha K \theta 1 - \omega \frac{x}{\rho_0^s} 1 \quad (7)$$

$$g_m = g_m^0 - \frac{M}{\rho_0^s} b \text{tr} \varepsilon - \left(s_m^0 - \ell\right) \theta + \frac{M}{\left(\rho_0^s\right)^2} m + \delta \frac{x}{\left(\rho_0^s\right)^2} \quad (8)$$

$$S = S_0 + 3\alpha K \text{tr} \varepsilon + \frac{C_\varepsilon}{T_0} \theta + \left(s_m^0 - \ell\right) m + \gamma x \quad (9)$$

$$A = A_0 + \frac{\omega}{\rho_0^s} \text{tr} \varepsilon + \gamma \theta - \delta \frac{m}{\left(\rho_0^s\right)^2} - \tau \frac{x}{\left(\rho_0^s\right)^2} \quad (10)$$

By using the saturating fluid state equation:

$$dg_m = \frac{dp}{\rho^s} - s_m d\theta, \text{ equation (8) becomes:}$$

$$p = p_0 - Mb \varepsilon + \rho_0^s \ell \theta + M \frac{m}{\rho_0^s} + \delta \frac{x}{\rho_0^s} \quad (11)$$

where p is the pore pressure and p_0 the pore pressure at the initial time.

3.1 SIGNIFICANCE OF MATERIAL CHARACTERISTICS:

3.1.1 The classical characteristics:

λ, μ are the lamé coefficients, M is the Biot modulus, b is the Biot coefficient, α is thermal dilatation coefficient, K is the bulk modulus, C_ε is the volumic heat capacity, T_0 is the initial temperature, s_m^0 is the initial mass entropy of fluid, ℓ is the latent heat of increasing fluid mass.

3.1.2 The characteristics related to our model:

The variation of pore pressure of fluid due to the external increasing of the mass m is the same than associated to the internal increasing of mass due to dehydration x . The coefficient δ can be then identified to M .

$T_0 \gamma$ is the latent heat of dehydration: it represents the consumed heat by the dehydration reaction to produce a unit mass of water vapour.

Equation (7) inverted shows that the volume strain related to chemical reaction of dehydration is:

$$\text{tr} \varepsilon^c = \frac{\omega}{K} \frac{x}{\rho_0^s} \quad (12)$$

We can distinguish in the last expression two different contributions; one is due to the internal supply of mass fluid in the porous space, the other is induced by shrinkage effect related to chemical volume change (dehydration shrinkage). Indeed, equation (12) can be written as follows:

$$\text{tr} \varepsilon^c = \frac{Mb}{K} \frac{x}{\rho_0^s} + 3\beta \frac{x}{\rho_0^s} \quad (13)$$

where the coefficient β may be considered as a chemical-dilatation coefficient.

τ is a material parameter which expresses the thermodynamic imbalance between the chemical constituents involved in the dehydration reaction.

4. Evolution laws

4.1 HEAT CONDUCTION LAW AND MASS TRANSFER

For the temperature evolution, Fourier law is adopted (14). The mass transfer in the concrete is governed by the Darcy's law (15)

$$Q = -C \text{grad} \theta \quad (14)$$

$$\frac{M}{\rho^s} = -\kappa \text{grad} p \quad (15)$$

where C is the thermic conductivity and κ is the permeability coefficient.

4.3 KINETICS OF DEHYDRATION

An evolution law of the Arrhenius type is adopted for the kinetics of dehydration. If the degree of conversion for the reaction is denoted by c , the Arrhenius kinetic reaction equation is given by:

$$\frac{dc}{dt} = -A_0 c^n \exp\left(-\frac{E_a}{RT}\right) \quad (16)$$

where A_0 , E_a , n and R are, respectively, the reaction rate constant, the activation energy, the order of reaction and the universal gas constant.

If the heating rate is constant, we derive from (16) and the initial condition $c = 0$ [5]:

$$x = x_f \left(1 - \left(1 + (n-1) \frac{A_0 E_a}{hR} g(y) \right)^{\frac{1}{1-n}} \right) \quad (17)$$

$$\text{where } g(y) = \left(\frac{e^{-y}}{y} - \int_y^\infty \frac{e^{-u}}{u} du \right) + \left(\int_{y_0}^\infty \frac{e^{-u}}{u} du - \frac{e^{-y_0}}{y_0} \right),$$

$y = \frac{E_a}{RT}$, $y_0 = \frac{E_a}{RT_0}$, T_0 is the initial temperature, h is the constant heating rate and x_f is the total mass loss.

5. Equation discretization and numerical solution

The numerical solution is carried out by using finite element technique (2D dimension, axisymmetric and plane stress problems are treated). A system of matrix differential equations is obtained and may be integrated in time by using Crank-Nicholson implicit algorithm. Note that the problem is nonlinear since the material parameters are temperature dependant. Therefore at each step of Crank-Nicholson algorithm, Newton-Raphson procedure is used. After solving the differential equations in terms of displacement, pressure and temperature, the strains and the stresses are calculated using equation (7). A numerical study have shown that the results are time step independant.

6. Numerical computations

The numerical simulations has been performed to fit experimental data that are available in the literature [6] in the case of HPC cylinders 16×32 subjected to different constant rate of heating on their surface. The classical poroelastic material parameters used in our numerical study has been collected from the literature [3, 6]. The reaction rate constant, the activation energy and the order of reaction A_0 , E_a , n has been determined to obtain a good accordance with the experimental results obtained by [6] (see Fig.1.). The parameter γ has also been numerically determined such that the calculated temperature gradient in the specimen is in agreement with the measured temperature gradient (see Fig.2.).

Temperature Dependence of material parameters:

Young modulus $E = E_0 * (1 - (T - 20) * 0.46/480)$

Bulk modulus of concrete $K = E / (3 * (1 - 2 \nu))$

Bulk modulus of water vapour considered as ideal gas

$K_g = p$; $\phi = \phi_0 * (1 + x/1000.)$

$b = 1 - K/K_g$; $M = 1 / ((b - \phi) / K_g + \phi / K_g)$

$\rho_g = (18 * 10^{-3} / 8.3) * p / (T + 273)$

$C_t = \rho * (900. + 80. * T/120. - 4. * (T/120.)^2)$ (J.m⁻³.°C⁻¹)

$C = 2. - 0.24 * T/120. + 0.012 * (T/120.)^2$ (W.m⁻¹.°C⁻¹)
Dynamic viscosity of water: $\eta = 3.85 * 10^{-14} * T + 10^{-11}$ (kg.m⁻¹.s⁻¹)

Permeability coefficient $\kappa = \kappa_i / \eta$

At the room temperature:

$E_0 = 56.7$ GPa; concrete density: $\rho = 2500$ Kg/m³; $\nu = 0.19$; bulk modulus of solid: $K_s = 72.5$ GPa; $\alpha = 0.8 * 10^{-5}$ °C⁻¹; $\beta = -0.1 * 10^{-5}$; $\ell = 463$ J.kg⁻¹; $\gamma = 4 * 10^6$ J.°C⁻¹.kg⁻¹; porosity: $\phi_0 = 0.06$ and Intrinsic permeability: $\kappa_i = 10^{-22}$ m².

The numerical simulations show that the chemical dilatation coefficient β has a great influence on the state of stress in the specimen. Indeed, when β varies from the value 10^{-6} to 8.10^{-6} , the axial stress at the heated surface of the specimen changes from a compressive state to a tensile state for temperature higher than 180°C (see Fig.7.). Furthermore, the value of this parameter can be considered as responsible of the explosive spalling reported in the literature since for some values of β , the axial stress exceeds the tensile strength of concrete. Another numerical study have shown that a great heating rate may induce the explosion of the specimen (Fig.4.- 6.).

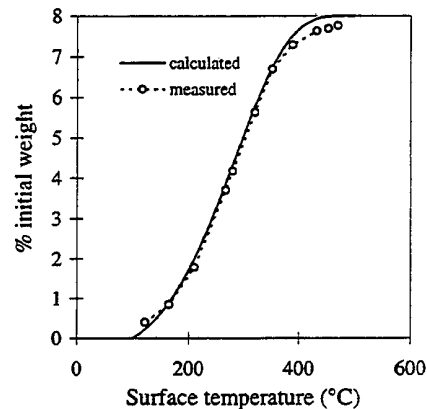


Fig.1. mass loss in HPC concrete specimens heated at 1°C/mn: measured by [6] and calculated.

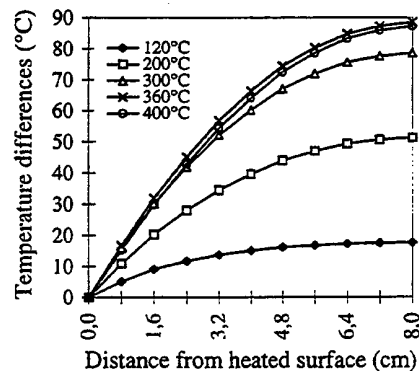


Fig.2. Temperature difference between the center and the surface of the specimen heated at 1°C/mn.

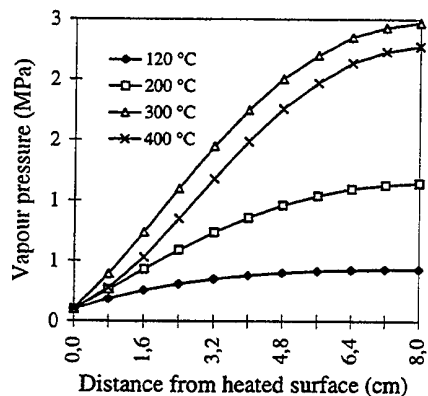


Fig.3. Pressure on a radius of the specimen heated at 1°C/mn .

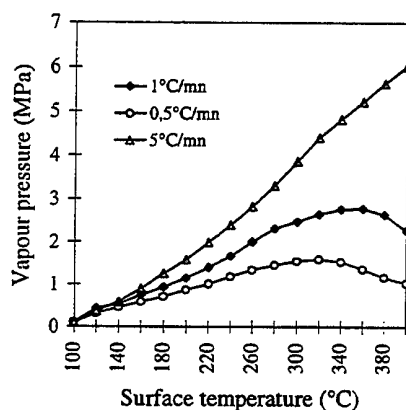


Fig.4. Vapour pressure at the center of the specimen subjected to different rate of heating .

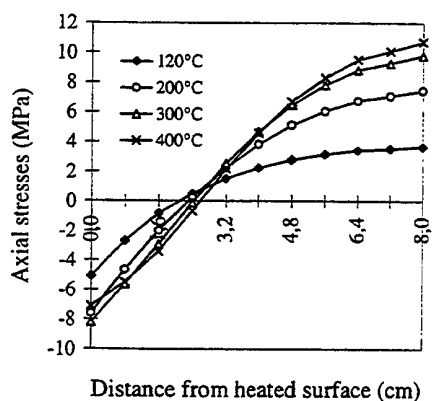


Fig.5. Axial stress vs. Radius at different surface temperature (rate of heating = 1°C/mn).

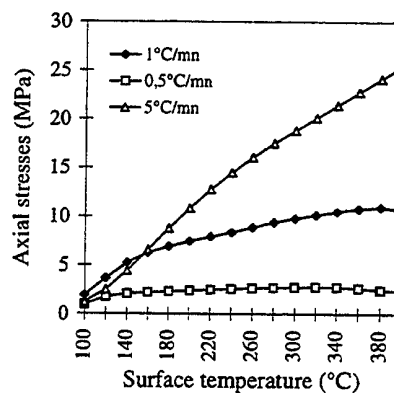


Fig.6. Axial stress at the center of the specimen subjected to different rate of heating .

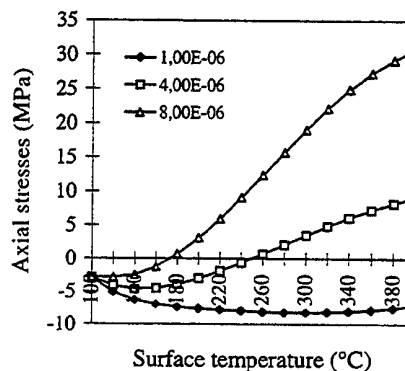


Fig.7. Axial stress at the surface of the specimen for different value of the chemical dilatation coefficient (rate of heating = 1°C/mn).

References

- (1) Bazant Z.P. and Kaplan M.F., Concrete at high temperatures, Longman, England, (1996).
- (2) Castillo C., Durani A.J., Effect of transient high temperature on strength concrete. ACI Materials Journal.
- (3) Coussy O., Mechanics of porous continua, John Wiley & Sons, Chichester, England, (1995).
- (4) Ulm F.J. and Coussy O., Modeling of thermochemomechanical coupling of concrete at early ages, J. of . Engrg. Mech., 121, N°7, July, 1995.
- (5) Wu Y. And Katsube N., A constitutive model for thermomechanical response of decomposing composites under high heating rates, Mech. Of Materials, 22, 189-201, 1996.
- (6) Noumowe A.N. and al., Thermal stresses and water vapour pressure of high performance concrete at high temperature, 4th Int. Symp. on utilization of High-Strength/High Performance Concrete, 561-570, Paris, 1996.

Session 2E

RESIDUAL STRESSES II

Chair: G. F. M. Souza

Co-Chair: L. Lindhorst

**On the Quantitative Predictions of Residual Stresses in a
Quenched Strip of Amorphous Plastics**

H. Ghoneim

**Fabrication Process Tailoring to Minimize Thermal
Residual Stresses in Metal Matrix Composites**

Christos C. Chamis

**Theoretical Analysis of Residual Stresses Removal by
Heat Supply**

M. Ishihara, Y. Tanigawa, R. Kawamura, N. Noda

**Determination of Residual Welding Stresses under
Consideration of Structural Transformations Using a
Multi-Purpose Finite Element Program**

O. Voß, I. Decker, H. Wohlfahrt

**Thermal Stresses Analysis of a Steps Axle with Boiling
Boundary**

J. R. Chen, J. B. Chen, H. G. Wang

On the Quantitative Predictions of Residual Stresses in a Quenched Strip of Amorphous Plastics

H. Ghoneim

Department of Mechanical Engineering, Rochester Institute of Technology
Rochester, NY 14623 USA

This paper addresses some of the challenges facing analysts when attempting to quantitatively predict the development of thermal residual stresses in processed amorphous plastic products. In particular, the paper focuses on the importance of selecting the appropriate constitutive equations describing the material behavior and the importance of the accurate assessment of the material parameters involved. An illustrative example is presented. The example illustrates the effect of the choice of the shift function on the residual-stresses development in a free quenched one-dimensional polystyrene strip.

Key Words: Thermal Residual Stresses, Viscoelasticity, Quenching, Volume Relaxation.

1. Introduction

The quantitative prediction of the residual-stresses buildup in processed plastic products is very difficult. For example, in the case of injection molding, analysts have to adopt appropriate constitutive equations which capture the nonlinear, anisotropic, viscoelastic behavior of the resin over the wide range of applied temperature and pressure. Also, a proper material-property database is needed in order to assess the material parameters existing in the constitutive equations. Moreover, the simulation program has to account for the fountain-flow and the boundary-conditions effects.

This paper discusses the importance of the appropriate choice of the constitutive equations and the material-parameters assessment on the qualitative prediction of the residual-stresses buildup. To simplify the task, the paper focuses on the residual-stresses development in a one-dimensional quenched strip. In this case the problems of the surface boundary condition and fountain flow are obviated, the effect of the pressure can be ignored, and the flow-induced anisotropy is alleviated.

2. Constitutive Equations

For the one-dimensional viscoelastic behavior we adopt the Boltzman integral [1],

$$\sigma = 6 \int_0^t \mu(t-\xi) \frac{\partial \varepsilon}{\partial \xi} d\xi - 2 \int_0^t \mu(t-\xi) \frac{\partial \varepsilon_v}{\partial \xi} d\xi \quad (1)$$

$$\varepsilon_v = \int_0^t J(t-\xi) \frac{\partial \sigma_m}{\partial \xi} d\xi + \int_0^t \alpha(t-\xi) \frac{\partial T}{\partial \xi} d\xi \quad (2)$$

where T is the absolute temperature, σ is the in-plane stress, ε is the in-plane strain, ε_v is the dilatational strain, σ_m is the mean stress, $\mu(t)$ is the shear-relaxation modulus, $J(t)$ is the dilatational-creep compliance, and $\alpha(t)$ is the "thermal-expansion" compliance. Also, we assume

$$\mu(t) = \mu_l - (\mu_l - \mu_g) M_1(t) \quad (3)$$

$$J(t) = \kappa_l - (\kappa_l - \kappa_g) M_2(t) \quad (4)$$

$$\alpha(t) = \alpha_l - (\alpha_l - \alpha_g) M_2(t) \quad (5)$$

where μ_l , κ_l and α_l are the shear modulus, compressibility and volumetric thermal-expansion coefficient for the liquid state, respectively. Similarly, μ_g , κ_g and α_g are for the glassy state. $M_1(t)$, and $M_2(t)$ are the shear-relaxation and the dilatational-creep functions, respectively [2]. They are taken as

$$M_1(t) = \sum_i (w_s)_i \text{Exp} \left\{ \int_0^t \frac{-dt'}{(\tau_s)_i} \right\}, \text{ and} \quad (6)$$

$$M_2(t) = \sum_i (w_D)_i \text{Exp} \left\{ \int_0^t \frac{-dt'}{(\tau_D)_i} \right\} \quad (7)$$

where w_i and τ_i are the weighting parameters and the relaxation or retardation times of mode i for the deviatoric (subscript S) and the dilatational (subscript D) domains.

Furthermore, we assume that the material is thermorheologically simple, i.e., $M_1(t)$ and $M_2(t)$ shift without distortion according to the following relation,

$$(\tau_D)_i = a_D(\tau_D)_{r,i} \text{ and } (\tau_S)_i = a_S(\tau_S)_{r,i} \quad (8)$$

where the subscript r denotes the reference state, a_D and a_S are the dilatational and deviatoric (shear) shift functions, respectively. They depend on the temperature, pressure and the structural state of the material. The thermorheologically-simple material assumption (equation 8) implies that M_1 as well as M_2 has the same shape at every thermomechanical state on a logarithmic time scale and that at different temperatures M_1 as well as M_2 may be brought into coincidence by a parallel shift along the logarithmic time scale producing a master curve. It should be mentioned that for some polymers and within certain temperature and pressure range, distortion of the shear-relaxation function has been experimentally noticed [2].

Following the argument of Espinoza and Aklonis [3], the relaxation and retardation spectra are assumed to move identically and without distortion, that is, $a_D = a_S = a$. The observation that the shear-relaxation modulus [4] as well as the dilatational-creep compliance [5], of some amorphous polymers in isothermal volume relaxation experiments, shifts along the logarithmic time with the change of the specific volume supports this assumption. Furthermore, the shift function is assumed to depend on the temperature and the structural state. Two shift functions are studied in the current analysis in order to demonstrate the effect of the shift function on the quantitative prediction of the residual-stresses buildup. The two functions are:

$$1. \text{Log}(a) = \frac{Q/T}{1 - T_2/T_f} - \frac{Q}{T_r - T_2} \quad (9_a)$$

$$2. \text{Log}(a) = \frac{Q}{T_f - T_2} - \frac{Q}{T_r - T_2} \text{ for } a \leq a_c,$$

$$\text{and } \text{Log}(a) = Q'/T_f - Q'/T_r \text{ for } a \geq a_c \quad (9_b)$$

where Q and T_2 are material constants, and a_c is the critical value of "a" which defines the transition between the melt and the glassy states. Q' is chosen such that the slope of $\text{Log}(a)$ is

continuous at a_c ; $Q' = Q\{T_r/(T_r - T_2)\}^2$.

Equation (9_a) is a modification of the Gibb's function. It reduces to the well-known Williams-Landel-Ferry (WLF) equation in the equilibrium state when $T_f = T$ and to the Arrhenius form in the glassy state when T_f is constant [6]. Equation (9_b) is a modification of the shift function adopted by the Cornell Injection Molding Group (CIMP). This equation fits reasonably well the experimental shift data of polystyrene and polycarbonate [7]. However, the equation is composed of two different expressions applied at the two different regions and consequently is numerically inconvenient. The fictive temperature T_f represents the structural state and is taken to be proportional to the transient specific-volume change [1],

$$T_f = T_0 + \int_0^t \{1 - M_2(t - \xi)\} \frac{\partial T}{\partial \xi} d\xi \quad (10).$$

The best choice of the variable to represent the structural state is still a debatable issue, however, the fictive temperature has been recognized as one of the appropriate choices [6].

Determination of the residual stresses in a free-quenched strip requires the simultaneous solution of equations (1) and (2) augmented with (3)-(10) at all material points (layers) across the thickness of the strip and over the whole history of quenching. Evolution of the temperature profile can be obtained by applying the one-dimensional heat conduction equation with free convection boundary conditions at the surfaces. The strain is solved for iteratively at any time by enforcing the free-end boundary condition, i.e., the lateral force to vanish.

3. Material Parameters Assessment

As mentioned before, we can solve for the evolution of the in-plane residual stresses across the thickness of the strip throughout the history of quenching - provided that all material properties are available. These material properties are:

1. the compressibility and volumetric thermal-expansion coefficients for the glassy (κ_g and α_g) and the melt states (κ_l and α_l);
2. the shear-relaxation moduli (μ_g and μ_l); the shear-relaxation spectrum, i.e., $(w_s)_i$ and

- (τ_s)_i; and the dilatational-creep spectrum, i.e., (w_D)_i and (τ_D)_i;
- the material constants of the shift function, Q and T₂.

The coefficient of thermal expansion and the compressibility can be obtained from the PVT diagram, using Tait's equations. The shear-relaxation and the dilatational-creep spectra can be determined from curve-fitting experimental data of the shear-relaxation modulus and dilatational-creep compliance, respectively. The shift function used to generate the master shear-relaxation and/or dilatational-creep compliance defines the values of Q and T₂. Fitting the isothermal volume-relaxation experimental data can also be used to generate the dilatational-creep compliance and the constants Q and T₂. It should be mentioned that although, in principle, assessment of the material properties is a direct task, finding reliable and consistent experimental data poses one of the greatest challenges to obtaining reliable and accurate values of the material parameters.

4. Example and Discussion

Prediction of the residual stresses buildup in a 2.6 mm thick polystyrene strip from 130 °C to 23 °C is presented. The example is meant to illustrate the importance of the proper shift function choice. It is imperative to acknowledge that the material parameters of the constitutive equations should not be determined by curve-fitting of the primary targeted experimental data. That is, for the current example, we cannot use the experimental data of the residual-stresses profile of the polystyrene strip to obtain any of the material constants. They should be obtained from completely different sets of experimental data.

The material parameters adopted for the current analysis are presented in Tables 1-3.

Table 1 Tait's constants

Constant	Glass	Liquid
C ₁ (cm ³ /gm)	0.986	1.007
C ₂ (cm ³ /gm-°C)	2.44 10 ⁻⁴	5.79 10 ⁻⁴
C ₃ (Pa)	2.26 10 ⁸	2.02 10 ⁸
C ₄ (1/°C)	1.36 10 ⁻³	3.00 10 ⁻³

Table 2 shear-relaxation and dilatational-creep parameters (T_r = 100 °C).

w _s	τ _s (sec)	w _D	τ _D (sec)
0.587	3.021	0.1	2.130 10 ⁻⁵
0.348	2.892 10 ¹	0.07	8.520 10 ⁻⁴
6.232 10 ⁻²	1.228 10 ²	0.11	7.455 10 ⁻²
2.736 10 ⁻³	1.557 10 ³	0.17	1.278
4.191 10 ⁻⁴	3.474 10 ⁴	0.165	2.556
1.111 10 ⁻⁴	1.071 10 ⁶	0.385	34.08
1.091 10 ⁻⁴	2.426 10 ⁷	μ ₂ (MPa)	745
4.964 10 ⁻⁵	2.096 10 ⁸	μ ₁ (MPa)	0.0

Table 3 Shift-function's parameters

	Model-1	Model -2
Q (K)	1255	1372
T ₂ (K)	326.7	334.3

Tait's constants are obtained from cumulative PVT data from literature for commercial-grade polystyrene. Shear-relaxation parameters are determined from curve fitting of the experimental data from Alkonis and Tobolski [8], and the dilatational-creep parameters are taken from Greiner and Schwarzl [9]. The parameters Q and T₂ are determined by best- fitting of the volume relaxation prediction of the current model with the corresponding experimental data a of Greiner and Schwarzl.

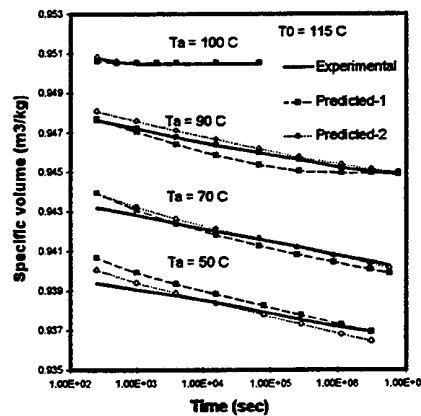


Fig. 1 Volume-relaxation for polystyrene upon quenching from 115 °C to indicated temperature

The predicted results using the shift functions (9_a), and (9_b), labeled predicted-1 and 2 respectively, are shown in Fig. 1. The corresponding predicted shift in the shear-relaxation modulus, for both shift functions,

with aging time are also compared with the relevant experimental data of Matsuoka [4] and displayed in Fig. 2. It should be mentioned that the second set of data (Fig. 2), are used to readjust the material parameters Q , T_2 and the average value of the shear-relaxation and creep-retardation times. It can be observed from the results that model 2, using equation (9_b), can match the experimental data better. However, both models can not generate accurate fits.

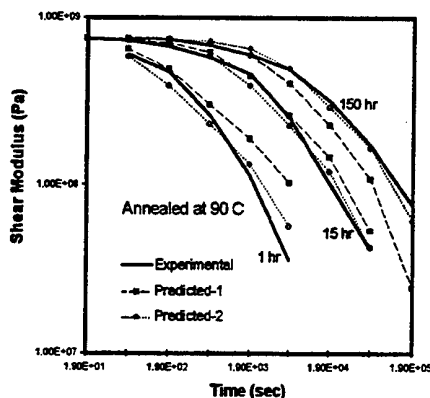


Fig 2 Shear-relaxation modulus for polystyrene annealed at 90 °C for different times.

Once the material parameters are determined, the constitutive equations proposed are used to predict the residual-stresses buildup in the freely quenched plate, and the predicted results are compared with the corresponding experimental results of Isayev and Crouthamel [10]. The predicted and experimental results are displayed in Fig. 3. It is clear that both models overpredict the residual stresses, and that the prediction of model 1 is substantially higher than that of model 2.

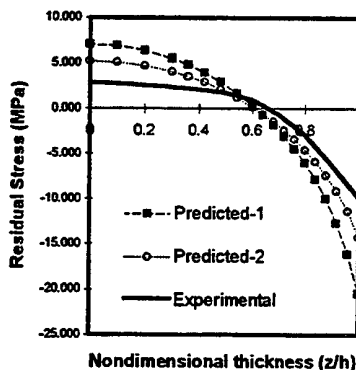


Fig. 3 Residual-stress for a 2.6 mm thick polystyrene plate quenched from 130 °C to 23 °C

5. Conclusion

The results presented in figures 1-3 are consistent and indicate: 1) both models of the shift functions could not match the experimental data required to obtain the material parameters (figures 1 and 2), and could not predict good residual stresses; and 2) model 2 matched the experimental data used for the parameter assessment better than model 1, and predicted a better residual-stress profile. These observations strongly suggest that the choice of the shift function is important; the more accurate the shift function is, a better prediction of the residual stresses is produced.

References

- 1) Ghoneim, H., and Hieber C.A., Incorporation of Density Relaxation in the Analysis of Residual Stresses in Molded Parts, Polymer Engineering and Science, In print.
- 2) Scherer, G.W., Relaxation in Glass and Composites, Wiley, New York, 1986.
- 3) Espinoza, A., and Aklonis, J.J., Modeling Viscoelastic Behavior of Glasses During Physical Aging, Polymer Engineering and Science, Vol. 33, pp. 486-496, 1993.
- 4) Matsuoka, S., Bair, H.E., Bearder S.S., Kern, H.E., and Ryan, J.T., Analysis of Non-Linear Stress Relaxation in Polymeric Glasses, Polymer Engineering and Science, Vol. 18, pp. 1073-1080, 1978.
- 5) Struik, C.E., Dependence of Relaxation Times of Glassy polymers on Their Specific Volume, Polymer Paper, Vol. 29, pp. 1347-1353, 1988.
- 6) Mijovic, J., Principal Features of Structural relaxation in Glassy Polymers. A Review, Polymer Engineering and Science, Vol. 34, pp. 381-389, 1994.
- 7) Cornell Injection Molding Program, Progress Report No. 19, 1996.
- 8) Alkonis, J.J., and Tobolsky, A.V., Journal of Applied Physics, Vol. 36, 1965.
- 9) Greiner, R., and Schwarzl, F.R., Volume Relaxation and Physical Aging of Amorphous Polymers 1. Theory of Volume Relaxation After Single Temperature Jumps, Colloid Polymers and Science, Vol. 267, pp. 39-47, 1988.
- 10) Isayev, A.I., and Crouthamel, D.L., Polym. Plast. Technol. Eng., Vol. 22, p. 209, 1984.

FABRICATION PROCESS TAILORING TO MINIMIZE THERMAL RESIDUAL STRESSES IN METAL MATRIX COMPOSITES

Christos C. Chamis
NASA Lewis Research Center
Cleveland, Ohio 44135

Metal-matrix composites (MMC) are potential candidate materials for applications requiring high operational temperatures (400 to 1100° C). In addition, high specific strengths and specific moduli are possible because the densities of the reinforcing materials are relatively low. This combination of properties makes these materials especially attractive for use in the aerospace industry. But, a crucial problem limiting the use of many MMCs is the high residual (final) thermal micro-stresses developed during the fabrication process, as a result of the large temperature differential and the mismatch between the thermal expansion coefficients (CTE) of the fiber and matrix. In order to control the high thermal residual micro-stresses in unidirectional MMCs developed during the cooling phase of the fabrication process, a computational method is presented to optimize the fabrication process of MMC and the thermomechanical properties of a compatible fiber-matrix interphase (compliant layer).

KEY WORDS: Graphite-fiber, copper-matrix, composite-mechanics, nonlinearities, micro-stresses.

Introduction

The objective of the method is to minimize the residual microstresses at the end of the fabrication process (i.e., phase 3 shown in Figure 1) by optimizing the temperature and consolidation pressure time profiles (histories) concurrently with the compliant layer properties (modulus, CTE, and strength) and other composite parameters (compliant layer thickness and fiber volume ratio), while the in situ constituent materials integrity is ensured throughout the process. Tailoring of the fabrication process has resulted in reducing residual microstresses in the matrix [1]. The addition of a suitable interphase placed between the fiber and matrix may produce MMCs with further reductions in the thermal residual stresses [2]. The present computational method was developed to concurrently tailor the fabrication process and the interphase of MMCs for minimal residual stresses.

The thermomechanical response of MMCs during cool-down of the fabrication process is simulated based on unified nonlinear micro-mechanical encoded in METCAN (metal matrix composite analyzer [3]). The theory is based on a

micromechanics unit cell shown in Figure 2. The nonlinearities due to temperature and stress in the three different phases (fiber, matrix and interphase) are described by a generic multi-factor interaction model of product form (MFIM) as follows:

$$\frac{P_i^t}{P_{oi}} = \left[\frac{T_{Mi} - T^t}{T_{Mi} - T_o} \right]^q \left[\frac{S_i^t - \sigma_i^t}{S_i^t} \right]^p \quad i = m, d, f$$

where P_i^t is any thermomechanical property at time t in phase i m or d P_{oi} is the corresponding reference property; T_{Mi} is the temperature at which mechanical properties approach zero, S_i^t is the strength at time t ; σ_i^t is the microstress in the i phase at time t ; and the exponents q and p are selected so that P_i^t passes through P_{oi} and some other point P_i^{t1} .

The minimization of residual micro-stresses is formulated as a constrained

nonlinear mathematical programming (NLP) problem and is numerically solved with the modified feasibility directions method.

- Objective function: $\min(\max(\omega_1 \sigma_{mA11}, \omega_2 \sigma_{mA22}))$
 $\min(\zeta)$
- subject to constraints: $\omega_1 \sigma_{mA11}^A \leq \zeta$ and $\omega_2 \sigma_{mA22}^A \leq \zeta$
- Upper and lower bounds:
 - Fabrication process parameters: $T_0 \leq T \leq T_M$
 $0 \leq p \leq 345 \text{ MPa}$
 $10 \text{ sec} \leq t \leq 18000 \text{ sec}$
 - Interphase property: $34.6 \text{ GPa} \leq E_d \leq 220.8 \text{ GPa}$
 $1.69 \text{ cm}^3/\text{cm}^3 \text{ } ^\circ\text{C} \leq \alpha_d \leq 67.8 \text{ cm}^3/\text{cm}^3 \text{ } ^\circ\text{C}$
 $34.5 \text{ MPa} \leq S_d \leq 414.0 \text{ MPa}$
 - Micromechanical parameters: $0.05 \leq k_f \leq 0.15$
 $0.05 \leq k_t \leq 0.15$

An ultra-high modulus graphite (P100)/copper MMC was used to demonstrate the proposed method for the concurrent optimization of the process and interphase properties. Figure 3 shows the current and the resultant optimum fabrication processes for Case 1 (fabrication process optimization only) and Case 2 (concurrent optimization of the fabrication process and interphase characteristics). In both cases the optimized processes follow similar patterns during the cool-down phase. Compared to the current process, two significant differences exist that lead to the reduction of the final residual matrix microstresses: (1) The optimization temperature histories in Figure 3(a) decrease more rapidly to room temperature and are held constant until the end of the process; (2) as shown in Figure 3(b), the predicted optimal consolidation pressure histories gradually increase as the consolidated temperature drops, reaching significantly higher values than the pressure of the current process and finally dropping to zero. More interestingly, the temperature drop takes place when the pressure is high, such that the thermal stresses are forced to develop when the matrix and interphase are highly nonlinear and nearly in a flow state; hence, high strains do not cause high stresses. The pressure is removed when the temperature reaches room values as it does not contribute further. This illustrates the importance of the consolidation pressure history.

The corresponding longitudinal and transverse matrix microstresses, σ_{mA11} and σ_{mA22} , are shown in Figure 4. The final residual microstress σ_{mA11} in Case 1 decreased by 21 percent compared to the

respective microstresses value of the current process. In comparison, Case 2 had a 41 percent reduction for σ_{mA11} . The additional reductions in Case 2 are attributed to the interphase optimization. The optimum microstress σ_{mA22} in Case 1 was nearly equivalent to that of the current process; however, the final microstress σ_{mA22} in Case 2 decreased by 24 percent because of the optimized interphase properties. Compared to the initial properties of the interphase (assumed same as copper), the optimized interphase has (1) a significantly higher CTE, (2) a slightly higher modulus and strength, and (3) an increased interphase thickness and fiber volume ratio.

The final longitudinal composite properties for Cases 1 and 2 increased in stiffness and strength (tensile) along with the CTE when compared to the current process. Also, Case 2 is superior to the current process and Case 1; it showed the most improvement in lowering the residual stresses and improving the final composite material properties. In conclusion, the results indicate that consolidation pressure histories are the most important fabrication parameters, while the CTE is the most significant interphase property.

REFERENCES

- [1] Saravanos, D.A., Murthy, P.L.N., and Morel, M., Optimum Fabrication Process for Unidirectional Metal-Matrix Composites: A Computational Simulation. NASA TM 102559, 1990.
- [2] Ghosn, L. J. and Lereh, B.A., Optimum Interface Properties for Metal Matrix Composites. NASA TM 102295, 1989.
- [3] Murthy, P.L.N., Hopkins, D.A. and Chamis, C.C., Metal Matrix Composite Micromechanics: In-Situ Behavior Influence on Composite Properties. NASA TM 102302, 1989.

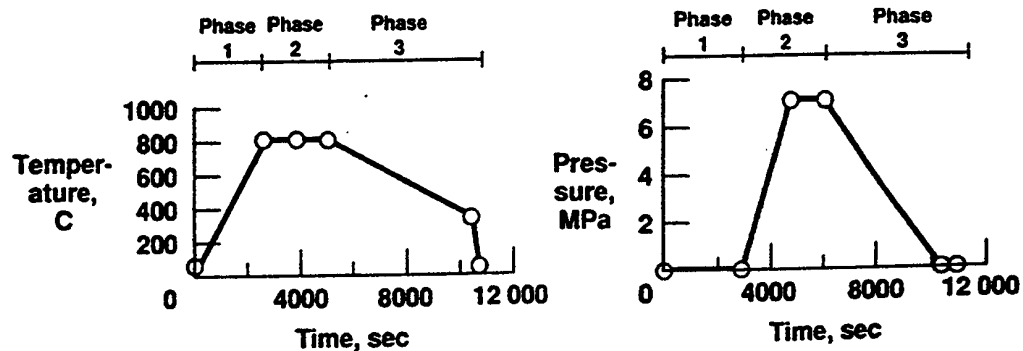


Figure 1. Typical fabrication process cycle for graphite/copper composite.

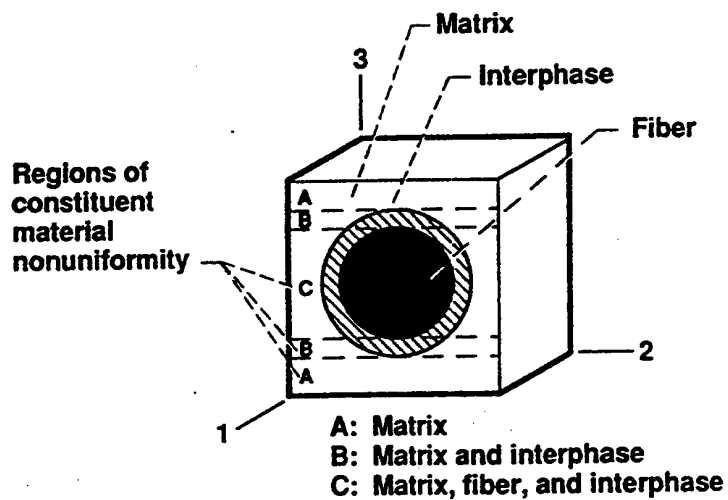


Figure 2. Micromechanics cell and regions for metal matrix composite mechanics.

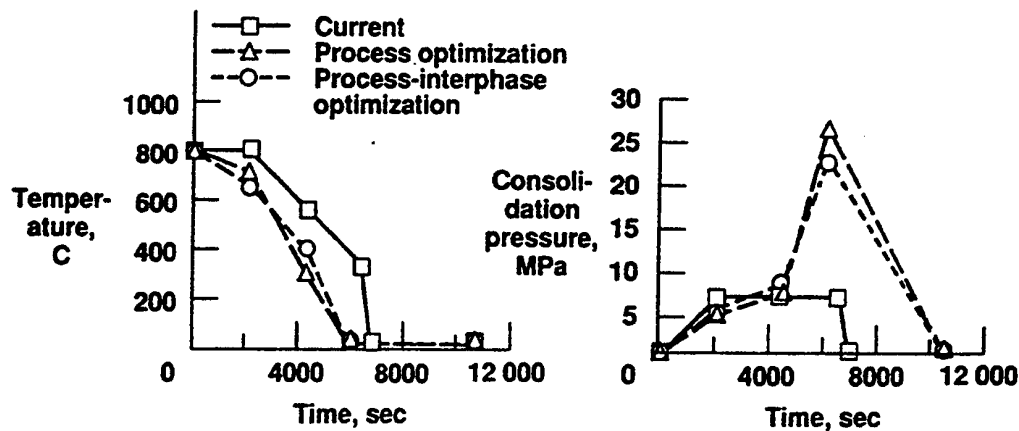


Figure 3. Concurrent and optimized fabrication process for graphite/copper composite.

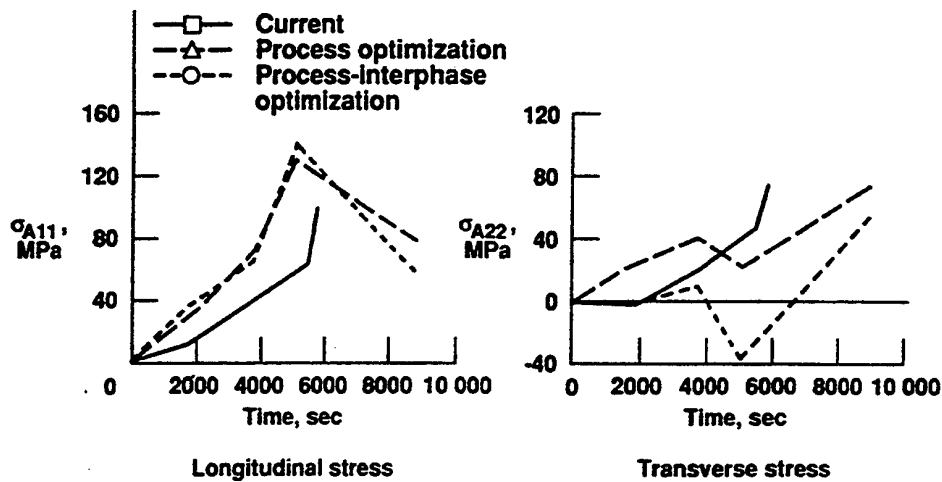


Figure 4. Current and optimized micro residual stresses in graphite/copper composites.

Theoretical Analysis of Residual Stresses Removal by Heat Supply

M. Ishihara^{*}, Y. Tanigawa^{**}, R. Kawamura^{**}, N. Noda^{*}

^{*} Department of Mechanical Engineering, Shizuoka University, 3-5-1 Jyohoku Hamamatsu Shizuoka, 432 JAPAN.

^{**} Department of Mechanical Systems Engineering, Osaka Prefecture University, 1-1 Gakuencho Sakai Osaka, 593 JAPAN.

This paper treats how to remove residual stresses which occur in plates due to welding. The analytical model is a rectangular thin plate which has residual stresses previously due to welding. And it is subjected to heat supply in order to remove residual stresses. We make use of the strain increment theorem for the theoretical analysis of thermoelastoplastic deformation of the plate, and introduce two-dimensional treatment based on Kirchhoff-Love's hypothesis. The analytical solution is obtained for the thermoelastic deformation. On the other hand, for the plastic deformation, the solution is evaluated with the aid of the finite difference method. Strain increment is calculated by successive elastic solution. Some numerical calculations are carried out in order to investigate how heating conditions such as heating time, heating area, heating position and the amount of heat influence on removal of residual stresses.

Key Words : Residual Stresses, Welding, Thermoelastoplastic Problem, Theoretical Analysis

1. Introduction

This paper treats how to remove residual stresses which occur in plates due to welding.

The welding process has been used for the fabrication of various structural elements. But the process causes plastic strains, especially compressive one, in the elements because they are subjected to a large amount of heat in a small area. Moreover these plastic strains produce residual stresses in the elements when they are cooled to room temperature. And these residual stresses affect the behavior of the elements such as brittle fracture, stress corrosion cracking, fatigue and buckling. Therefore it is very important to remove residual stresses from the elements, and there are several kinds of methods for it, for example, annealing, applying mechanical tension and applying vibration. Since residual stresses are closely related to compressive plastic strains caused by heat loading, it is important to control these strains in order to remove residual stresses.

In the previous studies [1,2], we were concerned with some transient thermoelastoplastic bending problems. In the studies, we found out that the compressive plastic strains caused by heat loading were controllable by heating conditions such as heating time, heating area and the amount of heat.

Therefore, in the present study, we aim at the control of plastic strains by applying heat to structural elements under appropriate conditions in order to remove residual stresses. The analytical model is a rectangular thin plate which has residual stresses previously due to welding. And it is subjected to heat

supply in order to remove residual stresses. For the temperature field, the analytical solution is obtained by integral transforms [3]. And for the theoretical analysis of thermoelastoplastic deformation of the plate, we introduce two-dimensional treatment based on Kirchhoff-Love's hypothesis. The analytical solution is obtained for the thermoelastic deformation. On the other hand, for the plastic deformation, the solution is evaluated with the aid of the finite difference method because we make use of the strain increment theorem [4]. Strain increment is calculated by successive elastic solution [4]. Some numerical calculations are carried out in order to investigate how heating conditions such as heating time, heating area, heating position and the amount of heat influence on removal of residual stresses.

2. Theoretical Analysis

2.1 HEAT CONDUCTION PROBLEM

We consider a rectangular plate as shown in Figure 1.

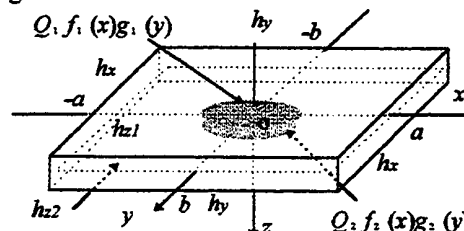


Fig. 1 A rectangular plate with a partially distributed heat supply.

Plate dimension is $2a \times 2b \times 2h$. Initial temperature

of the plate is the same as the temperature of surrounding medium which is kept constant. From time $t = 0$ to $t = t_0$, the plate is subjected to a partially distributed and symmetric heat supply $Q_1 f_1(x) g_1(y)$ at the upper surface ($z = -h$) and $Q_2 f_2(x) g_2(y)$ at the lower surface ($z = +h$). After that, the heat supply is removed and the plate is cooled by surrounding medium. Let h_x, h_y, h_{x1}, h_{x2} be the relative heat transfer coefficients on each surface.

2.1.1. *Heating Process.* For the heating process, the heat conduction equation, the initial condition and boundary conditions are given, respectively as

$$\frac{\partial T}{\partial t} = \kappa \left(\frac{\partial^2 T}{\partial x^2} + \frac{\partial^2 T}{\partial y^2} + \frac{\partial^2 T}{\partial z^2} \right) \quad (1)$$

$$t = 0 ; T = 0 \quad (2)$$

$$x = \pm a ; \frac{\partial T}{\partial x} \pm h_x T = 0 \quad (3)$$

$$y = \pm b ; \frac{\partial T}{\partial y} \pm h_y T = 0 \quad (4)$$

$$\left. \begin{aligned} z = -h ; \frac{\partial T}{\partial z} - h_{x1} T &= -\frac{Q_1}{\lambda} f_1(x) g_1(y) \\ z = +h ; \frac{\partial T}{\partial z} + h_{x2} T &= +\frac{Q_2}{\lambda} f_2(x) g_2(y) \end{aligned} \right\} \quad (5)$$

where T , κ and λ are temperature change, the thermal diffusivity and the thermal conductivity, respectively. By introducing the finite Fourier transform [3] over the variable x and y , and the Laplace transform over the variable t for the temperature function $T(x, y, z, t)$, we can obtain the temperature solution in the heating process as

$$\begin{aligned} T = & \sum_{n=1}^{\infty} \sum_{m=1}^{\infty} [c_n d_m \cos(\xi_n x) \cos(\zeta_m y) \\ & \cdot \sum_{j=1}^{\infty} f_j(\mu_j, t) \{ \dot{A}_j \cos(\gamma_j z) + \dot{B}_j \sin(\gamma_j z) \}] \\ & + \sum_{n=1}^{\infty} \sum_{m=1}^{\infty} [\frac{c_n d_m}{D} \cos(\xi_n x) \cos(\zeta_m y) \\ & \cdot \{ \dot{A}' \cosh(\delta z) + \dot{B}' \sinh(\delta z) \}] \end{aligned} \quad (6)$$

Explanation of symbols in Eq. (6) is omitted.

2.1.2. *Cooling Process.* T' , the temperature change in the cooling process, satisfies the Eqs. (1), (3), and (4) whose solution is T' instead of T , and satisfies the equations

$$t = t_0 ; T' = T(x, y, z, t_0) \quad (7)$$

$$\left. \begin{aligned} z = -h ; \frac{\partial T'}{\partial z} - h_{x1} T' &= 0 \\ z = +h ; \frac{\partial T'}{\partial z} + h_{x2} T' &= 0 \end{aligned} \right\} \quad (8)$$

instead of Eqs. (2), (5), respectively. Comparing equations for heating process and one for cooling

process, we can find out that the temperature solution T' takes the form

$$T'(x, y, z, t) = T(x, y, z, t) - T(x, y, z, t - t_0) \quad (9)$$

2.2 THERMOELASTOPLASTIC BENDING PROBLEM

2.2.1 *Derivation of Basic Equations.* In this subsection, we derive the basic equations which govern the thermoelastoplastic behavior of the plate. Here we consider the plate is free from traction. We assume that the plate is sufficiently thin. Therefore, we can introduce the assumption that the plane perpendicular to the neutral plane ($z = 0$) before deformation remains the plane perpendicular to it after deformation and that the axial stress σ_z is negligible compared with other stress components. According to the assumption above, in-plane strain components are given as

$$\varepsilon_{ij} = \varepsilon_{ij0} - z(w_{,ij}) ; (i, j = x, y) \quad (10)$$

where ε_{ij0} denotes in-plane strain components on the neutral plane and w denotes deflection of the plate. If we define ε_{ij}^p and $\Delta \varepsilon_{ij}^p$ as plastic strain already accumulated and plastic strain increment by increased thermal loading, respectively, the thermoelastoplastic stress-strain equations take the form

$$\varepsilon_{ij} = \frac{1+\nu}{E} \left(\sigma_{ij} - \frac{\nu}{1+\nu} \sigma_{kk} \delta_{ij} \right) + \alpha T \delta_{ij} + \varepsilon_{ij}^p + \Delta \varepsilon_{ij}^p \quad (11)$$

where σ_{ij} and ε_{ij} are stress components ($\sigma_z = 0$) and total strain components ($i, j = x, y, z$), respectively, and α , E and ν are the coefficient of linear thermal expansion, Young's modulus and Poisson's ration, respectively. Moreover, δ_{ij} denotes Kronecker's delta. Now we define resultant forces and moments per unit width as

$$N_{ij} = \int_{-b/2}^{b/2} \sigma_{ij} dz \quad (12)$$

$$M_{ij} = \int_{-b/2}^{b/2} \sigma_{ij} z dz \quad (13)$$

and plastic and thermal resultant forces and moments as

$$\{N_{ij}^p, \Delta N_{ij}^p\} = E \int_{-h}^h \{\varepsilon_{ij}^p, \Delta \varepsilon_{ij}^p\} dz \quad (14)$$

$$\{M_{ij}^p, \Delta M_{ij}^p\} = E \int_{-h}^h \{\varepsilon_{ij}^p, \Delta \varepsilon_{ij}^p\} z dz \quad (15)$$

$$N^T = \alpha E \int_{-h}^h T dz \quad (16)$$

$$M^T = \alpha E \int_{-h}^h T z dz \quad (17)$$

If we combine Eqs. (10), (11) and integrate it in the domain $-h \leq z \leq h$, we can express ε_{ij0} by resultant forces defined by Eqs. (12), (14) and (16). From ε_{ij0} above-mentioned and Eq. (10), we can represent in-plane strain components by resultant forces and deflection w as

$$\varepsilon_{ij} = \frac{1+\nu}{2hE} \left\{ N_{ij} - \frac{\nu N_{kk} - N^T}{1+\nu} \delta_{ij} + \frac{N_{ij}^p + \Delta N_{ij}^p}{1+\nu} \right\} - z(w_{,ij}) ; (i, j = x, y) \quad (18)$$

If we combine Eqs. (10), (11) and integrate it in the domain $-h \leq z \leq h$ with z multiplied, the resultants moments are given as

$$M_{ij} = -(1-\nu)D \left\{ w_{,ij} + \frac{\nu(w_{,kk})}{1-\nu} \delta_{ij} \right\} - \frac{M^T}{1-\nu} \delta_{ij} - \frac{1}{1+\nu} \left\{ M_{ij}^p + \frac{\nu M_{kk}^p}{1-\nu} \delta_{ij} \right\} - \frac{1}{1+\nu} \left\{ \Delta M_{ij}^p + \frac{\nu \Delta M_{kk}^p}{1-\nu} \delta_{ij} \right\} ; (i, j = x, y) \quad (19)$$

where D is flexural rigidity of the plate denoted by

$$D = \frac{E(2h)^3}{12(1-\nu^2)} \quad (20)$$

Now we consider the basic equations for the in-plane behavior. Equilibrium equations and compatibility condition in-plane direction are

$$\frac{\partial N_x}{\partial x} + \frac{\partial N_y}{\partial y} = 0, \quad \frac{\partial N_x}{\partial x} + \frac{\partial N_y}{\partial y} = 0 \quad (21)$$

$$\frac{\partial^2 \varepsilon_x}{\partial y^2} + \frac{\partial^2 \varepsilon_y}{\partial x^2} = 2 \frac{\partial^2 \varepsilon_{xy}}{\partial x \partial y} \quad (22)$$

Eq. (21) is satisfied by the "resultant force function" F defined as

$$N_x = \frac{\partial^2 F}{\partial y^2}, \quad N_y = \frac{\partial^2 F}{\partial x^2}, \quad N_{xy} = -\frac{\partial^2 F}{\partial x \partial y} \quad (23)$$

which takes the same form as Airy's stress function. If we combine Eq. (18) and Eq. (22), we may obtain the equation of compatibility represented by resultant forces. Considering Eq. (23) furthermore, the basic equation for the in-plane behavior is obtained as

$$\nabla^2 \nabla^2 F = -\nabla^2 N^T - [g_N(x, y) + \Delta g_N(x, y)] \quad (24)$$

where ∇^2 denotes the two-dimensional Laplace operator and the function $g_N(x, y)$ is defined as

$$g_N(x, y) = \frac{\partial^2 N_x^p}{\partial y^2} + \frac{\partial^2 N_y^p}{\partial x^2} - 2 \frac{\partial^2 N_{xy}^p}{\partial x \partial y} \quad (25)$$

and $\Delta g_N(x, y)$ is obtained by replacing N_{ij}^p with ΔN_{ij}^p in the above equation. The boundary conditions concerning to the in-plane deformation are represented in terms of the resultant force function F as [5]

$$\left. \begin{aligned} x = \pm a ; \quad \frac{\partial F}{\partial x} = 0, F = 0 \\ y = \pm b ; \quad \frac{\partial F}{\partial y} = 0, F = 0 \end{aligned} \right\} \quad (26)$$

Equilibrium equations of resultant forces and moments which cause out-of-plane deformation are given as

$$\frac{\partial N_x}{\partial x} + \frac{\partial N_y}{\partial y} = 0 \quad (27)$$

$$\frac{\partial M_x}{\partial x} + \frac{\partial M_y}{\partial y} = N_x, \quad \frac{\partial M_{xy}}{\partial x} + \frac{\partial M_{yy}}{\partial y} = N_y \quad (28)$$

If we substitute Eq. (28) into (27) and consider Eq. (19), we can obtain the basic equation for out-of-plane behavior as

$$D \nabla^2 \nabla^2 w = -\frac{1}{1-\nu} \nabla^2 M^T - [g_M(x, y) + \Delta g_M(x, y)] \quad (29)$$

where the function $g_M(x, y)$ is defined as

$$g_M(x, y) = \frac{1}{1-\nu^2} \frac{\partial^2}{\partial x^2} (M_x^p + \nu M_y^p) + \frac{1}{1-\nu^2} \frac{\partial^2}{\partial y^2} (M_y^p + \nu M_x^p) + \frac{2}{1+\nu} \frac{\partial^2 M_{xy}^p}{\partial x \partial y} \quad (30)$$

and $\Delta g_M(x, y)$ is obtained by replacing M_{ij}^p with ΔM_{ij}^p in the above equation. The boundary conditions concerning to the out-of-plane deformation are represented in terms of the deflection w as

$$\left. \begin{aligned} x = \pm a ; \quad D \left\{ \frac{\partial^2 w}{\partial x^2} + \nu \frac{\partial^2 w}{\partial y^2} \right\} = -\frac{M^T}{1-\nu} - \frac{M_x^p + \nu M_y^p}{1-\nu^2} - \frac{\Delta M_x^p + \nu \Delta M_y^p}{1-\nu^2} \\ y = \pm b ; \quad D \left\{ \frac{\partial^2 w}{\partial y^2} + \nu \frac{\partial^2 w}{\partial x^2} \right\} = -\frac{M^T}{1-\nu} - \frac{M_y^p + \nu M_x^p}{1-\nu^2} - \frac{\Delta M_y^p + \nu \Delta M_x^p}{1-\nu^2} \end{aligned} \right\} \quad (31)$$

$$\left. \begin{aligned} x = \pm a ; \quad D \frac{\partial}{\partial x} \left\{ \frac{\partial^2 w}{\partial x^2} + (2-\nu) \frac{\partial^2 w}{\partial y^2} \right\} = -\frac{1}{1-\nu} \frac{\partial M^T}{\partial x} - \left\{ \frac{1}{1-\nu^2} \frac{\partial}{\partial x} (M_x^p + \nu M_y^p) + \frac{2}{1+\nu} \frac{\partial M_{xy}^p}{\partial y} \right\} - \left\{ \frac{1}{1-\nu^2} \frac{\partial}{\partial x} (\Delta M_x^p + \nu \Delta M_y^p) + \frac{2}{1+\nu} \frac{\partial (\Delta M_{xy}^p)}{\partial y} \right\} \\ y = \pm b ; \quad D \frac{\partial}{\partial y} \left\{ \frac{\partial^2 w}{\partial y^2} + (2-\nu) \frac{\partial^2 w}{\partial x^2} \right\} = -\frac{1}{1-\nu} \frac{\partial M^T}{\partial y} - \left\{ \frac{1}{1-\nu^2} \frac{\partial}{\partial y} (M_y^p + \nu M_x^p) + \frac{2}{1+\nu} \frac{\partial M_{xy}^p}{\partial x} \right\} - \left\{ \frac{1}{1-\nu^2} \frac{\partial}{\partial y} (\Delta M_y^p + \nu \Delta M_x^p) + \frac{2}{1+\nu} \frac{\partial (\Delta M_{xy}^p)}{\partial x} \right\} \end{aligned} \right\} \quad (32)$$

2.2.2. Analysis of Practical Problem. In order to solve Eq. (24) under Eq. (26), we separate the resultant force function into elastic solution F^e and plastic solution F^p as

$$F = F^e + F^p \quad (33)$$

F^e satisfies Eqs. (24), (26) without the function

$g_N(x, y)$ and $\Delta g_N(x, y)$, and can be obtained from Eqs. (6), (9) and (16) as

$$\begin{aligned} F^e/\alpha E &= \frac{A_0^F}{2}x^2 + \frac{B_0^F}{2}y^2 + C_0^F \\ &+ \sum_{i=1}^{\infty} \{A_i^F \cosh(\alpha_i^F y) + B_i^F \alpha_i^F y \sinh(\alpha_i^F y)\} \cos(\alpha_i^F x) \\ &+ \sum_{j=1}^{\infty} \{C_j^F \cosh(\beta_j^F x) + D_j^F \beta_j^F x \sinh(\beta_j^F x)\} \cos(\beta_j^F y) \\ &+ \sum_{n=1}^{\infty} \sum_{m=1}^{\infty} \left[\frac{c_n d_m}{\xi_n^2 + \zeta_m^2} f^N(\xi_n, \zeta_m, t) \cos(\xi_n x) \cos(\zeta_m y) \right] \end{aligned} \quad (34)$$

$A_i^F, B_i^F, C_j^F, D_j^F$ are unknown constants and determined by Eq. (26). Explanation of other symbols in Eq. (34) is omitted. On the other hand, F^p satisfies Eqs. (24), (26) without N^T , and can be obtained with the aid of the finite difference method.

In order to solve Eq. (29) under Eqs. (31), (32), we separate the deflection into elastic deflection w^e and plastic one w^p as

$$w = w^e + w^p \quad (35)$$

w^e satisfies Eqs. (29), (31), (32) without $g_M(x, y)$, $\Delta g_M(x, y)$, M_{ij}^p and ΔM_{ij}^p , and can be obtained from Eqs. (6), (9) and (17) as the similar form to Eq. (34). On the other hand, w^p satisfies Eqs. (29), (31), (32) without M^T , and can be obtained with the aid of the finite difference method.

2.3 STRAIN INCREMENT THEOREM AND SUCCESSIVE ELASTIC SOLUTION

Strain increment components can be calculated from von Mises yield criterion and Prandtl-Reuss equations. This procedure was developed by Mendelson [4]. We define "modified total strain" as

$$\varepsilon'_{ij} \equiv \varepsilon_{ij} - \varepsilon_{ij}^p \quad (36)$$

Subtracting mean normal strain from diagonal elements of Eq. (36) leads to

$$e'_{ij} = e_{ij}^e + \Delta e_{ij}^p \quad (37)$$

where e'_{ij} and e_{ij}^e denote "modified deviatoric strain tensor" and elastic deviatoric strain tensor, respectively. According to Mendelson's procedure, Prandtl-Reuss equations represented only by strain components are given as

$$\Delta \varepsilon_{ij}^p = (\Delta \varepsilon_p / \varepsilon_{et}) \cdot e'_{ij} \quad (38)$$

where ε_{et} denotes "modified equivalent total strain" and is defined as

$$\varepsilon_{et} \equiv \sqrt{(2/3)e'_{ij} \cdot e'_{ij}} \quad (39)$$

and $\Delta \varepsilon_p$ denotes the equivalent plastic strain increment. Let σ_0 and m be the initial yield stress and work hardening parameter, respectively, and let the uniaxial stress-strain relation take the form

$$\begin{aligned} \varepsilon &= \sigma/E & ; (\sigma \leq \sigma_0) \\ \varepsilon &= (\sigma_0/E) \cdot (\sigma/\sigma_0)^m & ; (\sigma \geq \sigma_0) \end{aligned} \quad (40)$$

Then $\Delta \varepsilon_p$ is related to ε_{et} and the preloading equivalent stress $\sigma_{e,j-1}$, and is expressed

$$\Delta \varepsilon_p = \frac{3\varepsilon_{et} - 2(1+\nu)\sigma_{e,j-1}/E}{3 + 2(1+\nu)/\{m(\sigma_{e,j-1}/\sigma_0)^{m-1} - 1\}} \quad (41)$$

The equivalent stress σ_e is defined as

$$\sigma_e \equiv \sqrt{(3/2)s_{ij} \cdot s_{ij}} \quad (42)$$

where s_{ij} denotes the deviatoric stress tensor.

Now, consider the calculation of the strain increment which is caused by the temperature increment from time t to $t + \Delta t$. In the first place, if we assume $\Delta \varepsilon_{ij}^p = 0$, then the functions g_N , Δg_N , g_M and Δg_M are evaluated by Eqs. (25), (30) because ε_{ij}^p is already calculated. Then, resultant forces N_{ij} and deflection w are calculated from Eqs. (23), (24), (26), (29), (31) and (32) by the method which is described in the preceding section. Therefore, the stress and the total strain components are calculated by Eqs. (11), (18), and the first approximate solution of $\Delta \varepsilon_{ij}^p$ can be calculated by Eq. (38). Second, we assume that $\Delta \varepsilon_{ij}^p$ takes the value of this first approximate solution and proceed in a similar manner. This procedure is iterated until $\Delta \varepsilon_{ij}^p$ converges sufficiently. After convergence, we include $\Delta \varepsilon_{ij}^p$ into ε_{ij}^p and proceed to the next time step from $t + \Delta t$ to $t + 2\Delta t$.

References

- (1) Tanigawa, Y., Ishihara, M., Morishita, H. and Kawamura, R., Theoretical Analysis of Two-Dimensional Thermoelastoplastic Bending Deformation of Plate Subject to Partially Distributed Heat Supply, *Trans. JSME*, Vol. 62, No. 595, pp. 737-744, 1996.
- (2) Ishihara, M., Tanigawa, Y., Kawamura, R. and Noda, N., Theoretical Analysis of Thermoelastoplastic Deformation of a Circular Plate Due to a Partially Distributed Heat Supply, *J. Thermal Stresses*, Vol. 20, No. 2, pp. 203-225, 1997.
- (3) Sneddon, I. N., The Use of Integral Transforms, McGraw-Hill, New York, 1972.
- (4) Mendelson, A., Plasticity, Theory and Application, Macmillan, New York, 1968.
- (5) Takeuti, Y., Analysis of Thermal Stresses, Nisshin, Tokyo, 1971.

Determination of Residual Welding Stresses under Consideration of Structural Transformations Using a Multi-Purpose Finite Element Program

O. Voß, I. Decker, H. Wohlfahrt

Welding Institute, Technical University of Braunschweig, Germany

Different austenitization temperatures reached at different locations during the welding process have a strong influence on the developing thermal stresses. Assuming the welding process as a decoupled thermomechanical problem, an approach based on a maximum-temperature cooling-time diagram has been made to determine the microstructure and hardness distribution in the HAZ as well as the residual welding stresses. Because of the high temperature and stress gradients laser beam welds on mild steel have been used to validate the model. The experimentally obtained data has been found in good agreement with the results of the finite element calculations.

Keywords: welding, finite element simulation, structural transformation, maximum-temperature cooling-time diagram

1. Introduction

Welding residual stresses affect strongly the performance capability of the joined parts. Therefore the calculation of the temperature distribution and the resulting residual stresses is an important step in optimizing the welding process. Depending on the type of welded material microstructural transformations can occur during heating (ferrite + perlite \rightarrow austenite) and cooling (austenite \rightarrow martensite, bainite or ferrite + perlite, depending on the temperature cycle), causing a redistribution of the thermal stresses and strains because of accompanying volume variations and changes of the material properties.

Finite element simulations which consider microstructural transformations during a heat treatment are in general based on the time-temperature-transformation diagram (TTT-diagram) [1,2]. For predicting the microstructure in the heat affected zone (HAZ) of a weld, special welding-TTT-diagrams have been developed [3]. The characteristic temperature cycle for the determination of those diagrams is a fast heating to an austenitization temperature of 1350°C and no holding time before cooling. Welding-TTT-diagrams neglect the real temperature profile that shows a gradient of the maximum temperature reached as a function of the distance from the weld center. In the case of high-energy-density-beam welding this gradient is very steep and, therefore, the spacial variation of

the austenitization temperature is high in a narrow workpiece portion around the weld [4].

2. The maximum-temperature cooling-time diagram

A rising austenitization temperature causes larger and more stable austenite grains and, therefore, during cooling a delay of the ferrite nucleation. The bainite and ferrite regions in the welding TTT-diagram are displaced to longer cooling times [5] (figure 1).

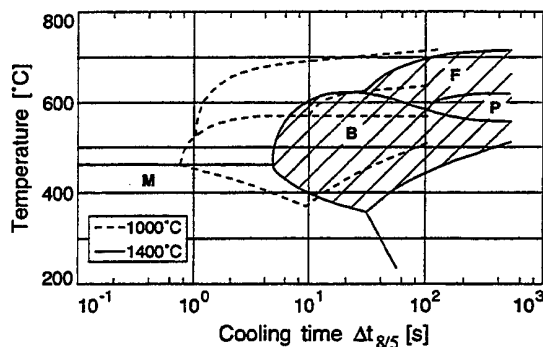


Figure 1: TTT-diagram for two different austenitization temperatures (steel A in [5])

Using several TTT-diagrams for different austenitization temperatures a maximum-temperature cooling-time diagram (figure 2) has been developed by [5] for a steel A (chemical composition shown

in table 1). This diagram reveals, depending on the maximum temperature reached and the cooling time between 800 and 500°C ($\Delta t_{8/5}$), which part of the HAZ shows a martensite (M), a martensite and bainite (M+B), a ferrite and bainite (F+B), or a ferrite and perlite (F+P) structure, as well as the corresponding hardness distribution (figure 2).

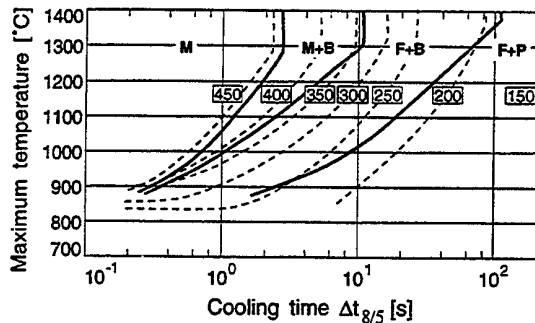


Figure 2: Maximum-temperature cooling-time diagram (steel A in [5])

3. The finite element model

Assuming the welding process as a decoupled thermomechanical problem, the microstructure in the HAZ can be determined from a measured or calculated thermal cycle, using the maximum-temperature cooling-time diagram. This allows to perform the calculation of the mechanical stresses and strains with full temperature and microstructural dependence: all material properties, especially the coefficient of thermal expansion and the yield stress are adapted whenever structural transformations occur. This approach offers a great variety of applications, because it can be integrated in any two or three dimensional model of a multi-purpose finite element program (e. g. ANSYS or ABAQUS), it is independent of the type of welding process or heat treatment and can be used for every steel alloy with microstructural transformations, if the material data is known.

Due to the high temperature and stress gradients laser beam welds on mild steel have been chosen as an example to validate the model. Any welding simulation is a highly nonlinear problem because of the temperature depending material data and the plastic deformations. To get suitable information about the microstructure, a large number of finite elements have to be placed in the HAZ, which is small compared to the overall dimensions of the joined parts.

The laser beam welds presented in this paper were done on 50 x 250 mm plates of St 52-3 with different thicknesses. Because of the small element width needed in the HAZ (0.1 mm) a fully three

dimensional finite element simulation is very time consuming. However, the residual stresses that develop in long welds far away from the edges can be approximated by help of a two dimensional plain strain model. To achieve reasonable computation times, the results of the three dimensional temperature model have been transferred to a two dimensional plain strain model as shown in figure 3.

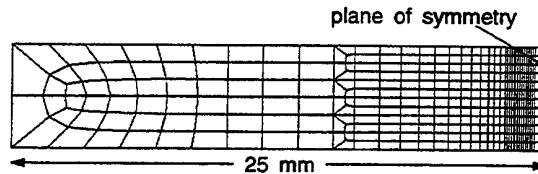


Figure 3: Finite element model (plain strain) for the stress-strain analysis

4. Results and discussion

The alloy chosen for the experiments is St 52-3 because of its similar chemical composition and mechanical properties to the steel A used by [5] (see table 1).

Steel	Chemical composition [%]				
	C	Si	Mn	P	S
steel A	0.16	0.40	1.50	0.008	0.024
St 52-3	≤0.20	≤0.55	≤1.60	≤0.040	≤0.040

Table 1: Chemical composition of a steel A and St 52-3

The microstructure, hardness distribution and welding residual stresses for different welding parameters and various plate thicknesses in the case of bead-on-plate laser beam welds have been compared with finite element calculations. As an example for the good agreement between experiment and numerical calculations one full set of results is presented in this paper.

Figure 4 compares the width of two experimentally obtained and calculated HAZs. Even though the martensite region and the areas with bainite grains are of the same size, it is noticeable that the weld reinforcement is not comparable, because weld pool effects like the surface tension have been neglected. With increasing computer capabilities weld pool modelling can be added to the finite element model to get better results in the melted region. Because of the good accordance of the results for the microstructure, it can be expected, that the calculated hardness distribution is also in good agreement with the experimental data. The ultrasonic contact impedance (UCI) measurement shown in figure 5 and the line plots for the three selected

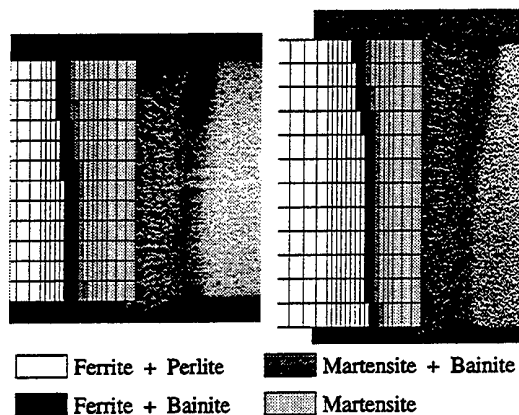


Figure 4: Comparison between the calculated and measured microstructure for St 52-3 (left: $d = 5$ mm, $P = 5$ kW, $v = 1.2$ m/min; right: $d = 6$ mm, $P = 5$ kW, $v = 1.3$ m/min)

scanning lines in figure 6 reveal, that the chosen hardness for martensite of 450 HV should be lowered in the simulations. The deviation can be explained with the slightly differing chemical compositions of steel A and St 52-3.

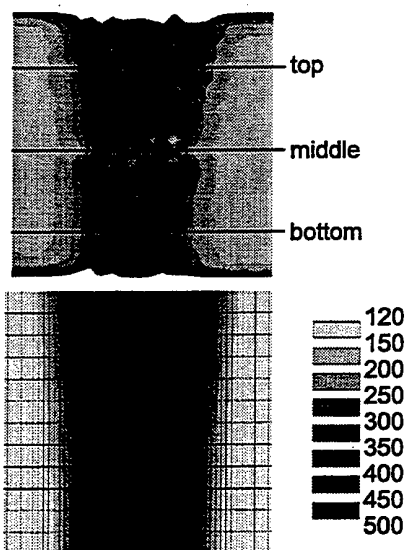


Figure 5: Comparison between UCI-measured hardness and the finite element result (St 52-3, $d = 5$ mm, $P = 5$ kW, $v = 1.2$ m/min)

The rise in the measured hardness near the top and bottom side of the plate can not be observed in the finite element result. It results from the fact, that the specimen was embedded in plastic while performing the UCI-measurement.

In order to receive accurate results for the residual welding stresses, the effect of the increase in volume

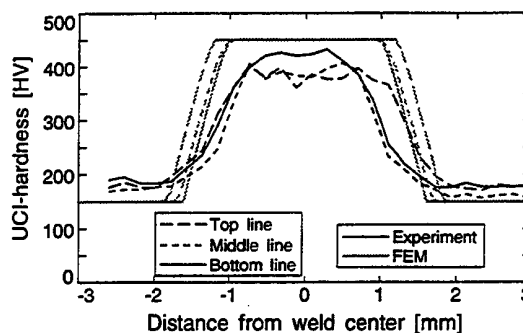


Figure 6: Comparison between UCI-measured hardness and the finite element result along selected lines (St 52-3, $d = 5$ mm, $P = 5$ kW, $v = 1.2$ m/min)

due to martensite formation has to be added to the normal thermal strain, causing an extra compressive stress that redistributes the thermal stresses. Figure 7 indicates that the X-ray stress measurements from the topside of the welded plate are in good agreement with the calculated results. The transverse stresses show a well developed compressive stress in the transformed area (the tensile transverse stress of about 110 MPa in the center of the weld shown in figure 7 is an experimental error, because of the surface topography of the weld seam).

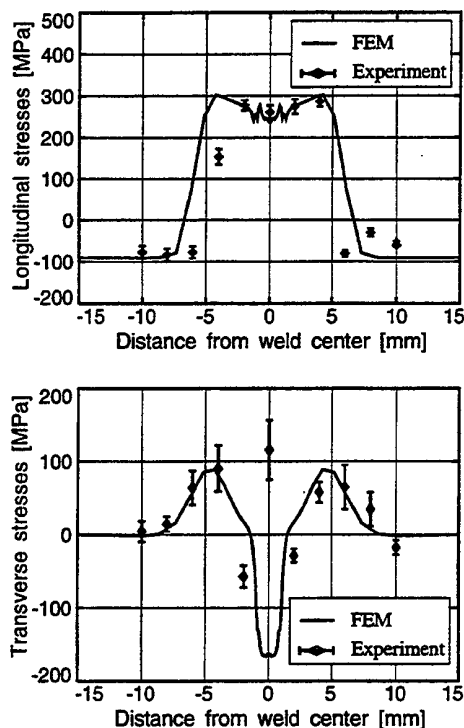


Figure 7: Longitudinal and transverse residual welding stresses (St 52-3, $d = 5$ mm, $P = 5$ kW, $v = 1.2$ m/min)

5. Conclusion

The decreasing austenitization temperatures occurring with increasing distance from the weld center, have a strong influence on the microstructural transformations in the HAZ. Combining several TTT-diagrams to a maximum-temperature cooling-time diagram allows this effect to be taken into account.

The welding process can be assumed as a decoupled thermomechanical problem. Integrating this approach in a multi purpose finite element program, enables the calculation of the thermal stresses and strains using material properties with the full temperature and microstructure dependence. The results obtained are in good agreement with the experimental data.

In the literature only very limited data about the material properties as a function of temperature can be found, therefore, interpolations and extrapolations still have to be performed. As long as secure material data is not available a coupled thermal and metallurgical calculation like revealed in [6], does not appear to be not necessary.

6. Acknowledgments

This work is funded by the Deutsche Forschungsgemeinschaft under the grant WO 344/23.

7. References

- [1] *Leblond, J.B.; Devaux, J.; Devaux, J.C.*: Modellierung metallurgischer Umwandlungsprozesse. CAD-CAM Report, No. 6 (1990), pp. 78-89
- [2] *Buchmayr, B.; Kirkaldy, J.S.*: Modeling of the Temperature Field, Transformation Behavior, Hardness and Mechanical Response of Low Alloy Steels during Cooling from the Austenite Region. J. Heat Treat 8 (1990), pp. 127-136
- [3] *Seyffarth, P.*: Grosser Atlas Schweiß-ZTU-Schaubilder. Düsseldorf: Dt. Verl. für Schweißtechnik, DVS-Verl. 1992
- [4] *Voß, O.; Hillebrand, H.; Decker, I.; Wohlfahrt, H.*: Vereinfachtes Modell zur Berücksichtigung von Gefügeumwandlungen beim Laserstrahlschweißen. 14. CAD-FEM Users Meeting 1996 in Bad Aibling: pp. I-21/1-10, CAD-FEM GmbH, Grafting
- [5] *Berkhout, C.F.; van Lent, P.H.*: Anwendung von Spitzentemperatur-Abkühlzeit (STAZ)-Schaubildern beim Schweißen hochfester Stähle. Schweißen und Schneiden 20, No. 6 (1968), pp. 256-260
- [6] *Bergheau, J.M.; Leblond, J.B.*: Coupling between Heat Flow, Metallurgy and Stress-Strain Computations in Steels. The Approach developed in the Computer Code SYSWELD for Welding and Quenching. Vth Engineering Foundation Conf. on Modelling of Casting, Welding and Advanced Solidification Processes, Davos, 1990

Thermal Stresses Analysis of a Steps Axle with Boiling Boundary

J. R. Chen J. B. Chen H. G. Wang

Dept. of Basic Science, Kunming University of Science and Technology, Kunming, 650093, Yunnan, P.R. CHINA

Based on the practice of the steps axle workpiece during quenching, the increment form about thermal elastoplastic constitutive equation, including variable physical properties and phase transformation, is put forward and solved by means of Finite Element Method in this paper. The transient stresses field and the residual stresses field are obtained. The varied factors are discussed.

Key Word: Thermal stresses Phase transformation Configuration factor Quenching

1. Introduction

The steps axle is one kind of common metallic workpieces during quenching. When the steps axle is heated over the temperature of Austenite and kept for enough time, then put into the quenching medium along the line of axle vertically, the surface of workpiece is contacted directly with the medium, so the intense heat transfer is formed. During that course, the surface of workpiece is in the state of pool subcooling boiling^[1]. The inhomogeneity of cooling leads to the various temperature grade at the different points in the workpiece, which cause the various thermal stress. Meanwhile the heat radiation for the shape influence and the heat latent released by phase transformation producers influence the distributions of the transient stresses and the residual stresses and make the numerical solution more difficult.

In this paper, on the basis of the previous^[2], the transient temperature field of the steps axle was obtained under the pool subcooling boiling. The thermal elastoplastic constitutive equation, including variable physical properties and phase transformation, is put forward and solved by means of Finite Element Method. The transient stresses field and the residual stresses field of the steps axle during quenching with water are obtained and the effects of phase transformation and shape are discussed. The results are satisfying.

The metallic workpiece is shown as fig.1. The material is carbon steel, which consists of the following composition (%): C 0.44, Si 0.12, Mn 0.66,

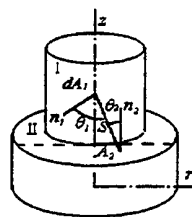


Fig.1 The model and configuration factor schematic drawing

$P < 0.035$, $S < 0.035$. The temperature of heating is 860°C , and water is acted as quenching medium.

2. The variable physical properties, the configuration factors and the heat conduction governing equation

2.1 THE VARIABLE PHYSICAL PROPERTIES

During the quenching process of metallic workpiece, based on difference of the cooling velocity and the critical temperature, the high temperature Austenite structure can be transformed into Ferrite, Pearlite, Bainite, Martensite and a small amount residual Austenite structure. Because of different physical properties of the various structures, lead to difference of the transient stresses and the residual stresses of the steps axle workpiece.

During quenching of metallic workpiece, the physical properties is a non-linear function not only of temperature, but also of phase transformation compositions. Put phase transformation conditions and phase compositions^[3] into the physical properties,

the expressions of physical properties can be written as following:

$$\left. \begin{aligned} k &= \sum_{k,L} \zeta_L^k \xi_L k_L(T) + (1 - \sum_{k,L} \zeta_L^k \xi_L) k_A(T) \\ C_p &= \sum_{k,L} \zeta_L^k \xi_L C_{pL}(T) + (1 - \sum_{k,L} \zeta_L^k \xi_L) C_{pA}(T) \\ \rho &= \sum_{k,L} \zeta_L^k \xi_L \rho_L(T) + (1 - \sum_{k,L} \zeta_L^k \xi_L) \rho_A(T) \\ E_{ijmn} &= \sum_{k,L} \zeta_L^k \xi_L E_{ijmn,L}(T) + (1 - \sum_{k,L} \zeta_L^k \xi_L) E_{ijmn,A}(T) \\ \alpha &= \sum_{k,L} \zeta_L^k \xi_L \alpha_L(T) + (1 - \sum_{k,L} \zeta_L^k \xi_L) \alpha_A(T) \end{aligned} \right\} (1)$$

Where, k , C_p , ρ , E_{ijmn} , α are heat conduction coefficient, specific heat, specific volume, Young's model and heat expansion coefficient, respectively; ζ_L^k , ξ_L are the phase transformation condition and the phase volume fraction^[3], $k_A(T)$, $C_{p,A}(T)$, $\rho_A(T)$, $E_{ijmn,A}(T)$, $\alpha_A(T)$ are heat conduction coefficient, specific heat, specific volume, Young's model and heat expansion coefficient of Austenite under the corresponding temperature respectively.

For other physical properties, the expressions are similar to (1).

2.2 THE CONFIGURATION FACTORS

Few persons consider the effect of the surface shape on workpiece during heat transfer. But it is proved by practice that because of the existence of radiation, while the each surface of workpiece release heat energy, they absorb the heat energy radiated by other surface and the quantity of the absorbed energy is relevant to surface shape of the workpiece to a great extend.

Any point on the surface of workpiece can radiate energy in the manner of hemisphere, and the ratio of the energy that can reaches other surfaces of the workpiece to the total radiated energy is called the configuration factor of the point. Obviously, the configuration factor is related to the shape of surface only.

From the calculating expression of the configuration factor^[4]:

$$F_{dA_1-A_2} = \int_{A_2} \frac{\cos \theta_1 \cos \theta_2}{\pi S^2} dA_2 \quad (2)$$

We can obtain the configuration factor $F_{dA_1-A_2}$. With the same analytical method, the con-

figuration factor $F_{dA_2-A_1}$ can be obtained shown in Fig.2.

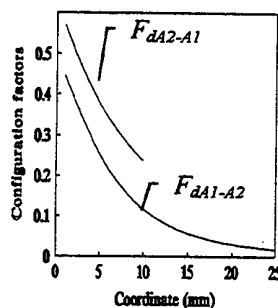


Fig.2 The configure factors

2.3 THE HEAT CONDUCTION GOVERNING EQUATION SET

In order to depict the course of heat transfer of the steps axle under the pool subcooling boiling more accurately, the following governing equation set^[2,3] is used:

$$\begin{aligned} \rho C_p \frac{\partial T}{\partial t} &= k \left(\frac{\partial^2 T}{\partial r^2} + \frac{1}{r} \frac{\partial T}{\partial r} + \frac{\partial^2 T}{\partial z^2} \right) \\ &\quad - \varepsilon \sigma [T^4 - T_b^4 (F_{1,\Pi-d(r,z)} - F_{d(r,z)-1,\Pi})] + \rho r \\ \rho r &= \rho \left[\frac{\partial q}{\partial \xi_L} \xi_L \zeta_L^k \right] \\ -k \frac{\partial T}{\partial n} &= h(T) \Delta T \\ T((r,z),0) &= \hat{T}(r,z) \end{aligned} \quad (3)$$

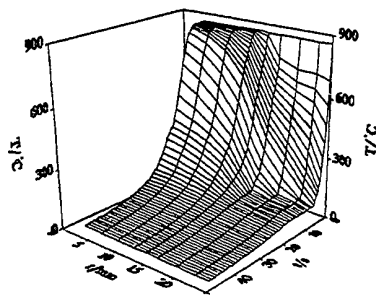


Fig.3 The distribution of temperature on the step section

The equation (3) is solved by means of F. E. M, the temperature field of workpiece can be ob-

tained. The trend of temperature varied with time and coordinates on step section are shown as fig.3.

3. Thermal elastoplastic constitutive equation with the phase transformation

Let γ_{ij}^e and γ_{ij}^T stand for the elastic strain and temperature strain respectively. From (1), we can get:

$$\gamma_{ij}^e = [E_{ijmn}]^{-1} \sigma_{mn} \quad (4)$$

$$\gamma_{ij}^T = \int_0^T \alpha \delta_{ij} dT$$

In which, δ_{ij} is the symbol of Kronecker. Different the equation (4), we can get as follow:

$$d\gamma_{ij}^e = E_{ijmn}^{-1} d\sigma_{mn} + \frac{dE_{ijmn}^{-1}}{dT} \sigma_{mn} dT \quad (5)$$

$$d\gamma_{ij}^T = \alpha \delta_{ij} dT$$

Adopt the isotropy strengthen model as this:

$$\bar{\sigma} = F(\int d\bar{\gamma}^{pl}, T) \quad (6)$$

Where $\bar{\gamma}^{pl}$ and $\bar{\sigma}$ stand for equivalent plastic strain and equivalent stress, respectively. Thus, we can get:

$$\frac{\partial \bar{\sigma}}{\partial \sigma_{ij}} d\sigma_{ij} = \frac{\partial F}{\partial \bar{\gamma}^{pl}} d\bar{\gamma}^{pl} + \frac{\partial F}{\partial T} dT \quad (7)$$

Let $\bar{\gamma}_{ij}^{pr}$ stands for the unite expression of all phase transformations strain component and γ_{ij} stands for the total strain. The increments form of them are $d\gamma_{ij}^{pr}$ and $d\gamma_{ij}^{[5]}$. Thus:

$$d\gamma_{ij} = d\gamma_{ij}^e + d\gamma_{ij}^{pl} + d\gamma_{ij}^T + d\gamma_{ij}^{pr} \quad (8)$$

Put equation (5), (7) into (8), we can get:

$$d\sigma_{ij} = E_{ijmn}^{ep} \left\{ d\gamma_{mn} - \left[\frac{dE_{ijmn}^{-1}}{dT} \sigma_{mn} + \alpha \delta_{mn} \delta_{ij} \right] dT - d\gamma_{mn}^{pr} \right\} + \frac{\partial \bar{\sigma}}{\partial \sigma_{mn}} \cdot E_{ijmn} \cdot \frac{\partial F}{\partial T} + \frac{\partial F}{\partial \bar{\gamma}^{pl}} + \frac{\partial \bar{\sigma}}{\partial \sigma_{rs}} \cdot E_{ijkl} \cdot \frac{\partial F}{\partial \sigma_{kl}} \quad (9)$$

Where E_{ijmn}^{ep} is

$$E_{ijmn}^{ep} = E_{ijmn} \left[1 - \frac{\frac{\partial \bar{\sigma}}{\partial \sigma_{rs}} \cdot E_{ijkl} \cdot \frac{\partial F}{\partial \sigma_{kl}}}{\frac{\partial F}{\partial \bar{\gamma}^{pl}} + \frac{\partial \bar{\sigma}}{\partial \sigma_{rs}} \cdot E_{ijkl} \cdot \frac{\partial F}{\partial \sigma_{kl}}} \right] \quad (10)$$

4. The calculating results and discussion

Based on the known temperature distribution, equation (9) is solved by means of F. E. M. The results are discussed as follows.

4.1 THE DISTRIBUTION OF THE TRANSIENT STRESSES AND THE RESIDUAL STRESSES

In Fig.4, σ_z , σ_r , σ_θ of different times on the step section are given:

Fig.4 shows:

(1) The transient stresses in different times are different, which expresses that the cooling velocity of different points are different on the step section.

(2) The maximum of stresses appears during the time 5 ~ 20s. During this course, the center of the workpiece is in the high temperature plastic zone and the stresses of the points can be released due to metal plastic deformation. Meanwhile, the crack is readily formed as a matter that the surface is in low temperature zone.

(3) The maximum of σ_z , σ_r , σ_θ appear mostly on the surface and near the surface, where the cracks are easily formed.

(4) After 25s, the changing ranges of stresses descends gradually. After 40s, the changes will tend to stability and the stresses distribution tend to the residual stresses distribution.

4.2 INFLUENCE ON STRESSES FIELD BY PHASE TRANSFORMATION AND SHAPE

Calculating results show: In every point of the model during quenching with water, Martensite transformation content is more than 96% and only small amount is Ferrite, Pearlite, Bainite and residual Austenite. The influence on the transient stresses by phase transformation comes mainly from Martensite transformation.

During Martensite transformation, latent heat will be released, which retards the cooling velocity. The stresses considered phase transformation change smaller than not considered it, and Martensite transformation retards the thermal stresses. Meanwhile, it also shows that if ignored the influence of phase

transformation, the serious error will be produced during calculating.

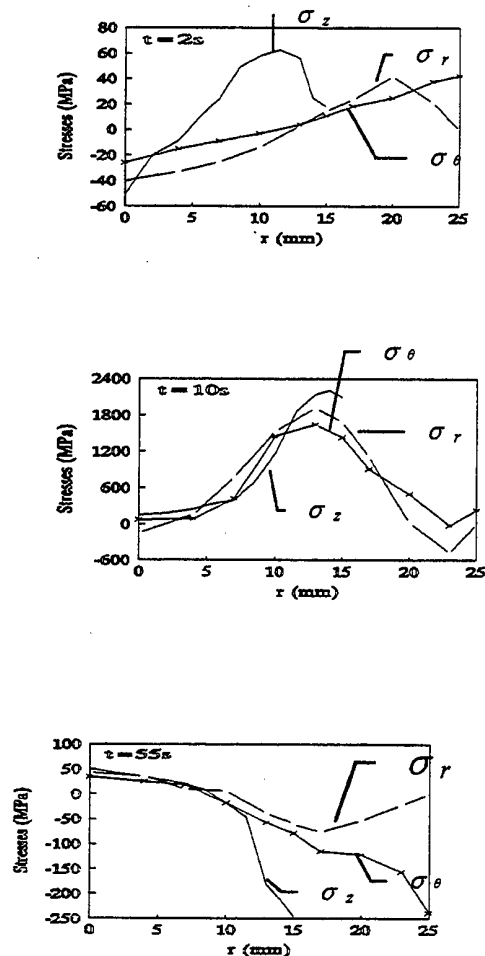


Fig.4 The distributions of the transient stresses on step section

The radiation term has certain effect on the transient stresses under high temperature condition. The radiation plays a role of supplementary external heat source. Its intensity is determined not only by the surface temperature, but also by the surface shape.

The phase transformation and the heat radiation retard the cooling velocity, and lighten the thermal stresses. Because cooling velocity is lowed, the quenching process lasts longer than that in which the phase transformation and the heat radiation are ig-

nored. Anyway, the residual stresses field is the thermal stresses.

5. Conclusion

From above, the conclusions can be obtained as following:

(1) It is feasible to solve the transient stress distribution and the residual stress distribution of the steps axle by equation (9) based on equation (3). Also, the results are satisfying.

(2) The phase transformation and shape influence heavily on distribution of the transient stresses and the residual stresses during quenching with water of steps axle, which must be considered. Though both factors retards the action of thermal stresses during quenching, the thermal stresses takes the main part.

(3) The heat radiation influences mainly during initial stage of quenching, while the phase transformation does when temperature is below M_s . Both of them influence on the residual stresses distribution. Compared each other, the phase transformation acts more heavily.

Reference

- (1) J.R.Chen *et al.*, The Problems of Heat Conduction Involving Subcooling Boiling Boundary and Phase Transformation during Quench Hardening, *J. of Metal Heat Treatment*, 14(1), 1993, 42-47
- (2) J.R.Chen *et al.*, The Coupled Heat Transfer Problem with Pool Subcooling Boiling, Radiation and Phase Transformation, *Proceedings of Thermal stresses'95*, 1995, 299-302, JAPAN.
- (3) J. R. Chen *et al.*, A Study on Heat Conduction with Variable Phase Transformation Composition during Quench Hardening, *J. of Materials Processing Technology*, 63, 1997, 554-558
- (4) R. Siegel, J. R. Howell, Thermal Radiation Heat Transfer, Second Edition, Hemisphere and McGraw-Hill, 1981.
- (5) H.G.Wang *et al.*, The Thermal Elasto-Plastic Constitutive Equation Including Phase Transformation of Carbon Steel during Quenching, *Mechanics and Engineering*, Yunnan Science and Technology Press, 1995, 62-68

Session 2F

HEAT CONDUCTION

Chair: R. A. Heller

Co-Chair: L. R. Rakotomanana

**On a Refined Heat Conduction Theory for
Microperiodic Layered Solids**

Józef Ignaczak, Zbigniew F. Baczyński

**Similarities and Differences between Heat Conduction
and Moisture Diffusion**

A. Szekeres, R. A. Heller, and S. Thangjitham

Heat Propagation in a Non-Homogeneous Body

L. R. Rakotomanana

**On the Fourier's Law of Heat Conduction in a
Nonlinear Fluid**

J. Jaric, Z. Golubovic

**The Sputtering Temperatures of a Cooling Cylindrical
Rod with an Insulated Core in a Two-Fluid Medium**

Rasajit K. Bera

On a Refined Heat Conduction Theory for Microperiodic Layered Solids

Józef Ignaczak and Zbigniew F. Baczyński

Center of Mechanics, Institute of Fundamental Technological Research,
Polish Academy of Sciences, Świątokrzyska 21, 00-049 Warsaw, POLAND

A refined averaged theory of rigid heat conductor with a microperiodic structure is used to solve a one-dimensional initial-boundary value problem of heat conduction in a periodically layered plate with a large number of homogeneous isotropic layers. In such a theory, the temperature $\theta = \theta(x, t)$ ($0 \leq x \leq L, t \geq 0$) is approximated by $\theta(x, t) = \theta_0(x, t) + \eta(x) \theta_1(x, t)$, where $\theta_0(x, t)$ represents a macro-temperature, $\theta_1(x, t)$ is a temperature corrector, and $\eta = \eta(x)$ is a prescribed periodic micro-shape function; and the functions $\theta_0 = \theta_0(x, t)$ and $\theta_1 = \theta_1(x, t)$ are to be found by solving an initial-boundary value problem described by a system of linear partial differential equations with averaged coefficients subject to suitable initial and boundary conditions. A uniqueness theorem for the averaged problem is proved, and two particular initial-boundary value problems for a periodically layered semi-space are solved in a series form. Numerical examples are included.

Key Words: Microperiodic Layered Composites, Nonsteady Heat Conduction Problems.

1. Introduction

A formal solution to the one-dimensional initial-boundary value problem for a parabolic heat conduction equation in a layered plate has been obtained before by a number of authors (cf. e.g. Eqs. (2)-(20) in [1]; and references in [2]). When the plate is made of a large number of layers with different constant isotropic thermal properties, an analysis of the formal solution becomes involved, and usually ends up with an approximate numerical solution. The present paper deals with the problem by using a one-dimensional averaged heat conduction theory in which the plate composed of a large number of layers is replaced by a plate with smeared thermal properties, and the classical formulation of the problem is replaced by an averaged description. The description, referred to a micro-periodic layered plate, consists of a system of two partial differential equations with constant coefficients for two unknown temperatures $\theta_0 = \theta_0(x, t)$ and $\theta_1 = \theta_1(x, t)$ ($0 \leq x \leq L, t \geq 0$) subject to suitable initial and boundary conditions; and an approximate solution takes the form $\theta(x, t) = \theta_0(x, t) + \eta(x) \theta_1(x, t)$,

where $\eta = \eta(x)$ is a micro-periodic shape function (cf. [2] and [3]). In Section 2, the basic field equations of the averaged theory and formulations of associated initial-boundary value problems for a microperiodic layered plate are presented. In Section 3, a uniqueness theorem for the problems of Section 2 is proved. In Sections 4 and 5, the series solutions for a periodically layered semi-space subject to a sudden

boundary heating and a laser surface heating, respectively, are obtained. In Section 6, a numerical analysis of the solution corresponding to the laser surface heating of the layered semi-space, is presented. Finally, in Section 7 results and conclusions are summarized.

2. Basic field equations

Consider a layered infinite heat conducting plate of finite dimensionless thickness L composed of n identical subunits which are thermally bonded to form a spatially periodic pattern as shown in Fig. 1

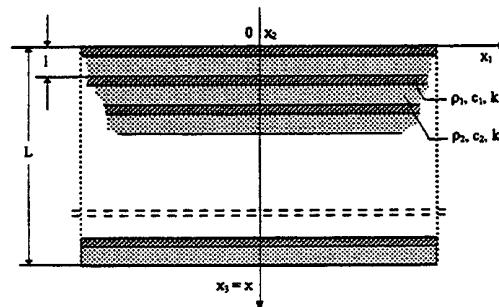


Fig. 1. Configuration and coordinate system of a microperiodic layered plate.

Each subunit consists of two layers which, in general, have different dimensions and are made of different homogeneous isotropic rigid heat conducting materials.

Let l_i, ρ_i, c_i , and k_i ($i = 1, 2$), in this order,

denote the physical dimension, density, specific heat, and thermal conductivity of the i -th layer in a subunit. If the interface conditions between any two adjacent layers are assumed to be of an ideal thermal contact type, i.e. the temperature and heat flux are continuous across an interface, and a thermal load is uniformly distributed over the boundary planes $x = 0$ and $x = L$ for every time $t \geq 0$, a heat conduction process in the layered plate can be described by a solution to the classical one-dimensional problem in which a parabolic heat conduction equation is to be satisfied for each layer, and suitable initial, interface and boundary conditions are to be met. If n is a large number ($n \rightarrow \infty$), the classical problem is approximated by the dimensionless averaged initial-boundary value problem (cf. [2] and [3]).

Find a pair (θ_0, θ_1) defined for $0 \leq x \leq L$ and $t \geq 0$, that satisfies the field equations

$$\begin{aligned} \left(\frac{\partial^2}{\partial x^2} - \frac{\partial}{\partial t} \right) \theta_0 + \frac{1}{\kappa} (\alpha - \beta) \frac{\partial}{\partial x} \theta_1 &= 0 \\ \left(\frac{\partial}{\partial t} + \alpha \gamma \right) \theta_1 + \kappa \gamma \frac{\partial}{\partial x} \theta_0 &= 0 \end{aligned} \quad (1)$$

for $0 < x < L$ and $t > 0$

subject to the initial conditions

$$\begin{aligned} \theta_0(x, 0) = f(x), \quad \theta_1(x, 0) = g(x) \\ \text{for } 0 < x < L \end{aligned} \quad (2)$$

and the boundary conditions

$$\theta_0(0, t) = h(t), \quad \theta_1(L, t) = i(t) \quad \text{for } t > 0 \quad (3)$$

where f, g, h , and i are prescribed functions. The constants α, β, γ , and κ in eqs. (1) are related to the thermal properties of a subunit of the layered plate and a microshape function $\eta = \eta(x)$ by

$$\begin{aligned} \alpha &= \frac{\langle k \dot{\eta}^2 \rangle}{\langle \rho c \eta^2 \rangle} \\ \beta &= \frac{\langle k \dot{\eta}^2 \rangle}{\langle \rho c \eta^2 \rangle} \left[1 - \frac{\langle k \dot{\eta}^2 \rangle}{\langle k \rangle \langle k \dot{\eta}^2 \rangle} \right] \\ \gamma &= \frac{\langle \rho c \rangle}{\langle k \rangle} \quad \kappa = \frac{\langle k \dot{\eta} \rangle}{\langle \rho c \eta^2 \rangle} \end{aligned} \quad (4)$$

where $\langle F \rangle$ stands for the mean value of a function

$F = F(x)$ on the interval $[0, 1]$ defined by

$$\langle F \rangle = \int_0^1 F(x) dx \quad (5)$$

and $\dot{\eta} = d\eta/dx$.

From the definitions of α, β, γ , and κ , we get

$$\alpha > \beta > 0 \quad \gamma > 0 \quad \kappa \neq 0 \quad (6)$$

Also, a modification of the problem (1)-(3), involving heat-flux boundary conditions is obtained if eqs. (3) are replaced by

$$\begin{aligned} -\langle k \rangle \frac{\partial}{\partial x} \theta_0(0, t) &= q_0(t) \\ \langle k \rangle \frac{\partial}{\partial x} \theta_1(L, t) &= q_1(t) \quad t > 0 \end{aligned} \quad (7)$$

where q_0 and q_1 are prescribed functions.

Once a solution (θ_0, θ_1) to the problem (1)-(3)

or [(1), (2), (7)] is found, a temperature θ in the plate is computed from the formula

$$\theta(x, t) = \theta_0(x, t) + \eta(x) \theta_1(x, t) \quad (8)$$

Due to an oscillatory character of $\eta(x)$ on $[0, L]$, θ represents an oscillating function over the plate thickness for every $t > 0$. Also, for a smooth pair (θ_0, θ_1) on $[0, L] \times [0, \infty)$, θ is a continuous function on $[0, L] \times [0, \infty)$, but $\partial\theta/\partial x$ may have discontinuities across the interfaces, due to continuity of $\eta(x)$ on $[0, L]$ and discontinuities of $\dot{\eta}(x)$ at the interfaces.

3. Uniqueness theorem

Theorem. The initial-boundary value problem (1)-(3) or [(1), (2), (7)] may have at most one solution.

Proof of this theorem is based on the statement that a solution of the problem (1)-(3) or [(1), (2), (7)] corresponding to a zero thermal load satisfies a global conservation law in the form

$$\begin{aligned} E(t) &= \int_0^L \int_0^t \left[\left(\frac{\partial}{\partial \tau} + \beta \gamma \right) \frac{\partial}{\partial x} \theta_0(x, \tau) \right]^2 d\tau dx \\ &\quad + \frac{1}{2} \int_0^L \left[\left(\frac{\partial}{\partial t} + \beta \gamma \right) \theta_0(x, t) \right]^2 dx \\ &\quad + \gamma(\alpha - \beta) \int_0^L \left[\frac{\gamma \beta}{2} \theta_0^2(x, t) + \int_0^t \left[\frac{\partial}{\partial \tau} \theta_0(x, \tau) \right]^2 d\tau \right] dx = 0 \end{aligned} \quad (9)$$

The function $E = E(t)$ represents the total thermal energy released over the time interval $[0, t]$ in the layered plate subject to a thermal load. By virtue of ineqs. (6), $E(t) \geq 0$, and eq. (9) asserts that the total thermal energy of the plate subject to a zero thermal load vanishes for $t \geq 0$.

4. Temperature in a layered semi-space subject to sudden boundary heating

We let $L = n \rightarrow \infty$, and solve the following initial-boundary value problem. Find a pair (θ_0, θ_1) that satisfies the field equations

$$\left(\frac{\partial^2}{\partial x^2} - \frac{\partial}{\partial t} \right) \theta_0 + \frac{1}{\kappa} (\alpha - \beta) \frac{\partial}{\partial x} \theta_1 = 0 \quad (10)$$

$$\left(\frac{\partial}{\partial t} + \alpha \gamma \right) \theta_1 + \kappa \gamma \frac{\partial}{\partial x} \theta_0 = 0$$

for $x > 0, t > 0$

the initial conditions

$$\theta_0(x, 0) = \theta_1(x, 0) = 0 \quad \text{for } x > 0 \quad (11)$$

and the boundary condition

$$\theta_0(0, t) = H(t) = \begin{cases} 1 & \text{for } t > 0 \\ 0 & \text{for } t < 0 \end{cases} \quad (12)$$

Moreover, θ_0 and θ_1 are to vanish as $x \rightarrow \infty$ for every $t > 0$. Using a Laplace transform technique similar to that of [4], [5] and [6], the following series solution of the problem (10)-(12) is obtained

$$\theta_0(x, t) = \int_0^t N(x, \tau) d\tau \quad (13)$$

$$\theta_1(x, t) = -\frac{\kappa}{\alpha} \int_0^t \{1 - \exp[-\alpha \gamma(t - \tau)]\} \frac{\partial}{\partial x} N(x, \tau) d\tau \quad (14)$$

where $N = N(x, t)$ is the series of Neumann's type for an integro-differential equation associated with eqs. (10)

$$N(x, t) = \frac{x}{2\sqrt{\pi}} t^{-3/2} \exp\left(-\lambda t - x^2/4t\right) + \frac{x}{2\sqrt{\pi}} \sum_{n=1}^{\infty} \frac{(\lambda\beta\gamma)^n}{n!(n-1)!} \int_0^t \exp[-\beta\gamma(t-s)] \times (t-s)^{n-1} s^{n-3/2} \exp\left(-\lambda s - x^2/4s\right) ds \quad (15)$$

and $\lambda = \gamma(\alpha - \beta)$.

The solution (13)-(15) converges uniformly for any positive and finite x and t ; and for the admissible range of the constants α, β , and γ [cf. (6)].

5. Temperature in a layered semi-space subject to laser surface heating

In this case we look for a pair (θ_0, θ_1) that satisfies the field eqs.

$$\left(\frac{\partial^2}{\partial x^2} - \frac{\partial}{\partial t} \right) \theta_0 + \frac{1}{\kappa} (\alpha - \beta) \frac{\partial}{\partial x} \theta_1 = 0 \quad (16)$$

$$\left(\frac{\partial}{\partial t} + \alpha \gamma \right) \theta_1 + \kappa \gamma \frac{\partial}{\partial x} \theta_0 = 0$$

for $x > 0, t > 0$

the initial conditions

$$\theta_0(x, 0) = \theta_1(x, 0) = 0 \quad \text{for } x > 0 \quad (17)$$

and the boundary condition

$$-\langle k \rangle \frac{\partial}{\partial x} \theta_0(0, t) = Y(t) \quad \text{for } t \geq 0 \quad (18)$$

where [7]

$$Y(t) = Y_0 t^n \exp(-b t^m) \quad (19)$$

Here, Y_0, b, m , and n are positive constants.

Moreover, θ_0 and θ_1 are to vanish as $x \rightarrow \infty$ for every $t > 0$. Clearly, $Y(t)$ represents a "skewed" Gaussian temporal profile of the laser pulse.

A solution to the problem (16)-(19) is obtained in the form [6]

$$\theta_0(x, t) = \int_0^t Y(\tau) M(x, t - \tau) d\tau \quad (20)$$

$$\theta_1(x, t) = -\kappa \gamma \int_0^t \hat{Y}(\tau) \frac{\partial M}{\partial x}(x, t-\tau) d\tau \quad (21)$$

where

$$\hat{Y}(t) = \int_0^t \exp[-\alpha \gamma(t-\tau)] Y(\tau) d\tau \quad (22)$$

and

$$M(x, t) = \frac{1}{\langle k \rangle \sqrt{\pi}} t^{-1/2} \exp(-\lambda t - x^2/4t) + \frac{1}{\langle k \rangle \sqrt{\pi}} \sum_{n=1}^{\infty} \frac{(\lambda \beta \gamma)^n}{n!(n-1)!} \int_0^t \exp[-\beta \gamma(t-\tau)] \times (t-\tau)^{n-1} \tau^{n-1/2} \exp(-\lambda \tau - x^2/4\tau) d\tau \quad (23)$$

The series solution (20)-(23) converges uniformly for any finite x and $t > 0$, and for the admissible range of parameters α, β , and γ , described by ineqs. (6).

6. Numerical analysis

Numerical analysis is restricted to the heating of a layered semi-space subject to a surface laser pulse. Each of the two-layer units is assumed to be made of the boron-epoxy layers, and $\eta = \eta(x)$ is a piece-wise linear function over the unit. So, the parameters $\alpha, \beta, \gamma, \kappa, \langle k \rangle$, and λ take the values:

$$\alpha = 7.17843 \times 10^{-5} [\text{m s}^{-1}] \quad \beta = 3.04197 \times 10^{-5} [\text{m s}^{-1}]$$

$$\gamma = 2.0873 \times 10^6 [\text{s m}^{-2}] \quad \kappa = -3.0842 \times 10^{-5} [\text{m s}^{-1}]$$

$\langle k \rangle = 1.0625 [\text{W/m.K}] \quad \lambda = 86.3403$. The skewed Gaussian temporal profile of the laser pulse is assumed as

$$Y(t) = Y_0 \exp(-10^3 t), \quad \text{so, } n=m=1, \quad b=1000 \text{ in}$$

eq.(19). In addition, we put $Y_0 = 3 \times 10^7 [\text{Wm}^{-2}]$,

$$\theta^* = 1[\text{K}], \text{ and } l^* = 0.004[\text{m}], \text{ so } t^* = \gamma(l^*)^2 =$$

$$33.397 [\text{s}], \text{ and } t = 0.029943 t^* [\text{s}^{-1}]. \text{ Here, } \theta^*,$$

l^* , and t^* stand for the temperature, length and time units, respectively. With such a choice of input data, a number of Figures showing $\theta_0(x, t)$ and $\theta_1(x, t)$

versus t for several fixed x 's, as well as temporal profiles of $\theta(x, t)$ for the fixed x 's, are presented.

7. Results and conclusions

A refined averaged heat conduction theory for a microperiodic layered rigid plate has been used to:

(i) formulate a one-dimensional initial-boundary value problem for a periodically layered plate; (ii) prove a uniqueness theorem for the problem; and (iii) solve two particular initial-boundary value problems for a layered semi-space in a closed series form. In such a theory, the temperature $\theta = \theta(x, t)$ is approximated by $\theta(x, t) = \theta_0(x, t) + \eta(x)\theta_1(x, t)$;

where $\theta_0(x, t)$ and $\theta_1(x, t)$ are the macro-

temperature and temperature-corrector, respectively; and $\eta = \eta(x)$ is a prescribed microperiodic shape function. A numerical analysis of $\theta(x, t)$ for the layered semi-space subject to a laser surface heating indicates that: (a) a contribution of the macro-temperature $\theta_0(x, t)$ to the total temperature $\theta(x, t)$

is dominant over the whole space-time domain $x > 0, t > 0$, except for a thin boundary layer in which the temperature-corrector $\theta_1(x, t)$ plays a significant

role; and (b) the temperature $\theta(x, t)$ is sensitive not only to a change of the material parameters but also to a change of the laser pulse characteristics.

REFERENCES

- [1] Tanigawa, Y., Akai, T., Kawamura, R., and Oka, N., Transient heat conduction and thermal stress problems of a nonhomogeneous plate with temperature dependent material properties, *J. Thermal Stresses*, vol. 19, No 1, pp.77-102, 1996.
- [2] El-Zebidy, A.F.M., Nonstationary heat conduction problems in microperiodic layered media, Ph.D. Thesis, submitted to IPPT, Polish Academy of Sciences, Warsaw, pp.1-122, April 1996.
- [3] Woźniak, C., Baczyński, Z.F., and Woźniak, M. Modelling of nonstationary heat conduction problems in microperiodic composites, *ZAMM*, vol. 76, No 4, pp.223-229, 1996.
- [4] Jakubowska, M., Kirchhoff's type formula in thermoelasticity with finite wave speeds, *J. Thermal Stresses*, vol. 7, No 3-4, pp. 259-283, 1984.
- [5] Hetnarski, R. B., and Ignaczak, J., Generalized thermoelasticity: closed-form solutions, *J. Thermal Stresses*, vol. 16, No 4, pp. 473-498, 1993.
- [6] Ignaczak, J., and Baczyński, Z.F., On a refined heat conduction theory for microperiodic layered solids, to be published.
- [7] Hetnarski, R.B., and Ignaczak, J., Generalized thermoelasticity: response of semi-space to a short laser pulse, *J. Thermal Stresses*, vol. 17, No 3, pp.377-396, 1994.